

CISM International Centre for Mechanical Sciences 569  
Courses and Lectures

Vincenzo Parenti-Castelli  
Werner Schiehlen *Editors*

# ROMANSY 21 – Robot Design, Dynamics and Control

Proceedings of the 21st CISM-IFTOMM  
Symposium, June 20–23, Udine, Italy



International Centre  
for Mechanical Sciences



Springer

# **CISM International Centre for Mechanical Sciences**

Courses and Lectures

Volume 569

## **Series editors**

### **The Rectors**

Friedrich Pfeiffer, Munich, Germany

Franz G. Rammerstorfer, Vienna, Austria

Elisabeth Guazzelli, Marseille, France

### **The Secretary General**

Bernhard Schrefler, Padua, Italy

### **Executive Editor**

Paolo Serafini, Udine, Italy



The series presents lecture notes, monographs, edited works and proceedings in the field of Mechanics, Engineering, Computer Science and Applied Mathematics. Purpose of the series is to make known in the international scientific and technical community results obtained in some of the activities organized by CISM, the International Centre for Mechanical Sciences.

More information about this series at <http://www.springer.com/series/76>

Vincenzo Parenti-Castelli  
Werner Schiehlen  
Editors

# ROMANSY 21 - Robot Design, Dynamics and Control

Proceedings of the 21st CISM-IFTOMM  
Symposium, June 20–23, Udine, Italy

*Editors*

Vincenzo Parenti-Castelli  
Department of Industrial Engineering  
University of Bologna  
Bologna  
Italy

Werner Schiehlen  
Institute of Engineering and Computational  
Mechanics  
University of Stuttgart  
Stuttgart  
Germany

ISSN 0254-1971                      ISSN 2309-3706 (electronic)  
CISM International Centre for Mechanical Sciences  
ISBN 978-3-319-33713-5              ISBN 978-3-319-33714-2 (eBook)  
DOI 10.1007/978-3-319-33714-2

Library of Congress Control Number: 2016939114

© CISM International Centre for Mechanical Sciences 2016

This work is subject to copyright. All rights are reserved by the Publisher, whether the whole or part of the material is concerned, specifically the rights of translation, reprinting, reuse of illustrations, recitation, broadcasting, reproduction on microfilms or in any other physical way, and transmission or information storage and retrieval, electronic adaptation, computer software, or by similar or dissimilar methodology now known or hereafter developed.

The use of general descriptive names, registered names, trademarks, service marks, etc. in this publication does not imply, even in the absence of a specific statement, that such names are exempt from the relevant protective laws and regulations and therefore free for general use.

The publisher, the authors and the editors are safe to assume that the advice and information in this book are believed to be true and accurate at the date of publication. Neither the publisher nor the authors or the editors give a warranty, express or implied, with respect to the material contained herein or for any errors or omissions that may have been made.

Printed on acid-free paper

This Springer imprint is published by Springer Nature  
The registered company is Springer International Publishing AG Switzerland

# Preface

The First CISM-IFTToMM Symposium on Theory and Practice of Robots and Manipulators was held during September 5–8, 1973, in Udine, Italy, not long after IFTToMM had been founded in 1969. The first ROMANSY, or Ro.Man.Sy., as the Symposium used to be referred to, marks the beginning of a long-lasting partnership between two international institutions, CISM, the Centre International des Sciences Mécaniques and IFTToMM, the International Federation for the Promotion of Mechanism and Machine Science.

As the 21st CISM-IFTToMM Symposium returns to Udine, RoManSy2016 will continue to preserve this tradition, by encouraging papers that are of a broad interest to the participants, providing an environment, and setting for meaningful technical and personal interactions among the delegates. In particular, the conference solicits papers providing a vision of the evolution of the robotics disciplines and signaling new directions in which these disciplines are foreseen to develop.

The paper topics of the 21st Symposium include, but not limited to, the following:

- Kinematics and Dynamics for Robotics
- Control and Perception of Robots
- Novel Robot Design
- Humanoid Robots
- Medical Devices
- Innovations and Applications

The 21st Symposium takes place during June 20–23, 2016 in Udine, Italy and will be enriched by two keynote papers presented by I-Ming Chen from Singapore and Oussama Khatib from Stanford, USA. These papers deal with innovations in infrastructure service robots and highlight the success of the ongoing ROMANSY symposia series.

For the steering of future ROMANSY symposia an advisory board has been established chaired by one CISM representative and one IFTToMM representative. In particular, the advisory board will encourage and review proposals for

forthcoming ROMANSY symposia. The Advisory Board 2016 is composed of the following members:

- Vincenzo Parenti-Castelli, Italy (CISM Representative)
- I-Ming Chen, Singapore (IFoMM Representative)
- Philippe Bidaud, France
- Marco Ceccarelli, Italy
- Oussama Khatib, USA
- Werner Schiehlen, Germany
- Atsuo Takanishi, Japan
- Teresa Zielinska, Poland

The International Scientific Committee (ISC) is responsible as in the past for the promotion and the review of the submitted papers in cooperation with the Programme Committee Co-Chairs. The following scientists have been serving on the ISC 2016:

- Vigen Arakelyan, France
- Giuseppe Carbone, Italy
- Greg Chirikjian, USA
- Victor Glazunov, Russia
- Clément Gosselin, Canada
- Qiang Huang, China
- Yan Jin, UK
- Andres Kecskemethy, Germany
- Yukio Takeda, Japan
- Marek Wojtyra, Poland

The ISC reviewed 54 papers and accepted 47 of them. In this volume the two keynote lectures and the contributed papers after a final revision are published.

The Programme Committee Co-Chairs are thankful for the great service provided by the CISM staff. In particular, Mrs. Paola Agnola, Mrs. Marika Minisini, and Prof. Paolo Serafini did an excellent job even when the changes in the CISM printing office required a special attention.

Italy  
Germany

Vincenzo Parenti-Castelli  
Werner Schiehlen

# Contents

## Part I Keynote Papers

<b>Innovations in Infrastructure Service Robots</b> . . . . .	3
I-Ming Chen, Ehsan Asadi, Jiancheng Nie, Rui-Jun Yan, Wei Chuan Law, Erdal Kayacan, Song Huat Yeo, Kin Huat Low, Gerald Seet and Robert Tiong	

<b>The New Robotics Age: Meeting the Physical Interactivity Challenge</b> . . . . .	17
Oussama Khatib	

## Part II Kinematics for Robotics

<b>Robust Inverse Kinematics at Position Level by Means of the Virtual Redundant Axis Method</b> . . . . .	21
Francisco Geu Flores, Sebastian Röttgermann, Bettina Weber and Andrés Kecskeméthy	

<b>Redundancy Resolution of a 9 DOF Serial Manipulator Under Hard Task Constraints</b> . . . . .	31
Narendrakrishnan Neythalath, Mathias Brandstötter and Michael Hofbaur	

<b>Geometry and Direct Kinematics of Six-DOF Three-Limbed Parallel Manipulator</b> . . . . .	39
Zh. Baigunchekov, M. Kalimoldaev, M. Utenov and T. Baigunchekov	

<b>Learning Global Inverse Kinematics Solutions for a Continuum Robot</b> . . . . .	47
Thomas George Thuruthel, Egidio Falotico, Matteo Cianchetti and Cecilia Laschi	



<b>A Study of a Wheel Shape for Increasing Climbing Ability of Slopes and Steps</b> . . . . .	55
K. Tanaka, H. Ishii, D. Endo, J. Mitsuzuka, D. Kuroiwa, Y. Okamoto, Y. Miura, Q. Shi, S. Okabayashi, Y. Sugahara and A. Takanishi	
<b>Position Kinematics of a 3-RRS Parallel Manipulator</b> . . . . .	65
Halil Tetik, Rohit Kalla, Gokhan Kiper and Sandipan Bandyopadhyay	
<b>Kinematic Analysis of a Single-Loop Translational Manipulator</b> . . . . .	73
Raffaele Di Gregorio	
<b>A Measure of the Distance Between Two Rigid-Body Poses Based on the Use of Platonic Solids</b> . . . . .	81
Claudio Mazzotti, Nicola Sancisi and Vincenzo Parenti-Castelli	
<b>Part III Dynamics for Robotics</b>	
<b>Properties of the Dahl Model Applied to Modelling of Static Friction in Closed-Loop Kinematic Chains</b> . . . . .	93
Marek Wojtyra	
<b>Mechanics of Mobile Robots with Mecanum Wheels</b> . . . . .	103
Klaus Zimmermann, Igor Zeidis, Florian Schale and Pedro Alonso Flores-Alvarez	
<b>Design of Partially Balanced 5R Planar Manipulators with Reduced Center of Mass Acceleration (RCMA)</b> . . . . .	113
Vigen Arakelian	
<b>An Alternative Approach to the Dynamics Analysis of Closed-Loop Mechanisms</b> . . . . .	123
Wei Li and Jorge Angeles	
<b>Lagrangian Based Dynamic Analyses of Delta Robots with Serial-Parallel Architecture</b> . . . . .	133
Jan Brinker and Burkhard Corves	
<b>Part IV Control and Perception of Robots</b>	
<b>Adaptive Model Predictive Control Design for Underactuated Multibody Systems with Uncertain Parameters</b> . . . . .	145
Fabian Schnelle and Peter Eberhard	
<b>Control and Experiments with Energy-Saving SCARA Robots</b> . . . . .	153
Makoto Iwamura and Werner Schiehlen	
<b>Control Design for Pneumatic Manipulation Robot</b> . . . . .	163
Anton Aliseychik, Viktor Glazunov, Igor Orlov, Vladimir Pavlovsky and Marina Shishova	

**Adaptive Edge Features Estimation for Humanoid Robot  
Visual Perception . . . . . 171**  
Tianwei Zhang and Yoshihiko Nakamura

**Disturbance Rejection Controller for Biped Walking  
Using Real-Time ZMP Regulation . . . . . 179**  
Zhangguo Yu, Maoxing Zheng, Qinqin Zhou, Xuechao Chen,  
Libo Meng, Weimin Zhang, Aiguo Ming and Qiang Huang

**Part V Novel Robot Design**

**Human-Powered Robotics—Concept and One-DOF Prototype . . . . . 191**  
Yusuke Sugahara

**Gripping Tests on an Underactuated Self-adapting Hand  
Prototype . . . . . 199**  
Cesare Rossi and Sergio Savino

**Combined Structural and Dimensional Synthesis of Serial Robot  
Manipulators . . . . . 207**  
D. Ramirez, J. Kotlarski and T. Ortmaier

**Development of the Acroboter Service Robot Platform . . . . . 217**  
László Bencsik, Ambrus Zelei and Gábor Stépán

**The Inversion of Motion of Bristle Bots: Analytical  
and Experimental Analysis . . . . . 225**  
Giancarlo Cicconofri, Felix Becker, Giovanni Noselli,  
Antonio Desimone and Klaus Zimmermann

**Design of a Compliant Environmentally Interactive Snake-Like  
Manipulator . . . . . 233**  
Sergio Jainandunsing, Just L. Herder, Yukio Takeda  
and Daisuke Matsuura

**Part VI Humanoid Robots**

**Joint Mechanism Coping with Both of Active Pushing-off  
and Joint Stiffness Based on Human . . . . . 243**  
Takuya Otani, Kenji Hashimoto, Takaya Isomichi,  
Shunsuke Miyamae, Masanori Sakaguchi, Yasuo Kawakami,  
Hun-ok Lim and Atsuo Takanishi

**Design of a Dexterous Hand for a Multi-hand Task . . . . . 251**  
Neda Hassanzadeh, Reza Movassagh-Khaniki  
and Alba Perez-Gracia

<b>Facial Expression Design for the Saxophone Player Robot WAS-4</b> . . . . .	259
Kei Matsuki, Keisuke Yoshida, Salvatore Sessa, Sarah Cosentino, Keiko Kamiyama and Atsuo Takanishi	
<b>Disturbance Force Generator for Biped Robots</b> . . . . .	267
Kenji Hashimoto, Kosuke Nishikawa, Juri Shimizu, Aiman Omer, Hun-ok Lim and Atsuo Takanishi	
<b>LARMbot: A New Humanoid Robot with Parallel Mechanisms</b> . . . . .	275
Daniele Cafolla, Mingfeng Wang, Giuseppe Carbone and Marco Ceccarelli	
<b>Human-Inspired Humanoid Balancing and Posture Control in Frontal Plane</b> . . . . .	285
Vittorio Lippi, Thomas Mergner, Maksymilian Szumowski, Magdalena Sylwia Zurawska and Teresa Zielińska	
<b>Compliant Actuator Dedicated for Humanoidal Robot—Design Concept</b> . . . . .	293
Magdalena Sylwia Zurawska, Maksymilian Szumowski and Teresa Zielinska	
<b>Part VII Service Robots</b>	
<b>Design of a 3-UPS-RPU Parallel Robot for Knee Diagnosis and Rehabilitation</b> . . . . .	303
Pedro Araujo-Gómez, Miguel Díaz-Rodríguez, Vicente Mata, Angel Valera and Alvaro Page	
<b>End-Effector for Disaster Response Robot with Commonly Structured Limbs and Experiment in Climbing Vertical Ladder</b> . . . . .	311
Takashi Matsuzawa, Kenji Hashimoto, Tomotaka Teramachi, Kazuhiro Uryu, Xiao Sun, Shinya Hamamoto, Ayanori Koizumi and Atsuo Takanishi	
<b>Design of a Tendon-Drive Manipulator for Positioning a Probe of a Cooperative Robot System for Fault Diagnosis of Solar Panels at Mega Solar Power Plant</b> . . . . .	321
Mitsuru Endo, Mai Endo, Takao Kakizaki, Yasuhiro Nakamura, Tsukasa Hebiishi and Kenji Otani	
<b>Physical Human-Robot Interaction: Increasing Safety by Robot Arm's Posture Optimization</b> . . . . .	329
Omar W. Maarroof and Mehmet İsmet Can Dede	

**Part VIII Medical Devices**

**Assessing the Orbital Stability for Walking with Four Prosthetic Feet at Different Speeds.** . . . . . 341  
 Lulu Gong and Ruowei Zhao

**Development of Rotary Type Movers Discretely Interacting with Supporting Surface and Problems of Control Their Movement** . . . . . 351  
 Eugeny Briskin, Alexander Maloletov, Nikolay Sharonov, Sergey Fomenko, Yaroslav Kalinin and Alexander Leonard

**Parameter Optimization for Exoskeleton Control System Using Sobol Sequences** . . . . . 361  
 Sergey Jatsun, Sergei Savin and Andrey Yatsun

**Study of RE-Gait® as the Device That Promotes Walking Using a Two-Dimensional Emotion Map** . . . . . 369  
 Eiichirou Tanaka, Yusuke Osawa, Keiichi Muramatsu, Keiichi Watanuki, Shozo Saegusa and Louis Yuge

**Development of Road Condition Categorizing System for Manual Wheelchair Using Mahalanobis Distance** . . . . . 377  
 Kazuyuki Kojima, Hiroki Taniue and Jun’Ichi Kaneko

**Control of a Self-adjusting Lower Limb Exoskeleton for Knee Assistance.** . . . . . 385  
 Viet Anh Dung Cai, Philippe Bidaud, Viet Thang Nguyen, Consuelo Granata and Minh Tam Nguyen

**Part IX Innovations and Applications**

**Pilot Experiments with the Human-Friendly Walking Assisting Robot Vehicle (hWALK).** . . . . . 395  
 Jorge Solis

**Conceptual Design of a Cable Driven Parallel Mechanism for Planar Earthquake Simulation.** . . . . . 403  
 Daisuke Matsuura, Shota Ishida, Muhamad Akramin, Emek Barış Küçükatabak, Yusuke Sugahara, Shinji Tanaka, Nobuo Fukuwa, Minoru Yoshida and Yukio Takeda

**Comparison of Dynamic Properties of Two KUKA Lightweight Robots.** . . . . . 413  
 Łukasz Woliński and Marek Wojtyra

**Comparison of Serial and Quasi-Serial Industrial Robots for Isotropic Tasks** . . . . . 421  
 Alexandr Klimchik, Evgeni Magid, Ilya Afanasyev and Anatol Pashkevich

**On the Dynamics and Emergency Stop Behavior of Cable-Driven Parallel Robots** . . . . . 431  
Philipp Tempel, Alexander Verl and Andreas Pott

**Automatic Robot Taping: Strategy and Enhancement.** . . . . . 439  
Qilong Yuan, Teguh Santoso Lembono and I-Ming Chen

**Part I**  
**Keynote Papers**

# Innovations in Infrastructure Service Robots

I-Ming Chen, Ehsan Asadi, Jiancheng Nie, Rui-Jun Yan,  
Wei Chuan Law, Erdal Kayacan, Song Huat Yeo,  
Kin Huat Low, Gerald Seet and Robert Tiong

**Abstract** Infrastructure service robotics is a discipline studying robotic systems and methodology for buildings and civil infrastructure construction, inspection, and maintenance. The target could be buildings, estates, parks, bridges, power plants, power transmission lines, underground tunnels, sewage pipes, port facilities, etc. In this article, several new infrastructure service robots projects for construction services and deep tunnel inspection carried out in Singapore will be introduced. With new actuators, low cost sensors, and open source robotics software, infrastructure robots represent a new breed of intelligent systems that help the society to overcome manpower shortage and ageing workforce. These projects are examples of user-led and user-inspired robotics R&D effort led by government agencies, universities, and industrial alliance of local and overseas robotics and construction machinery manufacturers, start-up companies, and system integrators. The ultimate goal is to strengthen the robotics R&D capability in Singapore and to foster a robotics industry and the ecosystem that transform Singapore into a Smart Nation.

**Keywords** Professional service robot · Construction robot · Large-diameter tunnel inspection robot

---

I.-M. Chen (✉) · E. Asadi · J. Nie · R.-J. Yan · W.C. Law · E. Kayacan · S.H. Yeo ·  
K.H. Low · G. Seet  
School of Mechanical and Aerospace Engineering, Nanyang  
Technological University, Singapore, Singapore  
e-mail: michen@ntu.edu.sg

R. Tiong  
School of Civil and Environment Engineering, Nanyang  
Technological University, Singapore, Singapore

# 1 Introduction

Infrastructure service robotics is a discipline studying robotic systems and methodology for buildings and civil infrastructure construction, inspection, and maintenance. According to the classification by International Federation of Robotics (IFR), such service robots include *professional cleaning systems* for floors, windows, walls, tank, hulls and pipes, *inspection and maintenance systems* for facilities, plants, tanks, tubes, and pipes, and *construction and demolition systems* for nuclear plants, building, civil/heavy structures, and road constructions. Developing robotic technology for infrastructure services has the following significance:

- (1) **Economics and sustainability**—Robotic technology would be able to reduce the reliance on unskilled workers and also skilled workers operating on sophisticate construction machinery.
- (2) **Productivity**—Robotic technology will streamline and further optimize current construction process for shorter project period, and also assure quality consistency of the construction project.
- (3) **Safety and health**—Robotic technology will reduce the human exposure to hazardous and inaccessible environment during construction.

Due to the recent advancement in robotic technology and cost down on key robotic components, such as low cost 3D imaging sensors, high precision 3D laser scanners, high density lightweight actuators, open source robotics software, AI and cloud computing, standardized plug-and-play components, and robust wireless communication and control, developing innovative robotic systems to service public infrastructure and private estates become affordable. However, there are still a number of technical challenges to overcome before these professional service robotic systems making massive inroad into real world services. These challenges include:

- Complete understanding of existing human workflow and processes and also the limitations in the application domain
- Performance evaluation, validation, and optimization of sub-systems and the overall robotic system for field operations
- Designing robustness robotic manipulation, mobility and perception modules for field operations
- Developing machine learning and intelligence for robotic systems that can adapt to environment and task variations in the fields.
- Designing suitable level of human-robot interaction and machine autonomy for effective operations

In this paper, we introduce three new infrastructure service robot projects for construction services and deep tunnel inspection carried out in Singapore. The basic design consideration and technology developed and integrated into the system will be presented. Preliminary results on these robots in lab trials will be described.



Finally, the paper will be concluded with some thoughts on further development and commercialization of these professional service robots.

## 2 Mobile High-Rise Spray Painting Robot

### 2.1 Motivation

Despite the rapid technology evolution, construction services are mostly labors-dependent and performed with conventional techniques and occasionally in dangerous situations. Beside the low efficiency in this sector, the needs for building, construction and maintenance are growing rapidly all around the world while the construction industry is facing a future shortage of skilled workers and wage increases. It is evident that inefficient management of resources and use of unskilled workers can result in a considerable decline in construction quality and productivity. Hence, there is a high demand for introducing novel robotic technologies that can be applied to boost productivity by focusing on quality and time saving, as well as to enhance safety and to reduce cost compared to the traditional method.

An overview of the relevant state of art on construction robots indicates a lack of advanced and multi-purposes robots for construction painting; particularly for interior finishing where only very few robots were designed and developed. The feasibility analysis and economic impact of robotizing interior finishing services for productivity improvement on the construction sites were initially studied by Rosenfeld et al. (1993), and Warszawski and Rosenfeld (1994, 1997). Later, Kahane and Rosenfeld (2004) developed a method for evaluating the effects of human-and-robot integration on automating a construction task and examined the method using an interesting multi-purpose robot, named TAMIR, for block laying and wall painting. The painting system consists of a commercial 6-DOF robot arm mounted on a computer controlled 3-DOF mobile platform. The robot was designed for research and development purposes, and it had an average reach access. Aris et al. (2005) mainly investigated the problem of automating upright spray painting for only ceiling finishing by designing a 3-DOF robot. The ceiling painter is derived horizontally by making use of a single-phase induction motor and a chain-sprocket mechanism and moved vertically via a zigzag ladder structure. The painting workspace of the robot is significantly small relative to the platform size. Another study (Naticchia et al. 2007) introduced a scaled down interior painting set up for laboratory use that consists of a 6-DOF manipulator to be mounted on a 2-DOF Hexapod for horizontal movement. The research also studied reproducing colored artworks by developing a multi-colored spraying tool. A roller-based interior wall painting robot was proposed by Sorour et al. (2011), which includes a horizontally moving platform (3-DOF), and a painting arm (2-DOF) with a roller brush, attached to end-effector, which solely scans the walls vertically up to 2.7 m. As a very low-cost robot, Keerthanaa et al. (2013) designed an airbrush spraying system for

interior finishing of simple and small spaces. The robot was equipped with a four-wheel platform, conveyor shafts, and chain-sprocket that allow transferring spraying system vertically up to limited height.

To the best of our knowledge, none of the previously reported paint robots is capable of delivering all desirable functionalities for interior finishing of the ceiling and walls of high-rise warehouses within a stand-alone automated system. All the existing indoor paint robots have low or average reach access and do not suit for painting high rise ceilings and corners. Besides, most of the paint robots are merely able to paint walls or to paint ceiling due to the insufficient mobility or autonomy of robots. High ceiling painting is inevitable and common in building construction, especially in industrial workshops. Traditional high ceiling painting is manually done by means of ladders or hydraulic lifts and often results in unreliable painting quality. It is hard to obtain consistent quality because of the unstable working position and movement of the worker thus yielding a big difference in productivity in accordance with the level of worker's skill and experience. Moreover, the high-place operation will create lethal dangers to painting workers. This project aims to develop an advanced paint robot that enables automating the execution of interior painting of high-rise ceilings and walls. A modular system is considered in this work, and the robot is designed with five primary subsystems: a 3-DOF mobile robot, a 1-DOF long reach mechanism, a 6-DOF commercial robot arm, a spraying system and a control and safety system. The proposed system configuration enables free access to a large workspace for painting ceilings and walls up to 10 m height and can improve the productivity due to the precise robot movement and even paint distribution throughout the whole painting patches.

## ***2.2 Overall System***

This project aims to develop a stand-alone robot with a higher degree of mobility compared to other existing indoor paint robots and with particular functionalities for automating the entire process of interior finishing of high-rise spaces. Unlike the other existing interior paint robots, the proposed robot includes a novel long reach mechanism that enables paint delivery to high-rise walls and ceilings. Modular design is considered in this work to reduce the design complexity at conceptual and technical levels, and to accelerate the manufacturing cycle as well as to increase the flexibility of system integration and upgrade. By considering a modular system, the robot is designed with five primary subsystems: a 3-DOF mobile robot, a long 1-DOF reach mechanism, a 6-DOF commercial robot arm, a spraying system and a computer-controlled system. Besides, the robot consists of several subsidiary modules such as hydraulic outrigger stabilizers, the cable-hose suspension system and diverse types of covers to protect the equipment and sensors against paint pollution.

The proposed system configuration enables free access to a large workspace for painting ceilings and walls up to 10 m height and sufficient maneuverability to paint

corners and non-planar surfaces. Using the proposed paint robot can improve the productivity due to the precise robot movement and even paint distribution throughout the whole spray pattern that ensures all painting patches receives a certain amount of paint precisely and consistently.

### 2.3 Robotic System Realization

The mobile robot, the first module, is designed to carry heavy payloads with zero-turn maneuverability by utilizing a combination of two driving wheels and six passive ones. The second module, long reach mechanism, comprises a dual mast telescopic lift mechanism that is derived up to certain heights via deploying hydraulic cylinders in conjunction with a series of cables, and it is centrally embedded in the mobile platform. The third module is a six degree-of-freedom robot arm, outfitted with a spray-painting gun and time-of-flight camera on its end-effector, to be located on a right spot on top of the long reach mechanism. The commercial airless spraying system is selected for the fourth module, together with an electrically actuated spray gun that allows high-quality interior finishing without the need for the air compressor. All spraying subsystems are mounted on the mobile robot that enables the free navigation of the robot within the construction site. To accomplish the painting task freely in large spaces, having a high level of autonomy and safety is vital. As the fifth module, the mobile robot will be endowed with several levels of autonomous capabilities for traveling through the construction site, for levelling the mobile robot attitude, for adjusting the altitude of lift mechanism, for planning the manipulator motion, for executing the spray painting task and for safety management.

A preliminary design of the robot is depicted in Fig. 1, in which the upper part covers of the robot and detailed design of subsidiary modules are not shown. Figure 2 demonstrates the manipulator arm currently set up in the lab to conduct

**Fig. 1** Preliminary design of high rise spray painting robot: 1—mobile robot (3-DOF), 2—spray painting system, 3—dual mast telescopic mechanism (1-DOF), 4—control box, 5—manipulator (6-DOF)

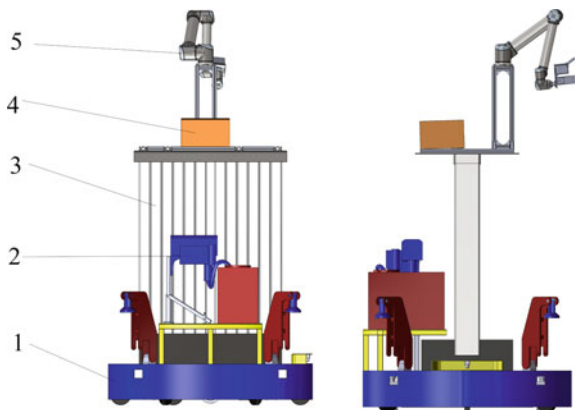




**Fig. 2** Manipulator setup outfitted with camera, spray gun and protective covers

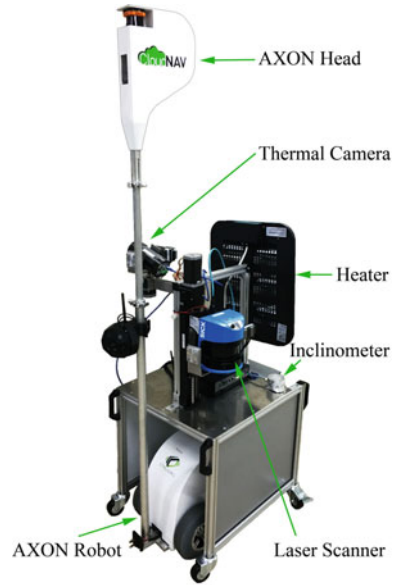
preliminary experiments for developing motion planning and vision processing algorithm. The robot arm is effectively outfitted for a real paint operation by considering protective covers for both the arm and the camera coupled to the end-effector as an eye-in-hand system.

### 3 Post-construction Quality Assessment Robot

#### 3.1 Motivation









Post construction quality assessment of buildings is an indispensable procedure in construction industry that is currently executed by manual inspectors. In a standard daily operation, a large number of inspectors are needed to finish the wholly manual assessment in the traditional way. Such a manual assessment procedure may import several errors into inspection because of executing the operation in incorrect way or the use of inaccurate inspection tools. What is more, the manual inspector may get tired after some time and the inspection accuracy may decrease over time. In most of the time, manual inspection has to be done during the daytime. Considering this time consuming, tiresome and unexciting procedure, an automated post construction quality assessment robot system is proposed in Fig. 3. The proposed robot system consists of a mobile robot, a 2D laser scanner, a thermal camera with a heater and an inclinometer (Axon Robot is from CtrlWorks Pte Ltd). This robot system can assess five different types of defects on the floors and walls, such as evenness, alignment, inclination, cracks and hollowness.

**Fig. 3** Automated construction quality assessment system



### 3.2 Quality Assessment Methodology

In traditional assessment, cracks of grounds, walls and ceiling are visually inspected. Evenness of ground and walls is inspected by using a 1.2 m spirit level, and alignment of two walls is inspected by using a set square in Fig. 4. In the assessment process of alignment, one edge of the setsquare tightly contacts with

Manual Assessment		Automated Assessment	
Tools	Assessment Items	Sensors	Assessment Items
 Visual checking	Cracks of grounds, wall, and ceiling	 UTM-03LX laser scanner	Navigation, localization, mapping and obstacle avoidance
 1.2m Spirit Level	Evenness of ground and walls	 LMS500 laser scanner	Evenness of ground and walls, and verticality of two walls
 Set Square	Verticality of two walls	 FLIR A310 thermal camera	Hollowness and cracks of ground and walls
 CONQUAS Rod	Hollowness of ground (By distinguishing the sound)	 AGS005 inclinometer	Inclination of ground

**Fig. 4** Manual assessment tools and autonomous assessment sensors

one wall (Ani et al. 2014), and the distance between the other one edge and the other wall is calculated. Beyond doubt, measurement error is imported into the operation during the assessment process, because it is a challenging task for the inspectors to accurately keep the setsquare horizontal. To assess the hollowness, the inspector needs to cover the whole ground with the end-effector of a CONQUAS rod. Then, the ground with hollowness is inspected by distinguishing the scuffing noise of the ground and the CONQUAS rod.

Considering this time consuming, tiresome and unexciting procedure of manual assessment, our proposed robotic system can accurately assess all these defects in real time. A Hokuyo UTM-03LX 2D laser scanner shown in Fig. 4 is used to localize the mobile robot and construct an environment map that can be used to store the accurate locations of defects. A Sick LMS 500 2D laser scanner is used to assess the evenness of ground and walls, and the alignment of two walls, which has a maximum measurement distance of 80 m, a measurement accuracy of 6 mm and a measurement range of 190°. The evenness is assessed by calculating the average deviation between raw sensor data and its extracted line segment, which have been mostly used to build a 2D environment map and localize a mobile robot (Yan et al. 2014, 2015a, 2015b). The alignment of walls is assessed by calculating the angle of two extracted planes. The inclination of ground is assessed by directly obtaining inclination angle in X- and Y-axis from a POSITAL inclinometer. To assess cracks and hollowness, thermal camera and a heater are used to obtain thermal images and RGB images. Then, these images are recognized by using support vector machine (SVM) method.

### 3.3 *Experimental Results*

Assessment results of evenness, crack and hollowness are shown in Figs. 5 and 6. In Fig. 5, the laser scanner is horizontally put on the ground of a constructed testbed. In the construction of this testbed, wall 1 is an even wall and wall 2 is an uneven wall. It can be seen from the comparison result of the average deviation for two walls that the average deviation of wall 1 is larger than that of wall 2. In Fig. 6a, the assessment result of a tile with cracks is shown by comparing the raw images and the processed images with SVM. In Fig. 6b, even though the color difference in the raw thermal image is not very clear, the process images can show the hollowness result well. These promising results show that the proposed automated construction quality assessment robot system works well in the identification of different types of defects.

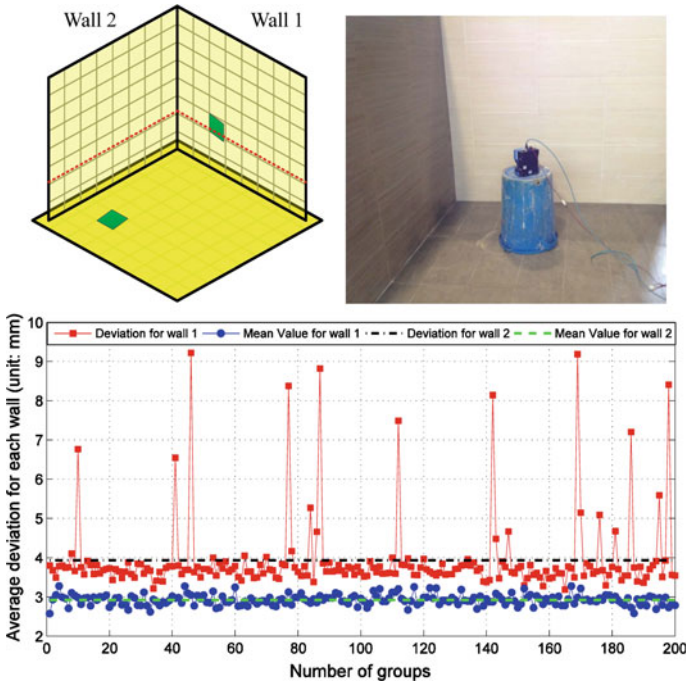
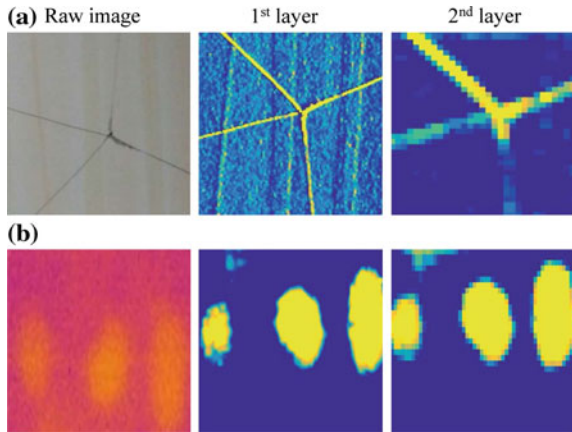


Fig. 5 Assessment result of evenness

Fig. 6 Assessment result of crack and Hollowness. **a** An example of crack assessment **b** An example of hollowness assessment



## 4 Deep Tunnel Sewerage System Inspection Robot

### 4.1 Motivation

The Deep Tunnel Sewerage System (DTSS) is a public wastewater utility based in Singapore, a solution to meet Singapore's long term needs for used water collection, treatment, reclamation and disposal. It has diameter of 6 m, and it is located 20–50 m underground. In order to prolong the service life of the sewers, the maintenance task such as inspecting the structural integrity of the tunnel is necessary. Human cannot easily access to DTSS because of high water flow, the presence of contagions or bio-hazardous materials, explosive gases and oxygen deprivation (Walter et al. 2012), as well as the absence of light in DTSS. Also, the tunnel is partially filled with water and muddy ground that is not easy for human to walk across. Significant study on pipeline and tunnel robot has been done due to its ability to access underground spaces and to achieve easier and better inspection in tunnels. However, most of the existing robots are designed for small or medium pipelines and tunnels (Law et al. 2015). There is a need to develop a tunnel robot to perform the maintenance of large-diameter tunnel.

### 4.2 Overall System

A generic locomotion mechanism for DTSS robot is designed that could cope with various tunnel conditions from dry, muddy, and partially filled water. On the other hand, a hoisting system will be configured for the launching, deploying and retrieving of the inspection robot. The setup of the inspection system consists of a number of subsystems, namely the auxiliary system and ground control station, the hoisting and winch system, and the robotic platform as shown in Fig. 7.

On the surface, the auxiliary system provides electrical power to the winch and the robotic platform as well as hydraulic power to actuate the A-frame. The control station houses the control units for the robotic platform and monitors displaying images from cameras and measurements from sensors.

The hoisting and winch system comprises an A-frame, a winch module and an umbilical cable. The A-frame is for lowering and lifting the robot along the access shaft without the needs of any other heavy-duty hoisting devices. The winch is mounted on the platform of the A-frame for easy transport and operation. An external 3-Phase AC power generator will supply the power to the winch module and provides power supply for the tethered robotic platform. The electrical power is transmitted through the multi-core umbilical cable carrying a Kevlar core, data optic fiber and multi-core copper wires.

The robotic platform has its own actuation and houses various sensors needed for the inspection of the sewer tunnel. In particular, it will have lightings to illuminate the tunnel and cameras to capture the tunnel images. A laser profiler and a



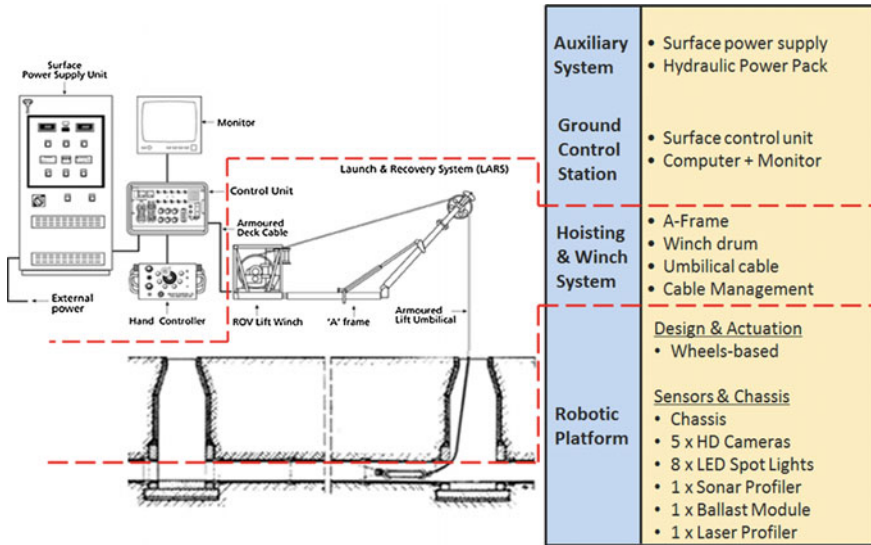


Fig. 7 Setup of inspection system

sonar profiler are utilized to scan the tunnel above and below the water surface respectively. A ballast control is used to vary weight of the robot to maintain the maneuverability and stability of the robot in accordance to the internal condition of the sewer.

### 4.3 System Designs

In Fig. 8, the semi-circular frame is designed for the mounting of 3 HD cameras and 4 LED spotlights, forming an inspection array radially at equal angle apart. It will be mounted on the chassis of the robotic platform facing towards the inner circumference of the sewer, covering the surface of the sewers above the water level.

The base plate is the main support structure of the robotic platform. All the mechanical parts will be mounted on the base plate, for instance, the front and rear camera, the locomotion mechanism, ballast, etc. Two waterproof enclosures, fixed on the base plate, are used to house the electrical components such as controller and drivers. The front facing camera is at a high position in the sewers, allowing an unblocked field of view of the sewer for navigation. Moreover, the robotic platform has low center of gravity and has large base to increase the robot stability.

Figure 8 also shows the situation when the robotic platform is deployed into the tunnel through the vertical shaft. The locomotion mechanism in this design can be tilted to certain angle that is perpendicular to the sewer surface before the robot lands onto the sewer to avoid the possible presence of soft debris along the bottom

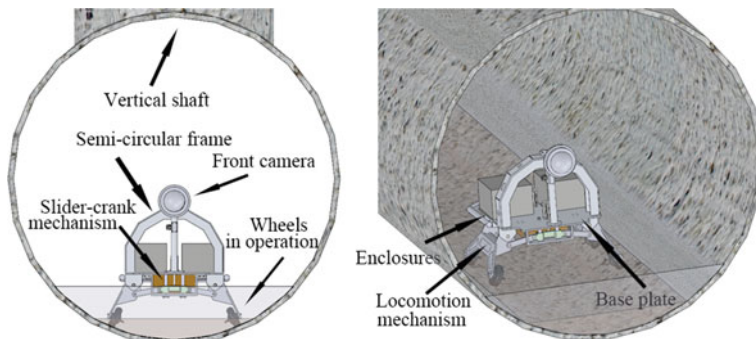


**Fig. 8** Robotic platform for DTSS

of the tunnel and to acquire better traction force over the sewer surface. This is achieved via a slider-crank mechanism that is used to transform translational motion into rotational motion.

## 5 Conclusions and Discussion

The infrastructure service robot projects introduced in this paper represent a new breed of service robots that are developed based on end-user input and more cost-effective, more compact, and more versatile than before. With advancement in sensors, actuators, and artificial intelligence, such robots could conduct service tasks autonomously with minimal human supervision. It is also possible to use such service robots with human collaboratively. The robot can perform simple, mundane, and large-scale tasks, whereas the human worker can conduct complex and sophisticated task that could be too expensive for robot to do. In such way, there could be “robot shift” and “human shift” co-existing in the work place. Such practices could create a paradigm shift in productivity for the future society with lots of professional service robots. Also there could be innovative workflow re-design due to such autonomous service robots along side with cloud services and big data analytics. The integration of infrastructure service robots, big data collected through the robots, and the value-add to the end users, as a complete service could be the future form of infrastructure service robotics companies.

**Acknowledgments** The research projects are supported by National Research Foundation of Singapore under TDIR2015-01-02, TDIR2015-01-03, and TDIR2015-01-04. Team members, Chen Qiu, Lijing Soh, Lili Liu, Varun Maruvanchery, Chin Leong Low, Burhan, and company co-developers, Aitech and CtrlWorkds are acknowledged. Lead public agencies, Jurong Town Corporation, Building Construction Authority, and Public Utility Board of Singapore are acknowledged.

## References

- Ani, A., Tawil, N., Johar, S., Razak, M., & Yahaya, H. (2014). Building condition assessment for new houses: a case study in terrace houses. *Journal Teknologi*, 70(1), 43–50.
- Aris, I., Parvez Iqbal, A. K., Ramli A. R., & Shamsuddin, S. (2005). Design and development of a programmable painting robot for houses buildings. *Journal of Teknologi*, Universiti Teknologi Malaysia, 42(A): 27–48.
- Kahane, B., & Rosenfeld, Y. (2004). Balancing human-and-robot integration in building tasks. *Computer-Aided Civil and Infrastructure Engineering*, 19, 393–410.
- Keerthanaa, P., Jeevitha, K., Navina, V., & Indira, G. (2013). Automatic wall painting robot. *International Journal of Innovative Research in Science, Engineering and Technology*, 2(7), 3009–3023.
- Law, W. C., Chen I. M., Yeo, S. H., Seet, G. L., & Low, K. H. (2015). A study of in-pipe robots for maintenance of large-diameter sewerage tunnel. In *Proceedings of 14th IFToMM World Congress in Mechanism and Machine Science Conference*, Taipei, Taiwan, 25–30 Oct 2015.
- Naticchia, B., Giretti, A., & Carbonari, A. (2007). Set up of an automated multi-color system for interior wall painting. *International Journal of Advanced Robotic Systems*, 4, 407–416.
- Rosenfeld, Y., Warszawski, A., & Zajicek, U. (1993). Full-scale building with interior finishing robot. *International Journal of Automation in Construction*, 2(4), 229–240.
- Sorour, M. T., Abdellatif, M. A., Ramadan, A. A., & Abo-Ismael, A. A. (2011). Development of roller-based interior wall painting robot. *World Academy of Science, Engineering and Technology, International Journal of Mechanical, Aerospace, Industrial, Mechatronic and manufacturing Engineering*, 5(11), 1785–1792.
- Walter, C., Saenz, J., Elkmann, N., Althoff, H., Kutzner, S., & Stuerze, T. (2012). Design considerations of robotic system for cleaning and inspection of large-diameter sewers. *Journal of Field Robotics*, 29(1), 186–214.
- Warszawski, A., & Rosenfeld, Y. (1994). Robot for interior finishing works in building—Feasibility analysis. *ASCE Journal of Construction Engineering and Management*, 120(1), 132–151.
- Warszawski, A., & Rosenfeld, Y. (1997). Economic analysis of robots employment in building. *Proceedings of the 14th International Symposium on Automation and Robotics in Construction (ISARC)* (pp. 177–184). Pennsylvania, USA: Pittsburgh.
- Yan, R. J., Wu, J., Yuan, Q., Yuan, C., Luo, L.-P., Shin, K.-S., et al. (2014). Natural corners-based SLAM with partial compatibility algorithm. *Proceedings of IMechE, Part I: Journal of systems and Control Engineering*, 228(8), 591–611.
- Yan, R. J., Wu, J., Shao, M.-L., Shin, K.-S., Lee, J.-Y., & Han, C.-S. (2015a). Mutually converted arc-line segment-based SLAM with summing parameters. *Proceedings of IMechE, Part C: Journal of Mechanical Engineering Science*, 229(11), 2094–2114.
- Yan, R. J., Wu, J., Lee, Y., & Han, C.-S. (2015b). Representation of 3d environment map using b-spline surface with two mutually-perpendicular LRFs. *Mathematical Problem in Engineering*, 2015(690310), 1–14.

## Author Biography



**I-Ming Chen** received his Ph.D. in Mechanical Engineering from California Institute of Technology, Pasadena, USA in 1994. He is an internationally renowned robotics researcher and has been with the School of Mechanical and Aerospace Engineering of Nanyang Technological University (NTU) in Singapore since 1995. Currently he is the Director of Robotics Research Centre in NTU.

His research interests are in collaborative robots, infrastructure robots, wearable sensors, human-robot interaction, reconfigurable automation, and parallel kinematics machines (PKM).

He is now serving on the editorial board of *Mechanism and Machine Theory*, *Robotica* (Cambridge Univ Press), and *Frontiers of Mechanical Engineering* (Springer-Verlag) as well as senior editor of *IEEE Transactions on Robotics*. He was Technical Editor of *IEEE/ASME Transactions on Mechatronics* from 2003 to 2009.

Professor Chen is a Fellow of IEEE and Fellow of ASME, General Chairman of 2017 IEEE International Conference on Robotics and Automation (ICRA 2017) in Singapore.

# The New Robotics Age: Meeting the Physical Interactivity Challenge

Oussama Khatib

**Abstract** The generations of robots now being developed will increasingly touch people and their lives. They will explore, work, and interact with humans in their homes, workplaces, in new production systems, and in challenging field domains. The emerging robots will provide increased operational support in mining, underwater, and in hostile and dangerous environments. While full autonomy for the performance of advanced tasks in complex environments remains challenging, strategic intervention of a human will tremendously facilitate reliable real-time robot operations. Human-robot synergy benefits from combining the experience and cognitive abilities of the human with the strength, dependability, competence, reach, and endurance of robots. Moving beyond conventional teleoperation, the new paradigm—placing the human at the highest level of task abstraction—relies on robots with the requisite physical skills for advanced task behavior capabilities. Such connecting of humans to increasingly competent robots will fuel a wide range of new robotic applications in places where they have never gone before. This discussion focuses on robot design concepts, robot control architectures, and advanced task primitives and control strategies that bring human modeling and skill understanding to the development of safe, easy-to-use, and competent robotic systems. The presentation will highlight these developments in the context of a novel underwater robot, Ocean One, called O2, developed at Stanford in collaboration with Meka Robotics, and KAUST.

---

O. Khatib (✉)

Robotics Laboratory Computer Science Department, Stanford University,  
Stanford, CA, USA

e-mail: khatib@robotics.stanford.edu

## Author Biography



**Biography of Oussama Khatib** Oussama Khatib received his Ph.D. from Sup' Aero, Toulouse, France, in 1980. He is Professor of Computer Science at Stanford University. His research focuses on methodologies and technologies in human-centered robotics including humanoid control architectures, human motion synthesis, interactive dynamic simulation, haptics, and human-friendly robot design. He is a Fellow of IEEE. He is Co-Editor of the Springer Tracts in Advanced Robotics (STAR) series and the Springer Handbook of Robotics, which received the PROSE Award for Excellence in Physical Sciences & Mathematics. Professor Khatib is the President of the International Foundation of Robotics Research (IFRR). He has been the recipient of numerous awards, including the IEEE RAS Pioneer Award in Robotics and Automation, the IEEE RAS George Saridis Leadership Award in Robotics and Automation, the

IEEE RAS Distinguished Service Award, and the Japan Robot Association (JARA) Award in Research and Development.

**Part II**  
**Kinematics for Robotics**

# Robust Inverse Kinematics at Position Level by Means of the Virtual Redundant Axis Method

Francisco Geu Flores, Sebastian Röttgermann, Bettina Weber  
and Andrés Kecskeméthy

**Abstract** Several techniques have been developed in the past to handle the inverse kinematics of serial robots passing through or close to singular configurations. As a common line, these approaches operate at velocity level, seeking a trade-off between tracking accuracy and joint velocity feasibility. While providing robust control, some difficulties arise in these methods for predicting end-effector errors and their spread in  $SE(3)$ . In a previous paper, the virtual redundant axis (VRA) method was introduced at velocity level, by which end-effector velocity errors could be concentrated in non-controllable directions. The present paper extends the VRA method to position level, allowing for a precise motion tracking and the handling of singularity paths in the same way as regular motions.

## 1 Introduction

Robust inverse kinematics algorithms, i.e. algorithms that are able to handle end-effector paths passing through or close to singularities, are useful when the task cannot avoid such singularities or when the robot motion is not known in advance. At singular configurations, the end-effector loses mobility in some  $SE(3)$  components, leading to so-called “degenerate directions” with locked translational or rotational motions, while some subsets of the robot joint variables redundantly operate in the nullspace of the degenerate directions, see e.g. Khatib (1987). Standard inverse kinematics algorithms thus collapse at singularities or lead to unfeasible

---

F.G. Flores (✉) · S. Röttgermann · B. Weber · A. Kecskeméthy  
Chair for Mechanics and Robotics, University of Duisburg Essen, Essen, Germany  
e-mail: francisco.geu@uni-due.de

S. Röttgermann  
e-mail: sebastian.roettgermann@uni-due.de

B. Weber  
e-mail: bettina.szyska@hotmail.com

A. Kecskeméthy  
e-mail: andres.kecsekemethy@uni-due.de



large joint velocities when passing close to them. In the past, several techniques have been developed to overcome these difficulties. As a common line, all these approaches work at velocity level, either by locally removing the degenerate components from the target velocities and controlling the redundant joint velocities through optimization, as e.g. in Khatib (1987) and Chiaverini and Egeland (1990), or by seeking a compromise between well-behaved joint velocities and tolerable end-effector errors, as e.g. in Wampler et al. (1986) and Nakamura and Hanafusa (1986). The latter approach, termed damped least squares (DLS) method, was refined several times, e.g. by Maciejewski and Klein (1988) and Buss and Kim (2005), and lead to the weighted damped least squares (WDLS) method, consisting of optimizing a trade-off between task accuracy and joint velocity feasibility under weighting of preferred directions. Also, Pechev (2008) proposed a feedback inverse kinematics (FIK) method using task space error feedback control which avoids matrix inversion. However, while ensuring robust inverse kinematics control, all velocity-based methods yield task errors difficult to predict and tend to spread out both in degenerate and non-degenerate directions.

To reduce these problems, Leontjev et al. (2012) proposed the virtual redundant axis (VRA) method, in which a virtual axis is added to the physical robot, such that velocities in the degenerate directions are absorbed by this virtual axis and physical tracking errors in non-degenerate directions are reduced. This paper extends the previous paper to position level, leading to (a) a much preciser and predictable motion of the end effector and (b) the possibility to handle singularity paths in the same way as regular inverse kinematics. The method is explained for the wrist singularity of a 6R KUKA robot, but can be extended to other types of singularities and/or paths.

## 2 State of the Art

### 2.1 Problem Formulation

Let the configuration of the robot manipulator be described by its joint variables  $\mathbf{q} \in \mathbf{R}^6$  and the robot's end-effector be described by the spatial reference frame  $\mathcal{K}_E \in \text{SE3}$ . Let furthermore  $\boldsymbol{\psi}_E$  be a parametrization of the pose of  $\mathcal{K}_E$  with respect to the robot's base frame  $\mathcal{K}_r$ , given by a collection of any form of rotation parameters and a position vector. The position and velocity direct kinematics of the robot is

$$\boldsymbol{\psi}_E = \mathbf{f}(\mathbf{q}) \quad (1)$$

$$\dot{\boldsymbol{\psi}}_E = \mathbf{J} \dot{\mathbf{q}}, \quad (2)$$

where  $(\dot{\cdot})$  in general denotes the time derivative of  $(\cdot)$ ,  $\mathbf{J} \in \mathbf{R}^{6 \times 6}$  is the robot's Jacobian, and  $\dot{\boldsymbol{\psi}}_E$  denotes the 6 dimensional "twist" vector collecting the angular velocity of the end-effector frame and the linear velocity of its origin. The problem addressed

in this paper is to compute joint angles  $\mathbf{q}$  that fulfill Eq. (1) as good as possible even in the presence of singularities or when approaching them, without leading to infeasible joint velocities.

## 2.2 WDLs Method with Feedback Correction

The WDLs method, originally proposed by Nakamura and Hanafusa (1986), and extended with feedback correction by Chiaverini et al. (1994), computes, at velocity level, robot joint increments  $\Delta\mathbf{q}$  within a time step  $\Delta t$  for a given task space increment  $\Delta\boldsymbol{\psi}_E = \boldsymbol{\psi}_E \Delta t$ , given in twist space, as

$$\Delta\mathbf{q} = [\mathbf{J}^T \mathbf{W}_{\text{DLS}}^2 \mathbf{J} + \lambda^2 \mathbf{I}]^{-1} \mathbf{J}^T \mathbf{W}_{\text{DLS}}^2 (\Delta\boldsymbol{\psi}_E + \mathbf{K}_{\text{err}} \boldsymbol{\psi}_{\text{err}}), \quad (3)$$

which is the exact solution to the unconstrained minimization problem

$$\underset{\Delta\mathbf{q}}{\text{minimize}} \quad 2 \|\mathbf{J} \Delta\mathbf{q} - (\Delta\boldsymbol{\psi}_E + \mathbf{K}_{\text{err}} \boldsymbol{\psi}_{\text{err}})\|_{\mathbf{W}_{\text{DLS}}^2}^2 + \lambda^2 \|\Delta\mathbf{q}\|_2^2. \quad (4)$$

In these equations,  $\|\cdot\|_{\mathbf{P}}$  is the norm using a positive semi-definite metric  $\mathbf{P}$ ,  $\mathbf{W}_{\text{DLS}}$  is a  $6 \times 6$  matrix weighting the components of the task space velocities,  $\lambda$  is the damping factor weighting the joint increments  $\Delta\mathbf{q}$ ,  $\boldsymbol{\psi}_{\text{err}}$  is the relative error from actual to desired end-effector pose, assumed to be of first order and thus also in twist space, and  $\mathbf{K}_{\text{err}}$  is the  $6 \times 6$  gain matrix attempting to reduce  $\boldsymbol{\psi}_{\text{err}}$ . Chiaverini et al. (1992) proposed to choose  $\lambda$  as a function of the smallest singular value  $\sigma_6$  of  $\mathbf{J}$  and a parameter  $\epsilon$  which defines the size of the singular region, according to

$$\lambda^2 = \begin{cases} 0 & \text{if } \sigma_6 \geq \epsilon \\ \left(1 - \left(\frac{\sigma_6}{\epsilon}\right)^2\right) \lambda_{\text{max}}^2 & \text{else,} \end{cases} \quad (5)$$

where the constant  $\lambda_{\text{max}}$  can be used to shape the solution in the neighborhood of the singularity.  $\mathbf{W}_{\text{DLS}}$  and  $\mathbf{K}_{\text{err}}$  are to be defined such that, in singular configurations, they eliminate the components of the prescribed velocities in degenerate directions. For the particular example of this paper (Fig. 1), which considers only hand-singularities during straight-line vertical end-effector motions with constant horizontal attitude, and assuming a twist-like end-effector pose parametrization  $\Delta\boldsymbol{\psi}_E = [\Delta\boldsymbol{\varphi}^T, \Delta\mathbf{r}^T]^T$ , with  $\Delta\boldsymbol{\varphi}$  and  $\Delta\mathbf{r}$  being decomposed in end-effector coordinates, this yields the matrices  $\mathbf{W}_{\text{DLS}} = \text{diag}\{w, 1, 1, 1, 1, 1\}$  and  $\mathbf{K}_{\text{err}} = \text{diag}\{\rho, 1, 1, 1, 1, 1\}$ , with weighting factor  $w$  and gain  $\rho$  defined according to

$$(1-w)^2 = \begin{cases} 0 & \text{if } \sigma_6 \geq \epsilon \\ \left(1 - \left(\frac{\sigma_6}{\epsilon}\right)^2\right) (1-w_{\min})^2 & \text{else,} \end{cases}$$

$$\rho = \begin{cases} 0 & \text{if } \sigma_6 \leq \epsilon \\ \frac{(\sigma_6 - \epsilon)^2}{9\epsilon^2} & \text{if } \epsilon < \sigma_6 < 4\epsilon \\ 1 & \text{otherwise.} \end{cases}$$

More general applications can foresee matrices  $\mathbf{W}_{\text{DLS}}$  and  $\mathbf{K}_{\text{err}}$  depending on the robot configuration  $\mathbf{q}$ .

### 3 Virtual Redundant Axis Method

The virtual redundant axis (VRA) method aims at eliminating all non-degenerate error components by adding virtual additional joints at the end-effector that will absorb non-controllable degenerate motions at singularities. Thus a virtual redundant robot arises with direct kinematics

$$\boldsymbol{\psi}_{\text{E}} = \bar{\mathbf{f}}(\bar{\mathbf{q}}) \quad (6)$$

$$\dot{\boldsymbol{\psi}}_{\text{E}} = \bar{\mathbf{J}} \dot{\bar{\mathbf{q}}}, \quad (7)$$

where vector  $\bar{\mathbf{q}} = [\mathbf{q}^T, \mathbf{q}_v^T]^T$  collects the robot axes as well as the  $m$ -virtual redundant axes  $\mathbf{q}_v$ , and  $\bar{\mathbf{J}} \in \mathbf{R}^{6 \times (6+m)}$  is the corresponding Jacobian.

For illustration purposes, the method is explained here for the example of the wrist singularity of a six-degrees-of-freedom robot whose end effector is moving with constant horizontal attitude along a vertical line (Fig. 1). When the robot reaches hand

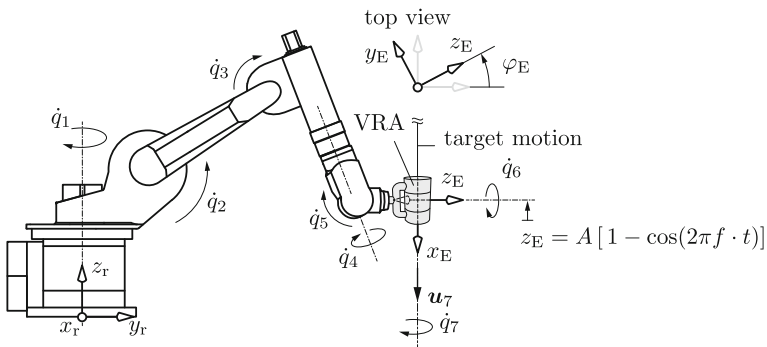


**Fig. 1** Robot with virtual redundant axis  $q_7$  and target motion

singularity, axes 4 and 6 are collinear, axis 5 is horizontal, and thus rotation about the perpendicular to axes 5 and 6 is instantaneously locked. This locked direction gives the direction of the sought virtual redundant axis (with joint variable  $q_7$ ), which due to the regarded particular motion can be assumed to constantly point in body-fixed end-effector x-direction and to be attached at its tip. More general situations may require floating axes as a function of the other robot axes.

### 3.1 VRA at Velocity Level

At velocity level, the “best” robot joint increments  $\Delta\bar{q}$  within a time step  $\Delta t$  for a given task space increment  $\Delta\psi_E = \dot{\psi}_E \Delta t$  can be assumed to be those minimizing the norm of joint variable increments, shifted by an offset, and fulfilling the kinematic velocity task, see Leontjev et al. (2012):

$$\begin{aligned} & \underset{\Delta\bar{q}}{\text{minimize}} \quad \|\Delta\bar{q} - \mathbf{c}\|_{\mathbf{W}_{\text{VRA}}}^2 \\ & \text{subject to} \quad \bar{\mathbf{J}} \Delta\bar{q} - \Delta\psi_E = \mathbf{0}. \end{aligned} \quad (8)$$

The offset  $\mathbf{c} = [0, \dots, 0, -q_7]^T$  is an error feedback that seeks to bring  $q_7$  to zero. The weights collected in  $\mathbf{W}_{\text{VRA}} = \text{diag}\{w_1, w_2, \dots, w_6, w_7\}$  are used to penalize the increments of the redundant axes during singularity, here  $\Delta q_4, \Delta q_6, \Delta q_7$ , while penalizing  $q_7$  increments more strictly when the robot is far away from singularity. Taking  $q_5$  as a measure for closeness to singularity (here with  $q_5 = 0.0$  at singularity), this can be achieved by choosing  $w_1 = w_2 = w_3 = w_5 = 0.0$ ,  $w_4 = w_6 = 1.0$ , and setting

$$w_7(q_5) = w_7^\infty \cdot (1 - \exp^{-\alpha \cdot q_5^2}) + w_7^* \cdot \exp^{-\alpha \cdot q_5^2}, \quad (9)$$

where  $w_7^\infty \gg w_7^*$ , and  $\alpha$  is a shaping factor. More general measures for closeness to singularities can be obtained from the singular value decomposition of the Jacobian  $\mathbf{J}$ . However, most industrial robots have clear geometrical measures for closeness to singularities that can be used also in that case.

The solution to the generalized least squares problem of Eq. (8) then is

$$\begin{bmatrix} \Delta\bar{q} \\ \boldsymbol{\mu} \end{bmatrix} = \begin{bmatrix} \mathbf{W}_{\text{VRA}} & \bar{\mathbf{J}}^T \\ \bar{\mathbf{J}} & \mathbf{0} \end{bmatrix}^{-1} \begin{bmatrix} \mathbf{W}_{\text{VRA}} \mathbf{c} \\ \Delta\psi_E \end{bmatrix}, \quad (10)$$

with Lagrange multipliers  $\boldsymbol{\mu}$ . This linear system can be readily computed using standard routines such as Lapack’s DGGLSE.

### 3.2 VRA at Position Level

The performance of the VRA method can be improved by formulating it at position level. In the following, it is assumed that the robot's end-effector path  $\boldsymbol{\psi}_E(t)$  is prescribed at discrete points  $t_i$  in time. Starting from an initial guess  $\bar{\boldsymbol{q}}^{(0)}(t_i)$ , the solution of Eq. (6) can be determined at time  $t_i$  by a sequence of  $N$  Newton steps (leaving out index  $t_i$  for better readability)

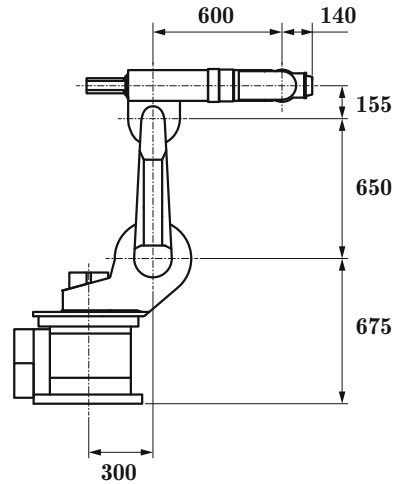
$$\bar{\boldsymbol{q}}(t_i): \bar{\boldsymbol{q}}^{(k)} = \bar{\boldsymbol{q}}^{(k-1)} + \Delta\bar{\boldsymbol{q}}^{(k)}, k = 1, 2, \dots, N, \quad (11)$$

where  $\Delta\bar{\boldsymbol{q}}^{(k)}$  is computed by solving Eq. (8) with  $\boldsymbol{c} = \mathbf{0}$  and  $\Delta\boldsymbol{\psi}_E \rightarrow \boldsymbol{\psi}_{\text{err}}^{(k-1)}$  as

$$\begin{bmatrix} \Delta\bar{\boldsymbol{q}}^{(k)} \\ \boldsymbol{\mu}^{(k)} \end{bmatrix} = \begin{bmatrix} \mathbf{W}_{\text{VRA}}^{(k-1)} & (\bar{\mathbf{J}}^{(k-1)})^T \\ \bar{\mathbf{J}}^{(k-1)} & \mathbf{0} \end{bmatrix}^{-1} \begin{bmatrix} \mathbf{0} \\ \boldsymbol{\psi}_{\text{err}}^{(k-1)} \end{bmatrix}. \quad (12)$$

Here,  $\boldsymbol{\psi}_{\text{err}}^{(k-1)}$  is the relative end-effector pose error from the configuration  $\bar{\boldsymbol{q}}^{(k-1)}$  at the end of Newton step  $k-1$  to the desired pose at time step  $t_i$ , assumed to be of first order and thus in twist space. The Newton iterations are carried out until either  $\|\Delta\bar{\boldsymbol{q}}_k\|_2$  or  $\|\boldsymbol{\psi}_{\text{err}}^{(k)}\|_2$  converges below predefined tolerances, yielding the solution  $\bar{\boldsymbol{q}}(t_i)$ . For the next time step, the initial guess is taken as  $\boldsymbol{q}^{(0)}(t_{i+1}) = \boldsymbol{q}(t_i)$  for the physical robot joints and as  $q_7^{(0)}(t_{i+1}) = \exp^{-\beta \cdot q_7^2(t_i)} \cdot q_7(t_i)$  for the virtual redundant joint, which ‘‘pulls’’  $q_7$  to zero when the robot is far from singularity, with  $\beta > 0$  being a user-defined shaping parameter.

Fig. 2 KUKA KR15/2



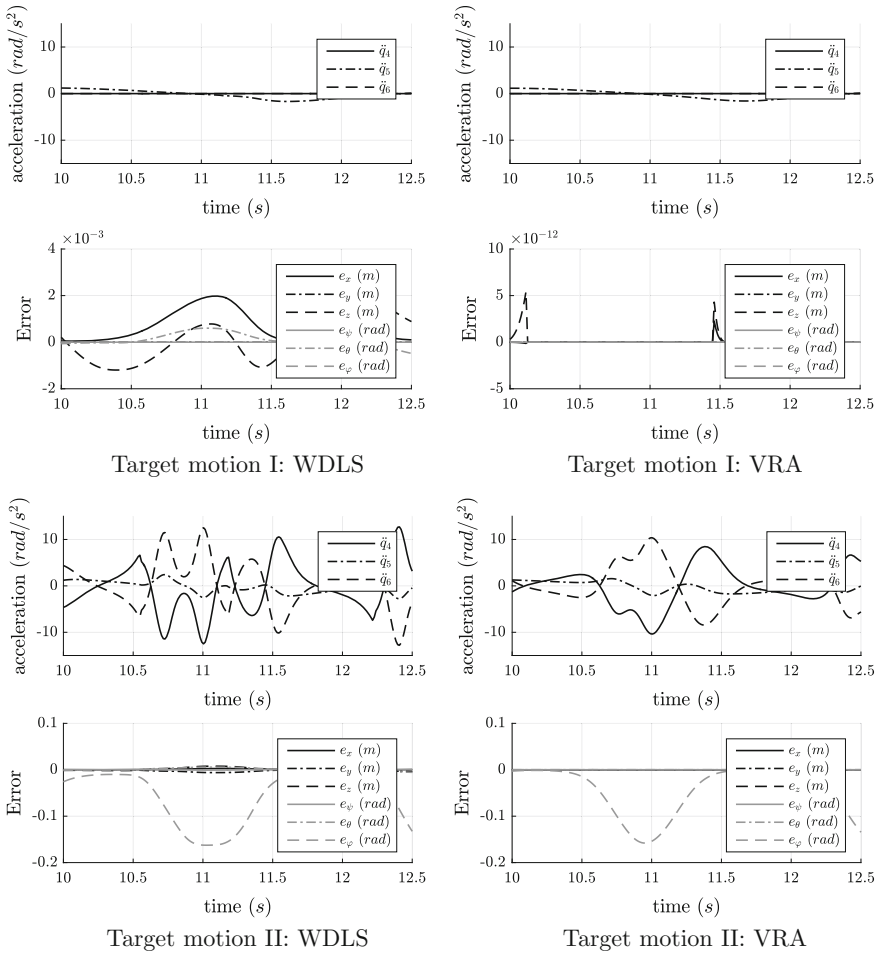


**Fig. 3** Robot response to pure heave motions with amplitude  $A = 0.2$  m and frequency  $f = 0.3$  Hz. Target motion I: at constant heading (yaw angle)  $\varphi_E = 0^\circ$ ; Target motion II: at constant heading (yaw angle)  $\varphi_E = 5^\circ$ . WDLS method with feedback correction with  $\epsilon = 0.08$ ,  $\lambda_{\max} = 0.04$ ,  $w_{\min} = 0.1$ , and  $\rho_{\max} = 1.0$ ; VRA method at position level with  $w_7^{\infty} = 4900$ ,  $w_7^* = 25.0$ ,  $\alpha = 2.0$ ,  $\beta = 1.0$ ,  $\text{tol} = 1.0 \cdot 10^{-12}$

## 4 Experimental Results

The performance of the WDLS and VRA methods were measured on a test bench consisting of a (real) KUKA robot as described in Figs. 1 and 2. The results are shown in Fig. 3. The joint accelerations were computed numerically from measured joint angles, and the displayed errors correspond to the residuals from computed to desired end-effector pose when evaluated in end-effector fixed twist space. As shown in the plots, the VRA method at position level succeeds in “absorbing” all the track

**Table 1** KUKA KR15/2 robot properties

Axis	Joint range	max. velocity
1	$\pm 185^\circ$	$152^\circ/s$
2	$+115^\circ$ to $-55^\circ$	$152^\circ/s$
3	$+70^\circ$ to $-210^\circ$	$152^\circ/s$
4	$\pm 350^\circ$	$284^\circ/s$
5	$\pm 135^\circ$	$293^\circ/s$
6	$\pm 350^\circ$	$604^\circ/s$

errors within the virtual redundant axis, leaving all other track error components below computing tolerance. Furthermore, the VRA joint motion at acceleration level is significantly smoother than that resulting from the WDLS method.

The methods were implemented without regarding computational efficiency. On a processor Intel(R) Core(TM) i7-950 @ 3.07GHz, the VRA at position level required 0.0289 s for computing a sample trajectory consisting of 1000 end-effector target poses, using 3 N steps in average, while the WDLS required 0.0412 s for the same trajectory. In both cases, this can be improved considerably, see Maciejewski and Klein (1988) (Table 1).

## 5 Conclusions

The VRA method at position level is shown to have superior properties compared to current velocity-based methods in terms of tracking precision and smoothness of the ensuing motion. Moreover, the VRA features no mode switching and only few tuning parameters, which makes it easy to implement and to use. While only one specific example was regarded in this paper, the VRA is extensible to multiple singularities and general virtual redundant axes, such as e.g. floating axes as functions of the robot configuration. These extensions are planned for future work.

## References

- Buss, S. R., & Kim, J. (2005). Selectively damped least squares for inverse kinematics. *Journal of Graphics, GPU, and Game Tools*, 10(3), 37–49.
- Chiaverini, S., & Egeland, O. (1990). A solution to the singularity problem for six-joint manipulators. In *Proceedings of 1990 IEEE International Conference on Robotics and Automation, 1990* (pp. 644–649). IEEE.
- Chiaverini, S., Egeland, O., & Kanestrom, R. K. (1992). Weighted damped least-squares in kinematic control of robotic manipulators. *Advanced Robotics*, 7(3), 201–218.

- Chiaverini, S., Siciliano, B., & Egeland, O. (1994). Review of the damped least-squares inverse kinematics with experiments on an industrial robot manipulator. *IEEE Transactions on Control Systems Technology*, 2(2), 123–133.
- Khatib, O. (1987). A unified approach for motion and force control of robot manipulators: The operational space formulation. *IEEE Journal of Robotics and Automation*, 3(1), 43–53.
- Leontjev, V., Flores, F. G., López, J., Ribickis, & Kecskeméthy, A. (2012). Singularity avoidance by virtual redundant axis and its application to large base motion compensation of serial robots. In *Proceedings of the 21th International Workshop on Robotics in Alpe-Adria-Danube Region, RAAD 2012* (pp. 77–84). Naples, Italy, September 10–13, 2012.
- Maciejewski, A. A., & Klein, Ch A. (1988). Numerical filtering for the operation of robotic manipulators through kinematically singular configurations. *Journal of Robotic Systems*, 5(6), 527–552.
- Nakamura, Y., & Hanafusa, H. (1986). Inverse kinematic solutions with singularity robustness for robot manipulator control. *Journal of Dynamic Systems, Measurement, and Control*, 108(3), 163–171.
- Pechev, A. N. (2008). Inverse kinematics without matrix inversion. In *Robotics and Automation, 2008. ICRA 2008* pp. 2005–2012. IEEE.
- Wampler, C. W., et al. (1986). Manipulator inverse kinematic solutions based on vector formulations and damped least-squares methods. *IEEE Transactions on Systems, Man and Cybernetics*, 16(1), 93–101.



# Redundancy Resolution of a 9 DOF Serial Manipulator Under Hard Task Constraints

Narendrakrishnan Neythalath, Mathias Brandstötter  
and Michael Hofbaur

**Abstract** Kinematic redundancy is a topic which has been discussed under various contexts to co-achieve a primary task along with additional tasks. However a structural analysis about kinematic redundancy to comprehend what really is happening underneath the hood has seldom been a topic of discussion. In this paper, kinematic redundancy is viewed from a slightly different perspective to deduce the constraints in the null space. Task distortion is explained in a geometrical sense and it lays the foundation for possible corrective measures for a better realization of the task. For the sake of generality, the considered primary task in this work is highly constraining in nature. A 9 DOF serial manipulator will be used instead of a conventional 7 DOF manipulator as the constraints imposed by the primary task results in insufficient null space dimensions.

## 1 Introduction

Robot systems are known as kinematically redundant, if a task can be performed with an infinitely large number of joint configurations. Such a kinematic structure would have more actuators than what is being demanded by the task for its successful execution. The motivation to design a redundant manipulator is to achieve a wider range of possible end effector orientations within the physical limits of the individual joints, to reduce the risk of collision, or to avoid singular configurations, see Stevenson et al. (2002). Previous works considered kinematic redundancy to minimize joint displacements (Liegeois 1977), avoid obstacles (Maciejewski and Klein 1985), minimize kinetic energy (Whitney 1969) and optimize joint torques (Hollerbach 1987).

---

N. Neythalath (✉) · M. Brandstötter · M. Hofbaur  
Joanneum Research, Institute for Robotics and Mechatronics, Klagenfurt, Austria  
e-mail: Narendrakrishnan.Neythalath@joanneum.at

M. Brandstötter  
e-mail: Mathias.Brandstoetter@joanneum.at

M. Hofbaur  
e-mail: Michael.Hofbaur@joanneum.at

More recent works involve generalized framework for multiple task management (Siciliano and Slotine 1991), algorithmic singularity avoidance (Chiaverini 1997) and problems with joint saturation (Omrnen et al. 2006; Flacco et al. 2012).

However we have noticed that the above mentioned research literature did not focus on the exact reasons for the distortion (partial fulfillment of the assigned task) experienced by additional tasks. In our work, the notion of null space and associated joint space tasks are therefore conceived and interpreted from a geometrical viewpoint. Task distortion will be expressed in terms of spatial orientation to the null space/row space. This spatial orientation denotes the geometric angle between the task vector and the basis vectors that span the null space. Such an interpretation will help to identify the family of additional tasks which will be in stark disagreement with the assigned primary task and thus provides a quantitative index to measure the task compatibility which has seldom been part of any research literature to the best of our knowledge. Ahead of delving into the intricate details, a brief primer to the concept of kinematic redundancy is provided.

The degree of kinematic redundancy is defined as the number of independent variables available in the mathematical model of the system for free alteration without influencing the given task execution. The available kinematic redundancy in the model can be resolved using the inverse kinematic mapping which exists between the generalized vectors (viz. position, velocity or acceleration) belonging to the joint and the task space. However a non-linear relationship which exists between the position vectors of the aforementioned spaces gives rise to inherent difficulties in the analysis of the system. Hence a common approach is to analyze and resolve the redundancy using the velocity vectors where the relationship decomposes into a linear mapping. Figure 1 illustrates the redundancy resolution of a serial manipulator in the presence of an obstacle moving with a velocity  $\mathbf{v}_o$ . This obstacle may be avoided by imparting  $\mathbf{v}_o$  in a direction opposite to the direction of approach of the obstacle at the critical point of the manipulator. The critical point is the point along the mechanical structure of the manipulator which is closest to the obstacle. As this task needs to be achieved within the null space of the primary task, it might be possible to fulfill the task only partially represented through  $\alpha\mathbf{v}_o$  where  $\alpha$  is a scalar value between 0 and 1. The joint space depicted in Fig. 1 is an  $n$  dimensional vector space of  $\mathbb{R}^n$  where  $n$  is the DOF of the robot. It contains two sub-spaces which are orthogonal to each other, namely a row space which is an  $m$  dimensional vector sub-space of  $\mathbb{R}^n$  where  $m$  is the dimension of the primary task and a null space which is an  $n - m$  dimensional vector sub-space of  $\mathbb{R}^n$ . However, in the event of kinematic singularities, the null space will grow into a higher dimensional space crushing the dimensions of the row space. This phenomenon will be dictated by the extent of linear dependencies existing in the system model. The task space (column space) is an  $m$  dimensional vector space of  $\mathbb{R}^m$  where  $m$  is the dimension of the primary task. The serial manipulator can be viewed as a system which maps a velocity vector from  $\mathbb{R}^n$  to  $\mathbb{R}^m$ . Such a forward transformation (direct kinematics) can be modeled by the manipulator's Jacobian  $\mathbf{J}$ . The forward transformation will collapse the components of the joint space velocity vector in the null space of  $\mathbf{J}$  to a zero vector and the components in the row space will be transformed over to the column space. If the generalized inverse of  $\mathbf{J}$ , represented

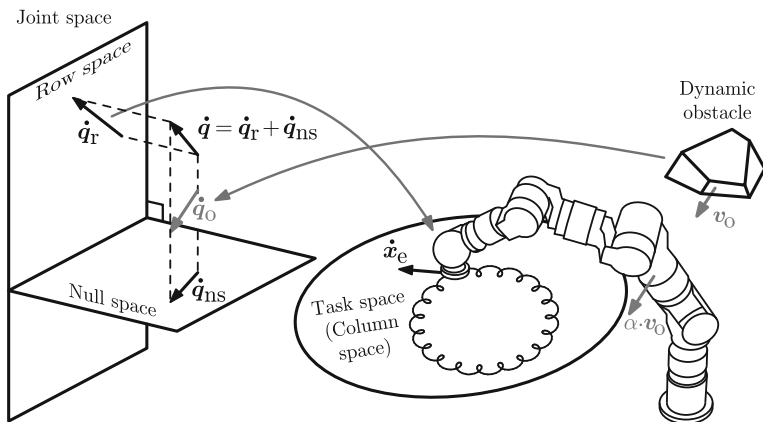


**Fig. 1** Kinematics of a serial manipulator

as  $\mathbf{J}^+$ , is allowed to operate on this transformed vector in the task space, only the components of the original vector in the row space can be retrieved. The addition of any vector from the null space to this row space vector will have no influence in the task space as they collapse to a zero vector during the forward transformation. But this addition of null space velocities will induce *self motion* inside the manipulator which can be used for performing other tasks.

The generalized inverse method resolves the redundancy as

$$\dot{\mathbf{q}} = \dot{\mathbf{q}}_r + \dot{\mathbf{q}}_{ns} = \mathbf{J}^+ \dot{\mathbf{x}}_e + (\mathbf{I} - \mathbf{J}^+ \mathbf{J}) \dot{\mathbf{q}}_0, \quad (1)$$

where  $\dot{\mathbf{q}}$  is the joint space velocity vector,  $\dot{\mathbf{x}}_e$  is the task space velocity vector,  $(\mathbf{I} - \mathbf{J}^+ \mathbf{J})$  represents the orthogonal null space projection matrix and  $\dot{\mathbf{q}}_0$  is an arbitrary joint space velocity. By acting on  $\dot{\mathbf{q}}_0$ , we can obtain different null space velocities. Hence the choice of  $\dot{\mathbf{q}}_0$  is entirely decided by the additional task at hand. For the

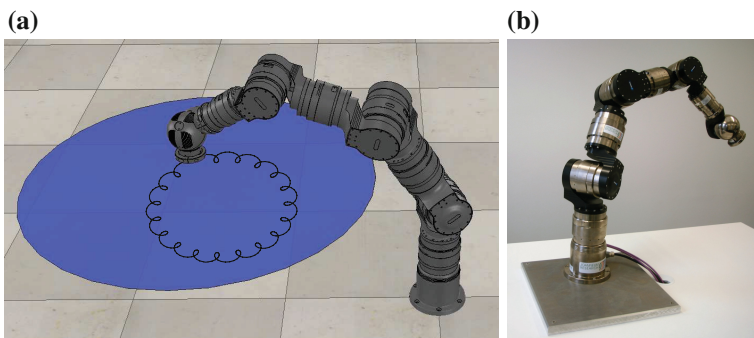


**Fig. 2** 9 DOF manipulator. **a** Simulation model represented in V-REP. **b** Robotic testbed

sake of simplicity, we will denote the orthogonal projection matrix ( $\mathbf{I} - \mathbf{J}^+ \mathbf{J}$ ) by  $\mathbf{Q}$ . Figure 2a illustrates the model of the 9 DOF serial manipulator used for simulation, whereas Fig. 2b depicts the corresponding real world robot.

## 2 Task Definition

For the purpose of our in-depth analysis, two exemplary tasks are defined. The primary task is a 5 DOF task of the end effector to move along a prescribed trajectory (shown in Fig. 2a) which is given as

$$\mathbf{x}_e = [0.02 \sin(20t) + 0.2 \sin(t) \quad 0.02 \cos(20t) + 0.2 \cos(t) \quad 0.512 \quad -\pi \quad 0]^T.$$

The first 3 components of  $\mathbf{x}_e$  refer to the  $x$ ,  $y$  and  $z$  coordinates of the end effector expressed in meters whereas the remaining 2 components signifies the end effector orientation expressed in radians.

The secondary task is defined as joint limit avoidance. The cost function to minimize the joint displacement was introduced by Zghal et al. (1990) as

$$H(\mathbf{q}) = \frac{1}{4} \sum_{i=1}^n \frac{(q_{i,\max} - q_{i,\min})^2}{(q_{i,\max} - q_i)(q_i - q_{i,\min})}, \quad (2)$$

where  $i$  is the joint index,  $[q_{i,\max}, q_{i,\min}]$  is the vector specifying the upper and lower bound for the  $i$ -th joint and  $q_i$  is the current joint position. The choice of the secondary task is arbitrary as the focus of this paper is more to analyze the null space constraints which lead to task distortion rather than the actual task itself.

## 3 Null Space Constraints

As obvious from (1) while trying to achieve the given secondary task in cohesion with the primary task, the secondary task may be subjected to distortion. The amount of distortion depends upon the magnitude of the null space projection of the computed secondary task velocity  $\dot{\mathbf{q}}_{\text{sec}}$ . It is obtained by the action of projection matrix  $\mathbf{Q}$  on  $\dot{\mathbf{q}}_{\text{sec}}$ . The operation of  $\mathbf{Q}$  on  $\dot{\mathbf{q}}_{\text{sec}}$  to obtain the null space velocity  $\dot{\mathbf{q}}_{\text{ns}}$  can be represented as

$$\dot{\mathbf{q}}_{\text{ns}} = \mathbf{Q} \dot{\mathbf{q}}_{\text{sec}}. \quad (3)$$

For a better illustration of this fact, we have taken a snapshot of the system at  $t = 3$ . The corresponding velocities are observed as  $\dot{\mathbf{q}}_{\text{sec}} = [0.313 \ 0.206 \ 0.106 \ -1.887 \ 0.015 \ -2.920 \ 0.053 \ -0.306 \ 0.141]^T$  rad/s and  $\dot{\mathbf{q}}_{\text{ns}} = [0.063 \ -0.187 \ 0.025 \ 0.174 \ -0.063 \ -0.184 \ 0.040 \ 0.177 \ 0.141]^T$  rad/s. In this case, the task distortion can be represented as the vector difference of these two vectors. This difference vector lies in the row space of the instantaneous analytical Jacobian  $\mathbf{J}_{\text{inst}}$  and represents the extent of disturbance caused to the primary task if the system would have been subjected to  $\dot{\mathbf{q}}_{\text{sec}}$  instead of  $\dot{\mathbf{q}}_{\text{ns}}$ . The task undergoes a huge distortion as suggested by the difference between the norms of  $\dot{\mathbf{q}}_{\text{sec}}$  ( $\|\dot{\mathbf{q}}_{\text{sec}}\| = 3.51$ ) and  $\dot{\mathbf{q}}_{\text{ns}}$  ( $\|\dot{\mathbf{q}}_{\text{ns}}\| = 0.4$ ). Physical explanation for such a distortion can be obtained by computing the angle  $\alpha$  between the null space and the additional task velocity which can be obtained as

$$\cos(\alpha) = \frac{\|\dot{\mathbf{q}}_{\text{ns}}\|}{\|\dot{\mathbf{q}}_{\text{sec}}\|}. \quad (4)$$

The spatial orientation of  $\dot{\mathbf{q}}_{\text{sec}}$  with respect to the null space is  $83.45^\circ$  in this case.  $\mathbf{J}_{\text{inst}}$  of the system at  $t = 3$  was observed to be:

$$\mathbf{J}_{\text{inst}} = \begin{bmatrix} -0.311 & -0.053 & -0.333 & -0.094 & -0.389 & -0.051 & -0.041 & 0.012 & 0 \\ 0.080 & 0.121 & 0.052 & -0.189 & 0.037 & -0.359 & -0.006 & -0.082 & 0 \\ 0 & -0.252 & 0.080 & -0.436 & 0.042 & -0.159 & 0 & 0 & 0 \\ 0 & 0.955 & 0.119 & 0.709 & -0.666 & 0.691 & -0.276 & 0.839 & 0 \\ 0 & 0.297 & -0.386 & 0.678 & 0.556 & 0.711 & 0.427 & 0.545 & 0 \end{bmatrix}$$

By Gaussian elimination, the instantaneous null space can be computed as

$$\mathbf{N}_{\text{inst}} = \begin{bmatrix} 0 & 0 & 0 & 0 & 0 & 0 & 0 & 0 & 1 \\ 0.829 & -0.219 & -0.436 & 0.025 & -0.256 & -0.010 & -0.037 & 0.084 & 0 \\ 0.069 & -0.022 & 0.293 & 0.029 & -0.403 & -0.004 & 0.861 & -0.074 & 0 \\ 0.114 & 0.457 & -0.162 & -0.483 & 0.015 & 0.523 & 0.041 & -0.494 & 0 \end{bmatrix}$$

At this moment, the null space is a manifold spanned by the 4 orthogonal row vectors of the matrix  $\mathbf{N}_{\text{inst}}$ . It is interesting to note that, the null space is in alignment with the joint axis 9 as indicated by the first row of the matrix  $\mathbf{N}_{\text{inst}}$  which would mean that any secondary task assignment along joint axis 9 will be realized completely. This could be easily verified by comparing the vectors  $\dot{\mathbf{q}}_{\text{sec}}$  and  $\dot{\mathbf{q}}_{\text{ns}}$ . Alternatively,  $\dot{\mathbf{q}}_{\text{ns}}$  can be computed from  $\mathbf{N}_{\text{inst}}$  as

$$\dot{\mathbf{q}}_{\text{ns}} = \sum_{i=1}^n (\dot{\mathbf{q}}_{\text{sec}} \cdot \mathbf{n}_{\text{inst}}(i)) \mathbf{n}_{\text{inst}}(i), \quad (5)$$

where  $n$  is the dimension of the null space and  $\mathbf{n}_{\text{inst}}(i)$  is the corresponding row of  $\mathbf{N}_{\text{inst}}$ . The dot product  $\dot{\mathbf{q}}_{\text{sec}} \cdot \mathbf{n}_{\text{inst}}(i)$  gives the projection of the secondary task velocity to the basis unit vectors of the null space which is then multiplied with  $\mathbf{n}_{\text{inst}}(i)$

to arrive at the projection vector. Finally all four individual projection vectors are added up to compute the null space velocity. As expected  $\dot{\mathbf{q}}_{\text{ns}}$  computed from (3) and (5) are identical. However (5) is a more intuitive representation because it shows the orthogonal basis vectors of the null space and helps us to visualize the null space. As the additional task velocity vector (represented in the joint space) approaches the normal to the null space, its null space projection gradually diminishes (projection onto the complimentary row space will reflect a corresponding increase) to a zero vector and the task undergoes a huge distortion. Row space is a vector space spanned by the linearly independent row vectors of  $\mathbf{J}_{\text{inst}}$  and is always normal to the null space. A velocity vector belonging to the row space of  $\mathbf{J}_{\text{inst}}$  (a linear combination of the individual rows) is  $\dot{\mathbf{q}}_{\text{sec}} = [-0.355 \ -2.525 \ -1.523 \ -3.198 \ 2.069 \ -4.888 \ 1.206 \ -3.802 \ 0]^T$  rad/s. The  $\dot{\mathbf{q}}_{\text{ns}}$  corresponding to the above vector is a zero vector. Hence if the additional task demands a velocity vector which belongs to the family of vectors obtained by a linear operation on the individual rows of  $\mathbf{J}_{\text{inst}}$  for its execution, it will be completely suppressed. In short, task compatibility between primary and additional tasks is just a measure of the spatial orientation of the velocity vector corresponding to the additional task with respect to the null space or the row space. If the solution space of the additional task involves more than one possible solution in the joint space, the ideal choice will be the vector which is farthest from the normal to the null space. It is also important to note that even if the additional task execution demands a velocity only in one of the joints, null space projection of this velocity vector may have components in other joints. For example, for a secondary task which is assigned only to joint axis 1 as  $\dot{\mathbf{q}}_{\text{sec}} = [0.313 \ 0 \ 0 \ 0 \ 0 \ 0 \ 0 \ 0 \ 0]^T$  rad/s,  $\dot{\mathbf{q}}_{\text{ns}}$  is spread across the first 8 joints as  $\dot{\mathbf{q}}_{\text{ns}} = [0.220 \ -0.041 \ -0.112 \ -0.009 \ -0.075 \ 0.016 \ 0.010 \ 0.003 \ 0]^T$  rad/s.

## 4 Null Space Transport

In this section, the transportation of the null space within the joint space during the task execution is briefly discussed. For the current task assignment, the null space possesses two distinct vector sub-fields. Due to the relaxation of one of the end effector euler angles ( $\gamma$  angle in this case), it is observed that null space is always in alignment with joint axis 9.

The primary task definition implies that joint axis 9 is normal to the task plane at every instant of time. Hence this component of the null space preserves its orientation during the task execution. However, it will be translated along the prescribed path of the end effector. The other component of the null space is a 3 dimensional vector sub-field spanned by the remaining set of basis vectors which is subjected to translation as well as rotation during the task execution. Figure 3 is a representational visualization of the movement of this vector sub-field in a 9 dimensional joint space. On encountering singular configurations, the null space will grow to a higher dimension along the axis of singularity.

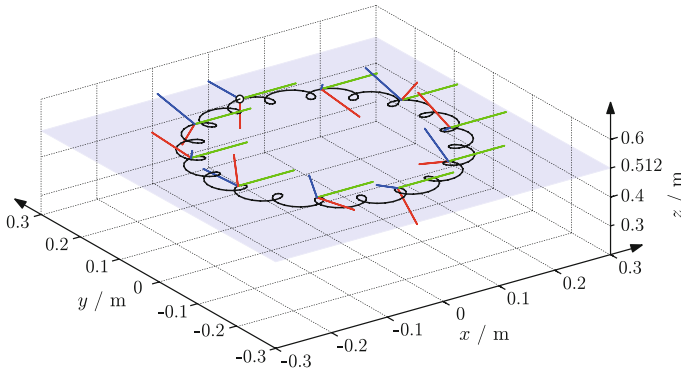


**Fig. 3** Red, green and blue axes span the 3 dimensional vector sub-field

## 5 Conclusions

It is interesting to comprehend the finer nuances of null space as it gives a vivid perception of the physical limitations of the manipulator. In case of a strong disagreement between the tasks, knowledge about the constraints in the null space may be used to alter some of the tasks to enforce cohesion between them wherever it is possible. If all the tasks are too rigid in nature, it may not be possible to modify them. In any event, a deeper insight regarding the null space will help us in making a clear distinction between the *possibilities* and *impossibilities* in terms of the task realization.

**Acknowledgments** This research was funded by the Austrian Ministry for Transport, Innovation and Technology (BMVIT) within the framework of the sponsorship agreement formed for 2015–2018 under the project RedRobCo.

## References

- Chiaverini, S. (1997). Singularity-robust task-priority redundancy resolution for real-time kinematic control of robot manipulators. In *IEEE Transactions on Robotics and Automation*.
- Flacco, F., De Luca, A., & Khatib, O. (2012) Motion control of redundant robots under joint constraints: Saturation in the null space. In *IEEE International Conference on Robotics and Automation*.
- Hollerbach, J. M. (1987). Redundancy resolution of manipulators through torque optimization. In *IEEE Journal of Robotics and Automation*.
- Liegeois, A. (1977). Automatic supervisory and control of the configuration and behavior of multi-body mechanisms. In *IEEE Transactions on Systems, Man, and Cybernetics*.
- Maciejewski, A. A., & Klein, C. A. (1985). Obstacle avoidance for kinematically redundant manipulators in dynamically varying environments. In *The International Journal of Robotics Research*.
- Omrcen, D., Zlajpah, L., & Nemec, B. (2006). Compensation of velocity and/or acceleration joint saturation applied to redundant manipulator. In *Jozef Stefan Institute Article*.

- Siciliano, B., & Slotine, J. J. E. (1991). A general framework for managing multiple tasks in highly redundant robotic systems. In *International Conference on Advanced Robotics (ICAR)*.
- Stevenson, R., Shirinzadeh, B., & Alici, G. (2002). Singularity avoidance and aspect maintenance in redundant manipulators. *International Conference on Control, Automation, Robotics and Vision*, 2, 857–862.
- Whitney, D. E. (1969). Resolved motion rate control of manipulators and human prostheses. In *IEEE Transactions on Man-Machine Systems*.
- Zghal, H., Dubey, R. V., & Euler, J. A. (1990). Efficient gradient projection optimization for manipulators with multiple degrees of redundancy. In *IEEE International Conference on Robotics and Automation*



# Geometry and Direct Kinematics of Six-DOF Three-Limbed Parallel Manipulator

Zh. Baigunchekov, M. Kalimoldaev, M. Utenov and T. Baigunchekov

**Abstract** In this paper the methods of structural synthesis and direct kinematics of six-DOF three-limbed parallel manipulator (PM) are presented. This PM is formed by connection of a mobile platform with a base by three dyads with cylindrical joints. Constant and variable parameters characterizing geometry of links and relative motions of elements of joints are defined. Direct kinematics of the PM is solved by iterative method.

**Keywords** Parallel manipulator · Limb · Geometry of link · Direct kinematics

## 1 Introduction

Most of the 6-DOF PM consist of six limbs (Merlet 2000; Gogu 2008–2014 and others). These PM possess the advantages of high stiffness, low inertia, and large payload capacity. However, such six-limbed fully PM have a limited workspace and complex kinematic singularities, which are their major drawbacks. Therefore in robotics literature (Yang et al. 2004; Mianovski 2007; Jin et al. 2009; Glazunov 2010 and other) a great interest to the PM with few number of limbs and larger workspace is observed.

---

Zh. Baigunchekov (✉) · T. Baigunchekov

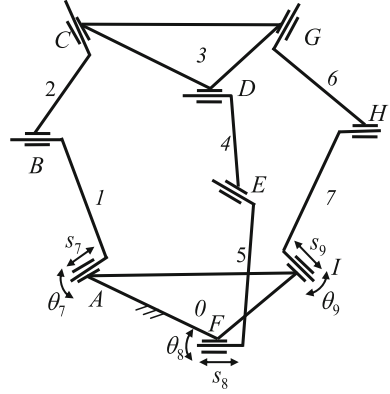
K.I. Satpayev Kazakh National Research Technical University, Almaty, Kazakhstan  
e-mail: bzh47@mail.ru

T. Baigunchekov  
e-mail: talgat.baigunchekov@gmail.com

M. Kalimoldaev  
Institute of Informatics and Computing Technologies, Almaty, Kazakhstan  
e-mail: mnk@ipic.kz

M. Utenov  
Al - Farabi Kazakh National University, Almaty, Kazakhstan  
e-mail: umu57@mail.ru

**Fig. 1** PM with cylindrical joints



Following the above-mentioned trends in the development of PM, we proposed a novel structure of six-DOF three-limbed PM with cylindrical joints (PM 3CCC) (Baigunchekov et al. 2009), as shown in Fig. 1. This PM is formed by connection of a mobile platform 3 with a base 0 by three spatial dyads  $ABC$ ,  $DEF$  and  $GHI$  of type CCC (C—cylindrical joint). Each of spatial dyads of type CCC do not impose restrictions on motion of the mobile platform, and six-DOF of the mobile platform are remained.

Each cylindrical joint has two-DOF: one rotation and one translation. In the considered PM the joints  $A$ ,  $F$  and  $I$  are active joints, and the joints  $B$ ,  $C$ ,  $D$ ,  $E$ ,  $G$  and  $H$  are passive joints. Six variable parameters  $s_7$ ,  $\theta_7$ ,  $s_8$ ,  $\theta_8$ ,  $s_9$ ,  $\theta_9$  of active joints  $A$ ,  $F$  and  $I$  are the generalized coordinates. The results of singularity analysis of the PM 3CCC are presented (Baigunchekov et al. 2012). In this paper the geometry of this PM is described and its direct kinematics is solved.

## 2 Geometry of the PM 3CCC

To describe the geometry of the PM 3CCC two right-hand Cartesian coordinate systems  $UVW$  and  $XYZ$  are attached to each element of each joint. The  $W$  and  $Z$  axes of the coordinate systems  $UVW$  and  $XYZ$  are directed along the axes of rotation and translation of the cylindrical joints.

Transformation matrix  $\mathbf{T}_{jk}$  between the coordinate systems  $U_jV_jW_j$  and  $X_kY_kZ_k$ , attached to the ends of the binary link with the  $j$ -th and  $k$ -th joints, has a form

$$\mathbf{T}_{jk} = \begin{bmatrix} t_{11} & t_{12} & t_{13} & t_{14} \\ t_{21} & t_{22} & t_{23} & t_{24} \\ t_{31} & t_{32} & t_{33} & t_{34} \\ t_{41} & t_{42} & t_{43} & t_{44} \end{bmatrix}, \quad (1)$$

where  $t_{11} = 1$ ,  $t_{12} = t_{13} = t_{14} = 0$ ,

$$\begin{aligned}
t_{21} &= a_{jk} \cdot \cos \gamma_{jk} + b_{jk} \cdot \sin \gamma_{jk} \cdot \sin \alpha_{jk}, \\
t_{22} &= \cos \gamma_{jk} \cdot \cos \beta_{jk} - \sin \gamma_{jk} \cdot \cos \alpha_{jk} \cdot \sin \beta_{jk}, \\
t_{23} &= -\cos \gamma_{jk} \cdot \sin \beta_{jk} - \sin \gamma_{jk} \cdot \cos \alpha_{jk} \cdot \cos \beta_{jk}, \\
t_{24} &= \sin \gamma_{jk} \cdot \sin \alpha_{jk}, \\
t_{31} &= a_{jk} \cdot \sin \gamma_{jk} - b_{jk} \cdot \cos \gamma_{jk} \cdot \sin \alpha_{jk}, \\
t_{32} &= \sin \gamma_{jk} \cdot \cos \beta_{jk} + \cos \gamma_{jk} \cdot \cos \alpha_{jk} \cdot \sin \beta_{jk}, \\
t_{33} &= \cos \gamma_{jk} \cdot \cos \alpha_{jk} \cdot \cos \beta_{jk} - \sin \gamma_{jk} \cdot \sin \beta_{jk}, \\
t_{34} &= -\cos \gamma_{jk} \cdot \sin \alpha_{jk}, \quad t_{41} = c_{jk} + b_{jk} \cdot \cos \alpha_{jk}, \\
t_{42} &= \sin \alpha_{jk} \cdot \sin \beta_{jk}, \quad t_{43} = \sin \alpha_{jk} \cdot \cos \beta_{jk},
\end{aligned}$$

$t_{44} = \cos \alpha_{jk}$ ,  $a_{jk}$ —a distance from the  $W_j$  axis to the  $Z_k$  axis measured along the direction of the common perpendicular  $t_{jk}$  between the  $W_j$  and  $Z_k$  axes;  $\alpha_{jk}$ —an angle between positive directions of the  $W_j$  and  $Z_k$  axes measured counterclockwise about positive direction of  $t_{jk}$ ;  $b_{jk}$ —a distance from direction of  $t_{jk}$  to direction of the  $X_k$  axis measured along the positive direction of the  $Z_k$  axis;  $\beta_{jk}$ —an angle between positive directions of  $t_{jk}$  and  $X_k$  axis measured counterclockwise about the positive direction of the  $Z_k$  axis;  $c_{jk}$ —a distance from direction of  $U_j$  axis to direction of  $t_{jk}$  measured along the positive direction of the  $W_j$  axis;  $\gamma_{jk}$ —an angle between positive directions of the  $U_j$  axis and  $t_{jk}$  measured counterclockwise about the positive direction of the  $W_j$  axis.

In comparison with the Denavit–Hartenberg transformation matrix, having four parameters, the transformation matrix (1) has six parameters fully characterizing the relative locations of the coordinate systems  $U_j V_j W_j$  and  $X_k Y_k Z_k$ , because a free rigid body in space has six generalized coordinates.

A binary link  $jk$  of type CC is shown in Fig. 2. Axes of the coordinate systems  $U_j V_j W_j$  and  $X_k Y_k Z_k$ , attached to the ends of this binary link, are chosen as follows: the  $W_j$  and  $Z_k$  axes are located along the axes of rotation and translation of the cylindrical joints  $j$  and  $k$ ; the origins  $O_j$  and  $O_k$  of the coordinate systems  $U_j V_j W_j$  and  $X_k Y_k Z_k$  are located in points of intersection of the  $W_j$  and  $Z_k$  axes with the common perpendicular  $t_{jk}$  between these axes; the  $U_j$  and  $X_k$  axes are located along the common perpendicular  $t_{jk}$ ; the  $V_j$  and  $Y_k$  axes are completed the right-hand Cartesian coordinate systems  $U_j V_j W_j$  and  $X_k Y_k Z_k$ .

At such choice of the coordinate systems  $U_j V_j W_j$  and  $X_k Y_k Z_k$  nonzero parameters of the matrix  $\mathbf{T}_{jk}$  are  $a_{jk}$  and  $\alpha_{jk}$ . Then from the matrix (1) we obtain a matrix of the binary link  $jk$  of type CC

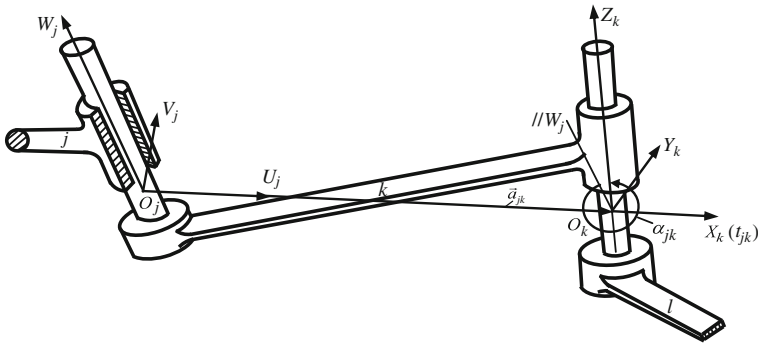


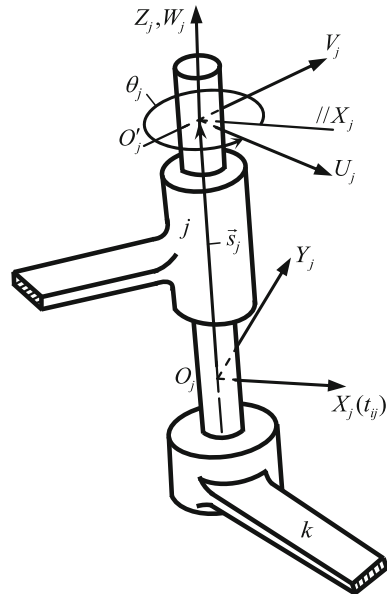
Fig. 2 Binary link  $jk$  of type CC

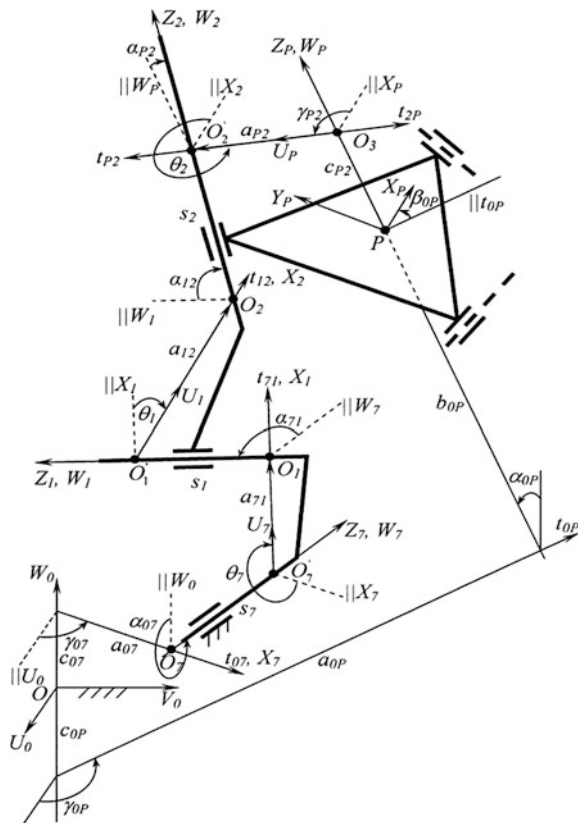
$$G_{jk}^{CC} = \begin{bmatrix} 1 & 0 & 0 & 0 \\ a_{jk} & 1 & 0 & 0 \\ 0 & 0 & \cos \alpha_{jk} & -\sin \alpha_{jk} \\ 0 & 0 & \sin \alpha_{jk} & \cos \alpha_{jk} \end{bmatrix}, \quad (2)$$

where parameters  $a_{jk}$  and  $\alpha_{jk}$  are constant, and they characterize the geometry of the binary link  $jk$  of type CC.

Nonzero parameters of the cylindrical joint  $j$  shown in Fig. 3 are  $\theta_j$  and  $s_j$ . Then from the matrix (1) we obtain a matrix of the cylindrical joint  $j$

Fig. 3 Cylindrical joint  $j$



**Fig. 4** The first limb


$$\mathbf{P}_j^C(\theta_j, s_j) = \begin{bmatrix} 1 & 0 & 0 & 0 \\ 0 & \cos \theta_j & -\sin \theta_j & 0 \\ 0 & \sin \theta_j & \cos \theta_j & 0 \\ s_j & 0 & 0 & 1 \end{bmatrix}, \quad (3)$$

where  $s_j$ —a distance from the  $X_j$  axis to the  $U_j$  axis measured along the directions of the  $Z_j$  and  $W_j$  axes;  $\theta_j$ —an angle between the positive directions of the  $X_j$  and  $U_j$  axes measured counterclockwise about the positive directions of the  $Z_j$  and  $W_j$  axes. Parameters  $s_j$  and  $\theta_j$  are variable, and they characterize relative translation and rotation motions of the  $j$ -th cylindrical joint elements.

Choosing the coordinate systems  $UVW$  and  $XYZ$ , as shown in Figs. 2 and 3, the constant and variable parameters of the PM 3CCC have been obtained. Constant and variable parameters of the first limb  $ABC$  of the PM 3CCC are shown in Fig. 4, where  $\theta_7$  and  $s_7$  are the generalized coordinates of the active joint  $A$ ;  $\theta_2$ ,  $s_2$  and  $\theta_3$ ,  $s_3$  are the variable parameters of the passive joints  $B$  and  $C$ ; all other parameters are the constant parameters characterizing the geometry of links. Constant and variable parameters of two other symmetrical legs are defined similarly.

### 3 Direct Kinematics

In direct kinematics of the PM 3CCC position of coordinate system  $X_P Y_P Z_P$  attached to the mobile platform 3 are defined with respect to the base frame  $U_o V_o W_o$  by known constant geometrical parameters of the links and the generalized coordinates  $s_i, \theta_i, (i = 7, 8, 9)$ .

For automation of calculation of the direct kinematics we use following designations:  $n$ —number of mobile links,  $m$ —number of input links,  $L$ —number of the closed loops,  $n_l$ —number of links in the  $l$ -th loop ( $l = 1, 2, \dots, L$ ),  $(l, a)$ —index of the  $a$ -th link in the  $l$ -th loop. Dependent variable parameters of the passive joints  $h_{(l,a)}^{(\omega)}$  are numerated  $1, 2, \dots, n - m$ , independent variable parameters of the active joints  $q_{(l,a)}^{(\omega)}$  are numerated  $n - m + 1, n - m + 2, \dots, n$ , where  $\omega$ —number of DOF of the joint  $(l, a)$ . For the considered PM 3CCC  $n = 7, m = 3, L = 2, n_1 = n_2 = 6, \omega = 2$ . PM 3CCC has two closed loops  $ABCDEF A$  and  $ABCGHIA$ .

Let made a Table 1 of conformity between the numbers of links and joints of the PM 3CCC.

Using the Table 1 of conformity between the numbers of links and joints we can write the loop-closure equations of the loops  $ABCDEF A$  and  $ABCGHIA$

$$\left. \begin{aligned} \mathbf{M}_{71} \cdot \mathbf{M}_{12} \cdot \mathbf{M}_{23} \cdot \mathbf{M}_{34} \cdot \mathbf{M}_{48} \cdot \mathbf{M}_{87} &= \mathbf{E} \\ \mathbf{M}_{71} \cdot \mathbf{M}_{12} \cdot \mathbf{M}_{25} \cdot \mathbf{M}_{56} \cdot \mathbf{M}_{69} \cdot \mathbf{M}_{97} &= \mathbf{E} \end{aligned} \right\} \quad (4)$$

or

$$\mathbf{M}_{l,1} \cdot \mathbf{M}_{l,2} \cdot \dots \cdot \mathbf{M}_{l,a} \cdot \dots \cdot \mathbf{M}_{l,n_l} = \mathbf{E}; \quad l = 1, 2, \quad (5)$$

where  $\mathbf{E}$  is a unit matrix,  $\mathbf{M}_{jk} = \mathbf{P}_{jk}^C \cdot \mathbf{G}_{jk}^{CC}, j, k = 1, 2, \dots, 9$ .

For the direct kinematics of the PM 3CCC the iterative method (Uicker et al. 1964) is used. According to this method unknown dependent variable parameters  $h_{(l,a)}^{(\omega)}$  are written through their initial approaches  $h_{(l,a)}^{(\omega)*}$  and deviations  $dh_{(l,a)}^{(\omega)}$  by expression

$$h_{(l,a)}^{(\omega)} = h_{(l,a)}^{(\omega)*} + dh_{(l,a)}^{(\omega)}, \quad (6)$$

where  $h_{(l,a)}^{(\omega)} \in \theta_{l,a}, s_{l,a}$ .

**Table 1** Conformity between the numbers of links and joints

$l$	1	1	1	1	1	1	2	2	2	2	2	2
$a$	1	2	3	4	5	6	1	2	3	4	5	6
$(l, a)$	7	1	2	3	4	8	7	1	2	5	6	9

The system of matrix Eq. (5) are transformed to the system of linear equations, from which the deviations  $dh_{(l,a)}^{(\omega)}$  are determined. Adding the determined deviations to their previous values, more exact values of the passive joints variable parameters have been obtained.

Position of the coordinate system  $X_P Y_P Z_P$  attached to the mobile platform 3 with respect to the base coordinate system  $U_o V_o W_o$  can be defined by matrix  $\mathbf{S}_P$

$$\mathbf{S}_P = \mathbf{G}_{07} \cdot \mathbf{M}_{71} \cdot \mathbf{M}_{12} \cdot \mathbf{M}_{23} \cdot \mathbf{G}_{3P}, \quad (7)$$

where  $\mathbf{G}_{07}$  is a transformation matrix between the coordinate system  $X_7 Y_7 Z_7$  and the absolute coordinate system  $U_o V_o W_o$ ,  $\mathbf{G}_{3P}$  is a transformation matrix between the coordinate systems  $X_P Y_P Z_P$  and  $X_3 Y_3 Z_3$  of the mobile platform 3.

## 4 Conclusions

A novel six-DOF three-limbed PM 3CCC is formed by connection of the mobile platform with the base by three spatial dyads with cylindrical joints. Constant and variable parameters of the PM 3CCC are defined on the basis of the transformation matrix of two systems of coordinates attached to each element of each joints. Constant parameters characterize geometry of links, and variable parameters characterize relative motions of the joint elements. The loop-closure matrix equations of the PM 3CCC are made up. The direct kinematics of the PM 3CCC is solved by iterative method of solution of the loop-closure matrix equations.

## References

- Baigunchekov, Z., Ceccarelli, M., et al. (2009). *Parallel Manipulator*, Patent No. 20725, Republic of Kazakhstan.
- Baigunchekov, Z., Izmambetov, M. (2012). Singularity analysis of parallel manipulator with cylindrical joints. In *Proceedings of the World Congress on Engineering WCE 2012*, London, UK, 4–6 July (Vol. 3, pp. 1733–1737).
- Glazunov, V. (2010). Design of decoupled parallel manipulators by means of the theory of screws. In *Mechanism and Machine Theory* (No. 45, pp. 239–250).
- Gogu, G. (2008–2014). *Structural Synthesis of Parallel Robots*, Parts 1–5. Dordrecht, Heidelberg, London, New-York: Springer.
- Jin, Y., Chen, I. M., & Yang, G. (2009). Kinematic design of a family of 6-DOF partially parallel manipulators. In *Mechanism and Machine Theory* (No. 44, pp. 912–922).
- Merlet, J. P. (2000). *Parallel Robots*. Dordrecht, Boston, London: Kluwer Academic Publishers.
- Mianovski, K. (2007). Singularity analysis of parallel manipulator POLMAN  $3 \times 2$  with Six degrees of freedom. In *Proceedings of the 12th IFToMM World Congress*, Besançon, France, June 18–21, 2007.

- Uicker, J. J., et al. (1964). An iterative method for the displacement analysis of spatial mechanisms. *Journal of Applied Mechanics*, 31. Trans. ASME Series E, 86, 309–314.
- Yang, G., Chen, I. M., Chen, W., & Lin, W. (2004). Kinematic design of six-DOF parallel-kinematics machine with decoupled-motion architecture. *IEEE Transactions on Robotics*, 20(20), 876–884.



# Learning Global Inverse Kinematics Solutions for a Continuum Robot

Thomas George Thuruthel, Egidio Falotico, Matteo Cianchetti  
and Cecilia Laschi

**Abstract** This paper presents a learning based approach for obtaining the inverse kinematics (IK) solution for continuum robots. The proposed model learns a particular global solution for IK problem by supervised learning without any prior knowledge about the system. We have developed an approach that solely relies on the sampling method and a unique IK formulation. The convergence of the solution, practically feasible sample data requirements and adaptability of the model is shown with simulations of a redundant continuum robot.

## 1 Introduction

Most robotic applications rely on task space controllers. The primary objective of such controllers is to guide the end effector trajectory, in case of manipulators, or the center of mass trajectory for legged locomotion. However, since these controllers can only act directly on the actuator space, a causal mapping between the task space and actuator space is required. Inverse Kinematic mappings are used to derive the configuration space coordinates given the task space coordinates.

Inverse kinematic models have been extensively studied for rigid bodied robots by using analytical and machine learning methods. Although analytical approaches, like iterative methods and inverse transform methods, have been fairly successful, they have fared poorly for complex systems. As expected, soft robots have been

---

T.G. Thuruthel (✉) · E. Falotico · M. Cianchetti · C. Laschi  
The BioRobotics Institute Scuola Superiore Sant'Anna, Pisa, Italy  
e-mail: thomasgeorge2571766@gmail.com

E. Falotico  
e-mail: e.falotico@sssup.it

M. Cianchetti  
e-mail: matteo.cianchetti@sssup.it

C. Laschi  
e-mail: cecilia.laschi@sssup.it

even more difficult to model analytically. Owing to their infinite degrees of freedom and elastic nature, even developing forward models have turned out to be difficult. There have been few developments in developing forward models based on piecewise constant curvature models (Webster and Jones 2010) and non-constant curvature models (Cianchetti and Laschi 2014). However, developing the inverse model would be even more challenging, although, there have been recent successes (Marchese et al. 2014). We believe that a machine learning approach would be better for complex soft robotic systems not only because of their ease of application and generalization ability but also because of their ability to adapt to changes in the starting system.

Like their rigid counterpart, learning the inverse kinematics model of soft bodies offers two major problems. Firstly, there exists an infinite number of possible solutions to the non-homogenous inverse kinematics equation for redundant systems. The other is related to the non-convexity of the solution set. A path based sampling approach for learning the inverse kinematics was used in Rolf et al. (2010). Their approach of using goal babbling for sampling enabled efficient detection and resolution of inconsistent samples. Further in (Rolf and Steil 2013), they have used this approach to learn the inverse kinematics of the bionic handling assistant. However, this approach still does not guarantee a global solution to the IK problem and the goal directed exploration leads to highly redundant learning data. Another approach is to develop multiple locally learned models to estimate the inverse kinematics (D'Souza et al. 2001; Vannucci et al. 2015; Susumu and Tachi 2001; Laschi 2014). The idea behind these approaches is the fact that IK solutions form a convex set in a spatially local set. In D'Souza et al. (2001), they have augmented the input representation to the inverse model for learning an appropriate particular solution to the IK problem by adding additional cost functions. Nonetheless, their method involves learning the differential inverse kinematics which leads to drifting of error during integration. Distal supervised learning approaches have also been applied for the IK learning problem in (Benoudjit 2014; Jordan and Rumelhart 1992). However, indirect training of the inverse model in this way is difficult due to local minima problems, instability and presence of inaccuracies in the forward model. Another interesting research is the use of structured prediction for resolving the ill-posed IK problem (Peters 2011). But this method would not adapt well to changes in the original system and would not scale well with higher dimensional systems.

In this paper we try to address the shortcomings of the existing approaches. We propose a global solution to learning the IK problem by appropriately biasing and selecting the input/output representation to the learning system, similar to (D'Souza et al. 2001). However, unlike D'Souza et al. (2001), we learn the inverse kinematics on the position level. We are using a simple multi-layer perceptron as a function approximator, although, the method is independent of the learning architecture. We have tested the method on a kinematic simulator of the bionic handling assistant (BHA) (Steil 2012). We demonstrate the adaptable nature of the learned IK model and efficiency of the algorithm with respect to the amount of sample data required.

## 2 Formulation of the Inverse Kinematics Learning Problem

A straightforward representation for learning the IK of a system would be to generate samples of  $(q, x)$ , where,  $x \in \mathfrak{R}^m$ , is the vector containing the coordinates of the end effector and  $q \in \mathfrak{R}^n$ , is the vector containing the joint space configuration vector, and to learn the mapping  $x \rightarrow q$ . Since there are infinite number of such functions, the learning system will learn a particular function depending on the sample data, averaging over samples that map to the same output ( $x$ ). However, naively learning such a system will lead to errors due to the non-convexity of the solution set. As mentioned in D'Souza et al. (2001), the differential IK formulation (1) forms a convex solution set locally.

$$\dot{x} = J(q)\dot{q} \quad (1)$$

where,  $J$  is the Jacobian matrix. A differential IK learning system would approximate the mapping  $(\dot{x}, q) \rightarrow (\dot{q})$ . The limitations of this approach have been discussed before. The proposed method can be understood more clearly from the Taylor series expansion of the forward kinematics equation given in (2)

$$\Delta x = J(q)\Delta q + \Delta q^T H(q)\Delta q + \dots \quad (2)$$

Here  $H$  is the Hessian matrix. Now, for small changes in  $q(\Delta q)$ , Eq. (2) can be approximated by (3). Note that this approximation becomes more erroneous as the value of the  $\Delta q$  increases.

$$\Delta x \approx J(q)\Delta q \quad (3)$$

Learning the mapping  $(\Delta x, q) \rightarrow (\Delta q)$  would be very similar to learning the differential inverse kinematics. However, now we are no longer dealing with IK problem in the velocity level. The non-convexity of the solution set is still maintained, at least reasonably, as long as  $\Delta x$  is small (spatially localized). The non-convex properties break down if we consider the higher order elements, hence the need for the approximation. Once the mapping is learned, we can incrementally add up local solutions to reach a desired end effector point. However, this method will still have the same shortcomings of the differential IK approach. Additionally, since the value of  $\Delta x$  and  $\Delta q$  is bounded during the learning process, using input values which are greater than that used during learning while testing will lead to undesirable behavior. Consequently, we modify the learning variables to develop a more practical and effective mapping. Equation (3) can be expanded and represented as shown below:

$$J(q_i)q_{i+1} = x_{i+1} - f(q_i) + J(q_i)q_i \quad (4)$$

This simple rearrangement now presents the learning algorithm with a new mapping;  $(x_{i+1}, q_i) \rightarrow (q_{i+1})$ . Where,  $q_{i+1}$  is the joint configuration that archives the end effector position  $x_{i+1}$ . Now if a neural network is trained for approximating this mapping while ensuring the spatial locality in the sample data (by keeping  $|q_{i+1} - q_i| < \epsilon$ ), it will have all properties of the mapping learned based on Eq. (3). In addition, and more importantly, now the inputs and outputs are bounded only by the kinematic constraints of the system; i.e. the inputs and outputs belongs to target space and configuration space and not a subset of it. This enables us to provide target positions for the end effector which is much farther away from local region and still obtain a corresponding joint configuration that brings the end effector closer to the target position. After each step, the end effector position will come closer to the target position as the accuracy of the IK approximator increases as  $|x_{i+1} - x_i|$  decreases, until convergence. Therefore, because of our unique formulation, we can get IK solutions for any point in the task space irrespective of its locality from the starting point, unlike the case of differential IK solvers.

### 3 Training the Neural Network

For approximating the function that maps the current joint configuration and next end effector to the next joint configuration we are using a multilayer perceptron with Tan-sigmoid transfer function in the hidden layer and a linear transfer function in the output layer. Bayesian regularization backpropagation method is used for training the neural network. The inputs and outputs are normalized in the pre-processing stage and divided randomly into sets for training and testing in the ratio 70:30 respectively. A validation test is generally not used as the algorithm prevents overfitting by Bayesian regularization (Hagan 1997) (Fig. 1).

**Robot Model.** The training data is obtained from a kinematic model of the BHA (Steil 2012). The model uses a constant curvature approximation for modelling the

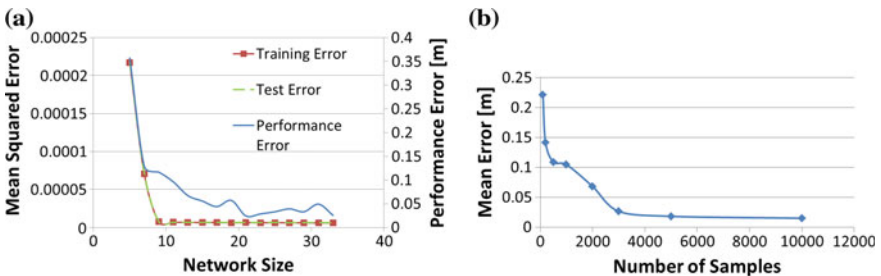
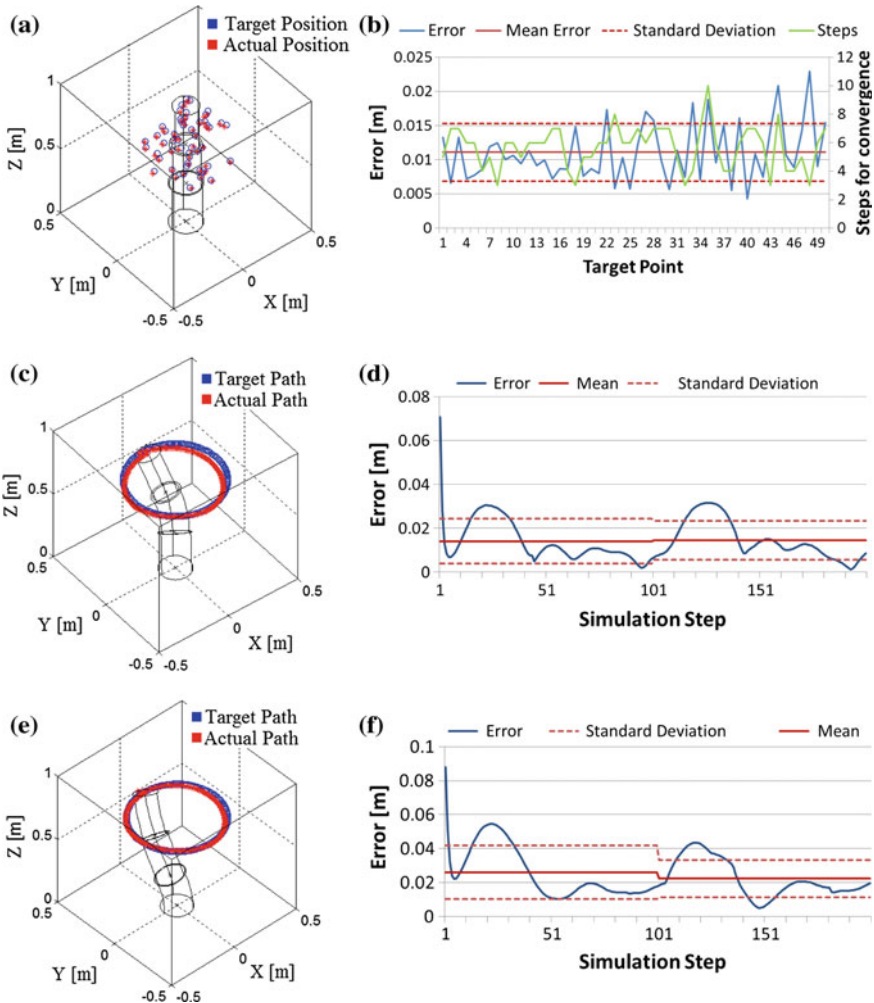


Fig. 1 a Neural network selection, b Performance of IK solver with number of samples

continuum kinematics of the manipulator. The robot is composed of three segments; each segment is actuated by the three pneumatic actuators. The kinematic model takes in as input the length of each actuator and outputs the three dimensional coordinates of the end effector with respect to a reference frame fixed at the origin. Figure 2a shows the schematic of the BHA. The model is a very good representation of the real BHA with a relative error of 1 %.



**Fig. 2** a Fifty randomly selected target points and their IK solutions, b Error values for each target point with their steps for convergence, c Trajectory tracking experiment and results, d Error values with mean and standard deviation for each rotation (100 steps), e Trajectory tracking experiment with last three joints fixed, f Error values with mean and standard deviation for each rotation (100 steps)

**Training data.** Sample data are obtained by continuous motor babbling. The soft and continuous nature of soft robots makes it a safe exploration strategy. This would be the easiest way to ensure that all the solution space of the IK problem is reached, although, probably not the most efficient. Nevertheless, motor babbling would provide more information than goal babbling. The input/output pairs are generated ensuring that  $|q_{i+1} - q_i| < \epsilon$ , where  $\epsilon$  is decided by trial and error. Keeping  $\epsilon$  too low will increase the amount of samples required for learning and keeping it high will affect the convex nature of the solution set. Also, random noise, ranging from  $\pm 2\%$  of the soft manipulator length ( $\pm 17$  mm) is added to the actual end effector position to simulate real world conditions (Rolf and Steil 2013). The artificially added noise also helps in avoiding overfitting while learning. The size of the neural network is determined by training a fixed sample data with increasing network size. The training and testing errors are recorded along with the performance error of the IK solver, which is obtained by checking the solution provided by the IK solver for a fixed fifty end effector targets (Fig. 1a). Finally, the lowest network size which provides the preferred behavior is selected (20, in our case). Figure 1b shows the performance of the IK solver with respect to the number of required samples, again, for fifty random target points. These tests are performed as follows: the manipulator starts at an upright home position  $[0, 0, 0.9 \text{ m}]$  and then the IK solver estimates the solutions for reaching each target point. The error shown in Fig. 1b is the final distance between the target position and end effector position. The proposed method requires significantly less samples for learning the IK when compared to (Rolf and Steil 2013), in spite of the higher noise added.

## 4 Simulations and Analysis

Three types of experiments are conducted on the learned IK model to validate and analyze the proposed approach. The first one is a simple ‘reaching a point’ simulation. Fifty points are randomly chosen (Fig. 2a) and the IK solver gives its estimate of the joint configurations. The forward model is used to compare the desired positions and the IK estimates. The errors along with the mean and standard deviation are shown in Fig. 2b. Since the points are not near to the starting point, the solver takes an average of 5.68 steps to converge to a value within a range of 1 mm with a standard deviation of 1.504.

The second experiment is a circular trajectory tracking simulation. The target trajectory is a circle centered at  $[0, 0, 0.7 \text{ m}]$  with a radius of 0.2 m and the end effector starting at the home position  $[0, 0, 0.9 \text{ m}]$ . The same path is followed twice. The path is discretized into 200 individual points, 100 points for one rotation. Figure 2c shows a comparison of the path derived from the IK solver with the target path. Figure 2d shows the magnitude of error in following the path along with the mean and standard deviation for each rotation. The large error in the beginning is

because the manipulator starts from the home position which is away from the target path.

The final simulation has the same circular target trajectory, but with the last three joints locked at a fixed value. The IK solver is given no knowledge about the freezing of the three joints. Therefore, the IK solver still outputs the next configuration for all the joints in each iteration, however, only the first six joints will be modified accordingly and the last three joints will maintain their initial configuration. The trajectory followed in this new setting is shown in Fig. 2e. The corresponding absolute errors with mean and standard deviation for each rotation are shown in Fig. 2f. Note that for the last two experiments only one step is needed to get the appropriate IK solution as the target points are nearby.

The results show that solutions provided by the IK solver are still good despite losing three degrees of actuation. This shows that the IK solver is able to provide a meaningful solution at any joint configuration. However, note that this is only possible because of the redundancy present in the system. Interestingly, this means that we could exploit the redundancy of the system for executing secondary tasks, by compromising correspondingly on the primary task.

## 5 Conclusion

In this paper, we have proposed an approach for learning a particular global IK solution for a redundant continuum robot. Our method differs from the countless others solely based on the sampling approach and the unique IK formulation. The particular solution selected is dependent on the sample data and the generalization properties of the neural network. We have proved with the help of realistic simulations, that the learned IK solution is truly robust, stable and global. This learned IK solutions can now be used for control. Since the IK solution does not depend on the load acting on the system and other parameters like friction, this can be directly used for controlling the position of a soft robot, provided that the forward kinematics is well defined. Simple PID controllers can be used to control the joint configuration as prescribed by the IK solver. The joint dynamics can be considered independent of each other, making it easy to control each of the joint parameters separately. Moreover, the same approach can be used for learning the inverse statics of continuum robots. Researchers have been able to learn the inverse statics of continuum robots for a non-redundant case (Giorelli et al. 2015). We believe that our approach can be easily extended for learning the inverse statics of a redundant continuum robot also.

**Acknowledgement** The authors would like to acknowledge the support by the European Commission through the I-SUPPORT project (HORIZON 2020 PHC-19, #643666). The authors would like to thank Italian Ministry of Foreign Affairs, General Directorate for the Promotion of the “Country System”, Bilateral and Multilateral Scientific and Technological Cooperation Unit, for the support through the Joint Laboratory on Biorobotics Engineering project.

## References

- Botond, B., Nguyen-Tuong, D., Csato, L., Bernhard, S. & Peters, J. (2011) Learning inverse kinematics with structured prediction. In *IEEE/RSJ International Conference on Intelligent Robots and Systems (IROS)* (pp. 698–703).
- D'Souza, A., Vijayakumar, S., & Schaal, S. (2001). Learning inverse kinematics. *Proceedings, IEEE/RSJ International Conference on Intelligent Robots and Systems, 1*, 298–303.
- Foresee, F. D. & Hagan, M. T. (1997) Gauss-Newton approximation to Bayesian regularization. In *Proceedings of the 1997 International Joint Conference on Neural Networks* (pp. 1930–1935).
- Giorelli, M., Renda, F., Calisti, M., Arienti, A., Ferri, G., & Laschi, C. (2015). Neural network and jacobian method for solving the inverse statics of a cable-driven soft arm with nonconstant curvature. *IEEE Transactions on Robotics, 31*(4), 823–834.
- Jordan, M., & Rumelhart, D. (1992). Forward models: Supervised learning with distal teacher. *Cognitive Science, 16*, 307–354.
- Renda, F. Giorelli, M. Calisti, M. Cianchetti, M. & Laschi, C. (2014) Dynamic model of a multi-bending soft robot arm driven by cables. *IEEE Transactions on Robotics 30*, 1109–1122.
- Marchese, A. D., Komerowski, K., Onal, C. D., Rus, D. (2014). Design and control of a soft and continuously deformable 2D robotic manipulation system. In *Proceedings of the IEEE International Conference on Robotics and Automation* (pp. 2189–2196).
- Melingui, A., Merzouki, R., Mbede, J. B., Escande, C. & Benoudjit, N. (2014) Neural networks based approach for inverse kinematic modeling of a compact bionic handling assistant trunk. In *IEEE 23rd International Symposium on Industrial Electronic* (pp. 1239–1244).
- Rolf, M. & Steil, J. J. (2012) Constant curvature continuum kinematics as fast approximate model for the Bionic Handling Assistant. In *IEEE/RSJ International Conference on Intelligent Robots and Systems (IROS)* (pp. 3440–3446).
- Rolf, M., & Steil, J. J. (2013). Efficient exploratory learning of inverse kinematics on a bionic elephant trunk. *Neural Networks and Learning Systems, IEEE Transactions on, 25*(6), 1147–1160.
- Rolf, M., Steil, J. J., & Gienger, M. (2010). Goal babbling permits direct learning of inverse kinematics. *IEEE Transactions on Autonomous Mental Development, 2*(3), 216–229.
- Susumu, E. O. & Tachi, S (2001) Inverse kinematics learning by modular architecture neural networks. In *Proceedings of IEEE International Conference on Robotics and Automation* (pp. 1006–1012).
- Vannucci, L., Cauli, N., Falotico, E., Bernardino, A. & Laschi, C. (2014) Adaptive visual pursuit involving eye-head coordination and prediction of the target motion. In *Proceedings of the 14th IEEE-RAS International Conference on Humanoid Robots (Humanoids 2014)* (pp. 541–546). : IEEE.
- Vannucci, L., Falotico, E., Di Lecce, N., Dario, P. & Laschi, C. (2015). Integrating feedback and predictive control in a bio-inspired model of visual pursuit implemented on a humanoid robot. In *Lecture Notes in Computer Science (including subseries Lecture Notes in Artificial Intelligence and Lecture Notes in Bioinformatics)*, (vol. 9222, pp. 256–267).
- Webster, R. J., & Jones, B. A. (2010). Design and kinematic modeling of constant curvature continuum robots: A review. *International Journal of Robotics Research, 29*, 1661–1683.



# A Study of a Wheel Shape for Increasing Climbing Ability of Slopes and Steps

**K. Tanaka, H. Ishii, D. Endo, J. Mitsuzuka, D. Kuroiwa, Y. Okamoto, Y. Miura, Q. Shi, S. Okabayashi, Y. Sugahara and A. Takanishi**

**Abstract** The objective of this study was to design a new model of wheel shape for increasing climbing ability of slopes and steps. We made a new model using a statics for calculating the ability easily and found that the arc-shaped notch type seems to be the best and implemented to our robot. In this paper, we introduce the detail of the proposed model and simulation results.

**Keywords** Wheel shape · Locomotion performance · Mobile robot

---

K. Tanaka (✉) · H. Ishii · D. Endo · J. Mitsuzuka · D. Kuroiwa · Y. Okamoto  
Y. Miura · A. Takanishi  
Department of Science and Engineering, Waseda University, Tokyo, Japan  
e-mail: [waseda-tanaka@toki.waseda.jp](mailto:waseda-tanaka@toki.waseda.jp)

H. Ishii  
e-mail: [hiroyuki@aoni.waseda.jp](mailto:hiroyuki@aoni.waseda.jp)

D. Endo  
e-mail: [daiki7091@gmail.com](mailto:daiki7091@gmail.com)

J. Mitsuzuka  
e-mail: [murasakiimo@akane.waseda.jp](mailto:murasakiimo@akane.waseda.jp)

D. Kuroiwa  
e-mail: [changeup@toki.waseda.jp](mailto:changeup@toki.waseda.jp)

Y. Okamoto  
e-mail: [yuya\\_okamoto@fuji.waseda.jp](mailto:yuya_okamoto@fuji.waseda.jp)

Y. Miura  
e-mail: [u390862@gmail.com](mailto:u390862@gmail.com)

A. Takanishi  
e-mail: [takanisi@waseda.jp](mailto:takanisi@waseda.jp)

Q. Shi  
Intelligent Robotics Institute and School of Mechatronical Engineering,  
Beijing Institute of Technology, Beijing, China  
e-mail: [shiqing@bit.edu.cn](mailto:shiqing@bit.edu.cn)

# 1 Introduction

Locomotion performance is one of the main issues for land-based mobile robot. A lot of studies focused on this ability and a lot of mechanisms have developed to suit a variety of environments and applications. Our research group also have studied on locomotion performance in developing an environmental monitoring system using multiple mobile robots outdoors such as forest and riverside area. The locomotive ability of climbing slopes and steps are required in this environment where a lot of obstacles are located.

We have developed a platform called WAMOT (Waseda Animal Monitoring robot) that have high mobility on uneven terrain using only two motors (Tanaka et al. 2014a). We have already proposed a new leg shape: elliptic leg that is in the middle of the wheel and the leg (Tanaka et al. 2014b). However, the maximum climbing ability of the slopes of the robot: 18 [deg] was so low that we could not operate the robot at particular area where the slope gradient is large, though that of the steps was very high.

In previous research, a lot of wheel shapes are proposed to suit the target environment. Loper used Tri-Lobe wheel that three small wheels mounted to a central hub (Herbert et al. 2008). CLOVER used special wheel like gear and used in a volcanic environment (Nagatani et al. 2014). These mechanisms are useful in each environment, but these wheels mechanisms have not well maintained using mechanical model and not meet our target environment. Spoke type wheel is well known as simple wheel and a lot of studies are focused on its climbing steps performance and its stability (Smith et al. 1998; Shankar et al. 2013). However, almost of these studies have not mentioned the way for satisfying both these climbing abilities.

The objective of this study was to design a new model of wheel shape for increasing climbing ability of slopes and steps. We made a new model with a statics in order to calculate the ability easily and considered whether the model is accurate or not by using dynamics simulation. Four wheeled and symmetrical designed robots were used for making the model because we consider that this type is the most general in mobile robots. Finally, we implemented an arc-shaped notch wheel to the WAMOT (Fig. 1) because we found that this type of wheel is best in terms of climbing ability of slopes and steps.

---

S. Okabayashi

Department of Fashion Sociology, Bunka Gakuen University, Tokyo, Japan  
e-mail: sook@aoni.waseda.jp

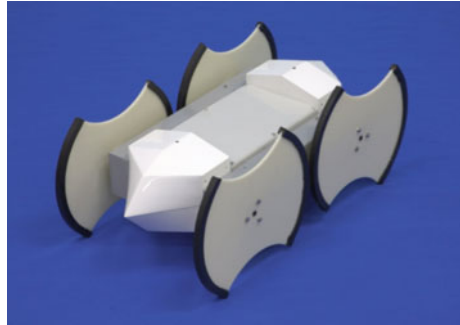
Y. Sugahara

Department of Mechanical Sciences and Engineering,  
Tokyo Institute of Technology, Tokyo, Japan  
e-mail: sugahara@mech.titech.ac.jp

A. Takanishi

Humanoid Robotics Institute (HRI), Waseda University, Tokyo, Japan

**Fig. 1** WAMOT with an arc-shaped notch type wheel



## 2 Overall Design of WAMOT

New type of WAMOT (Fig. 1) has four wheels and the two wheels on each of the left and right sides are connected by a timing pulley. Therefore, they move at the same speed and the robot has only two motors. The wheels can be replaced easily, we can compare the different type of wheel to understand each characteristic.

The robot is designed symmetrical about three axes, this can simplify the control of the robot and reduce the producing cost. The outer covering was attached to the robot for increasing the grass penetration ability, this is effective for moving grassy fields such as riverside and forest.

The two motors (30 W of ECi40, Maxson) of the robots are speed controlled by the motor control board (ESCON 24/3, Maxson) and programmed to move forward on the other board (Genuino Uno Rev3, Arduino). A 4300 mAh Li-Po battery is mounted on the robot and can drive it forward for about 4 h.

## 3 A Study on a New Wheel Shape

### 3.1 A Study of Climbing Steps

The wheel shape is greatly affected to the climbing steps. Comparison of three wheel shapes in terms of climbing steps ability is introduced in this section. In general, the robot cannot get high friction to the ground outdoors, so we assume that the robot cannot climb with only friction force.

Figure 2a shows a climbing steps of a circle type wheel. The maximum height potential of the climbing steps ( $H_{max}$ ) is as follows;

$$H_{max} = r \tag{1}$$

where  $r$  is wheel radius.

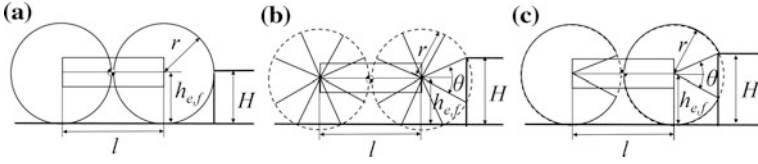


**Fig. 2** Comparison of three types of wheel in terms of climbing steps ability. This is the first phase of climbing

Figure 2b, c show a climbing steps of spoke and notch type. Since there is a prong hook on the wheel, the robot can climb the steps higher than its own height of wheel axis. However,  $H_{max}$  become down a little at spoke type because prong hook also can down the position of the forward axis ( $h_{e,f}$ ).  $H_{max}$  at spoke type is as follows;

$$H_{max} = r(\cos \frac{\theta}{2} + \sin \frac{\theta}{2}) \quad (2)$$

where  $\theta$  is the notch angle of the wheel.

When the circular part is touched to the ground during the robot climbing at notch type,  $H_{max}$  become larger.

$$H_{max} = r(1 + \sin \frac{\theta}{2}) \quad (3)$$

$H_{max}$  shows the maximum height potential of climbing ability of the robot. The robot can climb high step when the center of the gravity is at a forward and downward.

When the robot to climb up to the last, we have to consider the rear wheel. The effective length between the axis of the rear wheel and the contact point to the step ( $l_e$ ) should be shorter than that of between the axis and the center of gravity ( $l_g$ ).

Assuming that the center of gravity is located the center of the robot, the robot can finish climbing the step when the  $H$  meet the following formula.

$$\sqrt{r^2 - (H - h_{e,b})^2} < \frac{l}{2} \sin(\arctan(\frac{H}{l})) \quad (4)$$

where  $l$  is the length of the robot,  $h_{e,b}$  is the position of backward axis.

### 3.2 A Study of Climbing Slopes

The wheel shape is also greatly affected to the climbing slopes. Comparison of three wheel shapes in terms of climbing slopes ability is introduced in this section.

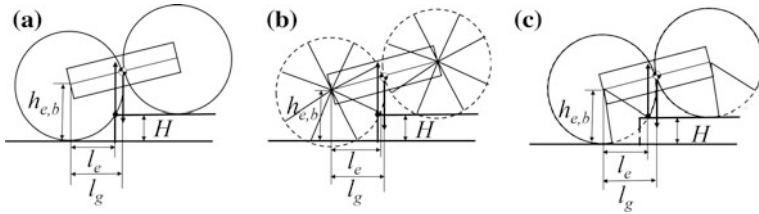


**Fig. 3** Comparison of three types of wheel in terms of climbing steps ability. This is the final phase of climbing. **a** Circle type **b** Spoke type **c** Notch type

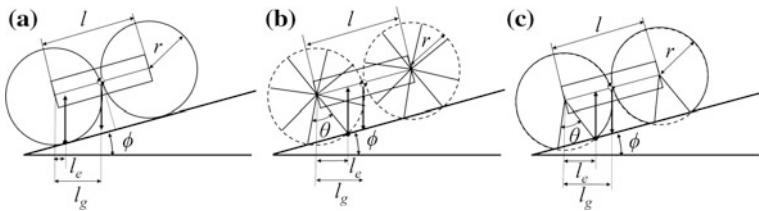


**Fig. 4** Comparison of three types of wheel in terms of climbing slopes ability. **a** Circle type **b** Spoke type **c** Notch type

We assume that the robot climb at so slow speed that we have not to consider the effect of acceleration.

Figure 3a shows a climbing slope of circle type wheel. In general, circle type has high climbing ability. The maximum angle of the climbing steps  $\phi_{max}$  is as follows (Fig. 4);

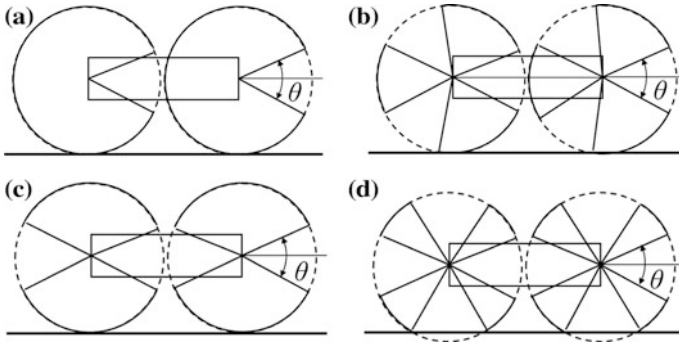
$$\phi_{max} = \arctan\left(\frac{l}{2r}\right) \tag{5}$$

Figure 3b, c show a climbing slope of spoke and notch type. There are prong hook on the wheel,  $l_e$  should be shorter than  $l_g$ . The maximum angle of the climbing steps  $\phi_{max}$  is as follows;

$$\phi_{max} = \arctan\left(\frac{\frac{l}{2} - r \sin \frac{\theta}{2}}{r \cos \frac{\theta}{2}}\right) \tag{6}$$

### 3.3 A Study on the Number of Notches

The number of notches is important for designing the wheel. A lot of notches may reduce the time the robot climb over the steps. However, since the angle of the



**Fig. 5** Four case of calculating the number of notches. **a**  $n = 4k + 1$  **b**  $n = 4k + 3$  **c**  $n = 4k + 2$  **d**  $n = 4k + 4$

notch is not considered good, climbing steps ability become low such as spoke type. Here, we calculate the angle range that does not lower the climbing ability. Therefore, we consider that the circle part of the wheel should touch to the ground when the notch part of wheel can catch the steps (Fig. 5).

The result of range angle is shown in Table 1 and example are shown in Fig. 6. After all, we only have to consider odd or twice the odd number of notches. The twice one is considered good in terms of reducing the time the robot climb over the steps. For example, when the angle of the notch is decided to be  $\pi/2$ , the best number of notches become 2.

**Table 1** Angle range in each case

Pattern	$n = 4k + 1$	$n = 4k + 2$	$n = 4k + 3$	$n = 4k + 4$
Angle range	$0 < \theta < \frac{\pi}{n}$	$0 < \theta < \frac{2\pi}{n}$	$0 < \theta < \frac{\pi}{n}$	Any angle is not suitable

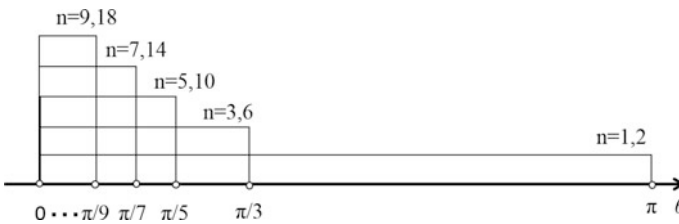


**Fig. 6** Optimal number of notches

### 3.4 A Study of the Edge Shape of the Notch

The edge shape of the notch is also affected to the climbing step ability. Rounded edge shape reduced the length of the effective radius ( $r_e$ ) and effective notch angle ( $\theta_e$ ) (Fig. 7). This reduces the climbing step ability and increase the climbing slope ability.

The climbing step ability and the climbing slope ability are calculated as below.

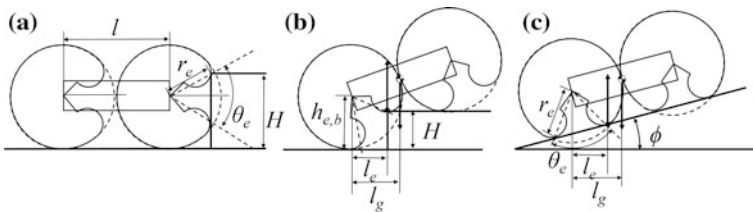
$$H_{\max} = r_e \left( 1 + \sin \frac{\theta_e}{2} \right) \tag{7}$$

$$\phi_{c, \max} = \arctan \left( \frac{\frac{l}{2} - r_e \sin \frac{\theta_e}{2}}{r_e \cos \frac{\theta_e}{2}} \right) \tag{8}$$

The robot can finish climbing the step when the  $H$  meets the following formula.

$$\sqrt{r_e^2 - (H - h_{e,b})^2} < \frac{l}{2} \sin \left( \arctan \left( \frac{H}{l} \right) \right) \tag{9}$$

Arc-shaped notch reduced does not reduce the maximum height potential of the climbing steps of the robot. This type of notched also increases the finishing climb steps ability because arc-shaped can shorten  $l_e$  (Fig. 8).





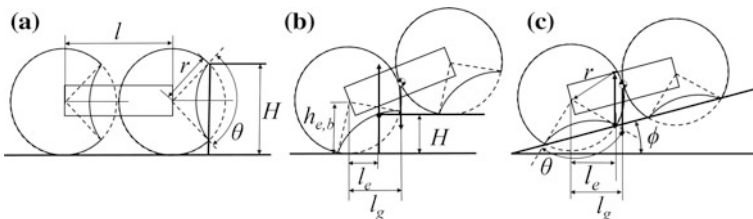






**Fig. 7** Rounded edge shape design. **a** First phase of climbing step **b** Final phase of climbing step **c** Climbing slope



**Fig. 8** Arc-shaped notch shape design. **a** First phase of climbing step **b** Final phase of climbing step **c** Climbing slope

**Table 2** Dynamic simulation results

Wheel type	Wheel	Standard (n = 4)	Standard (n = 3)	Standard (n = 2)	Standard (n = 1)	Rounded edge	Arc-shaped notch	
Image								
Climbing steps ability	Theoretical	140	232	235	235	210	235	
	Simulation	140 (25)	205 (125)	235 (125)	235 (115)	210 (180)	235 (180)	
Climbing slopes ability	Theoretical	47	28	28	28	35	28	
	Simulation	45	27	27	26	34	28	



## 4 Verification

To verify the validity of the proposed model, we did the dynamics simulation on v-rep that is provided for the educational use without charge. For adapting to the WAMOT, the size ( $l = 300$  [mm],  $r = 140$  [mm],  $\theta = 86^\circ$ ) was set. We selected the notch angle in terms of making spoke type ( $n = 4$ ).

Climbing steps ability test was conducted in steps of 5 [mm]. To prevent the robot climb up using a high frictional force, we set the friction rate ( $\mu = 0.4$ ) between the wheel and ground. In this test, we considered that the robot has ability if it was successful once among various distance tries. Table 2 shows the result of the test. We show the maximum height of the steps when the front wheel climbed in the upper column of simulation. We also add the result of the maximum height of the steps when the rear wheel climbed in the lower column of simulation.

Climbing slopes ability test was conducted in steps of  $1^\circ$ . In this test, we considered that the robot has ability if the robot climb up 2 [m] of the slope. Table 2 shows the result of the test.

## 5 Discussion

We can estimate the climbing ability of slopes and steps of mobile robots using the proposed model. The theoretical value is very similar to dynamic simulation value in Table 2. This shows that we can estimate the climbing ability easily by using proposed calculation formula. We can select and design the wheel shape to meet the required specifications of the target environment.

From this study, we found that the two parameter  $r_e$  and  $\theta_e$  are important for considering the design of the wheel. These parameters affect the climbing ability of the steps and slopes greatly. Arc-shaped notch design is most effective shape because not only it does not reduce the maximum potential height of the climbing steps of the robot but also increase the finishing climb steps ability. Arc-shaped notch type can get more high ability by changing the notch angle, although it seems inferior to rounded edge shape in terms of climbing slope ability at a glance.

This model is significant not only useful for wheel type of mobile robot, but this model also can apply to the other mobile robot such as crawler and legged type. Many mobile robots can use this model by only considering contacting point on the ground.

The limitation of the model is that this model cannot use to high speed mobile robot. The model should contain the idea of zero moment point (Vukobratovic et al. 2004) for taking acceleration into account.

## 6 Conclusions

A new model of wheel shape was designed for increasing climbing ability of slopes and steps. This model makes easy to estimate the climbing ability of slopes and steps of mobile robots.

In future works, we want to make a more detailed model that takes account the actual errors. And we want to do an experiment using Arc-shaped notch type wheel in a natural environment.

## References

- Herbert, S. D., et al. (2008) Loper: A quadruped-hybrid stair climbing robot. In *Proceedings of 2008 IEEE International Conference on Robotics and Automation* (pp. 799–804).
- Nagatani, K., et al. (2014) Development and field test of teleoperated mobile robots for active volcano observation. In *Proceedings of 2014 IEEE/RSJ International Conference on Intelligent Robots and Systems (IROS)* (pp. 1932–1937) September 2014.
- Shankar, K., et al. (2013) Motion planning and control for a tethered, rimless wheel differential drive vehicle. In *Proceedings of 2013 IEEE/RSJ International Conference on Intelligent Robots and Systems (IROS)* (pp. 4829–4836) November 2013.
- Smith, A. C., et al (1998) The motion of a finite-width rimless wheel in 3D. In *Proc. 1998 IEEE International Conference on Robotics & Automation* (pp. 2345–2350) May 1998.
- Tanaka, K., et al. (2014a). Design of operating software and electrical system of mobile robot for environmental monitoring. In *Proceedings of 2014 IEEE International Conference on Robotics and Biomimetics* (pp. 1763–1768) December 2014.
- Tanaka, K., et al. (2014b). Mechanical design of a mobile robot with eclipse legs for environmental monitoring. In *Proceedings of 2014 IFToMM Asian Conference on Mechanism and Machine Science*, July 2014.
- Vukobratovic, M., et al. (2004). Zero-moment point—thirty five years of its life. *International Journal of Humanoid Robotics*, 1(1), 157–173.

# Position Kinematics of a 3-RRS Parallel Manipulator

Halil Tetik, Rohit Kalla, Gokhan Kiper  
and Sandipan Bandyopadhyay

**Abstract** The 3-RRS parallel manipulator presented in this study comprises of parallel revolute joint axes in each leg. The manipulator is composed of a base and a moving platform which are in the shape of equilateral triangles. Moving platform has two rotational and one translational degrees-of-freedom. This study formulates the forward and inverse kinematics of the parallel manipulator. A 16<sup>th</sup> order polynomial in terms of one of the passive joint variables is obtained for the forward kinematic analysis. Numerical results and the corresponding pose of the manipulator for inverse and forward kinematics are presented.

**Keywords** 3-RRS parallel manipulator • Inverse kinematics • Forward kinematics

## 1 Introduction

Parallel manipulators (PM) having less than 6 degrees-of-freedom (DoF) attracted a lot of attention in the past few decades due to their architectural simplicity, low cost and easier control (Fan et al. 2009). Some of the most successful designs of PMs used in the industry are with less than 6-DoF (Chen et al. 2014).

This study deals with a 3-DoF 3-RRS PM which possesses one translational DoF and two rotary ones (Liu and Bonev 2008). Inverse kinematic analysis of a 3-RRS

---

H. Tetik (✉) · G. Kiper  
Department of Mechanical Engineering, Izmir Institute of Technology, Izmir, Turkey  
e-mail: haliltetik1989@gmail.com

G. Kiper  
e-mail: gokhankiper@iyte.edu.tr

R. Kalla · S. Bandyopadhyay  
Department of Engineering Design, Indian Institute of Technology Madras,  
Chennai, India  
e-mail: rohitkalla9@gmail.com

S. Bandyopadhyay  
e-mail: sandipan@iitm.ac.in

PM has been performed by (Li et al. 2001), where the analysis is performed by using a geometrical approach. (Itul and Pisla 2009) presented the inverse and forward kinematic model for a 3-RRS PM. For the forward position analysis, the set of position equations are suggested to be solved numerically; no analysis as to the number of solutions is presented.

In this study, first, the geometry of the 3-RRS PM is described. Then the kinematic constraints are formulated in terms of the loop-closure equations which are solved consequently. Inverse position analysis is done analytically. To solve the forward kinematic problem, the mathematical manipulation proposed by (Srivatsan and Bandyopadhyay 2013), is applied to a set of three non-linear equations in terms of passive joint variables. Finally, a 16<sup>th</sup> order polynomial in terms of the tangent of the half of one of the passive joint angles is obtained. The formulation is illustrated via numerical examples.

## 2 Position Analysis

The architecture of the PM investigated in this study is presented in Fig. 1. The 3-RRS PM consists of a fixed base, a moving platform and three identical limbs. The  $i$ th limb is composed of three joints: active revolute (R) joint fixed on the base at the point  $O_{0i}$ ; passive R joint located at the point  $O_{ij}$ ; and a passive spherical (S) joint between the links having a length  $l_2$  and the platform, located at the points  $O_{7j}$ , for  $i = 1, 2, 3$  and  $j = 4, 5, 6$ .

In Fig. 1, a fixed coordinate frame  $O_0$ -XYZ is attached to the base. Its origin,  $O_0$ , is chosen as the center of the circle with a radius of  $b$ , which is the circle tangent to all the three revolute joint axes at the base. The X-axis is along the vector  $\overline{O_0O_1}$  and the Z-axis is perpendicular to the base plane. A moving coordinate frame,  $O_7$ -UVW, is attached to the platform. The origin,  $O_7$ , is attached at the

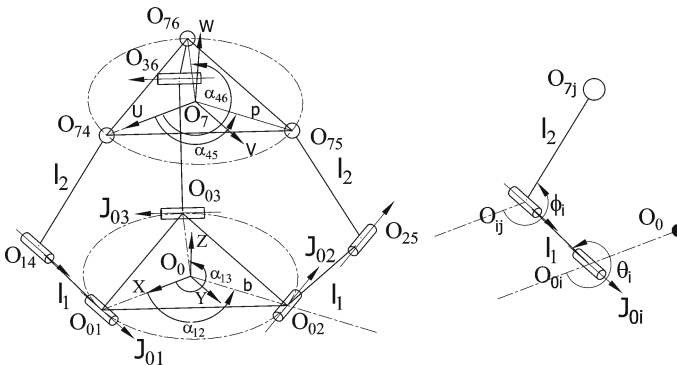


Fig. 1 Kinematic model of the 3-RRS PM

center of a circle with a radius  $p$ , which is the circle passing through the three spherical joint centers. The  $U$ -axis is along  $\overline{O_7O_{74}}$  vector and  $W$ -axis is perpendicular to the plane of the platform. In any leg, the axes of the active and passive R joints are parallel to each other. As a specific case, to achieve a symmetric form, the points  $O_{0i}$  and  $O_{7j}$  are placed at the vertices of the base and moving platform triangles. Therefore,  $\alpha_{12} = \angle O_{01}O_0O_{02} = 120^\circ$ ,  $\alpha_{13} = \angle O_{01}O_0O_{03} = 240^\circ$ ,  $\alpha_{45} = \angle O_{74}O_7O_{75} = 120^\circ$ , and  $\alpha_{46} = \angle O_{74}O_7O_{76} = 240^\circ$ . The input variables are  $\theta_1, \theta_2$ , and  $\theta_3$ ; passive revolute joint variables are  $\phi_1, \phi_2$ , and  $\phi_3$ .

**Constraint Equations.** Each limb is constrained to move in plane and the relation in between the  $X$  and  $Y$  coordinates of the spherical joint centres can be given as  $O_{7j,y} = \tan(\alpha_{1j})O_{7j,x}$ . Constraint equations due to this planar motion are derived by (Tsai 1999) for a 3-RPS PM and these equations are also valid for the 3-RRS PM:

$$O_{7y} = -u_y p \quad (1)$$

$$O_{7x} = p(u_x - v_y)/2 \quad (2)$$

$$u_y = v_x \quad (3)$$

where  $O_{7x}$  and  $O_{7y}$  are the  $X$  and  $Y$  coordinates of the platform center,  $u_x, u_y, v_x$  and  $v_y$  are the corresponding elements of the rotation matrix explained below.

$O_{7z}$  remains independent, indicating the translational DoF along the  $Z$ -axis. To determine the elements of the rotation matrix  $[\mathbf{R}]$  between coordinate frames of the base and moving platform, the following rotation sequence is applied: first rotate about the fixed  $Z$ -axis by an angle of  $\psi_z$ , then about the fixed  $Y$ -axis by an angle of  $\psi_y$  and finally about the fixed  $X$ -axis by an angle of  $\psi_x$ . This results in:

$$[\mathbf{R}] = \begin{bmatrix} u_x & v_x & w_x \\ u_y & v_y & w_y \\ u_z & v_z & w_z \end{bmatrix} = \begin{bmatrix} c_y c_z & -c_y s_z & s_y \\ s_x s_y c_z + c_x s_z & c_x c_z - s_x s_y s_z & -s_x c_y \\ s_x s_z - c_x s_y c_z & s_x c_z + c_x s_y s_z & c_x c_y \end{bmatrix} \quad (4)$$

where  $s$  and  $c$  stand for  $\sin$  and  $\cos$ , respectively, and subscripts  $x, y$  and  $z$  stand for rotation angles  $\psi_x, \psi_y$  and  $\psi_z$ , respectively.  $[\mathbf{R}]$  is bound to the 6 orthogonality conditions for rotation matrices. Besides, Eq. (3) further constrains  $[\mathbf{R}]$ . Therefore, only two elements of  $[\mathbf{R}]$  are independent. Considering the workspace of the 3-RRS PM, the suitable choices of independent parameters are  $w_x$  and  $w_y$ , while  $O_{7z}, w_x$  and  $w_y$  are the independent workspace parameters. For given  $w_x$  and  $w_y$ , first  $\psi_x, \psi_y$  and  $\psi_z$  can be determined:

$$\psi_y = \sin^{-1}(w_x), \text{ where, } s_y \neq \pm 1 \quad (5)$$

$$\psi_x = \sin^{-1}(-w_y/c_y) \quad (6)$$

Imposing Eq. (3) in Eq. (4), and dividing by  $c_z$ , we can determine  $\psi_z$  as

$$\begin{aligned} -s_x s_y &= (c_x + c_y) \tan \psi_z \\ \Rightarrow \psi_z &= \tan^{-1} (-s_x s_y / (c_x + c_y)) \end{aligned} \quad (7)$$

Substituting  $\psi_x$ ,  $\psi_y$  and  $\psi_z$  given by Eqs. (5)–(7),  $[\mathbf{R}]$  can be determined from Eq. (4). Equations (1)–(2) give the dependent position parameters.

**Inverse Position Analysis.** Inverse kinematics problem is to find the input angles  $\theta_1$ ,  $\theta_2$  and  $\theta_3$  for a given pose of the moving platform. The loop-closure equation can be written as:

$$\begin{aligned} \overrightarrow{O_0 O_{7j}} &= [\mathbf{R}_Z(\alpha_{1i})] \left\{ \begin{bmatrix} b \\ 0 \\ 0 \end{bmatrix} + [\mathbf{R}_Y(\theta_i)] \begin{bmatrix} l_1 \\ 0 \\ 0 \end{bmatrix} + [\mathbf{R}_Y(\phi_i)] \begin{bmatrix} l_2 \\ 0 \\ 0 \end{bmatrix} \right\} \\ \overrightarrow{O_0 O_{7j}} &= \overrightarrow{O_0 O_7} + [\mathbf{R}] \cdot [\mathbf{R}_Z(\alpha_{4j})] \begin{pmatrix} p \\ 0 \\ 0 \end{pmatrix} \end{aligned} \quad (8)$$

for  $i = 1, 2, 3$  and  $j = i + 3$ .  $[\mathbf{R}_Y]$  and  $[\mathbf{R}_Z]$  are the elementary CCW rotation matrices about  $Y$ -, and  $Z$ -axes, respectively. We express the points  $O_{7j}$  in terms of the given pose parameters using Eq. (8). The  $X$  and  $Z$  components of Eq. (8) are:

$$l_2 c_{\phi_i} c_{\alpha_{1i}} = O_{7jx} - c_{\alpha_{1i}}(b + l_1 c_{\theta_i}) \quad (9)$$

$$l_2 s_{\phi_i} = -O_{7jz} - l_1 s_{\theta_i} \quad (10)$$

Solving  $c_{\phi_i}$  and  $s_{\phi_i}$  from the Eqs. (9)–(10), and using the identity  $c_{\phi_i}^2 + s_{\phi_i}^2 = 1$ :

$$\begin{aligned} l_2^2 (c_{\alpha_{1i}} + 1)^2 - [O_{7jx} c_{\alpha_{1i}} (b + l_1 c_{\theta_i})]^2 - [c_{\alpha_{1i}} (O_{7jz} - l_1 s_{\theta_i})]^2 &= 0 \\ \Rightarrow A_i c_{\theta_i} + B_i s_{\theta_i} + C_i &= 0 \end{aligned} \quad (11)$$

where  $A_i = 2l_1 c_{\alpha_{1i}} (-O_{7jx} + b c_{\alpha_{1i}})$ ,  $B_i = 2l_1 O_{7jz} c_{\alpha_{1i}}$  and  $C_i = O_{7jx}^2 - 2b O_{7jx} c_{\alpha_{1i}} + c_{\alpha_{1i}}^2 (b^2 + l_1^2 - l_2^2 + O_{7jz}^2)$ . Applying tangent of half angle substitution to Eq. (11) and solving for  $\theta_i$ :

$$\theta_i = 2 \operatorname{atan2} \left( -B_i \pm \sqrt{A_i^2 + B_i^2 - C_i^2}, C_i - A_i \right) \quad (12)$$

$A_i = C_i$  results in singularity, which is not considered in this paper and it is assumed that  $A_i \neq C_i$ . Due to the  $\pm$  sign in Eq. (12), each  $\theta_i$  has two possible values, which yields at most 8 solutions. Therefore the PM has 8 assembly modes for the inverse kinematics.

**Forward Position Analysis.** The coordinates of the points  $O_{7j}$  can be calculated in terms of input variables  $\theta_i$  and passive R joint variables  $\phi_i$  by making use of the Eq. (8). Since the moving platform is in the form of an equilateral triangle, the distances between  $O_{7j}$  are constant and can be calculated by the cosine theorem. Using Eq. (8):

$$3p^2 = d^2 = |O_{74}O_{75}|^2 \Rightarrow f_1(\phi_1, \phi_2) = 0 \quad (13)$$

$$3p^2 = d^2 = |O_{75}O_{76}|^2 \Rightarrow f_2(\phi_2, \phi_3) = 0 \quad (14)$$

$$3p^2 = d^2 = |O_{76}O_{74}|^2 \Rightarrow f_3(\phi_1, \phi_3) = 0 \quad (15)$$

Equations (13)–(14) can be rewritten as:

$$f_{10} + f_{11}s\phi_2 + f_{12}c\phi_2 = 0 \quad (16)$$

$$f_{20} + f_{21}s\phi_2 + f_{22}c\phi_2 = 0 \quad (17)$$

Solving for  $c\phi_2$ ,  $s\phi_2$  from there,

$$s\phi_2 = \frac{f_{12}f_{20} - f_{10}f_{22}}{f_{11}f_{22} - f_{12}f_{21}}, \quad c\phi_2 = \frac{f_{10}f_{21} - f_{11}f_{20}}{f_{11}f_{22} - f_{12}f_{21}} \quad (18)$$

Since,  $c^2\phi_2 + s^2\phi_2 = 1$ , from Eq. (16)–(17), assuming  $f_{11}f_{22} - f_{12}f_{21} \neq 0$ :

$$(f_{12}f_{20} - f_{10}f_{22})^2 + (f_{10}f_{21} - f_{11}f_{20})^2 - (f_{11}f_{22} - f_{12}f_{21})^2 = 0 \quad (19)$$

At this point we apply the tangent of half angle substitution for the angles  $\phi_1$  and  $\phi_3$  for Eqs. (13)–(15):  $t_1 = \tan(\phi_1/2)$  and  $t_3 = \tan(\phi_3/2)$ . Equation (17) involves  $t_1$  and  $t_3$ , only. Rearranging Eq. (17), it is seen that it is a 4<sup>th</sup> order polynomial in  $t_1$ :

$$a_0 + a_1t_1 + a_2t_1^2 + a_3t_1^3 + a_4t_1^4 = 0 \quad (20)$$

Coefficients  $a_i$  in Eq. (20) are also 4<sup>th</sup> order polynomials in  $t_3$ . Also rearranging Eq. (15) in terms of  $t_1$  results in a quadratic equation:

$$b_0 + b_1t_1 + b_2t_1^2 = 0 \quad (21)$$

The coefficients  $b_i$  are also 2<sup>nd</sup> order polynomials in terms of  $t_3$ . Eliminating  $t_1$  from Eqs. (20)–(21) using polynomial division, we obtain:

$$\frac{b_2^3 H}{[a_4b_1^3 - b_1(2a_4b_0 + a_3b_1)b_2 + (a_3b_0 + a_2b_1)b_2^2 - a_1b_3^3]^2} = 0 \Rightarrow H = 0 \quad (22)$$

where

$$\begin{aligned}
 H = & a_4 \{ a_4 b_0^4 + b_1 [ -a_3 b_0^3 + b_1 ( a_2 b_0^2 - a_1 b_0 b_1 + a_0 b_1^2 ) ] \} + b_2 ( a_3^2 - 2a_2 a_4 ) b_0^3 + \\
 & b_2^2 [ ( a_2^2 - 2a_1 a_3 + 2a_0 a_4 ) b_0^2 + ( -a_1 a_2 + 3a_0 a_3 ) b_0 b_1 + a_0 a_2 b_1^2 ] + \\
 & ( -a_2 a_3 + 3a_1 a_4 ) b_0^2 b_1 + ( a_1 a_3 - 4a_0 a_4 ) b_0 b_1^2 - a_0 a_3 b_1^3 + \\
 & b_2^3 [ ( a_1^2 - 2a_0 a_2 ) b_0 - a_0 a_1 b_1 ] + a_0^2 b_2^4
 \end{aligned}$$

Equation (22) is valid provided that  $b_2 \neq 0$  and also denominator in Eq. (22) is nonzero. Equation (22) is a 16<sup>th</sup> order polynomial in terms of  $t_3$ . The value of  $t_3$  can be numerically computed from Eq. (22). For any  $t_3$  value,  $t_1$  is determined from Eqs. (20)–(21) and  $\phi_2$  is given by Eq. (16). There are at most 16 assembly modes of the moving platform for the forward kinematics. Once the platform points  $O_{7j}$  are determined from Eq. (8), the location of the platform is determined.

$t_3 = -2.07$ $\phi_1 = -56.04^\circ$ $\phi_2 = -92.32^\circ$ $\phi_3 = -128.40^\circ$ $w_x = -0.034$ $w_y = -0.18$ $O_{7,z} = 1.14$		$t_3 = -1.73$ $\phi_1 = -52.21^\circ$ $\phi_2 = -103.26^\circ$ $\phi_3 = -119.88^\circ$ $w_x = -0.09$ $w_y = 0.01$ $O_{7,z} = 1.14$		$t_3 = -1.55$ $\phi_1 = -116.11^\circ$ $\phi_2 = -108.70^\circ$ $\phi_3 = -114.26^\circ$ $w_x = 0.10$ $w_y = -0.11$ $O_{7,z} = 1.18$	
$t_3 = -1.50$ $\phi_1 = -117.81^\circ$ $\phi_2 = -48.51^\circ$ $\phi_3 = -112.58^\circ$ $w_x = 0.25$ $w_y = -0.45$ $O_{7,z} = 1.12$		$t_3 = -0.85$ $\phi_1 = -66.85^\circ$ $\phi_2 = -126.22^\circ$ $\phi_3 = -80.99^\circ$ $w_x = -0.20$ $w_y = 0.46$ $O_{7,z} = 1.16$		$t_3 = -0.73$ $\phi_1 = -74.88^\circ$ $\phi_2 = -68.66^\circ$ $\phi_3 = -72.22^\circ$ $w_x = -0.2$ $w_y = 0.2$ $O_{7,z} = 1.2$	
$t_3 = -0.56$ $\phi_1 = -135.65^\circ$ $\phi_2 = -83.84^\circ$ $\phi_3 = -58.95^\circ$ $w_x = 0.27$ $w_y = -0.06$ $O_{7,z} = 1.12$		$t_3 = -0.47$ $\phi_1 = -123.46^\circ$ $\phi_2 = -101.73^\circ$ $\phi_3 = -50.74^\circ$ $w_x = 0.08$ $w_y = 0.17$ $O_{7,z} = 1.13$		$t_3 = 0.53$ $\phi_1 = 97.19^\circ$ $\phi_2 = 124.38^\circ$ $\phi_3 = 55.72^\circ$ $w_x = -0.16$ $w_y = -0.16$ $O_{7,z} = -0.22$	
$t_3 = 0.70$ $\phi_1 = 77.16^\circ$ $\phi_2 = 132.07^\circ$ $\phi_3 = 69.88^\circ$ $w_x = 0.10$ $w_y = -0.15$ $O_{7,z} = -0.22$		$t_3 = 0.73$ $\phi_1 = 74.56^\circ$ $\phi_2 = 67.86^\circ$ $\phi_3 = 72.45^\circ$ $w_x = -0.11$ $w_y = 0.12$ $O_{7,z} = -0.27$		$t_3 = 0.89$ $\phi_1 = 133.47^\circ$ $\phi_2 = 57.43^\circ$ $\phi_3 = 83.36^\circ$ $w_x = -0.51$ $w_y = -0.08$ $O_{7,z} = -0.20$	
$t_3 = 1.17$ $\phi_1 = 57.04^\circ$ $\phi_2 = 121.93^\circ$ $\phi_3 = 98.87^\circ$ $w_x = 0.30$ $w_y = 0.06$ $O_{7,z} = -0.23$		$t_3 = 1.56$ $\phi_1 = 115.73^\circ$ $\phi_2 = 107.43^\circ$ $\phi_3 = 114.55^\circ$ $w_x = 0.21$ $w_y = -0.24$ $O_{7,z} = -0.25$		$t_3 = 1.65$ $\phi_1 = 112.62^\circ$ $\phi_2 = 43.42^\circ$ $\phi_3 = 117.63^\circ$ $w_x = -0.10$ $w_y = 0.16$ $O_{7,z} = -0.18$	
				$t_3 = 2.27$ $\phi_1 = 87.89^\circ$ $\phi_2 = 55.20^\circ$ $\phi_3 = 132.54^\circ$ $w_x = 0.26$ $w_y = 0.30$ $O_{7,z} = -0.20$	

Fig. 2 Forward kinematic solutions



### 3 Numerical Example

Several numerical examples are worked out in order to check forward and inverse kinematic solutions using *Mathematica*. As an example, consider the case where  $b = 0.55$  m,  $p = 0.275$  m,  $l_1 = 0.7$  m and  $l_2 = 0.775$  m. For the inverse kinematic analysis, as a generic example for given pose parameters  $O_{7z} = 1.2$  m,  $w_x = -0.2$  and  $w_y = 0.2$ , the possible corresponding joint angles are found as  $(\theta_1, \theta_2, \theta_3) = (-71.60^\circ, -66.09^\circ, -68.57^\circ)$ ,  $(-133.61^\circ, -144.85^\circ, -136.47^\circ)$ . Each leg has two possible configurations, leading to a total of  $2 \times 2 \times 2 = 8$  different configurations of the manipulator for a given pose of the moving platform. To verify the forward kinematic formulation, let  $\theta_1 = -133.61^\circ$ ,  $\theta_2 = -144.85^\circ$  and  $\theta_3 = -136.47^\circ$ , which is one of the eight solutions above. The solution of the 16<sup>th</sup> order univariate polynomial in terms of  $t_3$  results in sixteen distinct real solutions. The numerical values obtained for  $t_3$ , corresponding passive joint variables  $\phi_i$  and task space variables  $O_{7z}$ ,  $w_x$  and  $w_y$  are presented in Fig. 2. Notice that the 6th set of solutions matches with the task space parameters used in the inverse kinematic analysis. Figure 2 depicts the poses of the PM for the corresponding solutions.

### 4 Conclusion

A detailed analysis for the forward and inverse kinematics analysis of the 3-RRS PM is presented in this study. For the forward kinematics, all but one dependent joint variables are eliminated to obtain a 16<sup>th</sup> order polynomial. This suggests that an upper bound for the forward kinematics solutions of the 3-RRS PM is 16, which proves that polynomial obtained is the smallest one. The formulations are implemented in *Mathematica* and several numerical examples are presented. Indeed 16 real solutions are obtained for some configurations.

The formulations developed here will be implemented for the control of a 3-RRS PM in Izmir Institute of Technology. This manipulator will be the base part of a 6-DoF hybrid manipulator which will be used for pick and place applications. Further studies would include the identification of singularities and safe working zone, (see, Srivatsan and Bandyopadhyay 2014) and dynamic analyses of the PM.

### References

- Arun Srivatsan, R., & Bandyopadhyay, S. (2013). On the position kinematic analysis of MaPa-Man: A reconfigurable three-degrees-of-freedom spatial parallel manipulator. *Mechanism and Machine Theory*, 62, 150–165.
- Arun Srivatsan, R., & Bandyopadhyay, S. (2014). Determination of the safe working zone of a parallel manipulator. In *Computational Kinematics* (pp. 201–208). Netherlands: Springer.

- Chen, X., Xie, F. G., Liu, X. J., Xie, F., & Sun, T. (2014). A comparison study on motion/force transmissibility of two typical 3-DoF parallel manipulators: the sprint Z3 and A3 tool heads. *International Journal of Advanced Robotic System*, 11(5), 1–10.
- Fan, C., Liu, H., & Zhang, Y. (2009). Kinematics and singularity analysis of a novel 1T2R fully-decoupled parallel mechanism. In *Intelligent Computing and Intelligent Systems, 2009. ICIS 2009. IEEE International Conference* (Vol. 2, pp. 312–316). IEEE.
- Itul, T., & Pislá, D. (2009). Kinematics and dynamics of 3-DoF parallel robots with triangle platform. *Journal of Vibroengineering*, 11(1),
- Li, J., Wang, J., Chou, W., Zhang, Y., Wang, T., & Zhang, Q. (2001). Inverse kinematics and dynamics of the 3-RRS parallel platform. In *Robotics and Automation, 2001. Proceedings 2001 ICRA. IEEE International Conference* (Vol. 3, pp. 2506–2511). IEEE.
- Liu, X. -J., & Bonev, I. A. (2008). Orientation capability, error analysis, and dimensional optimization of two articulated tool heads with parallel kinematics. *Journal of Manufacturing Science and Engineering*, 130(1), 011015–011015–9.
- Tsai, L. -W. (1999). *Robot Analysis: The Mechanics of Serial and Parallel Manipulators*. Wiley.

# Kinematic Analysis of a Single-Loop Translational Manipulator

Raffaele Di Gregorio

**Abstract** A particular way to identify single-loop not-overconstrained architectures for translational parallel manipulators (TPMs) is proposed and discussed. Then, the position and the velocity analyses of one out of the identified architectures is presented.

**Keywords** Kinematic analysis • Translational manipulators • Single-loop mechanisms • Isotropic manipulators

## 1 Introduction

A great number of TPMs have been proposed in the literature [see Kong and Gosselin (2007) for Refs. and examples]. Most of them feature three kinematic chains (limbs) with equal topology, which join the end effector (platform) to the frame (base), and one actuated joint per limb. TPMs' synthesis criteria mainly rely on using either the screw theory (e.g., Kong and Gosselin 2007) or the intersection of displacement sub-groups (Hervé and Sparacino 1991). The first approach looks for limbs whose passive (i.e., without actuators) structures apply to the platform only one torque, and use three of such limbs in an arrangement that make them apply three non-coplanar torques to the platform. This approach identifies limbs with connectivity<sup>1</sup> 5. The second approach looks for limbs (mechanical generators)

---

<sup>1</sup>The term “connectivity” (Davidson and Hunt 2004) referred to two links of a mechanism indicates the number of degrees-of-freedom (dof) of the relative motion between those two links. Here, the phrase “limb connectivity” stands for the connectivity between platform and base when connected only by that limb.

---

R. Di Gregorio (✉)  
Department of Engineering, University of Ferrara, Ferrara, Italy  
e-mail: raffaele.digregorio@unife.it

that generate Shoeflies motions<sup>2</sup> and combines three of them so that the rotation axes of the Shoeflies motion generated by at least two limbs are not parallel. This approach identifies limbs with connectivity 4 and overconstrained architectures that can become not-overconstrained by adding idle passive pairs; also, it highlights that two limbs, that is, a single-loop architecture, are sufficient to obtain a TPM.

Reducing the limb number from three to two yields simplified architectures and, in general, a wider workspace. In addition, not-overconstrained architectures are interesting since they do not require small dimensional tolerances for all the links. On the other side, three-limbed overconstrained architectures are stiffer and make it possible to put all the actuators on the base.

A good compromise could be a single-loop not-overconstrained architecture with two actuators on the base and the third one near to the base. According to Chebychev-Grübler-Kutzbach formula and Euler's formula (Angeles 1988), a spatial single-loop not-overconstrained architecture with three dof must contain nine joint variables. Therefore, the combination of one limb with connectivity 4, which constrains the platform to a Shoeflies motion, and another limb with connectivity 5, whose passive structure applies to the platform only one torque with a component parallel to the rotation axis of that Shoeflies motion, yields a single-loop not-overconstrained architecture where the platform can only perform spatial translations (i.e., a TPM architecture). In short, any limb identified through the second approach when suitably combined with any limb identified through the first approach yields a single-loop not-overconstrained TPM architecture.

Here, these concepts are implemented with the **PRRR-PRPU**<sup>3</sup> architecture shown in Fig. 1. The **PRRR** limb is the mechanical generator of Shoeflies displacements. In this limb, the P-pair sliding direction and the three R-pair axes are all parallel to the  $y_b$  axis of the Cartesian reference  $O_b-x_b y_b z_b$ , fixed to the base; consequently, this coordinate axis has the direction of the rotation axis of the generated Shoeflies motion. The passive structure of the **PRPU** limb applies to the platform only one torque perpendicular to the cross link of the U-joint. This torque has a direction that does not change during motion and is parallel to the  $y_b$  axis. Indeed, the **PRPU** limb is so sized that the axes of the two intermediate R pairs are parallel to each other and are constrained to translate with respect to the base by keeping the direction of the  $x_b$  axis; whereas, the axis of the third R pair is perpendicular to those of the two intermediate and is fixed to the platform that keeps it perpendicular to the  $y_b$  axis, too.

Both the finite and the instantaneous kinematic analyses of the **PRRR-PRPU** architecture shown in Fig. 1 are presented in the following sections. Section 2

<sup>2</sup>The displacement sub-groups of Shoeflies,  $\{X(\mathbf{u})\}$ , are the unions of the spatial translation sub-group,  $\{T\}$ , with one rotation-around-an-axis sub-group,  $\{R(C, \mathbf{u})\}$ , where  $\mathbf{u}$  and  $C$  are the unit vector and a point of the rotation axis. Since the unit vectors are  $\infty^2$ , as many are the Shoeflies sub-groups.

<sup>3</sup>P, R, and U stand for prismatic pair, revolute pair and universal joint, respectively. Bold letters indicate the actuated pairs; whereas, the hyphen separates the strings which give the limb topologies by moving from the base to the platform.

addresses its position analysis. Section 3 deduces its instantaneous input-output relationship and presents its singularity analysis. Eventually, Sect. 4 draws the conclusions.

## 2 Position Analysis

With reference to Fig. 1,  $A_1$  is the center of the U joint.  $O_p$  is the platform reference point whose coordinates,  $(x, y, z)^T$ , measured in  $O_b-x_b y_b z_b$  will be used to identify the platform pose (the platform can only translate with respect to the base).  $A_2$  is the foot of the perpendicular from  $O_p$  to the axis of the R pair that joins the platform to

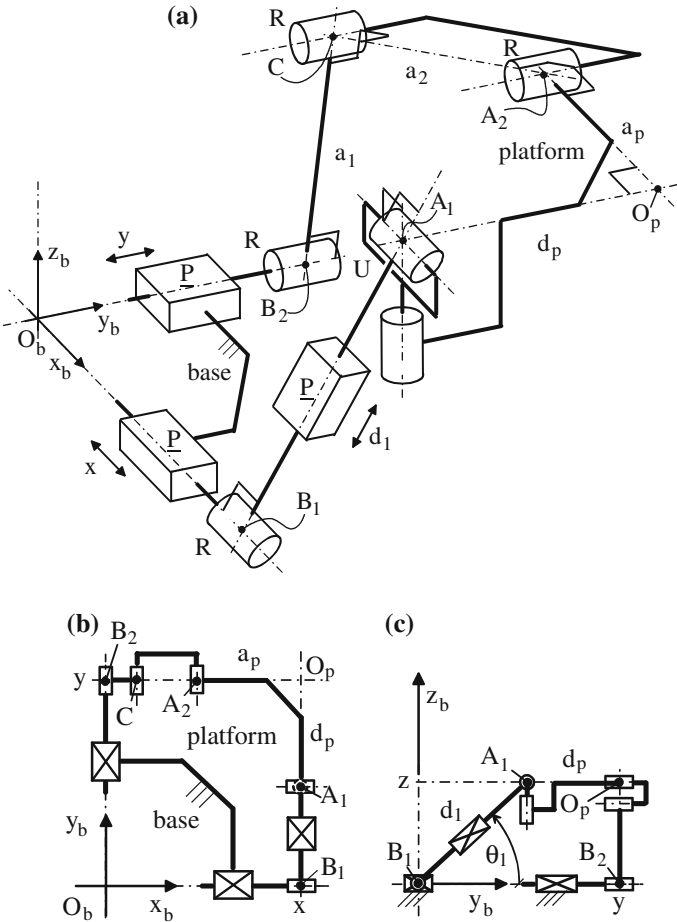


Fig. 1 PRRR-PRPU architecture: a 3D view, b top view, c front view

the **PRRR** limb.  $O_p$ ,  $A_1$ , and  $A_2$  are the vertices of a right triangle, fixed to the platform, which lies on a plane parallel to the  $x_b y_b$  coordinate plane.  $a_p$  and  $d_p$  are the lengths of the segments  $O_p A_2$  and  $O_p A_1$ , respectively.  $B_1$  is the foot of the perpendicular from  $A_1$  to the axis of the R pair between the two actuated P pairs of the **PRPU** limb, and  $d_1$  is the length of the segment  $A_1 B_1$ .  $B_2$  and  $C$  are the feet of the perpendiculars from  $A_2$  to the axes of the two intermediate R pairs of the **PRRR** limb; whereas,  $a_1$  and  $a_2$  are the lengths of the segments  $B_2 C$  and  $C A_2$ , respectively. Hereafter,  $\mathbf{i}_b$ ,  $\mathbf{j}_b$ , and  $\mathbf{k}_b$  will denote the unit vectors of the coordinate axes  $x_b$ ,  $y_b$ , and  $z_b$ , respectively.

The  $x$  and  $y$  coordinates of  $O_p$  coincides with the actuated joint variables of the two P pairs adjacent to the base [see Fig. 1b]; whereas, the third actuated joint variable,  $d_1$ , can be explicitly expressed as a function of the  $O_p$  coordinates as follows [see Fig. 1c]

$$d_1 = \sqrt{(y - d_p)^2 + z^2} \quad (1)$$

which also yields

$$z = \pm \sqrt{d_1^2 - (y - d_p)^2} \quad (2)$$

Therefore, if the  $O_p$  coordinates,  $x$ ,  $y$ , and  $z$ , are assigned (Inverse Position Analysis (IPA)), the actuated-joint variables,  $x$ ,  $y$ , and  $d_1$ , are determined uniquely and straightforwardly with Eq. (1). Conversely, if the actuated-joint variables are assigned (Direct Position Analysis (DPA)), the  $O_p$  coordinates can assume two set of values which share the same  $x$  and  $y$  values, but have the opposite  $z$  values given by Eq. (2). These two solutions of the DPA yield a workspace symmetric with respect to the  $x_b y_b$  coordinate plane.

The workspace, represented by using the  $O_p$  coordinates, is the intersection volume of two right circular cylindrical shells. One is due to the **PRPU** limb and has the axis parallel to the  $x_b$  axis and passing through the point  $(0, d_p, 0)^T$ , and the inner and outer radii equal to the minimum and maximum values of  $d_1$ . The other is due to the **PRRR** limb and has the axis parallel to the  $y_b$  axis and passing through the point  $(a_p, 0, 0)^T$ , and the inner and outer radii equal to  $|a_1 - a_2|$  and  $(a_1 + a_2)$ , respectively.

### 3 Instantaneous Kinematics

The translational nature of the studied **PRRR-PRPU** architecture has been stated in Sect. 1 through finite-kinetostatics considerations. Nevertheless, the instantaneous-kinematics analysis has to investigate whether platform's angular velocity,  $\boldsymbol{\omega}$ , can be different from zero at particular configurations (constraint singularities (Zlatanov et al. 2002)) of this TPM before deducing its instantaneous input-output relationship.

In the studied architecture,  $\omega$  must simultaneously satisfy the following two vector equations, the first coming from the **PRPU** limb and the second from the **PRRR** limb:

$$\omega = (\dot{\theta}_1 + \dot{\theta}_2) i_b + \dot{\theta}_3 k_b \quad (3a)$$

$$\omega = (\dot{\theta}_4 + \dot{\theta}_5 + \dot{\theta}_6) j_b \quad (3b)$$

where  $\theta_1$ ,  $\theta_2$ , and  $\theta_3$  are the joint variables of the three R pairs of the **PRPU** limb; whereas,  $\theta_4$ ,  $\theta_5$ , and  $\theta_6$  are the joint variables of the three R pairs of the **PRRR** limb. Equating the right-hand sides of Eqs. (3a) and (3b) yields

$$(\dot{\theta}_1 + \dot{\theta}_2) i_b - (\dot{\theta}_4 + \dot{\theta}_5 + \dot{\theta}_6) j_b + \dot{\theta}_3 k_b = 0 \quad (4)$$

which can be satisfied if and only if the coefficients of the three independent unit vectors  $i_b$ ,  $j_b$ , and  $k_b$  are identically equal to zero. Since such coefficients are the same that appear in Eqs. (3a) and (3b) and the unit vectors  $i_b$ ,  $j_b$ , and  $k_b$  are constant vectors,  $\omega$  must always be equal to zero, that is, the studied TPM has no constraint singularity.

The absence of constraint singularities allows the deduction of the instantaneous input-output relationship by assuming that the velocities of all the platform points are equal. This condition yields [see Fig. 1c]

$$\dot{O}_p \equiv \dot{A}_1 = \dot{B}_1 + d_1 \dot{\theta}_1 (i_b \times u) + \dot{d}_1 u \quad (4)$$

where

$$\dot{B}_1 = \dot{x} i_b, \quad u = \cos \theta_1 j_b + \sin \theta_1 k_b \quad (5)$$

Also, the time derivative of the geometric relationship  $(y - d_p) = d_1 \cos \theta_1$  [see Fig. 1c], after some rearrangements, yields

$$\dot{\theta}_1 = \frac{\dot{d}_1 \cos \theta_1 - \dot{y}}{d_1 \sin \theta_1} \quad (6)$$

Eventually, the introduction of Eqs. (5) and (6) into Eq. (4) brings to the sought-after instantaneous input-output relationship:

$$\dot{O}_p = \dot{x} i_b + \dot{y} \left( j_b - \frac{\cos \theta_1}{\sin \theta_1} k_b \right) + \dot{d}_1 \left( \frac{1}{\sin \theta_1} k_b \right) \quad (7)$$

**Singularity Analysis.** Singularities (Gosselin and Angeles 1990; Ma and Angeles 1991; Zlatanov et al. 1995) are manipulator's configurations where the instantaneous input-output relationship fails to state a one-to-one correspondence

between instantaneous inputs (i.e., the actuated joints' rates) and outputs (i.e., the platform twist). Type-I (serial) singularities occurs when the actuated joints' rates are not determined even though the platform twist is assigned; vice versa, type-II (parallel) singularities occurs when the actuated joints' rates are not determined even though the platform twist is assigned; eventually, type-III singularities are configurations where both the two previous conditions are satisfied.

Type-I singularities are located at the workspace boundaries and correspond to configurations where the platform can carry large forces (even infinitely large) without using one or more of the actuators' torques. Type-II singularities are usually located inside the workspace and correspond to configurations where the platform cannot carry forces (even infinitesimal) along one or more directions without requiring that one or more actuators supply infinite generalized torques.

In the studied TPM, the  $x$  and  $y$  coordinates of  $O_p$  are also actuated-joint variables. Therefore, singularities may occur only in the relationship between  $\dot{z}$  and the actuated joints' rates,  $\dot{x}$ ,  $\dot{y}$ , and  $\dot{d}_1$ . Actually, after a simple expansion, Eq. (7) reduces itself to two identities plus the following scalar equation

$$\dot{z} \sin \theta_1 = \dot{d}_1 - \dot{y} \cos \theta_1 \quad (8)$$

The analysis of Eq. (8) reveals that type-II singularities occur when  $\theta_1$  is equal to zero, that is, when  $O_p$  lies on the plane  $z = 0$  [see Fig. 1c]; whereas, no type-I singularities are presents.<sup>4</sup> Also, Eq. (7) and Fig. 1c highlight that, when  $O_p$  lies on the plane  $y = d_p$ ,  $\theta_1$  is equal to  $\pm 90^\circ$  and the Jacobian matrix that relates the platform translation velocity,  $\dot{O}_p$ , to the actuated joints' rates,  $\dot{x}$ ,  $\dot{y}$ , and  $\dot{d}_1$  is equal to  $\mathbf{diag}(1, 1, \pm 1)$ ; hence, at these configurations, it has all its singular values equal to one. The configurations where the singular values of this Jacobian are all equal and non-null are named isotropic (Angeles and Lòpez-Cajùn 1992; Gosselin and Angeles 1991) and provide the best kinetostatics performances. The manipulator that can reach one or more isotropic configuration are named isotropic. Therefore, the studied TPM is an isotropic manipulator that can reach  $\infty^2$  isotropic configurations corresponding to the points of the plane  $y = d_p$ . Locating its useful workspace around the plane  $y = d_p$  yields the best kinetostatics design.

## 4 Conclusions

Many types of limb for TPMs have been proposed in the literature. The suitable combination of two out of such limbs, one with connectivity 4 and another with connectivity 5, generates a family of single-loop not-overconstrained TPM

---

<sup>4</sup>Equations (7) and (8) do not take into account mobility limitations due to the maximum and minimum values the actuated-joint variables can assume. If such limitations were considered, all the configurations lying on the workspace boundaries would result to be type-I singularities.



architectures. A great number of such architectures make it possible to put two actuators on the base and the third near to the base thus keeping many of the advantages of the three-limbed architectures.

A particular **PRRR-PRPU** architecture belongs to this family and has two actuators on the base and the third near to the base. The position analysis and the instantaneous kinematics of this TPM have been addressed. The results are that two simple explicit formulas solve its position analysis problems, the workspace boundaries are easy to find, it has no constraint singularity, its type-II singularity locus is a plane easy to keep far from the useful workspace, and it has a double infinity of isotropic configurations. Therefore, it is a good design alternative.

The conclusion is that analyzing the kinematics of the architectures of this family can still provide new and interesting TPMs.

**Acknowledgments** This work has been developed at the Laboratory of Advanced Mechanics (MECH-LAV) of Ferrara Technopole, supported by UNIFE funds, by Regione Emilia Romagna (District Councillorship for Productive Assets, Economic Development, Telematic Plan) POR-FESR 2007–2013, Attività I.1.1.

## References

- Angeles, J. (1988). *Rational kinematics*. New York, USA: Springer.
- Angeles, J., & Lòpez-Cajùn, C. S. (1992). Kinematic isotropy and the conditioning index of serial robotic manipulators. *The International Journal of Robotics Research*, 11(6), 560–571.
- Davidson, J. K., & Hunt, K. H. (2004). *Robots and screw theory: applications of kinematics and statics to robotics*. New York, USA: Oxford University Press.
- Gosselin, C. M., & Angeles, J. (1990). Singularity analysis of closed-loop kinematic chains. *IEEE Transactions on Robotics and Automation*, 6(3), 281–290.
- Gosselin, C., & Angeles, J. (1991). A global performance index for the kinematic optimization of robotic manipulators. *Journal of Mechanical Design*, 113(3), 220–226.
- Hervé, J. M., & Sparacino, F. (1991). Structural synthesis of parallel robots generating spatial translation. In *Proceedings of the 5th IEEE International Conference on Advanced Robotics* (pp. 808–813).
- Kong, X., & Gosselin, C. (2007). *Type synthesis of parallel mechanisms*. Berlin, Germany: Springer.
- Ma, O., & Angeles, J. (1991). Architecture singularities of platform manipulators. In *Proceedings of the 1991 IEEE International Conference on Robotics and Automation* (pp. 1542–1547). Sacramento (CA, USA).
- Zlatanov, D., Bonev, I. A., & Gosselin, C. M. (2002). Constraint singularities of parallel mechanisms. In *Proceedings of the 2002 IEEE International Conference on Robotics & Automation* (pp. 496–502). Washington, DC.
- Zlatanov, D., Fenton, R. G., & Benhabib, B. (1995). A unifying framework for classification and interpretation of mechanism singularities. *ASME Journal of Mechanical Design*, 117(4), 566–572.

# A Measure of the Distance Between Two Rigid-Body Poses Based on the Use of Platonic Solids

Claudio Mazzotti, Nicola Sancisi and Vincenzo Parenti-Castelli

**Abstract** This paper deals with the definition of a measure of the distance between two spatial rigid-body poses (i.e., positions and orientations). First, a platonic solid is attached to the rigid body, then the distance metric is defined as the root mean square distance between the homologous vertices of the platonic solid at the two rigid-body poses. The distance metric thus defined is intrinsically endowed with physical meaning, it depends only on the position and dimension of the platonic solid on the body, while it is independent of the reference systems, of the chosen platonic solid and of its orientation with respect to the body. Finally, some suggestions for the choice of the position and dimension of the platonic solid are discussed.

**Keywords** Spatial pose distance • Point cloud • Platonic solid

## 1 Introduction

A common problem in many mechanical applications (e.g., evaluation of positioning precision, path planning and mechanism synthesis) is to measure the distance between the actual pose (i.e., position and orientation) of a rigid body and a target pose with respect to which the rigid body has to be located. Thus, basically the problem is to measure the distance between two rigid-body poses. Since the

---

C. Mazzotti · N. Sancisi (✉) · V. Parenti-Castelli  
DIN - University of Bologna, Bologna, Italy  
e-mail: nicola.sancisi@unibo.it

C. Mazzotti  
e-mail: claudio.mazzotti4@unibo.it

V. Parenti-Castelli  
e-mail: vincenzo.parenti@unibo.it

N. Sancisi · V. Parenti-Castelli  
CIRI Health Sciences & Technologies, Bologna, Italy

special Euclidean group  $SE(3)$  collects all possible poses of a rigid body, in the literature this problem is usually referred to as the definition of a distance metric in  $SE(3)$ . This problem has been extensively studied in the last few decades and many researchers have proposed a variety of solutions, some of them reported in Di Gregorio (2008) and Chirikjian (2015).

A distance metric must be a real function of both the position and the orientation of the body, which means a function of dimensionally non-homogeneous quantities. Thus, a first challenge consists in combining these quantities into a single measure. Moreover, a distance metric  $d_m(p_1, p_2)$  between two rigid-body poses  $p_1$  and  $p_2$  must satisfy the following conditions:

- (i) symmetry:  $d_m(p_1, p_2) = d_m(p_2, p_1)$ ;
- (ii) positive definiteness:  $d_m(p_1, p_2) > 0$  if  $p_1 \neq p_2$  and  $d_m(p_1, p_2) = 0$  if  $p_1 = p_2$ ;
- (iii) triangle inequality:  $d_m(p_1, p_2) \leq d_m(p_1, p_3) + d_m(p_3, p_2)$ , where  $p_3$  is a third rigid-body pose.

Some papers present the concept of invariance (Park 1995; Chirikjian 2015). This is basically the desirable property of the metric to be independent (to some extents) of the choice of the reference systems on the rigid body or on the fixed frame.

In this paper, in order to define a distance metric  $d_m(p_1, p_2)$  that is dimensionally homogeneous, a point cloud is associated with the rigid-body reference system to represent the body pose. The use of points instead of more standard pose parameterizations is not new and it is the basis of representations by natural coordinates (García De Jalón et al. 1986), and of the definition of kinematic performance indices (Angeles and Lopez-Cajún 1992; Nawratil 2007), of algorithms for robust  $SE(3)$  control of manipulators (Cunha et al. 2008) and of distance metrics in  $SE(3)$  (Martínez and Duffy 1995; Chirikjian and Zhou 1998) as well. In the present study, the root mean square distance between homologous points at  $p_1$  and  $p_2$  is computed. If the points of the point cloud coincide with the vertices of a regular polyhedron, the mathematical formulation is reduced to a compact and simple expression. The distance metric thus defined is easy to implement, mathematically compact and intrinsically endowed with physical meaning. It is independent of both the choice of the reference systems and of the type of the chosen regular polyhedron. It is also independent of the polyhedron orientation with respect to the body, but not of its position on the body and of its dimension, for which some suggestions are presented. In this perspective, for a chosen polyhedron position, the proposed distance metric is an isotropic measure (i.e., differences in the body position and orientation have the same weight along and above all directions). Non-isotropic metrics could also be devised by the same procedure, for those applications that require such a condition.

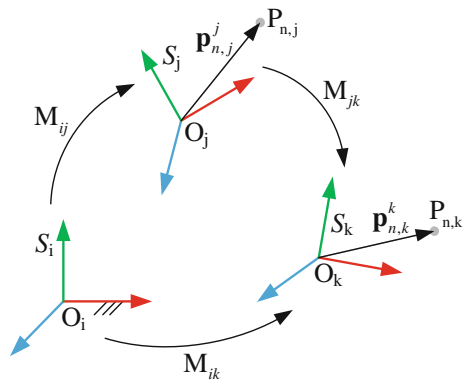
## 2 Formulation of the Proposed Distance Metric

The problem is to define a distance metric between two rigid-body poses. With reference to Fig. 1,  $S_i$  is the fixed reference system, whereas  $S_j$  and  $S_k$  are the two rigid-body reference systems, corresponding to the two rigid-body poses  $p_1$  and  $p_2$  whose distance has to be measured. Each reference system is right-handed, with coordinate axes  $x_q, y_q, z_q$  and origin  $O_q$ , where  $q = i, j, k$ . In this paper,  $P_{n,r}$  denotes the  $n$ th point  $P_n$  belonging to the system  $S_r$ , whereas  $\mathbf{p}_{n,r}^q$  denotes the position vector of the point  $P_{n,r}$  with respect to  $S_q$ , where  $r, q = i, j, k$  and in general  $r \neq q$ . The subscript  $n$  is omitted if the point is single, e.g., if it is the origin of a reference system. The relative pose of  $S_k$  with respect to  $S_j$  is represented by the  $4 \times 4$  homogeneous matrix  $\mathbf{M}_{jk} = \begin{pmatrix} \mathbf{R}_{jk} & \mathbf{o}_k^j \\ \mathbf{0} & 1 \end{pmatrix}$ , where  $\mathbf{R}_{jk}$  is the  $3 \times 3$  orthonormal rotation matrix that transforms the vector component from  $S_k$  to  $S_j$ ,  $\mathbf{o}_k^j$  is the position vector of the origin  $O_k$  of the system  $S_k$  expressed in  $S_j$ ,  $\mathbf{0}$  is the  $1 \times 3$  vector whose components are all equal to zero. As a consequence,  $\mathbf{p}_{n,k}^j = \mathbf{R}_{jk} \mathbf{p}_{n,k}^k + \mathbf{o}_k^j$ . In particular,  $\mathbf{M}_{jk} = (\mathbf{M}_{ij})^{-1} \mathbf{M}_{ik}$ , where  $\mathbf{M}_{ij}$  and  $\mathbf{M}_{ik}$  are the  $4 \times 4$  homogeneous matrices which represent the pose of  $S_j$  and  $S_k$  with respect to  $S_i$  respectively, whereas  $(\cdot)^{-1}$  is the inverse of the matrix inside brackets.

To define a distance metric, a point cloud composed of  $N$  points  $P_{n,r}$  (where  $n = 1, \dots, N$  and  $r = j, k$ ) is attached to the rigid body, such that its relative position and orientation does not change with the body pose, i.e.,  $\mathbf{p}_{n,j}^j = \mathbf{p}_{n,k}^k$ . The distance metric  $d_m$  is the root mean square distance of the homologous points  $P_{n,j}$  and  $P_{n,k}$  represented in the same reference system (e.g.,  $S_j$ ), that is:

$$d_m = \sqrt{\frac{1}{N} \sum_{n=1}^N |\mathbf{p}_{n,k}^j - \mathbf{p}_{n,j}^j|^2} = \sqrt{\frac{1}{N} \sum_{n=1}^N |\mathbf{o}_k^j + \mathbf{R}_{jk} \mathbf{p}_{n,k}^k - \mathbf{p}_{n,j}^j|^2} \quad (1)$$

**Fig. 1** The three reference systems:  $S_i$  is the fixed reference system, whereas  $S_j$  and  $S_k$  represent the body reference system at the two poses whose distance has to be measured



where  $|\cdot|^2$  is the square norm of the vector inside the brackets. Expanding the square norm in Eq. (1),  $d_m$  can be re-written as:

$$d_m = \sqrt{|\mathbf{o}_k^j|^2 + \frac{1}{N} \sum_{n=1}^N \left( |\mathbf{R}_{jk} \mathbf{p}_{n,k}^k|^2 + |\mathbf{p}_{n,j}^j|^2 + 2(\mathbf{o}_k^j \cdot \mathbf{R}_{jk} \mathbf{p}_{n,k}^k - \mathbf{o}_k^j \cdot \mathbf{p}_{n,j}^j - \mathbf{R}_{jk} \mathbf{p}_{n,k}^k \cdot \mathbf{p}_{n,j}^j) \right)} \quad (2)$$

If the origin  $O_j$  ( $O_k$ ) of  $S_j$  ( $S_k$ ) is placed at the centroid of the chosen point cloud:

$$\sum_{n=1}^N (\mathbf{o}_k^j \cdot \mathbf{R}_{jk} \mathbf{p}_{n,k}^k) = \mathbf{o}_k^j \cdot \mathbf{R}_{jk} \sum_{n=1}^N \mathbf{p}_{n,k}^k = 0 \quad \text{and} \quad \sum_{n=1}^N (\mathbf{o}_k^j \cdot \mathbf{p}_{n,j}^j) = \mathbf{o}_k^j \cdot \sum_{n=1}^N \mathbf{p}_{n,j}^j = 0 \quad (3)$$

Equation (2) consequently simplifies to:

$$d_m = \sqrt{|\mathbf{o}_k^j|^2 + \frac{1}{N} \left( \sum_{n=1}^N |\mathbf{R}_{jk} \mathbf{p}_{n,k}^k|^2 + \sum_{n=1}^N |\mathbf{p}_{n,j}^j|^2 \right) - \frac{2}{N} \sum_{n=1}^N (\mathbf{R}_{jk} \mathbf{p}_{n,k}^k \cdot \mathbf{p}_{n,j}^j)} \Rightarrow$$

$$d_m = \sqrt{|\mathbf{o}_k^j|^2 + \frac{2}{N} \sum_{n=1}^N r_n^2 - \frac{2}{N} \sum_{n=1}^N r_n^2 \cos(\alpha_n)} = \sqrt{|\mathbf{o}_k^j|^2 + \frac{2}{N} \sum_{n=1}^N r_n^2 (1 - \cos(\alpha_n))} \quad (4)$$





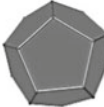
where  $r_n = |\mathbf{R}_{jk} \mathbf{p}_{n,k}^k| = |\mathbf{p}_{n,j}^j|$ , whereas  $\alpha_n$  is the angle between  $\mathbf{p}_{n,j}^j$  and  $\mathbf{R}_{jk} \mathbf{p}_{n,k}^k$ . If the  $N$  points of the point cloud lie on the surface of a sphere of radius  $R$ , Eq. (4) simplifies to:

$$d_m = \sqrt{|\mathbf{o}_k^j|^2 + 2R^2 \left( 1 - \frac{1}{N} \sum_{n=1}^N \cos(\alpha_n) \right)} \quad (5)$$

Equation (5) shows that  $d_m$  is given by the sum of two terms: the first term can be seen as the translational part of  $d_m$ , whereas the second term can be seen as the rotational part of  $d_m$ .

In this paper the  $N$  points of the point cloud are chosen coincident with the vertex of a regular polyhedron inscribed in a sphere of radius  $R$  and centered in the body reference system. This last hypothesis is chosen only to simplify the mathematical derivation using Eq. (5), but, as will be clarified further on, the final result does not formally change by centering the polyhedron at a different point. A regular polyhedron, usually called platonic solid, is a polyhedron whose faces are congruent regular polygons, which are assembled in the same way around each vertex. There are only five platonic solid, summarized in Table 1 together with the corresponding number of vertices.

**Table 1** The five platonic solids

	Tetrahedron	Octahedron	Cube	Icosahedron	Dodecahedron
<i>Platonic solid</i>					
<i>N</i>	4	6	8	12	20

The number  $N$  refers to the number of vertices

For platonic solids, the rotational part of Eq. (5) can be further simplified. The matrix  $\mathbf{R}_{jk}$  can be represented by means of the axis-angle parameterization, i.e.,  $\mathbf{R}_{jk} = \mathbf{R}_{jk}(\mathbf{u}, \theta)$ , where  $\mathbf{u}$  is the unit vector that identifies the direction of the finite screw axis between the two given poses, and  $\theta$  is the absolute value of the angle of rotation about this axis. It can be shown that  $d_m$  for all the five platonic solids results:

$$d_m = \sqrt{|\mathbf{o}_k^j|^2 + 2R^2 \left( \frac{2}{3} (1 - \cos(\theta)) \right)} \tag{6}$$

Therefore,  $d_m$  only depends on: (i) the position vector  $\mathbf{o}_k^j$ , (ii) the angle  $\theta \in [0, \pi]$  and (iii) the sphere radius  $R$ . As an alternative formulation, Eq. (6) can also be written as:

$$d_m = \sqrt{|\mathbf{o}_k^j|^2 + 2R^2 \left( 1 - \frac{\text{tr}(\mathbf{R}_{jk})}{3} \right)} \tag{7}$$

where  $\text{tr}(\cdot)$  is the trace of the matrix inside the brackets. Like in Eq. (5), the first term in Eqs. (6) and (7) represents the translational part of  $d_m$ , whereas the second term represents the rotational part. Indeed:

$$\begin{aligned} \text{if } |\mathbf{o}_k^j| = 0 &\Rightarrow d_m = R \sqrt{\frac{4}{3} (1 - \cos(\theta))} = R \sqrt{2 \left( 1 - \frac{\text{tr}(\mathbf{R}_{jk})}{3} \right)} \\ &\Rightarrow \max(d_m) = 2R \sqrt{\frac{2}{3}} \text{ for } \theta = \pi \\ \text{if } \mathbf{R}_{jk} = \mathbf{I} &\Rightarrow d_m = |\mathbf{o}_k^j| \\ \text{if } |\mathbf{o}_k^j| = 0 \text{ and } \mathbf{R}_{jk} = \mathbf{I} &\Rightarrow d_m = 0 \end{aligned}$$

where  $\mathbf{I}$  is the  $3 \times 3$  identity matrix. Thus, the rotational part of  $d_m$  is a function of the complement to one of the mean value of the  $\mathbf{R}_{jk}$  main diagonal elements. It is

worth noting that both the translational and the rotational part of  $d_m$  are homogeneous quantities, namely lengths. In particular, the sphere radius  $R$  can be seen as an intrinsic weight for the rotational part of  $d_m$ , thus  $R$  is similar to the characteristic length which was proposed by Angeles (2002) to combine translations and rotations, and which in this case takes on a clear geometrical interpretation.

### 3 Distance Metric Properties

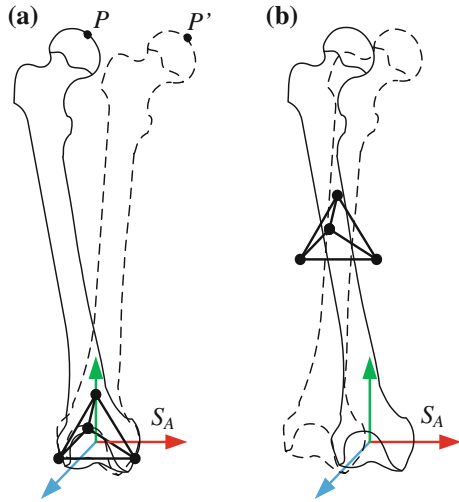
As clearly stated in Sect. 2, the value of  $d_m$  is based on point distances. Since the distance between two points satisfies the three conditions (symmetry, positive definiteness and triangle inequality) stated in Sect. 1,  $d_m$  consequently satisfies them and is thus a distance metric for SE(3). Moreover, the point distances are independent of the choice of the reference systems, thus  $d_m$  is also independent of this choice once the regular polyhedron pose is fixed on the body. Thus, the same result in Eqs. (6) and (7) holds if the platonic solid is not centered at the origin of the reference system: in this case  $|\mathbf{o}_k^j|$  is the distance between the centroid of the polyhedron at the two poses. The value of  $d_m$  does not depend on the chosen platonic solid, since the number of vertices  $N$  vanishes. Thus, there is no convenience in choosing a high number of points to obtain the measure: the spatial simplex, i.e., the tetrahedron, is sufficient to define  $d_m$  and it will be taken as a reference hereinafter. Moreover,  $d_m$  does not change with the tetrahedron orientation with respect to the body since it does not depend on  $\mathbf{u}$ . This orientation can thus be chosen arbitrarily since it does not affect the final result. As a further consequence,  $d_m$  can be seen as an isotropic distance metric, i.e., its value does not depend on the direction of the rotation axis between the poses, but only on the rotation difference  $\theta$ . On the contrary,  $d_m$  depends on the position and dimension of the tetrahedron:  $R$  does not vanish and  $\mathbf{o}_k^j$  changes with the tetrahedron position on the body. Suggestions for the choice of these parameters are proposed in the next Section.

### 4 Position and Dimension of the Tetrahedron

In this Section, some suggestions are presented about the choice of the proper position and dimension of the tetrahedron with respect to the body, by considering a specific application as an example.

A kinematic model of the knee replicating the joint natural motion is proposed in Sancisi and Parenti-Castelli (2011). For this particular application, the relative motion between the tibia (considered as the fixed frame) and the femur (considered as the moving body) is measured in vitro, then the model is synthesized in order to best fit the actual pose of the femur with respect to the target in vitro measured

**Fig. 2** Position of the tetrahedron with respect to the femur. The femur drawn with *solid (dashed) line* represents the actual (target) pose of the femur. For the sake of clarity, only the tetrahedron related to the actual pose is shown



femur pose. An anatomical reference system  $S_A$  is generally associated with each bone (Wu et al. 2002). At each step of the synthesis procedure, the problem is reduced to measuring and optimizing the distance between two body poses, i.e., the actual and the target pose of the femur. The distance between these two poses can be quantified by  $d_m$ . Since this metric is independent of the reference systems and of the orientation of the tetrahedron on the body, the result of the optimization will not depend on these parameters, but it will depend on the position on the body and on the dimension of the tetrahedron that, on the contrary, affect the measure.

As for the position, considering this particular application, a first solution is to place the tetrahedron in a point particularly important for the analysis, for instance centered at the origin of the anatomical system  $S_A$  of the femur (Fig. 2a) that is generally close to the joint. This choice is significant for the joint model synthesis (Sancisi and Parenti-Castelli 2011), since it allows a better control over the position of the bone part that is of interest. However, small rotation errors could imply greater position errors for some points of the body, e.g., the point  $P(P')$  of the actual (target) femur pose in Fig. 2a. Thus, this solution may not be optimal if the aim of the synthesis is to best replicate the motion of all points of the bone.

An alternative solution can be devised from the following considerations. The shape of the studied bones could be known from medical imaging. Equations (1)–(4) could be used to compute the root mean square distance  $\hat{d}_m$  of homologous points of this point cloud. In particular, Eq. (4) holds if the bone centroid is chosen as a reference for the computation of  $\mathbf{o}_k^j$  and  $\alpha_n$ . However, the index  $\hat{d}_m$  is not an isotropic distance metric as  $d_m$  is, and it also requires the definition of the bone shape, that is not always known. In this perspective, another possibility proposed here is to place the centroid of the tetrahedron coincident to the geometrical centroid of the femur. The main advantage of this particular choice is that in this case the isotropic distance metric  $d_m$  is correlated to the non-isotropic root mean square error  $\hat{d}_m$ , consequently



representing the average distance error between homologous points of the whole bone (Fig. 2b). Moreover, the approximate location of the bone centroid can be found in anthropometric tables (Dumas et al. 2007).

As for the tetrahedron dimension, a first solution is to consider the sphere radius  $R$  as a weight for the rotational part of  $d_m$ , and to set it as a consequence with respect to the translational part. For instance, in knee motion analysis, the choice of a lower value of the sphere radius  $R$  relative to a tetrahedron centered in the joint (Fig. 2a) allows a better control of the relative position between the bones at the joint. In contrast, in gait analysis, the choice of a higher value of  $R$  relative to a tetrahedron placed in the centroid of the bone (Fig. 2b) allows a better representation of the motion of the whole bone. As a second solution,  $R$  can be chosen as a representative dimension of the body, e.g., the radius of a sphere approximating the femur condyles. In this case, indeed,  $d_m$  would be representative of the root mean square distance between homologous points on the femur close to the joint.

## 5 Conclusions

A common problem in many mechanical applications is to measure the distance between the actual pose and the target pose of a rigid body, i.e., to define a distance metric between two given rigid-body poses.

In this paper a novel distance metric was proposed. A platonic solid was attached to the rigid body and the root mean square distance between homologous vertices at the two rigid-body poses whose distance has to be measured was computed. The distance metric thus defined is easy to implement, mathematically compact, isotropic, and intrinsically endowed with physical meaning as well. Moreover, it depends only on the position and dimension of the platonic solid on the body, while it is independent of the reference systems, of the chosen platonic solid and of its orientation with respect to the body. Finally, some suggestions for the choice of the position and dimension of the platonic solid were discussed by means of an example taken from a typical biomechanical application.

## References

- Angeles, J. (2002). *Fundamentals of robotic mechanical systems* (Vol. 2). New York: Springer.
- Angeles, J., & Lopez-Cajún, C. S. (1992). Kinematic isotropy and the conditioning index of serial robotic manipulators. *International Journal of Robotic Research*, 11(6), 560–571.
- Cunha, R., Silvestre, C., & Hespanha, J. (2008). Output-feedback control for stabilization on SE(3). *Systems & Control Letters*, 57(12), 1013–1022.
- Chirikjian, G. S. (2015). Partial Bi-Invariance of SE(3) Metrics. *Journal of Computing and Information Science in Engineering*, 15(1), 011008.
- Chirikjian, G. S., & Zhou, S. (1998). Metrics on motion and deformation of solid models. *Journal of Mechanical Design*, 120(2), 252–261.

- Di Gregorio, R. (2008). Review and comparison of the metrics proposed for measuring the distance between two rigid-body poses. In *Quaderni del DIEM – GMA, Atti della Seconda Giornata di Studio Ettore Funaioli* (pp. 47–58). Bologna: Esculapio. doi:10.6092/unibo/amsacta/2552. <http://amsacta.unibo.it/2552/>.
- Dumas, R., Chèze, L., & Verriest, J.-P. (2007). Adjustments to McConville et al. and Young et al. body segment inertial parameters. *Journal of Biomechanics*, 40, 543–553.
- García De Jalón, J., Unda, J., & Avello, A. (1986). Natural coordinates for the computer analysis of multibody systems. *Computer Methods in Applied Mechanics and Engineering*, 56, 309–327.
- Martinez, J. M. R., & Duffy, J. (1995). On the metrics of rigid body displacements for infinite and finite bodies. *Journal of Mechanical Design*, 117(1), 41–47.
- Nawratil, G. (2007). New performance indices for 6R robots. *Journal of Mechanism and Machine Theory*, 42, 1499–1511.
- Park, F. C. (1995). Distance metrics on the rigid-body motions with applications to mechanism design. *Journal of Mechanical Design*, 117(1), 48–54.
- Sancisi, N., & Parenti-Castelli, V. (2011). A new kinematic model of the passive motion of the knee inclusive of the patella. *Journal of Mechanisms and Robotics*, 3(4), 041003.
- Wu, G., Siegler, S., Allard, P., Kirtley, C., Leardini, A., Rosenbaum, D., et al. (2002). ISB recommendation on definitions of joint coordinate system of various joints for the reporting of human joint motion—Part I: Ankle, hip, and spine. *Journal of Biomechanics*, 35(4), 543–548. doi:10.1016/S0021-9290(01)00222-6.

**Part III**  
**Dynamics for Robotics**

# Properties of the Dahl Model Applied to Modelling of Static Friction in Closed-Loop Kinematic Chains

Marek Wojtyra

**Abstract** High parametric sensitivity of the Dahl model is observed when rigid body approach is used to analyse the static friction in close-loop mechanisms. The origins of sensitivity problems are investigated. The possibility of diminishing sensitivity problems by taking flexibility into account is discussed.

**Keywords** Static friction • Dahl model • Redundant constraints • Solution uniqueness

## 1 Introduction

Due to its nonlinear nature, friction is problematic in modelling. Most often encountered difficulties pertain to numerical stiffness of equations of motion (Armstrong-Hélouvry et al. 1994; Do et al. 2007) or to identification of model parameters (Hensen et al. 2002; Hadji and Mureithi 2014). It was also shown that the simulated motion of an overconstrained multibody system may be not unique when friction forces in joints are present (Frączek and Wojtyra 2011).

This study deals with problems of solution uniqueness and high parametric sensitivity that may occur when closed-loop mechanisms, even **without** redundant constraints, are modelled. The investigation is focused on the stiction phase and its vicinity. Two significantly different methods of friction modelling are examined, however, the results are in both cases similar: neither the stiction forces nor the moment of transition between static and kinetic friction regime can be credibly predicted when a rigid body model is employed.

The first investigated technique of friction modelling, the method of constraints addition and deletion, was proposed by Haug et al. (1986). Due to the necessity of constraints switching and the discontinuity at zero relative velocity, this approach is

---

M. Wojtyra (✉)

Institute of Aeronautics and Applied Mechanics,  
Warsaw University of Technology, Warszawa, Poland  
e-mail: mwojtyra@meil.pw.edu.pl

seldom used in practical calculations. However, examination of this model is advantageous, since some crucial issues are clearly visible. It is shown that in the stiction regime the multibody system becomes overconstrained and calculation of joint reactions is impeded: problems with solution uniqueness emerge.

The main object of investigation is the Dahl model (Dahl 1976). It is representative for a group of models with auxiliary “internal dynamics” state variables that describe the microslips during the stiction phase (Armstrong-Hélouvy et al. 1994). Apart from the Dahl model, this approach is adopted, e.g., in LuGre (Canudas de Wit et al. 1995) and Leuven (Swevers 2000) friction models. In this group of models, at a price of introducing additional differential equations, both stiction and sliding regimes are unified and governed by the same equations, and consequently, simulations are performed more efficiently (Do et al. 2007; Pennestrì et al. 2007). This article points out that—in the stiction regime and its neighbourhood—the multibody model behaviour is highly sensitive to changes of some less certain and hardly measurable parameters of the Dahl model of friction.

The problems associated with determining friction forces in the stiction regime are closely related to constraints redundancy, therefore, in further considerations flexibility of parts undergoing frictional contact is taken into account (flexibility of bodies is one of the main factors that decide how loads are distributed among kinematic pairs of an overconstrained mechanism, see Wojtyra and Frączek 2012). It is demonstrated that the secondary parameters of Dahl model no longer play the essential role in calculation of static friction forces. Instead, the elasticity is crucial for the results obtained in the stiction regime.

To illustrate the considered issues, a simple model of two-point foot-ground contact is investigated in the provided examples.

## 2 Constraints Addition-Deletion in Closed-Loop Mechanisms

Consider a rigid multibody system described by a  $n$ -element vector of dependent coordinates  $\mathbf{q}$ , subjected to  $m$  holonomic constraints  $\Phi(\mathbf{q}) = \mathbf{0}_{m \times 1}$ , and assume that constraints are independent, i.e., no redundant constraints exist. Let’s assume, for the sake of simplicity, that the considered system has exactly one degree of freedom ( $m = n - 1$ ) and forms a closed-loop kinematic chain with one or more loops.

The system equations of motion may be written in the following form:

$$\mathbf{M}(\mathbf{q}) \ddot{\mathbf{q}} + (\Phi_{\mathbf{q}}(\mathbf{q}))^T \boldsymbol{\lambda} = \mathbf{Q}(\mathbf{q}, \dot{\mathbf{q}}, t) + \mathbf{Q}^F(\mathbf{q}, \dot{\mathbf{q}}, \boldsymbol{\lambda}), \quad (1)$$

where  $\mathbf{M}$  denotes the mass matrix and  $\mathbf{Q}$  contains the external forces and all velocity dependent inertial terms. The generalized constraint reactions are represented by the product of the transposed constraint Jacobian  $\Phi_{\mathbf{q}}^T$  and the vector of

Lagrange multipliers  $\lambda$ . The generalized forces of sliding friction  $\mathbf{Q}^F$  are treated as additional external forces that depend on normal reactions (Haug et al. 1986).

Calculation of vector  $\mathbf{Q}^F$  is done in three steps. Firstly, generalized normal reactions  $\Phi_{\mathbf{q}}^T \lambda$  are used to calculate physical normal reactions  $\mathbf{N}_i(\mathbf{q}, \lambda)$  in each kinematic pair  $i$ . Then, the model of friction (e.g., the Dahl model), which establishes the relation between the normal and tangential force, is utilized to calculate the physical friction force  $\mathbf{F}_i(\mathbf{q}, \dot{\mathbf{q}}, \mathbf{N}_i)$  in each joint  $i$ . Finally, the physical friction forces acting in kinematic pairs are transformed into generalized friction forces  $\mathbf{Q}^F(\mathbf{q}, \mathbf{F}_1, \dots, \mathbf{F}_k)$ .

Equation (1) is valid as long as the multibody system is in motion. At a certain moment, the relative velocity in a kinematic pair can reach the zero value. After that event, motion of the system may continue instantaneously or can be stopped due to stiction occurrence. No relative joint motion is observed as long as the friction force remains within an allowable range. This condition for  $i$ th kinematic pair can be written as:

$$\|\mathbf{F}_i\| \leq \mu_i \left\| \mathbf{N}_i(\mathbf{q}, \Phi_{\mathbf{q}}^T \lambda) \right\|, \quad (2)$$

where  $\mu_i$  is a coefficient of static friction.

The joint locking due to static friction can be represented by a supplementary constraint imposed on the system, added when velocity of sliding reaches zero (Haug et al. 1986). The reaction associated with the additional constraint corresponds to the static friction force and can be utilized to calculate the physical joint friction force  $\mathbf{F}_i$ . To determine whether stiction occurs, condition (2) is repeatedly checked during simulation. If condition (2) is not satisfied, the supplementary constraint is deleted.

In the case of a 1-DOF mechanism, the relative velocities in all kinematic pairs become equal to zero at the same time. Thus, supplementary constraints  $\Psi(\mathbf{q}) = \mathbf{0}_{k \times 1}$  must be simultaneously added to all kinematic pairs with friction ( $k$  is the sum of relative degrees of freedom in these pairs). During the period of stiction, kinetic friction forces  $\mathbf{Q}^F$  as well as accelerations  $\ddot{\mathbf{q}}$  vanish and Eq. (1) has to be replaced by the following:

$$\begin{bmatrix} \Phi_{\mathbf{q}}(\mathbf{q}^*)^T & \Psi_{\mathbf{q}}(\mathbf{q}^*)^T \end{bmatrix}_{n \times (m+k)} \begin{bmatrix} \lambda \\ \kappa \end{bmatrix}_{(m+k) \times 1} = \mathbf{Q}(\mathbf{q}^*, \mathbf{0}, t)_{n \times 1}, \quad (3)$$

where  $\mathbf{q}^*$  represents the configuration at which mechanism is stopped,  $\Psi_{\mathbf{q}}$  denotes the Jacobian matrix of additional constraints, and  $\kappa$  is the vector of Lagrange multipliers that represents their generalized reactions.

Since in the case of a 1-DOF mechanism the number of additional constraints  $k$  exceeds the number of degrees of freedom (by  $k - 1$ ), the multibody system **becomes redundantly constrained** (the same is expected in mechanisms with more DOFs, whenever the number of additional constraints exceeds the number of DOFs). Mathematically, the system of linear equations, Eq. (3), is

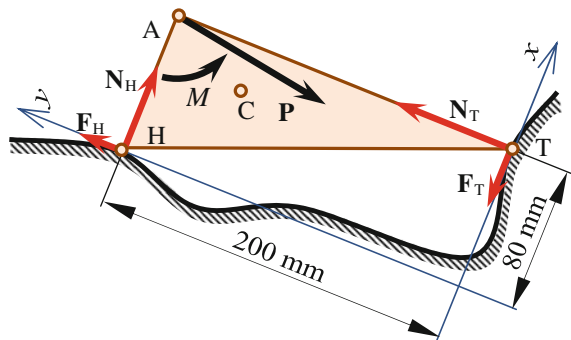
underdetermined. Most often, the indeterminacy pertains not only to  $\kappa$  (friction) but also to  $\lambda$  (normal reactions). As a consequence, neither normal reactions nor static friction forces can be uniquely determined as long as rigid body assumption holds (Wojtyra and Frączek 2012, 2013).

Motion of the stopped system is unique, nevertheless, the conditions for stiction occurrence, Eq. (2), must be repeatedly checked as the simulation proceeds. The essential problem is that, in many cases, two substantially different types of solutions for normal and friction forces can be found—one corresponding to sliding and the other corresponding to stiction. Thus, it is impossible to decide whether or not stiction conditions are fulfilled for given external loads.

*Example 1* A foot during two-point contact with an uneven terrain, presented in Fig. 1, serves as a simple example of a 1-DOF closed loop mechanism. The contact points at heel (H) and toe (T) can slide along the ground surface (“point on line” kinematic pairs). The coefficient of friction (for both kinetic and static friction) equals  $\mu = 0.5$ . A constant force  $\mathbf{P} = [-15, -95]^T$  [N], applied to the ankle (A) is accompanied by a torque  $M = 9$  [Nm]. Prior to the considered time instant the mechanism was not moving. The question is whether or not the conditions for stiction occurrence are fulfilled.

The discussed model of mechanism has no unique reaction solution. Let us focus on two out of infinitely many possibilities. The first solution is (all components in newtons):  $\mathbf{N}_H = [54, 0]^T$ ,  $\mathbf{F}_H = [0, 15]^T$ ,  $\mathbf{N}_T = [0, 80]^T$ ,  $\mathbf{F}_T = [-39, 0]^T$ , and the second one is:  $\mathbf{N}_H = [46, 0]^T$ ,  $\mathbf{F}_H = [0, 35]^T$ ,  $\mathbf{N}_T = [0, 60]^T$ ,  $\mathbf{F}_T = [-31, 0]^T$ . The condition for stiction occurrence, Eq. (2), is fulfilled for both contact points in the case of the first solution, whereas is not fulfilled in the other case. Both solutions are equally acceptable. There is no justification for rejecting one of them and preserving the other. Thus, the model offers no answer whether the foot slips or remains blocked by static friction.

**Fig. 1** Two-point foot-ground contact—dimensions and loads



### 3 Dahl Friction in Closed-Loop Mechanisms

The constraint addition-deletion approach is seldom used in practical applications since discontinuity at zero relative joint velocity and constraints switching causes a number of analytical and computational problems (Do et al. 2007; Pennestri et al. 2007). More frequently employed models treat stiction and sliding uniformly and provide the same equations for both regimes of friction. No additional constraints are imposed during the stiction phase, as friction force at zero relative velocity is described by equality rather than inequality.

The Dahl model (Dahl 1976) is based on the experiments that indicated an analogy between friction force—displacement relationship and stress—strain behaviour observed in material deformation tests. In the Dahl model an additional state variable  $z_i$  is introduced. This variable may be interpreted as the average deflection of asperities at contacting surfaces of  $i$ th kinematic pair. Deflection  $z_i$  is modelled in terms of the first-order differential equation, and physical friction force  $F_i$  is proportional to  $z_i$ :

$$\dot{z}_i = v_i - z_i \sigma_i |v_i| / F_{Ci}, \quad F_i = \sigma_i z_i, \quad (i = 1, \dots, k), \quad (4a, b)$$

where stiffness  $\sigma_i$  characterizes the elasticity of contact surfaces,  $v_i$  is the relative velocity of sliding, and  $F_{Ci}$  is the Coulomb friction force ( $F_{Ci} = \mu_i N_i$ ).

In the mathematical model, Eq. (1) is accompanied by Eqs. (4a, b), formulated for all pairs with friction. Variables  $\mathbf{z} = [z_1, \dots, z_k]^T$  are utilized to calculate the physical friction forces, which are then transformed to generalized friction force  $\mathbf{Q}^F(\mathbf{q}, \dot{\mathbf{q}}, \mathbf{z}, \dot{\mathbf{z}}, \lambda)$ .

An interesting question is, how the non-uniqueness problem, observed when constraint addition-deletion method is used, is reflected in models with Dahl friction? It can be shown that spring-like behaviour observed in the stiction regime combined with the coupling between joint microsrips are the key factors that decide on calculated friction.

Let  $x_i$  denote the relative displacement in the  $i$ th kinematic pair. According to the Dahl model, a microsrip  $\Delta x_i$  occurs in the static friction regime. Note that, in our case of a 1-DOF mechanism, microsrips in all kinematic pairs are coupled by the virtue of constraint equations and only one (say,  $\Delta x_p$ ) may be regarded as independent, hence:

$$[\Delta x_1 \quad \dots \quad \Delta x_i \quad \dots \quad \Delta x_k]^T \approx [w_1 \Delta x_p \quad \dots \quad w_i \Delta x_p \quad \dots \quad w_k \Delta x_p]^T = \mathbf{w}^T \Delta x_p, \quad (5)$$

where the ratios  $\mathbf{w}$  are constant at the given configuration of stiction  $\mathbf{q}^*$ .

Now, linearizing Eq. (4a, b) around  $v_{i0} = 0$  and  $z_{i0} = 0$  we get  $\dot{z}_i|_{v_{i0}, z_{i0}} \approx v_i$ . Note that  $\dot{x}_i = v_i$ , thus—when the model state is close to  $v_{i0}$  and  $z_{i0}$ —the change in  $x_i$  is close to the change in  $z_i$ :  $\Delta x_i \approx \Delta z_i = z_i - z_{i0} = z_i$ . Consequently, Eq. (4b) may be rewritten as:



$$F_i \approx \sigma_i w_i \Delta x_p, \quad (i = 1, \dots, k). \tag{6}$$

Equation (6) shows that at a given configuration of stiction  $\mathbf{q}^*$ , proportions between friction forces in kinematic pairs are fixed (and do not depend on external loads!). This is how the problem of indeterminacy of solution is solved, or rather circumvented. Unfortunately, credibility of the results rests entirely upon parameters  $\sigma_i$  fidelity.

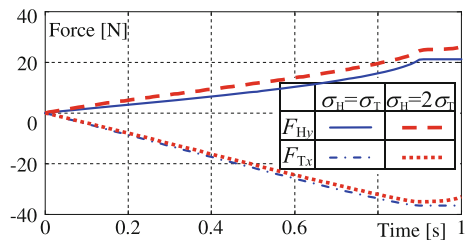
Note that the coefficients of friction,  $\mu_i$ , can be recognized as primary factors characterizing frictional properties of the system; they can be relatively easily found in scientific literature or trustworthily measured. The secondary parameters,  $\sigma_i$ , are less frequently measured or published. In many cases, rough estimations of these parameters are used during simulations (especially when a hardware prototype is unavailable). In that context, high sensitivity of the results to the values of secondary parameters is particularly unwelcome.

It is worth mentioning that in the kinetic friction mode, when velocity of sliding is high, the friction forces reach the values of  $F_{Ci}$  and proportions between them are no longer fixed (they vary in accordance to external loads).

*Example 2* We continue to study the mechanism from Fig. 1. Point C is the foot centre of mass, mass of the foot equals 5 [kg], and the moment of inertia is 0.01 [kg m<sup>2</sup>]. Force  $\mathbf{P}$  is constant whereas torque  $M$  changes in time:  $M(t) = \min(10t, 9)$  [Nm]. Note that at  $t \geq 0.9$  [s] the external loads are the loads investigated in Example 1.

The Dahl model of friction is used for both contact points (H and T). The first simulation was performed with  $\sigma_H = \sigma_T = 2 \times 10^6$  [N/m]. During this simulation, the model remained in the static friction regime. The second simulation was performed with  $\sigma_H = 4 \times 10^6$  [N/m]. At time  $t \approx 0.89$  [s] the model started to move. Friction forces calculated in both simulations are compared in Fig. 2. An influence of parameter  $\sigma_H$  value on calculated friction forces is clearly visible. Note that distribution of normal forces was also affected by the choice of  $\sigma_H$ .

**Fig. 2** Friction forces in simulations with  $\sigma_H = \sigma_T$  and  $\sigma_H = 2\sigma_T$



## 4 Dahl Friction in Flexible Body Models

Flexibility of bodies is a very important factor deciding on the distribution of reactions in overconstrained mechanisms (Wojtyra and Frączek 2012). Equally important role of flexibility may be expected when redundant constraints are introduced in order to model locking of the mechanism due to static friction. In fact, the frictional locking may be achieved strictly—by imposing additional constraints, or approximated—by applying sufficiently large friction forces accompanied by microslips at joints. In either case, flexibility may strongly influence (or even determine) normal and frictional reactions in the stiction regime.

When flexibility of bodies is taken into account, the number of system's degrees of freedom increases. As a result, when constraint addition-deletion method is used, dependent equations do not appear in the mathematical model of a multibody system in the stiction regime, and the problems with solution uniqueness do not emerge. Normal reactions and friction forces are unique and correspond to physics of the flexible system.

In the case of the Dahl model application, situation is a bit different. The deflections of flexible parts may be large enough to eliminate the rigid coupling between microslips. As it was pointed out, coupling boost the role of secondary parameters of friction models and lets them to importantly influence the distribution of friction forces.

There are many approaches to model flexibility of bodies. In this study a very simple model is used, just to show how flexibility influences the distribution of normal and frictional reactions. It is assumed that at contact point bodies may deflect ( $d_i$  is the normal deflection) and viscoelastic model of normal force is utilized with stiffness  $k_i$  and damping  $c_i$ , respectively:

$$N_i = k_i d_i + c_i \dot{d}_i. \quad (7)$$

*Example 3* The mechanism from previous examples is revisited. Firstly, the following set of flexibility parameters was utilized:  $k_H = k_T = 5 \times 10^4$  [N/m],  $c_H = c_T = 100$  [Ns/m]. Both simulations from Example 2 (with  $\sigma_H = \sigma_T$  and  $\sigma_H = 2\sigma_T$ ) were repeated. This time, however, no significant differences in results were observed. In both cases the mechanism remained in the static friction mode and calculated normal and frictional reactions were practically the same in both cases.

Next, stiffness parameter  $k_T$  was doubled ( $k_T = 1 \times 10^5$  [N/m]) and simulations with  $\sigma_H = \sigma_T$  and  $\sigma_H = 2\sigma_T$  were performed once more. The results were almost identical in both cases—the mechanism started to move at  $t \approx 0.88$  [s]. Again, the change in parameter  $\sigma_H$  affected the results almost imperceptibly.

The discussed results are illustrated by Fig. 3. The role of parameters  $\sigma_H$  and  $\sigma_T$  is diminished in contrast to rigid body model. This time the stiffness parameters are crucial for the results and decide on normal and friction forces distribution.

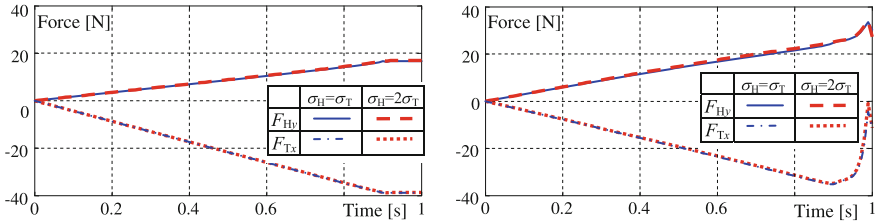


**Fig. 3** Friction in simulations with  $k_T = k_H$  (left) and  $k_T = 2k_H$  (right)

## 5 Conclusions

This study shows that application of Dahl model of friction to a rigid body mechanism with closed loop kinematic chains causes some unwelcome effects. Analogies to uniqueness problems encountered in overconstrained systems are indicated. Results of stiction regime simulations, achieved using rigid body model, may be considered as doubtful. High sensitivity of results to changes of parameter  $\sigma$  of the Dahl model is observed (this hardly measurable parameter sometimes is chosen quite arbitrarily).

It was also demonstrated that, when flexibility of mechanism bodies is taken into account, the selection of values of “secondary” parameters of model of friction only negligibly influences the results of simulations. The flexibility of bodies may be the key factor deciding on friction forces distribution during the stiction phase. It should be emphasized that the flexibility introduced to the model should properly reflect the real system properties. Otherwise, unrealistic solution would be found.

**Acknowledgments** This research was supported by the National Science Centre (Poland) grant no. DEC-2012/07/B/ST8/03993.

## References

- Armstrong-Hélouvry, B., Dupont, P., & Canudas de Wit, C. (1994). A survey of models, analysis tools and compensation methods for the control of machines with friction. *Automatica*, 30(7), 1083–1138.
- Canudas de Wit, C., Olsson, H., Astrom, K. J., & Lischinsky, P. (1995). A new model for control of systems with friction. *IEEE Transactions on Automation and Control*, 40(3), 419–425.
- Dahl, P. R. (1976). Solid friction damping in mechanical vibrations. *AIAA Journal*, 14(12), 1675–1682.
- Do, N. B., Ferri, A. A., & Bauchau, O. A. (2007). Efficient simulation of a dynamic system with LuGre friction. *Journal of Computational and Nonlinear Dynamics*, 2(4), 281–289.
- Frączek, J., & Wojtyra, M. (2011). On the unique solvability of a direct dynamics problem for mechanisms with redundant constraints and Coulomb friction in joints. *Mechanism and Machine Theory*, 46(3), 312–334.

- Hadji, A., & Mureithi, N. (2014). Nonlinear normal modes and the Dahl friction model parameter identification. In *ASME 2014 Pressure Vessels and Piping Conference Volume 4: Fluid-Structure Interaction*, V004T04A064 (pp. 1–10).
- Haug, E. J., Wu, S. C., & Yang, S. M. (1986). Dynamics of mechanical systems with Coulomb friction, stiction, impact, and constraints addition-deletion. *Mechanism and Machine Theory*, 21(5), 401–425.
- Hensen, R. H. A., van de Molengraft, M. J. G., & Steinbuch, M. (2002). Frequency domain identification of dynamic friction model parameters. *IEEE Transactions on Control Systems Technology*, 10(2), 191–196.
- Pennestrì, E., Valentini, P. P., & Vita, L. (2007). Multibody dynamics simulation of planar linkages with Dahl friction. *Multibody System Dynamics*, 17(4), 321–347.
- Swevers, J., Al-Bender, F., Ganesman, C. G., & Prajogo, T. (2000). An integrated friction model structure with improved presliding behavior for accurate friction compensation. *IEEE Transactions on Automatic Control* 45(4), 675–686.
- Wojtyra, M., & Frączek, J. (2012). Joint reactions in rigid or flexible body mechanisms with redundant constraints. *Bulletin of the Polish Academy of Sciences—Technical Sciences*, 60(3), 617–626.
- Wojtyra, M., & Frączek, J. (2013). Comparison of selected methods of handling redundant constraints in multibody systems simulations. *Journal of Computational and Nonlinear Dynamics*, 8(2), 021007 (1–9).

# Mechanics of Mobile Robots with Mecanum Wheels

Klaus Zimmermann, Igor Zeidis, Florian Schale  
and Pedro Alonso Flores-Alvarez

**Abstract** The mechanics of a robot with Mecanum wheels is studied. A Mecanum wheel is a wheel with rollers attached to its circumference. Each roller rotates about an axis that forms an angle with the plane of the disk. In robotics, a simplified approach, in which the equations of non-holonomic kinematic constraints are solved approximately by means of a pseudo-inverse matrix, is frequently applied. Such an approximate approach leads to “holonomization” of the system and allows Lagrange’s equations of the second kind to be used. In the present paper, the equations of motion are obtained on the basis of the principles of non-holonomic mechanics. The optimal torques to be applied to the wheels and the respective voltages to be fed to the electric in order to provide a prescribed trajectory for the robot’s center of mass are defined. The theoretical results are compared with measured data obtained by experiments with a prototype.

## 1 Introduction

For service robots and equipment for physically disabled persons, mobile systems with high maneuverability play an important role. The conventional wheel moves back into the focus of interest. Furthermore, the so-called omnidirectional wheels (e.g., “Mecanum wheels”, see Ilon 1975), generating constraints different from the conventional wheel, lead to investigations, based on the Mechanics and Control of

---

K. Zimmermann · I. Zeidis (✉) · F. Schale · P.A. Flores-Alvarez  
Department of Technical Mechanics, Technische Univesitaet Ilmenau, Ilmenau, Germany  
e-mail: igor.zeidis@tu-ilmenau.de

K. Zimmermann  
e-mail: klaus.zimmermann@tu-ilmenau.de

F. Schale  
e-mail: florian.schale@tu-ilmenau.de

P.A. Flores-Alvarez  
e-mail: pedro-alonso.flores-alvarez@tu-ilmenau.de

non-holonomic systems. At the present time, vehicles with Mecanum wheels (Fig. 1, left) are gaining ground for various applications. These wheels have rollers that are arranged at the circumference of the wheel. The rollers are orientated at an angle to the wheel plane and they can rotate about their own axis (Fig. 1, right). As a rule, this angle is equal to  $45^\circ$ . Such wheels have additional kinematical possibilities in comparison with conventional wheels. Due to these possibilities, a vehicle with Mecanum wheels can move forward-backward, leftward-rightward and rotate in an arbitrary way. Usually a Mecanum-wheeled vehicle has four wheels. By varying the rate and the direction of rotation of each wheel, one can implement, for example, a translational motion of the vehicle in any direction, as well as arbitrary turns and rotations on the spot.

The issues of kinematics of wheeled systems, including those with Mecanum wheels, are reviewed in Campion et al. (1996). The issues of kinematics, dynamics, and control of systems with Mecanum wheels in a non-holonomic treatment are considered, for example, in Wampfler et al. (1989), Zimmermann et al. (2009), Martynenko and Formal'skii (2007) for a number of particular cases. There are a great number of studies on robotics, in which the kinematics and dynamics of robots with four Mecanum wheels is approximately treated in terms of holonomic mechanics (see, e.g., Muir and Neumann 1990; Viboonchaicheep et al. 2003; Tsai et al. 2011). In these studies, pseudo-inverse matrices are used to resolve the kinematic constraint relations. Zimmermann et al. (2014) compared the equations derived on the basis of non-holonomic mechanics with the equations derived by using the approximate technique. In the present paper, the equations obtained by the methods of non-holonomic mechanics are used. On the basis of these equations, the optimal torques to be applied to the wheels and the respective voltages to be fed to the electric motors in order to provide a prescribed trajectory for the robot's center of mass are calculated. The back electromotive force (EMF) effect being taken into account.

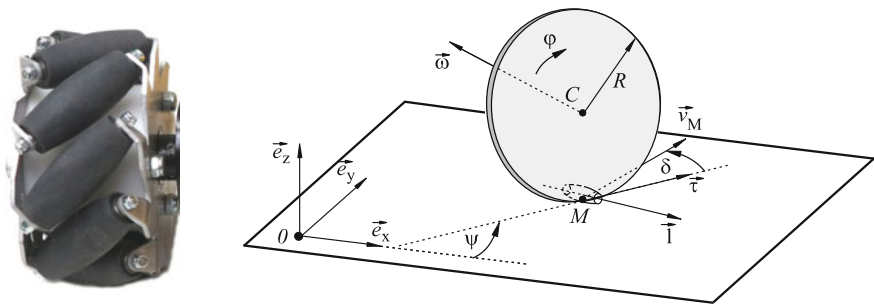


**Fig. 1** A Mecanum wheel (*left*) and the mechanical model (*right*)

## 2 Kinematics of a Mecanum Wheel

For a conventional wheel, the contact between the wheel and the supporting plane is characterized by the condition that the wheel is rolling without slip. This means that the velocity of the point by which the wheel contacts the plane at each current instant is equal to zero. Then the projections of the velocity of the contact point onto the direction lying in the wheel plane, as well as onto the direction perpendicular to this plane, are equal to zero. For a Mecanum wheel, only the projection of the velocity of the contact point onto the axis of rotation of the roller is equal to zero.

As a model of a Mecanum wheel we will consider the rolling of a disk of radius  $R$  centered at the point  $C$  on a horizontal plane. The plane of the disk is always vertical. Let  $\vec{l}$  denote the unit vector along the axis of attachment of the rollers,  $\vec{\tau}$  the unit vector lying in the wheel plane tangent to the rim at the point of contact. The kinematic constraint relation for a Mecanum wheel implies that the vector of velocity  $\vec{v}_M$  of the point  $M$  of contact of the wheel with the plane points along the line perpendicular to the axis of the roller, i.e., the projection of the velocity of the point  $M$  onto the roller axis is equal to zero (see Fig. 1, right). The kinematic constraint relation has the form

$$\vec{v}_M \cdot \vec{l} = 0. \quad (1)$$

The velocity  $\vec{v}_M$  is defined by the equation

$$\vec{v}_M = \vec{v}_C + \vec{\omega} \times \vec{CM}, \quad (2)$$

where  $\vec{v}_C$  is the velocity of the center  $C$  and  $\vec{\omega}$  is the angular velocity of the disk. Let  $\varphi$  be the angle of rotation of the disk about the axis passing through the point  $C$  perpendicular to the plane of the disk ( $\omega = \dot{\varphi}$ ). The kinematic relation (1) becomes

$$(\vec{v}_C - R\dot{\varphi}\vec{\tau}) \cdot \vec{l} = 0 \quad (3)$$

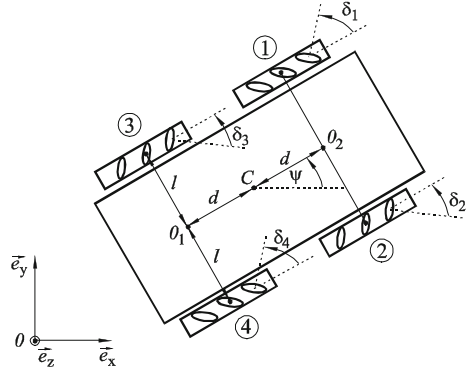
or

$$\vec{v}_C \cdot \vec{l} = R\dot{\varphi} \sin \delta, \quad \vec{\tau} \cdot \vec{l} = \sin \delta. \quad (4)$$

Here  $\delta$  is the angle between the vector of velocity  $\vec{v}_M$  and the vector  $\vec{\tau}$  (angle between the normal to roller axis and the vector  $\vec{\tau}$ ).

On the basis of the analysis of the kinematic constraints of type (4) it is shown that if a mechanical system is based on  $n$  Mecanum wheels in such a way that (a)  $n \geq 3$ ; (b) not all vectors  $\vec{l}_i$  are parallel to each other; (c) the points of contact of the wheels with the plane do not lie on one line, then it is always possible to find control functions  $\varphi_i$  ( $i = 1, \dots, n$ ) that implement any prescribed motion of the system's center of mass (see e.g. Martynenko and Formal'skii 2007).

**Fig. 2** A vehicle with four Mecanum wheels



Consider a model of a four-wheeled vehicle with Mecanum wheels (see Fig. 2). Let  $m_0$  be the mass of the body,  $m_1$  the mass of each of the wheels,  $J_0$  the mass moment of inertia of the body about the vertical axis passing through the center of mass,  $J_1$  the mass moment of inertia of each wheel about its axis of rotation, and  $J_2$  the moment of inertia of each wheel about the vertical axis passing through the center of the wheel.

The coordinates of the center mass of the system  $C$  in the reference frame (inertial system)  $\{O, \vec{e}_x, \vec{e}_y, \vec{e}_z\}$  are  $x_C$ ,  $y_C$ , and  $R$  is the radius of the wheels; the quantities  $|\vec{CO}_1| = |\vec{CO}_2| = d$  are the distances from the center of mass to the axes of the wheel pairs, and  $2l$  is the distance between the centers of the wheels of one axis. Let  $\psi$  be the angle between the vector  $\vec{O}_1\vec{O}_2$  and the vector  $\vec{e}_x$  (i.e. angle  $\psi$  describes the orientation of the vehicle). The corresponding kinematic relations are obtained on the basis of Eq. (4) for each wheel in the form

$$\dot{x}_C \sin(\psi + \delta_1) - \dot{y}_C \cos(\psi + \delta_1) - \dot{\psi}(l \sin \delta_1 + d \cos \delta_1) = R\dot{\varphi}_1 \sin \delta_1, \quad (5)$$

$$-\dot{x}_C \sin(\psi - \delta_2) + \dot{y}_C \cos(\psi - \delta_2) + \dot{\psi}(l \sin \delta_2 + d \cos \delta_2) = R\dot{\varphi}_2 \sin \delta_2, \quad (6)$$

$$-\dot{x}_C \sin(\psi - \delta_3) + \dot{y}_C \cos(\psi - \delta_3) - \dot{\psi}(l \sin \delta_3 + d \cos \delta_3) = R\dot{\varphi}_3 \sin \delta_3, \quad (7)$$

$$\dot{x}_C \sin(\psi + \delta_4) - \dot{y}_C \cos(\psi + \delta_4) + \dot{\psi}(l \sin \delta_4 + d \cos \delta_4) = R\dot{\varphi}_4 \sin \delta_4, \quad (8)$$

Equations (5)–(8) define four non-holonomic constraints. Note, that if translational motions ( $\dot{\psi} = 0$ ) or rotations about the center of mass ( $\dot{x}_C = \dot{y}_C = 0$ ) are allowed, then the constraints become holonomic.



### 3 Dynamic Equations

The equations of motion of the robot can be obtained by using any method of non-holonomic mechanics, for example, by deriving Lagrange's equations with multipliers or Appel's equations. The mechanical system under consideration has three degrees of freedom, its configuration is characterized by 7 Lagrangian variables,  $x_C, y_C, \psi, \varphi_1, \varphi_2, \varphi_3$ , and  $\varphi_4$ , subject to 4 constraints (5)–(8). For the case where all  $\delta_i = \pi/4$  ( $i = 1, \dots, 4$ ), the governing equations have the simplest form

$$\begin{aligned} \ddot{x}_C(mR^2 + 4J_1) + 4\dot{y}_C\dot{\psi}J_1 = R\sqrt{2}(M_1 \sin(\psi + \pi/4) \\ + M_2 \cos(\psi + \pi/4) + M_3 \cos(\psi + \pi/4) + M_4 \sin(\psi + \pi/4)), \end{aligned} \quad (9)$$

$$\begin{aligned} \ddot{y}_C(mR^2 + 4J_1) - 4\dot{x}_C\dot{\psi}J_1 = -R\sqrt{2}(M_1 \cos(\psi + \pi/4) \\ - M_2 \sin(\psi + \pi/4) - M_3 \sin(\psi + \pi/4) + M_4 \cos(\psi + \pi/4)), \end{aligned} \quad (10)$$

$$(J_C R^2 + 4J_1(l+d)^2)\ddot{\psi} = -R(l+d)(M_1 - M_2 + M_3 - M_4). \quad (11)$$

Here  $M_i$  are the torques applied to the respective wheels ( $i = 1, \dots, 4$ ),  $m = m_0 + 4m_1$  is the total mass of the system,  $J_C = J_0 + 4J_2 + 4m_1(l^2 + d^2)$  is the moment of inertia of the entire system relative to the center of mass.

If the torques  $M_i$  ( $i = 1, \dots, 4$ ) are defined as functions of time, then the angle of rotation of the robot about its center of mass  $\psi(t)$  can be expressed in terms of quadratures. For the solutions that correspond to the rotation of the robot about its center of mass at a constant angular velocity ( $\dot{\psi} = \Omega = \text{const}$ ), the torques applied to the wheels are related by

$$M_1 + M_3 = M_2 + M_4. \quad (12)$$

The motions with  $\Omega = \text{const}$  involve, apart from the rotation about the center of mass, the translatory motion of the robot ( $\Omega = 0, \psi = \text{const}$ ). Such motions are of interest for applications.

In this case, the system of Eqs. (9) and (10) is a nonhomogeneous system of linear differential equations with constant coefficients and can be solved in an explicit form.

We assume that the torques developed by each of the four identical DC motors are defined by (see e.g. Gorinevsky et al. 1997)

$$M_i(t) = c_u U_i(t) - c_v \dot{\varphi}_i(t), \quad (i = 1, \dots, 4). \quad (13)$$

Here,  $U_i(t)$  is the voltage applied to the respective motor,  $c_v \dot{\varphi}_i(t)$  is the torque due to the back EMF. The positive constant coefficients  $c_u$  and  $c_v$  are defined by the

magnitudes of the starting and nominal torques, the nominal angular velocity, and the nominal voltage. Substitute relations (13) into Eqs. (9)–(11) and eliminate the angular velocities of the wheels by using Eqs. (5)–(8) to obtain

$$\begin{aligned} \ddot{x}_C(mR^2 + 4J_1) + 4\dot{y}_C\dot{\psi}J_1 + 4\dot{x}_C\dot{v} = R c_u \sqrt{2}(U_1 \sin(\psi + \pi/4) \\ + U_2 \cos(\psi + \pi/4) + U_3 \cos(\psi + \pi/4) + U_4 \sin(\psi + \pi/4)), \end{aligned} \quad (14)$$

$$\begin{aligned} \ddot{y}_C(mR^2 + 4J_1) \ddot{y}_C - 4\dot{x}_C\dot{\psi}J_1 - 4\dot{y}_C\dot{v} = -R\sqrt{2}(U_1 \cos(\psi + \pi/4) \\ - U_2 \sin(\psi + \pi/4) - U_3 \sin(\psi + \pi/4) + U_4 \cos(\psi + \pi/4)), \end{aligned} \quad (15)$$

$$\left( J_C R^2 + 4J_1(l+d)^2 \right) \ddot{\psi} = -R(l+d)(M_1 - M_2 + M_3 - M_4). \quad (16)$$

## 4 Optimization of Driving Torques

If the trajectory of the center of mass of the robot is specified, i.e., the time histories  $x_C(t)$ ,  $y_C(t)$  and  $\psi(t)$  are given, then Eqs. (9)–(11) form a system of three equations for four unknown torques  $M_i(t)$ ,  $i = 1, \dots, 4$ . We can seek the solutions for which the sum of the squared torques applied to the wheels,

$$P = M_1^2(t) + M_2^2(t) + M_3^2(t) + M_4^2(t) \quad (17)$$

is a minimum at each time instant. In other words, we seek the torques that minimize the function  $P(M_1, M_1, M_1, M_4)$ . These torques are defined by

$$\begin{aligned} M_{1\min} = \sqrt{2}(\ddot{x}_C(mR^2 + 4J_1) + 4\dot{y}_C\dot{\psi}J_1^2) \sin(\psi + \pi/4)/(4R) \\ - \sqrt{2}(\ddot{y}_C(mR^2 + 4J_1) - 4\dot{x}_C\dot{\psi}J_1) \cos(\psi + \pi/4)/(4R) \\ - \ddot{\psi} \left( J_C R^2 + 4J_1(l+d)^2 \right) / (4R(l+d)), \end{aligned} \quad (18)$$

$$\begin{aligned} M_{2\min} = \sqrt{2}(\ddot{x}_C(mR^2 + 4J_1) + 4\dot{y}_C\dot{\psi}J_1) \cos(\psi + \pi/4)/(4R) \\ - \sqrt{2}(\ddot{y}_C(mR^2 + 4J_1) - 4\dot{x}_C\dot{\psi}J_1) \sin(\psi + \pi/4)/(4R) \\ + \ddot{\psi} (J_C R^2 + 4J_1(l^2 + d^2)) / (4R(l+d)), \end{aligned} \quad (19)$$

$$\begin{aligned} M_{3\min} = \sqrt{2}(\ddot{x}_C(mR^2 + 4J_1) + 4\dot{y}_C\dot{\psi}J_1) \cos(\psi + \pi/4)/(4R) \\ - \sqrt{2}(\ddot{y}_C(mR^2 + 4J_1) - 4\dot{x}_C\dot{\psi}J_1) \sin(\psi + \pi/4)/(4R) \\ - \ddot{\psi} (J_C R^2 + 4J_1(l^2 + d^2)) / (4R(l+d)), \end{aligned} \quad (20)$$

$$\begin{aligned}
 M_{4\min} = & \sqrt{2}(\ddot{x}_C(mR^2 + 4J_1) + 4\dot{y}_C\dot{\psi}J_1) \sin(\psi + \pi/4)/(4R) \\
 & - \sqrt{2}(\ddot{y}_C(mR^2 + 4J_1) - 4\dot{x}_C\dot{\psi}J_1^2) \cos(\psi + \pi/4)/(4R) \\
 & + \ddot{\psi}(J_C R^2 + 4J_1(l^2 + d^2))/(4R(l+d)).
 \end{aligned} \tag{21}$$

By applying a similar criterion (the minimum of the sum of the squares) to the voltages defined by Eqs. (14)–(16), we obtain

$$\begin{aligned}
 U_{1\min} = & \sqrt{2}(\ddot{x}_C(mR^2 + 4J_1) + 4\dot{y}_C\dot{\psi}J_1 + 4\dot{x}_C c_v) \sin(\psi + \pi/4)/(4Rc_u) \\
 & - \sqrt{2}(\ddot{y}_C(mR^2 + 4J_1) - 4\dot{x}_C\dot{\psi}J_1 + 4\dot{y}_C c_v) \cos(\psi + \pi/4)/(4Rc_u) \\
 & - \ddot{\psi}(J_C R^2 + 4J_1(l+d)^2)/(4R(l+d)c_u) - \dot{\psi}(l+d)c_v/(Rc_u),
 \end{aligned} \tag{22}$$

$$\begin{aligned}
 U_{2\min} = & \sqrt{2}(\ddot{x}_C(m + 4J_1) + 4\dot{y}_C\dot{\psi}J_1 + 4\dot{x}_C c_v) \cos(\psi + \pi/4)/(4Rc_u) \\
 & + \sqrt{2}(\ddot{y}_C(m + 4J_1^2) - 4\dot{x}_C\dot{\psi}J_1^2 + 4\dot{y}_C c_v) \sin(\psi + \pi/4)/(4Rc_u) \\
 & + \ddot{\psi}(J_C R^2 + 4J_1(l+d)^2)/(4R(l+d)c_u) + \dot{\psi}(l+d)c_v/(Rc_u),
 \end{aligned} \tag{23}$$

**Fig. 3** Mobile robot based on the 4 WD Mecanum wheel mobile kit from NEXUSrobot and controlled by a plugin based software “RobotController”



$$\begin{aligned}
U_{3 \min} = & \sqrt{2}(\ddot{x}_C(m + 4J_1) + 4\dot{y}_C\dot{\psi}J_1 + 4\dot{x}_C c_v) \cos(\psi + \pi/4)/(4Rc_u) \\
& + \sqrt{2}(\ddot{y}_C(m + 4J_1^2) - 4\dot{x}_C\dot{\psi}J_1^2 + 4\dot{y}_C c_v) \sin(\psi + \pi/4)/(4Rc_u) \quad (24) \\
& - \ddot{\psi}(J_C R^2 + 4J_1(l+d)^2)/(4R(l+d)c_u) - \dot{\psi}(l+d)c_v/(Rc_u),
\end{aligned}$$

$$\begin{aligned}
U_{4 \min} = & \sqrt{2}(\ddot{x}_C(mR^2 + 4J_1) + 4\dot{y}_C\dot{\psi}J_1 + 4\dot{x}_C c_v) \sin(\psi + \pi/4)/(4Rc_u) \\
& - \sqrt{2}(\ddot{y}_C(mR^2 + 4J_1) - 4\dot{x}_C\dot{\psi}J_1 + 4\dot{y}_C c_v) \cos(\psi + \pi/4)/(4Rc_u) \quad (25) \\
& + \ddot{\psi}(J_C R^2 + 4J_1(l+d)^2)/(4R(l+d)c_u) + \dot{\psi}(l+d)c_v/(Rc_u).
\end{aligned}$$

Constructing the optimal modes on the basis of integral criteria is reduced, as a rule, to numerical optimization procedures.

## 5 Conclusion

The kinematic and dynamic equations are derived for a four-wheeled robot with Mecanum wheels, subject to non-holonomic constraints (rolling without slipping). The optimal torques to be applied to the wheels and the voltages to be applied to the motors in order to provide a prescribed trajectory for the robot's center of mass are found. To evaluate the theoretical results, a prototype of a mobile platform with four Mecanum wheels that implements the principles presented in the paper was used (see Fig. 3). The experimental data agree with the theoretical predictions.

**Acknowledgments** This study was supported by the Development Bank of Thuringia and the Thuringian Ministry of Economic Affairs with funds of the European Social Fund (ESF) under grant 2011 FGR 0127.

## References

- Campion, G., Bastin, G., & D'Andrea-Novel, B. (1996). Structural properties and classification of kinematic and dynamic models of wheeled mobile robots. *IEEE Transactions on Robotics and Automation*, 12(1), 47–62.
- Gorinevsky, D. M., Formalsky, A. M., & Schneider, A. Yu. (1997). *Force control of robotics systems*. CRC Press LLC.
- Ilon, B. E. (1975). Wheels for a course stable selfpropelling vehicle movable in any desired direction on the ground or some other base, *US Patent 3876255*.
- Martynenko, Yu. G., & Formal'skii, A. M. (2007). On the motion of a mobile robot with roller-carrying wheels. *Journal of Computer and Systems Sciences International*, 46(6), 976–983.
- Muir, P. F., & Neumann, C. P. (1990). Kinematic modeling for feedback control of an omnidirectional wheeled mobile robot. *Autonomous robot vehicles* (pp. 25–31). New-York: Springer.
- Tsai, C. -C., Tai, F. -C., Lee, Y. -R. (2011). Motion controller design and embedded realization for mecanum wheeled omnidirectional robots. In *Proceedings of the 8th World Congress on Intelligent Control and Automation* (pp. 546–551). Taipei, Taiwan.

- Viboonchaicheep, P., Shimanda, A., & Kosaka, Y. (2003). Position rectification control for mecanum wheeled omni-directional vehicles. In *Proceedings of the 29th Annual Conference of IEEE Industrial Electronics Society* (pp. 854–859). Roanoke, USA.
- Wampfer, G., Salecker, M., & Wittenburg, J. (1989). Kinematics, dynamics, and control of omnidirectional vehicles with mecanum wheels. *Mechanics Based Design of Structures and Machines*, 17(2), 165–177.
- Zimmermann, K., Zeidis, I., & Behn, C. (2009). *Mechanics of terrestrial locomotion. With a focus on nonpedal motion systems*. Berlin: Springer.
- Zimmermann, K., Zeidis, I., & Abdelrahman, M. (2014). Dynamics of mechanical systems with mecanum wheels. In *Applied Non-Linear Dynamical Systems* (pp. 271–279). Wien, New York: Springer.

# Design of Partially Balanced 5R Planar Manipulators with Reduced Center of Mass Acceleration (RCMA)

Vigen Arakelian

**Abstract** This paper deals with the shaking force minimization in high-speed 5R planar parallel manipulators via center of mass acceleration control. The trajectories of the total mass center of moving links are defined as straight lines and are parameterized with “bang-bang” profile. Such a motion control allows the reduction of the maximum value of the center of mass acceleration and, consequently, the reduction in the shaking force. The suggested balancing technique is illustrated through computer simulations. The results obtained via ADAMS simulations showed that a reduction in the maximum value of the shaking force of 78 % has been obtained.

**Keywords** Shaking force • Balancing • Vibration reduction • Mechanism design • Center of mass acceleration

## 1 Introduction

Many industrial manipulators face the problem of frame vibrations during high-speed motion. Such a vibration can result from a number of conditions, acting alone or in combination. One of the main reasons is the unbalanced inertia forces leading to the increase of shaking force and shaking moment. It is known that a mechanical system with unbalance shaking force and shaking moment transmits substantial vibration to the frame. Thus, a primary objective of the balancing is to cancel or reduce the variable dynamic loads transmitted to the frame and surrounding structures. The balancing of manipulators is generally can be achieved in two steps: *i*) the cancellation (or reduction) of the shaking force and *ii*) the cancellation (or reduction) of the shaking moment.

---

V. Arakelian (✉)

Department of Mechanical and Control Systems Engineering, INSA, Rennes, France  
e-mail: vigen.arakelyan@insa-rennes.fr

V. Arakelian

Robotics Research Group, IRCCyN, Nantes, France

© CISM International Centre for Mechanical Sciences 2016

V. Parenti-Castelli and W. Schiehlen (eds.), *ROMANSY 21 - Robot Design, Dynamics and Control*, CISM International Centre for Mechanical Sciences 569,  
DOI 10.1007/978-3-319-33714-2\_13

The review of methods devoted to the shaking force balancing of manipulators has shown that the following principal approaches can be distinguished (Arakelian and Briot 2015).

*Shaking force balancing by adding counterweights.* One of the most simple and easily practicable methods is the balancing of manipulators by mass redistribution in order to keep the total center of mass of moving links stationary (Filaretov and Vukobratovic 1993; Agrawal and Fattah 2004; Arakelian and Briot 2015). It is obvious that the adding of the supplementary mass due to the counterweights is not desirable because it leads to the increase of the total mass, the overall size of the robot-manipulator and the efforts in joints. That is why in many designs of industrial robots (for example, KUKA R360, PUMA 200), the masses of the motors are often used as counterweights (Bayer and Merk 2011).

*Shaking force balancing by adding auxiliary structures.* Different approaches have been developed in order to balance the shaking force by adding auxiliary structures. The aim is the same: to keep the total center of mass of moving links stationary. However, in this case, the balancing is activated not by redistribution of the masses of the initial mechanism but through an auxiliary structure. The parallelogram and the pantograph have been used as auxiliary structures (Agrawal and Fattah 2004; Fattah and Agrawal 2003, 2005; Herder and van der Wijk 2010). However, such a balancing can be reached by creating relatively complex mechanical system and by an unavoidable increase of manipulator's sizes.

*Shaking force minimization via center of mass acceleration control.* The nature of this approach (Briot et al. 2012; Nenchev 2013) is based on the optimal control of the robot-manipulator center of masses. The aim of such a balancing method consists in the fact that the manipulator is controlled not by applying end-effector trajectories but by planning the displacements of the total mass center of moving links. The trajectories of the total mass center of moving links are defined as straight lines and are parameterized with “bang-bang” motion profiles. Such a control approach allows the reduction of the maximal value of the center of mass acceleration and, consequently, leads to the reduction in the shaking force.

However, despite the obvious advantages, observations and attempts of practical implementations showed that the latter approach also has some drawbacks. It is difficult to control a robot-manipulator based on the kinematic parameters of a virtual point as a center of masses. As a result, measurements and refinements of the displacements of the total mass center of moving links becomes pretty complex. Another imperfection of the mentioned method is the fact that the end-effector trajectory becomes a derivative of the trajectory of the center of masses, i.e. by using the known balancing method mentioned above it is possible to ensure only initial and final positions of the end-effector but not a straight line trajectory between them.

To eliminate these drawbacks, the present study proposes to combine the balancing through mass redistribution and the balancing via center of mass acceleration control. This allows one to reach more efficient balancing results, i.e. to increase the shaking force balancing rates and to control the displacements of the total mass center of moving links via the end-effector trajectory.

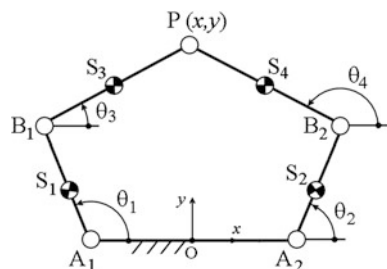
## 2 Shaking Force Balancing

A kinematic scheme of the 5R planar manipulator is shown in Fig. 1. The output axis  $P(x, y)$ , which corresponds to the axis of the end-effector, is connected to the base by two legs, each of which consists of three revolute joints and two links. The two legs are connected to a common axis  $P$  with the common revolute joint at the end of each leg. In each of the two legs, the revolute joint connected to the base is actuated. Such a manipulator can position the end-effector freely in a plane.

In the given planar 5R parallel mechanism each actuated joint is denoted as  $A_i (i = 1, 2)$ , the other end of each actuated link is denoted as  $B_i$  and the common joint of the two legs is denoted as  $P$ , which is also the axis of the end-effector. A fixed global reference system  $Oxy$  is located at the center of  $A_1A_2$  with the  $y$ -axis normal to  $A_1A_2$  and the  $x$ -axis directed along  $A_1A_2$ . The lengths of links are denoted as  $l_1 = A_1B_1$ ,  $l_2 = A_2B_2$ ,  $l_3 = B_1P$ ,  $l_4 = B_2P$  and  $l_0 = OA_1 = OA_2$ . The locations of the centers of mass are denoted as  $r_1 = l_{A_1S_1}$ ,  $r_2 = l_{A_2S_2}$ ,  $r_3 = l_{B_1S_3}$  and  $r_4 = l_{B_2S_4}$ .

The complete shaking force balancing of such a mechanism can be reached by adding 3 or 4 counterweights making the common center of mass stationary (Arakelian and Briot 2015). However, as mentioned above, such a solution leads to the increase of the total mass and the overall size of the robot-manipulator. Therefore, let us consider a partial balancing of the 5R mechanism via optimal redistribution of moving masses and reduction of the center of mass acceleration. Two steps will be considered: (i) optimal redistribution of the masses of input links to ensure the similarity of the output trajectory and the common center of mass trajectory; (ii) optimal control of the acceleration of the end-effector.

**Fig. 1** The planar 5R parallel manipulator





## 2.1 Reaching Similar Accelerations of the End-Effector of the 5R Planar Parallel Manipulator and Its Common Center of Mass

The coordinates of the common center of mass of the 5R planar manipulator can be expressed as:

$$x_S = \frac{m_1 x_{S_1} + m_2 x_{S_2} + m_3 x_{S_3} + m_4 x_{S_4}}{m} \quad \text{and} \quad y_S = \frac{m_1 y_{S_1} + m_2 y_{S_2} + m_3 y_{S_3} + m_4 y_{S_4}}{m}$$

with

$$\begin{aligned} m &= m_1 + m_2 + m_3 + m_4; x_{S_1} = r_1 \cos \theta_1 - l_0; y_{S_1} = r_1 \sin \theta_1; \\ x_{S_2} &= r_2 \cos \theta_2 + l_0; y_{S_2} = r_2 \sin \theta_2; x_{S_3} = l_1 \cos \theta_1 + r_3 \cos \theta_3 - l_0; \\ y_{S_3} &= l_1 \sin \theta_1 + r_3 \sin \theta_3; x_{S_4} = l_2 \cos \theta_2 + r_4 \cos \theta_4 + l_0; y_{S_4} = l_2 \sin \theta_2 + r_4 \sin \theta_4. \end{aligned}$$

where,  $m_i$  ( $i = 1, 2, 3, 4$ ) are the masses of moving links.

Given that the following relationships between angles  $\theta_3$ ,  $\theta_4$  and  $x$ ,  $y$  can be established:

$$\begin{aligned} \sin \theta_3 &= (y - l_1 \sin \theta_1) / l_3 \\ \cos \theta_3 &= (x - l_1 \cos \theta_1 + l_0) / l_3 \\ \sin \theta_4 &= (y - l_2 \sin \theta_2) / l_4 \\ \cos \theta_4 &= (x - l_2 \cos \theta_2 - l_0) / l_4 \end{aligned}$$

the coordinates of the common center of mass of the 5R planar manipulator can be rewritten as:

$$x_S = k_1 \cos \theta_1 + k_2 \cos \theta_2 + k_3 x + k_0 \quad \text{and} \quad y_S = k_1 \sin \theta_1 + k_2 \sin \theta_2 + k_3 y$$

where,

$$\begin{aligned} k_1 &= (m_1 r_1 + m_3 l_1 - m_3 r_3 l_1 / l_3) / m \\ k_2 &= (m_2 r_2 + m_4 l_2 - m_4 r_4 l_2 / l_4) / m \\ k_3 &= (m_3 r_3 / l_3 + m_4 r_4 / l_4) / m \\ k_0 &= l_0 (-m_1 + m_2 - m_3 + m_4 + m_3 r_3 / l_3 - m_4 r_4 / l_4) / m \end{aligned}$$

Now, it is easy to see that the mass redistribution of links connected directly to the frame can ensure the condition  $k_1 = k_2 = 0$  which, in turn, leads to the following

expressions for the coordinates of the common center of mass of the 5R planar manipulator:

$$x_S = k_3 x + k_0$$

$$y_S = k_3 y$$

As a result, acceleration of the common center of mass of the 5R planar manipulator will be:

$$\ddot{x}_S = k_3 \ddot{x}$$

$$\ddot{y}_S = k_3 \ddot{y}$$

This means that the acceleration of the end-effector of the manipulator and its common center of mass are similar, i.e. the minimization of the acceleration of the end-effector leads to the proportional minimization of the acceleration of the common center of mass of the manipulator.

## 2.2 *Optimal Control of the Acceleration of the End-Effector of the 5R Planar Manipulator*

The shaking forces  $F_{sh}$  of the planar 5R parallel manipulator with  $k_1 = k_2 = 0$  can be written in the form:

$$F_{sh} = m \ddot{s} = m \sqrt{\ddot{x}_S^2 + \ddot{y}_S^2} = m k_3 \ddot{s}_P = m k_3 \sqrt{\ddot{x}^2 + \ddot{y}^2}$$

where,  $\ddot{s}$  is the acceleration of the common center of mass of the manipulator,  $\ddot{x}_S$  is the acceleration of the common center of mass of the manipulator along  $x$  axis,  $\ddot{y}_S$  is the acceleration of the common center of mass of the manipulator along  $y$  axis,  $\ddot{s}_P$  is the acceleration of the end-effector of the manipulator,  $\ddot{x}$  is the acceleration of the end-effector of the manipulator along  $x$  axis and  $\ddot{y}$  is the acceleration of the end-effector of the manipulator along  $y$  axis.

As was mentioned in the recent study of Briot et al. (2012), the shaking force, in terms of norm, is minimized if the norm of the masses center acceleration is minimized along the generated trajectory. This means that if the displacement of the manipulator center of masses is optimally controlled, the shaking force will be minimized. For this purpose has been proposed to apply the “bang-bang” law ensuring two identical phases with constant acceleration and deceleration (Khalil and Dombre 2002). As was rightly noted in the study of Briot et al. (2012), the “bang-bang” law is based on theoretical considerations. In reality, the actuators are unable to achieve discontinuous efforts. Therefore, this law should be modified by a

trapezoidal profile in order to take into account the actuators properties in terms of maximal admissible effort variations. However, it was observed that for reasonable actuator parameters, the minimizations obtained in the cases of the “bang-bang” and trapezoidal profiles are very close (less than 1 %). The detailed discussion about it can be found in the mentioned publication.

### 3 Illustrative Example

To create a CAD model, the following geometric parameters of the 5R planar manipulator have been used:  $l_1 = l_2 = L_1 = 0.36$  m;  $l_3 = l_4 = L_2 = 0.3$  m;  $l_0 = 0.24$  m. The masses and the locations of the centers of mass of the moving links 3 and 4 are the following:  $m_3 = m_4 = 1$  kg,  $r_3 = r_4 = 0.15$  m. Now, taking into consideration the condition  $k_1 = k_2 = 0$  and assuming  $r_1 = r_2 = -0.06$  m, the masses of the links 1 and 2 can be determined:  $m_1 = m_2 = 3$  kg.

The trajectory of the end-effector  $P$  is given by a straight line limited between the initial position  $P_i$  with the coordinates  $x_i = -0.06$  m,  $y_i = 0.45$  m and the final position  $P_f$  with the coordinates  $x_f = 0.1364$  m,  $y_f = 0.4878$  m.

The input angles  $\theta_1$  and  $\theta_2$  will be determined from following expressions:

$$\theta_i = 2 \tan^{-1}(z_i), \quad i = 1, 2$$

where

$$z_i = \frac{-b_i + \sigma_i \sqrt{b_i^2 - 4a_i c_i}}{2a_i}, \quad i = 1, 2$$

with

$$\begin{aligned} \sigma_i = \pm 1 \quad (i = 1, 2); \quad a_1 = L_1^2 + y^2 + (x + l_0)^2 - L_2^2 + 2(x + l_0)L_1; \quad b_1 = b_2 = -4yL_1; \\ c_1 = L_1^2 + y^2 + (x + l_0)^2 - L_2^2 - 2(x + l_0)L_1; \quad a_2 = L_1^2 + y^2 + (x - l_0)^2 - L_2^2 \\ + 2(x - l_0)L_1; \quad c_2 = L_1^2 + y^2 + (x - l_0)^2 - L_2^2 - 2(x - l_0)L_1. \end{aligned}$$

The chosen configuration for simulations corresponds to  $\sigma_1 = 1$  and  $\sigma_2 = -1$ . Thus, for given coordinates  $x_i = -0.06$  m,  $y_i = 0.45$  m of the initial position  $P_i$ , the input angles are  $\theta_1^i = 1.856$ ,  $\theta_2^i = 1.609$  and for the final position  $P_f$  with  $x_f = 0.1364$  m,  $y_f = 0.4878$  m, the input angles are  $\theta_1^f = 1.247$ ,  $\theta_2^f = 1.141$ .

Now, let us apply a “bang-bang” motion profile to the end-effector  $P$  with parameters  $s = 0.2$  m and  $t = 0.02$  s.

The obtained variations of the input angles  $\theta_1$  and  $\theta_2$  are shown in Figs. 2 and 3.

The next step of simulations is to apply the obtained input angles and verify the law of motion of the output axis  $P$ . The displacement, velocity and acceleration of

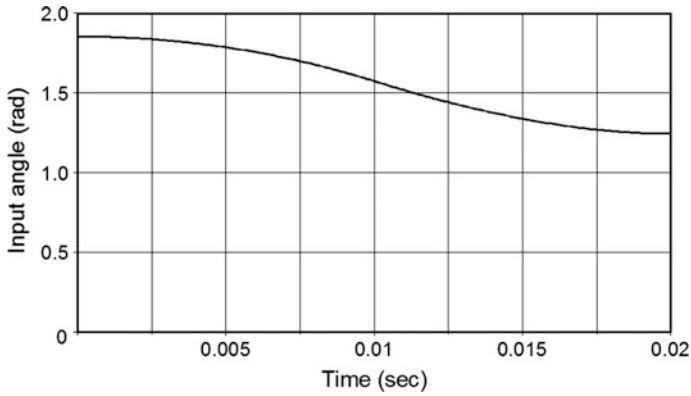


Fig. 2 Input angle  $\theta_1$

the output axis  $P$  is shown in Fig. 4. As can be seen from this figure, the input angles really ensure the displacements of the end-effector by the required “bang-bang” motion profile.

To show the efficiency of the developed method, two 5R planar parallel manipulators are compared: (a) an unbalanced manipulator, i.e.  $r_1 = r_2 = 0.18$  m and  $m_1 = m_2 = 1.2$  kg, with generation of input motions via five-order polynomial laws; (b) the manipulator designed by suggested approach.

In Fig. 5, the variations of the shaking forces for two simulated cases are presented. The obtained results showed that by suggested approach, the reduction of the maximal value of the shaking force is about 78 %.

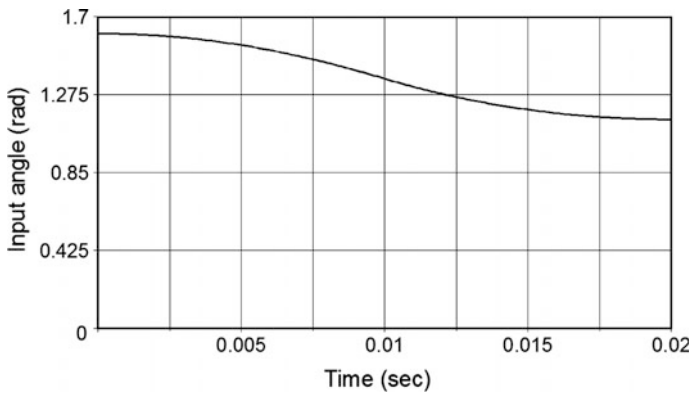
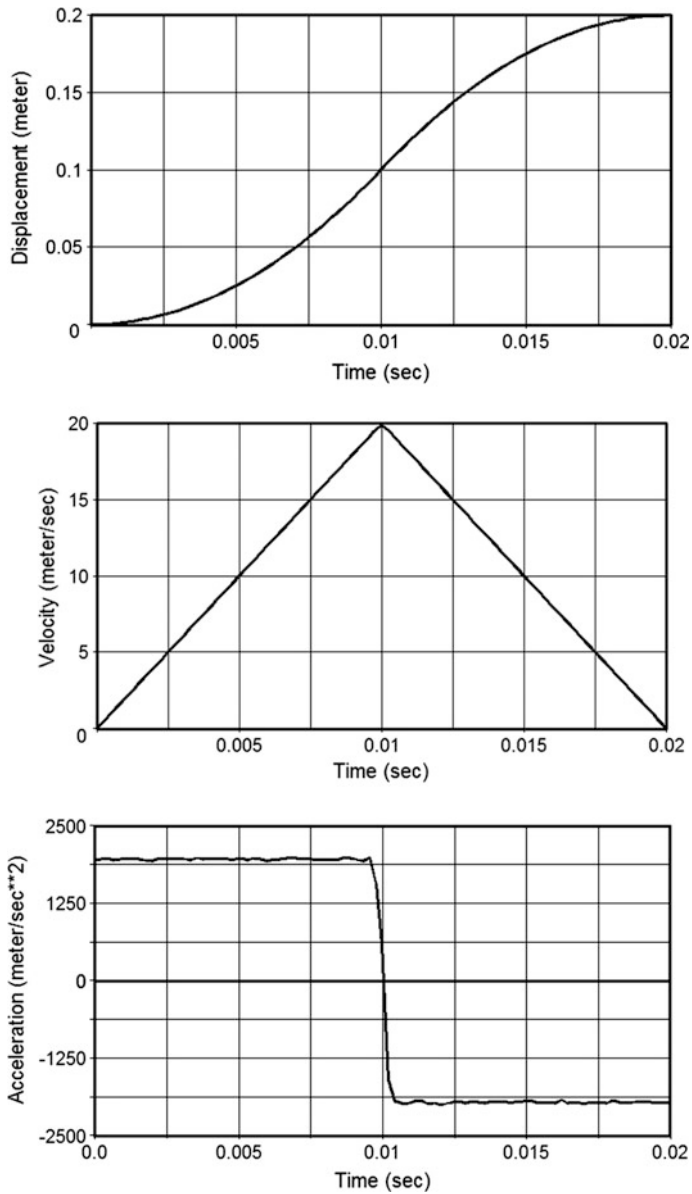


Fig. 3 Input angle  $\theta_2$



**Fig. 4** Displacement, velocity and acceleration of the end-effector of the 5R planar parallel manipulator

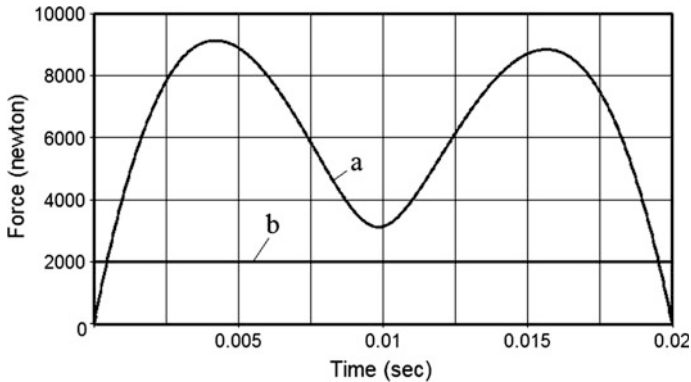


Fig. 5 Shaking forces for two simulated cases

## 4 Conclusions

In this paper, the principle of shaking force minimization in high-speed robots via center of mass acceleration control has been further developed and applied on the 5R planar parallel manipulator. The aim of the proposed solution consists in the fact that the manipulator is controlled not by applying end-effector trajectories but by planning the displacements of the total mass center of moving links. The trajectories of the total mass center of moving links are defined as straight lines and are parameterized with “bang-bang” profile. Such a motion control allows the reduction of the maximum value of the center of mass acceleration and, consequently, the reduction in the shaking force. However, observations showed that the mentioned approach despite its obvious advantages also has some drawbacks. It is difficult to apply such a balancing to parallel structures due to the complexity of relations between the output parameters and the displacements of the total mass center of moving links. In addition, it is difficult to control a robot-manipulator based on the kinematic parameters of a virtual point as a center of masses. As a result, measurements and refinements of the displacements of the total mass center of moving links becomes pretty complex. Another imperfection of the mentioned method is the fact that the end-effector trajectory becomes a derivative of the trajectory of the center of masses, i.e. by using the known balancing method mentioned above it is possible to ensure only initial and final positions of the end-effector but not a straight line trajectory between them.

To eliminate these drawbacks, the present study proposes to combine the balancing through mass redistribution and the balancing via center of mass acceleration control. This allows one to reach more efficient balancing results, i.e. to increase the shaking force balancing rates and to control the displacements of the total mass center of moving links via the end-effector trajectory.

The suggested technique is illustrated through computer simulations. The results obtained via ADAMS simulations showed that a reduction in the maximum value of the shaking force of 78 % has been obtained.

The proposed principle concerns only to the reduction of shaking forces, and for the reduction of shaking moments, a flywheel can be used (Arakelian and Smith 2008).

## References

- Agrawal, S., & Fattah, A. (2004). Reactionless space and ground robots: Novel design and concept studies. *Mechanism and Machine Theory*, 39(1), 25–40.
- Arakelian, V., & Smith, M. (2008). Design of planar 3-DOF 3-RRR reactionless parallel manipulators. *Mechatronics*, 18(10), 601–606.
- Arakelian, V., & Briot, S. (2015). *Balancing of linkages and robot manipulators, advanced methods with illustrative examples* (p. 291). Switzerland: Springer.
- Bayer, A., & Merk, G. (2011, August 24). Industrial robot with a weight balancing system. EP Patent 2301727.
- Briot, S., Arakelian, V., & Le Baron, J.-P. (2012). Shaking force minimization of high-speed robots via center of mass acceleration control. *Mechanism and Machine Theory*, 57, 1–12.
- Fattah, A., & Agrawal, S. (2003). Design and modeling of classes of spatial reactionless manipulators. In *Proceedings of the IEEE International Conference on Robotics and Automation (ICRA 2003)* (pp. 3225–3230). Taipei, Taiwan.
- Fattah, A., & Agrawal, S. (2005). Design arm simulation of a class of spatial reactionless manipulators. *Robotica*, 3, 75–81.
- Filaretov, V., & Vukobratovic, M. (1993). Static balancing and dynamic decoupling of the motion of manipulation robots. *Mechanism and Machine Theory*, 3(6), 767–783.
- Herder, J., & van derWijk, V. (2010, May 3). Force balanced Delta robot. NL Patent 2002839.
- Khalil, W., & Dombre, E. (2002). Modeling, identification and control of robots. London: Hermes Penton.
- Nenchev, D. N. (2013). Reaction null space of a multibody system with applications in robotics. *Mechanical Sciences*, 4, 97–112.

# An Alternative Approach to the Dynamics Analysis of Closed-Loop Mechanisms

Wei Li and Jorge Angeles

**Abstract** Dynamics analysis is crucial not only for model-based control, but also for design. This task, however, is quite challenging when it comes to closed-loop mechanisms. The authors resort to the *natural orthogonal complement*, to formulate the dynamics model of this kind of mechanisms; the technique is illustrated with an application to the well-known Bricard mechanism, which is overconstrained and hence, highly demanding in terms of meeting the constraints. It is shown that this approach offers a systematic way of producing the dynamic response of closed-loop mechanisms, which reduces the computation complexity, and hence is quite suitable for real-time control and mechanical design. Moreover, this approach is shown to be especially suitable for single-loop mechanisms, whose formulation cost is virtually the same as that for an open chain.

**Keywords** Dynamics analysis · Natural orthogonal complement · Bricard mechanism · Forward dynamics · Simulation

## 1 Introduction

The growing demand for higher control accuracy and higher speeds of operation is the motivation for the work reported here. The dynamics of closed-loop mechanisms is particularly challenging due to the presence of a number of kinematic constraints significantly higher than the degree of freedom (dof) of the mechanism at hand. The underlying mathematical model can be derived based on the Newton-Euler formulation (Dasgupta and Choudhury 1999) and the Euler-Lagrange formulation (Geng et al. 1992), but the number of variables involved in a multibody system calls

---

W. Li (✉) · J. Angeles

Department of Mechanical Engineering and Centre for Intelligent Machines,  
McGill University, 817, Sherbrooke Street West, Montreal, QC H3A 0C3, Canada  
e-mail: livey@cim.mcgill.ca

J. Angeles

e-mail: angeles@cim.mcgill.ca

© CISM International Centre for Mechanical Sciences 2016

V. Parenti-Castelli and W. Schiehlen (eds.), *ROMANSY 21 - Robot Design, Dynamics and Control*, CISM International Centre for Mechanical Sciences 569,  
DOI 10.1007/978-3-319-33714-2\_14



for algorithm-orientated methodologies suitable for preserving the stability of the integration scheme. Besides the above methods, there exist some other approaches, such as Hamilton's principle (Miller 2004) and the principle of virtual work (Tsai 2000). A comparison of these methods can be found in the literature (Merlet 2006). More recently, the application of the analysis of tree-structure systems was applied to parallel robots, while combining this concept with the recursive Newton-Euler formulation (Briot and Khalil 2015).

The main challenge of the dynamics modeling of parallel robots is to handle the constraints. Methods devised to handle constraints usually lead to differential-algebraic equations, which are more cumbersome to handle than purely differential equations. A case in point is the *augmented Lagrangian method*. In a version of this, the use of penalty functions was proposed (Bayo and Ledesma 1996) to cope with constraint violations, but this approach requires iterations within the simulation algorithm, which adds to the numerical complexity. This paper introduces a systematic approach to the formulation of the dynamics of closed-loop mechanisms, based on the *natural orthogonal complement* (NOC) (Angeles and Lee 1989), which is illustrated with an application to the Bricard mechanism (Bricard 1897). This mechanism is chosen due to its overconstrained nature, which is quite suitable to illustrate the effectiveness of the NOC. The same method was applied, although in a rather ad-hoc manner, to the dynamics of a robot of the Schönflies type (Cammarata et al. 2009). The NOC has also been adapted to real-time applications via its *decoupled* version for serial robots (Saha 2014). The foundations of the NOC are available in the literature (Angeles and Lee 1989; Angeles 2014); due to space limitations, only what pertains to closed-loop mechanisms is included here.

The paper organization follows: In Sect. 2, the displacement and kinematics relations of the Bricard mechanism are recalled; Sect. 3 establishes the dynamics model based on the NOC. Section 4 includes simulation results obtained with our algorithm, which are compared with those obtained from CAD software.<sup>1</sup> Section 5 includes our concluding remarks.

## 2 Displacement and Kinematic Relations

A sketch of the Bricard mechanism is shown in Fig. 1. Assuming the length of each link to be  $a$ , the Denavit-Hartenberg (DH) parameters (Hartenberg and Denavit 1964) describing the linkage geometry are

$$a_i = a, \quad b_i = 0, \quad \alpha_i = 90^\circ, \quad i = 1, \dots, 5; \quad \alpha_6 = -90^\circ \quad (1)$$

---

<sup>1</sup>SolidWorks motion analysis.

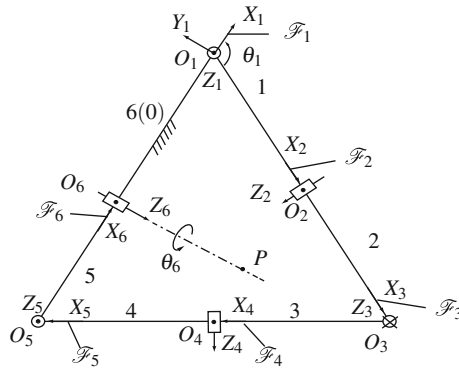


Fig. 1 The Bricard mechanism

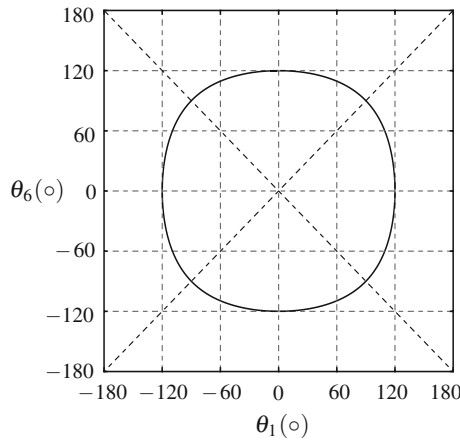


Fig. 2 \$\theta\_6\$ versus \$\theta\_1\$ relationship for the Bricard mechanism

The joint variables \$\theta\_i\$, for \$i = 1, \dots, 6\$, are defined accordingly. Because of the symmetries involved, the linkage geometry leads to (Angeles 1986)<sup>2</sup>:

$$\theta_1 = -\theta_3 = \theta_5, \quad \theta_2 = -\theta_4 = \theta_6 \tag{2}$$

The Bricard mechanism has one degree of freedom. We choose to actuate \$\theta\_1\$, and regard \$\theta\_6\$ as the linkage output, the two obeying the relation (Angeles 1986)

$$(\cos \theta_1 + 1)(\cos \theta_6 + 1) = 1 \tag{3}$$

<sup>2</sup>Some typos incurred in this reference were corrected here.

which is plotted in Fig. 2. Apparently, the  $\theta_6$ -versus- $\theta_1$  plot is doubly symmetric, with  $-\pi/3 \leq \theta_j \leq \pi/3$ , for  $j = 1, 6$ . Equation (3), upon differentiation w.r.t. time, yields

$$-\sin \theta_1 (\cos \theta_6 + 1) \dot{\theta}_1 - \sin \theta_6 (\cos \theta_1 + 1) \dot{\theta}_6 = 0 \quad (4)$$

Considering that the values for  $\theta_1$  and  $\theta_6$  lie within  $\pm 2\pi/3$ , we can simplify the above relation as

$$\frac{\dot{\theta}_6}{\dot{\theta}_1} = -\frac{\sin \theta_1 (\cos \theta_6 + 1)}{\sin \theta_6 (\cos \theta_1 + 1)} = -\frac{\tan(\theta_1/2)}{\tan(\theta_6/2)} \quad (5)$$

### 3 Dynamics Analysis Based on the NOC

#### 3.1 The Mathematical Model of the Mechanism

The mathematical model is now formulated by means of the NOC. The links of the Bricard mechanism are labelled as shown in Fig. 1. Let  $\mathbf{t}_j = [\boldsymbol{\omega}_j^T, \dot{\mathbf{c}}_j^T]^T$  denote the twist of the  $j$ th link, for  $j = 1, \dots, 5$ , in which  $\boldsymbol{\omega}_j$  is the link angular velocity,  $\dot{\mathbf{c}}_j$  is the velocity of the link centre of mass  $C_j$ , and we define  $\boldsymbol{\rho}_j$  as the vector  $\overrightarrow{O_j C_j}$ . Moreover, let  $\mathbf{t} = [\mathbf{t}_1^T, \mathbf{t}_2^T, \mathbf{t}_3^T, \mathbf{t}_4^T, \mathbf{t}_5^T]^T \in \mathbb{R}^{30}$  denote the *linkage twist*; the mathematical model governing the mechanism dynamics, before coupling all the links, is given by a system of five six-dimensional Newton-Euler equations, namely,

$$\mathbf{M}\dot{\mathbf{t}} = -\mathbf{W}\mathbf{M}\mathbf{t} + \mathbf{w}^A + \mathbf{w}^G + \mathbf{w}^C \in \mathbb{R}^{30} \quad (6)$$

where  $\mathbf{w}^A$ ,  $\mathbf{w}^G$  and  $\mathbf{w}^C$  represent the wrenches generated by active, gravity and non-working constraint forces and moments, respectively. Moreover,  $\mathbf{M}$  and  $\mathbf{W} \in \mathbb{R}^{30 \times 30}$  are block-diagonal matrices, i.e.,

$$\mathbf{M} = \text{diag}(\mathbf{M}_1, \dots, \mathbf{M}_5), \quad \mathbf{W} = \text{diag}(\mathbf{W}_1, \dots, \mathbf{W}_5) \quad (7)$$

with  $\mathbf{M}_j$  and  $\mathbf{W}_j \in \mathbb{R}^6$ , termed the link inertia and angular-velocity dyads, defined as

$$\mathbf{M}_j = \begin{bmatrix} \mathbf{I}_j & \mathbf{O}_{3 \times 3} \\ \mathbf{O}_{3 \times 3} & m_j \mathbf{1}_{3 \times 3} \end{bmatrix}, \quad \mathbf{W}_j = \begin{bmatrix} \boldsymbol{\Omega}_j & \mathbf{O}_{3 \times 3} \\ \mathbf{O}_{3 \times 3} & \mathbf{O}_{3 \times 3} \end{bmatrix}, \quad j = 1, \dots, 5 \quad (8)$$

where  $\mathbf{I}_j \in \mathbb{R}^{3 \times 3}$ ,  $m_j$  and  $\boldsymbol{\Omega}_j \in \mathbb{R}^{3 \times 3}$  represent the inertia tensor at the link center of mass, the mass, and CPM( $\boldsymbol{\omega}_j$ ) of the  $j$ th link, respectively.<sup>3</sup> Next, we derive the *twist-shaping matrix*  $\mathbf{T} \in \mathbb{R}^{30 \times 5}$ , as required by the NOC.

<sup>3</sup> $\mathbf{V} = \text{CPM}(\mathbf{v})$  is termed the *cross-product matrix* of any vector  $\mathbf{v} \in \mathbb{R}^3$ , and defined as  $\mathbf{V} = (\partial \mathbf{v} \times \mathbf{x} / \partial \mathbf{x})$ ,  $\forall \mathbf{x} \in \mathbb{R}^3$ .

### 3.2 Derivation of the Twist-Shaping Relations

The twist-shaping matrix  $\mathbf{T}$  maps the set of actuated joint rates to the twist  $\mathbf{t}$  of the system, as defined in the previous subsection. The actuated joint variable is  $\theta_1$  in our case, but firstly, we neglect the link couplings, i.e., we omit the last joint and regard the first five joints as if they were uncoupled, then the set of acutated joint rates becomes  $\dot{\boldsymbol{\theta}} = [\dot{\theta}_1, \dots, \dot{\theta}_5]^T \in \mathbb{R}^5$ , and  $\mathbf{t}$  can be expressed as a linear transformation of  $\dot{\boldsymbol{\theta}}$ , namely,  $\mathbf{t} = \mathbf{T}\dot{\boldsymbol{\theta}}$ , with

$$\mathbf{T} = \begin{bmatrix} \mathbf{t}_{11} & \mathbf{0} & \dots & \mathbf{0} \\ \mathbf{t}_{21} & \mathbf{t}_{22} & \dots & \mathbf{0} \\ \vdots & \vdots & \ddots & \vdots \\ \mathbf{t}_{51} & \mathbf{t}_{52} & \dots & \mathbf{t}_{55} \end{bmatrix} \in \mathbb{R}^{30 \times 5}, \quad \mathbf{0} \in \mathbb{R}^6 \tag{9}$$

where

$$\mathbf{t}_{ij} = \begin{cases} \begin{bmatrix} \mathbf{e}_j \\ \mathbf{e}_j \times \mathbf{r}_{ij} \end{bmatrix}, & \text{if } j \leq i \\ \begin{bmatrix} \mathbf{0} \\ \mathbf{0} \end{bmatrix}, & \text{otherwise} \end{cases} \tag{10}$$

with  $\mathbf{e}_j$  representing the unit vector parallel to the  $j$ th axis, and  $\mathbf{r}_{ij}$  the vector connecting the centers of mass of the  $j$ th and  $i$ th links, for  $j \leq i$  (Angeles 2014).

Next, we consider the link couplings. Since the mechanism has only one degree of freedom, the relations  $\dot{\theta}_i = \theta'_i(\theta_1)\dot{\theta}_1$ , for  $i = 2, \dots, 5$ , must hold, i.e.,

$$\dot{\boldsymbol{\theta}} = \boldsymbol{\vartheta}\dot{\theta}_1, \quad \boldsymbol{\vartheta} = [1, \theta'_2(\theta_1), \theta'_3(\theta_1), \theta'_4(\theta_1), \theta'_5(\theta_1)]^T \in \mathbb{R}^5 \tag{11}$$

For the Bricard mechanism, the relations below follow:

$$\dot{\theta}_1 = -\dot{\theta}_3 = \dot{\theta}_5, \quad \dot{\theta}_2 = -\dot{\theta}_4 = \dot{\theta}_6 \tag{12}$$

Moreover, from Eq. (5), we obtain  $\theta'_6(\theta_1) = -\tan(\theta_1/2) \cot(\theta_6/2)$ ,  $\boldsymbol{\vartheta}(\theta_1)$  then becoming

$$\boldsymbol{\vartheta}(\theta_1) = [1, \theta'_6(\theta_1), -1, -\theta'_6(\theta_1), 1, ]^T \tag{13}$$

from which we derive the twist-shaping vector  $\mathbf{t}_B \in \mathbb{R}^{30}$ :

$$\mathbf{t} = \mathbf{T}\dot{\boldsymbol{\theta}} = \mathbf{T}\boldsymbol{\vartheta}\dot{\theta}_1 = \begin{bmatrix} \mathbf{t}_{11} \\ \mathbf{t}_{21} + \theta'_6(\theta_1)\mathbf{t}_{22} \\ \mathbf{t}_{31} - \mathbf{t}_{33} + \theta'_6(\theta_1)\mathbf{t}_{32} \\ \mathbf{t}_{41} - \mathbf{t}_{43} + \theta'_6(\theta_1)(\mathbf{t}_{42} - \mathbf{t}_{44}) \\ \mathbf{t}_{51} - \mathbf{t}_{53} + \mathbf{t}_{55} + \theta'_6(\theta_1)(\mathbf{t}_{52} - \mathbf{t}_{54}) \end{bmatrix} \dot{\theta}_1 = \mathbf{t}_B\dot{\theta}_1 \tag{14}$$

with  $\mathbf{t}_B = \mathbf{T}\boldsymbol{\theta} \in \mathbb{R}^{30}$ . Then  $\dot{\mathbf{t}}$  can be derived as

$$\dot{\mathbf{t}} = \dot{\mathbf{T}}\boldsymbol{\theta}_1 + \mathbf{T}\dot{\boldsymbol{\theta}}_1 + \mathbf{T}\boldsymbol{\theta}\ddot{\boldsymbol{\theta}}_1 \quad (15)$$

Equation (6) can now be rewritten as

$$\mathbf{M}(\dot{\mathbf{T}}\boldsymbol{\theta}_1 + \mathbf{T}\dot{\boldsymbol{\theta}}_1 + \mathbf{T}\boldsymbol{\theta}\ddot{\boldsymbol{\theta}}_1) = -\mathbf{WMT}\boldsymbol{\theta}_1 + \mathbf{w}^A + \mathbf{w}^G + \mathbf{w}^C \quad (16)$$

All the quantities in the right-hand side of the above equation are known once the *state* of the linkage,  $\mathbf{x} = [\theta_1, \dot{\theta}_1]^T$ , is known, except for  $\mathbf{w}^C$ . Nevertheless, the foregoing vector can be eliminated by virtue of the *reciprocity relation* between feasible twist and constraint wrenches (Angeles 2014):

$$\mathbf{T}^T \mathbf{w}^C = \mathbf{0} \in \mathbb{R}^5 \quad (17)$$

Then, upon multiplication of both sides of Eq. (16) from the left by  $\mathbf{t}_B^T$ ,  $\mathbf{w}^C$  is eliminated, which leads to the desired model:

$$I(\theta_1)\ddot{\theta}_1 = -C(\theta_1, \dot{\theta}_1)\dot{\theta}_1 + \gamma + \tau \quad (18)$$

where  $I(\theta_1)$  is the generalized inertia,  $C(\theta_1, \dot{\theta}_1)\dot{\theta}_1$  is the generalized force of Coriolis and centrifugal terms,  $\gamma$  is the generalized gravity force, and  $\tau$  is the generalized active force, namely, the linkage driving torque. These terms are expanded below:

$$\begin{aligned} I(\theta_1) &= \mathbf{t}_B^T \mathbf{M} \mathbf{t}_B = \boldsymbol{\vartheta}^T \mathbf{T}^T \mathbf{M} \mathbf{T} \boldsymbol{\vartheta} \\ C(\theta_1, \dot{\theta}_1) &= \mathbf{t}_B^T \mathbf{M} \dot{\mathbf{t}}_B + \mathbf{t}_B^T \mathbf{W} \mathbf{M} \mathbf{t}_B \\ &= \boldsymbol{\vartheta}^T \mathbf{T}^T \mathbf{M} \dot{\mathbf{T}} \boldsymbol{\vartheta} + \boldsymbol{\vartheta}^T \mathbf{T}^T \mathbf{M} \mathbf{T} \dot{\boldsymbol{\vartheta}} + \boldsymbol{\vartheta}^T \mathbf{T}^T \mathbf{W} \mathbf{M} \mathbf{T} \boldsymbol{\vartheta} \\ \gamma &= \mathbf{t}_B^T \mathbf{w}^G = \boldsymbol{\vartheta}^T \mathbf{T}^T \mathbf{w}^G, \quad \tau = \mathbf{t}_B^T \mathbf{w}^A = \boldsymbol{\vartheta}^T \mathbf{T}^T \mathbf{w}^A \end{aligned} \quad (19)$$

thereby completing the modeling of the Bricard mechanism.

Finally, in order to show the generality of the NOC, we outline the modeling of a general multi-body system based on the above derivation. Assume that a given mechanical system has  $m$  moving bodies whose twists are given by  $\mathbf{t}_j$ , for  $j = 1, \dots, m$ ; moreover, we assume that the system has  $n$  degrees of freedom. The dynamics modeling via the NOC basically involves two steps: firstly, we write the system of dynamics equations for the uncoupled system, as in Eq. (6):

$$\mathbf{M}\dot{\mathbf{t}} = -\mathbf{W}\mathbf{M}\mathbf{t} + \mathbf{w}^A + \mathbf{w}^G + \mathbf{w}^C \in \mathbb{R}^{6m} \quad (20)$$

The second step is to reduce this system to coupled form with  $n$  equations and  $n$  generalized coordinates, the latter being the set of actuated joint variables  $\boldsymbol{\theta}$ . The key is to find the mapping

$$\mathbf{t} = \mathbf{T}\dot{\boldsymbol{\theta}}, \quad \mathbf{T} \in \mathbb{R}^{6m \times n} \quad (21)$$

Once relation (21) is obtained, based on the reciprocity relation  $\mathbf{w}_c^T \mathbf{t} \equiv \mathbf{0}$ , we have  $\mathbf{w}_c^T \mathbf{T} \dot{\boldsymbol{\theta}} \equiv \mathbf{0}$ , for an arbitrary  $\dot{\boldsymbol{\theta}}$ , and hence,  $\mathbf{w}_c^T \mathbf{T} = \mathbf{0}$  or, equivalently,  $\mathbf{T}^T \mathbf{w}_c = \mathbf{0}$ . Then, upon multiplication of both sides of Eqs. (20) by  $\mathbf{T}^T$ , we eliminate the constraint wrenches, which leads to the desired coupled model. The relation (21) is bound to exist once the assembly mode is chosen, since the set of independent variables is sufficient to characterize the configuration of the system.

### 4 Simulation Results

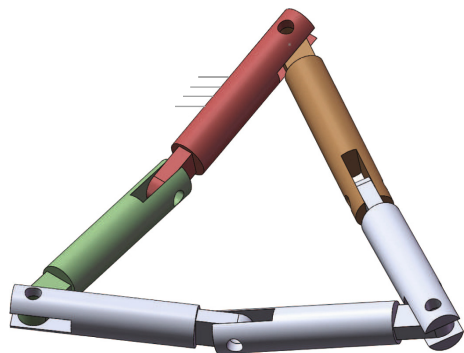
In order to simulate the mathematical model (18), we used a CAD system to obtain the numerical values of the inertial properties for each link of the mechanism, as shown in Fig. 3. Assuming homogeneous links made of 1060 Alloy, with a density of  $2700 \text{ kg/m}^3$ , the modeller<sup>4</sup> produced the numerical values

$$\begin{aligned}
 m &= 0.07 \text{ kg}, \quad l = 0.1 \text{ m}, \quad [\mathbf{I}_j]_{j+1} = \text{diag} (3.46, 55.93, 55.56) \cdot 10^{-6} \text{ kg m}^2 \\
 [\boldsymbol{\rho}_j]_{j+1} &= [0.052, 0, 0]^T \text{ m}, \quad j = 1, \dots, 5
 \end{aligned}
 \tag{22}$$

where  $[\cdot]_{j+1}$  means that vector or matrix  $(\cdot)$  is represented in  $\mathcal{F}_{j+1}$ . The initial values are chosen as  $\theta_1 = -30^\circ$ ,  $\dot{\theta}_1 = 0$ , while the actuator torque  $\tau_1 = \text{const} = 0.2 \text{ N}$ . In order to implement the simulation of the motion under the foregoing conditions, the model (18) is cast in state-variable form, namely,

$$\dot{\mathbf{x}} = \mathbf{f}(\mathbf{x}, \mathbf{u})
 \tag{23}$$

**Fig. 3** The CAD model of the Bricard mechanism



<sup>4</sup>SolidWorks 2013.

**Fig. 4** Simulation plot from the NOC model

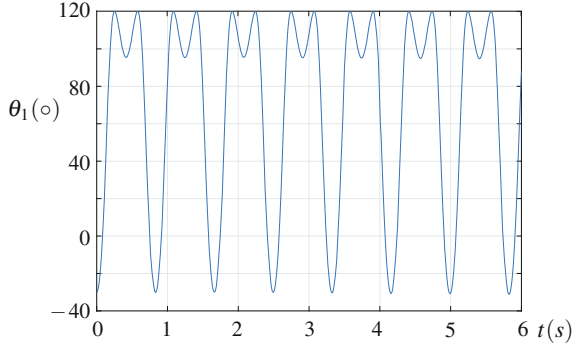
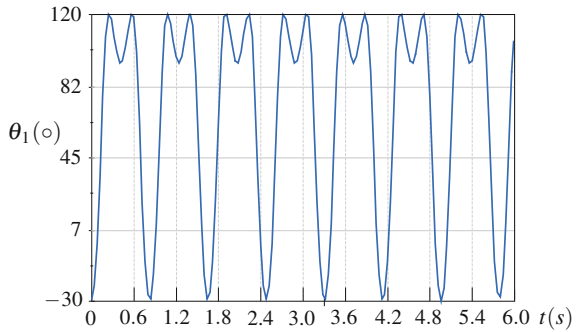


**Fig. 5** Simulation plot from CAD software



where

$$\mathbf{f}(\mathbf{x}, \mathbf{u}) = \begin{bmatrix} \dot{\theta}_1 \\ (-C\dot{\theta}_1 + \gamma + \tau_m)/I \end{bmatrix}, \quad \mathbf{x} = \begin{bmatrix} \theta_1 \\ \dot{\theta}_1 \end{bmatrix}, \quad \mathbf{u} = \begin{bmatrix} 0 \\ (\gamma + \tau_m)/I \end{bmatrix} \quad (24)$$

The time history thus obtained is shown in Fig. 4. In order to validate the simulation results, we resorted to the simulation capabilities of the CAD modeller, which produced the plot displayed in Fig. 5; this tallies with that of Fig. 4.

## 5 Conclusions

The authors proposed a systematic and effective approach to the dynamics analysis of closed-loop mechanisms, based on the NOC, which is demonstrated with the aid of the (overconstrained) Bricard mechanism. The complete displacement analysis, kinematics and dynamics are reported here. The proposed approach can be used in real-time control.

**Acknowledgments** The first author would like to acknowledge the support from the McGill Engineering Doctoral Awards (MEDA) and the Chinese Scholarship Council (CSC) for their financial support. The second author acknowledges the support received from NSRRC (Canada's Natural Sciences and Engineering Research Council) through Grant No. 2015-03864, and from McGill University's James McGill Professorship.

## References

- Angeles, J. (1986). Iterative kinematic inversion of general five-axis robot manipulators. *The International Journal of Robotics Research*, 4(4), 59–70.
- Angeles, J. (2014). *Fundamentals of Robotic Mechanical Systems. Theory, Methods, Algorithms* (4th ed.). New York: Springer.
- Angeles, J., & Lee, S. (1989). The modelling of holonomic mechanical systems using a natural orthogonal complement. *Canadian Society for Mechanical Engineering, Transactions*, 13(4), 81–89.
- Bayo, E., & Ledesma, R. (1996). Augmented lagrangian and mass-orthogonal projection methods for constrained multibody dynamics. *Nonlinear Dynamics*, 9(1–2), 113–130.
- Bricard, R. (1897). Mémoire sur la théorie de l'octaèdre articulé. *Journal de Mathématiques pures et Appliquées*, 113–148.
- Briot, S., & Khalil, W. (2015). Dynamic modeling of parallel robots. In *Dynamics of Parallel Robots* (pp. 139–199). Springer.
- Cammarata, A., Angeles, J., & Sinatra, R. (2009). The dynamics of parallel Schönflies motion generators: The case of a two-limb system. *Proceedings of the Institution of Mechanical Engineers, Part I: Journal of Systems and Control Engineering*, 223(1), 29–52.
- Dasgupta, B., & Choudhury, P. (1999). A general strategy based on the Newton-Euler approach for the dynamic formulation of parallel manipulators. *Mechanism and Machine Theory*, 34(6), 801–824.
- Geng, Z., Haynes, L. S., Lee, J. D., & Carroll, R. L. (1992). On the dynamic model and kinematic analysis of a class of Stewart platforms. *Robotics and Autonomous Systems*, 9(4), 237–254.
- Hartenberg, R. S., & Denavit, J. (1964). *Kinematic Synthesis of Linkages*. McGraw-Hill.
- Merlet, J.-P. (2006). *Parallel Robots* (Vol. 128). Springer.
- Miller, K. (2004). Optimal design and modeling of spatial parallel manipulators. *The International Journal of Robotics Research*, 23(2), 127–140.
- Saha, S. K. (2014). *Introduction to Robotics*. Tata McGraw-Hill Education.
- Tsai, L.-W. (2000). Solving the inverse dynamics of a Stewart-Gough manipulator by the principle of virtual work. *Journal of Mechanical Design*, 122(1), 3–9.



# Lagrangian Based Dynamic Analyses of Delta Robots with Serial-Parallel Architecture

Jan Brinker and Burkhard Corves

**Abstract** 30 years after the initial concepts, commercial Delta and Delta-like robots serve a niche market for high-speed pick-and-place applications. Expired patents and new fields of applications have led to increased research and development in recent years. The increased scientific focus on extended architectures with additional rotational dof resulted in different serial-parallel hybrid as well as fully-parallel designs. These concepts meet the industrial demands for novel complex handling tasks, increased payload capacities, and hygienic designs. This contribution presents kinematic and energy-based dynamic analyses for the classical Delta structure and six different extensions. Based on that, the required computation times and the influences of inertial effects are investigated.

**Keywords** Kinematics · Dynamics · Lagrangian formulation · Parallel robots · Delta robots

## 1 Introduction

In the 1980s, Clavel invented the Delta robot with three translational degrees-of-freedom (dof) dedicated to high-speed applications. Market analyses show a current tendency of adding serial mechanisms to the original parallel Delta architecture in order to obtain orientation capabilities. Such concepts consist of the basic Delta structure with three translational dof and an additional 3-dof rotational

---

J. Brinker (✉) · B. Corves  
Department of Mechanism Theory and Dynamics of Machines,  
RWTH Aachen University, Aachen, Germany  
e-mail: brinker@igm.rwth-aachen.de

B. Corves  
e-mail: corves@igm.rwth-aachen.de

head, i.e. a serial robotic wrist (type RRR), mounted on the platform. This wrist can be driven by three separate motors fixed on the frame (e.g. FANUC M-1 Series), attached to the platform, or attached to the distal links (e.g. FANUC M-3 Series). An extensive overview about the historical, academic, and industrial development of such mechanisms is presented by Brinker and Corves (2015). Research in the general fields of kinematics, dynamics, control, singular configurations, workspace, calibration, and mechanical design of Delta robots has been conducted extensively during the last decades. The most common analytical approaches for dynamic modeling are: the Principle of Virtual Work, the Newton-Euler Formulation, and the Lagrangian Formulation (Briot and Khalil 2015). The three approaches yield identical results, but the computational intensity may vary. A comparative study of these approaches shows that for the basic structure fastest processing times can be reached applying the Lagrangian Formulation (Brinker et al. 2015). Against this background, this contribution is concerned with complete energy-based models of Delta robots with six different extensions (i.e. additional motor(s) and, if applicable, intermediary telescopic shaft(s); cf. Fig. 1, right). One major challenge is that, due to the additional kinematic chains, partial derivatives may lead to cumbersome analytical expressions and thus, influence the computational costs of the approach. In this context, for each extension, the resulting computation times are compared against the other modeling approaches. The objectives of this contribution are (1) to assess the applicability of the Lagrangian approach to parallel robots with more complex architecture, (2) to identify the most advantageous modeling approach for the various extensions, and (3) to exemplarily illustrate the influences of the inertial effects of the additional bodies on the actuation torques of the basic structure depending on the imposed trajectory. To the best of our knowledge, the only scientific contribution concerning (dynamic) analyses of serial-parallel Delta robots are presented by Borchert et al. (2015) applying the Newton-Euler Formulation.

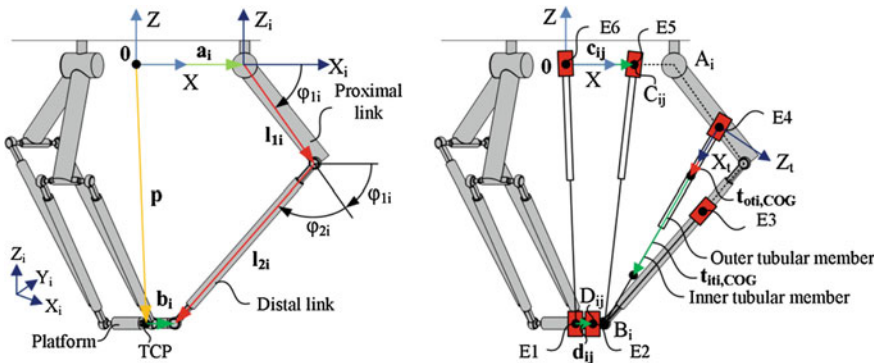


Fig. 1 Geometric relations and notations for the basic structure and six extensions

## 2 Geometric Relations

The position vectors of the actuated joints and the joints connecting the platform and the distal link are denoted by  $\mathbf{a}_i$  and  $\mathbf{b}_i$ . These joints lie on a circle with the radii  $a$  and  $b$ , respectively. The vectors pointing along the links of the  $i$ th chain are  $\mathbf{l}_{1i}$  and  $\mathbf{l}_{2i}$  (cf. Fig. 1, left). The motors driving the wrist can be attached to the frame, to the platform, to the distal, or to the proximal links, where the investigation of the latter is mere theoretical. The telescopic shaft is modeled as an outer and an inner tubular member with their ends attached to the basic structure by cardan joints. The vectors  $\mathbf{c}_{ij}$  and  $\mathbf{d}_{ij}$  describe the positions of the attachment points of the telescopic shaft, where the upper position, i.e.  $\mathbf{c}_{ij}$ , is equal to the motor position. The resulting six possible extensions (E) are determined by the position of the motors driving the additional rotational dof (marked in red; cf. Fig. 1, right).

Figure 1 (right) shows the geometric relations and notations for the basic structure and the six extensions. Accordingly, the motors can be placed into the Tool Center Point (TCP) (E1), on vector  $\mathbf{b}_i$ , i.e. the vector between the TCP and joints  $B_i$  (E2), on the distal link (E3), on the proximal link (E4), as well as on the frame with their coordinates related to the vector  $\mathbf{a}_i$  between  $\mathbf{0}$  and  $A_i$  (E5 and E6). E1 and E6 are modeled as 4-dof structures as commonly applied in industries (e.g. Kawasaki YF03 with direct drive and ABB IRB 360 with single telescopic chain, respectively). From abovementioned assumptions it follows for the extensions and the attachment points of the additional serial chain(s), respectively (cf. Table 1).

The factors  $x_j$  with  $0 < x_j \leq 1$  (for all  $j$ ) describe the proportion of a related vector to determine the motor position of the  $j$ th extension. As a simplification the platform-related attachment points of all configurations involving telescopic shafts (i.e. E3-E6) lie in  $B_i$ , i.e.  $x_0 = 1$ . For E1 and E2, the motors are attached directly to the platform and thus, no telescopic shaft is involved. For the sake of brevity, the index  $j$  denoting the extensions is neglected in the following.

**Table 1** Positions of the attachment points of the additional serial chain(s)

E	dof	$\mathbf{c}_{ij}$	$\mathbf{d}_{ij}$	Motor position
1	4	$\mathbf{p}$	$\mathbf{p}$	At TCP
2	6	$\mathbf{p} + x_2 \cdot \mathbf{b}_i$	$\mathbf{p} + x_2 \cdot \mathbf{b}_i$	Between TCP and $B_i$
3	6	$\mathbf{a}_i + x_3 \cdot \mathbf{l}_{1i} + x_3 \cdot \mathbf{l}_{2i}$	$\mathbf{p} + x_0 \cdot \mathbf{b}_i$	On distal link
4	6	$\mathbf{a}_i + x_4 \cdot \mathbf{l}_{1i}$	$\mathbf{p} + x_0 \cdot \mathbf{b}_i$	On proximal link
5	6	$x_5 \cdot \mathbf{a}_i$	$\mathbf{p} + x_0 \cdot \mathbf{b}_i$	Between $\mathbf{0}$ and $A_i$
6	4	$\mathbf{0}$	$\mathbf{p} + x_0 \cdot \mathbf{b}_i$	Between $\mathbf{0}$ and $A_i$

### 3 Kinematic Analyses

By solving the inverse kinematic problem, a relation between the given platform position  $\mathbf{p}$  and the desired angles of rotation of the three rotary actuators  $\varphi_{1i}$  driving the proximal links can be obtained.

**Position analysis.** The closure equation is given by:

$$\mathbf{p} = \mathbf{l}_{1i} + \mathbf{l}_{2i} + \mathbf{a}_i - \mathbf{b}_i \quad (1)$$

For detailed position analyses of the basic structure see Brinker et al. (2015). The vector along a telescopic shaft is then given as:

$$\mathbf{t}_i = -\mathbf{c}_i + \mathbf{p} + \mathbf{d}_i \quad (2)$$

The positions of the centers of gravity (COG) of the outer tube (ot) and inner tube (it) of the shaft are:

$$\mathbf{t}_{\text{oti, COG}} = \mathbf{c}_i + l_{\text{ot}}/2 \mathbf{t}_{i0} \quad (3)$$

$$\mathbf{t}_{\text{iti, COG}} = \mathbf{c}_i + (t_i - l_{\text{it}}/2) \mathbf{t}_{i0} \quad (4)$$

with  $l_{\text{ot}}$  and  $l_{\text{it}}$  as their lengths and  $t_i$  as current length of the complete shaft. For E3, the lengths of the tubes are set to:

$$l_{\text{ot}3} = l_{\text{it}3} = (1 - x_3)/(2l_{2i}) \quad (5)$$

For E4, E5, and E6, the following applies:

$$l_{\text{ot}4,5,6} = l_{\text{it}4,5,6} = (l_{1i} + l_{2i})/2 \quad (6)$$

**Velocity analysis.** Time differentiation of the closure equation results in:

$$\dot{\mathbf{p}} = \boldsymbol{\omega}_{1i} \times \mathbf{l}_{1i} + \boldsymbol{\omega}_{2i} \times \mathbf{l}_{2i} = (\dot{\varphi}_{1i} \cdot \mathbf{s}_{\text{Ai}}) \times \mathbf{l}_{1i} + \boldsymbol{\omega}_{2i} \times \mathbf{l}_{2i} \quad (7)$$

with  $\dot{\varphi}_{1i}$  and  $\mathbf{s}_{\text{Ai}}$  as actuation speed and axis of rotation of the proximal link (which corresponds to the  $Y_i$ -axis). By dot-multiplying (7) with the vector along the distal link the angular velocity of the same can be eliminated which, after rearranging, leads to a relation between the given platform velocity to the velocity of the actuated joint (i.e. the Jacobian matrix  $\mathbf{J}_{\mathbf{p}}$ ):

$$\dot{\varphi}_1 = (\dot{\varphi}_{11} \quad \dot{\varphi}_{12} \quad \dot{\varphi}_{13})^T = \mathbf{J}_{\mathbf{p}} \cdot \dot{\mathbf{p}} = (\mathbf{J}_{\mathbf{p}1}^T \quad \mathbf{J}_{\mathbf{p}2}^T \quad \mathbf{J}_{\mathbf{p}3}^T)^T \cdot \dot{\mathbf{p}} \quad (8)$$

where

$$\mathbf{J}_{\mathbf{p}_i}^T = ((\mathbf{s}_{A_i} \times \mathbf{l}_{1_i}) \cdot \mathbf{l}_{2_i})^{-1} \cdot \mathbf{l}_{2_i}^T \quad (9)$$

Assuming a central point of gravity, the velocities of the COG of the links are:

$$\mathbf{v}_{1_i, \text{COG}} = \boldsymbol{\omega}_{1_i} \times \mathbf{l}_{1_i}/2 \quad (10)$$

$$\mathbf{v}_{2_i, \text{COG}} = \dot{\mathbf{p}} - \boldsymbol{\omega}_{2_i} \times \mathbf{l}_{2_i}/2 \quad (11)$$

Rearranging (7) leads to

$$\boldsymbol{\omega}_{2_i} = \mathbf{l}_{2_i} \times (\dot{\mathbf{p}} - \boldsymbol{\omega}_{1_i} \times \mathbf{l}_{1_i})/l_2^2 \quad (12)$$

The velocity of the shaft, can be obtained by time differentiation of (2) or by the vector sum of the tangential velocity of the outer tube and the linear relative velocity of the inner tube:

$$\dot{\mathbf{t}}_i = -\dot{\mathbf{c}}_i + \dot{\mathbf{p}} = \dot{t}_i \mathbf{t}_{i0} + \boldsymbol{\omega}_{ti} \times \mathbf{t}_i \quad (13)$$

with the normalized vector  $\mathbf{t}_{i0}$  pointing along the shaft. Its linear and angular velocity can be computed by dot- and cross-multiplication of (13) with  $\mathbf{t}_{i0}$ :

$$\dot{t}_i = \dot{\mathbf{t}}_i \mathbf{t}_{i0} = -\dot{\mathbf{c}}_i \mathbf{t}_{i0} + \dot{\mathbf{p}} \mathbf{t}_{i0} \quad (14)$$

$$\boldsymbol{\omega}_{ti} = \mathbf{t}_{i0} \times \dot{\mathbf{t}}_i/t_i \quad (15)$$

The linear velocity is solely related to the inner tube. Hence, the velocities of the COG of the tubes are given by:

$$\dot{\mathbf{t}}_{oti, \text{COG}} = \dot{\mathbf{c}}_i + l_{ot}/2(\boldsymbol{\omega}_{ti} \times \mathbf{t}_{i0}) \quad (16)$$

$$\dot{\mathbf{t}}_{iti, \text{COG}} = \dot{\mathbf{c}}_i + \dot{t}_i \mathbf{t}_{i0} + (t_i - l_{it}/2)(\boldsymbol{\omega}_{ti} \times \mathbf{t}_{i0}) \quad (17)$$

## 4 Dynamic Analyses

The Lagrangian formulation describes the equations of motion of a mechanical system as a function of kinetic and potential energies. Three generalized coordinates are sufficient to describe the dynamics of a 3-dof Delta robot. However, to avoid difficult expressions due to the complex geometrical model, usually the Lagrangian equation of the first type with redundant coordinates requiring a set of constraint equations is applied. By solving the inverse dynamic problem the required actuation torques for a given trajectory (with known position, velocity, and acceleration) are determined. First, the kinetic and potential energies ( $T$  and  $U$ ) of each body need to be derived in order to obtain the Lagrangian equation:

$$L = T - \Pi \quad (18)$$

The actuation torques can then be derived by (see e.g. Miller and Clavel 1992):

$$\tau_i = \frac{d}{dt} \left( \frac{\partial L}{\partial \dot{\varphi}_{1i}} \right) - \frac{\partial L}{\partial \varphi_{1i}} - \lambda_i \frac{\partial \Gamma_i}{\partial \varphi_{1i}} \quad (19)$$

with  $p_x, p_y, p_z, \varphi_{11}, \varphi_{12}$ , and  $\varphi_{13}$  as generalized coordinates, the constraint equations  $\Gamma_i$ , and the multipliers  $\lambda_i$ . The energies of the basic Delta structure and its components were derived by Miller and Clavel (1992). The energies of the tubes and motors are introduced based on the different extensions:

$$T_{oti} = \frac{1}{2} I_{oti, COG} \boldsymbol{\omega}_{ii}^T \boldsymbol{\omega}_{ii} + \frac{1}{2} m_{oti} \dot{\mathbf{t}}_{oti, COG}^T \dot{\mathbf{t}}_{oti, COG} \quad (20)$$

$$T_{iii} = \frac{1}{2} I_{iii, COG} \boldsymbol{\omega}_{ii}^T \boldsymbol{\omega}_{ii} + \frac{1}{2} m_{iii} \dot{\mathbf{t}}_{iii, COG}^T \dot{\mathbf{t}}_{iii, COG} \quad (21)$$

$$T_{Mti} = \frac{1}{2} m_{Mti} \dot{\mathbf{c}}_i^T \dot{\mathbf{c}}_i \quad (22)$$

with  $I$  and  $m$  as mass moment of inertia and mass of the respective body. The additional motors are modeled as mass points with mass  $m_{Mti}$  having no moments of inertia. E1 and E2 can simply be modeled by adapting the platform mass. The model for E6 can be obtained by setting the motor positions to the origin of the global coordinate system, i.e.  $\mathbf{c}_{i6} = \mathbf{0}$ , and neglecting the masses and mass moments of inertia of two of the chains including the motors. As mentioned before, the distal, platform-related attachment point is assumed to be  $B_i$  for all extensions. Thus, for E3 the linear velocity is zero. The velocities of the additional motors are equal to the platform velocity for E1 and E2. For E3 and E4 the following relations apply:

$$\dot{\mathbf{c}}_{i3} = \dot{\mathbf{p}} - (1 - x_3)(\boldsymbol{\omega}_{2i} \times \mathbf{l}_{2i}) \quad (23)$$

$$\dot{\mathbf{c}}_{i4} = x_4(\boldsymbol{\omega}_{1i} \times \mathbf{l}_{1i}) \quad (24)$$

The potential energies for E3 are (see Brinker et al. (2015) for angle  $\varphi_{3i}$ ):

$$\Pi_{oti3} = -m_{oti}g(l_{1i} \sin \varphi_{1i} + x_3 l_{2i} \sin \varphi_{3i} \sin(\varphi_{1i} + \varphi_{2i}) + \frac{1}{2} l_{oti} \cos \varphi_{ii}) \quad (25)$$

$$\Pi_{iii3} = -m_{iii}g(l_{1i} \sin \varphi_{1i} + x_3 l_{2i} \sin \varphi_{3i} \sin(\varphi_{1i} + \varphi_{2i}) + t_i \cos \varphi_{ii} - \frac{1}{2} l_{iii}) \quad (26)$$

$$\Pi_{Mti3} = -m_{Mti}g(l_{1i} \sin \varphi_{1i} + x_3 l_{2i} \sin \varphi_{3i} \sin(\varphi_{1i} + \varphi_{2i})) \quad (27)$$

Similarly, for E4 and E5 it follows:

$$\Pi_{oti4} = -m_{oti}g(x_4l_{1i} \sin \varphi_{1i} + \frac{1}{2}l_{oti} \cos \varphi_{ti}) \quad (28)$$

$$\Pi_{iti4} = -m_{iti}g \left( x_4l_{1i} \sin \varphi_{1i} + \left( t_i - \frac{1}{2}l_{iti} \right) \cos \varphi_{ti} \right) \quad (29)$$

$$\Pi_{Mti4} = -m_{Mti}g x_4l_{1i} \sin \varphi_{1i} \quad (30)$$

$$\Pi_{oti5} = -\frac{1}{2}m_{z,i}gl_{oti} \cos \varphi_{ti} \quad (31)$$

$$\Pi_{iti5} = -m_{q,i}g \left( t_i - \frac{1}{2}l_{iti} \right) \cos \varphi_{ti} \quad (32)$$

$$\Pi_{Mti5} = 0 \quad (33)$$

with  $\varphi_{ti}$  measuring the angle between tube and negative Z-axis:

$$\varphi_{ti} = \arccos(-\mathbf{t}_{i0}^T \mathbf{e}_z) \quad (34)$$

## 5 Results

The proposed Lagrangian (L) modeling approach was implemented in Maple and Matlab and validated against the Newton-Euler (NE) and Virtual Work (VW) approaches. For kinematic and mass parameters, test trajectory, and detailed specifications see Brinker et al. (2015). The dimensions of the basic structure as well as the handling tasks and its specifications are highly interrelated to each other and above all to the extensions and their properties. As an example, the required torques to perform the test trajectory were derived for each actuator of the basic parallel kinematic structure extended by the respective telescopic shafts. The influence of the wrist and with it the rotational dof are not considered here.

Figure 2 displays the resulting actuation torques as function of time (corresponding to the imposed trajectory) and motor position (corresponding to the extensions E3, E4, and E5). It can be seen that moving the motor position from the origin to the attachment points  $A_i$  hardly influences the resulting torques. In respect of E4, the additional motor mass is not attached to the frame anymore, but to the proximal link of the basic structure. For each actuator, the resulting torque curves show a bend at the transition between E5 and E4. For E4, minimum and maximum torques decrease and increase, respectively, exponentially with increasing  $x_4$ . Interestingly, another bend can be seen at the transition between E4 and E3, which results from the varying definitions of tube lengths (cf. (5) and (6)). Both, maximum and minimum torques are reduced degressively with increasing  $x_3$ . Again, the reason for this course is the tube length, which is constantly adapted to the distance

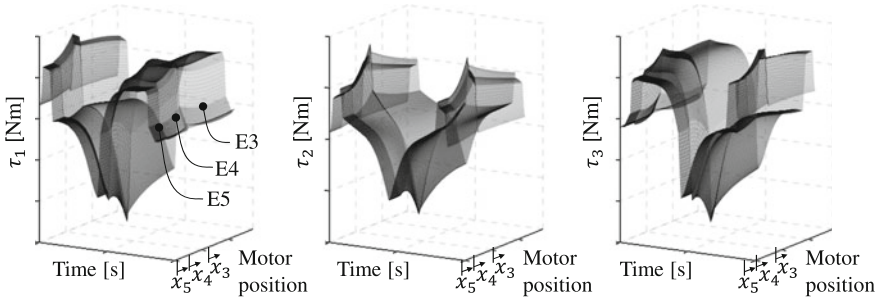


**Fig. 2** Comparison of actuation torques depending on time and motor position

between the motor and  $B_i$ . Consequently, the resulting torque curves are highly dependent on the extension. Highest values can be found attaching the telescopic shafts to the tip of the proximal joint. Here inertial effects are maximal.

For all approaches, the computation of actuation torques for E3 is the most expensive. Assume a normalized reference time of 1 s as a base for the longest computation time, the processing times for the six extensions are shown in Fig. 3. On average, VW is 30 % faster than NE for all extensions. For the less complex extensions, i.e. E1, E2, E5, and E6, L is the fastest approach (about 57 % faster than NE and 38 % faster than VW). Due to additional kinematic chains, for E3 and E4 partial derivatives become very cumbersome leading to considerable computation times. Computation costs are more than 200 (E3) and 12 (E4) times as great as the costs for NE. For better presentation, these values are excluded from Fig. 3. It should be noted that the efficiency of a model not only depends on the analyzed mechanical structure, but also on the computational scheme and the program structure (e.g. number and kind of mathematical operations).

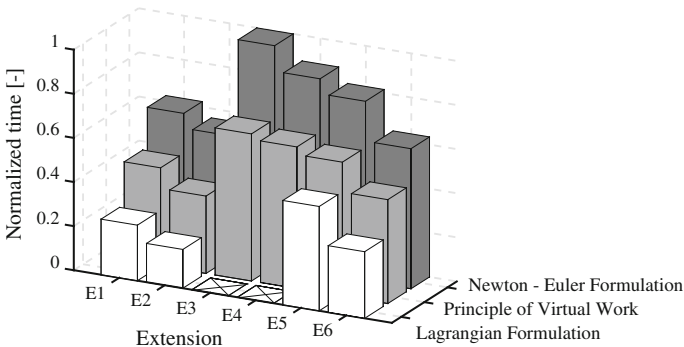


**Fig. 3** Comparison of the computation times



## 6 Conclusion

This paper introduced a holistic energy-based approach for the dynamic modeling of Delta robots with six different extensions (E) in order to obtain additional rotational dof. For extensions with rather simple kinematics, the Lagrangian approach is more efficient than other approaches. Due to the strong increase in complexity and cumbersome derivatives, E3 and E4 should preferably be modeled by other approaches, e.g. applying the Principle of Virtual Work. The properties of the extensions (e.g. motor position, diameters, lengths, and masses) highly influence the resulting driving torques. Against this background, future research will focus on the interrelations between the basic structure, the telescopic shafts, and the handling tasks with the aim of revealing the merits of each individual extension.

## References

- Brinker, J., & Corves, B. (2015, October 25–30). A survey on parallel robots with delta-like architecture. In *Proceedings of the 14th World Congress in Mechanism and Machine Science*. Taipei, Taiwan.
- Brinker, J., Corves, B., & Wahle, M. (2015, October 25–30). A comparative study of inverse dynamics based on Clavel's delta robot. In *Proceedings of the 14th World Congress in Mechanism and Machine Science*. Taipei, Taiwan.
- Briot, S., & Khalil, W. (2015). Dynamics of parallel robots—from rigid bodies to flexible elements. In *Mechanisms and Machine Science* (Vol. 35). Switzerland: Springer.
- Borchert, G., Battistelli, M., Runge, G., & Raatz, A. (2015). Analysis of the mass distribution of a functionally extended delta robot, *Robotics and Computer-Integrated Manufacturing*, 31, 111–120.
- Miller, K., & Clavel, R. (1992). The Lagrange-based model of delta-4 robot dynamics. *Robotersysteme*, 8, 49–54.

**Part IV**  
**Control and Perception of Robots**

# Adaptive Model Predictive Control Design for Underactuated Multibody Systems with Uncertain Parameters

Fabian Schnelle and Peter Eberhard

**Abstract** This paper deals with an adaptive control scheme consisting of a feedback linearization and a model predictive controller (MPC) which is aimed at a real-time capable implementation. To overcome the incalculable effect of uncertainties on the control behaviour, an unscented Kalman Filter (UKF) is used to adapt the prediction model of the MPC online. Robustness properties are derived by a fuzzy-arithmetical analysis. The proposed control scheme is applied to a serial manipulator with a passive joint containing uncertain parameters.

## 1 Introduction

In the course of weight and cost reduction in the design of manipulators and mechanisms, underactuated multibody systems gain a high relevance in the field of robotics. The functionality of model-based control approaches strongly depends on the accurate modeling of the dynamics. Model uncertainties resulting from a lack of knowledge may lead to an insufficient tracking behaviour and, therefore, have to be considered in the control design. Both trajectory tracking and compliance of constraints lead to the design of an MPC which is combined with a feedback linearization in order to simplify the nonlinear model. Uncertainties are incorporated in the control design by using an UKF to estimate their impact and, if necessary, to adapt the prediction model of the MPC. Robustness assessments are achieved by a fuzzy-arithmetical analysis.

---

F. Schnelle (✉) · P. Eberhard  
Institute of Engineering and Computational Mechanics,  
University of Stuttgart, Stuttgart, Germany  
e-mail: fabian.schnelle@itm.uni-stuttgart.de

P. Eberhard  
e-mail: peter.eberhard@itm.uni-stuttgart.de

## 2 Constrained Adaptive Nonlinear Control

The dynamics of complex mechanisms performing large motions and rotations can be described by the method of multibody systems. Following the principles of Newton and Euler and d'Alembert, the equation of motion can be derived and in case of underactuated serial manipulators be partitioned into an actuated and unactuated part denoted by the indices  $a$ , respectively  $u$

$$\begin{bmatrix} M_{aa}(q) & M_{au}(q) \\ M_{au}^T(q) & M_{uu}(q) \end{bmatrix} \begin{bmatrix} \ddot{q}_a \\ \ddot{q}_u \end{bmatrix} + \begin{bmatrix} k_a(q, \dot{q}) \\ k_u(q, \dot{q}) \end{bmatrix} = \begin{bmatrix} g_a(q, \dot{q}) \\ g_u(q, \dot{q}) \end{bmatrix} + \begin{bmatrix} u \\ \mathbf{0} \end{bmatrix} \quad (1)$$

with the generalized coordinates  $q$  and the input  $u$ . The matrix  $M$  is known as the mass matrix. The vector  $k$  summarizes the Coriolis, centrifugal and gyroscopic forces, whereby the generalized applied forces are expressed by the vector  $g$ . For end-effector trajectory tracking it is suitable to define the output as a linear combination of the actuated and unactuated generalized coordinates

$$y = q_a + \Gamma q_u, \quad (2)$$

whereby the matrix  $\Gamma$  weights the influence of the unactuated coordinates and can be derived as described in Seifried et al. (2011).

### 2.1 Feedback Linearization

Feedforward control structures are commonly used for tracking problems of end-effectors in order to take the large nonlinear motions into account and to simplify the control problem. The concept of feedback linearization, see Isidori (1995), in combination with a model predictive controller in order to penalize the deviations from the reference trajectory is applied. Applying the diffeomorphic coordinate transformation  $z^T = [y^T \ \dot{y}^T \ q_u^T \ \dot{q}_u^T]$ , the input-output normal form is derived and can be stated in the original coordinates as

$$\tilde{M}\ddot{y} = \tilde{g} - \tilde{k} + u, \quad (3)$$

$$(M_{uu} - M_{au}^T \Gamma) \ddot{q}_u = g_u - k_u - M_{au}^T \tilde{M}^{-1} (\tilde{g} - \tilde{k} + u). \quad (4)$$

For the sake of clarity, nonlinear terms are summarized in the matrices  $\tilde{M}$ ,  $\tilde{k}$  and  $\tilde{q}$  according to Seifried et al. (2011). Note that the internal dynamics (4) does not influence the output  $y$  and is thus unobservable. As a consequence a stable internal dynamics is necessary in order to design a feedback linearization. The minimum-phase property can be checked by the concept of zero dynamics, see Luca and Siciliano (1993). Then, the nonlinear feedback law

$$\mathbf{u} = \tilde{\mathbf{M}}\mathbf{v} + \tilde{\mathbf{k}} - \tilde{\mathbf{g}} \quad (5)$$

leads to the exactly linearized system  $\ddot{\mathbf{y}} = \mathbf{v}$ , which is the basis for the model predictive control design.

## 2.2 Model Predictive Control

Tracking a desired trajectory  $\mathbf{y}_d$  while considering input constraints at the same time lead to the design of a model predictive controller influencing the exactly linearized system in a desired way. The control objectives are realized by continually solving an optimal control problem given by the minimization of the quadratic cost function

$$J = \sum_{k=0}^{P-1} \|\mathbf{y}_k - \mathbf{y}_{d,k}\|_{\mathbf{Q}}^2 + \|\Delta\mathbf{v}_k\|_{\mathbf{R}}^2 \quad (6)$$

over the future  $M$  input rates  $\Delta\mathbf{V}_k^T = [\Delta\mathbf{v}_k^T \cdots \Delta\mathbf{v}_{k+M-1}^T]$  with respect to the system dynamics and the input constraints. Control parameters are the prediction horizon  $P$ , the control horizon  $M$  and the weighting matrices  $\mathbf{Q}$  and  $\mathbf{R}$ . The optimal solution  $\Delta\mathbf{V}_k^*$  can be obtained by transforming the optimal control problem into a linear-quadratic optimization problem and then applying optimization methods, see Maciejowski (2002).

## 2.3 Variable Constraint Mapping

Typical constraints on the input  $\mathbf{u}$  for multibody systems are restricted motor torques or limited workspace and have to be considered in the optimal control problem (6) as additional conditions

$$\mathbf{u}_{\min} \leq \mathbf{u}_k \leq \mathbf{u}_{\max}, \quad (7)$$

$$\Delta\mathbf{u}_{\min} \leq \Delta\mathbf{u}_k \leq \Delta\mathbf{u}_{\max}. \quad (8)$$

These constraints can not be applied directly to the optimization problem and must be expressed in terms of the optimization variable  $\Delta\mathbf{V}_k$  through the nonlinear mapping (5) between the physical input  $\mathbf{u}$  and the virtual input  $\mathbf{v}$ . Finding virtual input constraints  $\mathbf{G}_k\Delta\mathbf{V}_k \leq \mathbf{W}_k$  satisfying the physical input constraints (7) and (8) is object of the so-called constraint mapping, which is proposed by Kurtz and Henson (1997). Note that the constraint matrices  $\mathbf{G}_k$  and  $\mathbf{W}_k$  vary over the time due to the state-dependency of the mapping and determine the constraints on the planned future  $M$  input variables  $\Delta\mathbf{v}_k, \dots, \Delta\mathbf{v}_{k+M-1}$ . Thus, in each time step a prediction of the future states is required in order to compute the constraints over the control horizon  $M$ .

Recapitulate that by applying the variable constraint mapping technique an optimal input sequence  $\Delta \mathbf{V}_k^*$  is computed under consideration of the physical input constraints. A detailed explanation of the proposed method is given in Schnelle and Eberhard (2015).

## 2.4 Adaptive Control Using Unscented Kalman Filter

The main drawback of the presented feedback linearization/MPC scheme results from the fact that it relies on an exact cancellation of the nonlinear terms in order to get linear input-output behaviour and then applying model predictive control based on the exactly linearized model. As a consequence, in the presence of parametric uncertainties or unmodeled dynamics the feedback linearization is no longer exact and thus, the prediction model is less accurate and might lead to a wrong forecast and a resulting instability. The design of a robust control scheme considering uncertainties is necessary, see Sastry and Isidori (1989). Recapitulate that in case of uncertainties the feedback linearization (5) does not result in the linear system  $\dot{\mathbf{y}} = \mathbf{v}$ . To incorporate the dynamics of the uncertainties in the prediction model the linear state space model

$$\dot{\mathbf{x}} = \begin{bmatrix} \mathbf{0} & \mathbf{I} \\ -\mathbf{P}_1 & -\mathbf{P}_2 \end{bmatrix} \mathbf{x} + \begin{bmatrix} \mathbf{0} \\ \mathbf{I} + \mathbf{P}_3 \end{bmatrix} \mathbf{v}, \quad (9)$$

$$\mathbf{y} = [\mathbf{I} \ \mathbf{0}] \mathbf{x} \quad (10)$$

is introduced with the dense matrices  $\mathbf{P}_1$  and  $\mathbf{P}_2$  and the diagonal matrix  $\mathbf{P}_3$  containing  $2n_a n_a + n_a$  unknown parameters  $p_i$ . The number of actuated generalized coordinates is denoted by  $n_a$ . The linear model (9) approximates the potentially nonlinear dynamics from  $\mathbf{v}$  to  $\mathbf{y}$  by estimating and adapting the parameters  $p_i$ . Consequently, the prediction model of the MPC and thus the linear-quadratic optimization problem is adapted to the estimated model (9) in each time step. The UKF, see Julier and Uhlmann (1997), is applied for estimating the parameters  $p_i$  of the model (9) online. Unlike the Extended Kalman Filter (EKF), the UKF does not approximate the nonlinear process and observation model. Assuming Gaussian distributions on the measurement and the process model a deterministic sampling approach is utilized to calculate mean and covariance terms. Chosen sample points are propagated through the nonlinear system by an unscented transformation and capture the posterior mean and covariance accurately to the third order. Parameter estimation is realized by extending the state vector  $\mathbf{x}$  with the parameter vector  $\mathbf{p}^T = [p_1 \ \cdots \ p_{2n_a n_a + n_a}]$

$$\bar{\mathbf{x}} = \begin{bmatrix} \mathbf{x} \\ \mathbf{p} \end{bmatrix} \quad (11)$$

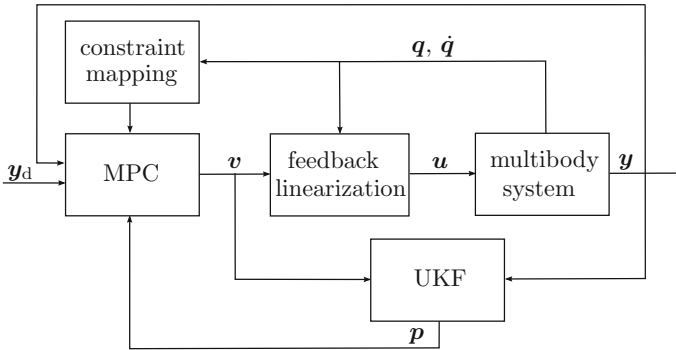


**Fig. 1** Control structure of the adaptive feedback linearization/MPC scheme estimating uncertainties by the UKF

resulting in the discrete nonlinear model

$$\bar{x}(k + 1) = f(\bar{x}(k), v(k)), \tag{12}$$

$$y(k) = [I \ 0 \ 0] \bar{x}(k). \tag{13}$$

obtained by discretizing (9) and (10). The proposed control structure including feedback linearization, MPC with constraint mapping and UKF for parameter estimation is depicted in Fig. 1.

### 3 Fuzzy Uncertainty Analysis

Uncertainties in mechanical systems often result from a lack of knowledge and an inexact parameter determination and thus are assumed as epistemic uncertainties. A suitable method of incorporating epistemic uncertainties into multibody systems is the implementation of uncertain model parameters as fuzzy numbers which are defined as convex fuzzy sets with a membership function  $\mu(x) \in [0 \ 1]$  only being equal to one for the nominal value. As the dynamics of the control structure is considerably influenced by the system parameters, dealing with fuzzy numbers requires a systematic calculation in the dynamical analysis which is known as fuzzy arithmetic. Based on the extension principle of Zadeh an efficient implementation can be realized by the transformation method, see Hanss (2002), where a fuzzy number is decomposed into several intervals. In addition, the method provides a way to quantify the effect of each fuzzy-valued parameter on the uncertainty of the system output by influence measures, see Gauger et al. (2008). Providing systematical tools to analyze the influences of parameter uncertainties, the fuzzy-arithmetical analysis allows a better understanding of the dynamical behaviour of mechanical systems, successfully applied to a flexible parallel manipulator, see Walz et al. (2015).

## 4 Application: Underactuated Manipulator with Passive Joint

The proposed adaptive nonlinear control scheme is applied to an underactuated manipulator with passive joint, depicted in Fig. 2. The manipulator consists of three rigid beams with length  $l_1 = 1$  m and  $l_{2,3} = 0.5$  m, of which the first and second beam are driven by motor torques  $T_1$  and  $T_2$ , whereas the third beam is linked to the second beam by a torsional spring-damper combination. Introducing the generalized coordinates  $\mathbf{q}^T = [\alpha \ \beta \ \gamma]$  and the input  $\mathbf{u}^T = [T_1 \ T_2]$  the equation of motion (1) can be derived. In order to investigate the impact of uncertainties on the control structure, the system parameters are described as symmetric triangular fuzzy numbers with the membership function

$$\mu(x) = \begin{cases} 1 + (x - \hat{p}_i)/(\alpha_i \hat{p}_i), & \text{for } (1 - \alpha_i)\hat{p}_i < x \leq \hat{p}_i, \\ 1 + (x - \hat{p}_i)/(\alpha_i \hat{p}_i), & \text{for } \hat{p}_i < x < (1 + \alpha_i)\hat{p}_i, \\ 0, & \text{otherwise,} \end{cases} \quad (14)$$

where  $\hat{p}_i$  denotes the nominal value of the  $i$ th parameter and  $\alpha_i$  describes its deviation and are given in Table 1. To track a desired trajectory  $\mathbf{r}_d$ , see Fig. 2, the end-effector position  $\mathbf{r}$  is approximated by the linearly combined output  $\mathbf{y}^T = [\alpha \ \beta] + [0 \ l_3/(l_2 + l_3)] \gamma$  by solving the inverse kinematics.

To demonstrate the need of an adaptive control scheme, a standard control approach consisting of feedback linearization and asymptotic tracking control

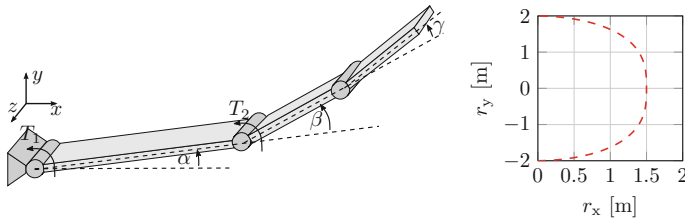


**Fig. 2** Schematic model of the underactuated manipulator with passive joint (*left*) and reference trajectory of the end-effector  $\mathbf{r}_d$  (*right*)

**Table 1** Parameter variations

Parameter $\hat{p}_i$	Nominal value $\hat{p}_i$	Deviation $\alpha_i$ (%)
Mass $m_1$	6.875 kg	$\pm 20$
Mass $m_2$	3.4375 kg	$\pm 20$
Mass $m_3$	3.4375 kg	$\pm 20$
Stiffness $c$	50 Nm/rad	$\pm 20$
Damping $d$	0.5 Nms	$\pm 20$



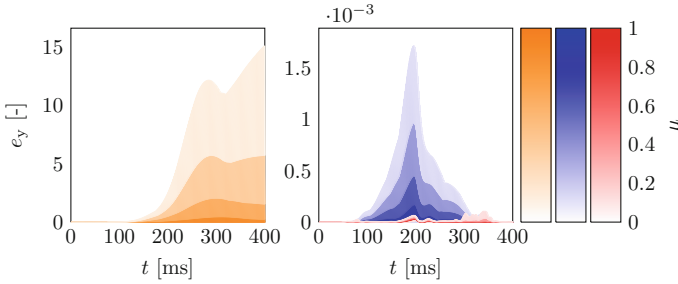


**Fig. 3** Fuzzy-valued quadratic tracking error  $e_y = \|\mathbf{y}_d - \mathbf{y}\|_2^2$  of feedback linearization combined with tracking control ■, with MPC ■ and with adaptive MPC ■

$\mathbf{v} = \ddot{\mathbf{y}}_d + \mathbf{k}_1(\dot{\mathbf{y}}_d - \dot{\mathbf{y}}) + \mathbf{k}_2(\mathbf{y}_d - \mathbf{y})$  is compared with the proposed control scheme consisting of both non-adaptive and adaptive MPC. The fuzzy-valued simulation results of the tracking errors  $e_y$ , depicted in Fig. 3, demonstrate a significant difference in the tracking behaviour between standard and adaptive control schemes in case of uncertainties. Obviously, the UKF adapts the model parameters  $\mathbf{p}$  due to the existing parametric uncertainties and consequently guarantees a better prediction of the future states leading to more suitable control actions and smaller tracking errors. For this application it can be stated that the proposed adaptive control scheme is robust against given fuzzy-valued uncertainties. Performing the simulations in MATLAB on an 8xIntel Core i7-2600CPU (3.40 GHz, 16 GB DDR3) the overall computation time for the control algorithm is 8.3 ms and lies under the sampling time of 10 ms.

## 5 Conclusion

A nonlinear control scheme consisting of a feedback linearization and an adaptive constrained MPC has been presented, which both guarantees accurate trajectory tracking and robustness against parametric uncertainties while satisfying input constraints. The application to a serial manipulator has constituted the need of adaptivity in the control design which has been realized by an UKF. Simulation results have depicted the insufficient tracking behaviour of combining feedback linearization with non-adaptive control schemes like asymptotic tracking control, whereas the proposed adaptive design has lead to small tracking errors. It has become clear that the fuzzy-arithmetical analysis is a suitable tool to quantify the effect of uncertainties on the dynamical behaviour of mechanical systems and to derive robustness assessments. Besides that, the algorithm features a potential real-time capable implementation.

## References

- De Luca, A., & Siciliano, B. (1993). Inversion-based nonlinear control of robot arms with flexible links. *Journal of Guidance, Control and Dynamics*, 16(6), 1169–1176.
- Gauger, U., Turrin, S., Hanss, M., & Gaul, L. (2008). A new uncertainty analysis for the transformation method. *Fuzzy Sets and Systems*, 1273–1291.
- Hanss, M. (2002). The transformation method for the simulation and analysis of systems with uncertain parameters. *Fuzzy Sets and Systems*, 277–289.
- Isidori, A. (1995). *Nonlinear Control Systems*. London: Springer-Verlag.
- Julier, S. & Uhlmann, J. (1997). New extension of the Kalman filter to nonlinear systems. In *AeroSense'97*, pp 182–193. International Society for Optics and Photonics.
- Kurtz, M., & Henson, M. (1997). Input-output linearizing control of constrained nonlinear processes. *Journal of Process Control*, 7, 3–17.
- Maciejowski, J. (2002). *Predictive Control with Constraints*. Upper Saddle River: Prentice Hall.
- Sastry, S. S., & Isidori, A. (1989). Adaptive control of linearizable systems. *IEEE Transactions on Automatic Control*, 34(11), 1123–1131.
- Schnelle, F. & Eberhard, P. (2015) Constraint mapping in a feedback linearization/MPC scheme for trajectory tracking of underactuated multibody systems. In *Proceedings of the 5th IFAC Conference on Nonlinear Model Predictive Control (NMPC 2015)*, Seville, Spain.
- Seifried, R., Burkhardt, M. & Held, A. (2011). Trajectory control of flexible manipulators using model inversion. In *Proceedings of the ECCOMAS Thematic Conference on Multibody Dynamics 2011*, Brussels, Belgium.
- Walz, N., Burkhardt, M., Eberhard, P., & Hanss, M. (2015). A comprehensive fuzzy uncertainty analysis of a controlled nonlinear system with unstable internal dynamics. *ASCE-ASME Journal of Risk and Uncertainty in Engineering Systems*, 1(4), 041008.

# Control and Experiments with Energy-Saving SCARA Robots

Makoto Iwamura and Werner Schiehlen

**Abstract** In this paper, we consider the design and control of an energy saving robot utilizing springs and reaction wheels. Firstly, we refer to the simultaneous optimization problem of spring parameters and trajectories with respect to the energy consumption based on optimal control theory. In particular, we report on the practical design problem to realize the proposed energy saving manipulator concept. In order to verify the proposed method, a prototype 2DOF manipulator is developed by using linear springs and reaction wheels for actuation. The experimental results show the effectiveness of the proposed energy saving manipulator concept.

## 1 Introduction

In the manufacturing industry, machines and robots controlled by actuators are used to increase productivity and achieve high quality products. However, these actuators are consuming a great amount of energy accelerating and braking continuously. Hence, saving the energy of such systems is a very important issue.

Existing methods for reducing the energy consumption of industrial robots in manufacturing systems have been recently reviewed by Paryanto et al. (2015). There are three main approaches found as follows.

- Energy-efficient motion planning
- Optimal robot operation parameters
- Scheduling robot operations

Recuperated energy saving potential and approaches in industrial robotics were considered by Meike and Ribickis (2011). These authors present experimental and

---

M. Iwamura

Department of Mechanical Engineering, Fukuoka University, Fukuoka, Japan  
e-mail: iwamura@fukuoka-u.ac.jp

W. Schiehlen (✉)

Institute of Engineering and Computational Mechanics,  
University of Stuttgart, Stuttgart, Germany  
e-mail: werner.schiehlen@itm.uni-stuttgart.de

© CISM International Centre for Mechanical Sciences 2016

V. Parenti-Castelli and W. Schiehlen (eds.), *ROMANSY 21 - Robot Design, Dynamics and Control*, CISM International Centre for Mechanical Sciences 569,  
DOI 10.1007/978-3-319-33714-2\_17

simulation results for two complementary alternatives: a capacitive energy buffer on the robot's DC-bus and a novel approach, the robot EnergyTeam. The principle of the robot EnergyTeam is a DC-bus merging among a various number of industrial robot power controllers thus enabling a controlled energy flow among the robots that decelerate and, therefore recuperate energy, and those that simultaneously require a peak power supply for the acceleration.

A path planning approach for the amplification of electrical energy exchange in multi axis robotic systems was presented by Hansen et al. (2013). The energy-based system model includes the robot dynamics, mechanical and drive losses, as well as the exchange of electrical energy. The nonlinear optimization problem is solved using global methods, considering kinematical and dynamic limitations. Simulations results are presented that prove the performance of the algorithm and demonstrate the beneficial effect of electrical energy exchange. Minimum time criteria can be retained if required and the approach is applicable to different multi axis manipulator types.

Resonant robotic systems were considered by Babitsky and Shipilov (2003). These robotic systems include spring accumulators and use control design with minimal energy consumption.

The standard task of industrial robots is a planned repetitive motion with a short cycle time. Such periodic motions result in phases of high accelerations and deceleration featuring high energy losses. Therefore, local energy storage transforming kinetic energy in reusable potential energy is attractive. Springs are reliable passive mechanical components for energy storage. Methods for reducing the consumed energy of controlled multibody systems by utilizing passive storage elements such as springs have been recently examined, see Schiehlen and Guse (2005); Schiehlen and Iwamura (2009).

A first application to robot systems was presented in Schiehlen and Iwamura (2010) where a simultaneous optimization method of spring parameters and trajectories was used. We showed the effectiveness of the proposed method by numerical simulations only.

In theory, we can achieve zero energy consumption by our method, but in practice the method can not be directly applied to a conventional manipulator since it utilizes the free frictionless vibrations of the system. In this paper we use the linear springs and controlled reaction wheels to develop a prototype 2DOF energy saving manipulator. Finally, and most important, the effectiveness of the proposed approach is verified through lab experiments.

## 2 Design and Control of Energy Saving Manipulator

The energy saving control method using springs proposed in Schiehlen and Iwamura (2010) utilizes natural modes of vibration of the system. On the other hand, existing robot manipulators have direct drive or geared motors at the joints and therefore free vibrations do not occur. Therefore, the proposed method can not be directly applied

to conventional manipulators. Hence in this chapter, we consider the practical design problem to realize the proposed energy saving manipulator concept. We develop a prototype 2DOF manipulator to validate realizability and effectiveness as shown in Iwamura et al. (2015).

### 2.1 Design of Energy Saving Manipulator

We consider a horizontal manipulator model equipped with rotational springs as shown in Fig. 1a. However, for the rotational spring it is usually difficult to adjust its stiffness and mounting position, and so we impose in our experimental setup rotational stiffness between neighboring links by using two linear springs and a special spring holder as shown in Fig. 1b. We denote by  $k_{ii}$  the linear spring stiffness,  $l_{ii}$  the distance between the joint and spring mounting point on the holder, then the applied torque  $T_i$  by springs about a joint can be approximated as

$$T_i = -2k_{ii}l_{ii}^2 \sin \theta_i \cos \theta_i \simeq -2k_{ii}l_{ii}^2 \theta_i (\equiv -k_i \theta_i). \tag{1}$$

From the above equation, it is understood that we can convert linear spring stiffness  $k_{ii}$  to corresponding rotational spring stiffness  $k_i$  by

$$k_i = 2k_{ii}l_{ii}^2. \tag{2}$$

Next, let us consider the installation position of actuators. Since the proposed method utilizes the free vibration of the system, all joints must be able to rotate freely. Therefore, we will not install motors at the joints, instead, we introduce controlled reaction wheels at an arbitrary point on the link and add driving torques from them as shown in Fig. 2.

The equations of motion of the links and the reaction wheels in Fig. 2 can be derived as follows

$$M_{\theta\theta}\ddot{\theta} + M_{\phi\theta}^T\ddot{\phi} + \mathbf{h} = -\mathbf{K}(\theta - \theta_n), \tag{3}$$

$$M_{\phi\theta}\ddot{\theta} + M_{\phi\phi}\ddot{\phi} = \boldsymbol{\tau}, \tag{4}$$

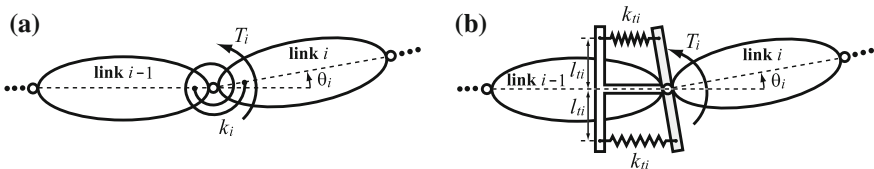


Fig. 1 Structure of proposed energy saving robot. **a** Mathematical model, **b** engineering design

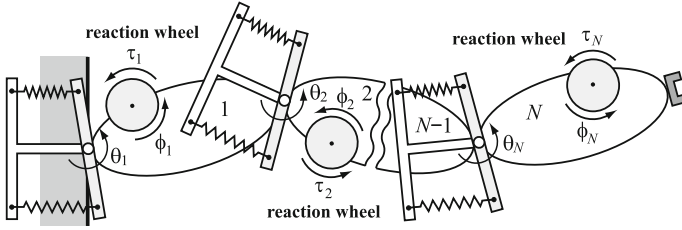


Fig. 2 Structure of proposed energy saving robot

where  $\theta = [\theta_1, \theta_2, \dots, \theta_N]^T$  is the vector of joint variables,  $\phi = [\phi_1, \phi_2, \dots, \phi_N]^T$  is the vector of rotation angles of reaction wheels,  $M_{\theta\theta}$ ,  $M_{\phi\theta}$ ,  $M_{\phi\phi}$  are the inertia matrices,  $h$  is the vector of centrifugal and Coriolis forces,  $\tau = [\tau_1, \tau_2, \dots, \tau_N]^T$  is the vector of driving torques of reaction wheels,  $K = \text{diag}[k_1, k_2, \dots, k_N]$  is the stiffness matrix,  $\theta_n$  is the vector of spring mounting positions.

By eliminating  $\phi$  from Eqs. (3) and (4), and defining  $M \equiv M_{\theta\theta} - M_{\phi\theta}^T M_{\phi\phi}^{-1} M_{\phi\theta}$ ,  $u \equiv -M_{\phi\theta}^T M_{\phi\phi}^{-1} \tau$ , then the following equations of motion are obtained

$$M\ddot{\theta} + h = -K(\theta - \theta_n) + u. \quad (5)$$

Since Eq. (5) has the same form as Eq. (3) in Schiehlen and Iwamura (2010), the energy saving control method proposed in Schiehlen and Iwamura (2010) can be directly applied to this novel energy saving manipulator systems. For more details see Iwamura et al. (2015), too.

## 2.2 Control of Energy Saving Manipulator

The minimum energy trajectory between the initial position  $\theta_0 = [\theta_{10}, \theta_{20}, \dots, \theta_{N0}]^T$  and the final position  $\theta_f = [\theta_{1f}, \theta_{2f}, \dots, \theta_{Nf}]^T$  can be expressed as

$$\theta(t) = \theta_m + \Phi q(t) (\equiv \theta_d(t)), \quad (6)$$

$$q(t) = [-q_{e1} \cos \omega_1 t, -q_{e2} \cos \omega_2 t, \dots, -q_{eN} \cos \omega_N t]^T, \quad (7)$$

where  $\omega_i$  is the  $i$ th natural frequency of the free vibrations and  $q_{ei}$  follows from the desired robot trajectory.

Theoretically, if we move the links to the position  $\theta_0$  by applying the external torques for the first time only, then repetitive movement between  $\theta_0$  and  $\theta_f$  can be achieved continuously without any additional input torque  $u$ . However, practically, due to the existence of friction and air resistance, the link motions attenuate gradually with time. Hence, let the desired trajectory  $\theta_d(t)$  be given by Eq. (6), and the following feedback controller be introduced

$$\mathbf{u} = \mathbf{M}\{\ddot{\boldsymbol{\theta}}_d - \boldsymbol{\alpha}(\dot{\boldsymbol{\theta}} - \dot{\boldsymbol{\theta}}_d) - \boldsymbol{\beta}(\boldsymbol{\theta} - \boldsymbol{\theta}_d)\} + \mathbf{h} + \mathbf{K}(\boldsymbol{\theta} - \boldsymbol{\theta}_n). \quad (8)$$

By substituting Eq. (8) into the equations of motion (5), it can be seen that the behavior of the error vector  $\mathbf{e}(t) \equiv \boldsymbol{\theta}(t) - \boldsymbol{\theta}_d(t)$  is governed by the equation

$$\ddot{\mathbf{e}}(t) + \boldsymbol{\alpha}\dot{\mathbf{e}}(t) + \boldsymbol{\beta}\mathbf{e}(t) = \mathbf{0}, \quad (9)$$

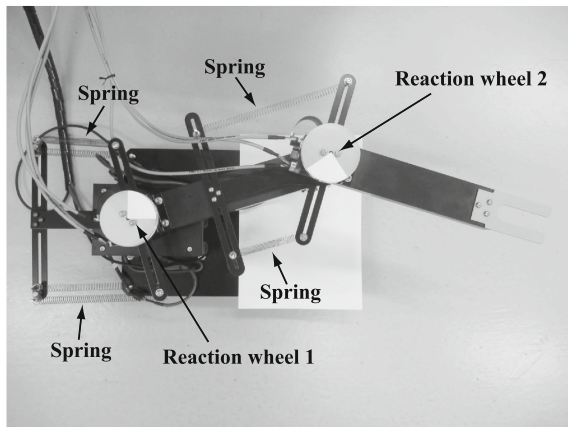
where  $\boldsymbol{\alpha}$  and  $\boldsymbol{\beta}$  are constant matrices that guarantee asymptotic stability. Equation (9) means that  $\boldsymbol{\theta}(t)$  converges to  $\boldsymbol{\theta}_d(t)$ , which means that proposed energy saving control method is realized.

### 3 A Prototype 2DOF Manipulator and Experimental Results

To validate the proposed energy saving control method, and practical design and control approach, we develop a prototype 2DOF manipulator shown in Fig. 3. In this experimental device, reaction wheels are driven by DC motors and installed such that their rotational center coincide with the joint axes. The rotary encoders are used to measure rotational angles of the links. And the electro-magnetic breaks are equipped to the joints so that we can keep holding the links at an arbitrary positions.

As an example, let us consider the repetitive movement between  $\boldsymbol{\theta}_0 = [0, 0]^T$  deg and  $\boldsymbol{\theta}_f = [60, 60]^T$  deg representing the initial and final configuration of the robot. The robot cycle time between two points are set as  $t_f^* = 2$  s. If we choose  $r_i$  as  $r_1 = 1$ ,  $r_2 = 3$ , the optimal rotational spring stiffnesses can be obtained as  $\mathbf{k} = [k_1, k_2]^T = [0.374, 0.085]^T$  Nm/rad from Iwamura et al. (2015). By using Eq. (2),  $\mathbf{k}$  is converted to the linear spring stiffnesses as  $\mathbf{k}_l = [k_{l1}, k_{l2}]^T = [18.706, 4.237]^T$  N/m. Then we

**Fig. 3** Picture of the prototype 2DOF manipulator



adjust the linear spring stiffnesses of the experimental device as close as possible to the optimal values. After that we conduct trajectory tracking control experiments by using the control law of Eq. (8). Figures 4 and 5 show the results of the trajectory tracking test for the 1st and 2nd joint angles respectively. In these figures, blue line shows the optimal (reference) trajectory calculated by Eqs. (6) and (7), and red line shows the actual trajectory measured by encoders. From these figures, it can be seen that the tracking error is fairly small and trajectory tracking is almost achieved. Figures 6 and 7 show the driving torques of 1st and 2nd actuators, respectively. In these figures, the red line shows the reaction wheel driving torque of proposed energy saving manipulator and blue line shows the joint driving torque required by the conventional manipulator to perform the same task. Let us compare the energy consumption of the proposed and the conventional manipulators by the following cost

**Fig. 4** Angle versus time (joint 1)

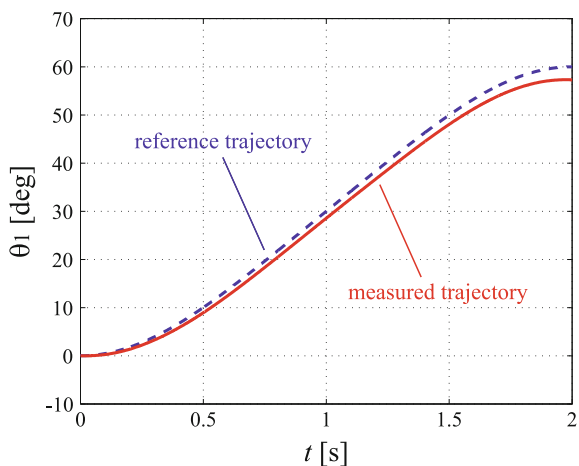


**Fig. 5** Angle versus time (joint 2)

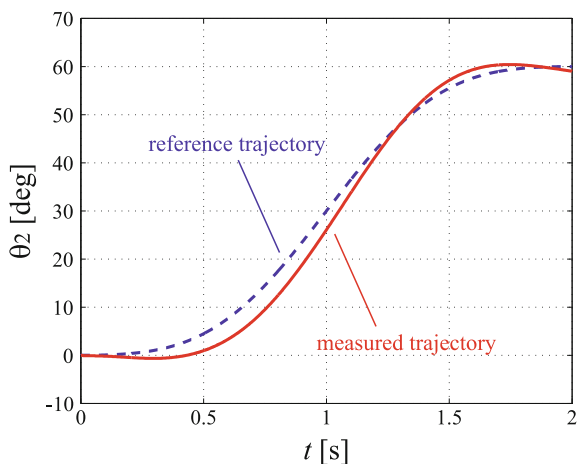




**Fig. 6** Torque versus time (actuator 1)

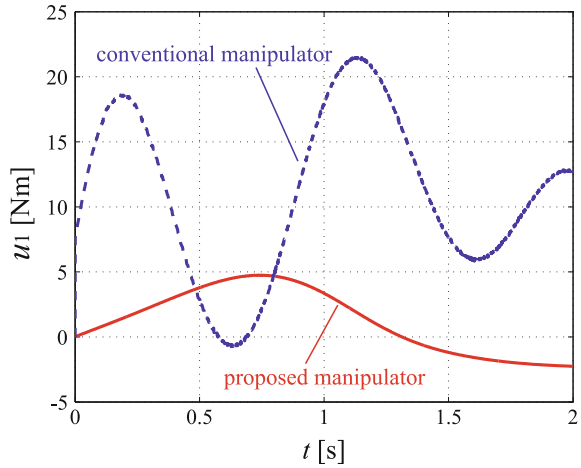
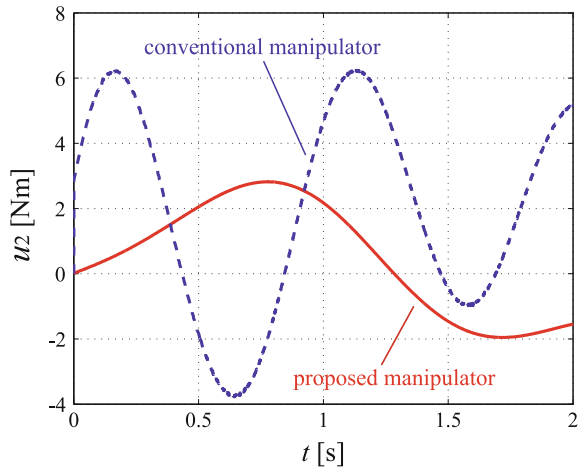


**Fig. 7** Torque versus time (actuator 2)

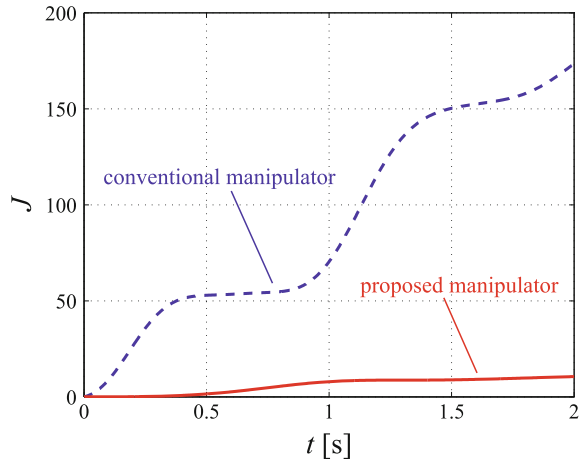


function

$$J(t) = \frac{1}{2} \sum_{i=1}^2 \int_0^t u_i^2(\bar{t}) d\bar{t}. \tag{10}$$

Figure 8 shows the result. The value of  $J(t_f)$  for the proposed manipulator was 10.57, in contrast for the conventional manipulator it was 173.5. It turns out that the energy consumption is reduced by 94%. In theory, see Schiehlen and Iwamura (2010), we could show by simulations an 100% reduction by optimization but 94% is still an excellent number. This result proves that the proposed concept is effective and it can strongly reduce the energy consumption.

**Fig. 8** Comparison of energy consumption



## 4 Conclusions

In this study, we considered a method for reducing energy consumption of SCARA robot by adding springs to the joints and utilizes the potential energy effectively. Firstly, we referred to a simultaneous optimization method for springs and trajectories based on the optimal control theory. Then, we discussed the engineering design and the control problems to be solved for the robot experiment. Finally, we developed a 2DOF energy saving manipulator prototype and validated the effectiveness of the proposed method through experiments.

## References

- Babitsky, V. I., & Shipilov, A. V. (2003). *Reasoning robotic systems*. Springer-Verlag.
- Hansen, C. Kotlarski, J. & Ortmaier, T. (2013). Path planning approach for the amplification of electrical energy exchange in multi axis robotic systems. In *2013 IEEE International Conference on Mechatronics and Automation (ICMA)*.
- Iwamura, M., Imafuku, S., Kawamoto, T., & Schiehlen, W. (2015). Development of an energy-saving manipulator using storage elements and reaction wheels. In J. M. Font-Llagunes (Ed.), *ECCOMAS Thematic Conference Multibody Dynamics 2015* (pp. 1388–1399). Barcelona: CIMNE.
- Meike, D. & Ribickis, L. (2011). Recuperated energy savings potential and approaches in industrial robotics. In *2011 IEEE Conference on Automation Science and Engineering (CASE)*, (pp. 299–303).
- Paryanto, P., Brossog, M., Bornschlegel, M., & Franke, J. (2015). Reducing the energy consumption of industrial robots in manufacturing systems. *The International Journal of Advanced Manufacturing Technology*, 78(5), 1315–1328.
- Schiehlen, W., & Guse, N. (2005). Power saving control of mechanisms. In H. Ulbrich & W. Gunthner (Eds.), *Vibration Control of Nonlinear Mechanisms and Structures* (pp. 277–286). Dordrecht: Springer.

- Schiehlen, W., & Iwamura, M. (2009). Minimum energy control of multibody systems utilizing storage elements. In *Proceedings of DETC, ASME paper DETC2009 86327*.
- Schiehlen, W., & Iwamura, M. (2010). Economical control of robot systems using potential energy. In V. Parenti-Castelli & W. Schiehlen (Eds.), *ROMANSY 18 Robot Design, Dynamics and Control* (pp. 323–330). Vienna: Springer.

# Control Design for Pneumatic Manipulation Robot

Anton Aliseychik, Viktor Glazunov, Igor Orlov, Vladimir Pavlovsky  
and Marina Shishova

**Abstract** The paper deals with a SCARA-like kinematics robot arm with pneumatic actuators. Dynamic model and control system are realized in the software package Matlab Simulink. Game Go selected as experimental task. The low-level control system is implemented on microcontroller STM32F4Discovery. Machine vision is realized on Android OS using OpenCV. Computer vision system as supporting technology will be demonstrated as important part of the presentation. It is important to note, different algorithms can be implemented as manipulator software and hardware technologies. The created robot passed experimental working off which allowed to draw conclusions about the created software and hardware effectiveness in the implementation of various manipulators control algorithms.

**Keywords** Manipulator · Control system · Matlab Simulink · Pneumatic drives · Machine vision

---

A. Aliseychik · V. Glazunov · I. Orlov (✉)  
Department of Mechanics and Control of Machines, Blagonravov Institute  
of Machines Science RAS, Moscow, Russia  
e-mail: orlovbel@gmail.com

A. Aliseychik  
e-mail: atooxa@gmail.com

V. Glazunov  
e-mail: vaglznv@mail.ru

V. Pavlovsky  
Robotics Laboratory, Keldysh Institute of Applied Mathematics RAS, Moscow, Russia  
e-mail: vlpavl@mail.ru

M. Shishova  
Research and Training Center “Intelligent Robotics”, Russian State University  
for the Humanities, Moscow, Russia  
e-mail: to-be-e-e-gin@ya.ru

**Fig. 1** ManGo robot

## 1 Manipulator ManGo

ManGo manipulator (Fig. 1) has a SCARA-like kinematic Orlov (2013), that mostly suits object manipulation tasks on a plane, including desk games. The first steps in kinematic analysis were carried out during the creation of robots design in CAD soft complex, the pneumatics of Italian company Pneumax was used as the executing drives. Optimal lengths of parts and attachment points of pneumatics were calculated to cover workspace of  $500 \times 500$  cm size, which is enough to work with almost every knowledge-based logical desk game.

## 2 Control System

Due to simple two-link kinematic scheme the solution of inverse kinematic problem for robot control is trivial. Therefore, the most reliable in this case trajectory kinematic control with position feedback. The usage of pneumatics involves both advantages (cheapness, higher speeds of motion, great efforts, etc.) and drawbacks, the main of which is the difficulty of accurate control. In order to solve this problem the valve PWM-control of the cylinders was realized. The control system of the manipulator ManGo for the “Go” game was realized on the bunch of “smartphone with Android OS—microcontroller Stm32F4”. Machine vision and decision-making system—on the smartphone, drive control system—on the controller.

## 2.1 Control Structure in Matlab

Matlab Simulink software package used to create the robot control system ManGo. Control system is divided into two components: the program decision-making and control of low-level system (firmware Stm32f4). These two components are connected by blocks of transmitting and receiving data: UART Rx and UART Tx respectively. Work firmware is built on iteration: each time a control program data arrive, the firmware performs only one operating cycle, sending the results back. Let us consider the controller firmware. At each iteration, the firmware takes three integer signal: two represent the desired coordinates of the manipulator on the playing field, and the third signal A is determined that the program would do in any given moment. A specific function is executed according to the signal value. Three types of functions exist: “go to the point”, “take the stone”, “put the stone”.

## 2.2 Machine Vision

Task of recognising Go board and stones is not new, as are most methods which were used in process of solving it. The main goal was to achieve a higher level of accuracy of recognition than of available solutions to the task, which was more or less successfully accomplished by combining known methods and binding them via a different approach.

Desk recognition on a picture can be divided into several steps:

- Picture preparation (converting into binary matrix)
- Searching for intersections and edges of the board
- Searching for neighbors and beginning of the grid building
- Completing the grid

The main steps of desk recognition algorithm on a certain example is described further.

**Pattern Recognition** Since lines on the board are thin and therefore poorly discernible (especially because of desk bent relatively to camera, natural non monotonous wood texture of the board surface and occasional glints), high quality of the picture is required. It is recommended to use camera with resolution of no less than 3 megapixels.

To get a binary picture with sharp outlines, without noise, Adaptive Threshold (Borgefors 1986; Huttenlocher and Felzenszwalb 2012; Meyer 1992; Telea 2004) is applied to the original picture (Fig. 2). Operations of dilatation and erosion follow next to smooth and clean the image.

**Searching for Line Intersections** Next step is patterns usage for desk edge search. It is important to find the bottom edge (top edge is harder to find because it's often blurred with desk surface), and at least one of the side edges, to determine the position of the desk on the picture. Patterns define how line intersections should look

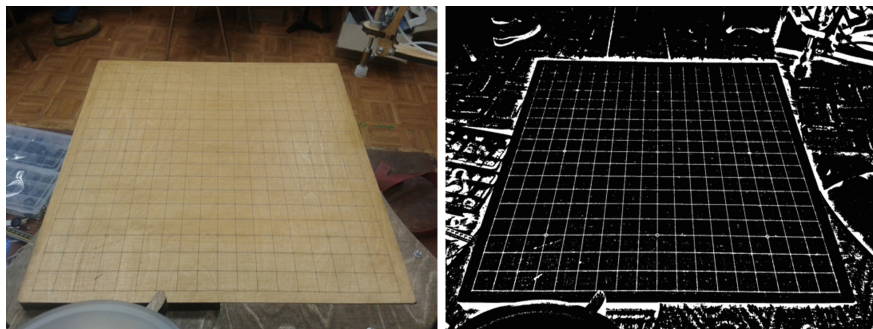


**Fig. 2** The original picture (on the *left*), picture after adaptive threshold (on the *right*)

like in binary picture. All that is needed is to apply these patterns during Hit-or-Miss transform Yu et al. (2012). However, because of image flaws, some edge points are missed and some detected points don't belong to the edge. OpenCV offers several methods of fitting line in array of points, but because of extra points these methods are not sufficient. The only option (though not very fast) is to run through pairs of points nearest to each other, choose those with more probable angle (since angle range is known for each edge). Line associated with pair of points is added to vector with one "vote" or, if a line with similar parameters has already been added, count of votes of latter increments. Line with biggest count is the one. Intersections inside the grid are found in the same way, through patterns.

**Grid Building** FLANN Lowe and Muja (2009) is a library, that implement nearest neighbor search method (interface for the library is contained in OpenCV). It uses point array in matrix form as input, and the result is k-dimensional tree, where k is a number of dimensions. In this case, the space is obviously two-dimensional. Each point of the desk has no more than four direct neighbors. In process of searching for four nearest for each point, restrictions are placed according to situation:

- Little distance between points, the distances between the point and each one of the neighbors shouldn't differ too much from each other;
- Right and left neighbors must lie on the same horizontal line;
- Top and bottom neighbors must lie on the same line, which is bent from the main vertical to no more than  $30^\circ$ .

Point becomes a part of the grid if it has no less than two neighbors.

During this part of the algorithm, vector of 6-slot arrays is created, each array associated with the single point. The first four slots contain neighbor indexes (or  $-1$ , if there is no neighbor in a certain direction), and the other two contain horizontal and vertical line numbers, to which the point belongs. Figure 3 shows how the points and their relations were found. The points on the top weren't found either because the distances between them were too small or detected points in the area were too scarce to find any relations. Next picture shows the found lines.

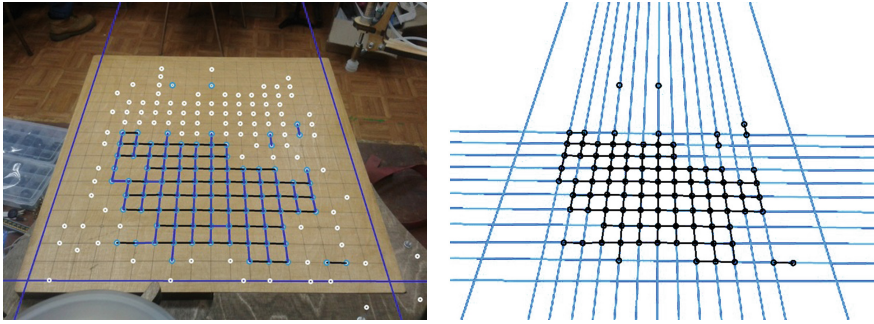


Fig. 3 Lines and relations found

Next step is completing the grid to a bounding rectangle. It can be done by calculating intersections of found lines, if there is any. That's why further actions take place:

1. If the point doesn't have one neighbor, it is calculated due to the coordinates of the point and the opposite neighbor. Afterwards, the new point is added to a vector of new possible points, and the counter of current is assigned 1.
2. Before adding the coordinate to the vector, it's important to check if there is a point with close coordinates. If so, the counter increments, and the coordinates are changed to the average between the old and the new one, if not, a new point is added.
3. In the end, the point is added to the grid, if the counter value is at least two.

The process continues until there is no more points to add. As a result is supposed to be a matrix  $N$  (width)  $\times$   $M$  (height) size.

**Finishing the Grid** As can be seen on Fig. 4, points lie on intersections of found lines and edges.

Number of missing points between the edges and rectangle can be calculated due to the grid that makes it possible to find average distance between points on each horizontal line. This way grid is expanded to zones L, R and B (Fig. 4, left).

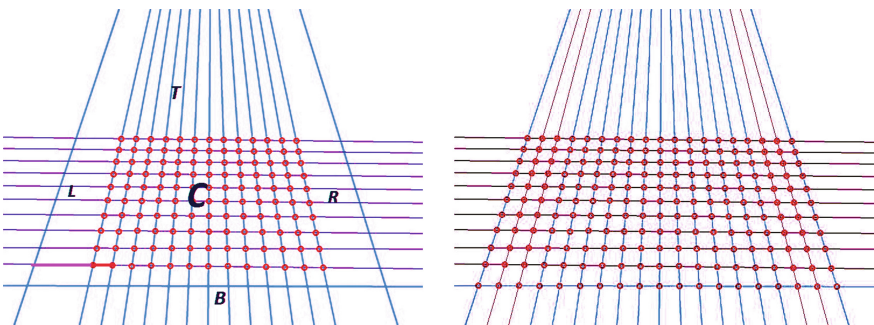
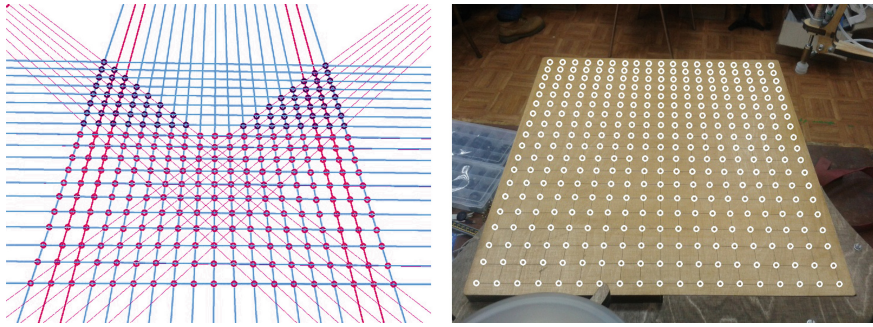


Fig. 4 Intersection points are found





**Fig. 5** Looking for diagonals, *horizontal lines*, intersections of diagonals and *horizontal lines*, *points* found on the desk (respectively)

To find the rest of the points the following actions are performed: 1. Diagonals, and their intersections with vertical lines are found, as shown on Fig. 5, left. 2. Now we can find the rest of horizontal lines. 3. Find the rest of the points as intersections of vertical and horizontal lines. Point search completed (Fig. 5, right).

**Black and White Stones Recognition** The idea of the algorithm is based upon the fact that illumination doesn't change during the game. The initial picture of empty desk is saved. The new picture (with stones on the desk) and the old one (without) are converted to HSV (Hue, Saturation, Value) format. Once the matrix of desk points on the picture is already found, the average value of brightness (Value), and intensity (Saturation) in the point surroundings are compared between two images. White stones will have the higher Value, black stones will have lower Value, while both will have the lowest Saturation. To remove the flecks off the stones, the picture is corrected by Gaussian blur.

### 3 Experiments

For acceptable control system maximum time to reach the 1 mm neighborhood of a chosen operating point should be 1–2s.

Experiments on real prototype (Figs. 6 and 7) demonstrated, that for dynamically tuned relay control small but imminent environmental and settings changes like temperature, working time and throttling coefficient can cause unacceptable increase of orientation time in some areas of desk. Quantitative characteristics of the throttling coefficients show difficult because the flow regulator with manual adjustment used. Figure 6 shows that location of such areas may vary with variation of settings.

And essential control system for well-working robot should resist small environmental changes. Unfortunately, proportional position and PI-control do not significantly improve robust of control. Thus today we are working on neural network approach.

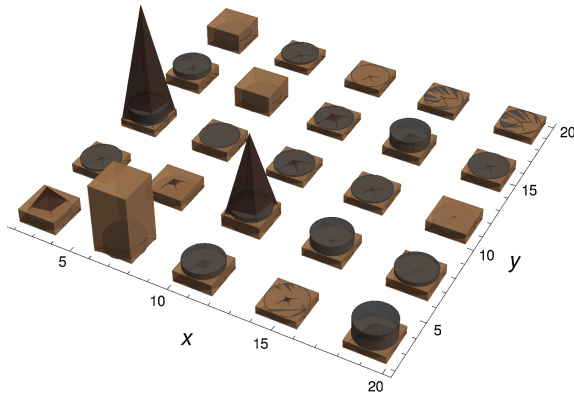


Fig. 6 Time to reach the point with different robot settings

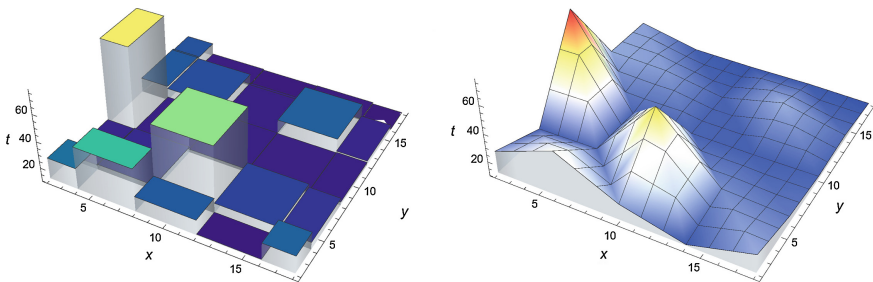


Fig. 7 Estimated time to achieve the position (on the left), Average time to reach the point with relay control (on the right)

## 4 Conclusion

The performed experiments have proven the effectiveness of software and hardware tools of intelligent robotics and their correspondence to the tasks. Detailed development of these instruments will provide shorter (faster) worktime of the robots, and improved logical features of the robots. Future plans are developing fully “assembled” intelligent robot-manipulator with planning and playing games abilities based on visual system and neural “nervous” system. The computer technologies that have been developed will be the universal tools for this activity.

The reported study was funded by RFBR, according to the research projects No. 15-08-08769 a, No. 16-38-60201 mol\_a\_dk and No. 16-31-00491 mol\_a.

## References

- Borgefors, G. (1986). Distance transformations in digital images. *Computer Vision, Graphics, and Image Processing*, 34(3), 344–371.
- Huttenlocher, D. P., & Felzenszwalb, P. F. (2012). Distance transforms of sampled functions. *Theory of Computing*, 8(1), 415–428.
- Lowe, D. G., & Muja, M. (2009). Fast approximate nearest neighbors with automatic algorithm configuration. *VISAPP*, 1, 331–340.
- Meyer, F. (1992). Color image segmentation. In *Proceedings of the International Conference on Image Processing and its Applications*, (pp. 303–306).
- Orlov, I. A. (2013). *Synthesis of Motions for Manipulation Systems for Spaces With Complex Relationships and Constraints*. Keldysh Institute of Applied Mathematics, Ph.D dissertation, [In Russian].
- Telea, A. (2004). An image inpainting technique based on the fast marching method. *Journal of Graphics*, 9(1), 23–34.
- Yu, D., Dahl, G., Mohamed, A., Jaitly, N., Senior, A., Vanhoucke, V., et al. (2012). Deep neural networks for acoustic modeling in speech recognition—the shared views of four research groups. *IEEE Signal Processing Magazine*, 29(6), 82–97.

# Adaptive Edge Features Estimation for Humanoid Robot Visual Perception

Tianwei Zhang and Yoshihiko Nakamura

**Abstract** Lidar scanner is a kind of sensor widely used in robotics visual perception, which provides accurate range data. Scan line grouping is an extremely fast plane segmentation and edge estimation method tailored for 2D Lidar scanners, which obtain 3D environment models by assembling 2D scan lines. In this paper, we propose an adaptive scan line split algorithm to overcome density shift problem of large scale scenes so that the scan line grouping method output more accurate plane segments and edges. The simulated experimental results indicate the proposed method is robust and promising in humanoid robotics applications.

## 1 Instruction

3D visual perception is an important technology for a number of applications related to robotic perception, wild environment mapping, automatic driving, cultural heritage modelling and architecture. In robotics, it is important for robots to be able to autonomously navigate and localize itself in both known or unknown environments. To fulfil navigation, localization, environment mapping and path planning tasks, various algorithms for different sensors are well studied in recent years (Nguyen et al. 2007).

Compared to other kinds of sensors, Laser scanner has many advantages, such as long range, more accurate range measurement, less noise, high angle resolution and high sampling frequency. However, the time cost of forming 3D point clouds constrains the application of 2D laser scanner in robotics. To obtain 3D space models, 2D laser scan lines need to be assembled due to their rolling angles, this phase may spend several seconds. Therefore, (Jiang and Bunke 1994) and (Gutmann et al. 2008) applied Ramer-Douglas-Peucker algorithm (RDP) (Douglas and Peucker

---

T. Zhang (✉) · Y. Nakamura  
Department of Mechano and Informatics, The University of Tokyo, Tokyo, Japan  
e-mail: zhang@ynl.t.u-tokyo.ac.jp

Y. Nakamura  
e-mail: nakamura@ynl.t.u-tokyo.ac.jp

1973) before scan line grouping phase. That is a way to save whole processing time by partly moving point clouds processing to pre-processing.

Different from wheel robot, a humanoid robot can step on or over obstacles, but fall down easily with bad contact conditions. So that the shape and texture of ground and obstacles' surfaces is the main task for visual perception. Many works have been done in plane segments estimation (Okada et al. 2001), surface normals estimation (Holzer et al. 2012; Bormann et al. 2015) and edge estimation (Asatani et al. 2011). Aiming at real-time humanoid robot continuous locomotion, we apply a modified RDP method before organising point clouds data (PCD) from 2D scan lines, adaptively extract edge point from scan lines and the sensed data is saved as straight line segments and endpoints. After assembling 3D PCD, a region growing method is employed to estimate plane segments by using the straight line segments. The contribution of this paper is that we propose an adaptive RDP method to split polyline segments which improved the accuracy of edge point estimation in both close and far areas.

The rest of the paper is organised as follows. Section 2 introduces related work in visual perception. PCD acquiring and edge point estimation are described in Sect. 3, experimental results are talked in Sect. 3 and this paper is concluded in Sect. 5.

## 2 Related Works

Platform estimation and surface reconstruction with depth sensors (Marton et al. 2009; Steinbrucker et al. 2013) are most widely studied families of methods for unknown environment perception. Point normal is one of the essential features of 3D point clouds. Rusu et al. introduced a normal estimation framework in (Rusu 2010), in which point normal is computed by analysing the eigenvectors and eigenvalues of a covariance matrix created by its  $k$ -nearest neighbours. Point clouds are captured from a single viewpoint, the orientation of normals are flipped toward viewpoint at the end. This framework has the limitation that the edge and corner points' normals lose their sharp features. Moreover, in (Ioannou et al. 2012), these boundary regions are estimated basing on the difference of estimated normals with different neighbour sizes. Recently, another normal estimation method designed for organized PCD, which supposed the structure of PCD data is fully known, in (Holzer et al. 2012) achieved real-time performance by building integral images of input PCD.

In (Okada et al. 2001), Okada et al. used a randomized 3D Hough transform to estimate platforms for stair climbing. Another work of Rusu (Bogdan Rusu et al. 2009) used Random sample consensus (RANSAC) to generate polygons upon point clouds which are represented by small volumes, called cells or voxels. RANSAC is fast but tends to combine small local platforms into big slopes, especially in large clutter scenes. In recent works, (Papon et al. 2013) extends an over-segmentation approach to real-time stereo data processing, it cluster voxels with same features, such as voxels' position, colour and normal features, to "supervoxels". Supervoxels

decrease PCD size complexity, real-time plane segmentation is achieved in (Papon et al. 2013) by using supervoxels as input. However, this method is designed for dense stereo data. In large scale scenes, the algorithm suffers from slow space dividing.

Jiang and Bunke proposed a plane segment estimation method in (Jiang and Bunke 1994), which grows platforms from straight line segments. These straight line segments are extracted as soon as the scan lines are acquired with original RDP algorithm. This plane estimation method is extremely fast since most input points are processed only in line segmentation phase. The sensed data is stored as straight line segments rather than single sampling points. (Gutmann et al. 2008) developed the former scan line grouping method by adding a polyline splitting strategy, which is comparing point numbers rather than compute the distance of all the point set. They also build a height map for humanoid robot walking planning basing on this planar segmentation method. However, the RDP polyline splitting method may result in wrong splitting as the distance grows further. In this paper, we proposed an adaptive threshold setting strategy to deal with the wrong polyline splitting when the sensing distance ranges.

### 3 Adaptive Straight Line Split

In this paper, the environment information is obtained from a Hokuyo UTM-30LX-EW 2D laser scanner. Comparing to high-frequency RGB-D stereo sensors, Microsoft Kinect, laser scanner has the superiorities of a larger field of view, further detectable range and suitability to bad lighting conditions. The chosen Hokuyo Lidar has  $270^\circ$  field of view, comparing with  $57.8^\circ$  of Kinect. Therefore, the robot can see more features without turning the neck, which is important for real-time mapping and perception. Moreover, depth cameras suffer from their baseline problem. Kinect works from about 0.6 to 4 m, while, Hokuyo UTM30 works in 0.1 to 60 m with  $\pm 1\%$  error. The baseline limitation makes a big problem for the humanoid robot. If the robot cannot see the staircase or obstacles in front of its foot, the stepping has to be finished without visual guidance. In our case, Hokuyo scanner can help the robot see the stair close to its standing feet accurately.

Hokuyo UTM-30LX-EW returns 1081 points each scan ( $0.25^\circ$  resolution) every 25 ms, to achieve dense 3D point clouds, the row data need are assembled according to the tilting angle of the scanner. This assembling processing limits the frame frequency. In (Osswald et al. 2011), the assembled 3D PCD is noisy with an error up to 5 cm, and the author points out that the error mainly comes from the estimation of the scanner's pose from the joint angle when robot tilts its head. To overcome this problem, our scanner is actuated by dynamixel MX-64 servo actuator which is fixed on the robot neck's joint. As shown in Fig. 1, the robot body keeps static when the scanner is tilting, and the tilting angle with respect to actuator's turning axis is recorded accurately by dynamixel MX-64. Accurate 3D scan can be achieved by assembling scan lines with their turning angle.

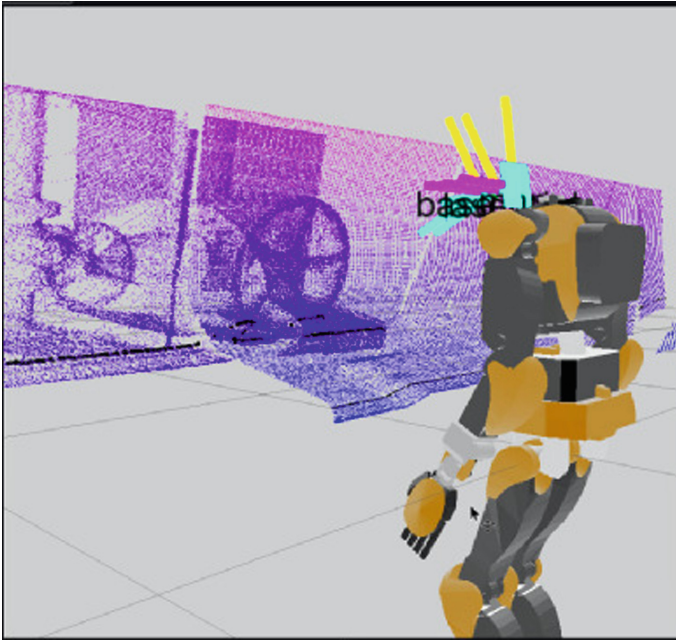


**Fig. 1** A Hokuyo scanner actuated by a dynamixel MX-64 servo mounted on HRP4’s neck. The 3D purple PCD is assembled from 2D scan lines (one shown in *black color*) according to its pitching angle accurately recorded by the actuator (shown as *blue square*)

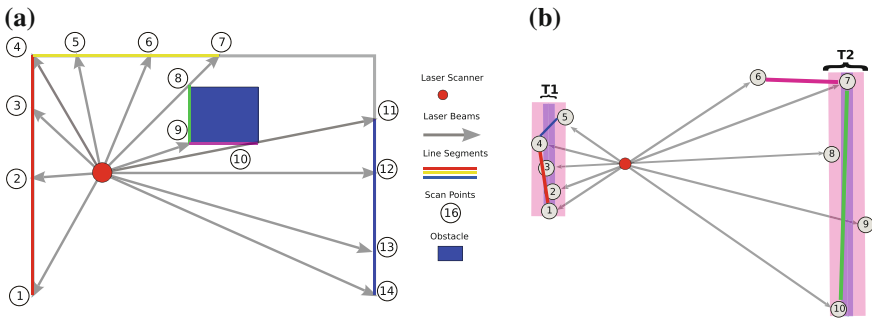


**Fig. 2** Hokuyo Lidar scanner 2D scan line **a**, Output of DP split, the 14 scan points are segmented to 5 line segments shown in different colors: ①④, ④⑦, ⑧⑨, ⑨⑩, ⑪⑭. In **b**,  $T_1$  is the split method threshold on the area close to sensor, while  $T_2$  is the threshold on the area far from sensor. ⑧ and ⑨ will be split if we use same threshold

One example of the 2D scan output is shown in Fig. 2. The RDP method is applied to split the polyline to straight line segments. The split method is shown in Algorithm 1, which processes the scan points in a recursive way: the distance from the query point to the line segment vector (between the start and end points) are

computed and compared with a threshold  $d_T$ , if it is bigger than the threshold, this line segment will be split on this query point, and the resulted two line segments will be added to the input of RDP.

The problem of the RDP is the setting of the threshold value. In the case of short range stereo vision, this threshold can be set to a fixed value according to the sensor's noise situation. However, in the case of Lidar scanner, the depth data ranges from 0.1 to 30 m, a fix parameter setting may lead to wrong split and wrong segmentation.

To deal with the large range difference of Lidar scanner raw data, an adaptive threshold set as:

$$d_T = \zeta * R \quad (1)$$

in which,  $R$  is the depth data set of the query point,  $\zeta$  is a value according to the sensor property.

---

### Algorithm 1 RDP split

---

**Input:** point cloud data set  $L : (L_1, L_2, \dots, L_n)$ , split distance threshold  $d_T$ , distance function  $D_n$ , gravity vector  $\vec{g}$

**Output:** edge points  $P$

```

1: for each  $L_i \in L$  do
2:   for each point  $p_i \in L_i$  do
3:      $p_s \leftarrow$  FIRST POINT OF  $L_i$ 
4:      $p_e \leftarrow$  END POINT OF  $L_i$ 
5:      $d_i \leftarrow$  COMPUTE_DISTANCE( $p_i$  to  $(p_s, \vec{p}_e)$ )
6:     if  $d_i > d_T$  then
7:        $\mathbb{P} \leftarrow p_i$ 
8:        $L \leftarrow$  push back( $p_s, \vec{p}_i$ ) and ( $p_i, \vec{p}_e$ )
9:     end if
10:   end for
11: end for
12: return  $P$ 

```

---

## 4 Experimental Results

In the experiments, see Fig. 3. a white rectangle board is put in front of the scanner, 1 m, 2 m respectively. and (c) and (f) are the wall located around 10 m away. In the upper scenes, the threshold  $d_T$  is fixed to 0.03 m, in the lower scenes,  $d_T$  is adaptive set as Eq. 1, and  $\zeta$  is set to 0.01. The results show that in short distance scenes split results are similar, however, when the scan distance ascends to 10 m, adaptive threshold result in much fewer edge points on the flat wall surface, therefore, adaptive threshold setting make RDP method robust to distance changing.



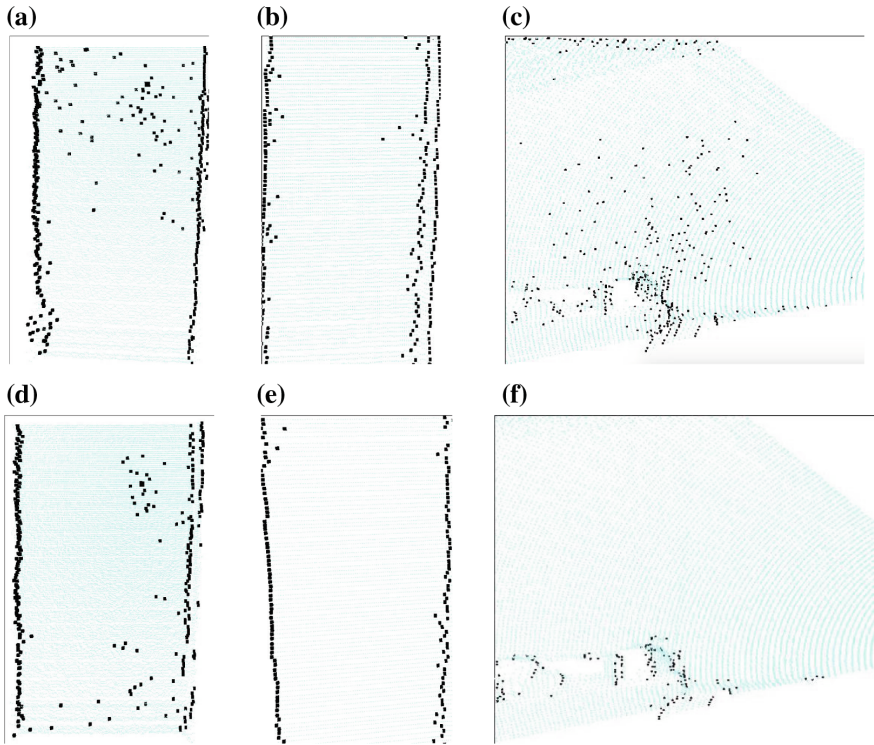


**Fig. 3** Extracted edge points **a** 1 m distance,  $d_T = 0.03$  m **b** 2 m distance,  $d_T = 0.03$  m **c** 10 m distance,  $d_T = 0.03$  m **d** 1 m distance, adaptive  $d_T$  **e** 2 m distance, adaptive  $d_T$  **f** 10 m distance, adaptive  $d_T$

## 5 Conclusion and Future Works

In this paper we propose an adaptive threshold setting strategy for scan line grouping plane finding method, and achieved better edge feature estimation performance even when the scan distance range from 0.1 to 30 m. These experiences suggest that the accurate edge point and straight line segments can be used for efficient plane segmentation and further humanoid applications, like footstep planning and state estimation. In future work, we will develop the method for point clouds registration and robot state estimation applications using straight line vector feature.

## References

- Asatani, M. Sugimoto, S. & Okutomi, M. (2011) Real-time step edge estimation using stereo images for biped robot. In *2011 IEEE/RSJ International Conference on Intelligent Robots and Systems (IROS)* (pp. 4463–4468). IEEE.
- Bormann, R., Hampp, J., Hagele, M., & Vincze, M. (2015). Fast and accurate normal estimation by efficient 3d edge detection. In *2015 IEEE/RSJ International Conference on Intelligent Robots and Systems (IROS)* (pp. 3930–3937). IEEE.
- Douglas, D. H., & Peucker, T. K. (1973) Algorithms for the reduction of the number of points required to represent a digitized line or its caricature. *Cartographica: The International Journal for Geographic Information and Geovisualization*, 10(2), 112–122.
- Gutmann, J.-S., Fukuchi, M., & Fujita, M. (2008). 3d perception and environment map generation for humanoid robot navigation. *The International Journal of Robotics Research*, 27(10), 1117–1134.
- Holzer, S., Rusu, R. B., Dixon, M., Gedikli, S., & Navab, N. (2012) Adaptive neighborhood selection for real-time surface normal estimation from organized point cloud data using integral images. In *2012 IEEE/RSJ International Conference on Intelligent Robots and Systems, IROS 2012, Vilamoura, Algarve, Portugal, October 7-12, 2012* (pp. 2684–2689). IEEE.
- Ioannou, Y., Taati, B., Harrap, R., & Greenspan, M. (2012). Difference of normals as a multi-scale operator in unorganized point clouds. In *2012 Second International Conference on 3D Imaging, Modeling, Processing, Visualization and Transmission (3DIMPVT)* (pp. 501–508). IEEE.
- Jiang, X., & Bunke, H. (1994). Fast segmentation of range images into planar regions by scan line grouping. *Machine Vision and Applications*, 7(2), 115–122.
- Marton, Z. C., Rusu, R. B., Beetz, M. (2009) On fast surface reconstruction methods for large and noisy point clouds. In *IEEE International Conference on Robotics and Automation, 2009. ICRA'09* (pp. 3218–3223). IEEE.
- Nguyen, V., Gächter, S., Martinelli, A., Tomatis, N., & Siegwart, R. (2007). A comparison of line extraction algorithms using 2d range data for indoor mobile robotics. *Autonomous Robots*, 23(2), 97–111.
- Okada, K., Kagami, S., Inaba, M., & Inoue, H. (2001) Plane segment finder: algorithm, implementation and applications. In *Robotics and Automation, 2001. Proceedings IEEE International Conference on 2001 ICRA* (vol. 2, pp. 2120–2125). IEEE.
- Osswald, S., Gutmann, J.-S., Hornung, A., & Bennewitz, M. (2011). From 3d point clouds to climbing stairs: A comparison of plane segmentation approaches for humanoids. In *2011 11th IEEE-RAS International Conference on Humanoid Robots (Humanoids)* (pp. 93–98). IEEE.
- Papon, J., Abramov, A., Schoeler, M., & Worgotter, F. (2013). Voxel cloud connectivity segmentation-supervoxels for point clouds. In *2013 IEEE Conference on Computer Vision and Pattern Recognition (CVPR)* (pp. 2027–2034). IEEE.
- Rusu, R. B., Sundaesan, A., Morisset, B., Hauser, K., Agrawal, M., Latombe, J.-C., et al. (2009). Leaving flatland: Efficient real-time three-dimensional perception and motion planning. *Journal of Field Robotics*, 26(10), 841–862.
- Rusu, R. B. (2010). Semantic 3d object maps for everyday manipulation in human living environments. *KI-Künstliche Intelligenz*, 24(4), 345–348.
- Steinbrucker, F., Kerl, C., Cremers, D. (2013). Large-scale multi-resolution surface reconstruction from rgb-d sequences. In *2013 IEEE International Conference on Computer Vision (ICCV)* (pp. 3264–3271). IEEE.

# Disturbance Rejection Controller for Biped Walking Using Real-Time ZMP Regulation

Zhangguo Yu, Maoxing Zheng, Qinqin Zhou, Xuechao Chen, Libo Meng, Weimin Zhang, Aiguo Ming and Qiang Huang

**Abstract** This paper proposes a disturbance rejection controller using real-time ZMP (Zero Moment Point) regulation which could maintain the stable walk of a humanoid robot when the robot is subjected to external disturbances. The controller detects the disturbance by an accelerometer, and computes the ZMP increment to overcome disturbance to ensure stability, and then calculate the increment of trajectory of center of mass according to ZMP increment using preview control. The

---

Z. Yu (✉) · M. Zheng · Q. Zhou · X. Chen · L. Meng · W. Zhang · A. Ming · Q. Huang  
Intelligent Robotics Institute, Beijing Institute of Technology, Beijing, China  
e-mail: yuzg@bit.edu.cn

M. Zheng  
e-mail: zhengmaoxing12@163.com

Q. Zhou  
e-mail: 1120120401@bit.edu.cn

X. Chen  
e-mail: chenxuechao@bit.edu.cn

L. Meng  
e-mail: menglibo@bit.edu.cn

W. Zhang  
e-mail: zhwm@bit.edu.cn

A. Ming  
e-mail: ming@mce.uec.ac.jp

Q. Huang  
e-mail: qhuang@bit.edu.cn

Z. Yu · X. Chen · W. Zhang · Q. Huang  
Key Laboratory of Biomimetic Robots and Systems (BIT), MOE, Beijing, China

A. Ming · Q. Huang  
Beijing Advanced Innovation Center for Intelligent Robots and System, Beijing, China

Q. Huang  
International Joint Research Laboratory of Biomimetic Robots and Systems,  
MOE, Beijing, China

effectiveness of our proposed method was confirmed by simulation in ADAMS and walking experiment on an actual humanoid robot, BHR-5.

## 1 Introduction

A humanoid robot is usually subjected to external disturbances during walking. It is very important for a humanoid robot to overcome disturbances during walking. Several methods were proposed to ensure humanoid robot to walk stably after being disturbed based on ZMP (Zero Moment Point) concept. A terrain adaptive control was discussed to reduce landing impact forces by setting the landing foot speed to zero (Hashimoto et al. 2009). Kamogawa et al. (2013) proposed a stability control method using ZMP compensation control and inverted pendulum control. A ZMP compensation method was proposed to improve the stability of locomotion while a robot suffered from disturbance (Prahlad et al. 2008). A walk control using feedback sensory reflex was proposed for quickly dealing with unexpected sudden events (Huang and Nakamura 2005). These methods gained the desired ZMP by estimate computation rather than acceleration measurement. This may lead to appreciable ZMP error to depress the stability of the robot.

In recent years, in order to maintain stable walking of the humanoid robot from large disturbances, foot placements control was proposed. Pratt et al. (2012) and Fu (2014) adjusted the step location using the capture region. Urata et al. (2011) adopted an online decision method of foot placement by using singular LQ preview regulation of an inverted pendulum model. These algorithm needed large amount of calculation.

In this paper we introduce a simple but fast disturbance rejection controller. The remainder of the paper is organized as follows. In Sect. 2, we give an overview of the anti-disturbance controller and the ZMP modification method using body acceleration when large disturbance effects on humanoid robot. The modification of trajectory of center of mass for disturbance rejection is provide in Sect. 3. In Sect. 4, simulation and experiment were conducted, and the results are provided.

## 2 ZMP Regulation

Figure 1 shows the overview of the proposed controller. The controller comprises three components. The disturbance detector detects whether the disturbance occurs based on the sensor that measures the acceleration of the center of mass (CoM) while the humanoid robot is walking. If humanoid robot suffers from a large external disturbance during walking, the controller will calculate the ZMP increment. Then the CoM trajectory modifier will output a new trajectory online. Humanoid robot is an incomplete constraint system and its support polygon is limited by the sole area.

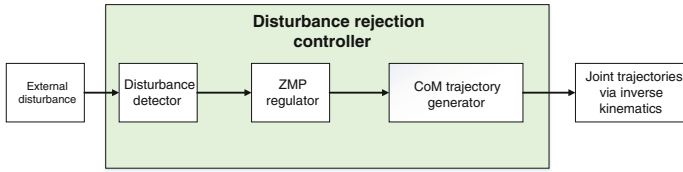


**Fig. 1** Overview of the disturbance rejection controller

When it suffers large external disturbances during walking, it is vital to modify the ZMP trajectory to maintain its balance.

### 2.1 ZMP Modification

We adopt the flywheel inverted pendulum model (Li et al. 2015) (Fig. 2) to simplify humanoid robot. We take Cartesian coordinates as shown in Fig. 3 and specify the x-axis as the ordinal walking direction. In the two-dimensional plane xoz (see Fig. 4), the dynamics analysis of the CoM is given by:

**Fig. 2** The flywheel inverted pendulum model

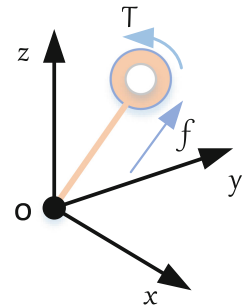


**Fig. 3** Dynamics model considering disturbance along x-direction

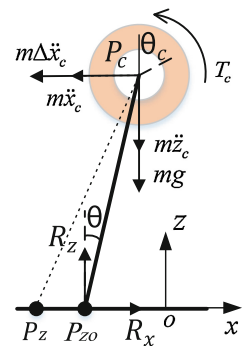


**Fig. 4** Forces and torques exerted on the CoM

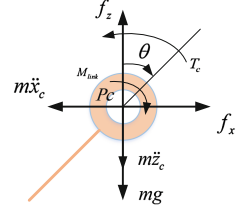
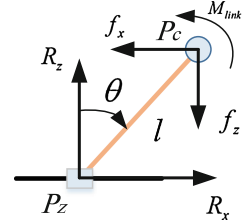


**Fig. 5** Forces and torques exerted at ZMP



$$\begin{aligned}
 m\ddot{x}_c &= f_x \\
 m\ddot{z}_c &= f_z - mg \\
 M_{link} &= T_c \\
 T_c &= J\ddot{\theta}
 \end{aligned} \tag{1}$$

where  $m$  is the mass of the humanoid robot,  $f_x$  and  $f_z$  are the components of ground reaction force on  $x$ -axis and  $z$ -axis respectively,  $M_{link}$  and  $T_c$  are the torques around  $y$ -axis and  $J$  is the rotational inertia of the upper body of the humanoid robot (Fig. 5).

The geometric relationships are shown as:

$$\begin{aligned}
 l^2 &= (x_c - x_{zmp})^2 + (z_c - z_z)^2 \\
 \tan \theta &= \frac{x_c - x_{zmp}}{z_c - z_z}
 \end{aligned} \tag{2}$$

Where  $x_c$  and  $z_c$  are the coordinate of the CoM,  $x_{zmp}$  and  $z_z$  are the coordinate of ZMP,  $l$  is the length of the flywheel inverted pendulum and  $\theta$  is the angle between the flywheel inverted pendulum and  $z$ -axis.

We also obtain the dynamics analysis of the point of ZMP  $P_z(x_{zmp}, z_{zmp})$  (see Fig. 3) as:

$$\begin{aligned}
 R_x &= f_x \\
 R_z &= f_z \\
 M_{link} + f_x \cdot l \cdot \cos \theta &= f_z \cdot l \cdot \sin \theta
 \end{aligned} \tag{3}$$

By substituting Eqs. (1) and (2) to Eq. (3) we obtain:

$$J\ddot{\theta} + m\ddot{x}_c z_c = (mg + m\ddot{z}_c)(x_c - x_{zmp}) \tag{4}$$

We suppose that humanoid robot is disturbed by external force in the x-direction and define the new acceleration as  $\ddot{x}_c + \Delta\ddot{x}_c$ . The external force we assume during walking is large enough that the original ZMP can not maintain the humanoid robot walking stably. Then we define the increment between the new ZMP and the original ZMP as  $\Delta P_z(\Delta x_{zmp}, \Delta z_{zmp})$  as shown in Fig. 3. According to Eq. (4), we derive the equation of the ZMP increment and the acceleration of the CoM in x-direction as:

$$J\ddot{\theta} + m(\ddot{x}_c + \Delta\ddot{x}_c)z_c = (mg + m(\ddot{z}_c + \Delta\ddot{z}_c))(x_c - x_{zmp} - \Delta x_{zmp}) \quad (5)$$

We can also suppose that humanoid robot is disturbed by external force in y-direction and the dynamics analysis is similar to the x-direction. We directly give the equation which shows the relationship between the ZMP increment and the acceleration of the CoM in y-direction as:

$$J\ddot{\theta} + m(\ddot{y}_c + \Delta\ddot{y}_c)z_c = (mg + m(\ddot{z}_c + \Delta\ddot{z}_c))(y_c - y_{zmp} - \Delta y_{zmp}) \quad (6)$$

To obtain the ZMP increment in x-direction and y-direction, it should be the input of the trajectory modifier. Therefore we rewrite Eqs. (5) and (6) to have the ZMP increment:

$$\begin{aligned} \Delta x_{zmp} &= \frac{(mg + m(\ddot{z}_c + \Delta\ddot{z}_c))(x_c - x_{zmp}) - m(\ddot{x}_c + \Delta\ddot{x}_c)z_c - J\ddot{\theta}}{mg + m(\ddot{z}_c + \Delta\ddot{z}_c)} \\ \Delta y_{zmp} &= \frac{(mg + m(\ddot{z}_c + \Delta\ddot{z}_c))(y_c - y_{zmp}) - m(\ddot{y}_c + \Delta\ddot{y}_c)z_c - J\ddot{\theta}}{mg + m(\ddot{z}_c + \Delta\ddot{z}_c)} \end{aligned} \quad (7)$$

## 2.2 Foot Placement with ZMP Increment

When the humanoid robot is disturbed by a large external disturbance during walking, the new planning ZMP is outside of the sole area. The controller modified the foot placement to ensure walking stability. The ZMP point of humanoid robot is mapped to the foot placement. The new foot placement is specified as:

$$\begin{aligned} x_f &= x_{fo} + \Delta x_{zmp} \\ y_f &= y_{fo} + \Delta y_{zmp} \end{aligned} \quad (8)$$

Where  $x_{fo}$ ,  $y_{fo}$  and  $x_f$ ,  $y_f$  are the original, and the new foot placement in x-direction and y-direction respectively.

### 3 Modification of CoM Trajectory

When the humanoid robot is disturbed by a large external disturbance during walking, the original planned ZMP might be out of the support polygon. So we should re-generate the ZMP trajectory for stable walking. We obtain the ZMP increment as Eq. (7) to maintain walking stably in Sect. 2. Thus the new ZMP is shown as follows:

$$\begin{aligned}x_z &= x_{zo} + \Delta x_{zmp} \\y_z &= y_{zo} + \Delta y_{zmp}\end{aligned}\tag{9}$$

Where  $x_{zo}$ ,  $y_{zo}$  and  $x_z$ ,  $y_z$  are the original and the new ZMP in x-direction and y-direction respectively.

After the ZMP trajectory is obtained, the trajectory of CoM of the humanoid robot in this paper can be gained by preview control theory Kajita et al. (2003). Thus, The increment of the CoM is also calculated from the ZMP increment by preview control theory.

## 4 Simulations and Experiments

To evaluate the performance of the proposed anti-disturbance controller, we conducted simulations and experiments on a biped robot BHR-5.

Some hypotheses are assumed for disturbance during walking as follows:

- (1) The disturbance is modeled as an instantaneous pushing force.
- (2) The disturbance is applied to the waist (approximately at the CoM).
- (3) The disturbance may occur on arbitrary walk step sequence of humanoid robot.

### 4.1 Simulations

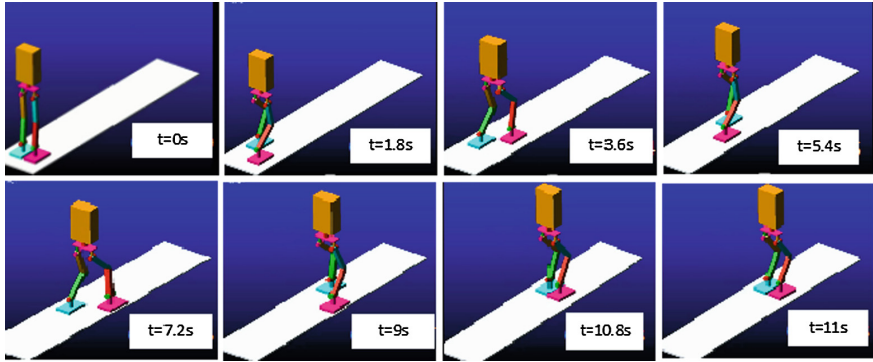
We used the physical parameters of BHR-5 prototype as shown in Table 1 to conduct the simulation in ADMS.

The disturbance modeled as an instantaneous pushing force exerted on the robot (along X direction, magnitude 100 N and duration 0.1 s) when the humanoid robot was about to take the fourth step. The new ZMP trajectory and new foot placement trajectory is calculated by Eqs. (8) and (9). As shown in the snapshots in Fig. 6, the robot could maintain stable walking successfully after a large external disturbance exerted on it. Figures 7 and 8 show the generated trajectory by the proposed controller.



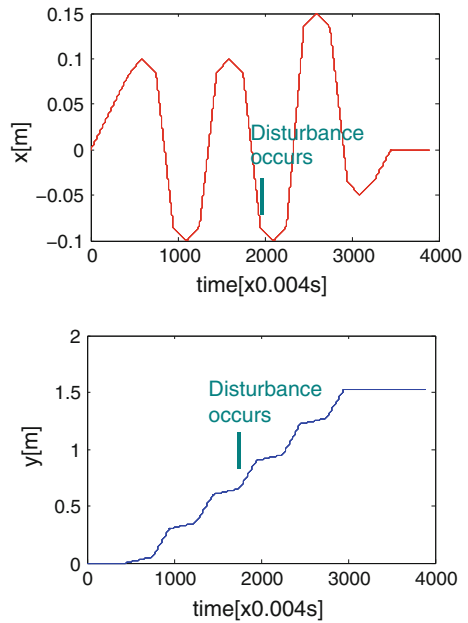
**Table 1** Parameters of the BHR-5 simulation model

Items	Value
Degrees of freedom	$2 \times 6$ (hip:3, knee:1, ankle:2)
weight	58.6 kg
Thigh length	0.312 m
Shank length	0.312 m
Distance between hips	0.17 m
Foot size	length: 0.28 m, width: 0.17 m



**Fig. 6** Snapshots of stable walking with disturbance exerted at 5.4 s (Disturbance is along x-direction, magnitude: 100 N and duration: 0.1 s)

**Fig. 7** ZMP trajectory generated by controller



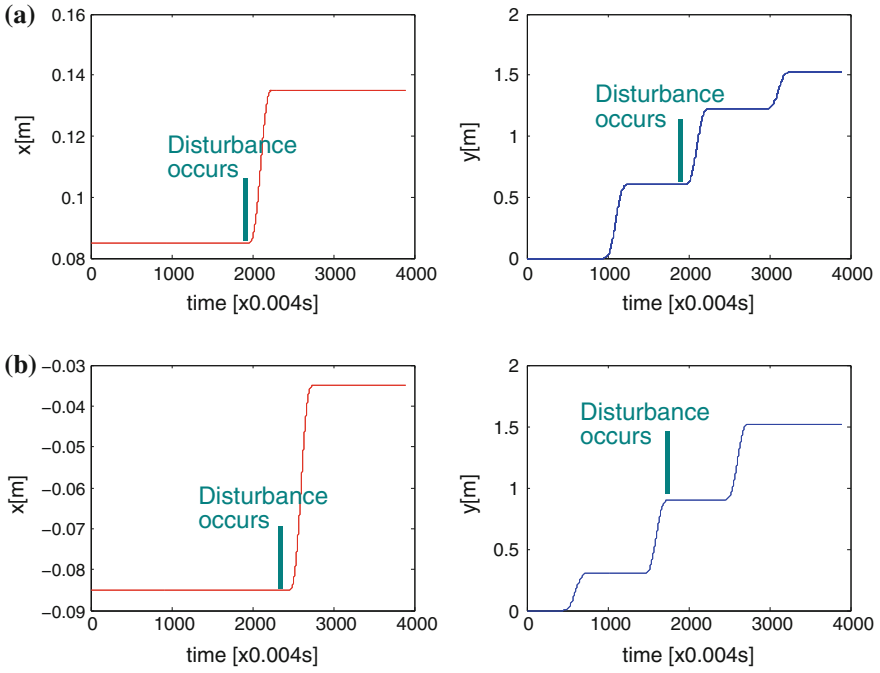


Fig. 8 Ankle trajectory generated by controller. **a** Right ankle trajectory. **b** Left ankle trajectory

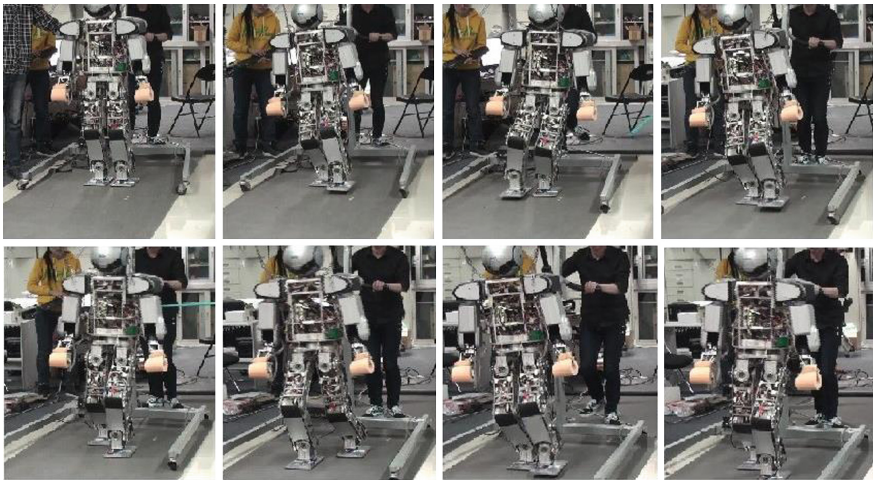


Fig. 9 Snapshots of stable walking with disturbance at approximately 5.4 s. Disturbance is along x-direction, magnitude 100 N and duration 0.1 s

## 4.2 Experiments

We used BHR-5 humanoid robot to conduct experiments to evaluate the effectiveness of the proposed anti-disturbance controller.

The disturbance detector shown in Fig. 1 is implemented by a six-axis acceleration-gyroscope sensor which is installed on the waist of the BHR-5 during walking.

Figure 9 shows the snapshots of this experiment. The disturbance occurred as shown in the fifth snapshot. Then the proposed controller worked to make the foot placement changed as shown in the sixth snapshot. It is shown that the disturbance rejection controller can maintain walking stably when the humanoid robot suffered a large external disturbance.

## 5 Conclusion

In this paper, we propose a disturbance rejection controller for biped walking using real-time ZMP regulation which achieves a stable walking after being subjected to external disturbance. The controller detects the disturbance with accelerometer, and computes the ZMP increment to overcome disturbance, and then calculate the increment of CoM trajectory. Simulation in ADAMS and experiment on a real robot validated the effectiveness of the proposed method.

**Acknowledgments** This work was supported in part by the NSFC under Grant 61320106012, 61375103, 61533004, 61273348, and 61321002, by the 863 Program under Grant 2014AA041602, 2015AA042305, and 2015AA043202, by the Key Technologies Research and Development Program under Grant 2015BAF13B01 and 2015BAK35B01, by the Beijing Natural Science Foundation under Grant 4154084, by the 111 Project under Grant B08043, and the Beijing Municipal Sci. and Tech. Project under Grant D161100003016002.

## References

- Fu, C. (2014). Perturbation recovery of biped walking by updating the footstep. In *2014 IEEE/RSJ International Conference on Intelligent Robots and Systems* (pp. 2509–2514).
- Hashimoto, K., & Hayashi, A., et al. (2009). Terrain-adaptive control to reduce landing impact force for human-carrying biped robot. In *AIM 2009. IEEE/ASME International Conference on Advanced Intelligent Mechatronics* (pp. 174–179).
- Huang, Q., & Nakamura, Y. (2005). Sensory reflex control for humanoid walking. *IEEE Transactions on Robotics*, 21, 977–984.
- Kajita, S., & Kanehiro, F., et al. (2003). Biped walking pattern generation by using preview control of zero-moment point. In *2003. Proceedings. ICRA'03. IEEE International Conference on Robotics and Automation* (pp. 1620–1626).
- Kamogawa, Y., & Yamada, K., et al. (2013). Stability control and pattern generation for biped humanoid robot. In *2013 13th International Conference on Control, Automation and Systems* (pp. 910–915).

- Li, J., Huang, Q., Yu, Z., et al. (2015). Integral acceleration generation for slip avoidance in a planar humanoid robot. *IEEE/ASME Transactions on Mechatronics*, 20, 2924–2934.
- Prahlad, V., Dip, G., & Meng-Hwee, C. (2008). Disturbance rejection by online zmp compensation. *Robotica*, 26, 9–17.
- Pratt, J., Koolen, T., De Boer, T., & Rebula, J. (2012). Capturability-based analysis and control of legged locomotion, part 2: Application to m2v2, a lower body humanoid. *The International Journal of Robotics Research*, 4, 1117–1133.
- Urata, J., & Nshiwaki, K., et al. (2011) Online decision of foot placement using singular lq preview regulation. In *2011 11th IEEE-RAS International Conference on Humanoid Robots* (pp. 13–18).

**Part V**  
**Novel Robot Design**

# Human-Powered Robotics—Concept and One-DOF Prototype

Yusuke Sugahara

**Abstract** This study proposes a concept for “human-powered robotics,” a design methodology for a robotic system which is controlled by directly using human motion as the power source. This paper describes the experimental fabrication and basic performance results of the 1-DOF prototype using powder clutches.

**Keywords** Human-powered robotics · Passive robotics · Human-robot cooperation

## 1 Introduction

### 1.1 Background and Research Purpose

In today’s modern world, there is an increasing need for robots to be able to perform their tasks within the human living environment, and thus, studies on the safety of service robotics are important.

On this issue, Goswami and Peshkin et al. proposed the concept of “Passive Robotics” (Goswami et al. 1990; Peshkin et al. 2001) to realize intelligent motion without driving power—the robot is driven by the force applied by a human, and its motion is controlled by controlling the braking force. The concept is advantageous for realizing intrinsic safety since the system in principle does not operate unless a human applies force. Robotic systems based on this concept have also been proposed by Hirata and Kosuge (Hirata et al. 2007, 2009; Suzuki et al. 2011), and the intelligent control of a walker, such as collision avoidance and fall prevention, as well as the application of a wearable walking helper and cooperative control of multiple robots, have been realized. While “Cobot” proposed by Peshkin et al. is controlled by controlling only the steering angle of its wheels through servo motors, all of the control methods proposed by Hirata et al. control the system’s moving direction, force

---

Y. Sugahara (✉)

Department of Mechanical Engineering, Tokyo Institute of Technology,  
Tokyo, Japan  
e-mail: sugahara@mech.titech.ac.jp

© CISM International Centre for Mechanical Sciences 2016  
V. Parenti-Castelli and W. Schiehlen (eds.), *ROMANSY 21 - Robot Design, Dynamics and Control*, CISM International Centre for Mechanical Sciences 569,  
DOI 10.1007/978-3-319-33714-2\_21

and velocity by controlling the torque of the powder brakes. Another technology that shares the concept of passive robotics is the EXPERT (Goto et al. 2013) intelligent surgical armrest proposed by Hongo et al., in which the arm is driven by the force applied by a human and through control of the braking torque, which has come onto the market as “iArmS” (DENSO 2015).

The above studies on passive robotics have one point in common: the motion of the end-effector is generated by the resultant force of the force applied by a human operator and the braking force generated by the robot, and in response the operator directly applies force to the end-effector. Therefore, this concept cannot be used for structures in which the operator contacts the external environment through the robot, or in which the force applied by the operator is output to the external environment through the robot. Moreover, it is impossible in principle to move the end-effector in the opposite direction of the applied force.

On the other hand, as exemplified by bicycles and wheelchairs, there are many types of machines that use the operator motion as the power source. When it becomes possible to control the output motion for these human-powered machines, it may also be possible to realize intelligent motion for active safety, such as path following, collision avoidance, and fall or slip prevention, by applying robotics technology, where the power is supplied by human motion. However in these human-powered machines, research findings in passive robotics cannot be applied immediately, because the operator’s force is output to the external environment through the system.

Therefore, author aimed to propose a concept for “human-powered robotics,” a core technology for the intelligent control of human-powered machines. This is the design methodology for the mechanism and controller for the servo control of motion by directly using human motion as the power source by controlling the transmitted torque.

The first stage in this study was to develop and evaluate a one-degree-of-freedom joint mechanism for a system using powder clutches and a torque sensor. The main goal was to achieve bidirectional servo control of the joint angle using the human motion of turning the handle as the power source.

## ***1.2 Relevant Studies***

Several studies have been conducted on the structure of a mechanical system to realize servo control of the joint by simultaneously using a power source and some devices that can control the transmitted torque. To enable direct joint torque control of the manipulator, Takase and Inoue (Takase and Inoue 1973) proposed the “clutch servo,” which is a joint mechanism driven by DC servo motors via powder clutches and wires. Inagaki et al. (Nishizawa et al. 1999; Takahama and Inagaki 1997) developed a legged robot whose joints are driven by the mechanically distributed output power of a gasoline engine. This system has two powder clutches, and the output of the engine is input to one clutch directly, and to the other clutch after the direction is inverted using spur gears. By controlling the transmitted torque of these

clutches, bidirectional servo control of the joint angle has been realized. Murakami (Murakami 2000) experimentally developed a joint mechanism that has the same structure by using a magnetic fluid clutch.

Although the purpose of these studies is different from this study because the power source is an electric motor or gasoline engine, the joint drive mechanism in this study was developed by referring to the mechanisms proposed in the relevant studies, as described below.

## 2 Design and Principle of Operation

The structure of KMR72 (Kokushikan Man-powered Robot—No. 72), the human-powered joint drive mechanism prototype developed in this study is shown in Fig. 1.

This mechanism, which was designed by referring to the system by Inagaki et al. (Nishizawa et al. 1999; Takahama and Inagaki 1997), can output bidirectional rotation and control output torque by using two powder clutches and controlling their transmitted torque.

The rotating motion applied by a human through the input handle is input to Clutch A directly and to Clutch B after its direction is inverted by the spur gears, shown by the arrows. The output shafts of the two clutches are mutually connected via a timing belt and they rotate in the same direction. Here, when Clutch A is excited and Clutch B is not excited, the power is transmitted to the output shaft only through Clutch A, and the output shaft rotates in the direction shown by the dotted arrow. On the contrary, when Clutch A is not excited and Clutch B is excited, the shaft rotates in the direction shown by the solid arrow. In this way, by manipulating the

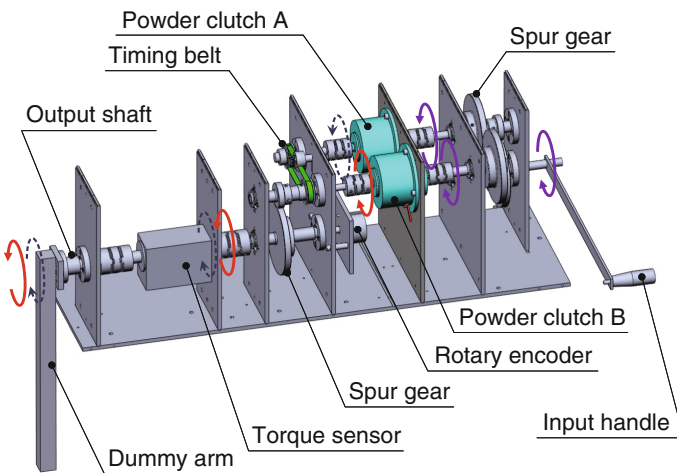


Fig. 1 Structure of the human-powered joint drive mechanism KMR72



transmitted torque of the two clutches, bidirectional rotation can be performed even though the rotation of the input handle is unidirectional. Here, a transmitted torque of the powder clutch can be controlled by its excitation current, because the torque is approximately proportional to the current.

In addition, the rotating speed of the input motion is increased three-fold before being input to the clutches and is reduced to one-third by the spur gears after the clutches. This makes the allowable torque of the whole mechanism three times the allowable torque of one clutch. Since the reduction ratio from input handle to output shaft is 1:1, this mechanism can output the same torque as the input torque applied by a human if the torque is within the allowable torque of the whole mechanism.

To detect the joint angle and torque, the output shaft is equipped with a torque sensor and a rotary encoder. There is also a dummy arm to which a weight can be attached for experimental purposes.

### 3 Controller

The computed torque method (Paul 1972) was used for position control of the joint angle.

The 1-DOF arm in this study can be modeled as shown in Fig. 2, and the equation of motion of this model can be written as follows:

$$\tau = J\ddot{\theta} + D\dot{\theta} + mgl \sin \theta \quad (1)$$

where  $\tau$  is the torque of the actuator,  $\theta$  is the angle of the actuator,  $J$  is the moment of inertia of the rotating system,  $D$  is the viscosity coefficient,  $m$  is the mass of the dummy arm,  $g$  is the gravitational acceleration and  $l$  is the distance between the center of mass of the arm and the rotation axis.

The computed torque method is a control method in which the actuator torque is computed through the dynamics of an arm and is used in a feed-forward manner,

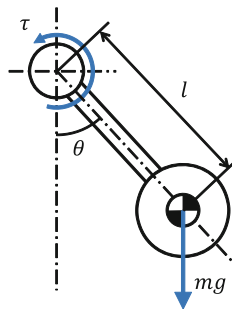


Fig. 2 Dynamic model of 1 DOF arm

and the actuator command torque for the 1-DOF arm is computed by the following equation:

$$\tau_d = J \left\{ \ddot{\theta}_d + K_v (\dot{\theta}_d - \dot{\theta}) + K_p (\theta_d - \theta) \right\} + D\dot{\theta} + mgl \sin \theta \tag{2}$$

where  $\ddot{\theta}_d$  is the desired angular acceleration,  $\dot{\theta}_d$  is the desired angular velocity,  $\theta_d$  is the desired angle,  $K_v$  and  $K_p$  are the velocity and proportional gains.

The command voltages for the powder clutch amps are computed from  $\tau_d$  in consideration of the proportionality of the exciting current and the transmitted torque. The command voltage is input to Clutch A if it is a negative value, and to Clutch B in the reverse case.

In addition,  $J$  and  $D$  were obtained through the parameter identification experiment by free vibration of the arm.

### 4 Experimental Results

Using the developed mechanism and control system, the position control experiments were conducted.

The experiment was conducted to position the dummy arm at the right under the output shaft, where  $\theta = 0$  deg, then move to 180 deg in 3 s, and move back to 0 deg in 3 s. The desired trajectory  $\theta_d(t)$  was generated by quintic interpolation. The transition of the joint angle and sequential images of this experiment are shown in Figs. 3 and 4. Even though there is a small vibration, the angle transition followed the desired angle in a satisfactory manner.

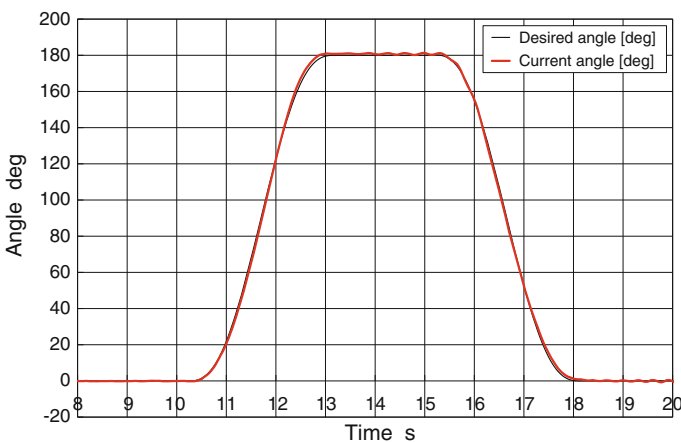


Fig. 3 Joint angle transition of the position control experiment

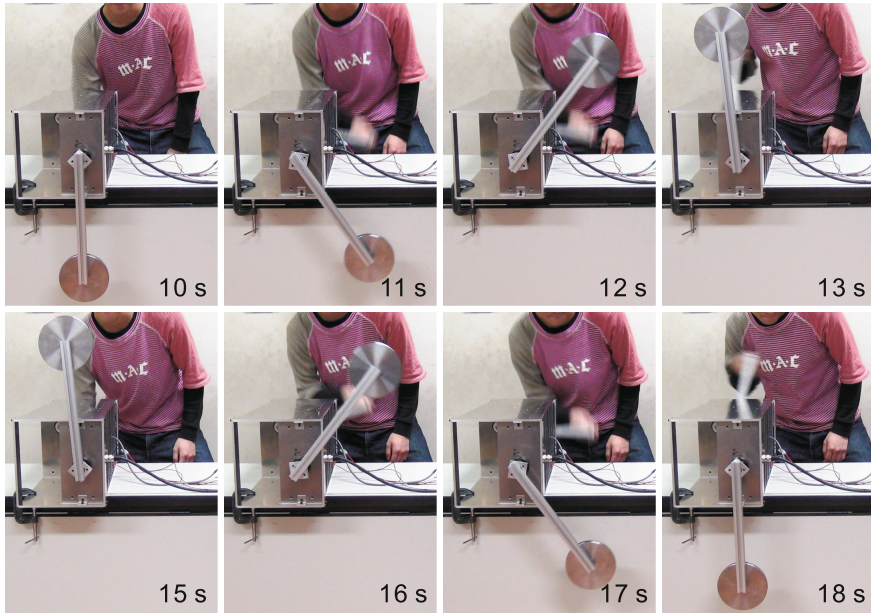


Fig. 4 Sequential photograph of the position control experiment

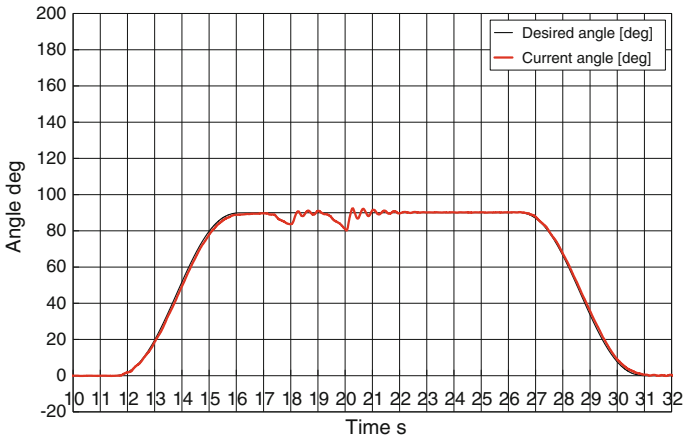


Fig. 5 Joint angle transition of the experiment with small disturbance

The second experiment was conducted to produce a disturbance by hand when the arm is at  $\theta = 90$ . The gains were the same as in the previous experiment. The joint angle transition is shown in Fig. 5. A large error in the current angle was observed at the time of the disturbance, but it quickly converged to the desired value.

As the experimental results show, even though the control performance is not sufficient for certain applications, and there is room for improvement in the mechanism and control system, it is confirmed that the mechanism and control system proposed in this study realize servo control of the joint angle by directly using human motion as its power source.

## 5 Conclusions and Future Work

A concept for “human-powered robotics” is presented. In the first stage of this study, a 1-DOF joint mechanism that can perform bidirectional servo control of the joint angle by using the human motion of turning the handle as its power source in a system using powder clutches is fabricated. The system’s basic performance is also evaluated. As can be seen in the experimental results, even though there is room for improvement of control performance, it is confirmed that the proposed system realizes servo control of the joint angle driven by the power of human motion.

As future work, author hopes to continue the redesign and evaluation of the mechanism and control system to improve the control performance. Author also intends to investigate the effective application fields of human-powered robotics, experimental fabrication and evaluation of the prototypes for those applications. In particular, application to life-support robots that have intrinsic safety, and personal mobility devices that bring convenience, high active safety and health enhancement functions, are also challenging.

**Acknowledgments** This work was partially supported by JKA and its promotional funds from the KEIRIN RACE, and by JSPS KAKENHI Grant Number 26420814.

## References

- DENSO. (2015). Supporting doctors to save lives. <http://www.globaldenso.com/en/innovation/story/iarms/>.
- Goswami, A., Peshkin, M. A., & Colgate, J. E. (1990). Passive Robotics: An Exploration of Mechanical Computation. In *Proceedings of the IEEE International Conference on Robotics and Automation* (pp. 279–284).
- Goto, T., Hongo, K., Yako, T., Hara, Y., Okamoto, J., Toyoda, K., et al. (2013). The concept and feasibility of Expert: Intelligent armrest using robotics technology. *Neurosurgery*, 72(S1), A39–A42.
- Hirata, Y., Hara, A., & Kosuge, K. (2007). Motion control of passive intelligent walker using servo brakes. *IEEE Transactions on Robotics*, 23(5), 981–990.
- Hirata, Y., Wang, Z., Fukaya, K., & Kosuge, K. (2009). Transporting an object by a passive mobile robot with servo brakes in cooperation with a human. *Advanced Robotics*, 23(4), 387–404.
- Murakami, I. (2000). Development of servomechanism with magnetic fluid clutch system. In *Proceedings of the Conference of the JSME Kanto Branch* (pp. 49–50). (in Japanese).

- Nishizawa, H., Kawasumi, S., & Inagaki, K. (1999). A leg mechanism driven by engine to improve cruising range. In *Proceedings of the Conference of the Robotics Society of Japan* (pp. 137–138). (in Japanese).
- Paul, R. P. (1972). *Modeling. Trajectory Calculation and Servoing of a Computer Controlled Arm*: Stanford University.
- Peshkin, M. A., Colgate, J. E., Wannasuphprasit, W., Moore, C. A., Gillespie, R. B., & Akella, P. (2001). Cobot architecture. *IEEE Transactions on Robotics and Automation*, 17(4), 377–390.
- Suzuki, S., Hirata, Y., Kosuge, K., & Onodera, H. (2011). Walking support based on cooperation between wearable-type and cane-type walking support systems. In *2011 IEEE/ASME International Conference on Advanced Intelligent Mechatronics (AIM)* (pp. 122–127).
- Takahama, T., & Inagaki, K. (1997). A design method for practically used walking machine. In *Proceedings of the IEEE/RSJ International Conference on Intelligent Robots and Systems* (pp. 414–419).
- Takase, K., & Inoue, H. (1973). *Robot arm using clutch servo*. *Biomechanism*, 2, 144–153. (in Japanese).

# Gripping Tests on an Underactuated Self-adapting Hand Prototype

Cesare Rossi and Sergio Savino

**Abstract** Tests on a prototype of an underactuated hand prosthesis, based on differential mechanisms, are described. The main aim was to examine the possibility of achieving a hand prosthesis economic, kinematically simple and easy to control; moreover inelastic tendon are used that allow the adjustment of the gripping force of an object just acting on the pulling force by the only actuator. In the paper the design of the prototype is briefly described and some results of experiments to test the hand suitability and capabilities, are shown

**Keywords** Underactuated mechanism · Mechanical hand prosthesis · Prototyping

## 1 Introduction

From a general point of view, designing a mechanical hand, the main problem consists in obtaining an articulated movement of the finger phalanxes that is able to adapt the fingers to the generic form of the object; this although it is not possible to have a high number of actuators able to govern the various degrees of freedom. The solution commonly adopted consists in using underactuated mechanisms having a lower number of actuators than the number of degrees of freedom.

Bicchi (2000) made an attempt at summarizing the evolution and the state of the art in the field of robot hands. This survey is focused mainly on three types of functional requirements that can be assigned to a mechanical hand in an artificial system, namely, manipulative dexterity, grasp robustness, and human operability.

---

C. Rossi (✉) · S. Savino (✉)

Department of Industrial Engineering, University of Naples “Federico II”, Naples, Italy  
e-mail: rossi\_cesare@fastwebnet.it

S. Savino  
e-mail: sergio.savino@fastwebnet.it

The experimental prosthetic hand by Dechev et al. (2001) is able to perform adaptive grab passive, i.e. the ability of the fingers to conform to the shape of a held object inside of the hand.

Most of the mechanical hand prostheses adopt or a rather small number of actuators (typically 4–5, see e.g. Grioli et al. 2012; Roccella et al. 2004; Roccella et al. 2007; Roccella et al. 2008; Cipriani et al. 2011) or a single actuator with elastic extendable tendons (see e.g. Gosselin et al. 2008; Baril et al. 2013; Brown and Asada 2007; Catalano et al. 2012; Bicchi 2000; Lotti and Vasura 2002).

Gosselin et al. presented the design and experimental validation of a robotic hand anthropomorphic underactuated with 15 degrees of freedom and a single actuator (Gosselin et al. 2008; Baril et al. 2013).

Brown and Asada (2007) lists a series of human hand postures and used the principal component analysis to calculate the synergies between the fingers, called “eigenpostures” these postures hand. They presented a new mechanism design to combine eigenpostures and drive a robot hand 17 degrees of freedom 5 fingers using only 2 DC motors.

In this paper we describe and test a prototype of an underactuated hand prosthesis based on a differential mechanisms. This prosthetic hand obtained the Italian patent N° 0001415546. By means of mobile pulleys in cascade both the adductor and the extensor tendons are actuated. The rotation and the sliding of the pulleys permitted to obtain a self-adapting device and the use of inelastic tendons.

Several investigations we carried on recently, consisting in examining the possibility of realizing a hand prosthesis economic, with a kinematic operating very simple, not bulky and lightweight; moreover the optimizing of several parameters was studied in order to obtain correctly working devices (Rossi and Savino 2014; Rossi et al. 2014; Penta et al. 2014; Penta et al. 2015; Niola et al. 2015; Carbone et al. 2015; Niola et al. 2015). This permitted to design and build a number of prototypes.

If compared to other mechanical hands, this device shows some advantages that can be summarized as follows:

1. Since only one actuator is necessary, thanks to the adaptive mechanism, it is particularly simple to control the device.
2. The grasping force can be controlled by just controlling the force exerted by the only actuator.
3. The inextensible tendons allows each finger to grab the object with a force that does not depend on the configuration of the finger or on the configuration of the other fingers. This does not happen in all the devices using extensible elastic tendons; using the latter, in fact, the fingers which phalanges have higher relative rotations will exert a grasping force that is lower than the one exerted by fingers which phalanxes have lower relative rotations.

## 2 The Design of the Hand

The five fingers can assume different configurations with a single motor by means of a pulley system in cascade, dimensioned to convey movement to the phalanges. Each finger consists of three elements, representing respectively the distal, medial and proximal phalanges, joined by hinges, and operated by a single inelastic tendon. The grasping of an object of any shape is obtained by operating the main inelastic tendon, which, through the system of pulleys, distributes the traction force between the various fingers, and closes each finger according to the resistance offered by the object to be grasped in the contact points. In this way, all the rotations of all the phalanxes will adapt to the object external surface or shape.

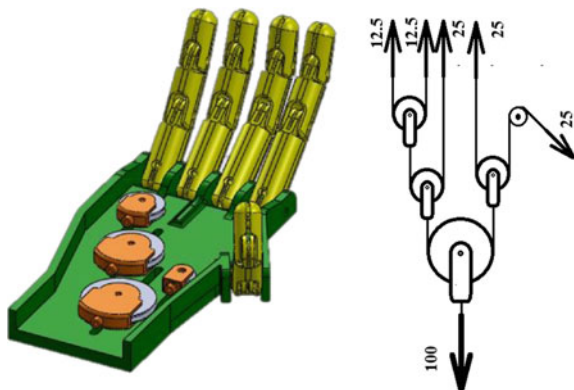
The each component of the prototype was designed by using a parametric CAD software; by means of it, tests on mechanisms were carried out, possible interferences between the individual components were studied, and dynamic simulations have were performed.

In Fig. 1 a CAD design of the hand is shown and a simple scheme of the pulley system is also reported.

By means of a parametric prototyping software, the behaviour of the single finger was studied. In particular, the action of the actuator tendon was obtained by applying forces having variable direction at the end of each of the tendon guides, while the action of the antagonist tendon was simulated by using elastic elements, see Fig. 2. The rigidity values of the elastic elements, were determined by means of dynamic simulation of the model. The system response in the presence of the only force of gravity has been studied by varying the values of stiffness of the springs. In this way the minimum values sufficient to guarantee the system to remain in its initial position, have been identified. In Table 1 the values of finger parameters are shown.

By further simulations it was possible to identify the minimum value of the force exerted by the actuator tendon to allow a complete closure of the finger with no objects to be gripped. The friction at each of the hinges was simulated by

**Fig. 1** The underactuated self adapting mechanical hand prostheses design





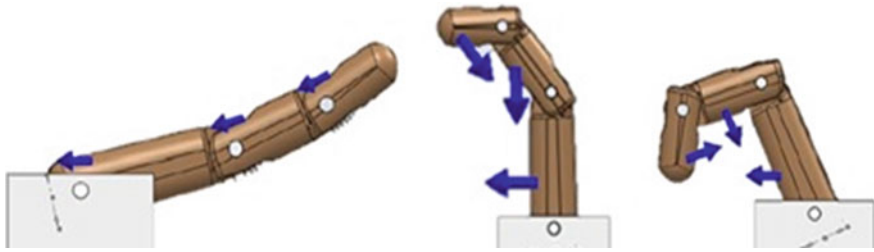


**Fig. 2** Virtual simulation of the finger closure

**Table 1** Finger parameters

Phalanx	Mass (kg)	Length (m)—distance between hinges	Stiffness (N/m)
proximal	0.01	0.045	15000
medial	0.0055	0.030	5000
distal	0.0030	0.025	1100

considering a coefficient of dynamic friction  $\mu = 100$ . In these conditions, a force applied to the tendon of 9 N was sufficient to the closure of the finger. In Fig. 2 some phases of the simulation are also shown. The simulation clearly shows that the direction of the forces changes depending on the configuration achieved by the finger. The CAD modeling allowed the study of the movement of all five fingers during the grasping of various objects, see Fig. 3. In this way it was possible, before the prototyping of the hand, to study and to analyze any interference between the components to have the opportunity to make directly changes to the model.

In Fig. 3 two tests studying and analyzing the position of the phalanges during the grasp of two objects having different sizes and geometries are also shown. In particular, on the left the object is an element with a non-symmetrical geometric section and on the right the object is a sphere. How it can be observed, the fingers of the hand always adapt themselves to the object to be grasped.

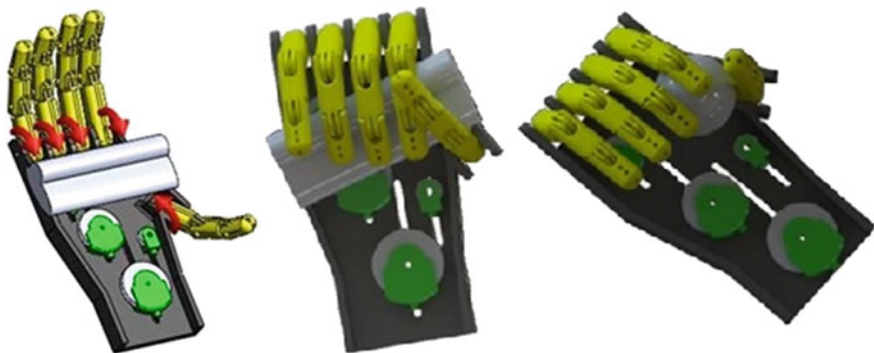


**Fig. 3** Simulation of the grasping

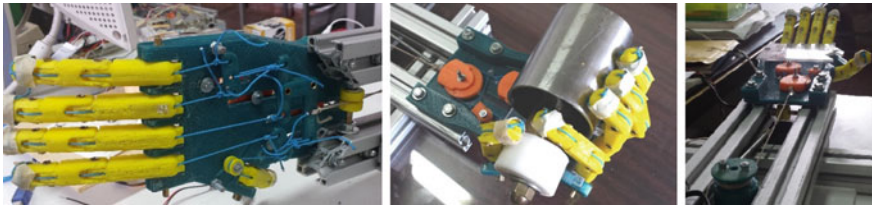


Fig. 4 The prototype

The prototype is shown in Fig. 4. In the upper part of the figure, on the left, a grasping is shown: it can be observed that the thumb and all the other fingers adapt themselves perfectly to the highly variable sections of the object.

### 3 Gripping Tests on the Prototype

In order to check the real capacity of grasping of the mechanical hand some gripping tests were performed with different objects and the force applied by the fingertip of each finger were measured. The prototype was equipped with a command button of the motor to perform the grip, and five FSR sensors, each of which was fixed on the distal phalanx of each finger. The experiments were performed by placing some test objects on the palm of the hand, initially opened, and performing the grip.

In the following the results relating to the grasp of two objects are shown: a piece of polystyrene and a hank of fabric. Figure 5 shows the grip test on a piece of polystyrene and the measured contact forces applied by the fingerstick of each

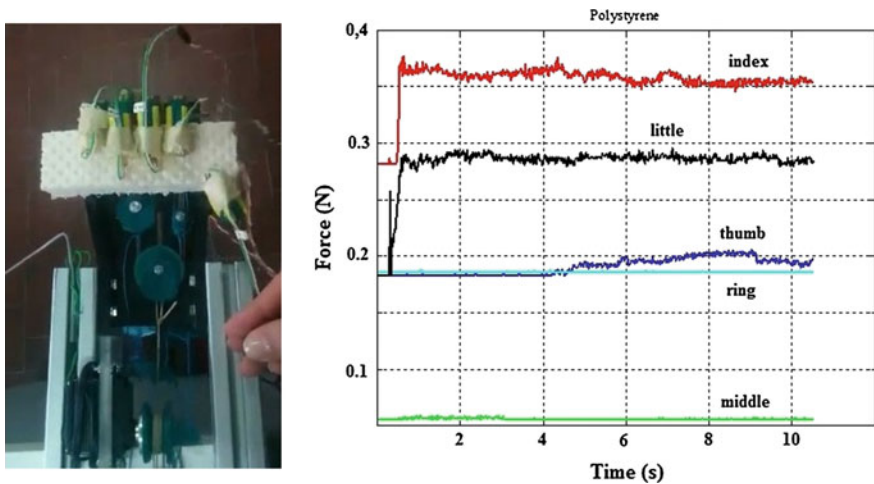
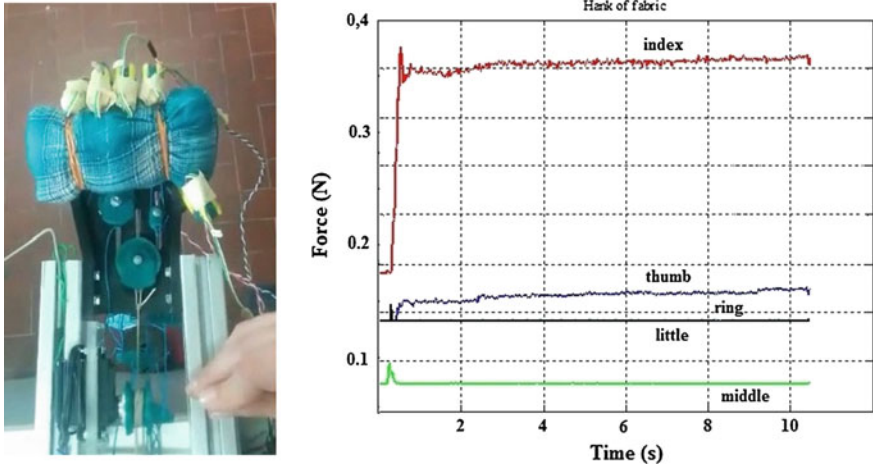


Fig. 5 The grip test on a piece of polystyrene



**Fig. 6** The grip test on an hank of fabric

finger were measured during the grasping. In Fig. 6 the test results for the grasping of an hank of fabric is shown. In the figures, for each type of grip, a graph of the forces measured on the fingertips, is also reported.

In the Tables 2 and 3 the average values obtained on three different tests, for each object, are reported.

With both objects, four fingers are involved in the grip (thumb index finger, ring finger and little finger) while on the middle finger a force on the fingertip lower than the other is observed. This evidence is entirely consistent with others analyses showing a dissipation of force for the middle finger bigger than the other.

In both tests the sum of the forces which the fingertips apply during the grasp, is only slightly more than 1 % of traction force of the tendon, but during the grasp also the other phalanges of the finger come into contact with the object and allow to apply force on it.

During the gripping of the piece of polystyrene, index and little finger exert a greater contact force, while for the hank of fabric, index finger and thumb show higher contact forces. This can be explained as follows: the piece of polystyrene,

**Table 2** Average values for tests on the piece of polystyrene

Grip	Force (N)					
	Thumb	Index	Middle	Ring	Little	Main ten
1	0.1833	0.3472	0.0614	0.1889	0.2627	86
2	0.1833	0.3232	0.0553	0.1857	0.2818	79
3	0.1906	0.3546	0.0556	0.1857	0.2812	81

**Table 3** Average values for tests on the hank of fabric

Grip	Force (N)					
	Thumb	Index	Middle	Ring	Little	Main ten
1	0.2667	1.111	0.0558	0.1857	0.1832	125
2	0.2489	0.7499	0.0558	0.1857	0.1834	125
3	0.2339	0.6916	0.0554	0.1857	0.1833	125

which has a long and narrow shape, facilitates the gripping by means of the index, middle, ring and little finger, while in the case of the hank of fabric, which has greater dimensions, the grasp is realized by blocking the object with the thumb.

## 4 Conclusions

Gripping tests on a prototype of a patent pending mechanical hand prototype were presented; they were carried on by means of a of a parametric prototyping software and by an instrumented prototype.

The results are encouraging since they showed the correct working of the hand prototype and a considerable “handiness” of the device that was simply made by PLA using a simple 3D printer.

Further investigations will essentially concern tests with all the phalanxes instrumented and by adopting a motion planning with the non-conventional techniques shown in (Rossi and Savino 2012).

## References

- Baril, M., Laliberte, T., Gosselin, C., & Routhier, F. (2013). On the design of a mechanically programmable underactuated anthropo-morphic prosthetic gripper. *Journal of Mechanical Design*, 135(12), 121008. doi:10.1115/1.4025493.
- Bicchi, A. (2000). Hands for dexterous manipulation and robust grasping: A difficult road toward simplicity. In *Ieee Transactions On Robotics And Automation* (Vol. 16, n. 6).
- Brown, C. Y. & Asada, H. H. (2007). Inter-finger coordination and postural synergies in robot hands via mechanical implementation of principal components analysis. In *Proc.eedingsof the 2007 IEEE/RSJ International Conference on Intelligent Robots and Systems*, San Diego (CA, USA), October 29–November 2.
- Carbone, G., Rossi, C. & Savino, S. (2015) Performance comparison between FEDERICA Hand and LARM Hand. *International Journal of Advanced Robotic Systems*, 12. doi:10.5772/60523, ISSN: 17298806.
- Catalano, M. G., Grioli, G., Serio, A., Farnioli, E., Piazza, C. & Bicchi, A. (2012). Adaptive synergies for a humanoid robot hand. In *Proceedings of IEEE-RAS International Conference on Humanoid Robots*, Osaka (Japan), October 2012.

- Cipriani, C., Controzzi, M., Carrozza, M. C. (2011) The smart hand transradial prosthesis. *Journal Of Neuro-engineering And Rehabilitation*, n. 8.
- Dechev, N., Cleghorn, W. L., & Naumann, S. (2001). Multiple finger, passive adaptive grasp prosthetic hand. *Mechanism and Machine Theory*, 36, 1157–1173.
- Gosselin, C., Pelletier, F., & Lalibertè, T. (2008). An anthropomorphic underactuated robotic hand with 15 Dofs and a single actuator. In *Proc. of 2008 IEEE International Conference on Robotics and Automation, Pasadena (CA, USA)*, 19–23 May.
- Grioli, G., Catalano, M., Silvestro, E., Tono, S., & Bicchi, A. (2012) Adaptive synergies: an approach to the design of under-actuated robotic hands. In *Intelligent Robots and Systems (IROS), 2012 IEEE/RSJ International Conference on* (pp. 1251–1256) 7–12 October 2012.
- Lotti, F. & Vasura, G. (2002). Design aspects for advanced robot hands. In *Proceedings of IEEE/RSJ International Conference on Intelligent Robots and Systems*, Lausanne, Switzerland, September 30–October 4.
- Niola, V., Penta, F., Rossi, C. & Savino, S. (2015) An underactuated mechanical hand: Theoretical studies and prototyping. *International Journal of Mechanics and Control*, 16(1), 11–19. ISSN: 15908844.
- Niola, V., Rossi, C., Savino, S., Carbone, G., Gaspareto, A. & Quaglia, G. (2015). An underactuated mechanical hand prosthesis by IFToMM ITALY. In *Proceedings of 14th IFToMM World Congress*, Taipei, Taiwan, October 25–30, 2015, doi:[10.6567/IFToMM.14TH.WC.PS13.005](https://doi.org/10.6567/IFToMM.14TH.WC.PS13.005).
- Penta, F., Rossi, C. & Savino, S. (2014). An underactuated finger for a robotic hand. *International Journal of Mechanics and Control*, 15(2). ISSN: 1590-8844.
- Penta, P., Rossi, C. & Savino, S. (2015). Gripping analysis of an underactuated finger. *Advances in intelligent systems and computing. Proceedings of 24th International Workshop on Robotics in Alpe-Adria-Danube Region* (pp 71–78) Bucharest, Romania, 27–29 May 2015. doi:[10.1007/978-3-319-21290-6](https://doi.org/10.1007/978-3-319-21290-6), ISBN: 9783319212906 (electronic version), 9783319212890 (print version).
- Roccella, S., Carrozza, M. C., Cappiello, G., Dario, P., Cabibihan, J. J., Zecca, M., Miwa, H., Itoh, K., Matsumoto, M. & Takanishi, A. (2004). Design, fabrication and preliminary results of a Novel anthropomorphic hand for humanoid robotics: RCH-1, In *Proceedings of 2004 IEEE/RSJ International Conference on Intelligent Robots and Systems*, Sendai, Japan, September 28–October 2, 2004.
- Roccella, S., Carrozza, M.C., Cappiello, G., Cabibihan, J. J., Laschi, C., Dario, P., Takanobu, H., Matsumoto, M., Miwa, H., Itoh, K. & Takanishi, A. (2007). Design and development of five-fingered hands for a humanoid emotion expression robot. *International Journal Of Humanoid Robotics* n. 4, 181–206.
- Roccella, S., Cattin, E., Vitiello, N., Giovacchini, F., Chiri, A., Vecchi, F. & Carrozza, M. C. (2008). Design of a hand exoskeleton (handexos) for the rehabilitation of the hand. *Gerontechnology* 7(2) 197.
- Rossi, C. & Savino, S. (2012). Robot trajectory planning by assigning positions and tangential velocities. *Robotics And Computer Integrated Manufacturing*, 29(1), 139–156. doi:[10.1016/j.rcim.2012.04.003](https://doi.org/10.1016/j.rcim.2012.04.003), ISSN 0736-5845.
- Rossi, C. & Savino, S. (2014). An underactuated multi-finger grasping device. *International Journal of Advanced Robotic Systems* 11(17). Article number 20.
- Rossi, C., Savino, S., Niola V. & Troncone, S. (2014). A study of a robotic hand with tendon driven fingers. *Robotica*. ISSN: 0263-5747, doi:[10.1017/S0263574714001179](https://doi.org/10.1017/S0263574714001179).

# Combined Structural and Dimensional Synthesis of Serial Robot Manipulators

D. Ramirez, J. Kotlarski and T. Ortmaier

**Abstract** The present work addresses the unification of the structural and dimensional synthesis of serial robot manipulators. Unlike related publications, the approach does not utilize simplifications of the kinematic structures. In addition, it is also capable of generating manipulators with up to six degrees of freedom. The approach reduces the computational effort by automatically generating the task-suitable architectures together with their corresponding optimisation parameters. Since the kinematics modelling is one of the main challenges, an algorithm for the numerical solution of the inverse kinematics is introduced. Finally, in order to demonstrate the capability of the method, the optimal manipulator for a pick and place operation is found using kinematic performance indices and particle swarm optimisation.

**Keywords** Serial manipulators · Robot design · Structural synthesis · Dimensional synthesis · Denavit-Hartenberg parameters

## 1 Introduction

The robot design process currently involves two isolated procedures: the structural synthesis and the dimensional synthesis (Merlet 2005). The first aims to find the number, type, and orientation of the robot joints in order to generate a manipulator

---

D. Ramirez (✉) · J. Kotlarski · T. Ortmaier  
Institute of Mechatronic Systems, Leibniz Universität Hannover, Hannover, Germany  
e-mail: danielandres.ramirez@imes.uni-hannover.de; danielramirez@usantotomas.edu.co;  
andresr36@gmail.com

J. Kotlarski  
e-mail: jens.kotlarski@imes.uni-hannover.de

T. Ortmaier  
e-mail: tobias.ortmaier@imes.uni-hannover.de

D. Ramirez  
Universidad Santo Tomás, Bogotá, Colombia

with a desired number of degrees of freedom (DOF). For this purpose, several methods like the Lie groups (Caro et al. 2010) and the screw theory (Kuo and Dai 2010) have been employed. In the dimensional synthesis, the optimal dimensions of the robot links are determined in order to accomplish a given task (Carbone et al. 2007). For this optimisation, many kinds of performance indices (Patel and Sobh 2015) as well as optimisation algorithms (Carbone et al. 2007; Lara-Molina et al. 2010) have been proposed.

Although the methods for the structural and dimensional synthesis are well established, the architectures produced as a result of the structural synthesis are not considered in the dimensional synthesis. Instead, the optimisation of the links dimensions is performed only for one structure, which is usually chosen a priori. Thus, the obtained manipulator that results from the dimensional synthesis is not necessarily the best mechanism for the given task.

Integrated synthesis of planar mechanisms has been developed for rigid body guidance in (Luu and Hayes 2012; Pucheta and Cardona 2011). Furthermore, dual quaternions have been used (Perez-Gracia and McCarthy 2006) in the synthesis of spatial mechanisms from a prescribed set of finite positions. Some authors have tried to unify the two aforementioned procedures for task-specific serial manipulators (defining the task as one or several paths). However, these attempts consider only manipulators with three DOF (Kucuk and Bingul 2006), simplified architectures (e.g. the last three axes intersecting at one point) (Patel and Sobh 2014, 2015), or a limited set of link geometries (i.e. the possible components are predefined modules) (Rubrecht et al. 2011).

The present work introduces a combined (structural and dimensional) synthesis of serial robot manipulators which does not assume any structural simplification. It is able to synthesize manipulators with up to six DOF while taking prismatic (P) and revolute (R) joints into account. In order to reduce the computational effort, the generation of all task-suitable architectures as well as the extraction of the minimal optimisation parameters is performed as the first step of the approach. Then, a generic numerical solution of the inverse kinematics for serial manipulators is presented. The optimisation procedure for an exemplary pick and place task with four DOF is addressed in the fourth section. Finally, the method's capability is demonstrated by synthesizing a manipulator for the mentioned task.

## 2 Generation of Suitable Architectures and Extraction of the Optimisation Parameters

The generation of suitable architectures to perform a required task is summarized here. A detailed description of the algorithm was previously published (Ramirez et al. 2015).

The architecture and geometry of a serial manipulator are described for the combined synthesis through a symbolic matrix of Denavit-Hartenberg (DH) parameters.

The first part of the synthesis aims to find the parameters that can be used during the optimisation as variables and the parameters that have to be constant in order to provide the required end effector (EE) DOF.

The necessary DOF to execute a given task can be used to define the required motion vector  $\xi_{req}$  as

$$\xi_{req} = [\xi_{req_1}, \xi_{req_2}, \xi_{req_3}, \xi_{req_4}, \xi_{req_5}, \xi_{req_6}]^T, \tag{1}$$

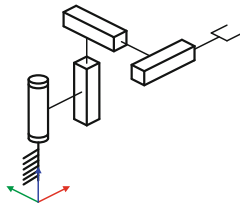
where  $\xi_{req_1}, \xi_{req_2},$  and  $\xi_{req_3}$  represent the translational DOF in direction of the axes  $x, y,$  and  $z$  while  $\xi_{req_4}, \xi_{req_5},$  and  $\xi_{req_6}$  represent the rotational DOF around the axes  $x, y,$  and  $z,$  respectively. It has to be noticed that  $\xi_{req}$  corresponds to the EE velocity of a serial manipulator  $\dot{\xi}$ :

$$\dot{\xi} = [\dot{\xi}_1, \dot{\xi}_2, \dot{\xi}_3, \dot{\xi}_4, \dot{\xi}_5, \dot{\xi}_6]^T = \begin{bmatrix} v_n \\ \omega_n \end{bmatrix} = J\dot{q}, \tag{2}$$

with  $J$  being the Jacobian matrix of the manipulator,  $v_n = [\dot{\xi}_1, \dot{\xi}_2, \dot{\xi}_3]^T$  the EE linear velocity,  $\omega_n = [\dot{\xi}_4, \dot{\xi}_5, \dot{\xi}_6]^T$  the EE angular velocity, and  $\dot{q}$  the joint rates vector. For a given task, if  $\xi_{req_i} = 0$  for any  $i = 1 \dots 6,$  then  $\xi_i$  should be also zero for the same  $i$  and for any  $\dot{q}$ . The suitability of a manipulator with respect to the task is evaluated using three conditions. Firstly, the null terms of  $\xi_{req}$  and  $\xi$  have to be the same. Secondly, the rank of the Jacobian matrix ( $\text{rank}(J)$ ) must be equal to the total number of required DOF. Thirdly, the independence of each EE DOF with respect to each DH parameter has to be verified. This evaluation is conducted in symbolic form in order to perform a global analysis. After the application of this conditions to the generated manipulators, it is possible to obtain a minimum set of architectures (i.e. without isomorphisms) to be considered during the subsequent optimisation.

Exemplarily, Fig. 1 shows a RPPP architecture, which is one of the 17 architectures that fulfil a required motion vector  $\xi_{req} = [\xi_{req_1}, \xi_{req_2}, \xi_{req_3}, 0, 0, \xi_{req_6}]^T$  (Ramirez et al. 2015). The corresponding DH parameters as well as the vector  $p$  with the optimisation parameters are also presented. In this case, the fixed parameters are  $\alpha_2 = \pi/2, \theta_3 = \pi/2,$  and  $\alpha_3 = \pi/2.$

**Fig. 1** Exemplary architecture generated for a task that requires three translational DOF and one rotational DOF around the z-axis (Ramirez et al. 2015)



R/P	$\theta_i$	$d_i$	$a_i$	$\alpha_i$
R	$q_1$	$d_1$	$a_1$	$\alpha_1$
P	$\theta_2$	$q_2$	$a_2$	$\pi/2$
P	$\pi/2$	$q_3$	$a_3$	$\pi/2$
P	$\theta_4$	$q_4$	$a_4$	$\alpha_4$

$$p = [d_1, a_1, \alpha_1, \theta_2, a_2, a_3, \theta_4, a_4, \alpha_4]$$



### 3 Kinematics Modelling

A central problem of the combined structural-dimensional synthesis is the solution of the inverse kinematics for a general serial manipulator including R and P joints. In this paper, the inverse kinematics is solved using a numerical approach, which exploits the advantages of both the pseudoinverse and the transpose of the Jacobian matrix.

The kinematics of a serial manipulator can be expressed as the relationship between the joint coordinates vector  $\mathbf{q}$  and the Cartesian coordinates vector (position and orientation) of the EE  $\mathbf{x}_{EE}$ :

$$\mathbf{x}_{EE} = \mathbf{f}(\mathbf{q}) . \quad (3)$$

The inverse kinematics problem consists of calculating  $\mathbf{q}$  from a given  $\mathbf{x}_{EE}$ :

$$\mathbf{q} = \mathbf{f}^{-1}(\mathbf{x}_{EE}) . \quad (4)$$

Most widespread numerical methods to solve (4) employ either the pseudoinverse or the transpose of the Jacobian  $\mathbf{J}$ . The first case corresponds to the Newton-Raphson method to solve nonlinear kinematic equations (Schwarz and Köckler 2011). The approach approximates the solution of the inverse kinematics  $\mathbf{q}$  to the vector  $\mathbf{q}_{p+1}$  using:

$$\mathbf{q}_{p+1} = \mathbf{q}_p + \mathbf{J}(\mathbf{q}_p)^\dagger \mathbf{K} \Delta \mathbf{x}_p , \quad (5)$$

with

$$\Delta \mathbf{x}_p = \mathbf{x}_{EE} - \mathbf{f}(\mathbf{q}_p) , \quad (6)$$

$$\mathbf{J}^\dagger = \mathbf{J}^T (\mathbf{J}\mathbf{J}^T)^{-1} , \quad (7)$$

and  $\mathbf{K}$  being a diagonal matrix to adjust the step size of the algorithm.

At the beginning of the algorithm  $\mathbf{q}_p$  corresponds to a given initial joint coordinates vector  $\mathbf{q}_0$ , which can be arbitrarily chosen. Though the approach usually has a high convergence rate, it diverges when  $\mathbf{J}(\mathbf{q}_p)$  is singular.

Another numerical method to solve the inverse kinematics corresponds to the gradient method for the solution of a system of nonlinear equations (Schwarz and Köckler 2011). This utilizes the transpose of  $\mathbf{J}$  in a similar way as (5):

$$\mathbf{q}_{p+1} = \mathbf{q}_p + \mathbf{J}(\mathbf{q}_p)^T \mathbf{K} \Delta \mathbf{x}_p . \quad (8)$$

Since the inversion of the Jacobian matrix is not necessary, this approach does not present problems with singularities. However, the convergence is slower in comparison to the Newton-Raphson method.

In order to take advantage of both approaches, a combined numerical solution of the inverse kinematics is proposed. This begins by using (5) and calculates the condition number  $\kappa$  of the Jacobian matrix  $\mathbf{J}(\mathbf{q}_p)$  at each step  $p$ . If  $\kappa \geq \kappa_{\max}$ , the algorithm switches to use (8) until  $\kappa < \kappa_{\max}$  and  $\mathbf{q}_p$  converges again. Then, Eq. (5) is used again to continue the process. The threshold  $\kappa_{\max}$  for the maximal allowed value of the condition number is given arbitrarily. Numerous tests showed that the algorithm is able to overcome singularities during the process and even find solutions near to singular poses with an appropriated convergence rate for  $200 < \kappa_{\max} < 600$ . The process is performed until  $\Delta \mathbf{x}_p < \epsilon$  for a given tolerance  $\epsilon$ . The proposed algorithm is presented in Algorithm 1. Detailed features of the algorithm are not discussed here due to space limitations.

---

**Alg. 1** Algorithm for the numerical solution of the inverse kinematics problem

---

**Require:**  $\mathbf{x}_{EE}$ ,  $\mathbf{q}_0$ ,  $\epsilon$ ,  $\kappa_{\max}$

```

 $\mathbf{q}_p \leftarrow \mathbf{q}_0$ 
repeat
   $\kappa \leftarrow \text{cond}(\mathbf{J}(\mathbf{q}_p))$ 
   $\Delta \mathbf{x}_p \leftarrow \mathbf{x}_{EE} - \mathbf{f}(\mathbf{q}_p)$ 
  if  $\kappa < \kappa_{\max}$  and  $\Delta \mathbf{x}_p < \Delta \mathbf{x}_{p-1}$  then
     $\mathbf{q}_{p+1} \leftarrow \mathbf{q}_p + \mathbf{J}(\mathbf{q}_p)^\dagger \mathbf{K} \Delta \mathbf{x}_{EE}$  {(from (5))}
  else
     $\mathbf{q}_{p+1} \leftarrow \mathbf{q}_p + \mathbf{J}(\mathbf{q}_p)^\text{T} \mathbf{K} \Delta \mathbf{x}_{EE}$  {(from (8))}
  end if
   $\mathbf{q}_p \leftarrow \mathbf{q}_{p+1}$ 
until  $\Delta \mathbf{x}_p < \epsilon$ 
return  $\mathbf{q}_p$ 

```

---

## 4 Optimisation Procedure

Due to the reasonable number of task-suitable architectures found through the generation of suitable architectures (Sect. 2), each of them can be optimised. Afterwards, the optimal configuration will be the one with the best performance of all architectures. The optimisation can be conducted for many kinds of requirements, e.g. accuracy, manipulability, size of the workspace, dynamical performance, etc. Exemplarily, the synthesis of a serial manipulator for a pick and place task will be introduced. Since the robot size influences other performance characteristics like stiffness and energy consumption, it will be used as optimisation criterion. Furthermore, the accuracy in the start pose ( $\mathbf{x}_{EE,s}$ ) and end pose ( $\mathbf{x}_{EE,e}$ ) are used as additional requirements of the design process. The indices that are used to evaluate the performance of the manipulator regarding these requirements as well as the optimisation algorithm are explained in the next sections.

## 4.1 Performance Indices

For the considered pick and place task, the robot size should be minimized maintaining a predefined accuracy in the start and end poses.

Several indices can be found in literature to evaluate the robot size. In this paper, the robot size index  $f_{\text{size}}$  is based on the structural length index (Waldron 2008), which compares the sum of the link lengths  $a_i$  and the joint offsets  $d_i$  to the volume of the reachable workspace. In our approach, the distance between the start and end points  $L_{\text{task}}$  will be used instead:

$$f_{\text{size}} = \frac{\sum_{i=1}^n |a_i| + |d_i|}{L_{\text{task}}}. \quad (9)$$

Since the condition number of  $\mathbf{J}$  ( $\kappa(\mathbf{J})$ ) is generally employed to analyse the error of the EE due to errors in the actuators, the local conditioning index (*LCI*) (Angeles and López-Cajún 1992) provides a good measure of the accuracy of the manipulator. However, in order to avoid the dimensional inhomogeneities of  $\mathbf{J}$ , the dimensionally homogeneous Jacobian matrix  $\tilde{\mathbf{J}}$  (Ranjbaran et al. 1995) must be used instead. The *LCI* is evaluated at the initial ( $\mathbf{q}_{\text{ini}}$ ) and end ( $\mathbf{q}_{\text{end}}$ ) point of the task. Then, the performance index corresponding to the accuracy of the manipulator is the minimum of these two values:

$$LCI_{\min} = \min \left( \kappa^{-1}(\tilde{\mathbf{J}}(\mathbf{q}_{\text{ini}})), \kappa^{-1}(\tilde{\mathbf{J}}(\mathbf{q}_{\text{end}})) \right). \quad (10)$$

## 4.2 Optimisation Problem

Exemplarily, the index  $f_{\text{size}}$  will be used as cost function and the minimum local conditioning index  $LCI_{\min}$  as constraint. Therefore, the optimal geometric parameters vector  $\mathbf{p}^*$  has to be found:

$$\mathbf{p}^* = \arg \min_{\mathbf{p}} (f_{\text{size}}(\mathbf{p})), \quad (11)$$

subject to

$$LCI_{\min} \geq LCI_{\min}^*, \quad (12)$$

where  $LCI_{\min}^*$  defines the lowest allowed value of  $LCI_{\min}$ . The parameters vector  $\mathbf{p}_{\min} \leq \mathbf{p} \leq \mathbf{p}_{\max}$  (lower bound  $\mathbf{p}_{\min}$ , upper bound  $\mathbf{p}_{\max}$ ) is obtained for each suitable architecture as explained in Sect. 2.

Since it is not possible to obtain an explicit expression for the cost function, a global optimisation method has to be used. In this case, the particle swarm optimisation algorithm (PSO) (Ebbesen et al. 2012) was chosen to solve the optimisation

problem. The optimisation process is performed for each suitable architecture. At the end of the process, the configuration (i.e. architecture including geometrical parameters) with the best performance is selected to perform the required task.

### 5 Exemplary Results

In order to demonstrate the capability of the proposed approach, the results of the synthesis for the aforementioned task are presented. This task requires three translational DOF and one rotational DOF around the vertical axis. The corresponding required motion vector is  $\xi_{req} = [\xi_{req_1}, \xi_{req_2}, \xi_{req_3}, 0, 0, \xi_{req_6}]^T$ . The required start and end poses of the EE ( $x_{EE,s}$  and  $x_{EE,e}$ ) are described using the position and orientation of the EE coordinate system (CS)<sub>EE</sub> with respect to the robot base coordinate system (CS)<sub>0</sub>. Table 1 gives the coordinates  $x, y, z$  and  $\varphi$  of the start and end poses.

The optimisation process was performed as explained in Sect. 4 for every suitable architecture (Ramirez et al. 2015). In each iteration of the optimisation, the inverse kinematics as introduced in Sect. 3 is computed to determine the joint coordinates corresponding to  $x_{EE,s}$  and  $x_{EE,e}$ . Afterwards, a point to point (PTP) interpolation is calculated in the joint space using a polynomial function of degree five (Biagiotti and Melchiorri 2008) in order to ensure the task feasibility.

The improvement in the numerical solution of the inverse kinematics is visualised in Fig. 2. As an example, for an RRRP architecture, the numerical inverse kinematics was performed with  $q_0 = [\pi/4, 0, \pi/4, 0.05]^T$  and  $x_{EE} = x_{EE,s}$ . Since  $q_0$

**Table 1** Start and end poses of the required task

Pose	$x$ [m]	$y$ [m]	$z$ [m]	$\varphi$ [rad]
$x_{EE,s}$	-0.5	0	0	$-\pi/2$
$x_{EE,e}$	0.5	0.6	0.7	0

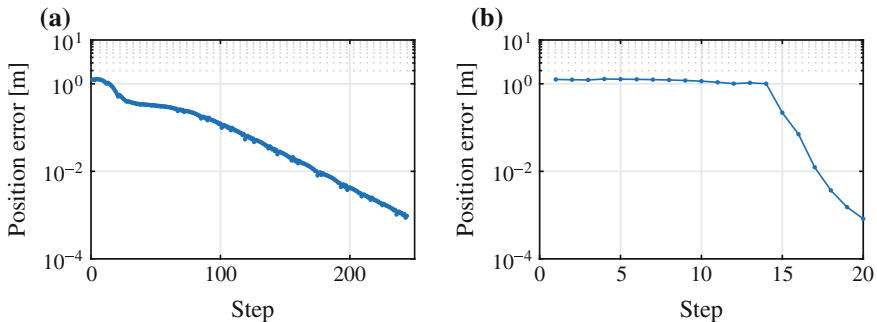


**Fig. 2** Evolution of the position error during the solution of the inverse kinematics **a** Using the transpose of  $J$  **b** Using the solution proposed in Algorithm 1

**Table 2** Architectures with the best performance after the optimisation procedure

Architecture	RPPP	RPRP	RPPR	PRPR	RRRP	PPPR
$f_{\text{size}}$	0.9613	1.0089	1.0881	1.0881	1.1212	1.2460
$LCI_{\text{min}}$	0.3613	0.1768	0.3163	0.2776	0.1	0.3077

**Table 3** DH parameters of the optimised manipulator

R/P	$\theta_i$ [rad]	$d_i$ [m]	$a_i$ [m]	$\alpha_i$ [rad]
R	$q_1$	0.318	0.227	0.5665
P	-1.9369	$q_2$	-0.058	$\pi/2$
P	$\pi/2$	$q_3$	0	$\pi/2$
P	-2.8224	$q_4$	0	0.9230

corresponds to a singular pose, the proposed algorithm (Fig. 2b) switches to use (8), but after step 13, it uses (7) for rapid convergence. Using only  $\mathbf{J}^T$  the convergence of the algorithm is slower (Fig. 2a). The represented position error corresponds to the norm of the first three terms of  $\Delta \mathbf{x}_p$ .

The architectures with the highest performance after the optimisation (RPPP, RPRP, RPPR, PRPR) and its performance indices are reported in Table 2. These results were obtained using 100 particles (swarm size) for each architecture and  $LCI_{\text{min}}^* = 0.1$ . The optimisation of every architecture was carried out several times with similar results.

The DH parameters of the best manipulator (RPPP) are shown in Table 3. As can be seen, the dimensions of the manipulator are reasonable for the given task. The capability of the method is demonstrated comparing the indices of the serial architectures that are usually employed for pick and place operations, namely PPPR (Gantry robot) and RRRP (Scara robot). The performance obtained for these manipulator are clearly poorer than the manipulator obtained with our method as reported in Table 2.

## 6 Conclusions

The paper presents an approach to combine the structural and dimensional synthesis of serial manipulators. Starting from a required task, every suitable architecture is considered during the dimensional optimisation process. In order to reduce the computational effort, the appropriate geometrical parameters of each architecture are deduced automatically. Due to an efficient numerical solution of the inverse kinematics, mechanisms with up to six DOF can be synthesized without any kinematic simplification. The benefits of considering all task-suitable architectures are observed

in the design of the manipulator for an exemplary pick and place operation. Here, the size of the robot was minimized and the accuracy was considered as a constraint during the optimisation. The obtained manipulator has a higher performance than the architectures typically employed for this kind of tasks.

## References

- Angeles, J., & López-Cajún, C. (1992). Kinematic isotropy and the conditioning index of serial robotic manipulators. *The International Journal of Robotics Research*, 11(6), 560–571.
- Biagiotti, L., & Melchiorri, C. (2008). *Trajectory Planning for Automatic Machines and Robots*. Berlin: Springer.
- Carbone, G., Ottaviano, E., & Ceccarelli, M. (2007). An optimum design procedure for both serial and parallel manipulators. *Proceedings of the Institution of Mechanical Engineers, Part C: Journal of Mechanical Engineering Science*, 221(7), 829–843.
- Caro, S., Khan, W., Pasini, D., & Angeles, J. (2010). The rule-based conceptual design of the architecture of serial schoenflies-motion generators. *Mechanism and Machine Theory*, 45(2), 251–260.
- Ebbesen, S., Kiwitz, P., & Guzzella, L. (2012). A generic particle swarm optimization matlab function. In: *Proceedings of the American Control Conference (ACC 2012)* (pp. 1519–1524).
- Kucuk, S., & Bingul, Z. (2006). Comparative study of performance indices for fundamental robot manipulators. *Robotics and Autonomous Systems*, 54(7), 567–573.
- Kuo, C., & Dai, J. (2010) Structural synthesis of serial robotic manipulators subject to specific motion constraints. In: *Proceedings of the ASME 2010 International Design Engineering Technical Conferences & Computers and Information in Engineering Conference*. Montreal.
- Lara-Molina, F. A., Rosario, J. M., & Dumur, D. (2010) Multi-objective design of parallel manipulator using global indices. *The Open Mechanical Engineering Journal* 4 (2010).
- Luu, T. J., & Hayes, M. (2012). Latest Advances in Robot Kinematics, chap. Integrated Type and Dimensional Synthesis of Planar Four-Bar Mechanisms (pp. 317–324). Springer Netherlands.
- Merlet, J. (2005). Optimal design of robots. In: *Proceedings of Robotics: Science and Systems*. Cambridge, USA.
- Patel, S., & Sobh, T. (2014). Using task descriptions for designing optimal task specific manipulators. In: *Proceedings of the 2014 IEEE/RSJ International Conference on Intelligent Robots and Systems (IROS 2014)* (pp. 755–760).
- Patel, S., & Sobh, T. (2015). Manipulator performance measures—a comprehensive literature survey. *Journal of Intelligent & Robotic Systems*, 77(3–4), 547–570.
- Patel, S., & Sobh, T. (2015). Task based synthesis of serial manipulators. *Journal of Advanced Research*, 6(3), 479–492.
- Perez-Gracia, A., & McCarthy, J. M. (2006). Kinematic synthesis of spatial serial chains using clifford algebra exponentials. *Proceedings of the Institution of Mechanical Engineers, Part C: Journal of Mechanical Engineering Science*, 220(7), 953–968.
- Pucheta, M. A., & Cardona, A. (2011). Topological and dimensional synthesis of planar linkages for multiple kinematic tasks. *Multibody System Dynamics*, 29(2), 189–211.
- Ramirez, D., Kotlarski, J., & Ortaimer, T. (2015). Automatic generation of a minimal set of serial mechanisms for a combined structural - geometrical synthesis. In: *Proceedings of the 14th IFToMM World Congress*.
- Ranjbaran, F., Angeles, J., Gonzalez-Palacios, M., & Patel, R. (1995). The mechanical design of a seven-axes manipulator with kinematic isotropy. *Journal of Intelligent and Robotic Systems*, 14(1), 21–41.
- Rubrecht, S., Singla, E., Padois, V., Bidaud, P., & de Broissia, M. (2011). Evolutionary design of a robotic manipulator for a highly constrained environment. In S. Doncieux, N. Bredeche, & J.

- Mouret (Eds.), *New Horizons in Evolutionary Robotics, Studies in Computational Intelligence* (Vol. 341, pp. 109–121). Berlin: Springer.
- Schwarz, H., & Köckler, N. (2011). *Numerische Mathematik*. Vieweg Teubner Verlag.
- Waldron, K.J. (2008). Design of arms. In: Dorf, R., Nof, S. (Eds.) *International Encyclopedia of Robotics: Applications and Automation* (Vol. 1), chap. A. Wiley.

# Development of the Acroboter Service Robot Platform

László Bencsik, Ambrus Zelei and Gábor Stépán

**Abstract** The domestic robot platform Acroboter exploits a novel concept of ceiling based locomotion. The robot platform is designed to perform pick and place tasks as well as carry other service robots with lower mobility. The crane-like Acroboter platform extends the workspace of these robots to the whole cubic volume of the indoor environment by utilizing the almost obstacle free ceiling. We summarize the evolution of the structure of the robot, the dynamic modelling concept and the control strategy which are the results of concurrent engineering.

## 1 Introduction

Service robot manufacturing is an exponentially growing area. The service robots are mainly ground based and use wheels, tracked locomotion system or sometimes legs. A common problem of the ground based concepts is related to the randomly placed obstacles on the floor which are typical in everyday indoor environment, like tables and chairs, edges of carpets and children's toys. On the other hand, ground based robots share the same workspace that humans use and cannot extend, when a special task would require this, like in case of reaching the top of a shelf. Furthermore, they waste valuable cubic volume from humans' workspace. In order to solve the above-described difficulties, it is straightforward to use flying robots which utilize the full cubic volume of the environment instead of moving on the floor. However

---

L. Bencsik (✉) · A. Zelei  
MTA-BME Research Group on Dynamics of Machines and Vehicles,  
Budapest, Hungary  
e-mail: bencsik@mm.bme.hu

A. Zelei  
e-mail: zelei@mm.bme.hu

G. Stépán  
Department of Applied Mechanics, Budapest University of Technology  
and Economics, Budapest, Hungary  
e-mail: stepan@mm.bme.hu



highly developed these flying applications like quadcopters are, their application for domestic purposes encounters crucial problems. The energy consumption of flying vehicles is typically high and the power that can be provided by batteries enables only short time operation. Furthermore, the loading capacity of flying drones are typically low. The novel concept of the crane-like robot called Acroboter (Stepan et al. 2009) combines the positive features of flying robots and the energy efficiency and loadability of ground based mobile platforms. The Acroboter platform has been developed within the European Union 6th Framework Project (IST-2006-045530) coordinated by the Department of Applied Mechanics, Budapest University of Technology and Economics.

The subsequent sections detail the design issues and prototype evolution of the Acroboter platform as well as the mechanical modelling approach and control aspects.

## 2 Concept of the Structural Design

There exist a few similar ceiling based, crane-like robot concepts, like the Flora service robot (Sato et al. 2004), which utilizes permanent magnets to keep and move its mobile cart on the ceiling. A tethered aerial robot presented in (McKerrow and Ratner 2007), of which the working unit is suspended on a single cable and equipped with two ducted fan actuators. A similar but simplified concept is the Winch-Bot that is presented in (Cunningham and Asada 2009). Here the cable winch is the only actuator on the robot, which can perform pick-and-place tasks. In the technical report (Dorigo et al. 2011) a parallel, distributed robotic system is introduced called Swarmanoid. The system has a few different type of units out of which there is one that can attach itself into the ceiling by a suspending cable and it can maneuver by using ducted fan actuators.

Similarly to the above-mentioned robotic systems, Acroboter can move on the almost obstacle free ceiling of a room, while transport the payload or a working unit similarly to gantry cranes, while it utilizes the pendulum-like motion efficiently (see sketch in Fig. 1 left).

A grid of anchor points (AP) is equipped on the ceiling. A climber unit (CU) moves from one to another anchor point by grasping two anchors at once or rotating around only one. The CU, which is a planar RRT robot, provides the main horizontal motion of the swinging unit (SU), which is the main working unit of Acroboter (see Fig. 1 right). The fine horizontal positioning of the final SU is performed by three pairs of ducted fan actuators (DF). The SU is equipped with a system of suspending and orienting cables. The main suspension cable (MC) is responsible for the elevation of the SU while the secondary cables (SC) of variable length are used for the precise stabilization of the orientation. The MC provides information signal and power transmission, too, although wireless communication between the main units is also implemented. The cable connector (CC) connects the main and secondary cables. The SU carries the end-effector of the robot which can be for example a

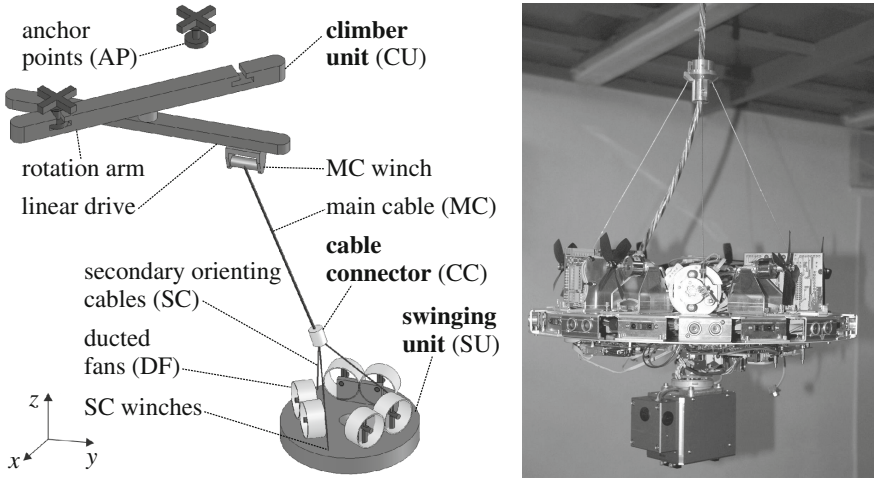


**Fig. 1** Sketch of the Acroboter (*left*), swinging unit prototype (*right*)

grasper, but it is also possible to interchange the grasper unit to other machines, such as a vacuum cleaner, with the help of the mechanical and electrical interface, which plays the role of a tool-changer situated at the bottom of the SU.

### 3 Dynamic Modelling Approach

In the classical modelling approaches of robots, the coordinates that describe the configuration of the model belong to the kinematic pairs involved. If the number of coordinates equals to the DoF then these joint coordinates are called *minimum set of generalized coordinates*. This approach is effective when open kinematic chains are modelled. When the dynamic modelling came into view, it was realized that Acroboter forms a complex multibody system, where the minimum set of coordinates is not effective as explained in the literature, e.g. (de Jalón and Bayo 1994). The windable cables, the CC and the SU together form a parallel kinematic structure, which also makes it very hard to use minimum number of coordinates. This problem can be resolved by means of *non-minimum set of generalized coordinates*. Out of the many possibilities we chose the so-called *natural coordinates*, which make real-time simulation possible and reduces computational costs even in case of highly complex multibody systems.

As we have more coordinates  $\mathbf{q} \in \mathbb{R}^n$  than DoF, we use geometric constraints that provide the relation between these dependent coordinates. Hence, the corresponding mathematical model is a differential algebraic equation (DAE). The equation of motion is written in the general form:

$$\mathbf{M}\ddot{\mathbf{q}} + \mathbf{C} + \boldsymbol{\varphi}_q^T \boldsymbol{\lambda} = \mathbf{H}\mathbf{u}, \quad (1)$$

$$\boldsymbol{\varphi} = \mathbf{0}, \quad (2)$$

where  $\mathbf{M}(\mathbf{q}) \in \mathbb{R}^{n \times n}$  is a positive definite mass matrix. In case of natural coordinates, the mass matrix is constant  $\mathbf{M}(\mathbf{q}) \equiv \mathbf{M}$ , which is a relevant advantage. Vector  $\mathbf{C}(\mathbf{q}, \dot{\mathbf{q}}) \in \mathbb{R}^n$  contains the centrifugal and Coriolis terms and all internal and external forces, including gravity. The holonomic and rheonomic geometric constraints are represented by  $\boldsymbol{\varphi}(\mathbf{q}, t) \in \mathbb{R}^m$ , thus the system has  $n - m$  DoF. The Jacobian matrix  $\boldsymbol{\varphi}_q = \partial \boldsymbol{\varphi} / \partial \mathbf{q} \in \mathbb{R}^{m \times n}$  defines the direction of the constraint forces, while their magnitude are represented by the corresponding Lagrange multipliers  $\boldsymbol{\lambda} \in \mathbb{R}^m$ . The  $l$  dimensional control input vector is  $\mathbf{u} \in \mathbb{R}^g$  and  $\mathbf{H}(\mathbf{q}) \in \mathbb{R}^{n \times g}$  is the generalized control input matrix. By using the method of Lagrange multipliers extended by the Baumgarte stabilization, the DAE equations of motion are arranged in a form, which can be handled by an ODE solver:

$$\begin{bmatrix} \mathbf{M} & \boldsymbol{\varphi}_q^T \\ \boldsymbol{\varphi}_q & \mathbf{0} \end{bmatrix} \begin{bmatrix} \ddot{\mathbf{q}} \\ \boldsymbol{\lambda} \end{bmatrix} = \begin{bmatrix} -\mathbf{C} - \mathbf{H}\mathbf{u} \\ -\dot{\boldsymbol{\varphi}}_q \dot{\mathbf{q}} - \dot{\boldsymbol{\varphi}}_t - 2\alpha(\boldsymbol{\varphi}_q \dot{\mathbf{q}} - \boldsymbol{\varphi}_t) - \beta^2 \boldsymbol{\varphi} \end{bmatrix}, \quad (3)$$

where  $\alpha$  and  $\beta$  are the Baumgarte stabilization parameters.

## 4 Control Issues

During the development of the control framework, several problems raised, which are solved partly by the modification of the structural design of the prototype and partly from the side of the control.

### 4.1 Singularities

By using the classical orientation representations like Euler-angles, (nutation, precession, rotation) it is obvious to chose the zero nutation at the hanging down position. In this scenario, the precession is not unequivocal in the vertical position. By the application of natural coordinates based description the mathematical singularity can be avoided besides the aforementioned advantages.

The vertical configuration is singular also from control viewpoint in case of the first prototype (Fig. 2 left) which possesses only two ducted fan actuators generating a resultant force  $F_x$  in the direction of the tubes and a torque  $T_z$  around the vertical axis. Near to the hanging down position, the desired acceleration perpendicular to the thrust force requires sudden rotation of the SU about  $z$ . First, the solution was provided by the application of a secondary ducted fan in cross direction (Fig. 2 centre), and the final prototype design (Fig. 2 right) makes it possible to generate approxi-

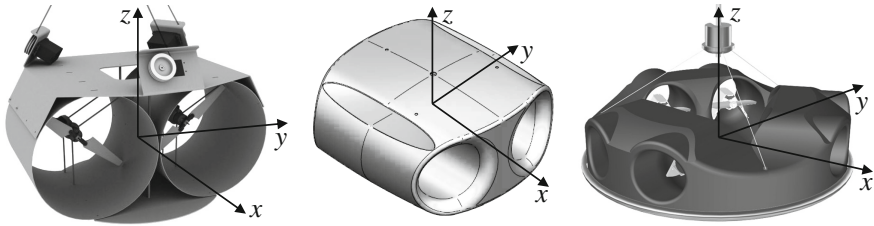


**Fig. 2** Evolution of the swinging unit: 2 ducted fans (*left*), additional cross direction fan (*centre*), 3 pairs of fans (*right*)

mately the same magnitude of thrust forces ( $F_x$  and  $F_y$ ) in any direction in the SU plane apart of the torque  $T_z$ . Consequently, the three pairs of ducted fan actuators represent 3 independent control inputs.

### 4.2 Underactuation

The complexity of the already intricate multibody control method is further complicated by the fact that the system is underactuated despite the large number of actuators, see Table 1. If the number  $g$  of the independent control inputs is less than the DoF of the system, then it is called *underactuated*, while if  $g = \text{DoF}$  than the system is *fully actuated*. Recently, more and more robotic systems have utilized the advantages of underactuation, like agile motion and energy efficient operation. The part of the dynamics which cannot be controlled directly is called *internal dynamics*; here the horizontal position of the cable connector can not be controlled directly.

### 4.3 Redundancy

The task of the robot is to keep the SU in the desired position and orientation in space, while there are no requirements for the motion of the CU and the CC. This means that the dimension of the task is only 6, all related to the SU only as the last column of Table 1 shows. Since the dimension of the prescribed task is smaller than the DoF, the

**Table 1** Degrees of freedom, actuators and prescribed DoF

Unit	DoF	Actuators	Prescribed DoF
Climber unit	3	3 (RRT)	$0 \mapsto 3$
Cable connector	3	1 (MC)	$0 \mapsto 1$
Swinging unit	6	$6 (F_x, F_y, T_z, 3 \text{ SC})$	6

**Table 2** Interpretations of redundancy

	Underactuated	Kin. redundant	Dyn. redundant
$\text{DoF} = g = l$	No	No	No
$\text{DoF} > g = l$	Yes	Yes	No
$\text{DoF} > g > l$	Yes	Yes	Yes

$l$ —dimension of task

$g$ —number of independent actuators

robot is not just underactuated but also *kinematically redundant*. Since the notions of both kinematic redundancy and underactuation appear, we proposed a classification of the different combinations of these ideas (Zelei et al. 2012) as it is summarized in Table 2. *An underactuated manipulator equipped with more independent control inputs than required to perform a specified task is called dynamically redundant underactuated system.*

In case of fully actuated robots, the above definition of dynamic redundancy is equivalent to the kinematic redundancy. In contrast, the inverse kinematics of underactuated systems cannot be solved uniquely without the consideration of the dynamics, so these are always kinematically redundant. However, if the task dimension  $l$  is equal to the number  $g$  of independent actuators, the determination of the control inputs is unique, and consequently the kinematics can also be calculated uniquely by using the internal dynamics. These systems are dynamically not redundant, the inverse dynamics can be solved uniquely. If the task dimension  $l$  is less than the number  $g$  of actuators, the system satisfies the above definition of dynamic redundancy, since even the inverse dynamic calculation is not unique.

The dynamic redundancy was resolved by the augmentation of the original set of tasks as Table 1 shows. The elevation of the CC was prescribed. The path of the main cable top mounting point was generated by a simplified model which utilizes the pendulum like motion. The inverse kinematics of the RRT structure was resolved by using geometric considerations.

#### 4.4 Control Algorithm

In spite of the underactuation, the system can be controlled by an extended inverse dynamical method. With the generalization of the method of Lagrange multipliers (3) the prescribed path of the robot is also defined as additional holonomic and rheonomic constraint equations called *servo-constraints* or *control-constraints* (Blajer and Kolodziejczyk 2007; Kovács et al. 2011):

$$\sigma = \mathbf{0}; \quad \sigma(\mathbf{q}, t) \in \mathbb{R}^l. \quad (4)$$

The task has same dimension as the number of independent control inputs  $l$ , consequently the above-mentioned dynamic redundancy is avoided. The geometric and

servo-constraints are *linearly independent* and also *consistent*, that is, there are no contradictory constraints, and they can be satisfied with *bounded control input*. The application of natural coordinates improves the solvability of the inverse kinematic problem, and the servo-constraints can be given conveniently.

The inverse dynamical calculation determines the desired acceleration  $\ddot{\mathbf{q}}$ , the input  $\mathbf{u}$  and adjunctively the vector  $\lambda$  of Lagrange multipliers uniquely, which satisfy the DAE system (1), (2) and (4). We extend the method of Lagrange multipliers (3) by including the control input  $\mathbf{u}$  which plays the role of the corresponding Lagrange multipliers of the servo constraints  $\sigma$ :

$$\begin{bmatrix} \mathbf{M} & \boldsymbol{\varphi}_q^T & -\mathbf{H} \\ \boldsymbol{\varphi}_q & \mathbf{0} & \mathbf{0} \\ \boldsymbol{\sigma}_q & \mathbf{0} & \mathbf{0} \end{bmatrix} \begin{bmatrix} \ddot{\mathbf{q}} \\ \lambda \\ \mathbf{u} \end{bmatrix} = \begin{bmatrix} -\mathbf{C} \\ -\dot{\boldsymbol{\varphi}}_q \dot{\mathbf{q}} - \dot{\boldsymbol{\varphi}}_t \\ \dot{\boldsymbol{\sigma}}_q \dot{\mathbf{q}} - \dot{\boldsymbol{\sigma}}_t - D(\boldsymbol{\sigma}_q \dot{\mathbf{q}} - \boldsymbol{\sigma}_t) - P\boldsymbol{\sigma} \end{bmatrix}, \quad (5)$$

where  $P$  and  $D$  are proportional and derivative gains of the linear compensator and play a similar role as Baumgarte gain parameters  $\alpha$  and  $\beta$ . The stabilization of the geometric constraints is unnecessary, because the geometric constraints are satisfied naturally, when the measured coordinate values are substituted.

## 5 Summary

The Acroboter domestic robot concept utilizes the advantages of both flying robots and crane-like systems. The problems of obstacle avoidance and energy efficiency are resolved together, furthermore, the robot platform utilizes the pendulum-like motion efficiently and provides large vertical workspace while it is still lightweight. As a secondary result of the development process of Acroboter we elaborated a general model-based motion control algorithm for underactuated and redundant multi-body systems. The control approaches were tested and applied in laboratory experiments for the Acroboter prototype.

**Acknowledgments** This work has been supported by the MTA-BME Research Group on Dynamics of Machines and Vehicles and by the Hungarian Scientific Research Fund, Hungary (OTKA) under grant numbers K-105433 and K-101714.

## References

- Blajer, W., Kolodziejczyk, K. (2007). Control of underactuated mechanical systems with servo-constraints. *Nonlinear Dynamics*, 50(4), 781–791. From the issue entitled Dynamical Systems: Theory and Applications.
- Cunningham, D., & Asada, H. H. (May 2009). (2009) The winch-bot: A cable-suspended, underactuated robot utilizing parametric self-excitation. *In IEEE International Conference on Robotics and Automation, Kobe, Japan, 12–17*,

- de Jalón, J. G., & Bayo, E. (1994). In *Kinematic and dynamic simulation of multibody systems: the real-time challenge*. Berlin: Springer.
- Dorigo, M., et al. (2011). Swarmanoid: A novel concept for the study of heterogeneous robotic swarms. Retrieved January 2016 from <http://people.idsia.ch/foerster/2013/02/SwarmanoidPaperTR.pdf>
- Kovács, I. I., Kövecses, J., Zelei, A., Bencsik, L. & Stépán, G. (2011). Servo-constraint based computed torque control of underactuated mechanical systems. In *Proceedings of ASME 2011 8th International Conference on Multibody Systems, Nonlinear Dynamics, and Control* (pp. 331–338) Washington, USA, 28–31 August 2011.
- McKerrow, P. J., & Ratner, D. (2007). The design of a tethered aerial robot. *Proceedings of IEEE International Conference on Robotics and Automation* (pp. 355–360), Rome, Italy, 10–14 April 2011.
- Sato, T., Fukui, R., Mofushita, H. & Mori, T. (2004). Construction of ceiling adsorbed mobile robots platform utilizing permanent magnet inductive traction method. In *Proceedings of 2004 IEEE/RSJ International Conference on Intelligent Robots and Systems* (pp. 552–558) Sendai, Japan, 28 September–2 October 2004.
- Stepan, G., Toth, A., Kovacs, L. L., Bolmsjo, G., Nikoleris, G., Surdilovic, D., Conrad, A., Gasteratos, A., Kyriakoulis, N., Chrysostomou, D., Kouskouridas, R., Canou, J., Smith, T., Harwin, W., Loureiro, R., Lopez, R. & Moreno, M. (2009). A ceiling based crawling, hoisting and swinging service robot platform. In *Proceedings of Beyond Gray Droids: Domestic Robot Design for the 21st Century Workshop at HCI 2009*.
- Zelei, A., Bencsik, L., Kovács, L. L. & Stépán, G. (2012) Redundancy resolution of the underactuated manipulator acroboter. In *proc. RoManSy 2012—19th CISM-IFTToMM Symposium on Robot Design, Dynamics and Control* (pp. 233–240), Paris, France, 12–15 June 2012.

# The Inversion of Motion of Bristle Bots: Analytical and Experimental Analysis

Giancarlo Cicconofri, Felix Becker, Giovanni Noselli,  
Antonio Desimone and Klaus Zimmermann

**Abstract** Bristle bots are vibration-driven robots actuated by the motion of an internal oscillating mass. Vibrations are translated into directed locomotion due to the alternating friction resistance between robots' bristles and the substrate during oscillations. Bristle bots are, in general, unidirectional locomotion systems. In this paper we demonstrate that motion direction of vertically vibrated bristle systems can be controlled by tuning the frequency of their oscillatory actuation. We report theoretical and experimental results obtained by studying an equivalent system, consisting of an inactive robot placed on a vertically vibrating substrate.

## 1 Introduction

Bristle bots are characterised by small size, robust and cheap design, and high speed of locomotion. Applications of bristle bots can be found in inspection technology (Becker et al. 2011), search and rescue systems (Hatazaki et al. 2007), and swarm robotic research (Giomi et al. 2013). The mechanism underlying their locomotion capabilities has been studied in (Ioi 1999; Becker et al. 2013; Giomi et al. 2013; Cicconofri and DeSimone 2015). To change motion direction of bristle-based mobile robots the following methods have been reported in the literature: changing the

---

G. Cicconofri (✉) · G. Noselli · A. Desimone  
SISSA, International School for Advanced Studies, Trieste, Italy  
e-mail: cicconof@sisssa.it

G. Noselli  
e-mail: gnoselli@sisssa.it

A. Desimone  
e-mail: desimone@sisssa.it

F. Becker (✉) · K. Zimmermann  
Technical Mechanics Group, Technische Universität Ilmenau, Ilmenau, Germany  
e-mail: felix.becker@tu-ilmenau.de

K. Zimmermann  
e-mail: klaus.zimmermann@tu-ilmenau.de



rotation direction of an unbalanced motor (Senyutkin 1977), using the phase shift between two unbalanced rotors (Ioi 1999) or changing the inclination of the bristle system using additional actuators (Schulke et al. 2011). Recent theoretical studies (DeSimone and Tatone 2012; Cicconofri and DeSimone 2015) have suggested that, for systems excited by vertical oscillations and moving along a straight line, direction of motion can be controlled by tuning the frequency of actuation. We provide in this paper an experimental validation of this prediction. Our results may be of interest in the field of inspection systems optimized for limited manoeuvring space, e.g. pipe inspection robots (Becker et al. 2011).

The paper is organized as follows. In Sect. 2 we accommodate the analysis presented in (Cicconofri and DeSimone 2015) for internally actuated robots in the context of an equivalent system, which consists of an inactive robot placed on a vibrating substrate. This setting provides cleaner and more efficient experimental study. In Sect. 3 we summarize the results of the experiments, and in Sect. 4 we outline possible directions for future work.

## 2 Setting, Modelling, and Analysis

Bristle bots are actuated by an internal vibrating mass. In order to better study their behaviour experimentally, however, we can avoid the encumbrance of an on-board motor by considering the setting depicted in Fig. 1. The setting consists of a (inactive) robot lying on a vertically vibrating substrate (shaker). As we show below, the resulting physical system, when considered in the shaker attached frame, is identical to that of a bristle bot moving on a still substrate and driven by an internal oscillating force.

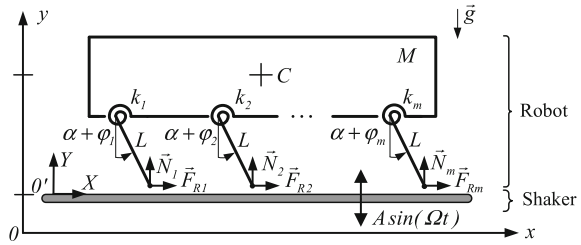
The robot is modelled as a two-dimensional rigid object, consisting of a row of  $m$  weightless support elements (bristles) of length  $L$  attached to a main body of mass  $M$ . The  $i$ th bristle is connected to the main body by a rotatory spring of stiffness  $k_i$ . The inclination of the bristles with respect to the vertical is given by  $\alpha + \varphi_i$ , where  $\alpha$  is the inclination angle in the unloaded configuration. The (horizontal) friction force acting at the contact point of the  $i$ th bristle with the shaker is modelled as

$$F_{Ri} = -\mu N_i \dot{P}_i, \quad (1)$$

where  $N_i$  is the normal reaction force acting on the tip of the bristle,  $\mu$  is a phenomenological friction coefficient, and  $\dot{P}_i$  the velocity of the contact point in the horizontal direction. We denote with a dot the derivative with respect to time.

**Simplifying assumptions and equations of motion.** We introduce two Cartesian coordinate systems in the vertical plane: the fixed reference frame ( $Oxy$ ) and the shaker-attached frame ( $O'XY$ ). The vertical displacement of the shaker at time  $t$  with

**Fig. 1** Schematic description of a model bristle bot lying on a shaker



respect to the  $x$  axis is given by  $A \sin(\Omega t)$ . We suppose that each bristle is always in contact with the shaker, and that the robot does not rotate with respect to the  $xy$ -plane. We have then

$$\varphi = \varphi_i, \quad i = 1, \dots, m \tag{2}$$

while all contact points have the same horizontal velocity  $\dot{P}_i = \dot{P} = \dot{x} + \dot{\varphi}L \cos(\alpha + \varphi)$ ,  $i = 1, \dots, m$ . Applying the principle of linear momentum we obtain

$$M\ddot{y} = N - Mg, \quad M\ddot{x} = -\mu N\dot{P},$$

where  $x$  and  $y$  are the coordinates of the centre of mass  $C$  in the fixed frame, and  $N = \sum_{i=1}^m N_i$  is the total normal force. With  $x = X$  and  $y = Y + A \sin(\Omega t)$ , the principle of linear momentum reads

$$M\ddot{Y} = N - Mg + MA\Omega^2 \sin(\Omega t), \quad M\ddot{X} = -\mu N\dot{P}. \tag{3}$$

Notice that  $X$  and  $Y$  are the coordinates of  $C$  in the shaker-attached frame. Finally, the principle of angular momentum gives

$$0 = -k\varphi + NL \sin(\alpha + \varphi) - \mu N\dot{P}L \cos(\alpha + \varphi), \tag{4}$$

where  $k = \sum_{i=1}^m k_i$ . Observe that Eqs. (3) and (4) are formally identical to the equations describing the same bristle bot model lying on a still substrate and actuated by an internal vertical force  $F(t) = MA\Omega^2 \sin(\Omega t)$ .

**Nondimensionalization and order of magnitude of parameters.** To normalize the dynamical variables we define the following parameters

$$\sigma = \sin(\alpha), \quad \chi = \cos(\alpha) \quad \text{and} \quad \epsilon = \frac{MgL\sigma}{k}.$$

We define then the *normalized* normal force  $n$ , angle difference  $\theta$ , and horizontal velocity  $w$  of the robot as

$$n = \frac{N}{Mg}, \quad \theta = \frac{\varphi}{\epsilon} \quad \text{and} \quad w = \frac{\dot{X}}{\epsilon\Omega L\chi}.$$

Applying all the definitions above, Eqs. (3) and (4) can be rewritten as the equivalent system in the dimensionless time  $\tau = \Omega t$

$$\begin{cases} -\gamma\ddot{\theta} \frac{\sin(\alpha + \epsilon\theta)}{\sigma} - \epsilon \left( \frac{\chi\gamma}{\sigma} \right) \dot{\theta}^2 \frac{\cos(\alpha + \epsilon\theta)}{\chi} = n - 1 + \eta \sin \tau \\ \dot{w} = -\lambda n \left( w + \dot{\theta} \frac{\cos(\alpha + \epsilon\theta)}{\chi} \right) \\ \theta = n \frac{\sin(\alpha + \epsilon\theta)}{\sigma} - \xi n \left( w + \dot{\theta} \frac{\cos(\alpha + \epsilon\theta)}{\chi} \right) \frac{\cos(\alpha + \epsilon\theta)}{\chi} \end{cases} \quad (5)$$

where

$$\xi = \frac{\mu Mg L^2 \chi^2 \Omega}{k}, \quad \lambda = \frac{\mu g}{\Omega}, \quad \gamma = \frac{(L\sigma\Omega)^2 M}{k} \quad \text{and} \quad \eta = \frac{AM\Omega^2}{Mg}. \quad (6)$$

In the following we suppose that  $\eta < 1$  is a small parameter, and  $\epsilon \lesssim \eta^2$ .

**Asymptotic analysis and average velocity.** We derive in this section an estimate of the average horizontal velocity of the robot, and we show how it can change sign for different values of the frequency of actuation. To obtain this estimate, we solve (5) by expanding the solution in power series in the (small) parameter  $\eta$ , that is

$$\theta = \theta_0 + \eta\theta_1 + \eta^2\theta_2 + \dots, \quad w = w_0 + \eta w_1 + \eta^2 w_2 + \dots, \quad n = n_0 + \eta n_1 + \eta^2 n_2 + \dots \quad (7)$$

Expanding (5) in powers of  $\eta$ , and matching coefficients of equal power, leads to a sequence of equations to be solved successively for the unknowns  $(\theta_j, w_j, n_j)$ , with  $j = 1, 2, \dots$ . It can be proved rigorously, see Cicconofri and DeSimone (2015), that (7) converge uniformly for every small enough  $\eta$ , and that only one periodic solution exist for each coefficient  $\theta_i$ ,  $w_i$  and  $n_i$  at each order. The resulting sum (7) for  $\theta$ ,  $w$ , and  $n$  is the only periodic solution of (5), and any other solution of the system converges asymptotically in time to it.

The zero-order system is given by

$$-\gamma\ddot{\theta}_0 = n_0 - 1, \quad \dot{w}_0 = -\lambda (w_0 + \dot{\theta}_0), \quad \theta_0 = n_0 - \xi (w_0 + \dot{\theta}_0),$$

and its only periodic solution is

$$\theta_0 = 1, \quad w_0 = 0 \quad \text{and} \quad n_0 = 1. \quad (8)$$

Now, imposing (8), the first order system reads

$$-\gamma \ddot{\theta}_1 = n_1 + \sin \tau, \quad \dot{w}_1 = -\lambda (w_1 + \dot{\theta}_1), \quad \theta_1 = n_1 - \xi (w_1 + \dot{\theta}_1). \quad (9)$$

We look here for solutions of the type

$$\theta_1 = \theta_1^s \sin \tau + \theta_1^c \cos \tau, \quad w_1 = w_1^s \sin \tau + w_1^c \cos \tau, \quad n_1 = n_1^s \sin \tau + n_1^c \cos \tau. \quad (10)$$

Replacing (10) in (9) and matching coefficients of sines and cosines respectively, we end up with six equations which allow us to determine  $\theta_1^s, \theta_1^c, w_1^s, w_1^c, n_1^s,$  and  $n_1^c$ . We obtain

$$\begin{aligned} \theta_1^s &= \frac{(\gamma - 1)(1 + \lambda^2) + \lambda \xi}{(\gamma - 1)^2 + ((\gamma - 1)\lambda + \xi)^2}, & \theta_1^c &= \frac{\xi}{(\gamma - 1)^2 + ((\gamma - 1)\lambda + \xi)^2}, \\ w_1^s &= \frac{-(\gamma - 1)\lambda}{(\gamma - 1)^2 + ((\gamma - 1)\lambda + \xi)^2}, & w_1^c &= \frac{-(\gamma - 1)\lambda^2 - \lambda \xi}{(\gamma - 1)^2 + ((\gamma - 1)\lambda + \xi)^2}, \\ n_1^s &= \frac{(\gamma - 1)(1 + \lambda^2) - (\gamma - 2)\lambda \xi - \xi^2}{(\gamma - 1)^2 + ((\gamma - 1)\lambda + \xi)^2}, & n_1^c &= \frac{\gamma \xi}{(\gamma - 1)^2 + ((\gamma - 1)\lambda + \xi)^2}. \end{aligned}$$

We then recover, in particular,  $w = \eta w_1 + \mathcal{O}(\eta^2)$ , where  $w_1$  is a periodic function with zero average. Indeed, the average velocity of the robot is of the order  $\sim \eta^2$ , however, we do not need to solve the second order system to recover a formula for it. We observe that, imposing (8), the second order expansion of the second equation in (5) gives

$$\dot{w}_2 = -\lambda(w_2 + \dot{\theta}_2) - \lambda n_1(w_1 + \dot{\theta}_1). \quad (11)$$

We know from the previously stated results in Cicconofri and DeSimone (2015) that (11) admits one periodic solution for  $w_2$  and  $\theta_2$ . Therefore, in particular,  $\dot{w}_2$  and  $\dot{\theta}_2$  have zero average. From (11) then follows that the average  $w^*$  of  $w_2$  can be written in terms of the solution of the first order system

$$w^* := \frac{1}{2\pi} \int_0^{2\pi} w_2 = \frac{-1}{2\pi} \int_0^{2\pi} n_1(w_1 + \dot{\theta}_1) = -\frac{1}{2} \left( \frac{\xi - \lambda}{(\gamma - 1)^2 + ((\gamma - 1)\lambda + \xi)^2} \right). \quad (12)$$

This last equation provides an explicit formula for the approximate (normalized) average horizontal velocity of the robot since

$$\frac{1}{2\pi} \int_0^{2\pi} w = \eta^2 w^* + \mathcal{O}(\eta^3).$$

Moreover, (12) shows how the sign of the average velocity depends on that of the difference between the two parameters  $\xi$  and  $\lambda$ , and ultimately on the frequency  $f := \Omega/2\pi$ , see (6). The formula predicts an average motion the negative direction for large values of  $f$ , and in the positive direction for small values of  $f$ . Figure 2

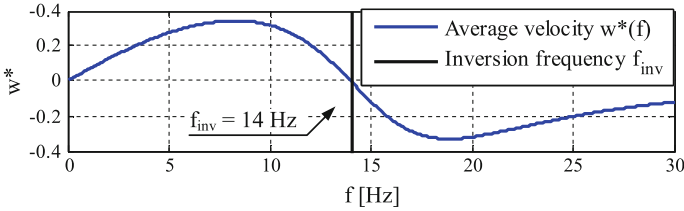


**Fig. 2** Average velocity  $w^*$  against excitation frequency  $f$ , with  $M = 10.5$  g,  $L = 8$  mm,  $\mu = 5$ ,  $k = 3.5 \cdot 10^{-3}$  Nm,  $g = 9.81 \frac{m}{s^2}$ ,  $\alpha = 35.2^\circ$

shows the frequency dependence of  $w^*$  when we fit (12) with the parameters of the prototype described below. The frequency such that  $w^* = 0$  is given by

$$f_{inv} = \frac{1}{2\pi} \cdot \frac{\sqrt{k/M}}{L \cos(\alpha)}, \tag{13}$$

which gives an approximation of the frequency at which the inversion of motion of the robot occurs. In the experiments below  $f_{inv} \simeq 14$  Hz.

### 3 Experiments

**Setup.** The experimental setup is shown in Fig. 3. It consists of a passive robot prototype lying on a platform attached to an electromagnetic shaker, which provides vertical excitation. The main body of the robot is made of polymer material with length  $\times$  width  $\times$  height = 55 mm  $\times$  35 mm  $\times$  9 mm., and mass  $M = 10.5$  g. The bristle functionality is realised by two 30 mm wide paper strips with a free length  $L = 8$  mm. With a mass of 55 mg, the paper strips meet sufficiently well the model assumption of massless bristles. The centre of mass of the robot is located in the middle between the ground-bristle contact points in order to avoid rotation of the main body, see model condition (2). In contrast to the model, the elasticity of the real bristles is equally distributed along their length. Their equivalent rotational stiffness and inclination angle are calculated to be  $k = 3.5 \cdot 10^{-3}$  Nm and  $\alpha = 35.2^\circ$ . Robot and shaker are equipped with markers for motion tracking.

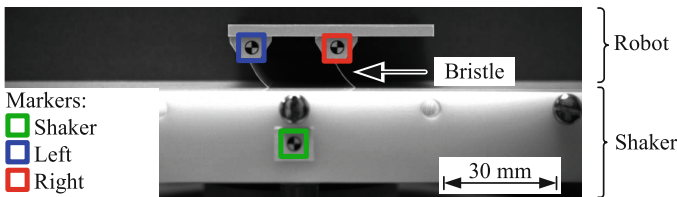


**Fig. 3** Experimental setup (single frame of a slow motion video)

**Experimental procedure and results.** The shaker is switched on producing vertical sinusoidal vibrations with controllable frequency and amplitude, leading to directed locomotion of the robot. At different frequencies we tune the amplitude of the shaker in order to match our analytic assumption  $\eta < 1$  and, in turn, to avoid the robot from losing contact with the ground. We recover a clear motion in the positive horizontal direction for frequencies below 10 Hz, and motion in the negative direction for frequencies above 18 Hz, in agreement with the theoretical predictions. Between 10 and 18 Hz we observe no directed locomotion.

**Two exemplarily locomotion characteristics.** We filmed the experiments with an high-speed camera. Figure 3 shows a frame of the videos. Locomotion is analysed by tracking the markers on the robot and the shaker. Figure 4 presents the tracking results for an excitation below the predicted inversion frequency, while Fig. 5 shows the tracking results for excitation above the inversion frequency.

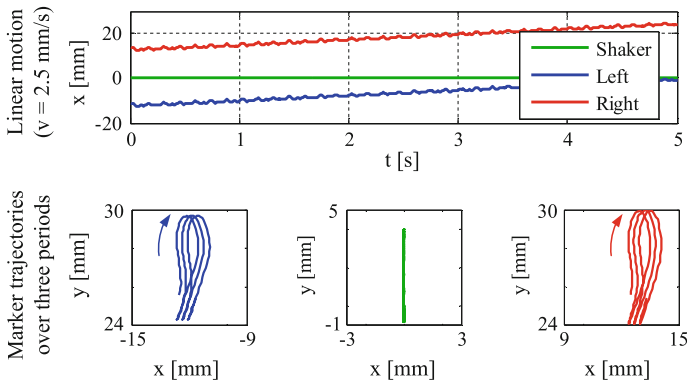


**Fig. 4** Locomotion behaviour of the prototype excited at 7 Hz

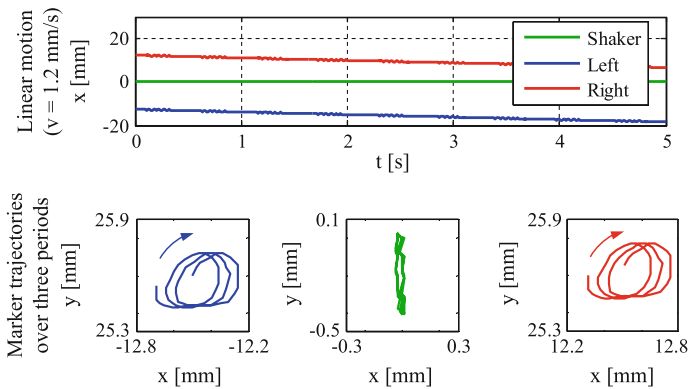


**Fig. 5** Locomotion behaviour of the prototype excited at 21 Hz

## 4 Conclusions and Outlook

We showed analytically and experimentally that the inversion of motion of bristle bots is possible by tuning the frequency of pure vertical excitation. Future work should focus on models accounting on more quantitatively accurate description of frictional interactions. Further experimental analysis is needed to find precisely the relation between robot parameters and locomotion characteristics.

**Acknowledgments** This research was partly supported by Deutsche Forschungsgemeinschaft Grant ZI 540/19-1 and ERC Advanced Grant 340685-MicroMotility.

## References

- Becker, F., Lysenko, V., Minchenya, V., Zeidis, I. & Zimmermann, K. (2013). An approach to the dynamics of a vibration-driven robot. In *Proc. of Romansy 19* (pp. 299–306). Vienna: Springer.
- Becker, F., Börner, S., Kästner, T., Lysenko, V., Zeidis, I. & Zimmermann, K. (2014). Spy bristle bot—A vibration-driven robot for the inspection of pipelines. In *Proc. of 58th IWK* (pp. 1–7).
- Cicconofri, G., & DeSimone, A. (2015). Motility of a model bristle-bot: A theoretical analysis. *International Journal of Non-Linear Mechanics*, 76, 233–239.
- DeSimone, A., & Tatone, A. (2012). Crawling motility through the analysis of model locomotors: Two case studies. *European Physical Journal E*, 35(85), 1–8.
- Giomi, L., Hawley-Weld, N., & Mahadevan, L. (2013). Swarming, swirling and stasis in sequestered bristle-bots. *Proceedings of the Royal Society A*, 469, 1–18.
- Hatazaki, K., Konyo, M., Isaki, K., Tadokoro, S. & Takemura, f. (2007) Active scope camera for urban search and rescue. In *IEEE IROS* (pp. 2596–2602).
- Ioi, K. (1999). A mobile micro-robot using centrifugal forces. In *Proceedings on International Conference on Advanced Intelligent Mechatronics* (pp. 736–741)
- Schulke, M., Hartmann, L. & Behn, C. (2011). Worm-like locomotion systems: development of drives and selective anisotropic friction structures. In *Proceedings of 56th IWK*.
- Senyutkin, A. (1977). *Bristle bot*. *Young Technician*, 6, 65–67. (in Russian).

# Design of a Compliant Environmentally Interactive Snake-Like Manipulator

Sergio Jainandunsing, Just L. Herder, Yukio Takeda  
and Daisuke Matsuura

**Abstract** Hyper redundant manipulators are robotic arms with many degrees of freedom. This allows them to navigate through a changing environment filled with objects. In this paper a new design for a hyper redundant manipulator is proposed. It makes use of underactuation and compliance to solve two problems, the path planning of the manipulator and the friction in the system. The proposed design consists of five segments. Each segment is a compliant cross axis flexure joint with four flexures. The proposed design is compared with a hyper redundant manipulator that also includes underactuation but is not compliant. It was found that compliance increases the range of motion and decreases the bending stiffness of the total manipulator while decreasing the lateral stiffness.

**Keywords** Hyper redundant manipulator · Compliant mechanism · Environmentally adaptive manipulator · Flexible robot arm

## 1 Introduction

Hyper redundant manipulators are robotic manipulators with many more degrees of freedom than necessary to reach a certain position. This allows the manipulator to bend and move around obstacles and reach its destination, since it has more than one way to reach its target. Applications of hyper redundant manipulators are abun-

---

S. Jainandunsing (✉) · J.L. Herder  
Delft University of Technology, Delft, The Netherlands  
e-mail: sergio.ijai@gmail.com

J.L. Herder  
e-mail: J.L.Herder@tudelft.nl

Y. Takeda · D. Matsuura  
Tokyo Institute of Technology, Tokyo, Japan  
e-mail: takeda@mech.titech.ac.jp

D. Matsuura  
e-mail: matsuura@mech.titech.ac.jp



dant. Some examples are: rescue robots, endoscopy and minimally invasive surgery, subsea, operating in space, bomb disposal and working in a nuclear environment. These are mentioned by Jones and Walker (2006), Davies et al. (1998), Chirikjian (1992) and Buckingham and Graham (2003).

In a previous study by Bakker et al. (2015), a new way for moving a hyper redundant manipulator between objects has been designed and implemented. Instead of calculating trajectories to move between the objects without touching them, the principle of underactuation was used to employ contact with the environment. In most cases there is no need for calculations to avoid the manipulator from touching the object, instead it is easier to use the environment to your advantage. When the manipulator comes in contact with an object the tip will start to curve around it and the rest of the manipulator follows.

Compliant mechanisms are mechanisms that make use of elastic deformation of flexible parts that bend instead of hinges. They have several advantages and disadvantages as mentioned in Lobontiu (2002) and Howell (2001). The advantages are summarized into two categories: cost reduction and increased performance such as no friction losses, no need for lubrication, no hysteresis, compactness, easy fabrication, maintenance free. Drawbacks are: the rotation of a flexure joint is not pure, the lateral stiffness is considerably lower compared to a regular joint and the flexure hinge is usually sensitive to temperature variations.

The goal of this paper is to develop a hyper redundant manipulator that uses the principles of under actuation and compliant mechanism. It has to be able to navigate through a 2D environment, while supporting its own weight. The design is compared with another design that uses only underactuation and is not compliant.

## 2 Methods

### 2.1 The Compliant Joint

Designing a compliant joint depends on the motion it needs to make, the range of motion, the stiffness, the lateral stiffness and the axis drift.

The lateral stiffness is defined as the stiffness perpendicular to the plane in which the manipulator can be controlled. The lateral stiffness has to be high enough in order for the manipulator to not bend downwards in the lateral plane (due to its own weight). The axis drift is of little importance, since the manipulator will use the environment to bend around its objects. By comparing the data of different compliant rotational joints found in the article by Machekposhti et al. (2012) and Trease et al. (2005), the cross axis joint shown in Fig. 1a was used in our study.

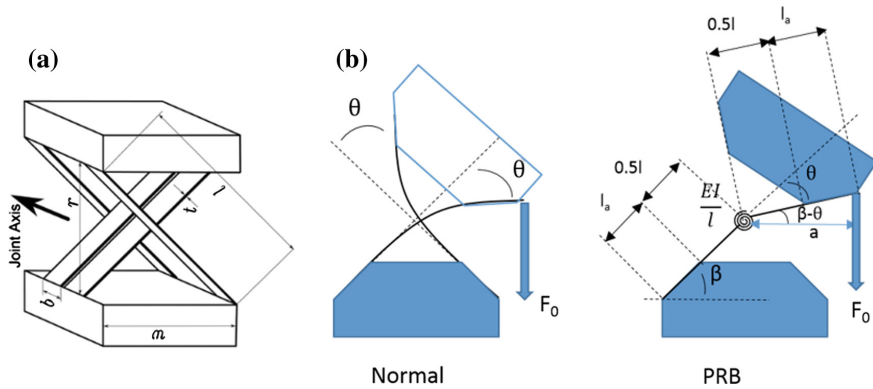


**Fig. 1** The compliant joint. **a** is the compliant cross axis joint from Chen et al. (2013). **b** is the Pseudo rigid body model

### 2.2 Pseudo Rigid Body Modelling

To calculate the dimensions of the flexures and have an estimation of the stress in the flexures, the non-linear problem is reduced to a pseudo rigid body model (PRBM). The pin-joint model described by Jensen and Howell (2002) is used. In Fig. 1b the pin-joint model is shown. The compliant cross axis joint can be described with linkages and torsion springs. Each segment has to be able to turn 90°. The torsion springs are assumed linear and the linkages have unlimited stiffness. The system is hereby reduced to a linear problem to give a close estimation.

Since there are large rotations, linear beam theory can no longer be applied to calculate the stiffness. To obtain the correct formulas for the stiffness (Eq. 1) and stress (Eq. 2), different assumptions need to be made to solve the Bernoulli-Euler equation when compared to small rotations. This was done by Howell (2001) and Jensen and Howell (2002).

$$K = \frac{EI}{l} = \frac{M_0}{\theta_0} \tag{1}$$

$$\sigma = \frac{M_0 * c}{I} \tag{2}$$

$E$  is the Youngs modulus,  $I$  is the moment of inertia,  $l$  is the flexure length,  $M_0$  is moment on the flexure,  $\theta_0$  is the angle of the flexure and  $c$  is the distance from central axis.

A segment was designed to bend 90°. A force of 2.4 N is needed for this. The force can be obtained with Eq. 3.  $M_0$  is the moment on the flexure and  $a$  is the moment arm.

$$F = \frac{M_0}{a} \tag{3}$$

### 2.3 Finite Element Analysis

A finite element software (Ansys workbench) was used to confirm the calculations made in the previous section and to check stresses in the material and the response of the material to a force. First one flexure was modelled and subsequently the whole joint. In the PRB calculations it was assumed that the force causes a constant moment along the length of the flexure. In reality there is a moment and a shear force working on the whole flexure. This explains the small difference observed in the stress.

When testing the lateral stiffness, Ansys did not converge when trying to apply a force perpendicular to the motion while the joint was under an angle. The lateral stiffness was measured by doing experiments with a prototype.

### 2.4 Optimization

Several prototypes were made after the initial PRBM and Ansys calculations. The PRBM and Ansys results from this paper are for the final prototype. To get to the final prototype some optimization needed to be done. From early experiments it was clear that the lateral stiffness of the prototype was too low. The goal was to reduce the distance covered by the tip of the manipulator by bending in lateral direction to 10% of the total length of the manipulator.

### 2.5 Prototype

The prototype and its experiment setup are shown in Fig. 2 together with the previous design (Bakker et al. 2015). The design consists out of five segments stacked on top of each other. This design was compared to the design of the previous one which only included underactuation. This is to investigate if adding compliant mechanism adds

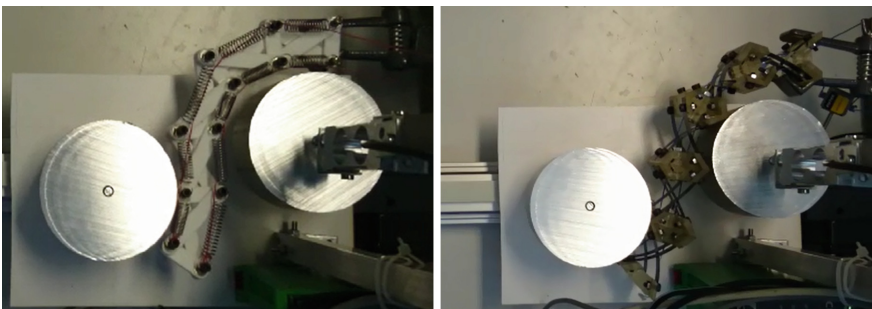


Fig. 2 Linkage-type prototype and Compliant design (right)

advantages. The previous design which only includes underactuation will be called the linkage-type manipulator. For fair comparison a prototype of the linkage-type manipulator was made at the same scale as the compliant version.

The stiffness is not the same for both prototypes, since the right springs could not be found. The stiffness for the linkage-type manipulator is 2.87 times higher than that for the compliant manipulator.

### 3 Experiments

#### 3.1 Conditions

The experiment setup is shown in Fig. 3a. In the experiment the two manipulators were compared. They each tried to traverse an obstacle course filled with cylinders. The force in the  $x$  and  $y$  directions on cylinder B as well as the force in one rope were measured. Instead of the manipulator moving forward through the obstacles, the obstacles moved towards the manipulator. This was done in order to achieve more stability and more precise results about the forces, since the manipulator has to be operated. Motion of the manipulator was controlled by two ropes, actuated by hand, to turn left or right. Interaction between the rope and the manipulator is shown in Fig. 3b. Where  $F$  is the force used to pull the rope and 1, 2 and 3 are the resulting forces of the rope on the system.

Four criteria were defined to measure the performance of the manipulators. The criteria are: the maximum force needed to navigate through the obstacle course, the forces on the environment, the range of motion and the lateral stiffness of the manipulator.

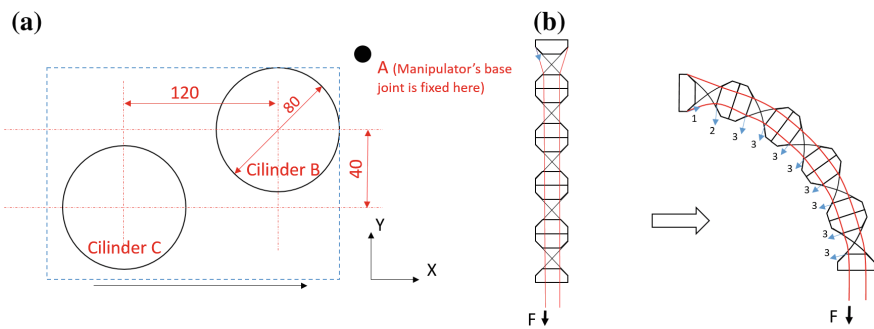


**Fig. 3** Experimental setup. **a** is the obstacle course. **b** is the interaction between the rope and the manipulator when pulling the rope

**Table 1** Comparison of two manipulators

Criteria	Compliant manipulator	Linkage-type manipulator
Maximum force in the rope	3.1 N	4.08 N
Maximum forces on the environment	1.86 N	0.882 N
Range of motion	$[-3/4\pi, 3/4\pi]$	$[-1/2\pi, 1/2\pi]$
Lateral stiffness	–	–

### 3.2 Results

In Table 1 a comparison between the two manipulators is given. The forces for the linkage-type manipulator are scaled with  $1/2.87$  to compensate for the increased stiffness of the prototype. The Lateral stiffness is determined by  $K_{lat} = \frac{\Delta M_{lat}}{\Delta \theta_{bot}}$ , where  $\Delta \theta_{bot}$  is the bending of the bottom segment in the lateral direction. Since this value was too low for the equipment to measure, a final verdict for this criteria cannot be given other than that both manipulators fulfill the goal of bending less than 10 % of their total length in the lateral direction.

### 3.3 Discussion

By removing the hinges (joints) with friction in the compliant manipulator presented in this paper, we observed several advantages. The stiffness can be influenced by adjusting the length, width, thickness, angle of the flexure or by the amount of flexures. The required stiffness in the compliant manipulator can be obtained with more precision, since no energy is lost due to friction. A more precise and sensitive control is obtained as compared to the linkage-type manipulator. When bending the compliant prototype, the moment arm increases till the flexure is bended  $90^\circ$ . This helps reducing the total force needed to bend the compliant prototype compared to the linkage-type prototype. This can be seen in the results. A segment of the linkage-type manipulator has a stiffness that is 287 % of the compliant manipulator. After scaling the force needed for the linkage-type manipulator is 132 % higher. This is because more energy is needed as explained above and because there is friction. The stiffness has an immediate effect on the forces acting on the environment. If the stiffness is higher the forces become higher. With the compliant manipulator it is easier to feel when an object is touched compared to the linkage-type manipulator, since there are no losses in friction. The stiffness of the linkage-type manipulator is higher, but the forces on the environment after scaling are lower. This is due to the friction in the system which caused an undesired effect. There is less force on the obstacle, but an increased force in the actuation.

The compliant manipulator possesses a high range of motion. The range of motion is coupled with the dimensions of the flexures. Increasing the length of the flexures increases the range of motion but decreases the stiffness, compared to the linkage-type manipulator whose linkages are its limitation.

The lateral stiffness is the downside of the compliant manipulator. In most cases it is coupled with the stiffness. This results in a problem when stiffness is desired to be low. A balance between the two needs are to be found.

The compliant manipulator has other advantages over the linkage-type manipulator which were not tested. The absence of friction(ropes are assumed frictionless) increases its durability and sensitivity. The driving forces are directly transferred to the user and no energy is lost as friction. It increases the accuracy of the manipulator. The compliant manipulator has greater form fitting capabilities than the linkage-type manipulator. The compliant manipulator has flexures which can adapt to the form, the linkage-type manipulator has stiff linkages.

The removal of hinges has advantages in certain applications, for instance in the medical field. Most equipment needs to be cleaned and made sterile. Some dirt can reside in the hinges which make it difficult to clean.

The compliant manipulator was designed to move in a 2D field in our study. Making it move in a 3D field is the next step. This can be accomplished in several ways. One is to design a compliant joint that can move in every direction. Another option is to take the segment that was designed in this research and rotate them on top of each other. In this way some segments can move in one way and the other segments in another allowing the manipulator to move in a 3D environment.

## 4 Conclusion

In this paper a new design for a hyper redundant manipulator is presented. The design makes use of two principles: compliance and underactuation. Underactuation allows the manipulator to adapt to the objects. It uses the object to make a turn rather than avoid touching it. This solves the difficult path planning hyper redundant manipulators have.

Compliance solves the problems due to friction and has other advantages as well. The design consists out of five segments stacked on top of each other. A segments contains four flexures that allows it to bend. Compliance allows the manipulator to achieve a higher range of motion and lowers the actuation force. Due to an undesired effect caused by the friction, the forces on the environment are higher for the compliant manipulator compared to the linkage-type manipulator. This friction however causes the actuation force of the linkage-type manipulator to increase since there is no friction compared to the linkage-type manipulator. The disadvantage was observed in the lateral stiffness.

## References

- Bakker, D. L., Matsuura, D., Takeda, Y., & Herder, J.L. (2015). Design of an environmentally interactive continuum manipulator. In *14th World Congress in Mechanism and Machine Science IFToMM2015, Taipei, Taiwan*.
- Brian, D. J., & Howell, L. L. (2002). The modeling of cross-axis flexural pivots. *Mechanism and Machine Theory*, *37*(5), 461–476.
- Buckingham, R., & Graham, A. (2003). Reaching the unreachable—Snake arm robots. In *International Symposium of robotics*. <http://www.ocrobotics.com/downloads/ISR03.pdf>.
- Chen, G., Zhang, S., & Li, G. (2013). Multistable behaviors of compliant sarrus mechanisms. *Journal of Mechanisms and Robotics*, *5*(2), 021005.
- Davies, J. B. C., Lane, D. M., Robinson, G. C., O'Brien, D. J., Pickett, M., Sfakiotakis, M., Deacon, B. (1998). Subsea applications of continuum robots. In *Proceedings of 1998 International Symposium on Underwater Technology* (pp. 363–369). doi:10.1109/UT.1998.670127.
- Gregory, S. C. (1992). *Theory and Applications of Hyper-Redundant Robotic Manipulators*.
- Howell, L. L. (2001). *Compliant Mechanisms*. Wiley.
- Jones, B. A., & Walker, I. D. (2006). Kinematics for multisection continuum robots. *IEEE Transactions on Robotics*, *22*(1), 43–55. doi:10.1109/TRO.2005.861458.ISSN:15523098.
- Lobontiu, N. (2002). *Compliant Mechanisms: Design of Flexure Hinges*. CRC Press.
- Machekposhti, F., Tolou, N., & Herder, J. L. (2012). The scope for a compliant homokinetic coupling based on review of compliant joints and rigid-body constant velocity universal joints. In *Proceedings of the ASME 2012 IDETC/CIE Conference*.
- Trease, B. P., Moon, Y.-M., & Kota, S. (2005). Design of large-displacement compliant joints. *Journal of mechanical design*, *127*(4), 788–798.

**Part VI**  
**Humanoid Robots**



# Joint Mechanism Coping with Both of Active Pushing-off and Joint Stiffness Based on Human

**Takuya Otani, Kenji Hashimoto, Takaya Isomichi, Shunsuke Miyamae, Masanori Sakaguchi, Yasuo Kawakami, Hun-ok Lim and Atsuo Takanishi**

**Abstract** Human steady running is modeled using a spring-loaded inverted pendulum (SLIP). However, human pushes off the ground actively when starting to run. In this study, we describe a knee joint mechanism for coping with both of an active pushing-off and joint stiffness needed to continue running. To achieve this, knee is equipped with a mechanism comprising a worm gear that improves torque transmission efficiency in order to achieve active movement and two laminated leaf springs for mimicking joint stiffness. We evaluated the performance of the laminated leaf spring and performed an experiment in which the developed running robot started to run. Using the proposed mechanisms, this robot could accomplish hopping with an active pushing-off motion and continued to run using its joint elasticity.

---

T. Otani (✉) · T. Isomichi · S. Miyamae  
Graduate School of Science and Engineering, Waseda University, Tokyo, Japan  
e-mail: t-otani@takanishi.mech.waseda.ac.jp

T. Isomichi  
e-mail: takaya\_isomichi@akane.waseda.jp

S. Miyamae  
e-mail: galspa1123@ruri.waseda.jp

T. Otani  
Japan Society for the Promotion of Science, Tokyo, Japan

K. Hashimoto  
Waseda Institute for Advanced Study, Waseda University, Tokyo, Japan  
e-mail: k-hashimoto@takanishi.mech.waseda.ac.jp

K. Hashimoto · H. Lim · A. Takanishi  
Humanoid Robotics Institute (HRI), Waseda University, Tokyo, Japan  
e-mail: holim@kanagawa-u.ac.jp

A. Takanishi  
e-mail: takanisi@waseda.jp

M. Sakaguchi · Y. Kawakami  
Faculty of Sport Sciences, Waseda University, Tokyo, Japan  
e-mail: msakaguc@ucalgary.ca

# 1 Introduction

For investigating human running mechanisms and human motion control, we have developed a bipedal humanoid robot that can mimic various characteristics of human running (see Otani et al. 2015a). Previous studies in human science have identified some characteristics of human running, for instance:

- The stance leg acts like a linear spring, and a human leg can be modeled as a spring-loaded inverted pendulum (SLIP) (Blickhan 1989).
- The knee and ankle joints in the stance leg act like torsion springs and these create the leg elasticity (Gunther and Blickhan 2002).
- The pelvis rotates in the frontal plane to increase jumping force (Otani et al. 2015b).
- Moment compensation is accomplished using the upper body and arm swinging (Hinrichs 1987).

Our robot has a pelvis and elastic legs, and can rotate its knee joint during the flight phase. The robot can attain jumping power and run using its active pelvic movement and leg elasticity. For steady running, its leg does not need to bend actively, but bends as a torsion spring during the stance phase. However, the robot cannot jump by the first pushing-off the ground when standing because it must store the energy in its elasticity using the resonance of its pelvic movement. In steady running, a human utilizes the leg elasticity for storing kinetic energy. However, human pushes off the ground by moving his/her hip and knee joints actively for jumping and starting to run (Bobbert et al. 1986). There are some studies about running humanoid robots; however, few robots can mimic this characteristic. Life-size real humanoid robots such as ASIMO (Takenaka et al. 2011) do not have leg elasticity. MABEL (Grizzle et al. 2009) has leg elasticity, however, the values of the legs' joint stiffness are different from that of a human. Therefore, we aimed to achieve both of an active pushing-off needed to start running and joint stiffness for steady running.

In this study, we sought to develop the knee joint mechanism coping with both of an active pushing-off and mimicking joint stiffness. For steady running, we had already developed a lower-body robot that can move its hip joint actively and has human-like joint stiffness in the knee and ankle joints. This robot cannot move its knee joint actively; however, the knee joint needs to move actively for pushing-off.

---

Y. Kawakami  
e-mail: ykawa@waseda.jp

M. Sakaguchi  
Faculty of Kinesiology, University of Calgary, Calgary, Canada

H. Lim  
Faculty of Engineering, Kanagawa University, Yokohama, Japan

A. Takanishi  
Faculty of Science and Engineering, Waseda University, Tokyo, Japan

To achieve both of an active movement and joint stiffness, we developed a new joint mechanism using laminated leaf springs made of carbon fiber reinforced plastic (CFRP) and a worm gear designed to improve the torque transmission efficiency. We then performed some experiments to evaluate the effectiveness of the proposed mechanism and succeeded to jump by an active pushing-off and run using leg elasticity.

## 2 Knee Joint Mechanism Coping with Both Active Pushing-off and Joint Stiffness

### 2.1 Joint Requirements for Running

Human running is concerned to be divided into a starting phase and a steady running phase. In the starting phase, human pushes off the ground after squatting a little by moving his/her hip and knee joints actively. On the other hand, during the stance phase of human steady running, the knee and ankle joints alternately lengthen and shrink like a spring, whereas the hip joint, unlike a spring, only lengthens (Novacheck 1998). The leg stiffness is a result of knee and ankle joint stiffness, which is important for attaining jumping force. As mentioned above, leg stiffness and joint stiffness vary according to running speed. To mimic these characteristics, we determined the requirements for the robotic joint based on human motion data, considering running speeds between 4 and 10 m/s. The requirements for achieving the joint stiffness of a running human leg were obtained from the results of our preliminary analysis and published running data (see Table 1) (Otani et al. 2015b).

### 2.2 Design of Knee Joint Mechanism

To cope with both active pushing-off and joint stiffness, we devised a new joint mechanism in which the angle between two leaf springs can be changed by an actuator in order to achieve active movement. The two leaf springs are connected through an actuator and transmit the joint torque to an upper link and lower link through the load point, which can be moved to change the effective length. When the angle between two leaf springs is actively changed, the joint rotates. When the

**Table 1** Requirements for knee joint

	Starting phase	Steady running phase	
		Swing	Stance
Torque (Nm)	29	15	180
Angular velocity	3.5	6.5	11
Joint stiffness (Nm/rad)	–	–	300–600

external torque is applied, the leaf springs bend and the joint angle also changes while the angle between the two leaf springs is not changed. If this mechanism is to act like a torsion spring, the angle between the two leaf springs should be fixed: only the leaf springs should bend to produce the joint torque.

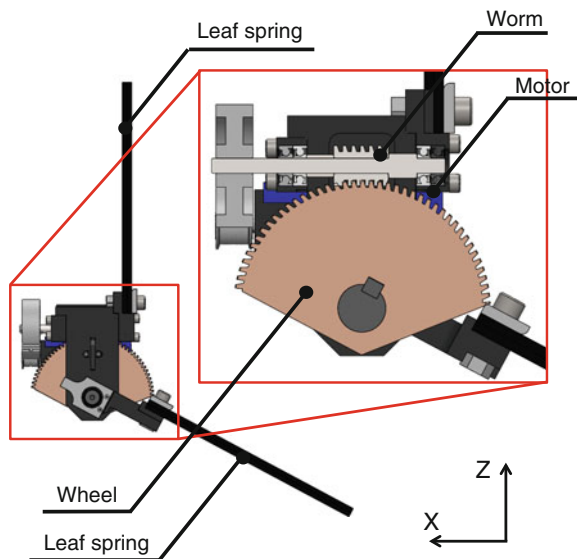
To accomplish this, we used a worm gear through which the torque from the input shaft to output shaft is transmitted; almost none of the torque from the output shaft to the input shaft is transmitted to the worm gear. However, generic worm gears are not able to be used for active knee movement because their transmission efficiency from the input to output shafts was too low. When these worm gears were used, the mechanism needed a higher output motor that was too heavy to keep the leg weight similar to that of a human. Therefore, we designed an original worm gear in which the transmission efficiency could be changed according to its lead angle. The theoretical formulas for transmission efficiency from the input shaft to output shaft  $\eta_1$  as well as from the output shaft to input shaft  $\eta_2$  are as follows:

$$\eta_1 = \frac{\tan \gamma}{\tan(\gamma + \rho)} \tag{1}$$

$$\eta_2 = \frac{\tan(\gamma - \rho)}{\tan \gamma} \tag{2}$$

where  $\rho$  is a parameter with a value of 0.14, determined by the material from which the worm gear is made and the angular velocity. Using these formulas, we designed the worm gear with the lead angle  $8.73^\circ$  to minimize the power of the motor. This knee mechanism can fix the angle between the two leaf springs in the stance phase and can actively control the joint angle (see Fig. 1).

**Fig. 1** CAD of the knee joint mechanism



### 2.3 Design of CFRP Leaf Spring

For incorporating the leaf springs into the developed joint mechanism, the leaf springs must withstand a large moment during the stance phase. An iron leaf spring could withstand a large load, but it would be very heavy and not be able to mimic the mass of a human leg. To solve it, we designed a leaf spring made of CFRP, which is strong and lighter than iron. However, when the CFRP leaf spring was made small enough to be installed into a robotic leg equivalent in size to a human leg, the stress on the leaf spring exceeded its strength. To resolve this problem, we stacked two leaf springs one upon another. When the number of leaf spring is one, the maximum stress  $\sigma$  is expressed as follows:

$$\sigma = \frac{6M}{bt^2} \tag{3}$$

where,  $M$  is the joint torque,  $b$  is the width of the leaf spring, and  $t$  is the thickness of the leaf spring. On the other hand, the thickness of each leaf spring  $t'$  is expressed as follows with the number of leaf springs  $n$ :

$$t' = \frac{t}{n} \tag{4}$$

Therefore, the maximum stress on one leaf spring in the laminated leaf spring is expressed as follows:

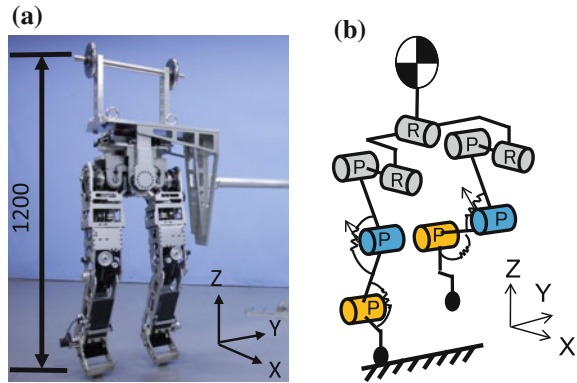
$$\sigma_{\text{laminated}} = \frac{6nM}{bt^2} \tag{5}$$

To increase the strength of the leaf spring with the same joint stiffness, we used these formulas to design a laminated leaf spring made of two CFRP leaf springs. Compared to an iron leaf spring whose joint stiffness is the same as that of the laminated CFRP leaf spring, the laminated leaf spring is almost the same in length and width, and the mass of the laminated leaf spring 200 g is much lower than that of the iron leaf spring 600 g (see Table 2). Furthermore, the mass of the joint mechanism using CFRP laminated leaf springs is 3000 g, which reduces approximately 21 % compared to 3800 g for the joint with iron leaf springs.

**Table 2** Leaf spring characteristics

Material	Iron (SK85)	CFRP
Size (mm)	250 × 90 × 3.4	220 × 70 × 8.8
Mass (g)	600	200

**Fig. 2** A bipedal robot with the developed joint mechanism. In (b), we used the harmonic drive for *gray joint*, the worm gear for *blue joint*, and passive joint for *yellow joint*. **a** Photo of the developed bipedal robot. **b** DoF of the robot



## 2.4 A Bipedal Robot with the Developed Joint Mechanism

We implemented the developed knee joint into the lower-body running robot (see Fig. 2). The robot also has an active pelvis mechanism. We used 150 W DC motors, timing belts, and harmonic drives to actuate the pelvis roll joint and hip joints. To perform human-like motions, the robot must be approximately the same size and weight as a human (Kouchi and Mochimaru 2005).

## 3 Evaluation of the Developed Joint Mechanism

### 3.1 Evaluation of CFRP Leaf Spring

We conducted experiments to evaluate the ability of the joint mechanism in mimicking human's knee joint stiffness. In the experiments, the robotic motion was restricted to the vertical direction using linear guides. At first, the robot was lifted, then lowered to apply a vertical downward force proportional to the mass of the robot. To determine the knee joint stiffness, we measured the knee joint angle using an encoder of the knee joint, and we measured the downward force using a force sensor located on the floor and calculated the joint torque.

The experimental results are summarized in Table 3. As the results show, we confirmed that the range of the joint stiffness of the developed joint was wider than that of a human knee joint.

**Table 3** Results of knee joint stiffness evaluation

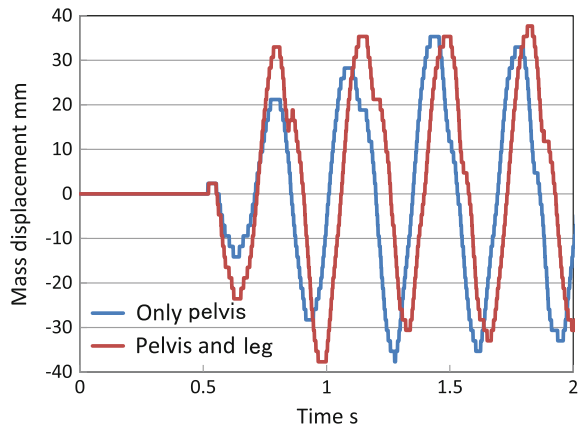
	Min. (Nm/rad)	Max. (Nm/rad)
Requirement for knee joint	300	600
Theoretical value	230	690
Measured value	230	680

### 3.2 Hopping with an Active Pushing-off and Joint Stiffness

We performed an experiment to evaluate the developed robot can use its active pushing-off and joint elasticity to start running. In this experiment, the robot initially stood then started to move its pelvis according to the pelvic oscillation control method (Otani et al. 2015a). When the robot was able to jump, it moved its hip pitch joint according to the running speed control method with a reference running speed of 0.2 m/s. To detect if the robot was in the stance phase or flight phase, we used the measured data of the ankle joint angle because the ankle joint bent when the robot landed. Moreover, we measured the vertical displacement of the center of mass using the data of a rotary encoder implemented in the guide. To compare the results with those using a leg pushing-off, we also performed an experiment that included the pushing-off. By comparing these experimental results, we aim to confirm the effectiveness of the developed knee joint mechanism. The amplitude of the pelvic oscillation and joint stiffness were selected based on human running data.

Figure 3 depicts the vertical displacement of the robot’s center of mass when the robot used only its pelvis and when it used its pelvis and a leg pushing-off. When the robot used only its pelvis, it could not hop with the first pelvic movement. On the other hand, the robot could hop with the first pelvic movement and leg’s pushing-off. Moreover, when the robot was able to hop with the first pushing-off, the hopping height was almost same as that of steady running. This result indicates that the joint mechanism was able to push off the ground actively and withstand the large torque during the stance phase of steady running. Therefore, these results confirm that the developed joint mechanism is effective for starting to run.

**Fig. 3** Mass vertical displacement in the hopping experiment



## 4 Conclusion

In this paper, we described the development of the knee joint mechanism coping with both of an active pushing-off and mimicking joint stiffness. To cope with active movement and joint stiffness, we developed a new joint mechanism using a worm gear improved the torque transmission efficiency for an active pushing-off and two laminated leaf springs to mimic joint stiffness. We evaluated the joint stiffness of the developed mechanism, and then performed a hopping experiment to evaluate the effectiveness of the proposed mechanism. The results confirm that the robot could hop and start running using an active pushing-off.

In the future, we will combine the SLIP model with upper body movement to develop a new stabilization control method.

**Acknowledgements** This study was conducted with the support of the Research Institute for Science and Engineering, Waseda University; Institute of Advanced Active Aging Research, Waseda University; Future Robotics Organization, Waseda University, and as part of the humanoid project at the Humanoid Robotics Institute, Waseda University. It was also financially supported in part by the JSPS KAKENHI Grant No. 25709019; Mizuho Foundation for the Promotion of Sciences; SolidWorks Japan K.K.; TohoTenax Co., Ltd.; and DYDEN Corporation; we thank all of them for the financial and technical support provided. Further, the high-performance physical modeling and simulation software MapleSim used in this research was provided by Cybernet Systems Co., Ltd. (Vendor: Waterloo Maple Inc.)

## References

- Blickhan, R. (1989) The Spring-mass model for running and hopping. *Journal of Biomechanics*, 22, 1217–1227 (1989).
- Bobbert, M. F., Huijing, P. A., & Schenau, G. I. (1986) A model of the human triceps surae muscle-tendon complex applied to jumping. *Journal of Biomechanics*, 19(11), 887–898.
- Grizzle, J. W., Hurst, J., Morris, B., Park, H. W., & Sreenath, K. (2009). MABEL, A new robotic bipedal walker and runner. *American Control Conference, 2009*, 2030–2036.
- Gunther, M., & Blickhan, R. (2002) Joint stiffness of the ankle and the knee in running. *Journal of Biomechanics*, 35, 1459–1474 (2002).
- Hinrichs, N. R. (1987) Upper extremity function in running. II: Angular momentum considerations. *International Journal of Sport Biomechanics*, 3, 242–263 (1987).
- Kouchi, M., & Mochimaru, M. (2005). *Human dimension database*. AIST: Digital Human Research Center.
- Novacheck, T. F. (1998). The biomechanics of running. *Gait and Posture*, 7, 77–95.
- Otani, T., Hashimoto, K., Yahara, M., Miyamae, S., Isomichi, T., Sakaguchi, M., et al. (2015a). Running with lower-body robot that mimics joint stiffness of humans. *In Proceedings of IEEE/RSJ International Conference on Intelligent Robots and Systems* (pp. 3969–3974).
- Otani, T., Hashimoto, K., Yahara, M., Miyamae, S., Isomichi, T., Hanawa, S., et al. (2015b). Utilization of human-like pelvic rotation for running robot. *Frontiers in Robotics and AI*, 2(17).
- Takenaka, T., Matsumoto, T., Yoshiike, T., & Shirokura, S. (2011). Running gait generation for biped robot with horizontal force limit. *JRSJ*, 29(9), 93–100.



# Design of a Dexterous Hand for a Multi-hand Task

Neda Hassanzadeh, Reza Movassagh-Khaniki  
and Alba Perez-Gracia

**Abstract** Kinematic synthesis applied to tree topologies is a tool for the design of multi-fingered robotic hands, for a simultaneous task of all fingertips. Dexterous multi-fingered robotic hands can be designed to perform collaborative tasks that are traditionally performed by more than one robotic manipulator. Such collaborative tasks require multiple robotic arms and a method to control their coordinate operation. In this work, the synthesis process for the design of a single robotic hand for a bimanual task is discussed, with application to the task of holding and peeling an orange.

## 1 Introduction

Many robotic tasks require the collaborative work of two or more robot manipulators, such as the combination of a positioning device with a robot performing an assembly task. To accomplish such tasks the coordination of the robots needs to be planned. Several works have been done on the control of such systems, with simultaneous control strategies and collision avoidance. In Dauchez et al. (1991), a relative description of the task has been proposed and a very simple collision avoidance algorithm, which permits a continuous progression of the task, has been developed. In William and Soloway (1997), a control architecture is presented for real-time, simultaneous sensor-based, shared control of remote, multiple-manipulator tele-robotic systems. Liu et al. (1999) study the problem of modeling and control of multiple cooperative underactuated manipulators handling a rigid object. In Sun and Mills (2002), a

---

N. Hassanzadeh · R. Movassagh-Khaniki · A. Perez-Gracia (✉)  
Department of Mechanical Engineering, Idaho State University,  
Pocatello 83209, USA  
e-mail: perealba@isu.edu

N. Hassanzadeh  
e-mail: hassneda@isu.edu

R. Movassagh-Khaniki  
e-mail: movareza@isu.edu

new adaptive, synchronized control algorithm is proposed for coordination of multiple manipulators in assembly tasks. These collaborative setups are designed mostly with non-dexterous end-effectors.

Kinematic synthesis has recently been applied to multiple end-effector systems, in order to increase the versatility in wristed hand designs. These systems can be defined, for synthesis purposes, as chains with a tree topology, with several common joints that branch to a number of serial chains, and possibly with several branching stages, ending with several end-effectors.

Kinematic and dynamic analysis of tree topologies is studied in de Jalon and Bayo (1994), Jain (2010) and Tischler et al. (1995), and type synthesis of tree topologies can be found in Lee and Tsai (2002) for grasping and manipulation requirements. The dimensional synthesis of the tree topologies has been explored in Simo-Serra et al. (2011), Simo-Serra et al. (2012) and more extensively in Simo-Serra and Perez-Gracia (2014). The synthesis of tree topologies, when applied to wristed multi-fingered hands, allows creating robotic hands for in-palm manipulation tasks, for instance, or complete arm-plus-hand designs.

In this application the interest is to switch from non-dexterous, bimanual manipulation to high-dexterity, single-hand manipulation, where the degree of dexterity needs to be adapted to the kind of task to be performed. In particular, the design of a hand for holding and performing an operation on an object is explored by designing a single three-fingered hand for peeling an orange. The example includes all the steps from motion capture and synthesis to hand implementation and testing in CAD environment.

## 2 In-Hand Manipulation and Dexterity

A possible definition of dexterity in robotic hand manipulation is the capability of changing the position and orientation of the manipulated object from a given reference configuration to a different one, arbitrarily chosen within the and workspace (Bicchi (2000), see also Ma and Dollar (2011)). Human hand has been used for many robotic hand designs, however the human hand is not particularly dexterous for in-palm manipulation, and so are most of the current robotic hands. The dexterity has been investigated in the design of robotic hands starting with the work of Salisbury and Roth (1983) by calculating different metrics related to mobility when holding an object. However, designs with a high dexterity are not widespread, possibly because of the increased complexity in the sensing and actuation.

## 3 Dexterous Hand Design Methodology

Usually for a given task, a large number of topologies for multi-fingered hands are available, and to select the most suited topology, some criteria must be considered. Number of positions and number of fingertips characterize the task, and the

solvability of the hand (see Makhmal and Perez-Gracia 2014) is a constraint in the search. In Tamimi et al. (2016), algorithms have been developed in order to enumerate all possible topologies for a set of user-defined restrictions and a task in the SE(3) group of rigid motion. In addition, mobility and connectivity of the hand-object system is checked for each topology.

Once a topology has been selected, dimensional kinematic synthesis is used to locate the axes corresponding to each joint of the hand, so that each of the end-effectors is capable to perform their designated displacements for the desired task; for details, see Simo-Serra and Perez-Gracia (2014). After the synthesis, post-synthesis optimization helps avoiding self-intersection and controlling the dimensions of the hand.

## 4 Orange Peeler Hand

### 4.1 Motivation

Holding and operating on an object is one of the prime goals for robotic tasks. The desired task is often a very delicate operation that requires a high level of precision, similar to the robots designed for precise surgical operations. One of the very well-known robots in this field is the Da Vinci™ Surgical System. The peeling of a grape placed on a table is demonstrated for this robot as an indication of its precision. The task targeted in this research is a peeling task while holding the object.

### 4.2 Task Definition

The Vicon™ motion capture system is used to capture the task performed by both human hands while holding and operating on the object. It is possible to scale the final hand for the same task on the smaller objects of approximate similar shape.

The targeted task requires two hands: one holds the orange and the other hand performs the cutting. Two fingertips are used to hold the object, while the other hand's end effector cuts through the orange peel. Figure 1 shows the configuration of the markers on thumb and index fingers and on the knife held by the other hand. Orange body and peel were also marked for their use in the intersection avoidance calculations for the final implementation. The system screen monitoring the markers is also shown in Fig. 1.

For the task to be performed by two different hands, the coordinated robot control needs to be added. Using the hand design procedure described in Sect. 3 this task can be achieved by a single hand with three end-effectors.

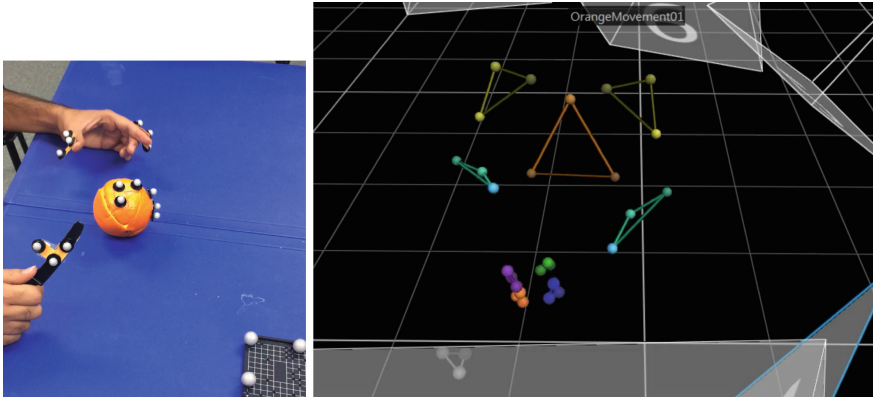


Fig. 1 Setup for the motion capture

### 4.3 Structural Synthesis

The structural synthesis was performed with the method described in Sect. 3. Amongst the resulting topologies, the final tree topology was selected with the parent pointer array  $p = \{0, 1, 1, 1\}$  and joint array  $j = \{1, 3, 3, 3\}$ , that is, a hand with one joint in the wrist and three fingers, each consisting three joints. Two fingers are designated for holding and positioning the orange while the third branch is considered as the cutter branch to peel through the orange. Figure 2 shows the graph representation of the hand.

When grasping an object, and assuming a stable grasp with soft fingers, the overall hand-plus-object system has mobility equal to 4. One of the degrees of freedom

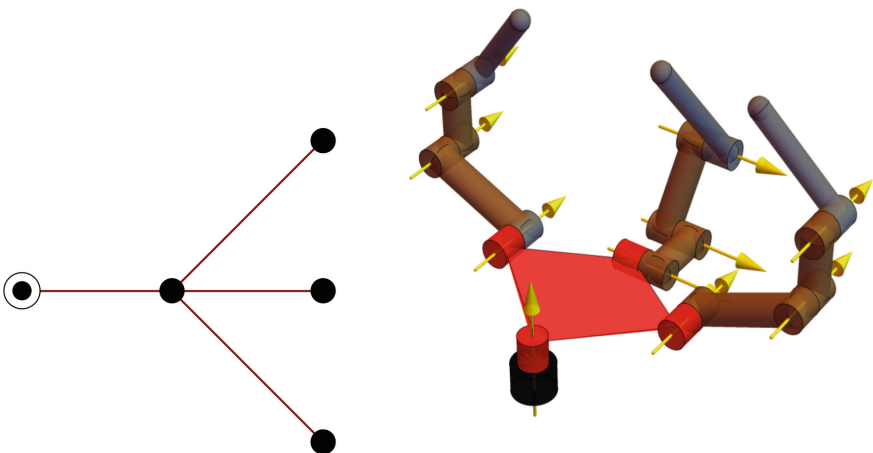


Fig. 2 Selected hand topology for the task and kinematic sketch

corresponds to the wrist rotation, while the other three are in-palm manipulation degrees of freedom. This topology is solvable for a total of  $m = 6$  positions, using the formulas developed in Makhal and Perez-Gracia (2014).

### 4.4 Dimensional Synthesis

For the dimensional synthesis, design equations were created and solved using *Art-TreeKS* (Simo-Serra and Perez-Gracia 2014) for the exact synthesis with 6 positions. The solution presented was obtained after 200 generations with a final error close to  $10^{-12}$ . Figure 3 shows the hand reaching the positions. Also Table 1 presents the



**Fig. 3** The final hand model reaching several positions

**Table 1** Plucker coordinates for the joints of the hand

Axis	Plucker coordinates
$S_1$	$(0.52, -0.81, -0.27) + \epsilon(-46.72, 29.88, -180.89)$
$S_2$	$(0.53, -0.34, -0.78) + \epsilon(-196.78, 19.13, -143.00)$
$S_3$	$(-0.27, 0.96, -0.04) + \epsilon(-20.15, -0.14, 132.52)$
$S_4$	$(0.72, -0.60, 0.34) + \epsilon(-66.52, -375.97, -512.76)$
$S_5$	$(-0.71, -0.57, -0.42) + \epsilon(-50.40, 82.83, -28.12)$
$S_6$	$(-0.98, 0.21, 0.02) + \epsilon(26.32, 90.24, 339.39)$
$S_7$	$(0.48, -0.86, -0.17) + \epsilon(-51.15, -1.03, -136.98)$
$S_8$	$(-0.22, 0.97, -0.11) + \epsilon(-62.32, 6.13, 173.44)$
$S_9$	$(-0.14, -0.93, 0.34) + \epsilon(95.94, -43.65, -78.43)$
$S_{10}$	$(0.52, -0.85, 0.07) + \epsilon(-32.05, -29.03, -113.25)$

resulting Plucker coordinates of the hand joints at the first position. Joint  $S_1$  corresponds to the wrist, joints  $S_2$ ,  $S_3$  and  $S_4$  correspond to the knife and the rest form the two holding fingers.

## 5 Results and Implementation

Link-based optimization is performed on the synthesis results, Yihun et al. (2014) and modelled following the procedure in Hasanzadeh et al. (2015). Performance characteristics being optimized include link length, intersection avoidance of the hand parts with the object and also self-intersection. The model of the optimized hand is presented in Fig. 3.

The motion of the holding fingers of the hand plus the orange system is analyzed by considering pointy fingertips with friction, modelled using the method presented in Staffetti and Thomas (2000), see Fig. 4 (*left*). Using this method, it is easy to impose different restrictions on the relative motion between fingertips and object, by eliminating some of the joints of the equivalent kinematic chain. The in-hand manipulation workspace of the center of the orange is calculated and shown in Fig. 4 using planar friction fingers, which allow only rotation about the normal direction at the contact point, and keeping the wrist fixed (Fig. 5).

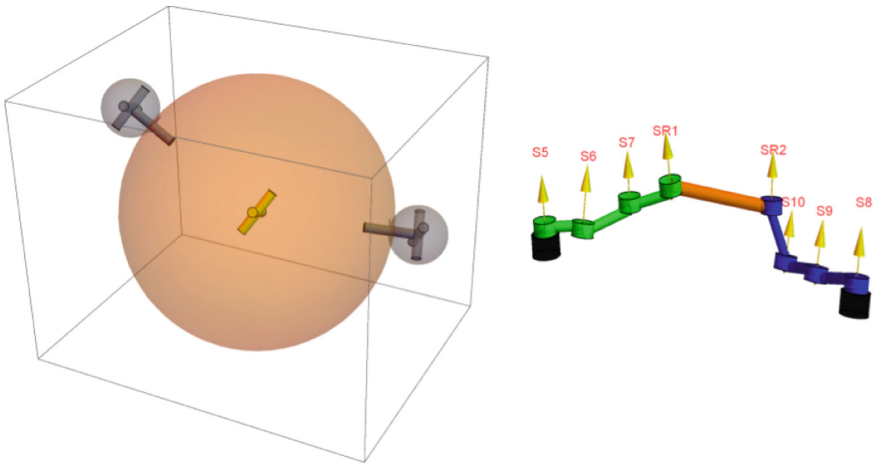
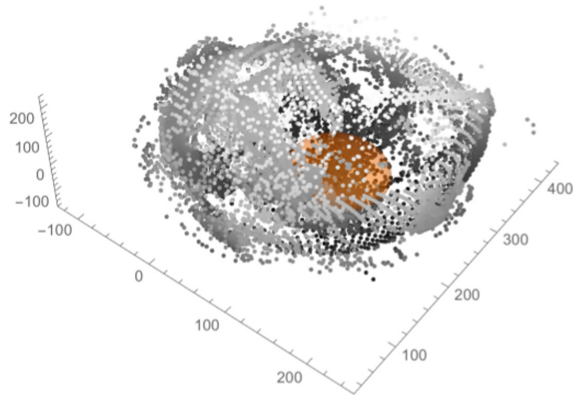


**Fig. 4** The model of the contact between fingertips and orange, *left*, and the resulting closed-chain for in-palm manipulation, *right*

**Fig. 5** The orange in the workspace of the fingers for the selected contact



## 6 Conclusions

In this work, a single, dexterous hand has been created for an orange-peeling task usually requiring two hands. A synthesis process has been used in which a hand topology is selected for a desired number of end-effectors, task positions, and object mobility, and then synthesized and optimized. The implementation and motion analysis are presented. The kinematic and mechanical design of the hand and the analysis of its performance are the first steps to assess the use of dexterous hands for tasks traditionally performed by collaborative manipulators with simpler end-effectors.

## References

- Bicchi, A. (2000). Hands for dexterous manipulation and robust grasping: A difficult road toward simplicity. *IEEE Transactions on Robotics*, 16(6)
- Dauchez, P., Delebarre, X., Bouffard, Y., & Degoulange, E. (1991). Ask description for two cooperative manipulators. In *Proceedings of the American Control Conference*.
- de Jalon, J. G. & Bayo, E. (1994). *Kinematic and Dynamic Simulation of Multibody Systems: The Real-Time challenge*. Verlag: Springer.
- Hasanzadeh, N., He, X., & Perez-Gracia, A. (2015). A design implementation process for robotic hand synthesis. In *ASME International Design Engineering Technical Conferences*.
- Jain, A. (2010). Graph-theory roots of spatial operators for kinematics and dynamics. In *Proceedings of the 2010 International Conference on Robotics and Automation* (pp. 2745–2750), Anchorage, Alaska, USA.
- Lee, J. J., & Tsai, L. W. (2002). Structural synthesis of multi-fingered hands. *Journal of Mechanical Design*, 124, 272–276.
- Liu, Y., Xu, Y., Bergerman, M. (1999). Cooperation control of multiple manipulators with passive joints. *IEEE Transactions on Robotics*, 5(2).
- Ma, R. R., & Dollar, A. M. (2011). On dexterity and dexterous manipulation. In *The 15th International Conference on Advanced Robotics*. Tallinn, Estonia.

- Makhal, A., & Perez-Gracia, A. (2014). Solvable multi-fingered hands for exact kinematic synthesis. In *Advances in Robot Kinematics*. Ljubljana, Slovenia.
- Salisbury, J. K., & Roth, B. (1983). Kinematic and force analysis of articulated mechanical hands. *Journal of Mechanisms, Transmissions and Automation in Design*, 105(1), 35–41.
- Simo-Serra, E., & Perez-Gracia, A. (2014). Kinematic synthesis using tree topologies. *Mechanism and Machine Theory*, 72C, 94–113.
- Simo-Serra, E., Moreno-Noguer, F., & Perez-Gracia, A. (2011). Design of non-anthropomorphic robotic hands for anthropomorphic tasks. In *Proceedings of the 2011 ASME International Design Engineering Technical Conferences, IDETC-CIE*. Washington D.C., USA.
- Simo-Serra, E., Perez-Gracia, A., Moon, H., & Robson, N. (2012). Design of multi fingered robotic hands for finite and infinitesimal tasks using kinematic synthesis. In *Advances in Robot Kinematics*. Innsbruck, Austria.
- Staffetti, E., & Thomas, F. (2000). Analysis of rigid body interactions for compliant motion tasks using the grassmann-cayley algebra. In *Proceedings of the 2000 IEEE/RSJ International Conference on Intelligent Robots and Systems*.
- Sun, D., & Mills, J. K. (2002). Adaptive synchronized control for coordination of multirobot assembly tasks. *IEEE Transactions on Robotics*, 18(4).
- Tamimi, A., Perez-Gracia, A., & Pucheta, M. (2016) Structural Synthesis of Hands for Grasping and Manipulation Tasks, *Advances in Robot Kinematics*, Grasse, France, June 27–30.
- Tischler, C. R., Samuel, A. E., & Hunt, K. H. (1995). Kinematic chains for robot hands—1. orderly number synthesis. *Mechanism and Machine Theory*, 30(8), 1193–1215.
- William, W., Harrison, R. L., & Soloway, D. (1997). Shared control of multiple-manipulator, sensor-based telerobotic systems. In *Proceedings of the 1997 IEEE International Conference on Robotics and Automation*, Albuquerque, NM, April 20–25.
- Yihun, Y., Bosworth, K., & Perez-Gracia, A. (2014). Link-based performance optimization of spatial mechanisms. *Journal of Mechanical Design*, 136(12).



# Facial Expression Design for the Saxophone Player Robot WAS-4

Kei Matsuki, Keisuke Yoshida, Salvatore Sessa, Sarah Cosentino,  
Keiko Kamiyama and Atsuo Takanishi

**Abstract** The implementation of strategies for intuitive and natural communication between robots and humans, depending on the specific situation, is becoming more and more important. Intuitive and human-like communication patterns for human-robot cooperation will ease communication cognitive load and allow the user to better focus on the task at hand. This work presents a basic facial expression system for a humanoid robot saxophonist, allowing the robot to change its expression during a musical performance to both send specific cues for synchronization to a partner human player, and also add emotional emphasis to the performance, as human players naturally do.

---

K. Matsuki · K. Yoshida · S. Sessa (✉) · S. Cosentino · K. Kamiyama  
Faculty of Science and Engineering, Waseda University, Tokyo, Japan  
e-mail: s.sessa@aoni.waseda.jp

K. Matsuki  
e-mail: kei\_matsuki@asagi.waseda.jp

K. Yoshida  
e-mail: unbacked-yossey@toki.waseda.jp

S. Cosentino  
e-mail: sarah.cosentino@aoni.waseda.jp

K. Kamiyama  
e-mail: kaguya009@yahoo.co.jp

A. Takanishi  
Department of Modern Mechanical Engineering, Waseda University, Tokyo, Japan  
e-mail: contact@takanishi.mech.waseda.ac.jp

A. Takanishi  
Humanoid Robotics Institute, Waseda University, Tokyo, Japan

# 1 Introduction

Music is a very complex form of communication among humans and musical performances of bands, where different layers of exchanges take place simultaneously, are exquisite examples of how humans interact by using sound and nonverbal cues to synchronize, and convey different cognitive and emotional information to different parties. In particular, musicians use specific gestures and facial expressions to communicate with other partners information about the music such as tempo, mood, metric. In addition, empathetic body language and facial expressions are often used by players to convey and enforce emotions evoked by music to the audience and the other partners. Kawase suggested that when the player and the audience interact in the music space the visual communication is largely used (Kawase et al. 2007). In particular, musicians express tempo with body oscillations and mood with facial expressions and gaze. A robot can be used as a perfect testbed for validating models of interaction among musical performers and to measure how non-verbal cues and music influence the feeling of the audience during a musical performance. There are already several studies on interactive musical robots that explore how the overall performance experience influences audience. The electronic organ player robot WABOT-2 (WAseda roBOT-2) (Kato et al. 1987) can play the instrument faster than any human, so it can reproduce impeccably musical pieces that take years to master. In addition, it has basic interaction skills, mostly for self-introduction. The piano-player Teotronico and the Toyota's Violinist robots are anthropomorphic musician robots that can use empathetic body language in the piece interpretation. Shimon and Haile (Hoffman and Weinberg 2010; Weinberg et al. 2005) are two drummer robots that react to sound produced by a human player in a creative duet. The humanoid flutist robot WF-4RVI (Waseda Flutist No.4 Refined VI), and more recently the humanoid saxophonist robot WAS-3 (WAseda Saxophonist No. 3), are particularly sophisticated among the others music robots because they can play standard wind instruments by a complex combination of soft materials and mechanisms mimicking the human functions (Petersen et al. 2009; Solis et al. 2007). Furthermore, several studies of human-robot interaction have been performed with these platforms to explore and validate models of musical interaction and improvisation (Cosentino et al. 2014; Petersen et al. 2010). In this paper, we describe the design of an iconic facial expression mechanism for WAS-4 (WAseda Saxophonist No. 4) based on observations of human saxophonists during performances. We studied then how this facial expression mechanism can be used to convey emotions related to the musical performance to enrich the overall audience experience. In particular, we performed experiments with different facial expressions and we analyzed the audience perception response in terms of moods and human similarity. This paper is organized as follow: in Sect. 2 we describe WAS-4 and its main features; in Sect. 3 we describe the methods use and the experiments performed to select desired facial expressions and refine the design of the facial expression mechanism, and the mechanism in

detail. Section 4 shows the results of the evaluation experiment on the generation of facial expression linked with musical performance. Finally, Sect. 5 presents the conclusions and future works on the subject.

## 2 Humanoid Saxophonist Player Robot WAS-4

WAS-4 is a saxophonist humanoid robot. It has been designed based on the human characteristics, especially the parts involved in the instrument playing (oral cavity, lips, and fingers). Its dimensions are 30 % larger than an average human. Fig. 1 shows

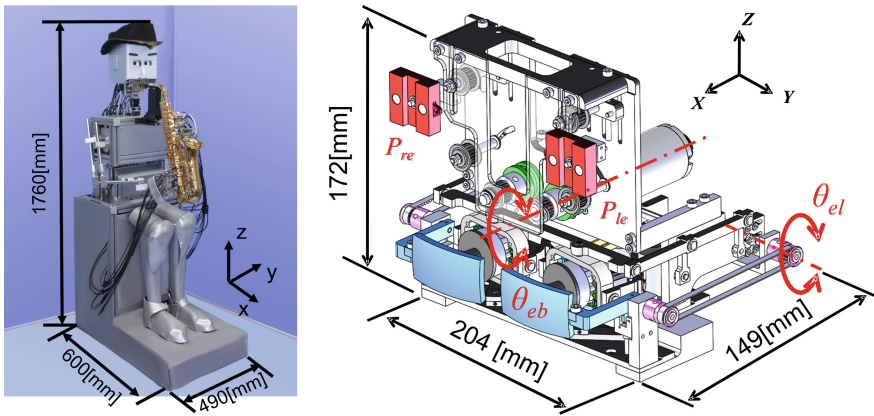


**Fig. 1** WASeda Saxophonist No. 4 (WAS-4) and its facial expression mechanism:  $P_{le}$ ,  $P_{re}$ : coordinates of left and right eyebrow,  $\theta_{eb}$ : rotation angle of the eyebrow motor,  $\theta_{el}$ : rotation angle of the left eyelid motor

**Table 1** WAS-4 Specifications

Function	Body parts	Number of DoF
Sound production	Lips	2
	Oral cavity	1
	Tongue	1
	Lung	2
Key stroke	Left hand	8
	Right hand	11
Posture	Hip	1
Facial expression	Gaze	2
	Eyebrow	1
	Eyelid	2
Total		31

an overall view of the WAS-4 and its new facial expressions mechanism. Table 1 shows the main functions of the robot, the corresponding mimicked human body parts and the relative Degrees of Freedom.

### 3 Method

#### 3.1 *Design and Development of the Facial Expressions Mechanism*

A pre-existing constraint of the design was to maintain unchanged the gaze mechanism. Furthermore, to avoid mechanism-generated noise that could influence the musical performance, we opted for an implementation with direct drive, instead of gears. Based on these specifications, we investigated the motions that the mechanism should reproduce. We focused on the upper face expressions, especially eyebrows and eyelid movements, because the mouth is used for playing the sax and the lower face is partially hidden by the instrument.

#### 3.2 *Facial Expression During Saxophone Performance*

We manually labeled videos of saxophonists during a musical performance to analyze the common facial expression used. 14 videos of different saxophonists playing two popular songs: “Autumn Leaves” and “Take the ‘A’ Train” were selected for a total duration of 57 min. The videos were cut in short segments of one-second length and labeled accordingly to the following movements: *raise one eyebrow*, *raise both the eyebrows*, *frowning*, *close one eyelid*, *close both eyelids*, *open the eyes*, *neutral position*. Figure 2 shows the time each movement is used as a percentage of the total playing time. From these results, we can see that closing both the eyelids and frowning are often used by saxophonists during playing. Upon discussion with a professional saxophonist, we found that raising the eyebrows and winking during a performance might be used as specific signals for the articulations and attacks. Therefore, we deduced that a mechanism for the synchronized motion of eyebrows, for eyebrows raising or frowning; and a mechanism for the independent motion of the eyelids for blinking or winking will be sufficient to generate the most common iconic facial expressions used by a human saxophonist during musical performances.

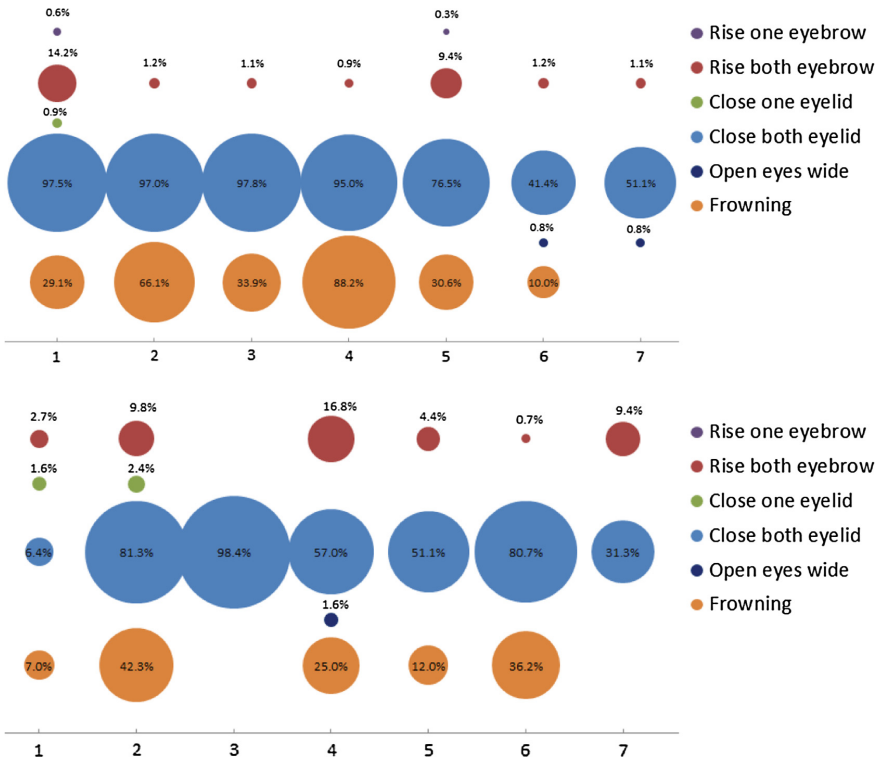


Fig. 2 Movements used during saxophone performances of top: “Autumn leaves” and bottom: “Take the ‘A’ train”, expressed in percentage of the total execution time

### 3.3 Mechanical Movement Specifications

We performed an assessment experiment with 8 subjects (5 Males, 3 Females, age: 21–25) to determine the speed specifications for the eyebrows and the eyelids in each movement. We marked the subject’s eyebrows and eyelids with color markers as shown in Fig. 3, then we video recorded the subject asking them to rise the eyebrows, frown, blink, and wink as fast as possible. From the videos, based on the movement of the markers, we determined the eyebrows and eyelids speed during different movements. We found that the speed specification based on the experiments are:

- eyebrows: (rise) 28.9 mm/s, (frowning) 27.9 mm/s
- eyelids: (both blinking or winking) 55.7 mm/s

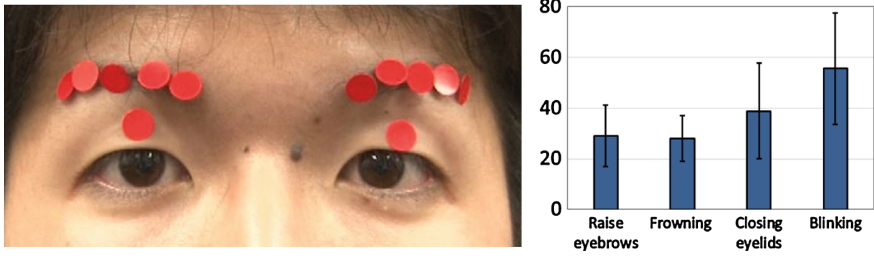


Fig. 3 Experiment setup and results to determine the speed specifications for eyebrow and eyelid

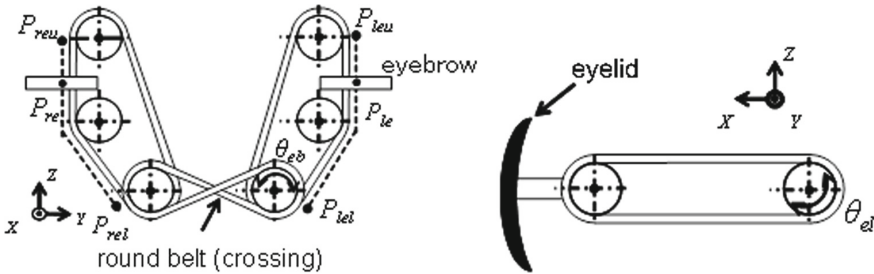


Fig. 4 (left) Eyebrow mechanism.  $P_{leu}$ ,  $P_{lel}$ ,  $P_{reu}$ ,  $P_{rel}$ : linear movement range limits points for respectively the left and right eyebrow, (right) Eyelid mechanism.  $\theta_{el}$ : rotation angle of the left eyelid motor

### 3.4 Design of the Eyebrows and Eyelids Mechanisms

We propose then two distinct mechanisms that comply with the kinematic specifications above. The eyebrows mechanism is achieved with just one active joint and using a brushed motor with direct drive. The belt rotates and raises or lowers simultaneously two magnets, which are coupled with the eyebrows that slide on the outer part of the robot face mask. The eyelids are instead controlled independently and directly, as they are separated from the main body of the robot face mask, adding two separate degrees of freedom. Figure 4(left) and (right) show respectively eyebrows and eyelids mechanisms.

## 4 Experiments and Results

We carried out two evaluation experiment to verify the validity of the implemented facial expression system. In the first experiment, we verified that the system meets the required speed specifications. We used data from the encoders and kinematic parameters to calculate the different movement speed. Table 2 shows the movements

**Table 2** Human and robot motion comparison

Movement	Human speed (mm/s)	Robot speed (mm/s)
Rise eyebrows	28.9	29.4
Frowning	27.9	31.9
Blinking	55.7	64.4

Motion patterns		
Pattern	Eye brow	Eyelids
No.1	neutral	neutral
No.2	raise	open
No.3	raise	close
No.4	frown	close

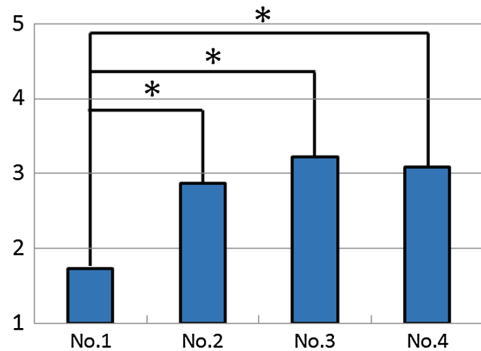


**Fig. 5** Perception experiment results (\* $p < 0.01$  Bonferroni correction)

speed of the mechanism compared to natural human movement. We confirmed that the speed specifications are met.

With the second experiment, we examined how the system affects the audience perception during a musical performance, in particular whether the performance and robot are perceived more natural and human-like. We recorded videos of the robot musical performance, without facial expression, and performing various facial expressions. We uploaded the videos on SurveyMonkey and a total of 28 participants responded to the on-line questionnaire. Subjects were between 20 to 35 y.o. (average 21.8,  $SD = 2.66$ ), 26 males and 2 females. We used an increasing 5-points Likert scale to evaluate naturalness with 1 being least natural and 5 very human-like. Using T-test with a Bonferroni correction, significant differences in the perception of the patterns were found ( $F(3, 84) = 2.71, p < 0.01$ ). From the results, shown in Fig. 5, we can affirm that the robot with a facial expression mechanism is perceived as more natural and human-like.

## 5 Conclusions

In this paper, we described the design and implementation of an iconic facial expression mechanism for WAS-4 (WAseda Saxophonist No. 4) based on observations of human saxophonists during performances, and we assessed the perception of audience in terms of naturalness and human-likeness of the facial expression able robot.

Results show that the robot able to perform facial expressions -albeit basic- is perceived as more natural. Future works in this direction will be to use these expressions also for synchronization with human partner musicians, and implementing more complex facial expressions to convey emotional empathy during a musical performance.

**Acknowledgments** The authors would like to express their thanks to the General Directorate for Cultural Promotion and Cooperation for its support to RoboCasa; Tokyo Womens Medical University/Waseda University Joint Institution for Advanced Biomedical Sciences (TWIns); and International Center for Science and Engineering Programs (ICSEP) of Waseda University. The authors would also like to express their gratitude to Life Performance Research and SolidWorks Corp for their support to the research.

## References

- Cosentino, S., Petersen, K., Lin, Z., Bartolomeo, L., Sessa, S., Zecca, M., & Takanishi, A. (2014). Natural human robot musical interaction: understanding the music conductor gestures by using the WB-4 inertial measurement system. In *Advanced Robotics* (pp. 1–12).
- Hoffman, G., & Weinberg, G. (2010). Shimon: An Interactive Improvisational Robotic Marimba Player. *CHI '10 Extended Abstracts on Human Factors in Computing Systems, CHI EA '10* (pp. 3097–3102). New York, NY, USA: ACM.
- Kato, I., Ohteru, S., Shirai, K., Matsushima, T., Narita, S., Sugano, S., et al. (1987). The robot musician wabot-2 (waseda robot-2). *Robotics*, 3(2), 143–155.
- Kawase, S., Nakamura, T., Draguna, M., Katahira, K., Yasuda, S., & Shoda, H. (2007). Communication channels performers and listeners use: a survey study. In *Proceedings of ICoMCS* (p. 76).
- Petersen, K., Solis, J., Ninomiya, T., Yamamoto, T., Takeuchi, M., & Takanishi, A. (2009). Development of the anthropomorphic saxophonist robot WAS-1: Mechanical design of the lip, tonguing, fingers and air pump mechanisms. In *IEEE International Conference on Robotics and Automation, 2009. ICRA '09* pp. 3043–3048. doi:[10.1109/ROBOT.2009.5152313](https://doi.org/10.1109/ROBOT.2009.5152313).
- Petersen, K., Solis, J., & Takanishi, A. (2010). Musical-based interaction system for the Waseda Flutist Robot. *Autonomous Robots*, 28, 471–488.
- Solis, J., Taniguchi, K., Ninomiya, T., Yamamoto, T., & Takanishi, A. (2007). The waseda flutist robot No. 4 refined IV: enhancing the sound clarity and the articulation between notes by improving the design of the lips and tonguing mechanisms. In *IEEE/RSJ International Conference on Intelligent Robots and Systems, 2007. IROS 2007*.
- Weinberg, G., Driscoll, S., & Parry, M. (2005). Musical interactions with a perceptual robotic percussionist. In *IEEE International Workshop on Robot and Human Interactive Communication, 2005. ROMAN 2005* (pp. 456–461).



# Disturbance Force Generator for Biped Robots

Kenji Hashimoto, Kosuke Nishikawa, Juri Shimizu, Aiman Omer,  
Hun-ok Lim and Atsuo Takanishi

**Abstract** This paper describes the mechanism and control of a disturbance force generator that is able to evaluate disturbance compensation control of biped robots quantitatively. The disturbance generator consists of a base, a motor drive system and a suspension system. In order to apply a disturbance force to a biped humanoid robot, a wire wound on a pulley of the disturbance generator is connected with robot's waist. The effectiveness of the disturbance force generator is verified through several disturbance experiments.

**Keywords** Disturbance force generator • Biped robot • Humanoid robot

---

K. Hashimoto (✉)

Waseda Institute of Advanced Study, Waseda University, Tokyo, Japan  
e-mail: hashimoto@aoni.waseda.jp

K. Nishikawa · J. Shimizu · A. Omer

Graduate School of Science and Engineering, Waseda University, Tokyo, Japan  
e-mail: k-nishikawa@takanishi.mech.waseda.ac.jp

J. Shimizu

e-mail: j-shimizu@takanishi.mech.waseda.ac.jp

A. Omer

e-mail: aimano@aoni.waseda.jp

H. Lim

Faculty of Engineering, Kanagawa University, Yokohama, Japan  
e-mail: holim@kanagawa-u.ac.jp

A. Takanishi

Department of Modern Mechanical Engineering, Waseda University, Tokyo, Japan  
e-mail: takanisi@waseda.jp

K. Hashimoto · H. Lim · A. Takanishi

Humanoid Robotics Institute (HRI), Waseda University, Tokyo, Japan

## 1 Introduction

We have developed a biped humanoid robot named WABIAN-2 as a human motion simulator (Ogura et al. 2003) and a human-carrying biped vehicle named WL-16 (Sugahara et al. 2006). For the practical application, biped robots must compensate for external forces from the environment. Therefore, we also have developed biped balancing controls against external disturbances (Takanishi et al. 1990; Hashimoto et al. 2011). There are also previous works on disturbance compensation control under unknown external forces (Hyon and Cheng 2007; Hyon et al. 2007; Urata et al. 2012). Most, however, do not use quantitative methods to apply disturbing forces. We should use disturbance generator which can control force magnitude and force application timing to evaluate biped balancing controls quantitatively.

In this paper, we report on a device that generates disturbing forces for use in testing balance controls for biped robots. The machine offers a reproducible, quantitative source of external force that can be applied to different kinds of mobile and immobile loads.

## 2 Mechanical Structure of Disturbance Force Generator

### 2.1 Preliminary Analysis

We conducted preliminary experiments to determine the impact force that occurs during a robot-human collision. Because it is difficult to determine impact force by actually colliding with a robot while walking, we created an equivalent system to provide similar results.

We tied a humanoid robot, WABIAN-2 and a human waist with a wire and placed a force sensor between them (see Fig. 1). We also placed a force sensor on a sliding cage to eliminate the influence of gravity applied to the force sensor. The robot and the human weigh 63 kg and 75 kg respectively. Before starting each experiment, we covered the subject's eyes to prevent prediction when the wire would tighten and impact would occur. We programmed the robot to assume a standing position and asked the subject to walk forward. Experimental results show that the collision force was impulsive and its peak value was 380 N. We set the maximum pulling force of a disturbance force generator to 500 N.

### 2.2 Mechanical Design

A disturbance force generator should have the following characteristics, (i) controllable force, (ii) controllable timing of force application, (iii) repetitiveness, and (iv) applied force measurement and registration. We developed a disturbance force generator as shown in Fig. 2 to fulfill the above requirements.

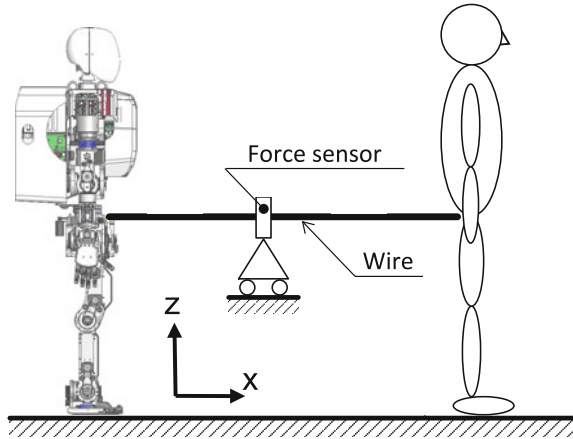


Fig. 1 Preliminary experiments to determine the impact force that occurs during a robot-human collision

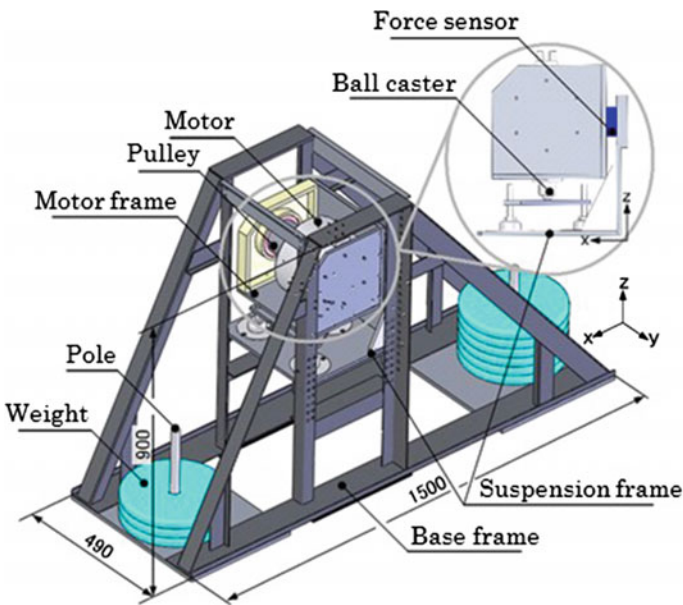


Fig. 2 Disturbance force generator

We selected a direct drive motor (SGMCS-25D, Yaskawa Electric Corporation) because it met the torque requirements and can keep the response time as short as possible (Table 1). We mounted the motor on a motor frame and placed a ball caster between the motor frame and suspension frame. The connection limits the

**Table 1** Specification of direct drive motor

Rated output	Rated torque	Rated current	Rated speed	Max. speed	Rotor moment of inertia
393 W	25 N m	2.7 A <sub>RMS</sub>	150 min <sup>-1</sup>	250 min <sup>-1</sup>	750 kg m <sup>2</sup> × 10 <sup>-4</sup>

motor's vertical motion but allowed free horizontal motion. A force sensor is used to provide a force feedback of the system. We placed the sensor between the motor frame and the vertical wall of the suspension frame, which can allow direct measurement of pulling force. There is an adjustable connection between the suspension frame and the base frame. We designed the adjustable connection so that the height of pulling wire can be adjusted within the range of  $-50$  and  $+100$  mm from the level of robot's pelvis measured while standing of 700 mm. The steel base frame is able to withstand high loads. Poles for weights used to immobilize the machine are on both ends of the base frame. The weight of the machine is about 70 kg and 150 kg, without and with a dummy load respectively.

A steel wire was chosen to connect a robot to the disturbance force generator. One end of the pulling wire is connected to robot's waist. The other end is wound on a pulley directly mounted on the output shaft of the motor.

### 3 Control System for Disturbance Force Generator

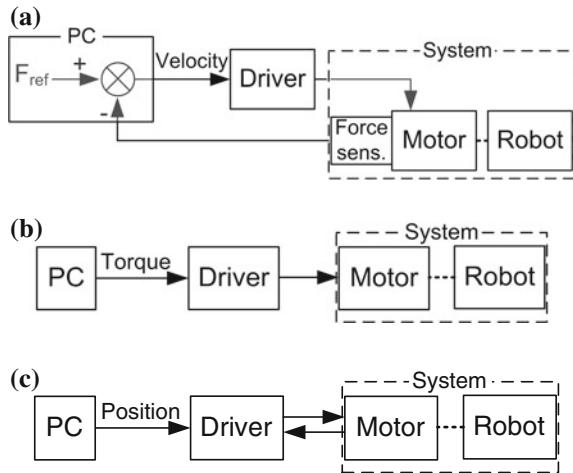
The purpose of the disturbance generator is to generate forces of varying magnitude and direction. The mechanism has only one DoF and a simple control system. Components include the motor, a motor driver, a force sensor, and a personal computer (PC). The motor is a three-phase AC direct drive type with an encoder. There is a SGD V-2R8A01A motor driver that provides three control modes for torque, velocity, and position. A PC with a QNX Neutrino RTOS 6.3 operating system provides high level control.

There are three stages in the control algorithm; (i) tightening a wire, (ii) applying force, and (iii) loosening the wire. During the first stage, we control wire winding speed. Using the velocity control with feedback from the force sensor, we tighten the wire in preparation for the second stage (Fig. 3a).

Second stage in the control algorithm is the phase where we apply the actual disturbance force. We use the open-loop torque control mode of the motor driver and send the torque set-point from the PC (Fig. 3b).

After applying the disturbing force, the control system goes to the final, third stage. We expect that after applying the disturbance, the robot will swing or fall down. Therefore, the motor loosens the wire by unwinding it in order to avoid further external force to the robot (Fig. 3c).

**Fig. 3** Control systems of disturbance force generator.  
**a** Closed-loop force/velocity.  
**b** Open-loop torque control.  
**c** Open-loop position control



### 4 Experimental Tests and Consideration

To evaluate the performance of the disturbance generator, we performed two kinds of experiments to verify force controllability and force reproducibility.

The first test showed that the system was easily entering oscillations and could not keep the wire tight when the load was moving. First we connected the wire of the disturbance force generator directly to the robot. This kind of connection is very stiff, resulting in very low damping ratio. As a consequence the system was difficult to be stabilized and susceptible to oscillations. To solve this problem, we inserted a set of springs between the load and the pulling wire. Furthermore, we limited spring extension by a wire loop (see Fig. 4). During the first experiment, the pulling wire was connected to a heavy, immobilized load and we conducted a set of pulling tests.

The results showed that there was a 50 ms delay in the real system response when the wire was directly connected to the load without spring connection (Fig. 5). The force magnitude was about 45 N greater than that of the desired force. By contrast, when connection was through the spring, there was a 200 ms delay in the system response, and the magnitude of recorded force exceeded that of the desired force by almost 150 N. The difference in delay resulted from significant

**Fig. 4** Spring connection.  
**a** Released condition.  
**b** Tightened condition

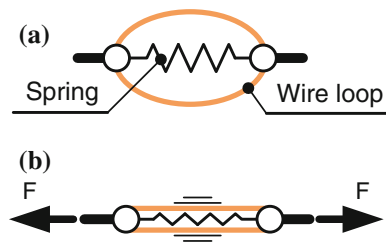
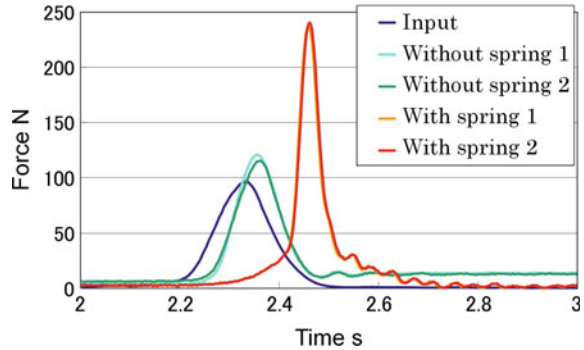


**Fig. 5** Force sensor data measured during pulling an immobilized load



decrease in system’s stiffness caused by the spring. Overshoot was caused by the sudden increase in system’s stiffness, when spring extension limiting wire tightened. As a result of the first experiment, we can find that the wire of the disturbance force generator should be directly connected to the load without a set of springs when a load is immobilized.

Second we connected a humanoid robot, WABIAN-2 to the disturbance force generator through the spring connection because the system was easily entering oscillations and could not keep the wire tight during robot walking (Fig. 6). The robot is 1480 mm tall, weighs 63 kg, and has 41 degrees of freedom (DoF). We programmed the robot to perform forward walking. Pulling experiments examined four different directions (forward, backward, leftward and rightward). There were three experiments for each direction, in which we applied the same pulling force during initial swing, mid-swing and terminal swing phases of gait. We repeated each experiment three times. Under these conditions, we were able to apply the same disturbing force to the robot repeatedly. Figure 7 shows one of experimental results when we added external force from the front side of the robot.

**Fig. 6** Overall system view

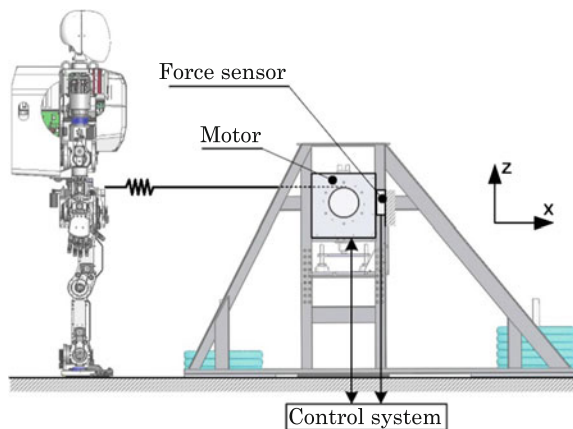
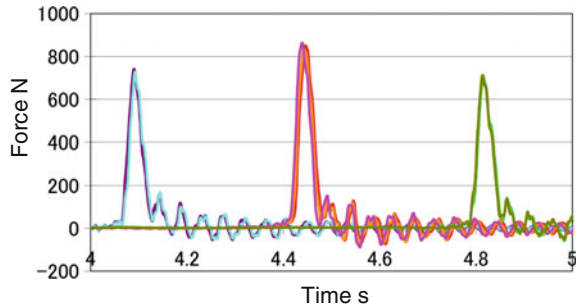


**Fig. 7** Force sensor data during forward pulling experiment



## 5 Conclusions

We presented a disturbance force generator with a direct drive motor to apply disturbing force to a moving humanoid robot. A series of experiments verify that the proposed system can apply an identical force to the robot in an accurately specified time. The force applied to an immobile robot, directly connected to the pulling wire, has nearly the same shape as the reference force, however, the wire of the disturbance force generator tended to vibrate when it is connected to a moving load. Use of a set of springs can inhibit the oscillation, however, it causes a delay in the resultant force, and the wire that limits spring extension causes an overshoot. Further research will focus on these problems of the connections of the pulling wire and other issues concerning force application to moving humanoid robots.

**Acknowledgments** This study was conducted as part of the Research Institute for Science and Engineering, Waseda University; Future Robotics Organization, Waseda University, and as part of the humanoid project at the Humanoid Robotics Institute, Waseda University. It was also supported in part by MEXT/JSPS KAKENHI (Grant Number: 25220005), Toyota Motor Corporation, SolidWorks Japan K.K., and DYDEN Corporation whom we thank for their financial and technical support.

## References

- Hashimoto, K., Lim, H. O., & Takanishi, A. (2011). Disturbance compensation control for biped vehicle. *Advanced Robotics*, 25(3), 407–426.
- Hyon, S. H., & Cheng, G. (2007). Disturbance rejection for biped humanoids. In *Proceedings of the IEEE International Conference on Robotics and Automation* (pp. 2668–2675).
- Hyon, S. H., Hale, J. G., & Cheng, G. (2007). Full-body compliant human-humanoid interaction: balancing in the presence of unknown external forces. *IEEE Transactions on Robotics*, 23(5), 884–898.
- Ogura, Y., Lim, H. O., & Takanishi, A. (2003). Stretch walking pattern generation for a biped humanoid robot. In *Proceedings of the IEEE/RSJ International Conference on Intelligent Robots and Systems* (pp. 352–357).

- Sugahara, Y., Hashimoto, K., Sunazuka, H., Kawase, M., Ohta, A., Tanaka, C., et al. (2006). Towards the biped walking wheelchair. In: *Proceedings of the first IEEE RAS/EMBS International Conference on Biomedical Robotics and Biomechanics* (pp. 781–786).
- Takanishi, A., Takeya, T., Karaki, H., & Kato, I. (1990). A control method for dynamic biped walking under unknown external force. In *Proceedings of the IEEE International Workshop in Intelligent Robots and Systems* (pp. 795–801).
- Urata, J., Nishiwaki, K., Nakanishi, Y., Okada, K., Kagami, S., & Inaba, M. (2012). Online walking pattern generation for push recovery and minimum delay to commanded change of direction and speed. In *Proceedings of the IEEE/RSJ International Conference on Intelligent Robots and Systems* (pp. 3411–3416).



# LARMbot: A New Humanoid Robot with Parallel Mechanisms

Daniele Cafolla, Mingfeng Wang, Giuseppe Carbone  
and Marco Ceccarelli

**Abstract** LARMbot humanoid robot is presented with its peculiar design as based on mechanisms with parallel architecture. The mechanical design is described as motivated by biomimetic inspiration to human anatomy and functionality. The mechanical structure of the main parts are discussed with performance characterization. A prototype is presented with a built solution with low-cost solution and user-oriented operation by using commercial components and 3D printing manufacturing.

**Keywords** Humanoid robots · Torso designs · Biped locomotors · Parallel mechanisms

## 1 Introduction

Humanoid robots, which are designed as directly inspired by human capabilities, are considered to be partners and servants for human beings during daily life (Kemp et al. 2008). Research on humanoid robots has made rapid progress and several humanoid robots have been developed with mobility and operability for performing typical daily tasks in human environments, like ASIMO of Honda (Hirose and Ogawa 2007), WABIAN of Waseda University (Ogura et al. 2006), HRP of AIST/KAWADA (Kaneko et al. 2009), LOLA of Technical University Munich (Buschmann et al. 2012), and HUBO of KAIST (Zucker et al. 2015).

---

D. Cafolla · M. Wang · G. Carbone · M. Ceccarelli (✉)

Laboratory of Robotics and Mechatronics DICEM, University of Cassino  
and South Latium, Cassino, Italy  
e-mail: ceccarelli@unicas.it

D. Cafolla  
e-mail: cafolla@unicas.it

M. Wang  
e-mail: wang@unicas.it

G. Carbone  
e-mail: carbone@unicas.it

Serial mechanisms in humanoids possess large workspace and dexterous maneuverability, which can guarantee the capability of imitating human-like movements. However, they are susceptible to bending at high load and vibration at high speed leading to lack of precision and poor dynamic performance (Sébastien and Bonev 2007). These drawbacks become an issue for the design of a humanoid robot since it requires more sophisticated sensor fusion schemes, model-based control algorithms and powerful driven systems. On the other hand, parallel mechanisms are well known for having better performance in terms of dynamic behaviour, accuracy, payload capability, stiffness so that they have been widely studied both in industry and academia (Ceccarelli 2004; Merlet 2006). Nevertheless, parallel mechanisms also have some drawbacks such as small workspace, complex direct kinematic, and singularity problems, which require a proper selection of mechanisms and optimized mechanical design (Carbone et al. 2009).

Human body is an extremely complex system with several muscles and tendons in each body part that act in parallel to each other to give mobility to the corresponding skeleton (Saladin 2008). With such a biomimetic inspiration a humanoid robot can be designed and operated with a kinematic structure made of several parallel mechanisms as suggested in (Ceccarelli and Carbone 2009). Sellaouti and Ouezhou (2005) have built a prototype called ROBIAN as based on hip and ankle designs with parallel mechanisms. Saltaren et al. (2007) have proposed orientation parallel mechanisms for the neck and shoulder of humanoid robots. Liang and Ceccarelli (2012) have designed a novel waist-trunk system by using parallel mechanisms. At Laboratory of Robotics and Mechatronics (LARM) in Cassino, a new biomimetic inspired humanoid robot, LARMbot, is under development as based on a biologically inspired parallel structures.

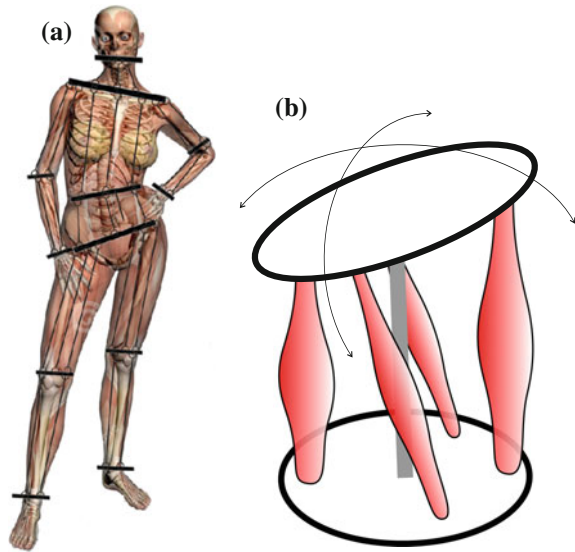
In this paper, a new humanoid conceptual design is described as motivated by an inspiration from design and function of human anatomy. The kinematic structure of a humanoid can be composed by several parallel mechanisms with different design solutions as depending of the body parts they will mimic in functionality and volume. The humanoid prototype LARMbot has been designed assembling CAUTO (CASSINO hUMANOID TORSO), in (Cafolla and Ceccarelli 2015) with the Cassino biped locomotor (Wang and Ceccarelli 2015). The main characteristics of the humanoid are outlined with features for low-cost manufacturing and operation.

## 2 Parallel Architectures in Human Anatomy

Human anatomy can be modeled with skeleton structures that are actuated by muscles acting in parallel as parallel manipulators. This conceptual design is summarized in Fig. 1 with a biomimetic inspiration for different design solutions as depending of the body parts they will mimic in functionality and volume.

Bones provide structural strength to the human frames. They provide support to the organs of the body, to transfer internal and external loads, and thus to perform

**Fig. 1** Models of human anatomy: **a** parallel mechanism for main parts, **b** scheme of muscle actuated parallel mechanism



useful tasks. It is important that the structural strength of a humanoid robot at least matches that of the human frame. The bones of the body are connected together at joints which permit various d.o.f.s (degree of freedom) of many movements of the human body. A considerable simplification can probably be made without significantly affecting its functionality. An example of this simplification concerns the shoulder joint. As the arm is raised, the initial range of movement is facilitated by the rotation of the ball and socket shoulder joint, but the later stages involve movement of the shoulder blade. In a robot, this movement could be performed by simply extending the range of movement of the shoulder joint and keeping the shoulder itself fixed with respect to the spine by using a parallel structure as shown in Fig. 1a. Figure 1b shows a conceptual scheme of the interaction of the two platforms of a parallel mechanism and its d.o.f.s.

In the human body muscles are the actuators that convert chemical energy into mechanical work. They are a form of linear actuators, and are joined to a bone at each end with tendons. They can only operate in tension, and the tensile force is created by muscle contraction. This means that they operate in opposing pairs to give even two-way motion, and this makes the control problem easier.

### 3 The LARMbot

The LARMbot design has been developed by looking at a humanoid structure that is composed by systems for manipulation, locomotion, and payload capability with human-like characteristics. Manipulation system is designed with traditional

anthropomorphic structure of 3 d.o.f.s carrying an artificial hand of five cable-driven articulated fingers. Future developments are under consideration to design the arm with parallel mechanism for larger payload capability. Locomotion system is designed referring to the scheme of Fig. 1b to develop a biped locomotor whose legs have the structure of a 3 d.o.f.s parallel mechanism whose end-effector is the foot plate. Torso system is designed by combining the serial structure of a spine with a cable-driven parallel mechanism as muscle-like actuation system.

The conceptual design have been elaborated on the basis of kinematic design whose solution has given the CAD mechanical structure in Fig. 2. In particular, Fig. 2a shows the CAUTO (CASSino hUMANoid TORso) design (Cafolla and Ceccarelli 2015) that is implemented as torso module in the full LARMbot humanoid in Fig. 2c. Figure 2b shows the Cassino biped locomotor that is designed with a leg structure for translatory motion of the foot. The waist plate contains gearing system to perform turning motion while walking. The Cassino biped locomotor is connected to CAUTO module through the waist plate giving the LARMbot full structure in Fig. 2c.

Most of the components are designed to use commercial parts, such as the vertebra-like joints, and the muscle-like leg actuators, while the frames are designed for low-cost 3D printing manufacturing, such as the vertebrae discs, the shoulders frame, the waist, and foot plates. The design feature can be summarized in with a light structure of 2.8 kg, compact size of  $(972.19 \times 414.60 \times 294.60)$  mm, payload capability of 0.86 kg that is limited by the current arm structure (as 3 kg if considering CAUTO and Biped locomotor only), fairly easy controlled actuation via commercial motors under Arduino control algorithms.

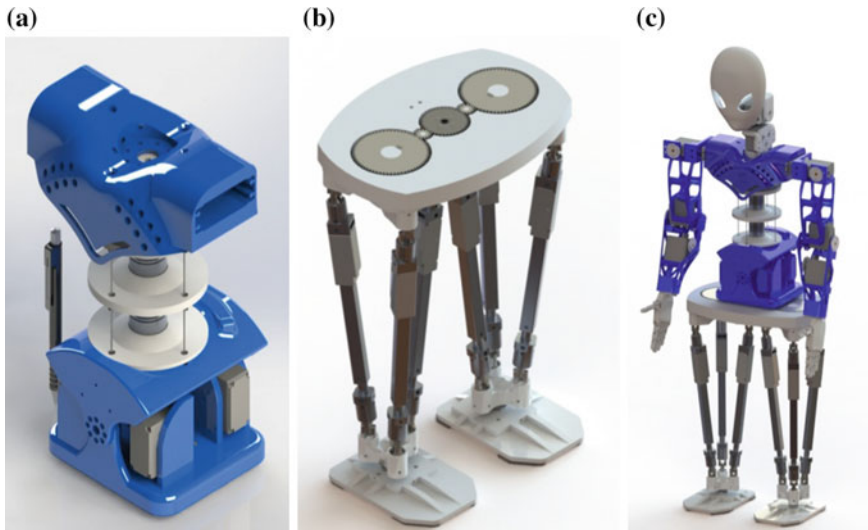


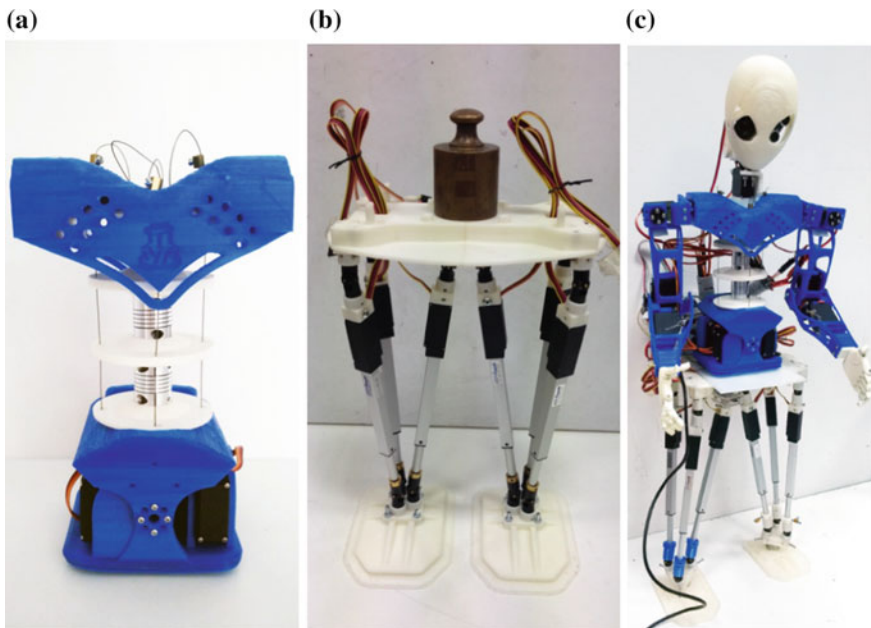
**Fig. 2** A CAD design of the humanoid LARMbot at LARM in Cassino: **a** torso, **b** biped locomotor, **c** full assembly

## 4 Prototype and Testing

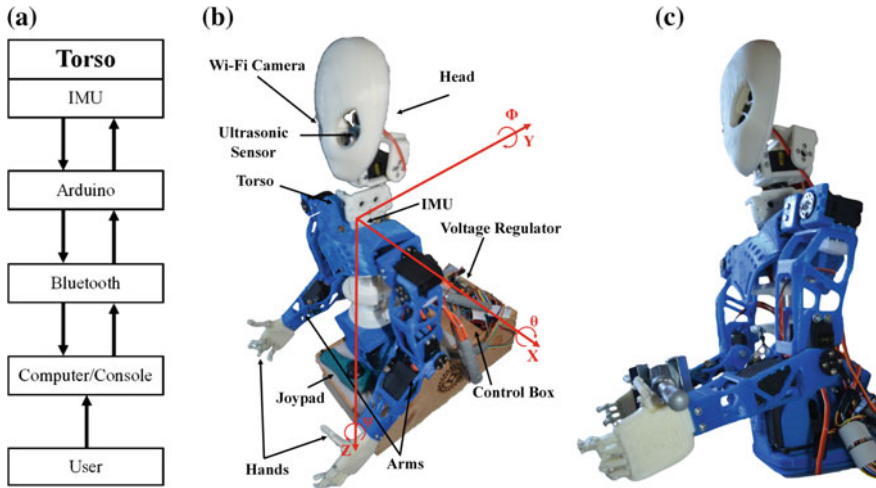
A prototype of LARMbot humanoid has been built as in Fig. 3 following the CAD design solutions in Fig. 2 by using commercial components and 3D printed manufacturing parts. Several tests have been worked out to validate the design features and to characterize the operation performance. Main test results are reported in Figs. 4, 5, 6 and 7.

Figure 4a shows a scheme for the experimental tests with the humanoid torso CAUTO. The torso is powered by a Li-Po battery of 11.1 V–2.2 Ah and is operated through Bluetooth the Arduino boards and its software. An Inertia Measurement Unit (IMU) is placed on the center of the neck along the spine axis to sense significant angles of motion and linear accelerations around the reference axes, Fig. 4b. A current sensor is used to monitor the power consumption. A control box contains 4 Arduino Nano, 4 HC-05 Bluetooth modules and 1 ACS714 current sensor and it is arranged at the bottom of the torso, Fig. 4b.

Tests results are reported in Fig. 5 for lifting a load of 0.86 kg with a motion of 20.40 s. The humanoid torso starts in a standstill position with the load on the arms, Fig. 5a, and then the load is lifted simultaneously by the two arms. In Fig. 4c the lifting test is measured as a smooth motion in angles with few acceleration peaks (less than  $3 \text{ m/s}^2$ ) for a limited power consumption (max 26 W).



**Fig. 3** A prototype of the LARMbot in Casino: **a** torso, **b** biped locomotor, **c** assembly



**Fig. 4** An experiment layout for testing of CAUTO as LARMBot torso: **a** a scheme of the operation control, **b** the laboratory setup, **c** lifting a load

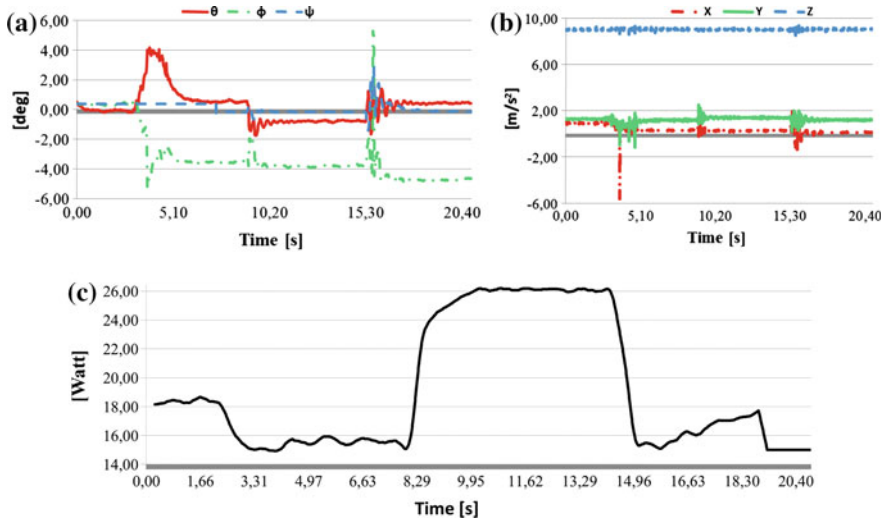


**Fig. 5** Results of the experimental test in Fig. 4c: **a** spine angular displacement, **b** spine acceleration, **c** power consumption

A prototype of the Cassino biped locomotor is built, as shown in Fig. 3b, whose a dynamic simulation is reported in (Wang and Ceccarelli 2015). Figure 6 shows two snapshots during an experimental test and results are shown in Fig. 7.

Experimental results in terms of ground contact forces, power consumption and rotation angles are measured for performance evaluation and design characterization

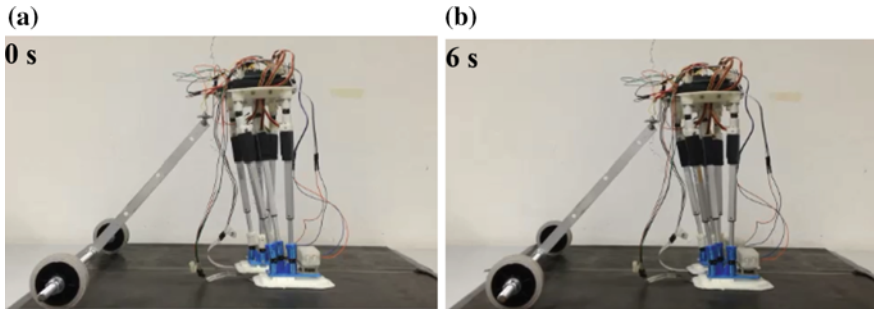


**Fig. 6** Two snapshots of an experimental test of LARMbot biped locomotor as rickshaw: **a** starting configuration; **b** during motion

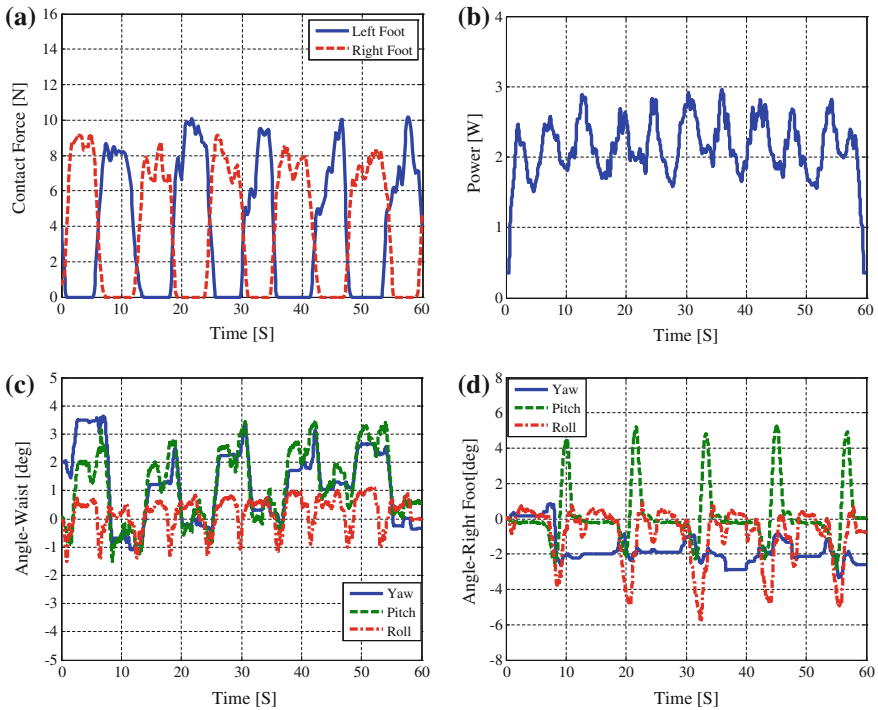


**Fig. 7** Measured results of the experimental test in Fig. 7: **a** ground contact forces; **b** power consumption; **c** angles of waist; **d** angles of right foot

of the built prototype of Cassino biped locomotor. In Fig. 7a, there are one or two minor jumps in each step (max 10.2 N), which are due to the corresponding foot landing impact on the ground and waist swinging. In Fig. 7b, the power consumption is measured with a maximum value of 2.9 and a peak value occurring when

waist is in the middle during swinging from back to front. In Fig. 7c, d, the rotation angles are plotted in terms of yaw, pitch and roll with proper limited ranges. The largest rotation motions of right foot are in pitch and roll when in the swinging phase, while the largest rotation motions of waist are in yaw and pitch when waist swings from back to front.

## 5 Conclusions

The LARMbot humanoid is presented with its peculiar design that is based on a biomimetic inspiration from human anatomy by using parallel mechanisms in torso and leg designs. The mechanical design has been developed in compact and light solution permitting the use of commercial components and 3D printing manufacturing of the parts. The LARMbot prototype has been experienced with basic motions confirming the design features for low-cost, powerful, compact design in human-like tasks. The proposed design structures permit a close-form formulation of kinematics and dynamics so that the control design has been achieved with straightforward algorithms for fairly easy operation programming.

## References

- Buschmann, T., Schwienbacher, M., Favot, V., Ewald, A., & Ulbrich, H. (2012). The biped walking robot Lola. *Journal of the Robotics Society of Japan*, 30(4), 363–366.
- Cafolla, D., & Ceccarelli M. (2015). Design and simulation of a cable-driven vertebra-based humanoid torso. *International Journal of Humanoid Robotics* (in print).
- Carbone, G., Liang, C., & Ceccarelli, M. (2009). Using parallel architectures for humanoid robots. In *Proceeding of the Kolloquium Getriebetechnik*, Aachen, September 16–18 (pp. 177–188).
- Ceccarelli, M. (2004). *Fundamentals of mechanics of robotic manipulation*. Dordrecht: Kluwer Academic Publishers.
- Ceccarelli, M., & Carbone, G. (2009). A study of feasibility for a leg design with parallel mechanism architecture. In *Proceedings of 2009 IEEE/ASME Conference on Advanced Intelligent Mechatronics (AIM 2009)*, Singapore, July 14–17 (pp. 1447–1452).
- Hirose, M., & Ogawa, K. (2007). Honda humanoid robots development. *Philosophical Transaction of the Royal Society*, 365(1850), 11–19.
- Kaneko, K., Kanehiro, F., Morisawa, M., Miura, K., Nakaoka, S., and Kajita, S. (2009). Cybernetic Human HRP-4C. In *Proceeding of 9th IEEE/RAS International Conference on Humanoid Robots (Humanoids 2009)*, Paris, December 7–10 (pp. 7–14).
- Kemp, C., Fitzpatrick, P., Hirukawa, H., Yokoi, K., Harada, K., & Matsumoto, Y. (2008). Humanoid robots. In B. Siciliano & O. Khatib (Eds.), *Springer handbook of robotics* (pp. 1307–1333). Berlin Heidelberg: Springer.
- Liang, C., & Ceccarelli, M. (2012). Design and simulation of a waist–trunk system for a humanoid robot. *Mechanism and Machine Theory*, 53, 50–65.
- Merlet, J. P. (2006). *Parallel robots* (2nd ed.). Dordrecht: Springer.
- Ogura, Y., Aikawa, H., Shimomura, K., Morishima, A., Lim, H. O., & Takanishi, A. (2006). Development of a new humanoid robot WABIAN-2. In *Proceedings of 2006 IEEE International Robotics and Automation (ICRA 2006)*, Orlando, (pp. 76–81).



- Saladin, K. S. (2008). *Human anatomy*. New York: McGraw Hill Higher Education.
- Saltaren, R. J., Sabater, J. M., Yime, E., Azorin, J. M., Aracil, R., & Garcia, N. (2007). Performance evaluation of spherical parallel platforms for humanoid robots. *Robotica*, 25(03), 257–267.
- Sébastien, B., & Bonev, I. (2007). Are parallel robots more accurate than serial robots? *CSME Transactions*, 31(4), 445–456.
- Sellaouti, R., & Ouezdou, F. B. (2005). Design and control of a 3DOFs parallel actuated mechanism for biped application. *Mechanism and Machine Theory*, 40(12), 1367–1393.
- Zucker, M., Joo, S., Grey, M. X., Rasmussen, C., Huang, E., Stilman, M., & Bobick, A. (2015). A general-purpose system for teleoperation of the DRC-HUBO humanoid robot. *Journal of Field Robotics*, 32(3), 336–351.
- Wang, M. F., & Ceccarelli, M. (2015). Design and simulation of walking operation of a Cassino biped locomotor, new trend in mechanism and machine science. *Springer*, 24, 613–621.

# Human-Inspired Humanoid Balancing and Posture Control in Frontal Plane

Vittorio Lippi, Thomas Mergner, Maksymilian Szumowski,  
Magdalena Sylwia Zurawska and Teresa Zielińska

**Abstract** Human balancing can be modeled for the sagittal and frontal planes using double inverted pendulum (DIP) biomechanics representations. The DIP approach has also been used in the DEC (disturbances estimation and compensation) model for balance control of a humanoid robot in the sagittal plane. In this paper, it is implemented on a 14 degrees of freedom humanoid for the frontal plane. Positive results open the possibility to use the DEC concept for a bio-inspired modular control architecture for both the sagittal and the frontal planes.

**Keywords** Human-like posture control · Modular control architecture · Humanoid · Balancing · Frontal plane

## 1 Introduction

Humanoid robots can be used to explore the mechanisms behind human posture and movement control using experiments in real world set-up (Cheng et al. 2007) and repeating human experiments with robots inspired by neurological theories (Mergner et al. 2006, 2009; Hettich et al. 2014).

---

V. Lippi (✉) · T. Mergner  
Neurologische Klinik, Neurozentrum, University of Freiburg,  
Breisacher Straße 64, Freiburg, Germany  
e-mail: vittorio.lippi@uniklinik-freiburg.de

T. Mergner  
e-mail: mergner@uni-freiburg.de

M. Szumowski (✉) · M.S. Zurawska · T. Zielińska  
Faculty of Power and Aeronautical Engineering,  
Warsaw University of Technology, Nowowiejska 24, Warsaw, Poland  
e-mail: mszumowski@meil.pw.edu.pl

M.S. Zurawska  
e-mail: mzurawska@meil.pw.edu.pl

T. Zielińska  
e-mail: teresaz@meil.pw.edu.pl

Various models of human posture control based on sensory input have been proposed. Two main approaches can be identified. The control engineering approach that uses internal model-based methods to describe known postural response criteria (Kooij et al. 1999; Kuo 2005). The second approach is mainly biologically inspired, trying to reproduce human response data in model simulations. In a reductionist biological approach, the Independent Channel, IC model (Peterka 2002) describes human reactive sway behavior as the result of three reflex-like sensory feedback loops (vestibular, joint angle proprioception, vision). Another bio-inspired model, which is used in this work, is the DEC (disturbance estimation and compensation) model (Mergner 2010). It uses multisensory input to estimate external or self-produced disturbances. Although the physical constraints in human and humanoid posture control are similar, the methods in humanoid robotics substantially differ from those in the correspondent human studies. Humanoid balancing research is mostly focused on the solution of the control problem rather than on the recording, analysis, and modeling of movements. Also, humanoid balancing is often based on the zero moment point control or related measures, which try to keep the center of pressure within the base of support under the feet (Goswami 1999). For controlling biped stance without making assumptions about the support surface, the robot profits from the use of an inertial measuring unit (IMU). In this work the bio-derived vestibular sensor presented in (Mergner et al. 2009) is used (Fig. 1).

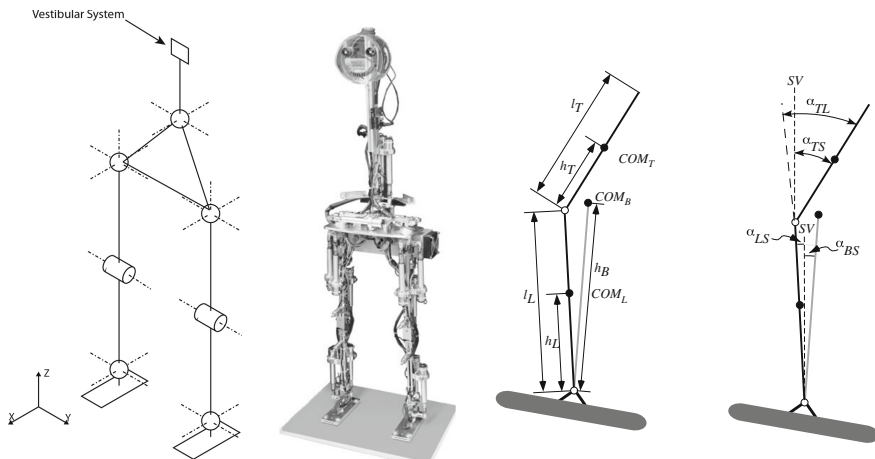


**Fig. 1** The Lucy robot. The diagram on the *left* shows the body segments, the position of the vestibular system, the joints and the 14 DOFs. Every joint is equipped with encoders of joint angle and angular velocity proprioceptive input) and torque. The *middle* shows a picture of Lucy. Actuation was force controlled. The *right* gives the conventions used

## 2 Generalization of DEC Concept to Frontal Plane

### 2.1 The DEC Concept

The DEC model is based on studies of human posture control and movement perception. First developed for the control of a single inverted pendulum body model (Mergner et al. 2006), its application has been extended to a double inverted pendulum (DIP), including hip and ankle joints (Hettich et al. 2014). Furthermore, the DEC control also was generalized for multiple DOFs and tested in simulations (Lippi et al. 2013) and in robotic experiments (Zebenay et al. 2015). This generalization was implemented in terms of a modular control architecture, in which for each DOF a control module is controlling a specific target variable. The variable can be the joint angle, the center of mass of all the body segments above the controlled joint, or the orientation in space of the link supported by the controlled joint. The DEC model uses multi-sensory fusions for internal reconstructions of the external disturbances having impact on body posture (Mergner 2010). It is inspired by neuroscience research on human perception of self-motion and on biped balancing responses to exactly known external disturbances. The concept uses estimates of external stimuli to provide compensatory feedback to the controller.

Figure 2 gives an overview of the DEC controller applied to the frontal plane. There are two control modules: One module for controlling balance of the whole-body COM (with the desired body COM angular displacement  $BS'$  as set point signal commanding actuation in the ankle joints of both legs). The other module serves the control of trunk-space ( $TS$ ) orientation in a pelvic/vertebral column joint on top of the pelvis. Positions are defined as tilt with respect to the gravitational vertical. Each module contains a servo control loop with a PD controller. In order to obtain a given desired trajectory, external disturbances must be compensated. Four external disturbances are acting on the body: (1) Support surface tilt, (2) Support surface translation, (3) Contact forces such as a push against, or a pull on the body, and (4) Field forces such as gravity. The disturbance estimates of 2–4 are fed to the PD controller as angle equivalents. The angle equivalent is computed dividing the disturbance torque by  $mgh$ , where  $m$  is the mass and  $h$  the height of the center of mass of all the links above the controlled joint. The angle equivalent corresponds then to a body lean that would produce in approximation an equivalent torque due to the gravity effect. This form of direct compensation of external disturbances allows the loop gain to be relatively small. The leg-space angle upon support surface tilt is estimated using the vestibular trunk-space angular velocity signal  $\dot{\alpha}_{ts}$  and the proprioceptive trunk to leg velocity signal  $\dot{\alpha}_{tl}$ , in the following form:

$$\hat{\alpha}_{ls} = \int (\dot{\alpha}_{ts} - \dot{\alpha}_{tl}) dt \quad (1)$$

The final estimate involves a velocity detection threshold and a gain factor, both of which were identified in human experiments. In the ankle module, this estimate

is obtained from the vestibular trunk-space angular velocity signal,  $\dot{\alpha}_{ts}$  (down channeled to leg segment), the proprioceptive trunk-leg angular velocity signal,  $\dot{\alpha}_{tl}$  and the leg-foot velocity signal  $\dot{\alpha}_{lf}$  as follows:

$$\hat{\alpha}_{fs} = \int (\dot{\alpha}_{ts} - \dot{\alpha}_{tl} - \dot{\alpha}_{lf}) dt \quad (2)$$

The estimation of the gravitational ankle torque is computed, assuming a small angle approximation for body-COM angle  $\sin(\alpha_{bs}) \approx \alpha_{bs}$ , as:

$$\hat{T}_{A_{grav}} = m_B h_B g \alpha_{bs} \quad (3)$$

Compensating the gravity and balancing the body in the ankle joint module requires the knowledge of COM. The estimate of body-space angle  $\hat{\alpha}_{bs}$  is computed as:

$$\hat{\alpha}_{bs} = \frac{(h_T \alpha_{ts} + l_L \alpha_{ls}) m_T + h_L \alpha_{ls} m_L}{h_B m_B} \quad (4)$$

where  $m_B$  is body mass,  $m_T$  is trunk mass,  $m_L$  is the mass of both legs,  $h_B$  is body COM height,  $h_T$  is trunk COM height,  $h_L$  is leg COM height and  $l_L$  is leg length. Assuming small angular changes,  $h_B$  is set constant.

## 2.2 Lower Body Kinematics

Neglecting knee movements, the lower body standing on the support surface forms a *four bar linkage system* with one degree of freedom. A simplified double inverted pendulum (DIP) model is then used, consisting of a virtual ankle joint (between the two physical feet) connected by a virtual link to the pelvis joint (connecting the trunk and the hip). A similar model has been proposed also for human balancing in the frontal plane in (Goodworth and Peterka 2012).

The virtual ankle joint position  $y_{virtual}$  is expressed as a weighted average of the positions of the two physical ankles

$$y_{virtual} = k y_{left} + (1 - k) y_{right} \quad (5)$$

where  $y_{left}$  and  $y_{right}$  are expressed with respect to the center of the hip. The factor  $k$  ranges from 1 (i.e. the virtual joint coincides with the left ankle) to 0 (i.e. the virtual joint coincides with the right ankle). The value of  $k$  is set arbitrarily. The position of  $y_{virtual}$  defines where the projection of the COM is supposed to be when its inclination,  $\alpha_{bs}$ , is  $0^\circ$ . This representation is convenient to express the weight shift between the legs that would be required to perform a step.

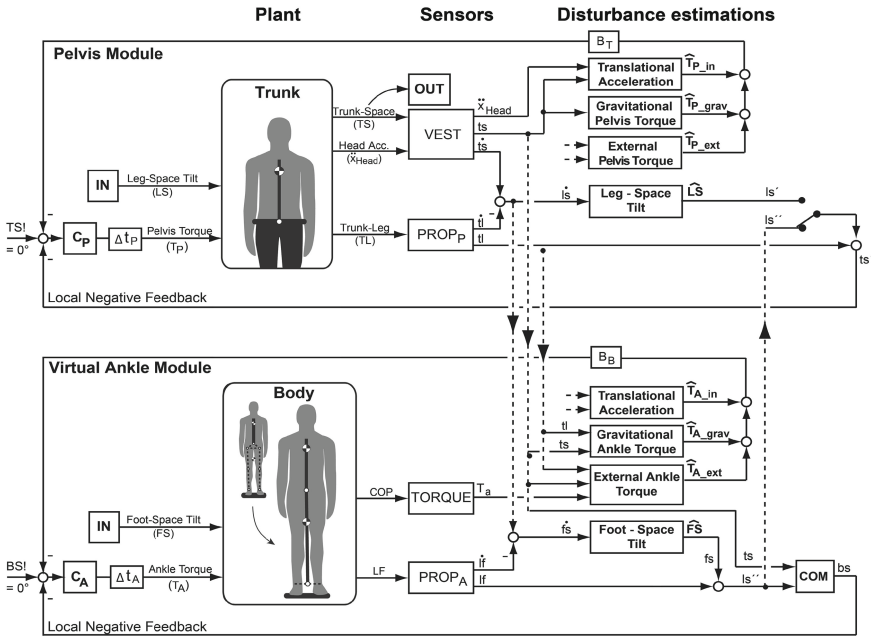


**Fig. 2** DEC control in the frontal plane, scheme adapted from (Hettich et al. 2014). The upper control module stabilizes trunk orientation in space (set point signal  $TS!$ ) in terms of an inverted pendulum based on the pelvic joint. The lower module stabilizes whole-body COM in space ( $BS!$ ), integrating a mapping from the lower limb kinematics also to an inverted pendulum model based on a virtual ankle joint. *Switch* The  $ls$  signal can optionally be up-channeled to the trunk control module from the control module for the legs, reconstructing  $ls$  on the basis of the  $fs$  estimate (Eq. 2). Each control module contains the four disturbance estimators

The DEC module controlling the virtual joint takes as input the position of the COM of the lower body with respect to the virtual joint and the length of the virtual link and its orientation in space. The computation of the COM is based on lower limbs position, assuming that the mass distribution is known. The desired torque for the virtual joint is distributed on the four actuated joints (ankles and hips). The ankle joints are producing only a small part of the torque (~20%). The reason is that due to the relatively short foot length the foot-ground contact may easily be lost in the frontal plane. The control system applied to the frontal plane is shown in Fig. 2.

### 3 Experiments

The control system has been tested on the *Lucy* robotic platform (Fig. 1). The robots construction was inspired by human-like anthropometrics (Winter 2009). The estimators in the controls had time delays of 60 ms. Experiments consisted of performing

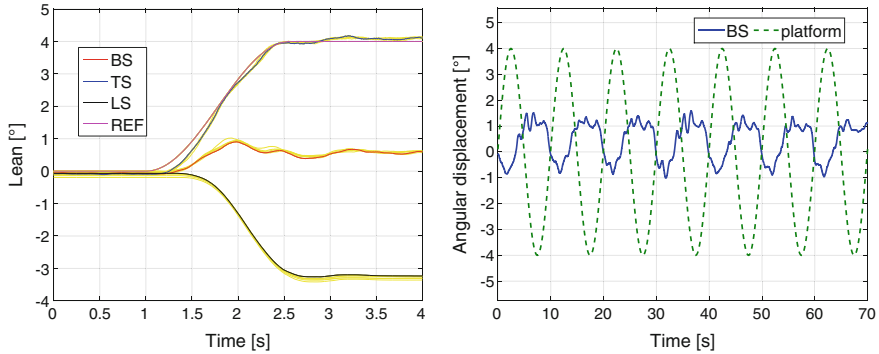


**Fig. 3** Voluntary trunk bending towards *left* (*up*). Angular positions of body COM, *BS*, of trunk in space, *TS*, and of virtual leg in space, *LS*, all with respect to the gravitational vertical (averages,  $n = 8$ ; *yellow* gives variability range; REF, desired trunk in space). The trunk movement is associated to with a compensatory lower body movement to the right, resulting from the total body COM control. *Right BS* response to sinusoidal support surface tilt in the frontal plane (0.1 Hz;  $4^\circ$ ). For a general comparison between human data and robot experiments see (Hettich et al. 2014)

voluntary lateral trunk lean movements (smoothed ramp-like trajectory,  $4^\circ$ ) and of applying support surface tilts in the frontal plane (see Fig. 3). The robot was controlled with the DEC concept in the frontal plane as described above and in the sagittal plane as described before in the Posturob II robot (see (Hettich et al. 2014) also for experimental set up and recordings). Leg rotation in the hips in the horizontal plane was controlled with a proportional derivative feedback on joint position. The control in the sagittal plane was implemented having a module controlling the pelvis joint and one for each of the following pairs of joints: hips, knees and ankles as presented in (Ott et al. 2016). The voluntary movement consisted in a lateral trunk bending, that evoked adjustments in the lower body. The external disturbance consisted in applying a support surface tilt disturbance in the frontal plane, with a frequency of 0.1 Hz and amplitude of  $4^\circ$ .

## 4 Results

The robot controlled with the DEC managed to balance through several trials within the experimental scenarios. The result for the voluntary movement is shown in Fig. 3. The reference signal is a raised-cosine velocity function of  $4^\circ$  amplitude. The response shows the typical coordination behavior emerging from the interaction of the two control modules, as shown in previous experiments for the sagittal plane (Zebenay et al. 2015; Lippi et al. 2013; Hettich et al. 2014; Ott et al. 2016).

The body sway response to support surface tilt is plotted in Fig. 3, right. The trunk was controlled to keep an upright position while the lower part of the body was controlled to balance the whole body COM. The COM sway was about 1° in amplitude.

## 5 Conclusion and Future Work

This work presents an application of the DEC concept for controlling in the frontal plane Lucy's biped stance in the ankle and hip joints. The control proved to be stable for both, external and self-produced disturbances, and it was robust with respect to the time delays in the system. Thus, the work shows that using a double inverted pendulum model allows controlling the balance of a robot's biped stance in the frontal plane. Preliminary tests showed that more DoFs can be included and that balance control in the three planes of space is possible. Further experiments are required to verify that the concept can be extended to more complex behavioral situations and bodily configurations such as lifting a foot to perform a step.

**Acknowledgments** Supported by the European Commission (FP7-ICT-600698 H2R)

## References

- Cheng, G., Hyon, S., Morimoto, J., Ude, A., Hale, J. G., Colvin, G., et al. (2007). CB: A humanoid research platform for exploring neuroscience. *Advanced Robotics*, 21, 10971114.
- Goodworth, A. D., & Peterka, R. (2012). Sensorimotor integration for multisegmental frontal plane balance control in humans. *Journal of Neurophysiology*, 107(1), 1228.
- Goswami, A. (1999). Postural stability of biped robots and the foot-rotation indicator (FRI) point. *The International Journal of Robotics Research*, 18(6), 523533.
- Hettich, G., Assänder, L., Gollhofer, A., & Mergner, T. (2014). Human hipankle coordination emerging from multisensory feedback control. *Human Movement Science*, 37, 123146.
- Kuo, A. D. (2005). An optimal state estimation model of sensory integration in human postural balance. *Journal of Neural Engineering*, 2(3), S235.
- Lippi, V., Mergner, T., & Hettich, G. (2013). A bio-inspired modular system for humanoid posture control. In E. Ugur, E. Oztop, J. Morimoto & S. Ishii (Eds.) Proceedings of IROS 2013 Workshop on Neuroscience and Robotics "Towards a Robot-Enabled, Neuroscience-Guided Healthy Society".
- Mergner, T. (2010). A neurological view on reactive human stance control. *Annual Review Control*, 34, 77198.
- Mergner, T., Huehe, F., Maurer, C., & Ament, C. (2006). Human equilibrium control principles implemented into a biped robot. In *Robot Design, Dynamics, and Control* (Vol. 487, pp. 271–279).
- Mergner, T., Schweigart, G., & Fennell, L. (2009). Vestibular humanoid postural control. *Journal of Physiology-Paris*, 103, 178194.
- Ott, C., Henze, B., Hettich, G., Seyde, T., Roa, M. A., Lippi, V. & Mergner, T. (2016). Comparison of bio-inspired and model-based approaches for posture control of humanoid robots. *Robotics Automation Magazine*.



- Peterka, R. J. (2002). Sensorimotor integration in human postural control. *Journal of Neurophysiology*, 88, 1097-1118.
- van der Kooij, H., Jacobs, R., Koopman, B., & Grootenboer, H. (1999). A multisensory integration model of human stance control. *Biological Cybernetics*, 80, 299-308.
- Winter, D. A. (2009). Anthropometry. In *Biomechanics and Motor Control of Human Movement* (4th ed., pp. 82-106).
- Zebenay, M., Lippi, V., & Mergener, T. (2015). Human-like humanoid robot posture control. In *Proceedings of the 12th International Conference on Informatics in Control, Automation and Robotics* (pp. 304-309). doi:[10.5220/0005542603040309](https://doi.org/10.5220/0005542603040309). ISBN: 978-989-758-123-6.

# Compliant Actuator Dedicated for Humanoidal Robot—Design Concept

Magdalena Sylwia Zurawska, Maksymilian Szumowski  
and Teresa Zielinska

**Abstract** The design concept of compliant actuator dedicated for humanoid robot is presented. Actuator consists of DC motor with serial and parallel springs. Evaluation of motor parameters and selection of springs' parameters was performed considering human motion data. Correctness of proposed design was justified by simulation. The following the reference trajectories for knee joint was investigated. Obtained results confirmed that the proposed concept of compliant actuator performs well with decreasing the motor power demand.

## 1 Introduction

Main goal of the humanoid robots research is to achieve human-like motion. The attention is focused on four main aspects: robots motion synthesis considering the complex models, utilisation of simplified models for motion design, assuring the required movements by the specific of mechanical structure, and obtaining the motion with minimum control but with the support of natural dynamics of mechanical system.

When investigating the human gait its synergy is emphasized. This feature is often adopted in robotics (Hauser et al. 2007). In other investigations complex movements realised by human are decomposed into a sequence of simple ones. This approach uses the so-called motion signatures and is applied for humanoids motion synthesis (Vasilescu and Alex 2002).

---

M.S. Zurawska · M. Szumowski (✉) · T. Zielinska  
Faculty of Power and Aeronautical Engineering, Warsaw University of Technology,  
Warsaw, Poland  
e-mail: mszumowski@meil.pw.edu.pl

M.S. Zurawska  
e-mail: mzurawska@meil.pw.edu.pl

T. Zielinska  
e-mail: teresaz@meil.pw.edu.pl

The methods of motion generation considering simplified models are completely different from those above. The simplified models describe the gait properties using its simplification to the dynamics of inverted pendulum (LIP) (Kajita et al. 2001), spring loaded inverted pendulum (SLIP) (Wensing and Orin 2013), or some extensions of the above (Komura et al. 2005).

Movement generation using the advantages of mechanical design can be considered as a separated method. In (Kondo et al. 2008) a bipedal robot with mechanical parts mimicking bone structure is presented, specifically it can be pelvis (Otani et al. 2013) or foot arch (Hashimoto et al. 2010).

One of the most important properties of musculo-skeletal system is its compliance. Main advantage of properly designed mechanical compliant system is that, that it reduce the amount of required energy and store it in deflected springs. In addition the compliance brings impact absorption what creates possibility for more robust torque control. Compliance in robotic structure can be *passive* or *active*. *Passive* approach rely on introducing the elastic elements or soft materials in not actuated parts (robot's feet) (Hashimoto et al. 2013). Other approach—*active* one—means integrate the elastic components—mostly springs—with actuators.

*Passive walker* robots use only potential energy and natural dynamics to maintain constant movement (McGeer 1990) on the inclined surface. Their movement is similar to human movement. Analysis of passive gaits is a good starting point to design the motion of actuated, energy efficient walking robots moving on horizontal surface. Such example is Cornell Ranger robot (Bhounsule et al. 2012). Here the researchers registered the joint torques during passive walking on the slope and applied it to the bipedal robots moving on flat terrain. It resulted in energy efficient walking.

Presented above concepts have their advantages and disadvantages. In our opinion *Passive walker* concept has significant advantage due to supporting the motion by natural dynamics of a robot. Compliant elements (springs) added to the actuator decrease force impact during foot touch-down, this makes the gait more similar to human one. Moreover, if properly designed, the compliant elements decrease the energy demand from actuators.

Our main aim was to develop compliant actuators for a two legged robot. To achieve such goal, we selected the structure of compliant actuator and specified its parameters, that means the motor parameters and the spring stiffness. Correctness of design was justified by simulations, obtained results are described in this paper.

## 2 Design Considerations on Elastic Actuators

Limbs of walking machines, unlike typical industrial manipulators, meet very different expectations. From one side they must bear a high torque for lifting the whole robot body, from the other side they must move fast enough in the transfer phase. Another challenge in walking machines is to manage the foot impact on the ground, force impulse causes stability problems, brings energy dissipations and, when repeated many times, it can damage the construction.

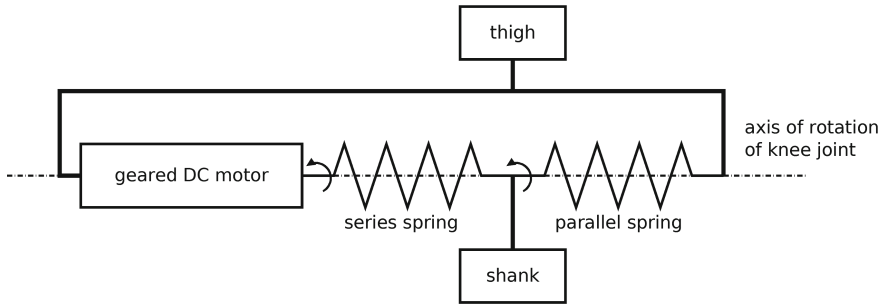


**Fig. 1** Configuration scheme of Parallel-Series Elastic Actuator (PSEA) mounted in the knee joint

Each of those problems is possible to avoid applying dedicated, properly designed actuator. In such actuator the reduction of force impulses is obtained by placing the spring in series to the actuator (Pratt and Williamson 1995), while the additional torque to maintain robot leg over the ground during the transfer phase is delivered by parallel spring reducing the motor torque demand. By adding to the geared DC motor a proper set of springs the power consumption (its mean and peak value) is reduced (Grimmer et al. 2012).

Referring to the above, authors of this paper decided to apply structure with parallel and series springs. First spring—parallel one—is located between the load and the actuator chassis. Second spring—serial one—is located between geared DC motor shaft and the load. Figure 1 represents such compliant scheme mounted in the knee joint.

## 2.1 Parameters Selection

Parameters selection for elastic actuator was done for the knee joint of humanoid robot 1.7 m tall. For this purpose angular trajectories, angular velocities and torque trajectories were taken into account. Those data were obtained from human motion recording (using Vicon system).<sup>1</sup> Human torques were normalised to the robot weight, having in mind that the robot weight differs from the human one. Weight of the robot was assumed to be 10 kg and its height equal to 90 cm what matches analogous human dimension.

Parallel spring parameters were selected considering minimization of energy peaks, parts availability and their price. Selection of torsional spring parameters was done considering a simplified, linear model:

<sup>1</sup>Data used for gait reconstruction were collected at *Pracownia Diagnostyki Narzadu Ruchu* at Warsaw children's hospital *Instytut Pomnik—Centrum Zdrowia Dziecka*. Authors thank to professor Malgorzata Syczewska, the hospital's Director, for her help and support during experiments.

$$M_{ps} = k_{ps} \cdot (\phi_{joint} - \phi_{ps0}), \tag{1}$$

where  $M_{ps}$ —torque due to the spring torsion [Nm],  $k_{ps}$ —parallel spring stiffness [Nm/rad],  $\phi_{joint}$ —joint angle [rad],  $\phi_{ps0}$ —angle in equilibrium position [rad].

Required torque in SEA branch is equal to:

$$M_{SEA} = M_{joint} - M_{ps}, \tag{2}$$

where  $M_{joint}$  is required torque in robot joint. Recorded value of angular velocity in joint  $\dot{\phi}_{joint}$  allows to compute values of power in SEA branch:

$$P_{SEA} = M_{SEA} \cdot \dot{\phi}_{joint}. \tag{3}$$

Selecting the spring (from the list of available in the market) and having in mind the possible amendments of equilibrium position the serial spring with following parameters was selected (applying the formulas (1)–(3)):  $k_{ps} = 5.5 \frac{Nm}{rad}$  and  $\phi_{ps0} = 0.2$  rad. With such parameters the required peak of motor power dropped from 144.4 W (needed power without spring) to 125.7 W (with spring) and the mean value of power dropped appropriately from 13.7 to 12.8 W.

Series spring was chosen basing on analysis presented in (Tsagarakis et al. 2009). It was decided to chose spring with stiffness of  $k_{ss} = 600 \frac{Nm}{rad}$ . Decision was made considering similar application as in mentioned article.

### 3 Simulation Research

#### 3.1 Control System

Virtual robot was modeled in ADAMS environment. Actuating system with compliant actuator was modeled using Matlab/Simulink environment. Simulation structure is presented in Fig. 2.

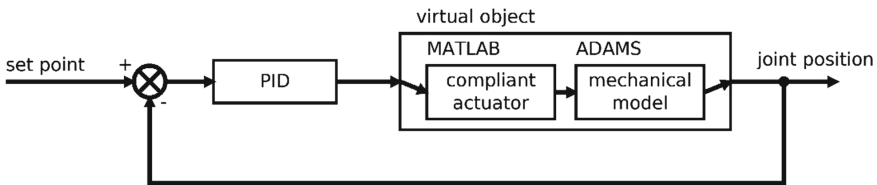
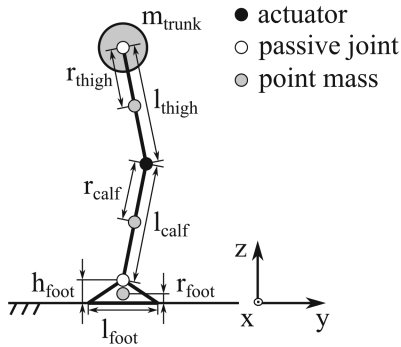


Fig. 2 Structure of simulation model with compliant actuating system



Lengths	Value [m]	Masses	Value [kg]
$l_{thigh}$	0.416	$m_{thigh}$	1.7
$l_{calf}$	0.418	$m_{calf}$	1.3
$l_{foot}$	0.25	$m_{foot}$	0.7
$h_{foot}$	0.066	$m_{trunk}$	2.6
$r_{thigh}$	0.180		
$r_{calf}$	0.181		
$r_{foot}$	0.033		

Fig. 3 Robot model considered in simulation

### 3.2 Developed Model

Model used for simulation is presented in Fig. 3. The compliant actuator is located in knee joint, the hip and ankle joints are passive.

### 3.3 Results

Simulation task was to reproduce the reference trajectories. Trajectories were taken from human motion data. We used angular knee trajectories for support phase and for swing phase.

Reference and obtained knee angular trajectories in support phase are shown in the Fig. 4(a). Reference and obtained knee angular trajectories in swing phase are

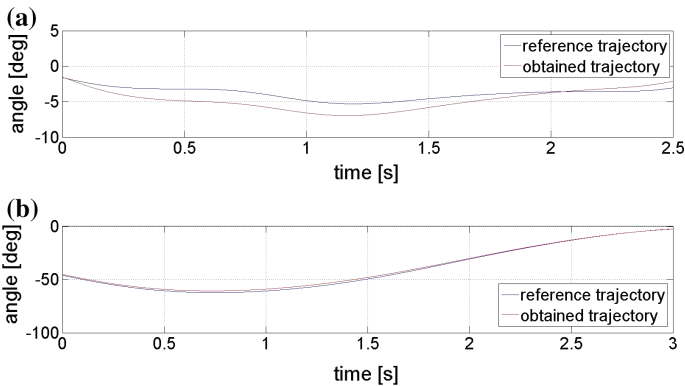
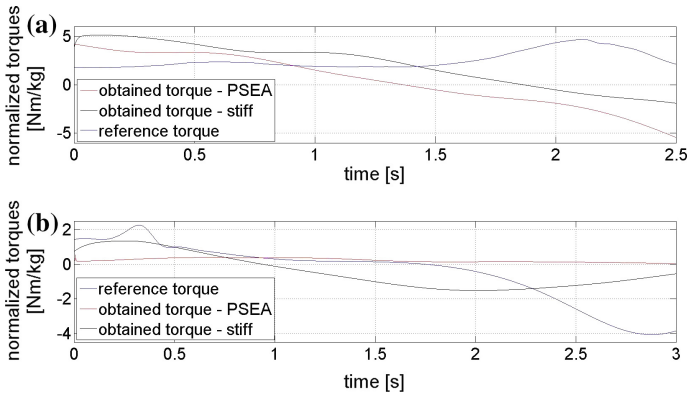


Fig. 4 Knee joint trajectories for the robot with compliant actuator (red) and the human trajectories (blue): a leg support phase, b leg transfer phase



**Fig. 5** Normalized knee joints torques in transfer phase: obtained with PSEA (red), obtained with stiff actuator (black) and human trajectories as the reference (blue): **a** leg support phase, **b** leg transfer phase

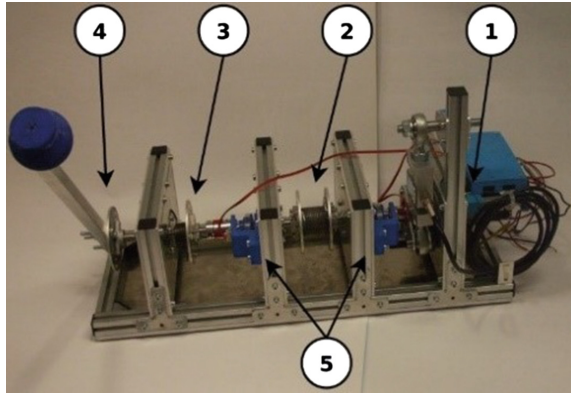
shown in the Fig. 4(b). As it can be noticed angular trajectory in transfer phase is more accurately reproduced with comparison to the trajectory in stance phase, the reason is that the PID controller parameters were tuned for the leg transfer phase. Maximum deviation of obtained and reference trajectory is about  $2^\circ$ . PID controller was chosen as a simple proof of algorithm concept.

Torques obtained in simulations (red), normalized by dividing by weight of a robot, are shown in the Fig. 5a (support phase) and Fig. 5b (transfer phase). Human joint torques (blue) are shown as the reference. The torque trajectories obtained with traditional (stiff) actuator are also demonstrated. For the compliant actuator with PID control the torque trajectories are smooth. The shape of obtained torques and human torques are not identical because the model of the robot is simplified comparing to human body and also the actuators differ from the biological muscles. Despite of the above the torque trajectories justify the advantage of compliant actuator over the traditional actuator (DC motor), the magnitude of torques obtained with compliant actuation is smaller.

## 4 Conclusion and Future Works

The results shown above confirmed that the model of compliant actuator is correct and selected parameters are sufficient. Simple control with PID controller can perform well enough, but for real implementation more advanced control will be considered (e.g. predictive or flatness based control). The prototype of compliant actuator is currently tested in the test bed Fig. 6. The future work will focus on the development of robot prototype with proposed compliant actuators.

**Fig. 6** Test bed for compliant actuator: 1—geared DC motor, 2—series spring, 3—parallel spring, 4—load and 5—absolute encoders



## References

- Bhounsule, P. A., Cortell, J., & Ruina, A. (2012). Design and control of ranger: an energy-efficient, dynamic walking robot. In *Proceedings of the Fifteenth International Conference on Climbing and Walking Robots and the Support Technologies for Mobile Machines* (pp. 441–448).
- Grimmer, M., Eslamy, M., Gleich, S., & Seyfarth, A. (2012). A comparison of parallel-and series elastic elements in an actuator for mimicking human ankle joint in walking and running. In *IEEE International Conference on Robotics and Automation*.
- Hashimoto, K., Takezaki, Y., Hattori, K., Kondo, H., Takashima, T., Lim, H., et al. (2010). A study of function of the human's foot arch structure using biped humanoid robot. In *IEEE/RSJ International Conference on Intelligent Robots and Systems* (pp. 2206–2211).
- Hashimoto, K., Motohashi, H., Takashima, T., Lim, H., & Takanishi, A. (2013). Shoes-wearable foot mechanism mimicking characteristics of human's foot arch and skin. In *Proceedings of the 2013 IEEE International Conference on Robotics and Automation* (pp. 678–683).
- Hauser, H., Neumann, G., & Ijspeert, A. J. (2007). Biologically inspired kinematic synergies provide a new paradigm for balance control of humanoid robots. In *IEEE-RAS International Conference on Humanoid Robots* (pp. 73–80).
- Kajita, S., Kanehiro, F., Kaneko, K., Yokoi, K., & Hirukawa, H. (2001). The 3D linear inverted pendulum mode: A simple modeling for a biped walking pattern generation. In *IEEE/RSJ International Conference on Intelligent Robots and Systems* (pp. 239–246).
- Komura, T., Nagano, A., Leung, H., & Shinagawa, Y. (2005). Simulating pathological gait using the enhanced linear inverted pendulum model (pp. 1502–1513).
- Kondo, H., Morishima, A., Ogura, Y., Momoki, S., Shimizu, J., Lim, H., et al. (2008). Algorithm of pattern generation for mimicking disabled person's gait. In *IEEE RAS/EMBS International Conference on Biomedical Robotics and Biomechanics* (pp. 724–729).
- McGeer, T. (1990). Passive dynamic walking. *The International Journal of Robotics Research*.
- Otani, T., Iizuka, A., Takamoto, D., Motohashi, H., Kishi, T., Kryczka, P., et al. (2013). Algorithm of pattern generation for mimicking disabled person's gait. In *Proceedings of the 2013 IEEE International Conference on Robotics and Automation* (pp. 659–664).
- Pratt, G. A., & Williamson, M. M. (1995). Series elastic actuators.
- Tsagarakis, N. G., Laffranchi, M., Vanderborght, B., & Caldwell, D. G. (2009). A compact soft actuator unit for small scale human friendly robots (pp. 4356–4362).



- Vasilescu, M., & Alex, O. (2002). Human motion signatures: Analysis, synthesis, recognition. In *International Conference on Pattern Recognition* (pp. 456–460).
- Wensing, P. M., & Orin, D. E. (2013). High-speed humanoid running through control with a 3D-slip model. In *IEEE/RSJ International Conference on Intelligent Robots and Systems* (pp. 5134–5140).

**Part VII**  
**Service Robots**

# Design of a 3-UPS-RPU Parallel Robot for Knee Diagnosis and Rehabilitation

Pedro Araujo-Gómez, Miguel Díaz-Rodríguez, Vicente Mata, Angel Valera and Alvaro Page

**Abstract** Nowadays, rehabilitation robots represent a field in which a variety of robotic devices have been proposed. One example of such devices is lower-limb rehabilitation robots. Specifically, the knee joint is one of the joints whose rehabilitation is foreseen as a potential task for a robot device. This paper describes the design of a robot for knee diagnosis and rehabilitation. First, we established the design specification by studying the mobility needed at the robot's end-effector to deal with diagnosis and rehabilitation treatments for knee injuries. The analysis led us to conclude that 4° of freedom (DoF), two translation (2T) and two rotational (2R), are needed in order to meet the design specifications. After that, we chose a parallel robot with a 3-UPS/RPU architecture from several conceptual designs of 4 DoF (2T2R) parallel robots. For the chosen robot, we developed the inverse kinematic model, and also we established the preliminary dimensions of the robot. Through simulations, we found the workspace of the robot showing that its end-effector is able to follow a prescribed task taken from studying the leg motion. Finally, we built a prototype, which is currently undergoing dynamic modelling, parameter identification and control design stages.

---

P. Araujo-Gómez (✉) · M. Díaz-Rodríguez (✉)  
Facultad de Ingeniería, Departamento de Tecnología y Diseño,  
Universidad de los Andes, Mérida, Venezuela  
e-mail: pfaraujo@ula.ve

M. Díaz-Rodríguez  
e-mail: dmiguel@ula.ve

V. Mata (✉)  
Centro de Investigación en Tecnología de Vehículos,  
Universidad Politécnica de Valencia, Valencia, Spain  
e-mail: vmata@ula.ve

A. Valera  
Departamento de Ingeniería y Sistemas y Automática,  
Universidad Politécnica de Valencia, Valencia, Spain  
e-mail: giuprog@isa.upv.es

A. Page  
Grupo de Tecnología Sanitaria del IBV, CIBER, Valencia, Spain

## 1 Introduction

Robot design has recently expanded into other non-traditional fields, mainly due to the emerge of new needs and demands; for instance, service robots addressing human and social needs (Alcocer et al. 2012). In the service robot field, rehabilitation robots are one such kind whose design and implementation focus on reducing the physical therapist's work, increasing the length of rehabilitation exercises, gathering information on the status of the patients recovery and, also enabling treatments to be done via teleoperation (telerobotics). However, the available devices are expensive and need appropriate protocols for therapy (Díaz et al. 2011), although some studies have reported evidence of the greater effectiveness of robotic therapy, as well as clear benefits in terms of reducing costs and the physical effort of the therapist (Alcocer et al. 2012). Most of the devices that have been developed focus on rehabilitation, without considering the task of diagnosis. In this respect, studies have shown that rehabilitation robots have great potential in term of precise diagnosis of the patient's injury, and they can also provide quantitative measures of the patient's recovery (Saglia et al. 2010). Diagnostic devices that are capable of performing rehabilitation tasks represent a potential field of research.

The various rehabilitation devices that have been developed differ in terms of the kind of treatment they focus on (Díaz et al. 2011). One of the major types of devices that has been proposed is the stationary type with many commercial and research prototypes having been developed. Some of them have undergone a great deal of development and others are basically still at an early stage. Yaskawa Electric produced a serial type robot for rehabilitation of the lower extremity called the TEM LX2 (Sakaki 1999), which makes it possible to apply exercises that are usually controlled by a trained therapist. Akdoğan and Adli (2011) developed a stationary device for rehabilitation of the knee with the ability to collect information about forces and positions during therapy. The LAMBDA project developed by Bouri et al. (2009) consists of a robot with 3° of freedom (DoF) with one rotational (1R) and two translational (2T) motions. The robot provides motion to the lower extremity in the sagittal plane, and its advantage is that it can be used for training in sports activities. Bradley (2009) developed a device that provides motion in the sagittal plane, the initial design of the robot is based on 2-DoF, but later the robot was modified to include 4-DoF. In addition, the device can be operated remotely; for instance, it can be used at home while the therapist can be in another place. All the above mention devices have a complex configuration and are task specific.

A wide variety of devices for knee rehabilitation have been proposed, but devices for the diagnosis of knee injuries, on the other hand, have barely been studied. We are interested in developing a robot that can carry out both tasks: rehabilitation and diagnosis. Therefore, the article presents the design of a robotic device based on a parallel robot configuration for knee diagnosis and rehabilitation. The next section presents the conceptual design of the robot including a review of the some of the current parallel robots accomplishing the required design specification. Section 3 presents the kinematic analysis of a 4-DoF robot. Section 4 presents the workspace

of the proposed robot, including a task in which the end-effector is able to follow a prescribed trajectory taken from studying the leg motion. Finally, the conclusions and ongoing research are presented.

## 2 Conceptual Design

### 2.1 Design Specification

Two members of the multidisciplinary team involved in the project (Page et al. 2013; Vallés et al. 2015) were assigned to research biomechanical aspects of the knee joint, and also to review current devices for knee rehabilitation and diagnosis. After a set of presentations and discussions involving most of the members of the project, we established the kinematic requirements, which are the DoF and the range of motion (RoM) required to accomplish both tasks: rehabilitation and diagnosis. For instance, the required RoM for diagnosis can be established according with the Pivot Shift Test (Wheless 1996). In term of rehabilitation requirements, the knee joint can rotate around the transverse axis and the vertical axis. Moreover, the knee can translate in the sagittal plane. Diagnosis and rehabilitation exercises generally occur in the plane and axis described above, therefore a robot with 2R2T DoF would cover a large number of procedures applicable to an injured knee.

### 2.2 Parallel Robot with 2T2R Degree of Freedom

Current research on parallel robots with 2T2R motions turns out to be limited. Chen et al. (2002) introduced a novel 4-DoF parallel robot with base mounted prismatic actuators and 2PRS-2PUS configuration. Fan et al. (2011) proposed a robot with four limbs containing two adjacent RPU limbs and two adjacent SPS limbs, connecting the base to the moving platform. In the aforementioned robots two of their arms form a plane, which limits the leg motion, so the 4-DoF available are two displacements (y and z) and two rotations (x and y axis). Other parallel robots with 2T2R have been proposed, but they present some difficulties from an assembly point of view, or they have been designed for very specific tasks. To sum up, Fig. 1 shows four conceptual designs which are based on Chen et al. (2002) and Fan et al. (2011), and our own design analysis.

Of the four conceptual design shown in Fig. 1, the 3UPS-RPU presents the following advantages: (1) High load-to-weight ratio thanks to the central strut, which represents an important factor for selecting the robot since it has to be able to hold in some cases up to the entire weight of the human body. (2) The central strut includes a revolute joint constraining the end-effector's motion to the sagittal plane (which is the required motion), the joint can also provide a wide rotational motion in the plane

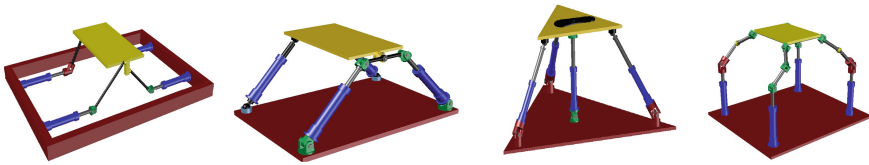


**Fig. 1** From left to right 2PRS+2PUS modified Chen et al. (2002), 2RPU+2SPS modified (Fan et al. 2011), 3UPS-RPU, and 2PRRR+2PUSR

in which the translational motions occur. Therefore, we selected the 3UPS-RPU as the architecture for the knee diagnosis and rehabilitation robot.

### 3 Kinematic Analysis of the 3UPS-RPU Parallel Robot

A global coordinate system  $O_F$  is attached to the center of the fixed platform, while a local coordinate system is attached at the center of the mobile platform  $O_M$ , both the  $O_F$  and  $O_M$  can be related through the  $(X, Y, Z)$  coordinates and the Euler angles  $(\delta, \gamma, \phi)$  by the following rotational matrix,

$${}^F R_M = \begin{bmatrix} c_\gamma c_\phi & -c_\gamma s_\phi & s_\gamma \\ s_\delta s_\gamma c_\phi + c_\delta s_\phi & -s_\delta s_\gamma s_\phi + c_\delta c_\phi & -s_\delta c_\gamma \\ s_\delta s_\gamma c_\phi + s_\delta s_\phi & c_\delta s_\gamma s_\phi + s_\delta c_\phi & c_\delta c_\gamma \end{bmatrix} \quad (1)$$

where  $s_* = \sin(*)$  and  $c_* = \cos(*)$

For the position analysis of each leg the D-H notation is used, Fig. 2 shows the parameters for the central strut, the U joints are considered as 2 consecutive revolute joints.

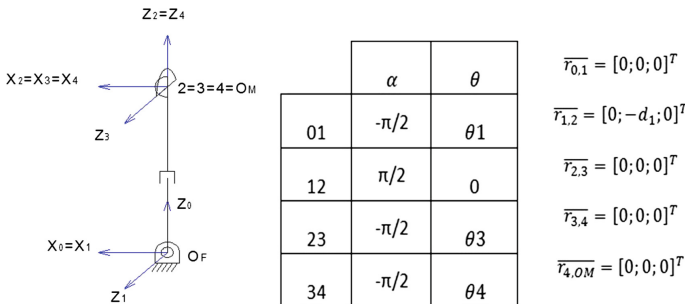


**Fig. 2** D-H parameters for position analysis of the central strut (RPU)

The position of the  $O_M$  with respect to the  $O_F$  can be found as follow,

$$\vec{r}_{F,M} = \vec{r}_{F,1} + {}^0R_1^1 \vec{r}_{1,2} = \begin{bmatrix} 0 \\ 0 \\ 0 \end{bmatrix} + \begin{bmatrix} c_1 & -s_1 & 0 \\ 0 & 0 & 1 \\ -s_1 & -c_1 & 0 \end{bmatrix} \begin{bmatrix} 0 \\ -d_1 \\ 0 \end{bmatrix} \quad (2)$$

$$[X \ Y \ Z]^T = [s_1 d_1 \ 0 \ c_1 d_1]^T \quad (3)$$

From Eq. 3  $Y = 0$  which means that the end-effector is constrained to move in the sagittal plane. In addition, we are interested in the inverse kinematics problem, thus, the actuator displacement  $d_1$  can be found as follows,

$$d_1 = \sqrt{X^2 + Z^2} \quad (4)$$

The U joint of the central strut also introduces another restriction which is that the end-effector rotation of the platform around  $O_F$  x axis is equal to zero. The second component of the vector normal to the mobile platform is null. This constraint can be written as follows,

$$-s_\delta c_\gamma r_m^2 s_{\beta_2} = 0 \quad (5)$$

where  $\beta_2$  represents the angle between the line defined by the center of the platform and one of the spherical joint and  $X_m$ , and  $r_m$  represents the radio of the mobile platform. From Eq. 5,  $\delta = 0$ .

Considering a similar approach for the remaining leg the following set of equation can be found,

$$d_2 = \sqrt{(X + c_\gamma c_\phi r_m - r_f)^2 + s_\phi^2 r_m^2 + (Z - s_\gamma c_\phi r_m)^2} \quad (6)$$

$$d_i = \left[ (X + (-1)^{(i-1)} c_\gamma c_\phi c_{\beta_{i-1}} r_m + (-1)^i c_\gamma s_\phi s_{\beta_{i-1}} r_m c_{\beta_{i-1}} r_f)^2 + (-s_\phi c_{\beta_{i-1}} r_m + (-1)^{(i-1)} c_\phi s_{\beta_{i-1}} r_m + (-1)^i s_{\beta_{i-1}} r_f)^2 + (Z + s_\gamma c_\phi c_{\beta_{i-1}} r_m + (-1)^{(i-1)} s_\gamma s_\phi s_{\beta_{i-1}} r_m)^2 \right]^{1/2} \quad (7)$$

for  $i = 3, 4$ , where  $r_f$  is the radius of the fixed platform.

The velocity of the actuated joints with respect to the end-effector velocity can be found by deriving Eqs. 4, 6, and 7. That is,

$$\vec{d} = J [\dot{X} \ \dot{Z} \ \dot{\phi} \ \dot{\gamma}]^T \quad (8)$$

where J represents the jacobian matrix.

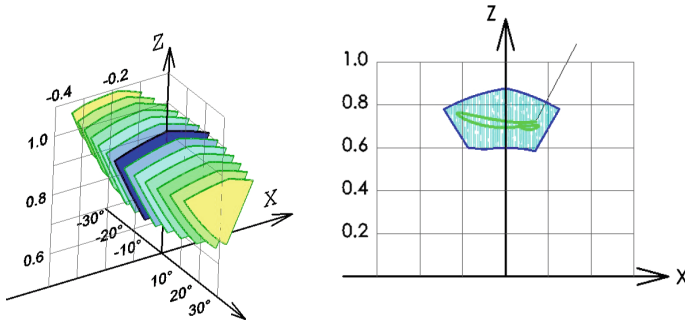
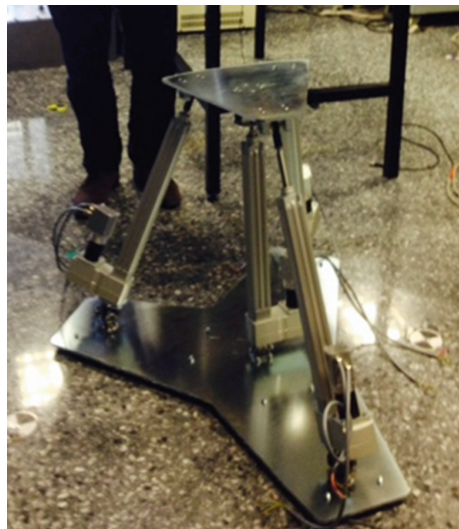


Fig. 3 3 UPS-RPU workspace, and a rehabilitation task performed within the workspace

### 4 Workspace Analysis

Equations 4–7 can be used to develop the workspace of the 3RPS-RPU parallel robot. The kinematics dimensions of the robot are found based on the required Range of Motion. The workspace has to be able to include motion allowing one leg to be moved along a normal walk. After a trial and error approach the following dimensions were found:  $r_f = 0.4$  and  $r_M = 0.2$  m, and  $\beta_2 = 40^\circ$  and  $\beta_3 = 50^\circ$ . The displacement of the prismatic joints are set to 0.60–0.90 m. An asymmetrical design ( $\beta_i$  are different) of the mobile platform was selected in order to eliminate a particular singularity of the robot that occurs when the  $\beta_i$  are similar. Figure 3 shows the workspace of the robot which was found by considering the motion in the X and Z direction ( $Y = 0$ ), and  $5^\circ$  intervals for rotation around the Z axis.

Fig. 4 Prototype of the 3UPS-RPU for knee diagnosis and rehabilitation





On the other hand, we simulate the case in which the robot is able to follow a prescribed task taken from studying the leg motion. Major rotations that occur in the joints of the ankle, knee and hip were determined in Andriacchi et al. (1997). Thus, the task to study correspond to a trajectory following the central point of the foot, whereas knee displacement and hip displacement are fixed. Figure 3 shows how the robot is capable of accomplishing the defined task.

Figure 4 shows the actual prototype which is currently undergoing dynamic modeling, parameter identification and control design stages.

## 5 Conclusion

In this paper we have presented the design of a robot for knee diagnosis and rehabilitation. The design specification was developed by studying the mobility needed at the robot end-effector to deal with diagnosis and rehabilitation treatments for knee injuries. Four degrees of freedom were established to accomplishing the design specification, in which two are translation (2T) and two rotational (2R). A 3-UPS/RPU architecture was selected from several conceptual designs of 4 DoF (2T2R) parallel robots. Then, the inverse kinematic model was developed, and the preliminary dimensions of the robot were found by trial and error. In addition, the workspace of the robot representing the end-effector X, Y and rotation around Z motion was developed through simulations. Moreover, a prescribed task taken from studying the leg motion was also analyzed. Finally, a first prototype of the robot has been built. Further work, which is currently being undertaken, focuses on dynamic modelling, parameter identification and control design of the robot. After that, clinical research will be carried out with patients.

## References

- Akdoğan, E., & Adli, M. A. (2011). The design and control of a therapeutic exercise robot for lower limb rehabilitation: Physiotherobot. *Mechatronics*, 21(3), 509–522.
- Alcocer, W., Vela, L., Blanco, A., Gonzalez, J., & Oliver, M. (2012). Major trends in the development of ankle rehabilitation devices. *Dyna*, 79(176), 45–55.
- Andriacchi, T. P., Natarajan, R. N., & Hurwitz, D. E. (1997). Musculoskeletal dynamics, locomotion, and clinical applications. *Basic Orthopaedic Biomechanics*, 2, 37–68.
- Bouri, M., Le Gall, B., & Clavel, R. (2009). A new concept of parallel robot for rehabilitation and fitness: The lambda. In *2009 IEEE International Conference on Robotics and Biomimetics (ROBIO)* (pp. 2503–2508). IEEE.
- Bradley, D., Acosta-Marquez, C., Hawley, M., Brownsell, S., Enderby, P., & Mawson, S. (2009). NeXOS—the design, development and evaluation of a rehabilitation system for the lower limbs. *Mechatronics*, 19(2), 247–257.
- Chen, W. -J., Zhao, M. -Y., Zhou, J. -P., & Qin, Y. -F. (2002). A 2T-2R, 4-DoF parallel manipulator. In *ASME 2002 International Design Engineering Technical Conferences and Computers*

- and Information in Engineering Conference* (pp. 881–885). American Society of Mechanical Engineers.
- Díaz, I., Gil, J. J., & Sánchez, E. (2011). Lower-limb robotic rehabilitation: Literature review and challenges. *Journal of Robotics* (Article ID 759764), 1–11.
- Fan, C., Liu, H., Yuan, G., & Zhang, Y. (2011). A novel 2T2R 4-DOF parallel manipulator. In *2011 Fourth International Symposium on Knowledge Acquisition and Modeling (KAM)* (pp. 5–8). IEEE.
- Page, A. et al. (2013). Methodologies for the design of biomechatronic systems. *Application for the Development of a Parallel Hybrid Robot for Diagnostics and Rehabilitation*. <https://mebiomec.ai2.upv.es/>.
- Saglia, J. A., Tsarakakis, N. G., Dai, J. S., & Caldwell, D. G. (2010). Control strategies for ankle rehabilitation using a high performance ankle exerciser. In *2010 IEEE International Conference on Robotics and Automation (ICRA)* (pp. 2221–2227). IEEE.
- Sakaki, T. (1999). TEM: Therapeutic exercise machine for recovering walking functions of stroke patients. *Industrial Robot: An International Journal*, 26(6), 446–450.
- Vallés, M., Cazalilla, J., Valera, Á., Mata, V., Page, Á., & Díaz-Rodríguez, M. (2015). A 3-PRS parallel manipulator for ankle rehabilitation: Towards a low-cost robotic rehabilitation. *Robotica*, 1–19.
- Wheless, C. R. (1996). *Wheless' textbook of orthopaedics*. DataTrace Internet Publishing.

# End-Effector for Disaster Response Robot with Commonly Structured Limbs and Experiment in Climbing Vertical Ladder

**Takashi Matsuzawa, Kenji Hashimoto, Tomotaka Teramachi, Kazuhiro Uryu, Xiao Sun, Shinya Hamamoto, Ayanori Koizumi and Atsuo Takanishi**

**Abstract** This paper describes the development of end-effector for disaster response robot with commonly structured limbs and experiment of climbing a vertical ladder. The end-effector is required to have the ability to hang on rungs and side rails and work as both hands and feet. We developed an end-effector with hook-like shape so that it can hang on both rungs and side rails, and grooves on the back of hook make it possible for the end-effector to play the role of both hands and feet, fixing on the rungs of ladder firmly. Moreover, the design of the end-effector

---

T. Matsuzawa (✉) · T. Teramachi · K. Uryu · X. Sun · S. Hamamoto · A. Koizumi  
Faculty of Science and Engineering, Waseda University, Tokyo, Japan  
e-mail: matsuzawa-t@akane.waseda.jp

T. Teramachi  
e-mail: t-teramachi@ruri.waseda.jp

K. Uryu  
e-mail: kuryu0101@moegi.waseda.jp

X. Sun  
e-mail: x-sun@asagi.waseda.jp

S. Hamamoto  
e-mail: 16231lorenzimu-su@fuji.waseda.jp

A. Koizumi  
e-mail: ayanori.k@ruri.waseda.jp

K. Hashimoto  
Waseda Institute for Advanced Study and Humanoid Robotics Institute,  
Waseda University, Tokyo, Japan  
e-mail: k-hashimoto@takanishi.mech.waseda.ac.jp

A. Takanishi  
Department of Modern Mechanical Engineering and Humanoid Robotics Institute,  
Waseda University, Tokyo, Japan  
e-mail: takanisi@waseda.jp

allows the robot to perform some locomotion style other than climbing, like bipedal walking. We made the experiment in climbing a ladder obeying Japanese Industrial Standards (JIS) performed by the robot. As a result, end-effectors enabled the robot's feet to reach the highest rung.

**Keywords** Legged robot • Rescue robot • Ladder climbing

## 1 Introduction

Various kinds of disaster, such as earthquake and tsunami taking place all over the world, expand the demand of the recovery work and field survey in a disaster site. However, in some situations it is hard for human to reach places where disaster occurs. Therefore, disaster robots are required to conduct tasks in extreme environments such as going through narrow places and moving on the ground with rubble. Therefore, competition like DRC (DARPA Robotics Challenge 2015) is held to test the capability of robots to deal with disaster.

Robots with crawlers such as Quince (Yoshida et al. 2013) are often used in a disaster site, but it is difficult for them to get over vertical ladders and narrow places. As for flying robots, some platforms of unmanned aerial vehicle (UAV) for several purposes such as load carriage (Pounds et al. 2011) and manipulation (Kondak et al. 2014) are developed, but they are not appropriate for tasks requiring direct contact like hammering test. In such disaster sites, robots with legs work more flexibly than crawler robots, especially in the case where there are vertical ladders. In addition, it is effective to make them have some locomotion style such as biped, quadruped (Fukuda et al. 2005; Kamioka et al. 2015) and crawling and choose the proper style when they move in a disaster site. Therefore, the long-term goal of our research is the development of the robot with high accessibility in extreme environment and is capable of performing diverse locomotion styles.

Extremity of environment can be measured, in our opinion, by three indexes: narrowness, unevenness and inclination. This paper focuses on vertical ladders, which are included in one of the highest degree of inclination, because vertical ladders are required to be got over, not only in disaster sites but also in ordinary maintenance of infrastructures with ladders. The specification of vertical ladder used in our research obeys JIS (Japanese Industrial Standards). Gorilla-III (Yoneda et al. 2008) and HRP-2 (Vaillant et al. 2014) succeeded in climbing vertical ladders in JIS. The robot made by HONDA also achieved to climb (Kanazawa et al. 2015). However, these robots did not reach the highest rung because they could not hang on side rails. Therefore, the objective of this paper is the achievement of climbing vertical ladder in JIS, making use of both rungs and side rails.

## 2 Development of End-Effector

The height of the robot in this research is 1290 mm, which is appropriate for adapting to human’s working environment (Matsuzawa et al. 2015). The robot has four commonly structured limbs for high accessibility, and can keep moving even if one of its limbs is broken (Fig. 1). Each limb consists of 7 Degrees of Freedoms (DoF in short) for achieving redundancy. The body has 1-DoF, considering the transition among locomotion styles such as biped walking and quadruped walking. Therefore, the robot has 29-DoFs in total. The shape of the end-effector should be designed so that it can be used as both hand and foot while climbing. Besides that, it should also be designed not only for climbing a vertical ladder but also for biped and quadruped walking. As a result, the requirements of the end-effector is as follows: (i) capability of hanging on a rung, (ii) capability of hanging on a side rail, (iii) flat base to ensure surface contact with the ground when the robot stands with two or four limbs. The robot hangs on rungs and side rails of a ladder like human when climbing. In the case of human, they hang on themselves by their hand to prevent falling. If the robot hangs on themselves by fingers, it is difficult to prevent drastic increase of size of the end-effector because the force necessary for hanging on the ladder on fingers becomes large and actuators with high torque output are necessary. On the other hand, if the end-effector has the shape like a hook, it does not need to be equipped with any actuator for hanging on the ladder. This prevents the increase in the weight of end-effectors. Consequently, the end-effector is designed to have the shape like a hook with grooves. The groove for foot has the shape of a triangle to make it easier to be fixed with rungs. As for the hook for hand, it is effective to have the shape which hang on both rungs and side rails.

As previously mentioned, the end-effector was designed like Fig. 2. The grooves, No. 1 and No. 2, are used for foot and No. 3 is designed for hand. The groove of

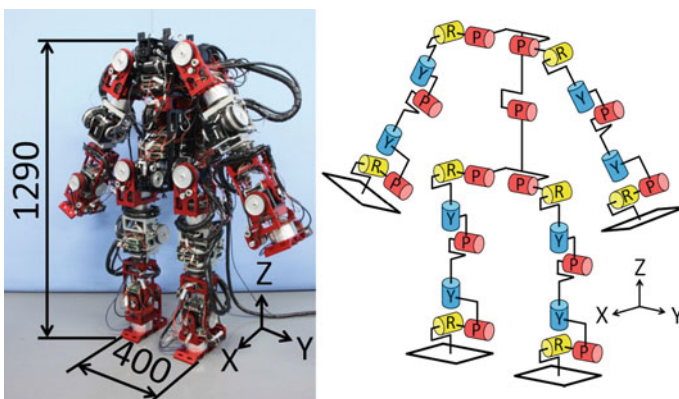
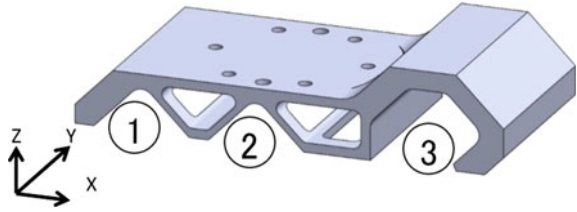
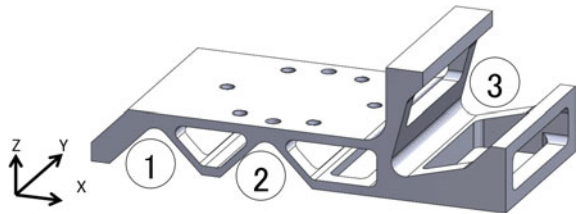


Fig. 1 Overview and Degrees of Freedom of the four-limbed robot

**Fig. 2** The groove upon the palm of hands



**Fig. 3** The groove in the back of hands



No. 1 makes it easier to avoid interference between rungs and lower limbs comparing with groove of No. 2 when the robot hangs on rungs with it during climbing. As for No. 2, it is useful in reducing the joint torque of the ankle because the moment arm length of No. 2 is shorter than that of No. 1. Therefore, the selection of two grooves depends on actual circumstances. Considering the shape of groove for hands, bigger moveable angle is required for wrist pitch joint, which is more than  $90^\circ$ . Therefore, we changed the position of groove for hands to the back of hand like Fig. 3. It makes the required moveable angle for wrist pitch joint smaller, less than  $90^\circ$  (Fig. 4).

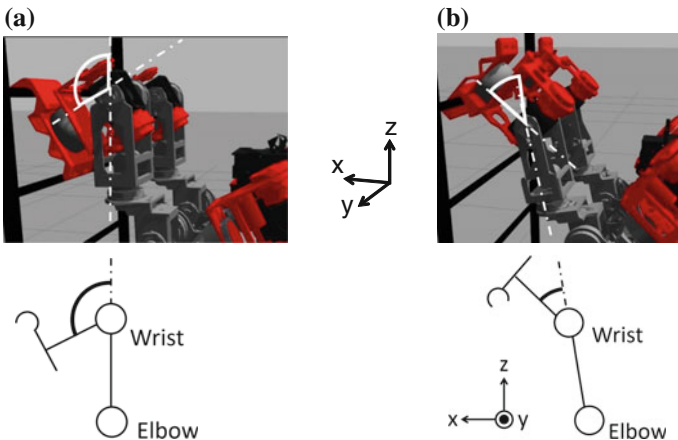
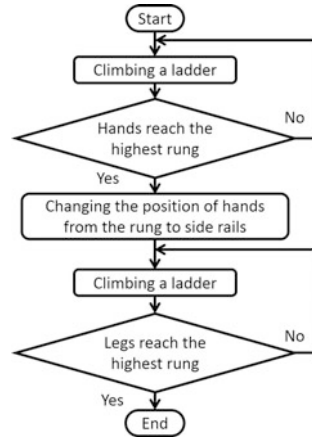


**Fig. 4** The required moveable angle for the pitch joint of the wrist. **a** The groove upon the palm of hands. **b** The groove in the back of hands

**Fig. 5** The motion of climbing a vertical ladder

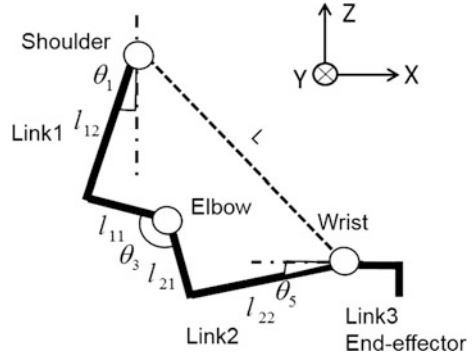


The size of groove is designed to be able to hang on rungs and side rails with diameter of 14–35 mm. The angle of each joint is calculated as follows: (i) decide the position and posture of the end-effector (ii) calculate the angle of each joint by inverse kinematics. Then, the motion pattern of the robot is generated based on the angle of each joint. Each joint moves based on the command of the angle. Figure 5 illustrates the flowchart of climbing motion. As for the pattern of limb motions in climbing vertical ladders, there are some options such as transverse gait, pace gait and trot gait. Transverse gait is the motion that four limbs move one by one in climbing, while pace and trot gait are motions that two limbs move simultaneously. When the robot reaches the highest rung, handing position is changed from rungs to side rails. After changing hand position, the robot moves with only legs, keeping hands holding with side rails and sliding up with the whole body. This makes it possible to shorten the time required to climb a ladder. When the legs reached the highest rung, the robot moves its legs to the catwalk. The robot climbs a ladder in this way.

### 3 Calculating the Angle of Each Joint

Angle of each joint is calculated by defining the position and posture of the end-effector. In this research, inverse kinematics is calculated as a 6-DoF limb by setting the angle of hip/shoulder pitch joint because it is easier to calculate, although the limb of the robot consists of 7-DoFs. Figure 6 illustrates the definition of the length of limbs and the vector of an initial position of the end-effector. The angle of each joint is defined as follows:

**Fig. 6** Geometric structure of a limb



Hip/shoulder pitch:  $\theta_1$ , Hip/shoulder roll:  $\theta_2$   
 Knee/elbow pitch:  $\theta_3$ , Ankle/wrist yaw:  $\theta_4$   
 Ankle/wrist pitch:  $\theta_5$ , Ankle/wrist roll:  $\theta_6$

At first,  $\theta_3$  is calculated geometrically by defining  $L$  as the distance between hip/shoulder joint and ankle/wrist joint (Fig. 6). Note that the elbow of the robot has the offset equal to  $l_{11}$  and  $l_{21}$ .

$$\theta_3 = 2\pi - \arccos \left\{ (l_{11}^2 + l_{12}^2 + l_{21}^2 + l_{22}^2 - L^2) / 2\sqrt{(l_{11}^2 + l_{12}^2) \cdot (l_{21}^2 + l_{22}^2)} \right\} - \arctan \left( \frac{l_{21}}{l_{11}} \right) - \arctan \left( \frac{l_{22}}{l_{21}} \right) \quad (1)$$

Next,  $\theta_1$  and  $\theta_2$  can be solved the position of ankle/wrist joint is calculated according to the goal position and posture of the end-effector after defining hip/shoulder joint as the origin. Then,  $\theta_1$  and  $\theta_2$  is calculated with the position of ankle/wrist joint.

In the end,  $\theta_4$ ,  $\theta_5$  and  $\theta_6$  is calculated as follows: (i) calculate the vector for the goal position of the end-effector, (ii) obtain a vector by multiplying all of rotation matrix about each joint of limb to the vector for initial position of the end-effector.

This result is in match of the vector for goal posture of the end-effector and the vector mentioned in (ii). In this way,  $\theta_4$ ,  $\theta_5$  and  $\theta_6$  can be calculated. In general, there are some solutions about inverse kinematics of 6-DoFs. This problem is solved by using the solution that makes the range of moveable angle widest.

## 4 Experiments

The motion of changing the position of hands from rungs to side rails is needed for the robot to move to the catwalk. Then, we conducted the experiment about the motion of climbing vertical ladders including the transition of the position of



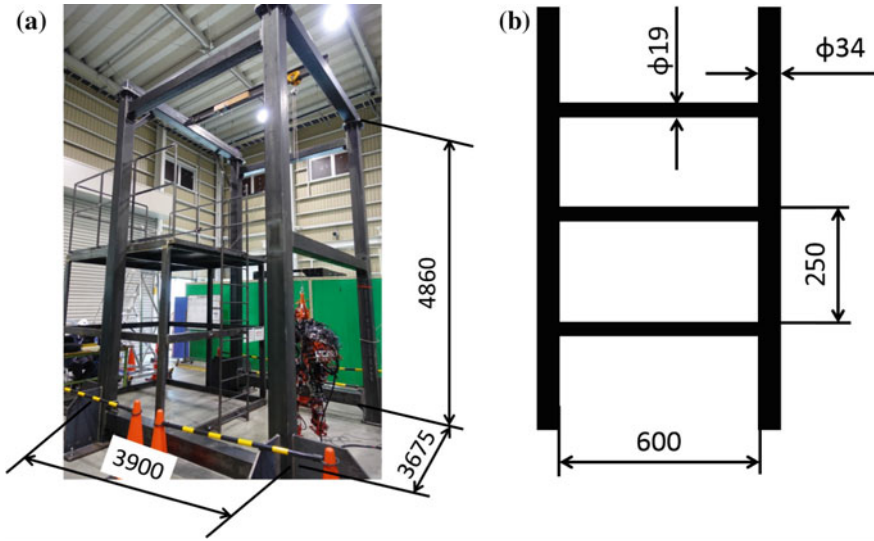


**Fig. 7** Experimental environment. **a** Overview. **b** Ladder

end-effector from rungs to side rails. Figure 7 illustrates the environment in this experiment. The height of the environment is 4860 mm, the width is 3675 mm, and the depth is 3900 mm. These sizes are designed for the experiment of climbing a ladder and moving from a ladder to a catwalk. The distance between rungs and side rails is 250 and 600 mm according to JIS. The diameter of rungs is 19 mm and side rails is 34 mm based on the specification of an escape ladder. The order of motion is as follows: (i) climb the ladder until the hands reach the highest rung, which uses a spline interpolation method to generate the trajectory of the end-effector (Sun et al. 2015), (ii) shift the hand from the rung to side rails (Fig. 8), (iii) climb the ladder while hands gripping side rails until the feet reach the highest rung (Fig. 9). We found that the robot could arrived at the highest rungs with shifting end-effectors from rungs to side rails.

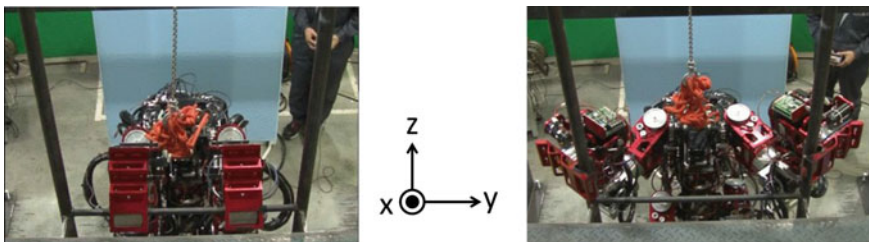


**Fig. 8** Moving hands from the highest rung to side rails

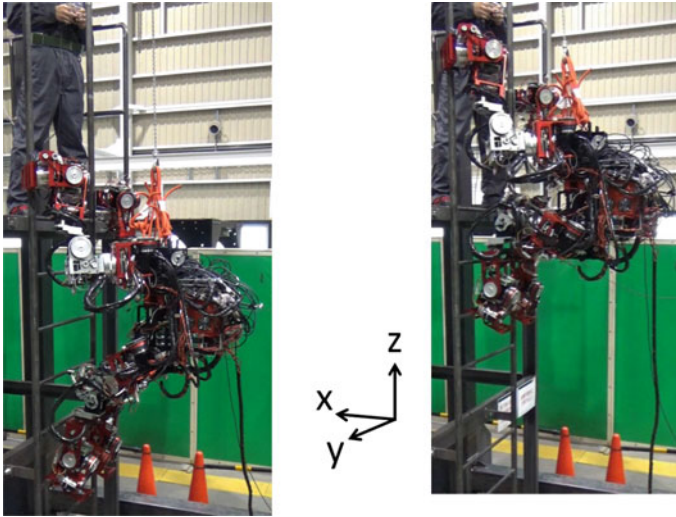


Fig. 9 Climbing the vertical ladder during gripping side rails

## 5 Conclusions and Future Works

In this research, we developed the commonly structured four-limbed robot and its end-effectors and it succeeded in climbing the ladder with shifting the position of the end-effector from rungs to side rails. This made the feet of the robot reach the highest rung. However, there are some issues to be solved in future. In the near future, we will improve the trajectory generation method of end-effectors, especially by using a redundant degree of freedom. For example, when the robot goes through side rails for moving from the ladder to a catwalk and climbs a ladder with a safety gage, it needs to avoid the collision between obstacles and the robot by utilizing the redundant degree of freedom cleverly. Therefore, we will introduce the trajectory generation method with 7-DoFs. Besides, the end-effector requires the integration a hook and hand with active degree of freedom. In a disaster site, the robot needs to perform not only climbing ladders but also manipulation tasks like handling doorknob, bulb and so on. As a result, the integration will contribute to the variety of tasks. As for other types of locomotion styles, the robot aims to get over steps and terrains.

**Acknowledgments** This research was conducted as a collaborative research between the Humanoid Robotics Institute (HRI), Waseda University and Mitsubishi Heavy Industries, Ltd. We would like to express thanks to SolidWorks Japan K. K., DYDEN CORPORATION and KITO CORPORATION.

## References

- Darpa Robotics Challenge Finals. (2015). Retrieved from December 7, 2015, <http://www.theroboticschallenge.org/>.
- Fukuda, T., et al. (2005). Multi-locomotion robot—energy-based motion control for dexterous brachiation. In *Proceedings of IEEE International Conference of Robotics and Biomimetics (ROBIO)* (pp. 4–9).
- Kamioka, T., et al. (2015). Dynamic gait transition between bipedal and quadrupedal locomotion. In *Proceedings of IEEE/RSJ International Conference on Intelligent Robots and Systems (IROS)* (pp. 2195–2201).
- Kanazawa, M., et al. (2015). Robust vertical ladder climbing and transitioning between ladder and catwalk for humanoid robots. In *Proceedings of IEEE/RSJ International Conference on Intelligent Robots and Systems (IROS)* (pp. 2202–2209).
- Kondak, K., et al. (2014). Aerial manipulation robot composed of an autonomous helicopter and a 7 degrees of freedom industrial manipulator. In *Proceedings of IEEE International Conference on Robotics and Automation (ICRA)* (pp. 2107–2112).
- Matsuzawa, T., et al. (2015). Development of disaster response robot with commonly structured limbs and experiment in climbing vertical ladder. In *Proceedings of International Conference on Advanced Mechatronics (ICAM)* (pp. 142–143).
- Pounds, P., Bersak, D., & Dollar, A. (2011). Grasping from the air: hovering capture and load stability. In *Proceedings of IEEE International Conference on Robotics and Automation (ICRA)* (pp. 2491–2498).
- Sun, X., et al. (2015). Event-based climbing motion planning for a quadruped robot. In *Proceedings of International Conference on Advanced Mechatronics (ICAM)* (pp. 78–79).
- Vaillant, J., et al. (2014). Vertical ladder climbing by the HRP-2 humanoid robot. In *Proceedings of IEEE International Conference on Humanoid Robots (Humanoids)* (pp. 671–676).
- Yoneda, H., et al. (2008). Vertical ladder climbing motion with posture control for multi-locomotion robot. In *Proceedings of IEEE/RSJ International Conference on Intelligent Robots and Systems (IROS)* (pp. 3579–3584).
- Yoshida, T., et al. (2013). Improvements to the rescue robot quince toward future indoor surveillance missions in the Fukushima Daiichi nuclear power plant. In *Field and Service Robotics Volume 92 of the series Springer Tracts in Advanced Robotics* (pp. 19–32).

# Design of a Tendon-Drive Manipulator for Positioning a Probe of a Cooperative Robot System for Fault Diagnosis of Solar Panels at Mega Solar Power Plant

Mitsuru Endo, Mai Endo, Takao Kakizaki, Yasuhiro Nakamura, Tsukasa Hebiishi and Kenji Otani

**Abstract** In recent years, several large-scale solar power plants, called mega solar power plants, have been built at various locations. Inspection of a faulty solar panel is important for the maintenance of solar panels. However, previous methods of determining a fault in a solar panel required removal of panels from the solar power plant. In this paper, a cooperative robot system using wire-parallel mechanism is proposed for the realization of on-site inspection. Based on Vector-Closure and manipulability, the design of the system is described.

## 1 Introduction

In Japan, there are huge solar power plants, which generate electricity in excess of 1 MW by using solar panels. Such solar power plants are called mega solar power plant. As of June 2014, 1,427 solar power plants were generating electricity, and a total of 2,709 MW of electricity was generated. Generally, a solar panel generates electricity from 150 to 250 W. Thus, in order to build a mega solar power plant, a minimum of 4,000 solar panels are required. Such a large number of solar panels

---

M. Endo (✉) · M. Endo · T. Kakizaki  
College of Engineering, Nihon University, Fukushima, Japan  
e-mail: m\_endo@mech.ce.nihon-u.ac.jp

M. Endo  
e-mail: mai.endo.ss.lab@gmail.com

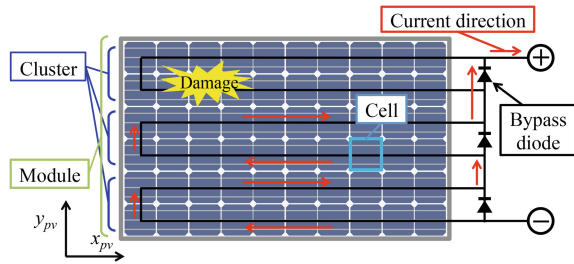
T. Kakizaki  
e-mail: kakizaki@mech.ce.nihon-u.ac.jp

Y. Nakamura · T. Hebiishi · K. Otani  
Fukushima Renewable Energy Institute of AIST, Fukushima, Japan  
e-mail: yas.nakamura@aist.go.jp

T. Hebiishi  
e-mail: t.hebiishi@aist.go.jp

K. Otani  
e-mail: k.otani@aist.go.jp

**Fig. 1** Configuration of a solar module



require frequent maintenance and inspection, as they may be damaged because of mechanical or electrical faults. The major reasons that may damage a solar panel are electrical faults, such as earth fault or snapping of a wire/wires, and mechanical faults, such as the degradation or destruction of the surface of a solar panel. Such mechanical faults cause a critical fault called hot spot, i.e., a point in a solar panel becomes extremely hot, over  $200^{\circ}\text{C}$ , and may lead to fire in some cases. Decrease in power generation is only 0.5 % per year Wohlgeomuth (2006); however, periodic inspections are required to avoid a worst-case scenario.

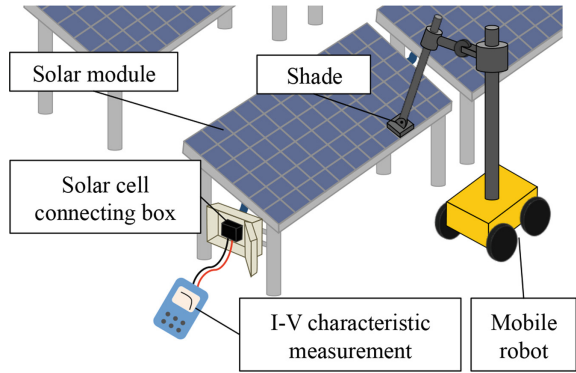
Figure 1 shows the construction of a general solar panel. The solar panel consists of several cells, which are the smallest unit as a battery. A line or lines of cells, which are connected serially, compose a cluster. Clusters are connected serially and compose a panel. In general, a panel is composed of three clusters. Each cluster is bypassed by a diode. When a cluster has a broken cell, the diode shorts automatically and the power supply to the cluster is cut off. Some modules, which are connected serially, compose a string. Some strings compose an array. A mega solar power plant is realized by connecting arrays.

The methods of inspecting faults in a solar panel proposed in previous studies involved using I-V characteristics. Such inspection methods require the removal of solar panels from a string. The removal of solar panels requires time, manpower, and money. To overcome these problems, a novel concept for the inspection of a solar panel by using mobile robots is proposed. As the proposed method realizes on-site inspection, the cost of maintenance will be decreased. In this paper, the previous design and the limitations of a robot of the proposed system are described. In addition to this, the design of a robot using a tendon-drive parallel manipulator based on Vector-Closure is described.

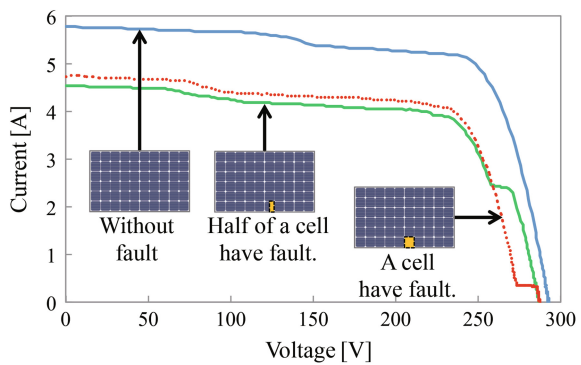
## 2 On-Site Inspection for Detecting a Broken Cell

Figure 2 shows a concept of the proposed system. The system consists of multiple mobile robots, sensors, which are installed on the infrastructure, and a server, which integrates the information received from the sensors and robots. The robots position inspection equipment on a solar panel, such as wiring path survey equipment or a shading plate.

**Fig. 2** Concept of the proposed system



**Fig. 3** I-V curves



When the system utilizes a shading plate, a broken cell is detected based on the I-V characteristic of a string. As shown in Fig. 3, a string without a broken cell has a simple arch on the graph showing the relationship between the generated current and voltage (I-V). In contrast, a string with a broken cell has a multiplex curve, which transforms based on the number of broken cells and how to brake, on the graph. When a cell is shaded, the cell stops generating electricity and acts as a broken cell PVPS (1995). To utilize mentioned above, the system specifies a broken cell as follows.

1. The system specifies a string with a broken cell or broken cells based on a sensor measuring the I-V characteristics.
2. Mobile robots shade all cells one by one, and the system checks the shape of the I-V curve.
3. When an unbroken cell is shaded, the shape of the I-V curve of the string changes. When a broken cell is shaded, the shape of the I-V curve of the string does not change, as the shaded cell does not generate electricity.

The robot must shade only the targeting cell to ensure that only one cell acts as a broken cell. Albeit shadow is small or slim, when it crosses the cell, the cell acts as a broken cell. Thus, the robot is designed as a mobile robot with a tendon-drive

parallel manipulator. The body of the robot is designed as a thin pole, and thin nylon wires are utilized for suspending the shading plate such that the shadow of the robot does not fall on the cells.

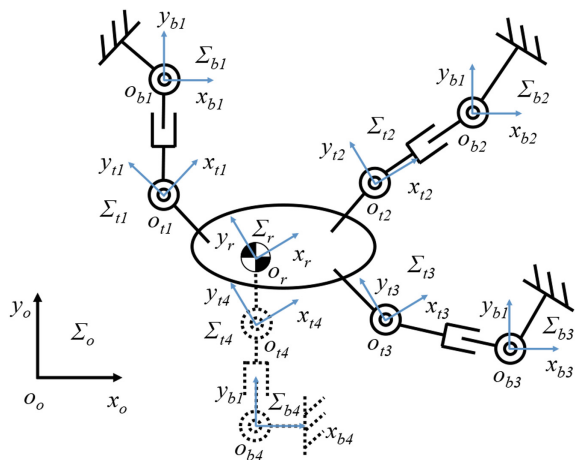
### 3 Workspace of the Tendon-Drive Parallel Manipulator

The wires of the tendon-drive parallel manipulator could apply force only in the pulling direction. Thus, an optimal analysis of the workspace of the manipulator is required. Figure 4 describes a model of the tendon-drive parallel manipulator. Since the shading plate positions the manipulator with respect to the cross-sectional direction, we can consider the manipulator as a planer system, If we assume that the wire never slacks, the winding of the wire may model translational joints, and the bending at each end of the wire may model rotational joints.

In addition to the model of the wires, based on Form-Closure or Vector-Closure, which is often considered at grasping by a robot hand for judging advisability of grasping Gordon and Raju (1991), the tendon-drive parallel mechanism must have  $n + 1$  wires to position at  $n$  DoF space Mikelsons et al. (2008). For planer 3-DoF positioning, generally the system employs four wires Gouttefarde et al. (2015). In this study, by considering gravity as a virtual wire, planer 3-DoF positioning was achieved using only three wires. Coordinate systems are defined as shown in Fig. 4.

Let  ${}^o\mathbf{P}_r \in \mathcal{R}^2$  and  ${}^o\theta_r \in \mathcal{R}$  denote the positions of the origin of  $\Sigma_r$  and orientation of  $\Sigma_r$  with respect to  $\Sigma_o$ , respectively. We define  $\mathbf{p} = [{}^o\mathbf{P}_r {}^o\theta_r]^T \in \mathcal{R}^3$  as a controlled variable vector of the manipulator. Let  $l_i \in \mathcal{R}$  denote the length of the  $i$ th wire. We define  $\mathbf{q} = [l_1 \dots l_4]^T \in \mathcal{R}^4$  as a manipulated variable vector. Then, a wire length  $l_i$  based on Euclidean norm is derived as follows

**Fig. 4** A model of a tendon-drive parallel manipulator and coordinate systems



$$l_i = \|\mathbf{P}_{bi}^o\| \quad (1)$$

$$= \|\mathbf{P}_{ti}^o - \mathbf{P}_{bi}^o\|. \quad (2)$$

Differentiating (2) with respect to time

$$\dot{l}_i = \begin{bmatrix} \frac{1}{l_i} \mathbf{R}^{ti} \mathbf{P}_{bi} \\ \frac{1}{l_i} \mathbf{R}^{ri} \mathbf{P}_{ti} \times \mathbf{R}^{ti} \mathbf{P}_{bi} \end{bmatrix}^T \dot{\mathbf{p}}. \quad (3)$$

Writing (3) in a matrix form, we obtain

$$\dot{l}_i = \mathbf{j}_i^T \dot{\mathbf{p}}, \quad (4)$$

where  $\mathbf{j}_i \in \mathcal{R}^3$  is a coefficient vector of the  $i$ th wire. As  $l_i$  is a member of the manipulated variable vector, we can yield

$$\dot{\mathbf{q}} = \mathbf{J}^T \dot{\mathbf{p}}, \quad (5)$$

where

$$\mathbf{J} = [\mathbf{j}_1 \ \cdots \ \mathbf{j}_4] \in \mathcal{R}^{3 \times 4}, \quad (6)$$

where  $\mathbf{J} \in \mathcal{R}^{3 \times 4}$  is a Jacobean.

Furthermore, let  $\tau_i \in \mathcal{R}$  denote the tensile strength of the  $i$ th wire.  $\boldsymbol{\tau} = [\tau_1 \ \cdots \ \tau_4]^T \in \mathcal{R}^4$  is a set of them, and  ${}^o\mathbf{f} = [{}^o f_x \ {}^o f_y \ N]^T \in \mathcal{R}^3$  denotes the forces and moment applied to the handling object such as a shading plate. Then, the relation between the variables mentioned above are obtained as follows by using Jacobean  $\mathbf{J}$ .

$${}^o\mathbf{f} = \mathbf{J}\boldsymbol{\tau}. \quad (7)$$

Since 4th element of  $\boldsymbol{\tau}$  corresponds the virtual wire described the gravity, we derive the tensile strength of each wire  $\tau$  as follows

$$\bar{\tau}_4 = \bar{\mathbf{J}}_4^{-1} ({}^o\mathbf{f} - \tau_4 \mathbf{j}_4), \quad (8)$$

where,  $\bar{\mathbf{J}}_i \in \mathcal{R}^{3 \times 3}$  denotes the matrix, which extracts the  $i$ th column from the Jacobean  $\mathbf{J}$ , i.e.,

$$\bar{\mathbf{J}}_i = [\mathbf{j}_1 \ \mathbf{j}_2 \ \cdots \ \mathbf{j}_{i-1} \ \mathbf{j}_{i+1} \ \cdots \ \mathbf{j}_m], \quad (9)$$

where  $m$  denotes the number of wires.  $\bar{\boldsymbol{\tau}}_i \in \mathcal{R}^3$  denotes the vector, which extracts the  $i$ th element from the tensile strength of wires  $\boldsymbol{\tau}$ , i.e.,

$$\bar{\boldsymbol{\tau}}_i = [\tau_1 \ \tau_2 \ \cdots \ \tau_{i-1} \ \tau_{i+1} \ \cdots \ \tau_m]. \quad (10)$$



Let  ${}^o\mathbf{P}_{ii} \in \mathcal{R}^2, {}^o\mathbf{P}_{bi} \in \mathcal{R}^2$  are positions of the origin of  $\Sigma_{ii}$  and  $\Sigma_{bi}$  with respect to  $\Sigma_o$ , respectively. We can determine  ${}^o\mathbf{P}_{ii}, {}^o\mathbf{P}_{bi}$  at arbitrary positions. Based on each position, space, which satisfies the condition of Vector-Closure, changes. When the condition of Vector-Closure is satisfied, all the members of  $\tau$  are positive, and all the wires tighten. Thus, the system can position the handling object. Therefore, by appropriately determining  ${}^o\mathbf{P}_{ii}, {}^o\mathbf{P}_{bi}$ , the workspace of the manipulator is designed.

It should be noted that a column  $\mathbf{j}_i$  of Jacobean  $\mathbf{J}$  represents the force or moment direction applied by the tensile strength of  $i$  th wire  $\tau_i$ . To realize Vector-Closure, one set of  $n$  force or moment directions of  $n + 1$  wires are linearly independent, and the following condition is satisfied.

$$\sum_{i=1}^{n+1} a_i \mathbf{j}_i = \mathbf{0}, \quad (11)$$

where  $a_i \in \mathcal{R}$  denotes a positive constant. In the proposed system, a set of force/moment directions of three wires out of four wires have to be linearly independent. The condition is satisfied, when one of  $\zeta_i \in \mathcal{R} (i = 1, 2, 3, 4)$  of following equation excepting 0.

$$\zeta_i = \det(\bar{\mathbf{J}}_i), \quad (12)$$

About another condition, from (11), we can derive follows:

$$[a_1 \ a_2 \ a_3]^T = -\bar{\mathbf{J}}_4^{-1} \mathbf{j}_4 a_4. \quad (13)$$

It should be noted that as all  $a_i$  are positive, all the elements of  $\mathbf{V}_c \in \mathcal{R}^3$  of the following equation must have positive values.

$$\mathbf{V}_c = -\bar{\mathbf{J}}_4^{-1} \mathbf{j}_4. \quad (14)$$

When conditions relating (12) and (14) are satisfied, Vector-Closure is realized. The boundary of Vector-Closure, i.e., the points that satisfy  $\mathbf{V}_c = \mathbf{0}$ , is the singular point.

## 4 Design of a Robot Based on Vector-Closure

The system requires positioning the entire surface of the solar panels. In this study, the size of each array, string, and panel is assumed based on the actual infrastructure of a mega solar power plant located in the Fukushima Renewable Energy Institute of National Institute of Advanced Industrial Science and Technologies. Figure 5 describes the size and angle of each array, string, and panel.

To include the entire surface of the panel in the workspace, we searched  ${}^o\mathbf{P}_{bi}, {}^r\mathbf{P}_{ii}$ . Figure 6a shows the designed values, and Fig. 6b shows the surfaces of the panel and

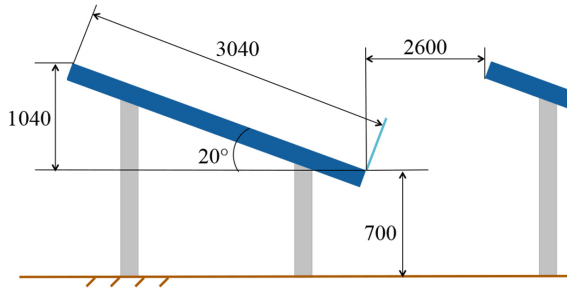


Fig. 5 Dimensional spec. of solar panels at mega solar power plant

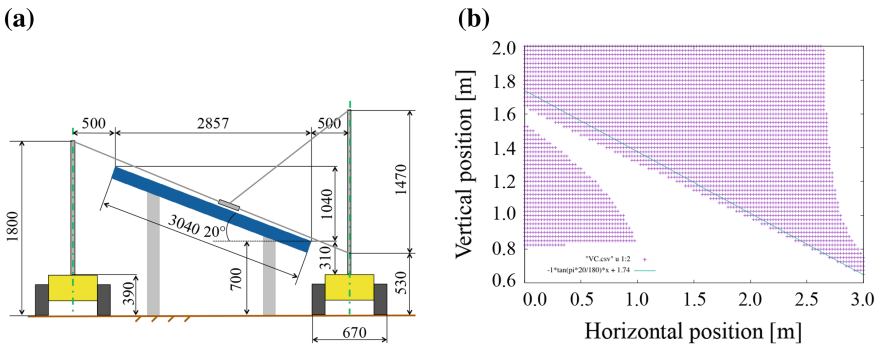
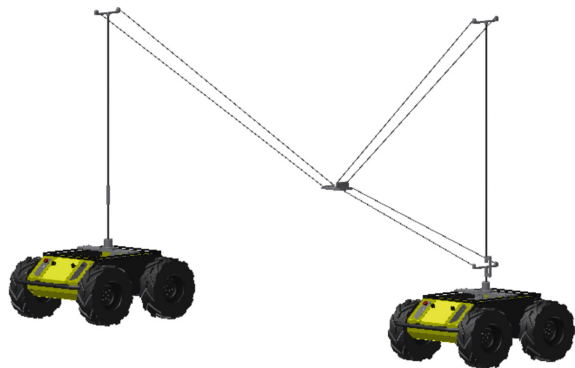


Fig. 6 Designed results. a Dimensional specification. b Vector-Closure space

Fig. 7 Designed cooperative robot for positioning a shading plate



space, which satisfy the conditions of Vector-Closure. As shown in Fig. 6b, the entire surface of the panel is included in space, which satisfies the conditions of Vector-Closure; i.e., the workspace.

Figure 7 shows the designed robot system based on the sizes mentioned above. A carbon rod is installed in the mobile robot (Husky A200, Clearpath Robotics). Nylon wires are employed for handling the shading plate, which is made of POM.

## 5 Conclusion

In this paper, a robot system, which inspects mechanical or electrical fault in a solar panel, is designed. The system is designed for inspection of solar panels at a mega solar power plant. Based on Vector-Closure, the workspace of the robot is analyzed, and the size of the robot is designed. The construction of the actual experimental system and experiments will be carried out in our future works.

## References

- Gordon, S. J., & Raju, G. J. (1991). Telerobotics grasping of unmodeled objects. In *Fifth International Conference on Advanced Robotics* (pp. 249–254).
- Gouttefarde, M., Lamaury, J., Reichert, C., & Bruckmann, T. (2015). A versatile tension distribution algorithm for n-DOF parallel robots driven by  $n + 2$  cables. *IEEE Transaction on Robotics*, *31*, 1444–1457.
- Mikelsons, L., Bruckmann, T., Hiller, M., & Schramm, D. (2008). A real-time capable force calculation algorithm for redundant tendon-based parallel manipulators. In *Proceedings on 2008 IEEE International Conference on Robotics and Automation* (pp. 3869–3874).
- IEA PVPS (1995). *Review of Failures of Photovoltaic Modules*. International Energy Agency.
- Wohlgemuth, J. H. (2006). Long term reliability of photovoltaic modules. In *Conference Record of the 2006 IEEE 4th World Conference on PV Energy Conversion* (pp. 2050–2053).

# Physical Human-Robot Interaction: Increasing Safety by Robot Arm's Posture Optimization

Omar W. MaarooF and Mehmet İsmet Can Dede

**Abstract** To have robot manipulators working alongside with humans is a necessity in service robots. Obviously, in these robotics applications, human safety has precedence over precision and repeatability, which are the most important qualification of the conventional industrial manipulators. The safety measures can be taken either in the hardware or in the software or in both. This work by using a redundant manipulator aims at providing a safety measure through controlling the self-motion of the manipulator. The self-motion of the manipulator is controlled to change the posture of the manipulator to minimize or maximize the forces it can exert along a given direction. In this way, by knowing the location of the human or a delicate piece that it should not harm, manipulator's posture is optimized to exert the minimum amount of forces during an unexpected collision. The control algorithm for this objective is described in this paper and it is evaluated through simulation tests on a redundant lightweight robot manipulator.

## 1 Introduction

Robot manipulators have been used in industrial production lines for many years. In recent years, robotic arms are started to be used in other areas of life as in surgeries, rehabilitation and in daily life services. In these new fields of use, human-robot interaction becomes a necessity. A new term, Socially Assistive Robotics (SAR), was defined in Feil-Seifer and Mataric (2005) for the service robots that work with humans. This new generation of robots are built to be directly in contact with new kind of users which are not necessarily the operators. As Forlizzi et al. (2004) suggest, these users are either disabled or elderly individuals who do not have full awareness of

---

O.W. MaarooF · M.İ.C. Dede (✉)

Department of Mechanical Engineering, Izmir Institute of Technology,  
Izmir, Turkey  
e-mail: candede@iyte.edu.tr

O.W. MaarooF

e-mail: omarmaarooF@iyte.edu.tr

robots but need robot service for every-day assistance. In recent years, robot manufacturers and researchers designed robots specifically for SAR applications.

SAR research field is focused on the physical Human–Robot Interaction (pHRI) since the safety and dependability measures for the robots used in SAR applications have an increased importance compared with precision and repeatability measures set for the conventional industrial robots. The need of safety and dependability measures were discussed in the studies of Haddadin et al. (2009) based on impact tests of a lightweight robot with a crash-test dummy for possible injuries that can happen in a SAR system and the severity of these injuries.

In research project with the acronym PHRIDOM, see (De Santis et al. 2008), the components of a robotic application are discussed based on safety and dependability in pHRI. The components mentioned were mechanics, actuation control techniques and real-time planning for safety measures. Sensors and fault handling were also discussed for dependability issues in a SAR design. In order to improve the safety and dependability of SAR systems, Pervez and Ryu (2008) give future directions of pHRI: multi-level protection strategy, failure management, safety enhancement through diversity and redundancy of sensors, and further work on robot control.

One of the approaches to avoid injuries in SAR applications is real-time planning. Some studies on evaluating the danger level based on the attributes of the human are provided by Najmaei et al. (2010), and impact force, effective robot inertia, the relative velocity, and the distance between the robot and the human are discussed by Kulić and Croft (2007). In these studies, real-time planning is performed based on the estimated danger levels. However, the human behavior is not easy to predict. Therefore, it is always possible to have a collision of the robot with the human during operation. For such cases, design of the robot and the controller plays a big part to avoid injuries. Haddadin et al. (2008) show how reactive control strategies can contribute to ensuring human safety during physical interaction.

In this work, increasing the safety during pHRI with respect to impact forces is studied. A new approach is proposed by utilizing a redundant robot to minimize the injury possibilities prior to detecting the contact. In order to accomplish this, posture optimization is employed to make a redundant robot arm to change its posture to minimize the impact forces along a given direction while carrying out the main task. This direction is selected to be along the vector from the end-effector to the assisted human. As a result of this, during a collision of the human and the end-effector, forces exerted on the human is minimized, which is another safety measure that can be employed in software. Previously, some researchers Walker (1990) controlled the self-motion of the redundant robot to resolve redundancy for reducing impact forces.

Our previously designed controller appeared in Maarroof et al. (2012) is selected for the purpose of controlling the self-motion of a redundant manipulator. The desired sub-task to be performed by this controller is selected to optimize the posture for static force exertion based on the work presented in (Chiu 1988).

A commercially available redundant robot arm, 7-Degrees-of-Freedom (DoF) LWA4-Arm by SCHUNK, is selected to be used in the tests of the developed controller since this robot arm was used in a SAR application in Martens et al. (2007). When the main-task is designated as following a 3D position trajectory, this robot arm

has 4 extra DoF, which makes the system more flexible in terms of possible number of different postures during operation. Simulation tests of the controller for minimizing the impact forces by optimizing the posture are carried out and results that are validating the efficiency of the new designs are given in the next sections.

## 2 Null Space Concept in Redundant Robot Arm Kinematics

Redundant manipulators have larger number of DoF,  $n$ , than the DoF required by the task,  $m$ . The end-effector pose in the task space, denoted by  $x(t) \in \mathfrak{R}^m$ , is defined as a function of joint position vector as  $x = k(q)$ .  $k(q) \in \mathfrak{R}^m$ , where  $m \in \mathfrak{N}$ , represents the forward kinematics calculation,  $q(t) \in \mathfrak{R}^n$  is the link position vector of an  $n$ -link manipulator and the relationships between the end-effector motion and the link motion in velocity and acceleration levels are obtained as  $\dot{x} = J(q)\dot{q}$  and  $\ddot{x} = J(q)\dot{q} + J(q)\ddot{q}$ , respectively.

$J(q) = \partial k(q) / \partial q \in \mathfrak{R}^{m \times n}$ , is the Jacobian matrix of the manipulator, and from here on, it will be referred as  $J$ .  $\dot{q}(t)$ ,  $\ddot{q}(t) \in \mathfrak{R}^n$  denote the link velocity and acceleration vectors, respectively. Since  $J$  is not a square matrix for redundant manipulators ( $m < n$ ), one can use the *pseudo-inverse*,  $J^+ = J^T(JJ^T)^{-1}$ , to obtain the inverse kinematics relations. This can be accomplished when  $J$  has full rank (the manipulator is not in a singular configuration). The pseudo-inverse is defined by (Golub and Van Loan 1983) such that the equalities in (1) are satisfied.

$$(J^+J)^T = J^+J, \quad (JJ^+)^T = JJ^+, \quad JJ^+J = J, \quad J^+JJ^+ = J^+. \quad (1)$$

However, in order to represent the inverse kinematics calculations in velocity and acceleration levels, joint velocities,  $\theta_N$ , and accelerations,  $\dot{\theta}_N$ , in the null space of  $J$  are included to the formulation as  $\dot{q} = J^+\dot{x} + \theta_N$  and  $\ddot{q} = J^+(\ddot{x} - \dot{J}\dot{q}) + \ddot{\theta}_N$ , respectively.

The velocities in the null space are designed so that the main task execution is not affected by these extra motion of the joints. The design of the self-motion controller to regulate the null space motion is explained in the next section.

## 3 Control Design for the Redundant Robot

In this work, controller's main objective is to track a desired end-effector motion demand taking into account the dynamics of the manipulator. In order to achieve this, a control torque input signal,  $\tau(t)$ , has to be designed. The torque command signal should also include necessary information to execute sub-tasks defined by an optimization measure that regulates the self-motion of the manipulator. The

controller design is a modification based on the controller developed by Hsu et al. (1989). In this paper, the motion tracking task taking place in task space is called as the main-task and regulating the self-motion of the manipulator for the selected optimization criterion is called as the sub-task.

**Control Design for the Main-Task.** The dynamic model for an n-link, robot manipulator can be represented as  $M(q)\ddot{q} + C(q, \dot{q}) + G(q) + F(\dot{q}) + \xi_d = \tau$ , where  $M(q) \in \mathfrak{R}^{n \times n}$  represents the generalized inertia matrix,  $C(q, \dot{q}) \in \mathfrak{R}^{n \times n}$  represents the torques due to centripetal-Coriolis effects vector,  $G(q) \in \mathfrak{R}^n$  is the gravity vector,  $F(\dot{q}) \in \mathfrak{R}^n$  represents the friction effects vector,  $\xi_d \in \mathfrak{R}^n$  is a vector containing the unknown but bounded, disturbance effects and  $\tau(t) \in \mathfrak{R}^n$  is the torque input vector which can be calculated, if the computed torque technique is used, as;

$$\tau = M_c \left\{ J^+ \left( \ddot{x}_d + K_v \dot{e} + K_p e - \dot{J} \dot{q} \right) + \ddot{\theta}_N \right\} + N_c \quad (2)$$

where  $x_d$  is the desired position defined in task space,  $e = x_d - x$  is the tracking error,  $K_v$  and  $K_p$  are the constant feedback gain matrices,  $M_c(q)$  is the computed generalized inertia matrix,  $N_c(q, \dot{q})$  is the computed nonlinear terms that appear in the dynamics equation of the robot, which are the Coriolis, centripetal, gravitational, frictional effects, and  $\ddot{\theta}_N$  is the designed joint acceleration vector designed in the null space of  $J$ . If the manipulator does not go through a singular condition, then the control law presented in (2) guarantees that the tracking error converges to zero exponentially given that we can calculate the generalized inertia matrix and nonlinear terms with some precision ( $M_c \cong M$ ,  $N_c \cong N$ ) as presented by Maarroof et al. (2012).

**Control Design for the Sub-Task.** For any subtask assigned, a vector function  $g(\cdot) \in \mathfrak{R}^n$  is designed. This vector function may be a function of time, current state, etc. The objective of the sub-task controller is to make the null space joint velocity to track the projection of  $g$  onto the null space of  $J$ . Since  $(I - J^+ J)$  projects vectors onto the null space of  $J$ , this can be formulated by an error signal calculation as presented in (3) which can approach to zero by a suitable controller.

$$\dot{e}_N = (I - J^+ J)g - \dot{\theta}_N \quad (3)$$

Assuming that the manipulator does not go through a singularity condition, it is required to design  $\dot{\theta}_N$  to meet the sub-task objective. The missing part in the control design given in (2), which is  $\dot{\theta}_N$ , is formulated in (4).

$$\dot{\theta}_N = (I - J^+ J)\dot{g} - \left( J^+ \dot{J} J^+ + \dot{J}^+ \right) Jg + K_N \dot{e}_N \quad (4)$$

In (4),  $K_N$  is a positive definite feedback gain matrix. With this formulation, the joint velocities in the null space converge to,  $(I - J^+ J)$  i.e.,  $\dot{e}_N$ , and the tracking error  $e$  converges to zero. The proof of this convergence is extensively explained in Maarroof et al. (2012).

**Objective Function for Sub-tasks in General.** The projection of function  $g$  into the null space of  $J$  can be considered as formulation of the desired null space joint velocities that are needed to accomplish a given subtask. In order to control the self-motion of the joint velocities, the gradient  $g$  (or its negative) of the objective function  $f(q)$  with a gain,  $k$ , can be used as  $g = k\nabla f$ . In the next section, the objective function for minimization of static force configuration is presented.

### 4 Posture Optimization for the Static Impact Force Minimization

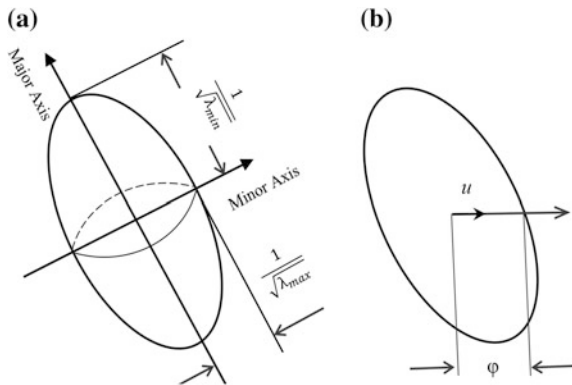
The objective for this sub-task is to keep the robot manipulator in a posture that minimizes the ability to withstand external static impact force from the environment in a given end-effector position and for specific direction of force. The manipulating force measure is a scalar,  $w_f$ , based on the static environment-manipulator reaction force/torque vector,  $F$ , relationship given in (5) given by Walker (1990).

$$w_f = 1/w_m = 1/(\sigma_1 \sigma_2 \dots \sigma_m) \tag{5}$$

Manipulating force ellipsoid is defined similar to the manipulability ellipsoid,  $w_m$ . In this case, large principal axis directions are associated with directions in which large static forces can be generated and vice versa.

The force ellipsoid is perpendicular to the manipulability ellipsoid in the sense that their magnitudes in each principal axis direction are inversely proportional. Force ellipsoid can be defined by;  $F^T(JJ^T)F$ . The optimal direction for exerting the maximum force is along the major axis of the force ellipsoid which coincides with the eigenvector of the matrix  $JJ^T$  corresponding to its largest eigenvalue  $\lambda_{max}$  as indicated in Fig. 1a. The force transfer ratio along a certain direction is equal to the distance from the center to the surface of the force ellipsoid along this vector as it can be observed in Fig. 1b. In Fig. 1b,  $u$ , is the unit vector along the desired force

**Fig. 1** Force ellipsoid.  
**a** Ellipsoid axes, **b** Force transfer ratio in direction  $u$





direction and  $\varphi$ . is the force transmission ratio along  $u$ . Since  $\varphi u$  is a point on the surface of the ellipsoid, it should satisfy the following equation:

$$(\varphi u)^T (JJ^T) (\varphi u) = 1 \tag{6}$$

Re-arranging (6), an impact force magnitude measure can be derived for  $\varphi$ . Chiu (1988) proposed to maximize the following kinematic function presented in (7) (task compatibility index) for maximum force configuration making use of  $\varphi$ .

$$f(q) = \varphi^2 = \frac{1}{u^T (JJ^T) u} \tag{7}$$

In this work, utilizing (7) to formulate the objective function as shown in (8), impact force sub-task objective is defined to limit the impact force with the environment at the lowest level as used by Tatlicioglu et al. (2009).

$$f(q) = k u^T (JJ^T) u \tag{8}$$

### 5 Simulation Test Results

A set of simulation results are presented in this section in order to evaluate the performance of the proposed controller. In these simulations, the aim is to utilize the virtual dynamic model of the 7-DoF LWA4-Arm produced by SCHUNK GmbH. The manipulator’s CAD model is retrieved from the producer’s website and the dynamic model is then transferred to the simulation environment, MATLAB® Simulink, in which simulations are carried out at a fixed-step sample time of 0.1 kHz.

The manipulator is initialized from a rest condition at the following link positions  $q = [0 \ -25 \ 0 \ -35 \ 0 \ -10 \ 0]^T$  in degrees. Figure 2 shows the desired task-space trajectories for all simulations. The main-task is selected as tracking a position trajectory in Cartesian space and the end-effector orientation is left free.

The 7-DoF manipulator has 4 extra DoF as a consequence of this task description, which provides more flexibility in optimization. In the controller that

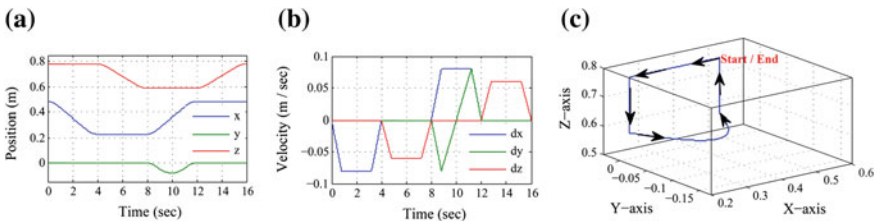


Fig. 2 Desired task-space trajectories: a in 3D, b position level, c velocity level

was presented in (2), the nonlinear terms that include computed centripetal and Coriolis, frictional and disturbance effects are neglected since robot moves in slow motion. However, gravitational effects are used in the nonlinear effect cancellation term,  $N_c$ .

In the simulation tests, the objective functions are set in one of them to minimize and in the other one to maximize the static impact force magnitude. Force direction, which is the direction that the static impact force to be minimized, is selected to be along  $x$ -axis direction,  $u = [1 \ 0 \ 0]^T$ . Figure 3a, shows position trajectory tracking error for the end-effector’s tip point in the static impact force minimization subtask. The error is bounded with 0.7 mm that indicates the main-task objective is satisfied.

The sub-task objective results for both sub-tasks are presented in Fig. 3b. It can be observed that the sub-task objective measure for maximization of manipulability along  $x$ -axis is kept at higher values in static impact force minimization task with respect to maximization task. As a final note, subtask controller performance is validated since the subtask error signal is bounded by 0.015 rad/s. A configuration change appears in the result presented in Fig. 3a after second 14. This sudden change results in higher velocity demands at joint level and thus, larger errors in the main-task trajectory tracking. Configuration change after second 14 is illustrated in Fig. 4a with virtual manipulator’s screenshots taken during the simulation.

After second 14, the second, fourth and sixth joints are moved with higher velocities to change the configuration as shown in Fig. 4a. As a result of this, the manipulability along  $x$ -axis is maximized and the static impact force is minimized and thus, the subtask objective is satisfied. In contrast, Fig. 4b reveals how the static impact force is maximized when robot arm configuration is changed to rotate manipulability ellipsoid placing the shortest diameter along the  $x$ -axis.

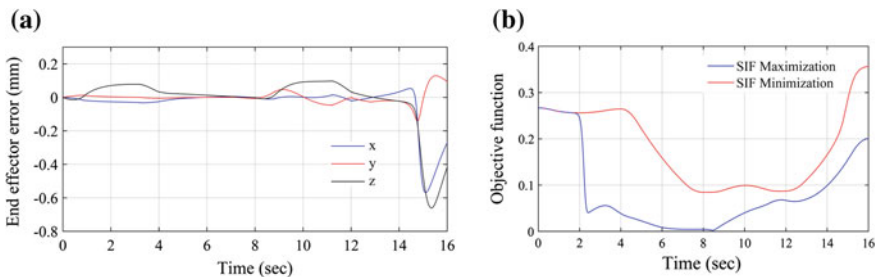


Fig. 3 a Tip point position error. b Objective function magnitude

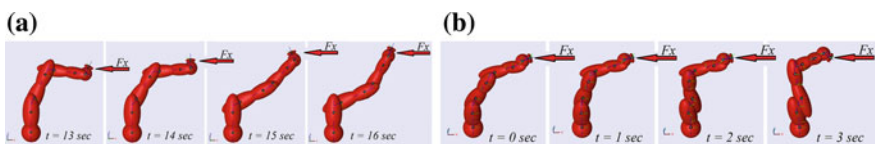


Fig. 4 Robot arm motion during simulation: a minimizing SIF, b maximizing SIF

## 6 Conclusions

The aim in this paper is to study a different safety measure in SAR applications by making use of redundant robot and the control of a redundant robot's self-motion. To achieve this, a general sub-task controller utilizing self-motion property of redundant robot manipulator was adapted to change the posture of the manipulator to minimize the static force exertion to the environment along a certain direction. The controller is then tested in simulations on a 7-DoF robot arm model. The main-task assigned for the manipulator was to track the position trajectory for the end-effector's tip point in Cartesian space, which allowed more DoF to be used for posture optimization. Test results indicated that the main-task objective is reached by keeping the tracing error bounded. It should be noted that maximum errors occurred during sudden configuration changes when higher joint velocities are required. This is a result of excluding centripetal and Coriolis terms in nonlinearity cancellation. The sub-task objective for minimizing the static force along  $x$ -axis, is also satisfied, which is observed by bounded errors in the sub-task error signal and the posture changes in the animation of the robot arm during tests. Overall, it can be stated that the stability and effectiveness of the designed controller is verified and this controller can be used in SAR applications using redundant manipulators to increase the safety of the application.

**Acknowledgments** This work is supported in part by The Scientific and Technological Research Council of Turkey via grant number 115E726.

## References

- Chiu, S. L. (1988). Task compatibility of manipulator postures. *The International Journal of Robotics Research*, 7, 13–21.
- De Santis, A., Siciliano, B., De Luca, A., & Bicchi, A. (2008). An atlas of physical human-robot interaction. *Mechanism and Machine Theory*, 43, 253–270.
- Feil-Seifer, D., & Matarić, M. J. (2005). Defining socially assistive robotics. In *Proceeding of the 9th International Conference on Rehabilitation Robotics*, June 2005, ICORR 2005 (pp. 465–468). IEEE.
- Forlizzi, J., DiSalvo, C., & Gemperle, F. (2004, June). Assistive robotics and an ecology of elders living independently in their homes. *Human-Computer Interaction*, 19(1), 25–59.
- Golub, G. H., & Van Loan, C. F. (1983). *Matrix computations*. Baltimore, MD: The Johns Hopkins Press.
- Haddadin, S., Albu-Schäffer, A., Luca, A. D., & Hirzinger, G. (2008). Collision detection and reaction: A contribution to safe physical human-robot interaction. In *Proceeding of the International Conference on Intelligent Robots and Systems*, Nice, France, September 2008, IROS 2008 (pp. 3356–3363). IEEE/RSJ.
- Haddadin, S., Albu-Schäffer, A., & Hirzinger, G. (2009). Requirements for safe robots: Measurements, analysis and new insights. *The International Journal of Robotics Research*, 28 (11–12), 1507–1527.
- Hsu, P., Mauser, J., & Sastry, S. (1989). Dynamic control of redundant manipulators. *Journal of Robotic Systems*, 6, 133–148.

- Kulić, D., & Croft, E. (2007). Pre-collision safety strategies for human-robot interaction. *Autonomous Robots*, 22, 149–164.
- Maarouf, O. W., Gezgin, E., & Dede, M. İ. C. (2012). General subtask controller for redundant robot manipulators. In *Proceeding of the 12th International Conference on Control, Automation and Systems*, (ICCAS), JeJu Island, South Korea, October 2012 (1352–1357). IEEE.
- Martens, C., Prenzel, O., & Gräser, A. (2007). The rehabilitation robots FRIEND-I & II: Daily life independency through semi-autonomous task-execution. Vienna, Austria: INTECH Open Access Publisher. ISBN: 978-3-902613-01-1.
- Najmaei, N., Lele, S., Kermani, M. R., & Sobot, R. (2010). Human factors for robot safety assessment. In *Proceeding of ASME International Conference on Advanced Intelligent Mechatronics (AIM)*, July 2010 (pp. 539–544). IEEE.
- Pervez, A., & Ryu, J. (2008). Safe physical human robot interaction-past, present and future. *Journal of Mechanical Science and Technology*, 22, 469–483.
- Tatlicioglu, E., Braganza, D., Burg, T. C., & Dawson, D. M. (2009). Adaptive control of redundant robot manipulators with sub-task objectives. *Robotica*, 27, 873–881.
- Walker, I. D. (1990). The use of kinematic redundancy in reducing impact and contact effects in manipulation. In *Proceeding of the International Conference on Robotics and Automation*, OH, USA, May 1990 (pp. 434–439). IEEE.

**Part VIII**  
**Medical Devices**

# Assessing the Orbital Stability for Walking with Four Prosthetic Feet at Different Speeds

Lulu Gong and Ruowei Zhao

**Abstract** The aim of this study is to evaluate the orbital stability for walking with four prosthetic feet at normal and slow speeds. Phase plane portraits, Poincaré maps and Floquet multipliers are used in this study. The Flex Foot, SACH foot, Seattle Foot and the optimized foot are taken as the research objects. The results demonstrate that walking with Flex Foot, Seattle Foot and the optimized foot at slow speed always exhibit smaller hip and ankle flexion, compared to walking at normal speed. While the walking speed has no obvious influence on the joint activities for walking with SACH foot. Walking with the four prosthetic feet at different speeds displays the orbital stability.

**Keywords** Prosthetic feet · Orbital stability · Poincaré map · Floquet multipliers · Gaits

## 1 Introduction

During gait, perturbations arise from internal sources (e.g., neuromuscular) and external sources (e.g., wind, surface friction and/or uneven surfaces) (see, e.g., Bruijn et al. 2013). Gaits are classified into two main types: periodic and non-periodic (see, e.g., Carbone and Gomez-Bravo 2015). Periodic gaits repeat the same sequence of steps every cycle (see, e.g., McGhee 1968). A periodic gait is one in which every limb operates with the same cycle time. Otherwise, the gait is non-periodic (see, e.g., Carbone and Gomez-Bravo 2015). It is well known that trajectories traced by lower limb joints of healthy human are periodic in time. Thus, the maximum Floquet multipliers (FM) can be used to quantify “Orbital Stability” of human gaits. The orbital stability quantifies the rate of convergence/divergence

---

L. Gong (✉) · R. Zhao  
School of Life Sciences and Technology, Tongji University, Shanghai, China  
e-mail: lulugong@tongji.edu.cn

R. Zhao  
e-mail: zhaoruwei@tongji.edu.cn

of continuous gait variables (e.g., joint angles) towards a limit cycle (see, e.g., Bruijn et al. 2013). Hurmuzlu and Moskowitz (1986) were the first to use the maximum FM in bipedal locomotion to estimate the stability of passive dynamic walkers. The great advantage of orbital stability lies in that the maximum FM can be obtained without using actual perturbations (see, e.g., Bruijn et al. 2013).

The prosthetic feet play an important role in ambulation for the amputees. Many studies compared the performance (e.g., energy efficiency) of conventional Solid Ankle Cushion Heel (SACH) foot and the energy storage and return (ESAR) foot (e.g., Seattle Foot and Flex Foot) (see, e.g., Hsu et al. 1999). Our previous study (Gong et al. 2013) showed that walking with Flex Foot exhibited the greatest hip flexion, knee flexion and ankle dorsiflexion during stance period, while walking with SACH foot had the smallest hip flexion, knee flexion and ankle dorsiflexion during the same period. Gaits using Seattle Foot displayed the intermediate performance compared with Flex Foot and SACH foot.

The speed is also important for prosthetic walking. The commercial prosthetic foot can mimic the behavior of a healthy ankle to maintain stable walking at slow speed, while the ankle provides additional energy for propulsion at the plantar flexion phase for walking at normal speed (see, e.g., Palmer 2002).

Therefore, the present study evaluated the orbital stability of prosthetic walking at normal and slow speeds with four prosthetic feet, i.e., Flex Foot, SACH foot, Seattle Foot and one non-specific optimized foot. Finally, we compared the influences of different walking speeds on the kinematics of lower limb joints for four prosthetic feet.

## 2 The 2-D Model and Basic Terminology of Human Walking

A 2-D model is adopted in our study since walking mainly happens in the sagittal plane, see Fig. 1. The planar model involves seven bodies, that is, the HAT, two thighs, two shanks and two feet. The HAT includes the head, two arms, upper part of the trunk and pelvis. The model has 7 degrees of freedom (DOFs) without considering the horizontal and vertical trajectories of the HAT. Thus, 7 generalized coordinates are used to describe the locomotion of the model, which are defined as:

- $\varphi_1$ —HAT angle with respect to the vertical,
- $\varphi_2(\varphi_5)$ —flexion angle of right (left) thigh with respect to the vertical,
- $\varphi_3(\varphi_6)$ —flexion angle of right (left) shank relative to right (left) thigh,
- $\varphi_4(\varphi_7)$ —plantar flexion angle of right (left) foot relative to right (left) shank.

One gait cycle starts with the heel strike event (HS) of one foot, and ends at next HS of the same foot. It includes two phases: the stance phase and the swing phase, see Fig. 2. The four typical events in the stance phase are HS, foot flat event (FF),

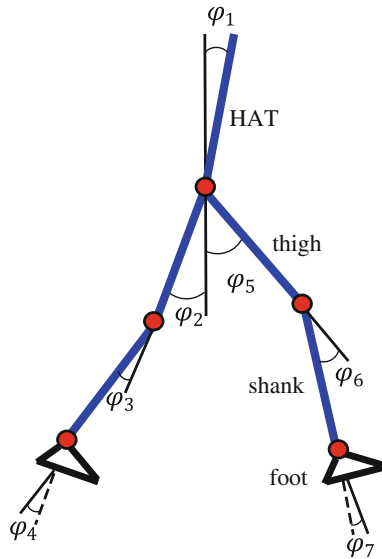


**Fig. 1** The seven-body planar model

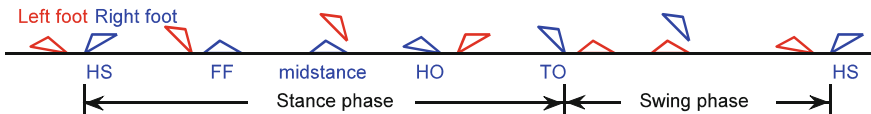


**Fig. 2** The schematic view of the typical phases and events of one gait cycle

heel off event (HO) and toe off event (TO). The stance phase can be further divided into three sub-phases: contact sub-phase (HS-FF), controlled dorsiflexion and powered plantar flexion (see, e.g., Jiménez-Fabián and Verlinden 2012 and Gong et al. 2013). Controlled dorsiflexion is from FF to the event of dorsiflexion reaching the maximum. The powered plantar flexion ends at TO.

### 3 Methods

We hypothesized that the joints are rotational and all the elements are nondeformable. Flex Foot, SACH foot, Seattle Foot and the optimized foot are taken as the research objects. The kinematic parameters of lower limb joints for walking with these prosthetic feet were obtained from numerical experiments by Ackermann (2005) and Hoang (2008). We investigated prosthetic walking at normal speed (1.33 m/s) and slow speed (1.00 m/s). There are data sets of four gait cycles for each prosthetic locomotion. The data of fast walking speed (1.68 m/s) of the



prosthetic feet are not shown because it is difficult to fulfill the constraints, especially the ones specifying maximal muscle neural excitations.

The state vector includes seven angular positions ( $\varphi_k, k = 1, \dots, 7$ ) and seven angular velocities ( $\dot{\varphi}_k, k = 1, \dots, 7$ ), which can be written as:

$$x = [\varphi_1, \varphi_2, \varphi_3, \varphi_4, \varphi_5, \varphi_6, \varphi_7, \dot{\varphi}_1, \dot{\varphi}_2, \dot{\varphi}_3, \dot{\varphi}_4, \dot{\varphi}_5, \dot{\varphi}_6, \dot{\varphi}_7]^T. \quad (1)$$

The angular positions of lower limb joints were extracted from numerical experiments. The angular velocities were calculated by numerically differentiating angular positions. Then, angular positions and angular velocities were averaged over four gait cycles. Phase plane portraits of lower limb joints were obtained by plotting averaged angular positions against respective averaged angular velocities.

In the state space, Poincaré section is a hypersurface transversing the trajectories at regular intervals and obtaining points of intersection. Any discrete event of the gait cycles (e.g., HS), can be used to define a Poincaré section. Poincaré map (i.e., first return map) is the map from the current intersection to the subsequent intersection on a Poincaré section. As for gaits, the Poincaré maps at the discrete events of the joints can be obtained by plotting the value of  $x$  at  $i^{\text{th}}$  gait cycle ( $x_i$ ), versus its value at  $(i + 1)^{\text{th}}$  gait cycle ( $x_{i+1}$ ), i.e., form the equation of

$$x_{i+1} = P(x_i). \quad (2)$$

The equilibrium state defines a periodic motion that returns to itself upon subsequent intersection, i.e.,

$$x_{eq} = P(x_{eq}), \text{ where } x_{eq} = \frac{1}{n} \sum_{i=1}^n x_i. \quad (3)$$

The difference between  $x_i$  and equilibrium state  $x_{eq}$ , can be calculated by

$$\delta x_i = x_i - x_{eq}. \quad (4)$$

Linearizing the map with respect to the equilibrium state yields a Jacobian matrix  $J_p$ , which meets  $\delta X_{i+1} = J_p \delta X_i$ . Here, the rows of matrix  $\delta X_i$  are the vector components of  $\delta x_i$  and the columns represent the separate gait cycles. By using the pseudo-inverse routine in MATLAB, the  $14 \times 14$  constant  $J_p$  is calculated from the linear least-square fit.

According to the Floquet theory, the system is stable when the absolute values of all eigenvalues of  $J_p$  (i.e., FM) are less than 1, which means that disturbances vanished over subsequent cycles (see, e.g., Müller and Schiehlen 1985). The more detailed description of the mathematical fundamentals can be found in our previous study (see, e.g., Gong 2008).

Ackermann (2005) has compared the energetic efficiency of the four prosthetic feet at different walking velocities, based on the kinematics and equations of motion

of the walking model. Therefore, we present a kinematic analysis based on phase plane portraits of different prosthetic feet at different speeds in present study.

### 4 Simulation and Results

We assume that the subjects walked with both left and right prosthetic feet. Thus, we plotted phase plane portraits, Poincaré maps and FM of right lower limb joints.

#### 4.1 Investigating Joint Kinematics by Phase Plane Portraits

Figures 3, 4, 5 and 6 show phase plane portraits of lower limb joints for prosthetic walking at different speeds, which were marked with values of typical foot contact events, i.e., HS, FF, HO and TO. For all the prosthetic feet, walking at slow speed has smaller hip and knee flexion, and greater ankle flexion during contact sub-phase (HS-FF), compared to walking at normal speed.

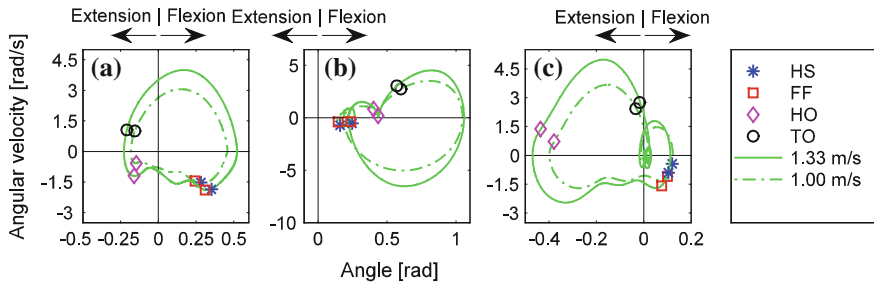


Fig. 3 Phase plane portraits of the joints for Flex Foot at different walking speeds

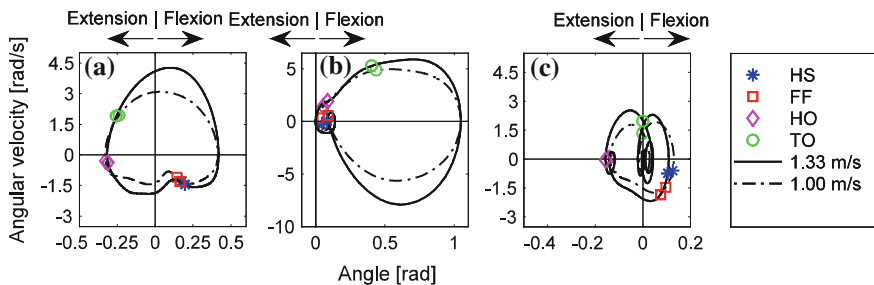
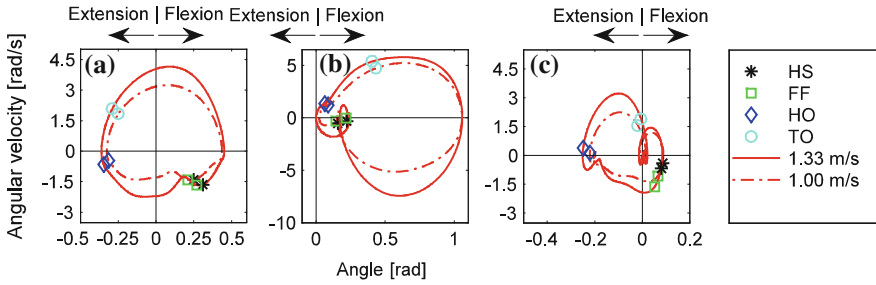
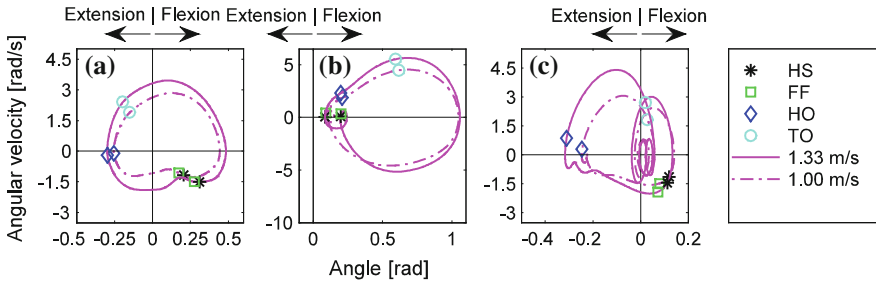


Fig. 4 Phase plane portraits of the joints for SACH foot at different walking speeds



**Fig. 5** Phase plane portraits of the joints for Seattle Foot at different walking speeds



**Fig. 6** Phase plane portraits of joints for the optimized foot at different walking speeds

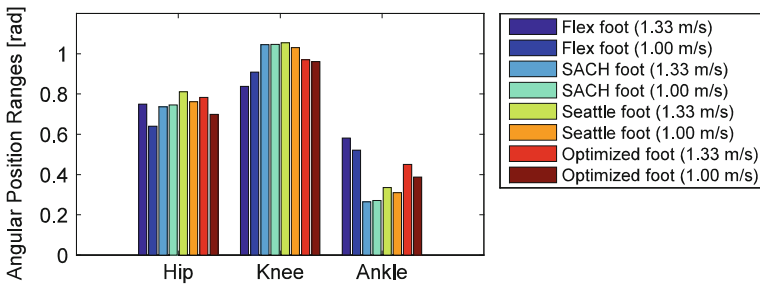


**Fig. 7** Averaged angular position ranges of lower limb joints for walking with different prostheses at different speeds

The averaged angular position ranges of right lower limb joints were calculated by subtracting the minimum from the maximum of averaged angular positions, see Fig. 7. Compared to the normal speed, walking with Flex Foot at slow speed demonstrates smaller hip and ankle angular ranges, and greater knee angular ranges.

Walking with Seattle Foot at slow speed displays smaller angle ranges of three lower limb joints than values at normal speed. Walking with the optimized foot at slow speed has smaller hip and ankle angular ranges than values at normal speed,

and there is no great differences of knee angular ranges between different speeds. While for SACH Foot, there are no obvious differences in angular ranges of lower limb joints between normal and slow walking speeds.

### 4.2 Investigating First Return Points by Poincaré Maps

Figure 8 demonstrates Poincaré maps (i.e., first return maps) for all locomotion at right HS event. All first return points cluster around the 45 diagonal line, which confirms the periodic nature of human gaits. Figure 8a and b show observable shift towards the lower left corner in hip and knee joints for four prosthetic feet walking at slow speed, compared to values of the same prosthetic feet at normal speed. However, Fig. 8c displays that there are no significant differences in ankle plantar flexion between walking at normal speed and at slow speed for all locomotion.

### 4.3 Assessing the Orbital Stability by FM

The eigenvalues of  $J_p$  for four prosthetic feet walking at different speeds are calculated at four sections, i.e., HS, FF, HO and TO. The results demonstrate that there are no differences for distributions and magnitudes of FM at these events for all locomotion. Figure 9 displays the distribution of FM at right foot contact events for

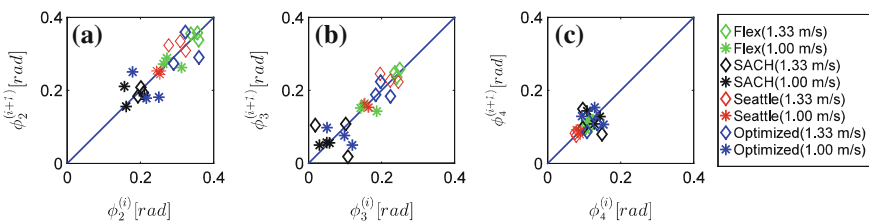


**Fig. 8** Poincaré maps of the joints for different prostheses at different walking speeds. **a** Hip. **b** Knee. **c** Ankle

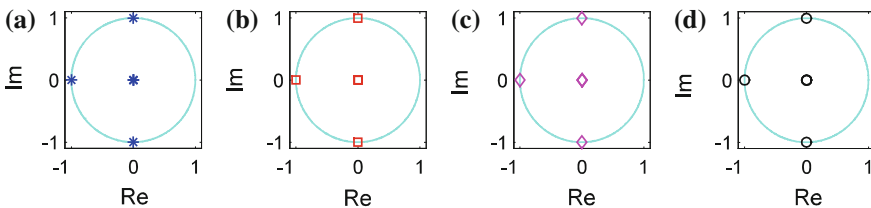


**Fig. 9** The FM at right foot contact events for walking with Flex Foot at slow speed. **a** Heel strike. **b** Foot flat. **c** Heel off. **d** Toe off

walking with Flex Foot at slow speed. That means that FM do not depend on the choice of Poincaré section. All magnitudes of FM fall into the range between  $-1$  and  $1$ , which implies the orbital stability for different prosthetic feet at different speeds. The results are consistent with those from related experiments made by Ackermann (2005), who obtained the numerical data of different walking velocities based on his experimental data of normal walking and the kinematic data of Winter (1991).

## 5 Conclusions

This study evaluates the orbital stability of prosthetic walking considering different speeds by using methods of phase plane portraits, Poincaré maps and Floquet multipliers. Simulation was made for walking with Flex Foot, SACH foot, Seattle Foot and the optimized foot at normal speed and at slow speed.

It turns out that human gaits using these four prosthetic feet at different speeds display the orbital stability. However, there are still different effects on kinematics of lower limb joints for prosthetic walking at different speeds. For walking with SACH foot, there are no obvious differences in joint activities between different speeds. While compared to walking at normal speed, walking with Flex Foot, Seattle Foot and optimized foot at slow speed exhibit smaller hip and ankle joint activities. These observations partially may be explained by the characteristics of energy storage and return feet, i.e., Flex Foot and Seattle Foot. The results indicate the proposed method in this study provides a feasible analytical tool to evaluate the performance of prosthetic feet.

**Acknowledgements** This research is supported by Chinese Scholarship Council (CSC), the National Natural Science Foundation of China (NSFC) Grant (No. 11402176) and the Fundamental Research Funds for the Central Universities.

## References

- Ackermann, M., & Gros, H. (2005). *Measurements of Human Gaits*. Interim Report ZB-144. Stuttgart: Institute B of Mechanics, University of Stuttgart.
- Bruijn, S. M., Meijer, O. G., Beek, P. J., & van Dieën, H. (2013). Assessing the stability of human locomotion: A review of current measures. *Journal of the Royal Society, Interface*, *10*, 20120999.
- Carbone, G., & Gomez-Bravo, F. (Eds.). (2015). *Motion and operation planning of robotic systems*. London: Springer.
- Gong, L. (2008). *Stability analysis of human locomotion with processed data*. Institute Report IB-42. Stuttgart: Institute of Engineering and Computational Mechanics, University of Stuttgart.
- Gong, L., Tang, Q., & Mo, H. (2013). Comparison and evaluation of human locomotion traits with different prosthetic feet using graphical methods from control area. *ICSI 2013, Part II, LNCS* (Vol. 7929, pp. 463–471).

- Hoang, K.-L. H. (2008). *Modellierung und Simulation von Oberschenkel-prothesen*. Master Thesis DIPL-126. Stuttgart: Institute of Engineering and Computational mechanics, university of Stuttgart (in German).
- Hsu, M. J., Nielsen, D. H., Yack, H. J., & Shurr, D. G. (1999). Physiological measurements of walking and running in people with transtibial amputations with 3 different prostheses. *Journal of Orthopaedic and Sports Physical Therapy*, 29, 526–533.
- Hurmuzlu, Y., & Moskowitz, G. D. (1986). Role of impact in the stability of bipedal locomotion. *International Journal of Structural Stability and Dynamics*, 1, 217–234.
- Jiménez-Fabián, R., & Verlinden, O. (2012). Review of control algorithms for robotic ankle systems in lower-limb orthoses, prostheses, and exoskeletons. *Medical Engineering & Physics*, 34, 397–408.
- McGhee, R. (1968). Some finite state aspects of legged locomotion. *Mathematical Biosciences*, 2, 67–84.
- Müller, P. C., & Schiehlen, W. O. (1985). *Linear vibrations*. Dordrecht: Martinus Nijhoff Publishers.
- Palmer, L. R. (2002). *Sagittal plane characterization of normal human ankle function across a range of walking gait speeds*. Master's thesis, Department of Mechanical engineering, MIT.
- Winter, D. A. (1991). *The biomechanics and motor control of human gait: Normal, elderly and pathological* (2nd ed.). Waterloo: University of Waterloo Press.

# Development of Rotary Type Movers Discretely Interacting with Supporting Surface and Problems of Control Their Movement

Eugeny Briskin, Alexander Maloletov, Nikolay Sharonov,  
Sergey Fomenko, Yaroslav Kalinin and Alexander Leonard

**Abstract** The problem of determining of motion quality indicators for walking robots of rotary type movers discretely interacting with supporting surface is formulated. The quality indicators have been introduced functionals, depending on equations of motion.

**Keywords** Walking machine · Walking mover · Discretely interacting with the surface · Energy efficiency · Optimization

## 1 Introduction

Experience of research and development of walking machines (Pavlovsky 2013) (example Briskin et al. 2014a, b, Fig. 1) shows that with the obvious advantages of some of the samples for permeability and maneuverability over wheeled and tracked machines, they lose speed and energy consumption per unit path.

---

E. Briskin · A. Maloletov · N. Sharonov (✉) · S. Fomenko · Y. Kalinin · A. Leonard  
Department of Theoretical Mechanics, Volgograd State Technical University,  
Volgograd, Russia  
e-mail: pochta0012@mail.ru

E. Briskin  
e-mail: dtm@vstu.ru

A. Maloletov  
e-mail: maloletov@gmail.com

S. Fomenko  
e-mail: fomenko.serg@mail.ru

Y. Kalinin  
e-mail: jkv83@mail.ru

A. Leonard  
e-mail: alex-leonard@yandex.ru

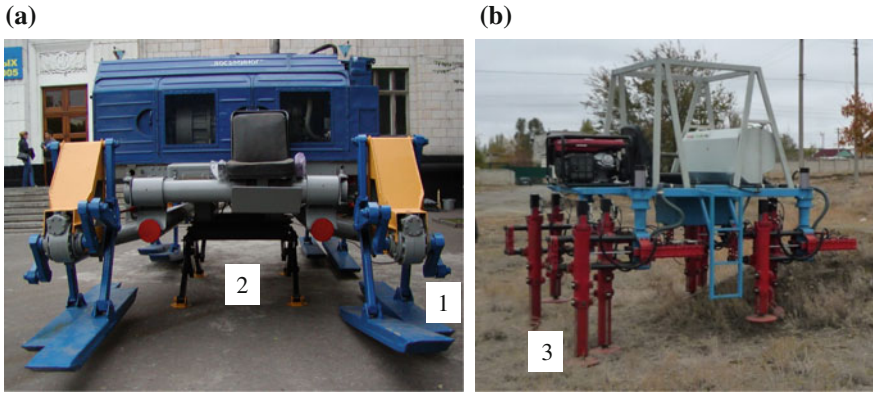
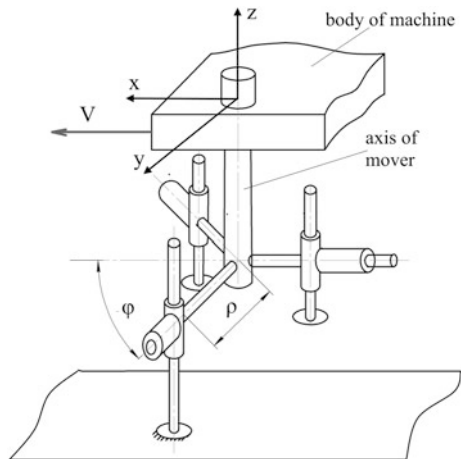


**Fig. 1** Walking machines “Vosminog” **a** with cycle walking movers *1* of course motion and lifting movers *2* designed to improve the profile practicability and “Ortonog” **b** with twin orthogonal-rotary walking movers *3*

The advantages are explained by the ability of transposition of walking mechanisms in any point of reasonable trajectory and/or usage supports of walking mechanisms with sufficiently large surface. The lacks are due to the unbalance of walking mechanisms, what is cause of additional inertial loads and high energy consumption. So the development of waking movers saving advantages of walking method of movement and at least partially free from specific lacks is an actual problem. In the basis of the problem of energy efficiency and increase the speed is the need of periodic acceleration to maximum speed and deceleration to zero in the time of interacting with the surface. However, the mover, composed of several walking mechanisms may allow the possibility of balancing under certain algorithms of its control.

The rotary-orthogonal (Briskin et al. 2014b) walking mover is one of such movers (Fig. 2), consisting of at least three orthogonal walking mechanisms with

**Fig. 2** Rotary-orthogonal mover for walking machine





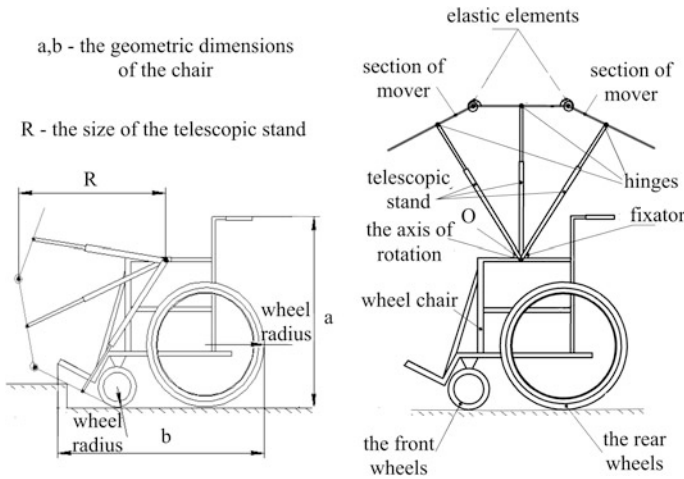


**Fig. 3** Vehicle with a mobile ramp (rotary-pie mover)

common drive of the rotational motion. The principle of operation rotary-orthogonal walking mover is based on the interacting only one walking mechanism with the ground. The other two mechanisms are in phase of transfer in this time.

The rotary-pie (VSTU 2015) movers may be used while improving the profile and cross-country ability of wheeled machines, for example for wheelchair (Fig. 3). Such movers may be named as rotary-pie movers. Rotary-pie movers is divided into section. They are used to overcome steps, small ditches and similar obstacles.

The rotational motion about a fixed axis unites these movers: in the first case around the vertical axis, in the second case around horizontal axis. They are more simple and more efficient compared to previously considered movers.

## 2 Statement of the Problems

Each of the movers has several indicators. The indicators have contradictory character. So we have task of looking for Pareto optimality solution (Multicriteria Optimization and Springer 1995; Briskin et al. 2014c). The indicators may be combined in a general indicator

$$J = \sum_{i=1}^N k_i H_i, \tag{2.1}$$

where  $k_i$  are weighting factors. The solution corresponding to the minimum of indicator  $J$  is the Pareto optimal for any given set of weighting factors  $k_i$ .

## 2.1 Rotary-Orthogonal Mover

Rotary-orthogonal mover can provide any flat motion. So the task of determining of program movement of mover and the whole walking machine is possible and legitimate. The program movement of walking machine with such mover will depend on the requirement for quality indicators. Among them are selected:

Dimensionless indicator of heat loss

$$H_1 = \frac{1}{GS} \int_0^{\tau} \sum_{j=1}^N \left[ \alpha_M L_j^2 + \alpha_p (F_{1j}^2 + F_{2j}^2 + F_{3j}^2) \right] dt \quad (2.2)$$

Dimensionless indicator of static balance

$$H_2 = \frac{1}{S^2 \tau} \int_0^{\tau} \sum_{j=1}^N \left( \rho_{C_{xj}}^2 + \rho_{C_{yj}}^2 \right) dt \quad (2.3)$$

Dimensionless indicator of comfort motion

$$H_3 = \frac{\tau^3}{S^2} \int_0^{\tau} \dot{V}^2 dt \quad (2.4)$$

Dimensionless indicator of longitudinal and transverse support reactions

$$H_4 = \frac{1}{G^2 \tau} \int_0^{\tau} R_y^2 dt; \quad (2.5)$$

$$H_5 = \frac{1}{G^2 \tau} \int_0^{\tau} R_x^2 dt \quad (2.6)$$

Here  $G$  is weight of machine,  $S = 2\rho_0 \cos\varphi_0$  is step length,  $\tau$  is time of one step,  $L_j$  is the torque developed by the engine,  $F_{1j}$ ,  $F_{2j}$ ,  $F_{3j}$  are forces developed by the drives of horizontal displacement  $j$  mover,  $\alpha_M$ ,  $\alpha_d$  are movers characterizing's constants,  $\rho_{C_{xj}}$ ,  $\rho_{C_{yj}}$  are thus the coordinates center of mass mover in the coordinate system rigidly connected with the machine body (Fig. 2),  $V$  is speed of center mass,  $R_x$ ,  $R_y$  are transverse and longitudinal support reactions.

$$\rho_{C_{xj}} = \frac{1}{M} \sum_{k=1}^3 \rho_{C_{xjk}} m_k, \quad \rho_{C_{yj}} = \frac{1}{M} \sum_{k=1}^3 \rho_{C_{yjk}} m_k \quad (2.7)$$

The quality indicators  $H_1, H_2, H_3$  depend from program motion type, among them, as more typical, is translational motion with a rectilinear movement of the center of mass. So the goal is to define the equations of this movement, providing the minimum of general quality indicator (2.1).

## 2.2 Rotary-Pie Mover

The goal of rotary-pie mover research is to define the optimal outer radius  $R$  of mover (mobile ramp). Optimality is assessed by general indicator, taking into account the maximum height of the obstacle, minimum of outer radius and minimum of the moment attached to the axis of rotation of wheelchair wheels. For rotary-pie mover as indicators of use

$$H_1 = R; \tag{2.8}$$

$$H_2 = L_{max} \tag{2.9}$$

where  $R$  is conventional radius of mobile ramp,  $L_{max}$  is the torque, applied to the axis  $O$  (Fig. 3) of mobile ramp.

## 3 Mathematical Model of Walking Machine Motion Dynamics with Rotary-Orthogonal Movers

Mathematical model allowing to study robot flat motion is based on the choice design scheme, corresponding synchronous motion of all movers allows to provide any movement of the suspension point of mover in the plane of the machine movement.

Thus we can consider the body of robot as material point and only one mover, consisting of three mechanisms of walking (Fig. 2). Generalized coordinates:  $\varphi$  is the angle of mover rotation,  $\rho_1, \rho_2, \rho_3$  are the distance from the axis of the support poles of walking mechanisms;  $x_O, y_O$  are coordinates of mover axis. So it take place the expression for the kinetic energy.

$$T = \frac{1}{2}M(V_{Ox}^2 + V_{Oy}^2) + \frac{1}{2}m \sum_{j=1}^N V_j^2 \tag{3.1}$$

Here  $M, m$  are correspondingly mass of robot and support column of walking mechanism;  $V_j$  ( $j = 1, 2, 3$ ) is velocity of supporting column, which are expressed by generalized velocity  $V_{Ox}, V_{Oy}, \dot{\varphi}, \dot{\rho}_1, \dot{\rho}_2, \dot{\rho}_3$

$$\begin{aligned}
 V_{jx} &= V_{Ox} - \dot{\rho}_j \sin(\varphi_j) - \rho_j \dot{\varphi}_j \cos(\varphi_j), \quad V_{jy} = V_{Oy} + \dot{\rho}_j \cos(\varphi_j) - \rho_j \dot{\varphi}_j \sin(\varphi_j) \\
 V_j &= \sqrt{V_{jx}^2 + V_{jy}^2}, \quad \varphi_j = \varphi + \frac{2\pi(j-1)}{3}
 \end{aligned}
 \tag{3.2}$$

Finally, we obtain the expression for kinetic energy in the form

$$T = \frac{1}{2}(M + 3m)(V_{Ox}^2 + V_{Oy}^2) + \frac{1}{2}m \sum_{j=1}^3 \left( \begin{aligned} &\dot{\rho}_j^2 - 2V_{Ox}(\dot{\rho}_j \sin \varphi_j + \rho_j \dot{\varphi}_j \cos \varphi_j) + \\ &+ \rho_j^2 \dot{\varphi}_j^2 + 2V_{Oy}(\dot{\rho}_j \cos \varphi_j - \rho_j \dot{\varphi}_j \sin \varphi_j) \end{aligned} \right)
 \tag{3.3}$$

After determine the virtual work, we can determine generalized force.

$$\delta A = L\delta\varphi - P_y\delta y_O - P_x\delta x_O + \sum_{j=1}^3 F_j\delta\rho_j
 \tag{3.4}$$

$P_x, P_y$  are external forces acting on the machine body,  $\delta\varphi, \delta x_O, \delta y_O, \delta\rho_j$  are corresponding virtual displacement.

We should consider holonomic connection providing immobility first supporting column

$$\begin{aligned}
 f_1(y, \rho_1, \varphi) &= y + \rho_1 \cos(\varphi) - \rho_0 \cos(\pi\mathcal{K}) = 0 \\
 f_2(x, \rho_1, \varphi) &= x - \rho_1 \sin(\varphi) + \rho_0 \sin(\pi\mathcal{K}) + h = 0
 \end{aligned}
 \tag{3.5}$$

where  $\rho_0, \pi\mathcal{K}$  is initial horizontal length of first supporting column and the angle of rotation of mover in the time of the beginning of interaction with supporting surface;  $h$  is the final distance between the vector of axis mover velocity and first supporting column,  $x, y$  is coordinates of immobility pad supporting column.

Then equation of motion will have form of Lagrange equations with undetermined multiplies  $\lambda_1, \lambda_2$ .

$$\begin{aligned}
 (M + 3m)\ddot{y} + m \sum_{j=1}^3 (\ddot{\rho}_j - \rho_j \dot{\varphi}_j^2) \cos \varphi_j - m \sum_{j=1}^3 (2\dot{\rho}_j \dot{\varphi}_j + \rho_j \ddot{\varphi}_j) \sin \varphi_j &= \lambda_1 - P_y \\
 (M + 3m)\ddot{x} + m \sum_{j=1}^3 (\rho_j \dot{\varphi}_j^2 - \ddot{\rho}_j) \sin \varphi_j - m \sum_{j=1}^3 (2\dot{\rho}_j \dot{\varphi}_j + \rho_j \ddot{\varphi}_j) \cos \varphi_j &= \lambda_2 - P_x \\
 m \sum_{j=1}^3 (\ddot{\varphi}_j \rho_j^2 + 2\dot{\varphi}_j^2 \rho_j \dot{\rho}_j - \rho_j \ddot{x} \cos \varphi_j - \rho_j \ddot{y} \sin \varphi_j) &= L - \lambda_1 \rho_1 \sin \varphi - \lambda_2 \rho_1 \cos \varphi \\
 m\ddot{\rho}_1 + m\ddot{y} \cos \varphi - m\ddot{x} \sin \varphi - m\rho_1 \dot{\varphi}^2 &= F_1 + \lambda_1 \cos \varphi - \lambda_2 \sin \varphi \\
 m\ddot{\rho}_2 + m\ddot{y} \cos \varphi_2 - m\ddot{x} \sin \varphi_2 - m\rho_2 \dot{\varphi}^2 &= F_2 \\
 m\ddot{\rho}_3 + m\ddot{y} \cos \varphi_3 - m\ddot{x} \sin \varphi_3 - m\rho_3 \dot{\varphi}^2 &= F_3
 \end{aligned}
 \tag{3.6}$$

The obtained equations are solved to determine the optimal program regime of motion and results  $\lambda_1, \lambda_2, L, F_1, F_2, F_3$  are substituted in (2.2–2.6) for the definitions of quality indicator.

### 4 Design Scheme and Quasi-static Mathematical Model of Rotary-Pie Mover When Overcoming the Ledge

Design scheme of rotary-pie mover takes into account three material solid body: wheelchair, wheel to which the torque force is applied, and external sector of the mobile ramp (rotary-pie movers) (Fig. 4). For overcoming the ledge by considered mechanical system it is necessary that its center of mass was located to the left of the point  $B$  (Martynenko 2005).

It is possible if applied movement of force  $L$  will vary in accordance the law

$$L = \frac{m_2 g l_2 r \sin \varphi_2}{R - r} \tag{4.1}$$

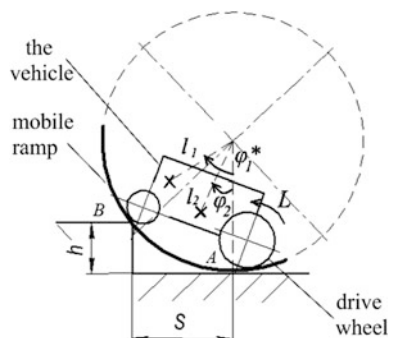
Here  $m_2$  is mass of wheelchair,  $g$  is acceleration of gravity,  $l_2$  is dimension the position of the center of mass of the wheelchair. Related graphs are given in Fig. 5.

The obtained results allow to define the Pareto-optimum region of valid parameters, providing overcoming the ledge with height  $h$ . The maximum possible height of the ledge corresponds to the point  $P$  lying at the intersection of straight lines  $R = R_{max}, L = L_{max}$ . The angle  $\varphi_2$  varies within

$$\arcsin \left( \frac{\sqrt{2Rh - h^2} m_1 + m_2}{m_2 l_2} - \frac{m_1 l_1}{m_2 l_2} \sin \varphi_1 \right) < \varphi_2 < \arcsin \left( \frac{d}{l_2} \sin \alpha \right) + \alpha \tag{4.2}$$

where  $d$  is the distance from the center of mass of the wheelchair to the axis of the drive wheel,  $\alpha$  is a constructive angle,  $m_1$  is mass of mobile ramp.

Fig. 4 Mathematical model of motion in overcoming obstacles



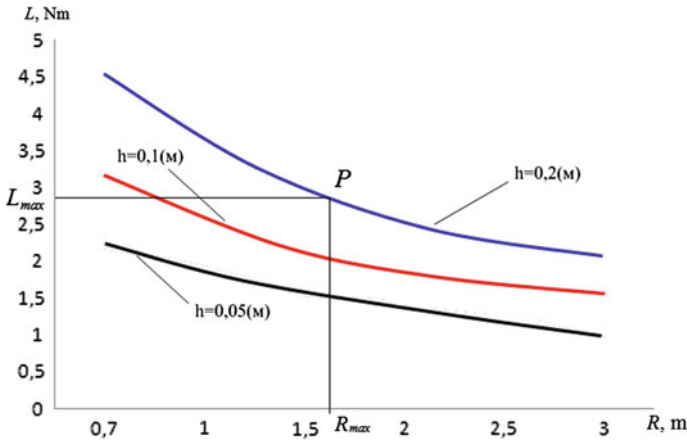


**Fig. 5** The dependence of engine torque  $L$  from a conventional radius  $R$  of the mobile ramp at different heights  $h$  to overcome obstacles

The requirement of stability of the wheelchair defines the minimum of angle  $\varphi_2$  and the condition of rotary-pie walking mover rolling over the ledge defined the maximum of angle  $\varphi_2$ .

The optimal value of the conditional radius  $R$  of the rotary-pie mover is defined from the condition of the minimum of complex criterion type (2.1):

$$J = k_1 H_1 + k_2 H_2 = k_1 R + k_2 L_{max} \tag{4.3}$$

$$\frac{dJ}{dR} = k_1 + k_2 \frac{m_2 g l_2 r \sin \varphi_{2max}}{(R - r)^2} = 0 \tag{4.4}$$

The developer, based on its experience alone sets the ratio of weighting coefficients and then determines the optimal value  $R_{opt}$ .

## 5 Conclusion

Rotary-orthogonal walking and rotary-pie walking movers are not a known wheel-walking mover developed under the leadership of famous Russian scientist Kemurdgian (1993).

However, such mover retain partially the advantages of the wheeled mover (high speed, simplicity, balance) and acquires properties of walking mover (discrete interacting with the ground).

This work is executed at financial support of the Ministry of Education and Science of the Russian Federation (state assignment № 9.862.2014/K).

## References

- Briskin, E. S., et al. (2014a). Problems of increasing efficiency and experience of walking machines elaborating. In *Advances on Theory and Practice of Robots and Manipulators: Proceedings of ROMANSY 2014. Mechanisms and Machine Science* (Vol. 22, pp. 383–390). Springer.
- Briskin, E. S., et al. (2014b, May). On the control of motion of a walking machine with twin orthogonal rotatory movers. *Journal of Computer and Systems Sciences International*, 53(3), 464–471.
- Briskin, E. S., et al. (2014c). On the energy efficiency of cyclic mechanisms. *Mechanics of Solids*, 49(1), 11–17.
- Briskin, E. S., Fomenko, S. S., Sharonov, N. G., & Serov, V. A. (2015). Vehicle for disabled people. 153154RU, A61G5/00. VSTU.
- Martynenko, Yu. G., & Formal'skii, A. M. (2005). A control of the longitudinal motion of a single-wheel robot on an uneven surface. *Journal of Computer and Systems Sciences International*, 44(4), 662–670.
- Pavlovsky, V. E. (2013). For elaboration of walking machines. Preprint of Keldysh Institute of Applied Mathematics of RAS (No 101., 32 pp.).
- Planetohodi, A. L., Kemurdzhian, M., et al. (1993). Mashinostroenie (in Russian).
- Statnikov, R. B., & Matusov, J. B. (1995). *Multicriteria optimization and engineering* (236 pp.). Springer.

# Parameter Optimization for Exoskeleton Control System Using Sobol Sequences

Sergey Jatsun, Sergei Savin and Andrey Yatsun

**Abstract** The focus of this paper is the control system of an exoskeleton that performs sit-to-stand motion. In previous publications it was shown that during such motion an exoskeleton can be modeled as a four bar serial mechanisms. That allows to simplify the control system design, which has been shown in the literature. This work provides further development of one of the existing approaches in designing control systems for exoskeletons performing sit-to-stand motion. In the paper a method for parameter optimization of the regulator is presented. The method is based on a multi stage procedure and combines the use of Sobol sequences with a nonlinear numerical optimization techniques. The results of the optimization and their analysis are presented. Relative advantages of using different objective functions are discussed.

**Keywords** Exoskeleton • Verticalization • Control system • Regulator • Optimization • Sobol sequence

## 1 Introduction

The design of robotic devices for enhancing human functional capabilities and improving the quality of life is a very important engineering and scientific field. Exoskeletons are an example of such type of devices. At the present stage of development exoskeletons have applications in production where they are used to improve the staff's efficiency, as well as in medicine for mechanotherapy of

---

S. Jatsun • S. Savin (✉) • A. Yatsun  
Department of Mechanics, Mechatronics and Robotics,  
Southwest State University, Kursk, Russia  
e-mail: sergey89mtkgtu@mail.ru

S. Jatsun  
e-mail: teormeh@inbox.ru

A. Yatsun  
e-mail: ayatsun@yandex.ru



patients. The latter area of application is socially significant since an exoskeleton can compensate for and help regain lost function of the musculoskeletal system (see works by Tsukahara et al. 2009; Jun et al. 2011).

During the design of tools for optimal synthesis of the exoskeleton's parameters special attention should be given to tools for regulator setting of the automatic control system based on the use of mathematical models of the mechanism's dynamic behavior. There is a considerable amount of work dedicated to specific problems such as gait generation and motion planning while maintaining stability (see papers by Kajita et al. 2001, 2003) interaction with environment (Park et al. 2006; Sentis 2010). Recent papers by Jatsun (2015a, b, c) discuss controlled motion of an exoskeleton during the verticalization process. An adaptive regulator for verticalization of the exoskeleton and a method for setting that regulator are proposed in article by Jatsun (2015b). The proposed regulator is a modified version of a multichannel PI regulator and its setting method is based on the use of a combination of two quality criteria. A series of assumptions allowing us to set the regulator by varying only two parameters were also made in the work. This paper shows further development of this approach connected with the use of a modified multichannel PID regulator with six independent coefficients. A method for its setting based on space probing and numerical optimization methods is proposed. Here we limit ourselves to the case when the exoskeleton performs verticalization.

## 2 Model of an Exoskeleton Performing Verticalization

During verticalization the exoskeleton can be considered as a planar four link mechanism whose links are connected in series with the given masses (see Fig. 1). We make the assumption that the first link is fixed at all times during verticalization. Conditions under which this assumption is permissible are determined in paper by Jatsun (2015c).

In Fig. 1 points  $O_i$ —hinges, to which rotary actuators are attached,  $C_i$ —centers of mass of the links,  $\varphi_i$ —absolute angles defining the orientation of the links relative to the horizontal plane, the links have masses  $m_i$  and lengths  $l_i$ ,  $M_{i,i+1}$ —torques generated by electric motors.

In order to determine the centers of mass of the links we assume that the mass of every link is given by the formulas:

$$m_1 = m_{foot}^h + m_{foot}^{ex}, \quad m_2 = m_{shin}^h + m_{shin}^{ex}, \quad (1)$$

$$m_3 = m_{hip}^h + m_{hip}^{ex}, \quad m_4 = m_{torso}^h + m_{torso}^{ex}. \quad (2)$$

where  $m_{foot}^h, m_{shin}^h, m_{hip}^h, m_{torso}^h$ —masses of the corresponding human body parts, while  $m_{foot}^{ex}, m_{shin}^{ex}, m_{hip}^{ex}, m_{torso}^{ex}$ —masses of the mechanism's links. We take the

**Fig. 1** Analytical diagram of the mechanism; 1-4—first-fourth links

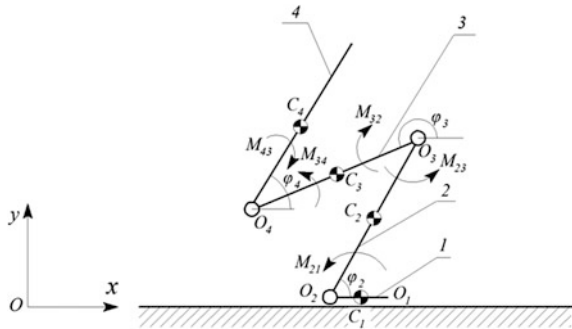


**Table 1** Masses and lengths human body parts as percentages of the whole body and height

Body part	Mass (%)	Length (%)
Torso	55.1	30
Pelvic region	13.66	9.3
Hip	10.5	23.2
Shin	4.75	24.7
Foot	1.43	4.25

masses of the mechanism’s links according to the characteristics of the exoskeleton model developed in the SWSU laboratory:

$$m_{foot}^{ex} = 0.5 \text{ kg}, m_{shin}^{ex} = 2 \text{ kg}, m_{hip}^{ex} = 3 \text{ kg}, m_{torso}^{ex} = 5 \text{ kg} \tag{3}$$

We get the weight of human body parts from medical literature. Publication by Plagenhoef et al. (1983) provides data on the distribution of body weight presented in Table 1.

Further we look at the case when the exoskeleton is put on a person of mass 50 kg and height 1.7 m. In papers by Jatsun et al. (2015) we can find kinematic analysis of the mechanism and its equations of motion. These relations will be used to describe the system control block in the next section.

### 3 Control System

Here we look at a multichannel automatic control system with an adaptive regulator, which is a modification of a PID regulator. A diagram of the control system is shown in Fig. 2.

The following denotations are used in Fig. 2:  $x_C^*, y_C^*$ —desired values of the coordinates of the center of mass,  $\varphi_2^*, \varphi_3^*, \varphi_4^*$ —desired values of generalised coordinates obtained by solving the inverse problem of kinematics,  $e_2, e_3, e_4$ —control error:  $e_i = \varphi_i^* - \varphi_i, i = 2, 3, 4$ .

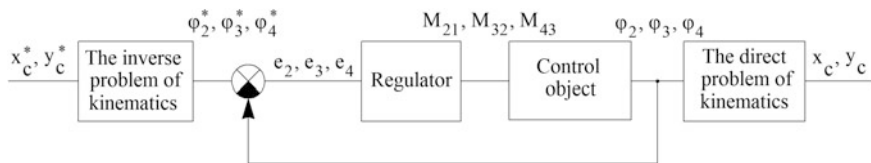


Fig. 2 Diagram of the control system

The regulator’s action is described by the following equation:

$$\vec{M} = \mathbf{B}^{-1} \mathbf{A} \left( \mathbf{K}_p \vec{e} + \mathbf{K}_d \frac{d}{dt} \vec{e} \right), \tag{4}$$

where  $\mathbf{A}$ —the mechanism’s generalized matrix of inertia,  $\vec{M}$ —control actions vector  $\vec{M} = [M_{21} \ M_{32} \ M_{43}]^T$ ,  $\mathbf{B}$ —a matrix that maps the vector of the motor torques to the generalised forces it produces,  $\mathbf{K}_p, \mathbf{K}_d$ —diagonal matrices with constant coefficients where:

$$\mathbf{K}_p = \begin{bmatrix} k_1 & 0 & 0 \\ 0 & k_2 & 0 \\ 0 & 0 & k_3 \end{bmatrix}, \mathbf{K}_d = \begin{bmatrix} k_4 & 0 & 0 \\ 0 & k_5 & 0 \\ 0 & 0 & k_6 \end{bmatrix}. \tag{5}$$

We introduce the following objective function for regulator setting:

$$J = \int_0^{t_f} \left( \vec{s}^T \mathbf{Q} \vec{s} + \vec{M}^T \mathbf{R} \vec{M} \right) dt, \tag{6}$$

where  $\vec{s} = [e_1 \ e_2 \ e_3 \ \dot{e}_1 \ \dot{e}_2 \ \dot{e}_3]^T$ —vector of control errors and their derivatives,  $\mathbf{Q}, \mathbf{R}$ —positively determined symmetrical matrices,  $t_f$ —time of verticalization.

We will use a three stage method to find the objective function’s minimum. In the first stage we define a region of regulator parameters in which optimisation will be carried out. In the next stage we perform space probing with the help of a Sobol sequence (also known as  $LP_\tau$  sequence) and find the value of the objective function on the obtained sequence (see papers by Sobol 1976). The last stage consists in the use of a numerical optimization algorithm of function  $J$ , based on the interior points method.

Let’s look at the realisation of the proposed method. We study a hypercube in six-dimensional space in the region of parameters  $k_i, i = \overline{1,6}$ , described by the inequality:

$$0 \leq k_i \leq 5000. \tag{7}$$

Let  $p$  be the  $LP_\tau$  sequence of points in the given hypercube, while  $J(p^j)$ —the value of the objective function when using regulator parameters  $k_i$ , corresponding

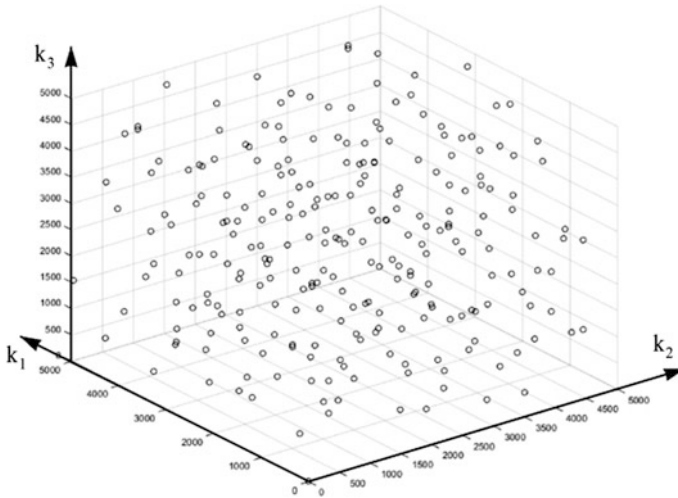


**Fig. 3** Projection of sequence  $p$  on a 3D space of parameters  $k_1, k_2, k_3$ . 250 points are shown

to the  $j$ th point of sequence  $p$ . Figure 3 shows a projection of sequence  $p$  on a 3D space of parameters  $k_1, k_2, k_3$ .

We find the objective function’s minimum value on sequence  $p$ , for a set of 1000 points of the sequence:

$$J_{\min} = \min_{1 \leq j \leq 1000} [J(p^j)]. \tag{8}$$

The minimum value  $J_{\min}$  is obtained at  $k_1 = 4785.2, k_2 = 683.6; k_3 = 839.8; k_4 = 371.1; k_5 = 1347.7; k_6 = 1308.6$ . in the second stage this point is used as the initial value for the numerical method of optimization. Optimization is done by means of the interior point method realized in MATLAB. The following values of matrices  $\mathbf{K}_p, \mathbf{K}_d$  were obtained as a result of the optimization:

$$\mathbf{K}_p = \begin{bmatrix} 5000 & 0 & 0 \\ 0 & 664.9 & 0 \\ 0 & 0 & 57.2 \end{bmatrix}, \mathbf{K}_d = \begin{bmatrix} 1000.4 & 0 & 0 \\ 0 & 769.2 & 0 \\ 0 & 0 & 487 \end{bmatrix}. \tag{9}$$

We notice that one of the obtained coefficients landed at the edge of the given hypercube. Figure 4 shows time graphs of generalized coordinates obtained under the use of a set (tuned) regulator. The graphs visually coincide with those of the desired values of generalized coordinates.

The disadvantage of this method is that the obtained regulator requires a rapid increase of torques at the beginning, which can cause difficulties during practical realization of the regulator. The time graphs of torques obtained under the use of the tuned regulator are shown in Fig. 5.

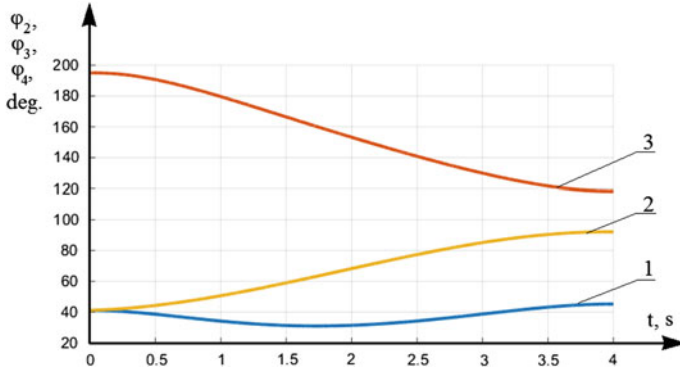


Fig. 4 Time graphs of generalized coordinates 1— $\varphi_2(t)$ , 2— $\varphi_3(t)$ , 3— $\varphi_4(t)$

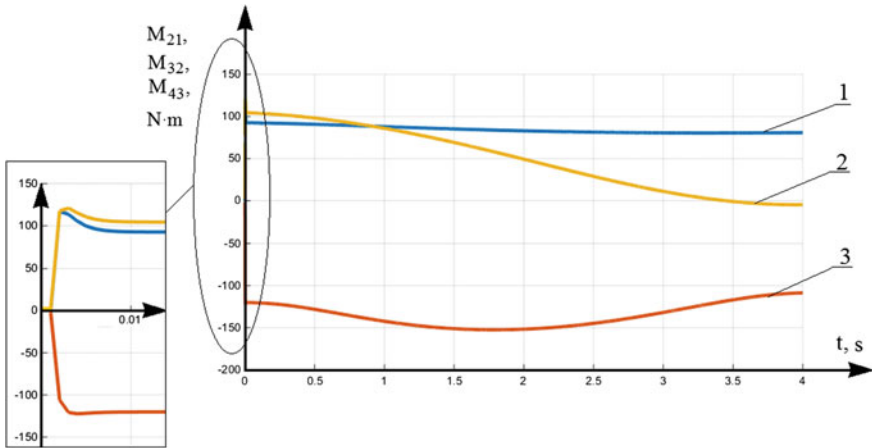
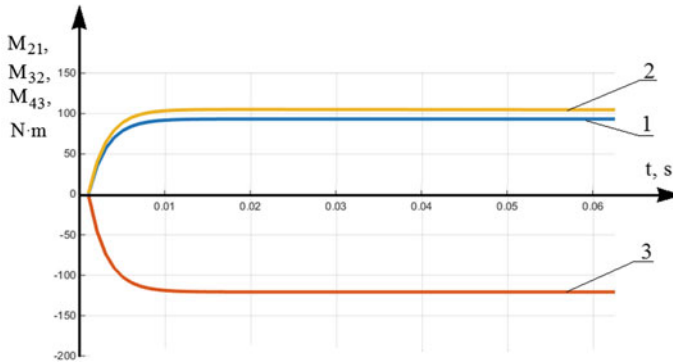


Fig. 5 Time graphs of torques 1— $M_{21}(t)$ , 2— $M_{32}(t)$ , 3— $M_{43}(t)$

The stated effect is linked to large values of gain coefficients selected during setting. In order to introduce additional limitations on the value of coefficients of matrices  $\mathbf{K}_p, \mathbf{K}_d$  we use a modified objective function:

$$J_m = \int_0^{t_f} \left( \vec{s}^T \mathbf{Q} \vec{s} + \vec{M}^T \mathbf{R} \vec{M} \right) dt + n_1 \|\mathbf{K}_p\| + n_2 \|\mathbf{K}_d\|, \quad (10)$$

where  $\|\cdot\|$ —the matrix’s spectral norm,  $n_1, n_2$ —weight coefficients. In as much as  $\mathbf{K}_p, \mathbf{K}_d$  are diagonal matrices with positive elements their spectral norm is equal to their biggest element.



**Fig. 6** Time graphs of torques 1— $M_{21}(t)$ , 2— $M_{32}(t)$ , 3— $M_{43}(t)$ ,  $t \in [0 \ 0.06]$

We set the regulator using the method stated above for the objective function,  $J_m$ . The following values of matrices  $\mathbf{K}_p, \mathbf{K}_d$  are obtained as a result of optimization:

$$\mathbf{K}_p = \begin{bmatrix} 1170 & 0 & 0 \\ 0 & 701.3 & 0 \\ 0 & 0 & 93.7 \end{bmatrix}, \mathbf{K}_d = \begin{bmatrix} 373.5 & 0 & 0 \\ 0 & 373.5 & 0 \\ 0 & 0 & 373.5 \end{bmatrix}. \quad (11)$$

Figure 6 shows time graphs of torques obtained by using a regulator with the given coefficients in the time interval  $t \in [0 \ 0.06]$ .

It may be noted that the increase in the value of things become much smoother and stretched over time, but the shapes of graphs  $\varphi_2(t), \varphi_3(t), \varphi_4(t)$  visually do not change.

## 4 Conclusion

The following results were obtained after the study. A three-stage method for setting the PID regulator parameters using  $LP_\tau$  sequences was proposed. The regulator was set using two different objective functions and a comparative analysis of the results carried out. It was shown that modifying cost function by adding to it spectral norms of the regulator gain matrices can result in “smoother” control action functions and can lead to obtaining gain matrices proportional to an identity matrix.

**Acknowledgments** Work is performed with RSF, Project № 14-39-00008 “The establishment of the research laboratory of modern methods and robotic systems to improve the human environment”.

## References

- Jatsun, S. F. (2015a). The modelling of the standing-up process of the anthropomorphic mechanism In S. F. Jatsun, L. Yu. Vorochaeva, A. S. Yatsun, & S. I. Savin (Eds.), *Proceedings of the International Conference on CLAWAR* (pp. 175–182).
- Jatsun, S. (2015b) Study of controlled motion of exoskeleton moving from sitting to standing position. In S. Jatsun, S. Savin, A. Yatsun, & A. Malchikov (Eds.), *Advances in Robot Design and Intelligent Control. Proceedings of the 24th International Conference on Robotics in Alpe-Adria-Danube Region (RAAD)*. Volume 371 of the series Advances in Intelligent Systems and Computing (pp. 165–172).
- Jatsun, S. F. (2015c). Locomotion control method for patients verticalization with regard to their safety and comfort. In S. F. Jatsun, S. I. Savin, A. S. Yatsun, & R. N. Turlapov (Eds.), *26th DAAAM International Symposium on Intelligent Manufacturing and Automation*.
- Jatsun, S. F., Savin, S. I., Yatsun, A. S., & Turlapov, R. N. (2015). Adaptive control system for exoskeleton performing sit-to-stand motion. In *The Tenth International Symposium on Mechatronics and its Applications ISMA* (p. 25).
- Jun, H. G., Chang, Y. Y., Dan, B. J., Jo, B. R., Min, B. H., Yang, H., et al. (2011). Walking and sit-to-stand support system for elderly and disabled. In *2011 IEEE International Conference on Rehabilitation Robotics (ICORR)* (pp. 1–5). IEEE.
- Kajita, S., Kanehiro, F., Kaneko, K., Yokoi, K., & Hirukawa, H. (2001). The 3D linear inverted pendulum mode: A simple modeling for a biped walking pattern generation. In *Proceedings. 2001 IEEE/RSJ International Conference on Intelligent Robots and Systems, 2001* (Vol. 1, pp. 239–246). IEEE.
- Kajita, S., Kanehiro, F., Kaneko, K., Fujiwara, K., Harada, K., Yokoi, K., et al. (2003, September). Biped walking pattern generation by using preview control of zero-moment point. In *Proceedings. ICRA'03. IEEE International Conference on Robotics and Automation, 2003*. (Vol. 2, pp. 1620–1626). IEEE.
- Park, J., & Khatib, O. (2006). Contact consistent control framework for humanoid robots. In *Proceedings 2006 IEEE International Conference on Robotics and Automation, 2006. ICRA 2006* (pp. 1963–1969). IEEE.
- Plagenhoef, S., Gaynor Evans, F., & Abdelnour, T. (1983). Anatomical data for analyzing human motion. *Research Quarterly for Exercise and Sport*, 54(2), 169–178.
- Sentis, L., Park, J., & Khatib, O. (2010). Compliant control of multicontact and center-of-mass behaviors in humanoid robots. *IEEE Transactions on Robotics*, 26(3), 483–501.
- Sobol, I. M. (1976). Uniformly distributed sequences with an additional uniform property. *USSR Computational Mathematics and Mathematical Physics*, 16(5), 236–242.
- Tsukahara, A., Hasegawa, Y., & Sankai, Y. (2009). Standing-up motion support for paraplegic patient with Robot Suit HAL. In *IEEE International Conference on Rehabilitation Robotics, 2009. ICORR 2009* (pp. 211–217). IEEE.

# Study of RE-Gait<sup>®</sup> as the Device That Promotes Walking Using a Two-Dimensional Emotion Map

Eiichirou Tanaka, Yusuke Osawa, Keiichi Muramatsu,  
Keiichi Watanuki, Shozo Saegusa and Louis Yuge

**Abstract** We developed a walking assistance apparatus RE-Gait<sup>®</sup> for not only the elderly but also apoplexy patients, which assist the ankle joint of the equipped person. By only assisting the ankle joint, the equipped person's leg can be raised. To keep up the user's motivation for exercise using this apparatus, it is necessary to assist not only physically but also mentally. Therefore we suggested the new method of promotion walking, using the walking assistance apparatus while listening to the beat sound, which was adjusted according to a two-dimensional emotion map. In this paper, the relation between emotion map and walking condition map is shown.

**Keywords** Walking assistance • Keeping up motivation • Two-dimensional emotion map

---

E. Tanaka (✉) · K. Muramatsu · K. Watanuki  
Graduate School of Science and Engineering, Saitama University, Saitama, Japan  
e-mail: tanakae@mech.saitama-u.ac.jp

K. Muramatsu  
e-mail: muramatsu@mech.saitama-u.ac.jp

K. Watanuki  
e-mail: watanuki@mech.saitama-u.ac.jp

Y. Osawa  
School of Engineering, Saitama University, Saitama, Japan  
e-mail: s12tm014@mail.saitama-u.ac.jp

S. Saegusa  
Faculty of Business Administration, Shujitsu University, Okayama, Japan  
e-mail: shosaegu@shujitsu.ac.jp

L. Yuge  
Graduate School of Biomedical & Health Sciences, Hiroshima University,  
Hiroshima, Japan  
e-mail: ryuge@hiroshima-u.ac.jp



## 1 Introduction

There are many elderly and apoplexy patients in Japan. Recently, various walking assistance devices have been developed (Colombo et al. 2000; Sankai 2010), and almost all devices assist for a hip joint and/or knee joint. However, the most fatigable muscle while walking is the TA (tibialis anterior) muscle, and equinus foot is likely to stumble. Therefore, we developed RE-Gait<sup>®</sup>, a walking assistance apparatus which assist the ankle joint of the equipped person. By only assisting the ankle joint, the equipped person's leg can be raised. This apparatus can use for not only the elderly but also apoplexy patients. The effectiveness of the method assisting only ankle joint was already shown in our papers (Kimura et al. 2013; Tanaka et al. 2015).

To keep up the user's motivation for exercise using this apparatus, it is necessary to assist not only physically but also mentally. Therefore we suggested listening to the beat sound, which was adjusted according to the walking cycle. We carried out the experiment where four subjects walked on the treadmill while listening to a beat sound. We asked them to give information on the condition of their feelings, from pleasant or not in each case of the beat sound. We also measured their heartbeat. By using these two parameters, the vector can be drawn on the two dimensional map. From these results of the vectors, we could recognize the relation between the beat sound and the emotion while walking and listening to the beat sound.

Furthermore, we carried out the experiment where subjects walked on the tread mill using the walking assistance apparatus while listening to a beat sound. These devices can be tuned based on a comfortable walking cycle. In this paper, the effectiveness of the method and the possibility of the control of the emotion while walking are shown.

## 2 Walking Assistance Apparatus for the Promotion of Exercise

**Development of RE-Gait<sup>®</sup>.** The previous type of our developed apparatus (Tanaka et al. 2015) had a flexible shaft and worm gear was relatively heavy weight (5.6 [kg]) for patients. Therefore, we developed RE-Gait<sup>®</sup>; a new type of the apparatus as shown in Fig. 1, which can be used not only for neuro-rehabilitation but also for the promotion of exercise, because it is very small (able to wear under the pants), light weight (One foot: 1 [kg]). The photo of wearing RE-Gait<sup>®</sup> are shown in Fig. 2. This apparatus assists the ankle joints of the equipped person with the motor controlled with a micro computer. The insole is attached to pressure sensors, and the apparatus can grasp the phase of the contact condition between the sole and the ground as shown in Fig. 3. In the reference (Tucker et al. 2015), motion intention estimation is important and it requires the human's control method for locomotion and the sensing to understand the state and intent. It is necessary to prepare the

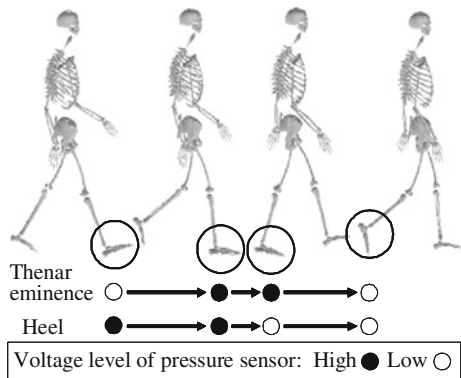


Fig. 1 RE-Gait<sup>®</sup> and wearing under the pants

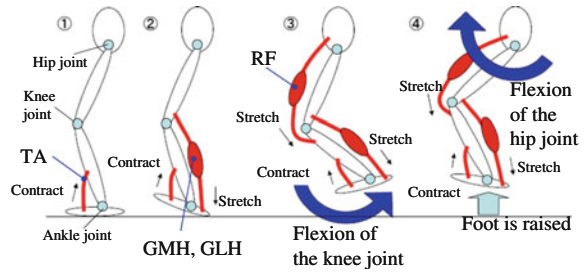
Fig. 2 Photo of wearing RE-Gait<sup>®</sup>



Fig. 3 Measurement of walking phase with pressure sensors



**Fig. 4** Mechanism to raise a foot by dorsiflexion assistance



hierarchical controller. However, if the robot has a complex controller, the equipped person may be hard to estimate the motion of the robot. Especially, the main targeted user is the elderly. Therefore, in our device, the motion is previously input, according to the contact condition of the pressure sensors.

**Mechanism to raise a foot by only assisting the ankle joint.** Our developed apparatus can raise the user's leg utilizing stretch reflex to bi-articular muscle of the user, by only assisting the ankle joint as shown in Fig. 4. The mechanism of raising a leg only by assisting the ankle joint can be explained as follows: (1) By the dorsiflexion of the ankle joint by the apparatus, GMH (Medial Head of Gastrocnemius muscle) of the bi-articular muscle is diminished by stretch reflex, and the knee joint is inflected. (2) By inflecting the knee joint, RF (Rectus Femoris muscle) of bi-articular muscle is also diminished by stretch reflex, and the foot is raised. By utilizing this method, the actuator for the knee joint does not have to be equipped and the load on the user's leg can be decreased.

### 3 Walking Promotion Experiment Using a Two-Dimensional Emotion Map

**Walking experiment using RE-Gait<sup>®</sup> while listening to a beat sound.** We already confirmed the effectiveness of the ankle assist apparatus in previous studies. By using the apparatus, the dorsiflexion and the plantarflexion are increased, it means to improve gait, and walking safety. From this result, it is better to use the apparatus to promote waking exercise. Furthermore, for long time use, we suggest the method to control the walking condition and feeling by adjusting the targeted cadence of the apparatus. At first, we carried out the measuring experiment while using RE-Gait<sup>®</sup>. Subjects were four able-bodied men (Age: 21–22). We measured the walking speed, the number of steps, their heartbeat, and carried out a feeling questionnaire after each experiment.

To confirm the influence of the walking condition of equipped persons, we compared the variation of the walking condition while using RE-Gait<sup>®</sup> or not. Subjects walked on a treadmill, and they tuned to the comfortable walking speed themselves, and they walked for three minutes. After taking an adequate rest, they

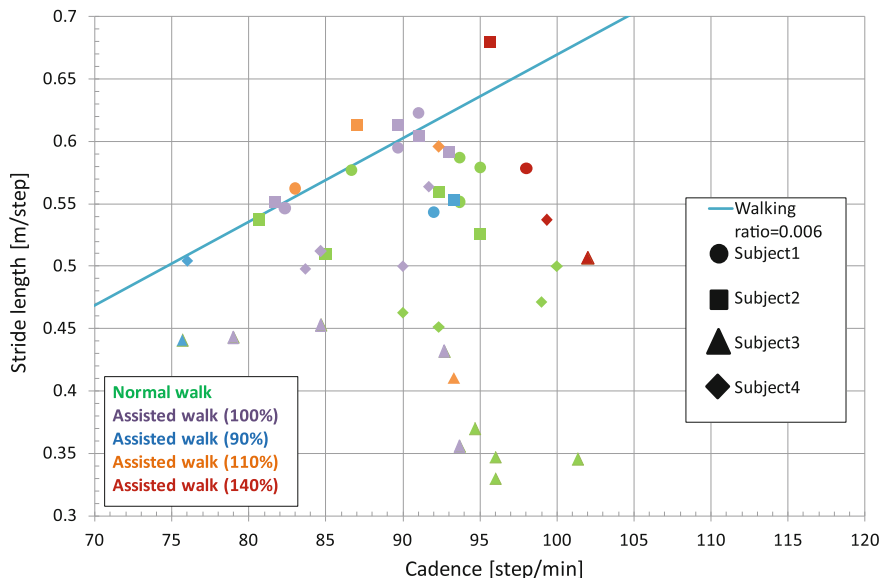


**Fig. 5** Variation of the condition from normal walk (Green) to assisted walk adjusted cadence of the apparatus by 100 (Purple), 90 (blue), 110 (Orange), and 140 % (Red)

walked again and used RE-Gait<sup>®</sup>. The targeted cadence of RE-Gait<sup>®</sup> was also tuned to be able to walk comfortably. We counted the number of steps and recorded the set speed of the treadmill, therefore we derived the cadence, stride length, and walking ratio. Figure 5 shows the result of the variation of the walking condition. From the reference (Diedrich and Warren 1995), the walking ratio of the free walk is about 0.006, therefore the line whose gradient is 0.006 is drawn. As shown in Fig. 5, by using RE-Gait<sup>®</sup>, the walking ratio of all subjects increased. Generally, the elderly’s walking ratio is about 0.004.

Next, to grasp the influence of the walking condition by tuning the targeted cadence of RE-Gait<sup>®</sup>, we carried out the experiment and compared the variation of walking condition of the assisted walk adjusted the targeted cadence of RE-Gait<sup>®</sup> comfortably (100 %) and adjusted by 90, 110, and 140 %. The result is shown in Fig. 5. The results of the 140 % of the targeted cadence slightly shift toward the right direction of the graph, however, the results between the 100 % (Purple dots) and the others are close.

Finally, we carried out the experiment and compared the variation of the condition of the assisted walk listening to the beat sound whose targeted cadence and beat was adjusted same as the 100, 90, 110, and 140 % of the cadence. The result is shown in Fig. 6. The results of the 90 % shift toward the left direction, and results of the 140 % shift toward the right and upper direction. Therefore, to control the walking condition, it is better to use both the apparatus and listening to the beat sound together.

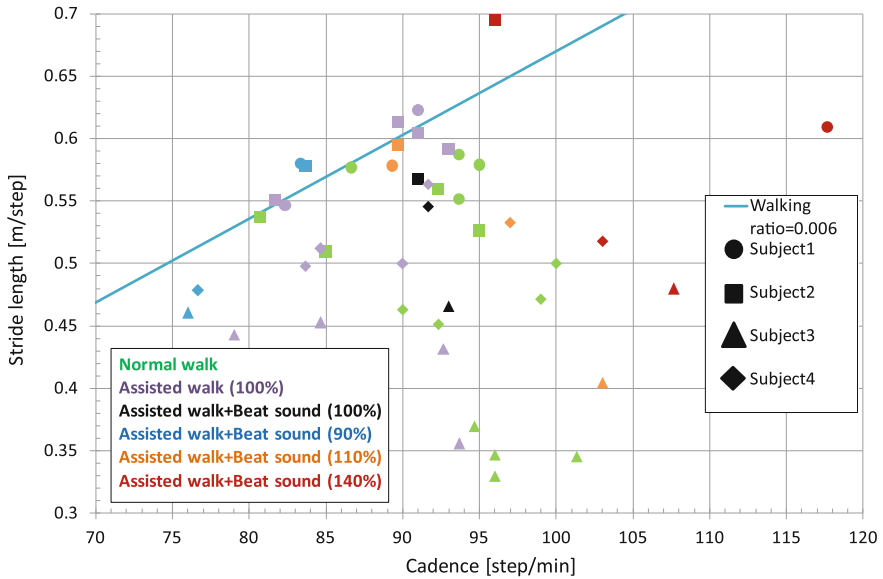


**Fig. 6** Variation of the condition from normal walk (Green) to assisted walk (Purple), and assisted walk listening to the beat sound whose targeted cadence and beat was adjusted as by 100 (Black), 90 (blue), 110 (Orange), and 140 % (Red)

**Two dimensional emotion map while using RE-Gait® and listening to a beat sound.** After the experiments we asked subjects to give information on the condition of their feelings, from pleasant or not by 7 levels in each case of the beat sound. We defined the result of this questionnaire as the horizontal axis of the two-dimensional emotion map. We also measured their heartbeat. We translated the variation of LF/HF (LF: low frequency, HF: High frequency) to the vertical axis of arousal, and the value of LF/HF when the subject walked while listening to the 100 % beat of the walking cycle was defined as an original point. We assumed each result of these calculated values were on the vertical axis. By using these two parameters, we could define the two-dimensional emotion vector on the map.

Figure 7 shows the result of the two dimensional emotion map of the assisted walk using RE-Gait®. The results of the 110 % exists on the upper and right axes, however, the most of all results of the 90 and 140 % exists in the third quadrant. It is unarousal and negative emotion. These shift methods cannot use for emotion control, because walking motivation of the subject decreases.

On the other hand, Fig. 8 shows the result of the two dimensional emotion map of the assisted walk using RE-Gait® and listening to the beat sound. Almost all data shift toward the right direction and some data of the 90 and 110 % exists in the first quadrant. From these results, the method of tuning to the 90 and 110 % for the targeted cadence of the apparatus and beat sound is effective to control walking keeping positive feeling. On the contrary, two data of the 140 % are in the left end on the vertical axis. From Fig. 6, the walking condition of the 140 % of Subjects

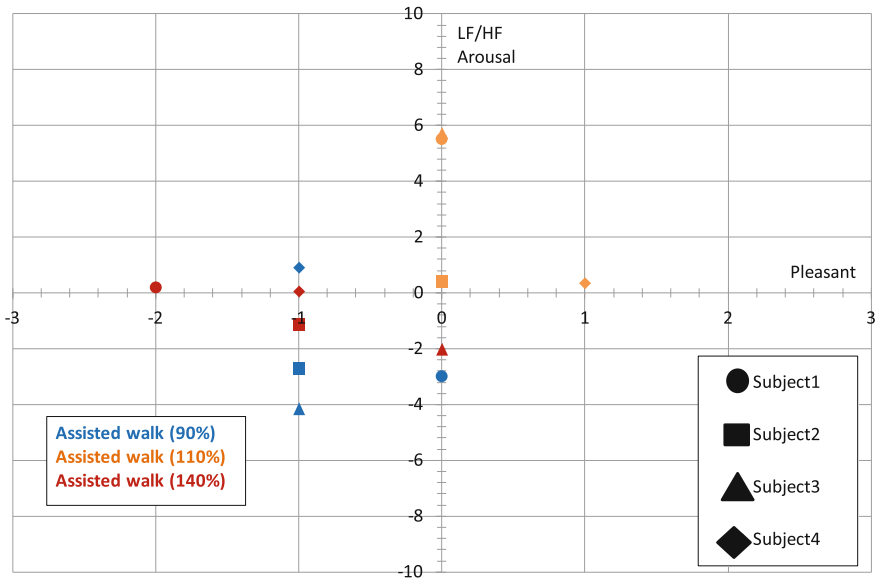


Fig. 7 Two dimensional emotion map of the assisted walk using the apparatus (100 %: original point, 90 %: blue, 110 %: orange, 140 %: red)

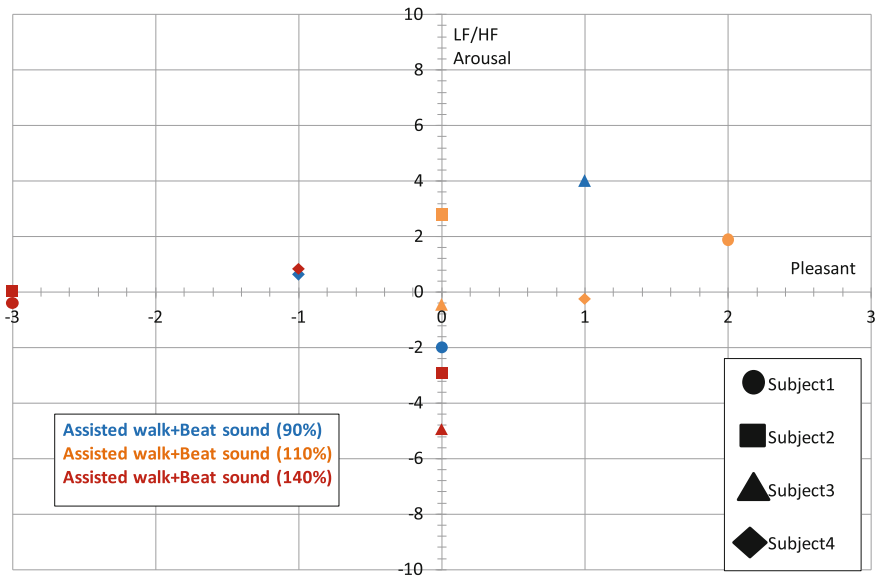


Fig. 8 Two dimensional emotion map of the assisted walk using the apparatus and listening to the beat sound (100 %: original point, 90 %: blue, 110 %: orange, 140 %: red)

land 2 are drastically improved, however, it is difficult for them to keep the motivation of walking.

From these results of the two dimensional emotion map, the effectiveness of the method to tune the cadence and beat sound was confirmed. Therefore, we suggest the method of walking promotion and keeping motivation of walking exercise as follows:

- (1) At first, the targeted beat sound is set at 100 % of the normal cadence.
- (2) When the value of LF/HF of hart beat increases, the targeted beat sound is set at 110 % of the normal cadence.
- (3) When the value of LF/HF increases higher than the normal value by about 5–10, the targeted beat sound is set at 90 % of the normal cadence.
- (4) When the value of LF/HF decreases lower than the normal balue by about 5–10, the targeted veat sound is set at 110 %
- (5) Repeat from (2) to (4) arbitraly with the computer program

As a future work, we will carry out the experiment with more subjects.

## 4 Conclusions

We developed the small and simple walking assistance apparatus, RE-Gait<sup>®</sup>. For keeping user's motivation of exercise walking, we suggested to use RE-Gait<sup>®</sup> and listen to the beat sound, which were tuned on the basis of comfortable cadence. Two dimensional emotion map was drawn and we comfirmed the relation between the walking condition and the subject's emotion. By using this result, the method for keeping motivation of the walking exercise can be utilised.

## References

- Colombo, G., et al. (2000). Treadmill training of paraplegic patients using a robotic orthosis. *Journal of Rehabilitation Research and Development*, 37(6), 693–700.
- Diedrich, F. J., & Warren, W. H. (1995). Why change gaits? *Dynamics of the Walk-Run Transition, Journal of Experimental Psychology: Human Perception and Performance*, 21(1), 183–202.
- Kimura, H., Tanaka, E., & Yuge, L. (2013). Clinical application of robotic orthosis for patients with lower limb paralysis. In *Inclusion, Participation & Empowerment (ISPO 2013) World Congress*, 82.
- Sankai, Y. (2010). HAL: Hybrid assistive limb based on cybernics. In *Robotics Research, The 13th International Symposium ISRR*, 25–34.
- Tanaka, E., Muramatsu, K., Watanuki, K., Saegusa, S., & Yuge, L. (2015). Walking assistance apparatus enabled for neurorehabilitation of patients and its effectiveness. *Mechanical Engineering Letters, JSME*, 1, 15-00530.
- Tucker, M. R., Olivier, J., Pagel, A., Bleuler, H., Bouri, M., Lambercy, O., del R Millán, J., Riener, R., Vallery, H., & Gassert, R. (2015). Control strategies for active lower extremity prosthetics and orthotics: A review. *Journal of neuroengineering and rehabilitation*, 12(1).

# Development of Road Condition Categorizing System for Manual Wheelchair Using Mahalanobis Distance

Kazuyuki Kojima, Hiroki Taniue and Jun'Ichi Kaneko

**Abstract** Wheelchairs are widely used for the people with difficulty in walking. In accordance with the enforcement of the law regarding the promotion of their smooth transfer, barrier-free systems have been provided in many public facilities. However, many small gaps, narrow lanes which interrupt wheelchair users still remain. They also interrupt electric wheelchairs and human support robots with wheels. This paper describes our Mahalanobis-distance based road condition categorizing system for such mobilities. This system enables us to detect the barriers and informs us where the barriers are. This paper describes the method and confirms its validity by conducting experiments.

## 1 Introduction

This paper describes our Mahalanobis-based road condition categorizing system for manual wheelchairs which are widely used for the people with difficulty in walking such as the injured, the aged and the paralyzed inferior limbs. In accordance with the enforcement of the law regarding the promotion of their smooth transfer, barrier-free systems have been provided in many public facilities. From the point of view of barrier-free and human-centered design, the road surface has smoothed, a difference in level has been eliminated, and a wheelchair ramp has been installed in the public spaces (Ballast 2013). However, many small gaps, narrow lanes which interrupt wheelchair users still remain. The reason is that such disturbances are unde-

---

K. Kojima (✉) · J. Kaneko  
Department of Mechano-Robotics, Graduate School of Science & Engineering,  
Saitama University, Saitama, Japan  
e-mail: kojima@mech.saitama-u.ac.jp

J. Kaneko  
e-mail: jkaneko@mech.saitama-u.ac.jp

H. Taniue  
Department of Engineering, Saitama University, Saitama, Japan  
e-mail: s12tm064@mail.saitama-u.ac.jp

© CISM International Centre for Mechanical Sciences 2016  
V. Parenti-Castelli and W. Schiehlen (eds.), *ROMANSY 21 - Robot Design, Dynamics and Control*, CISM International Centre for Mechanical Sciences 569,  
DOI 10.1007/978-3-319-33714-2\_42



tectable by non-handicapped people. These barriers also interrupt electric wheelchairs and human support robots with wheels. In this study, in order to detect and indicate the disturbances, network-connected manual wheelchair with torque sensors, an accelerometer and a GPS receiver is used. In this paper, we focus on the relationship between the road condition and handrim torque while driving the manual wheelchair. Using the relationship, based on the Mahalanobis-Taguchi system (Taniguchi et al. 2000), our proposed method enables categorizing road conditions.

## 2 Road Disturbances for Wheelchair Users

Figure 1 shows examples of road disturbances such as (a) small gap, (b) manhole cap, (c) braille blocks, (d) slope, (e) cracks and (f) narrow lane for wheelchair users. These disturbances are undetectable by non-handicapped people. Therefore, in spite

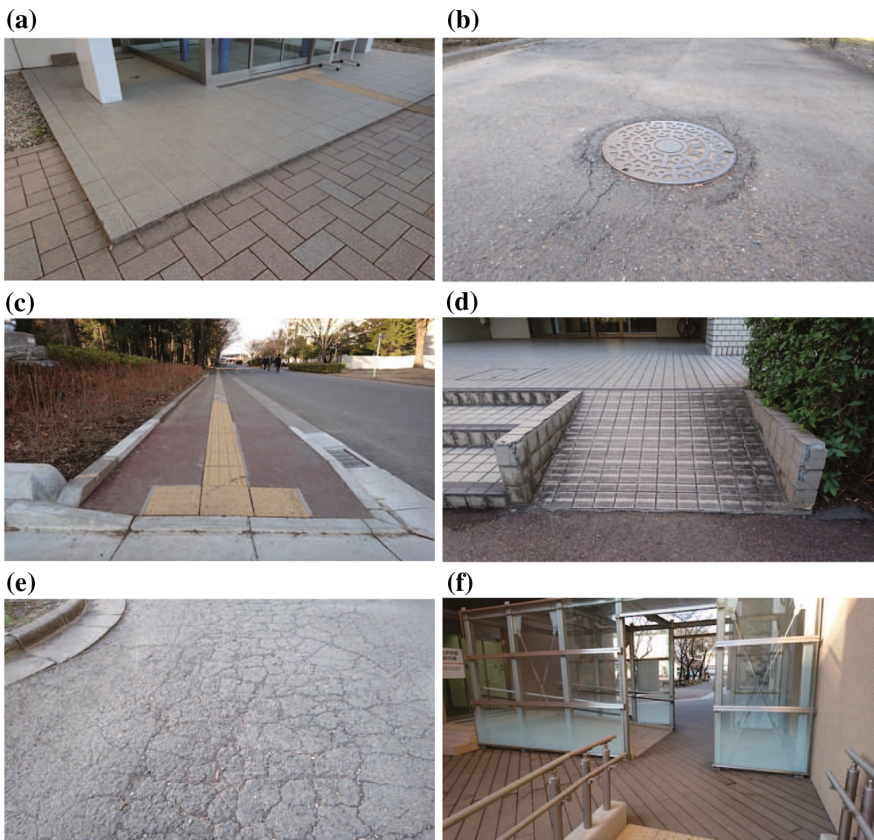


**Fig. 1** Road disturbances for wheelchair users. **a** Small gap. **b** Manhole cap. **c** Braille blocks. **d** Slope. **e** Cracks. **f** Narrow lane

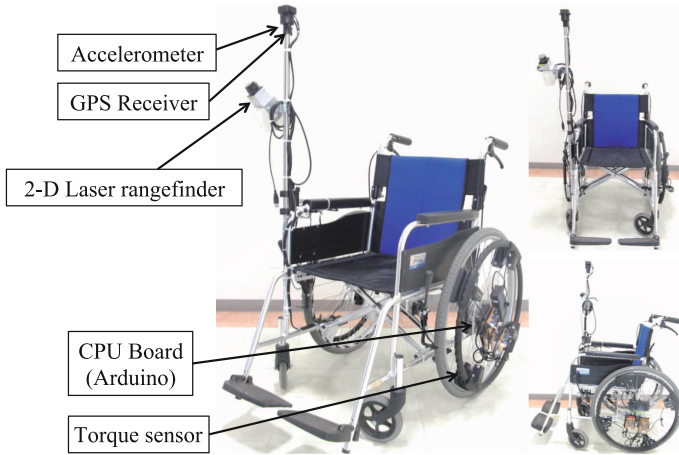


**Fig. 2** Proposed wheelchair

of the idea of barrier-free design, many of these disturbances still remain. For driving comfort for the wheelchair users, road repair in consideration of the wheelchair users is needed.

### 3 Wheelchair-Type Road Surface Inspection System

Figure 2 shows our proposed wheelchair-type road surface inspection system. We have been developing the wheelchair on which torque sensors, an accelerometer and a GPS receiver are implemented for gathering the road condition data onto our server PC (Sato et al. 2014; Taniue et al. 2015). Various researches using a sensors-implemented wheelchair has been made in the past decade (Redford 1993; Henderson 1994; Tolerico et al. 2007; Chugo et al. 2011; Sumida and Matsunaga 2012). These researches focused on behaviors of wheelchair users. On the other hand, we focus on road conditions. Our final purpose is to develop a system which display traffic disturbances for manual wheelchairs on the digital map automatically. For this purpose, this study aims to associate the measurement values with road conditions using Mahalanobis distance.

### 4 Characteristics of Time Series Handrim Torque

We measured handrim torque while driving the wheelchair at various road conditions. Figure 3 shows time series torque at (a) normal driving, (b) left tilting road, (c) slope and (d) step respectively. Those waveforms differ depending on the

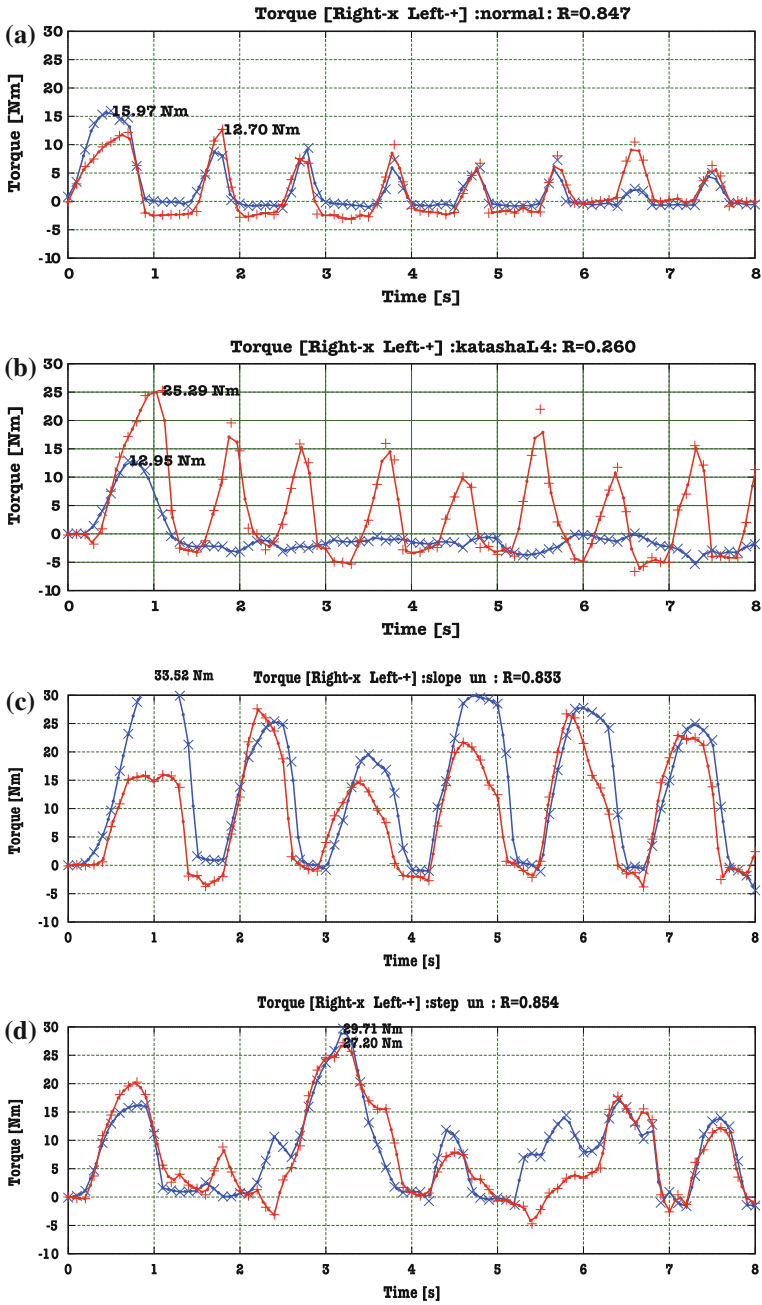


Fig. 3 Time series handrim torque. a Normal. b Left tilting road. c Slope. d Step

road conditions. During normal driving, approximately 1 Hz periodically waveform appears at both left and right handrims. While driving on a left tilting road, periodically waveform only appears on the left side handrim. Larger torque is needed while climbing a slope and an impact load arises when the wheelchair is crossing over a step. These waveforms have different magnitude and frequency. Therefore these waveforms can be categorized into a road condition using these features and some other values.

## 5 Unit Space and Mahalanobis Distance

Mahalanobis Taguchi system (MT system) was proposed by Taguchi in the field of quality engineering (Taniguchi et al. 2000). This method provides a guiding principles for judging if some condition is included in a kind of group by using Mahalanobis distance. Using this method, unit space is defined in consideration of correlations of all quantities in a certain state. In detail, Mahalanobis distance is defined using means, variances and correlations of the data set in following equations.

$$D(\mathbf{u}) = \sqrt{\frac{1}{k} \mathbf{u}^T \mathbf{R}^{-1} \mathbf{u}} \quad (1)$$

where  $\mathbf{R}$  is correlation coefficient matrix,

$$\mathbf{u} = (u_1, u_2, u_3, \dots)^T \quad (2)$$

$$u_i = \frac{x_i - m_i}{\sigma_i} \quad (3)$$

$x_i$  is measurement data,  $m_i$  is mean value of each data set, and  $\sigma_i$  is standard deviation. Therefore, the Mahalanobis distance is unitless and scale-invariant, and considering of the correlations of the data set.

## 6 Measurement and Calculation

Acquired time series torque data differs depending on the road conditions. In our previous experiments, we realized torque periodicity, maximum value, dominate frequency and phase difference rely on the road conditions. Therefore, in this study, Mahalanobis distance is derived from following eight kinds of data, (1) left maximum torque (Nm), (2) right maximum torque (Nm), (3) left average torque (Nm), (4) right average torque (Nm), (5) left dominant frequency (Hz), (6) right dominant frequency (Hz), (7) phase difference (rad), and (8) correlation coefficient.

After the data acquisition using our manual wheelchair, 247 sets of time series data are extracted and categorized into nine conditions, (1) left tilting road (neutral), (2) left tilting road (discomfort), (3) right tilting road (neutral), (4) right tilting road (discomfort), (5) normal, (6) rough surface, (7) slope (neutral), (8) slope (discomfort), and (9) step. The correlation coefficient matrix, the mean value vector and the standard deviation vector are derived for each condition. Note that categories include road comfort level based on questionnaire result using subjects. The matrices for ‘normal’ as an example case are shown in Eqs. (4)–(6).

$$R = \begin{pmatrix} 1.00 & 0.25 & 0.66 & 0.41 & -0.20 & -0.24 & 0.25 & -0.10 \\ 0.25 & 1.00 & 0.31 & 0.64 & -0.13 & -0.22 & -0.03 & 0.10 \\ 0.66 & 0.31 & 1.00 & 0.61 & -0.22 & -0.50 & 0.00 & 0.06 \\ 0.41 & 0.64 & 0.61 & 1.00 & -0.34 & -0.48 & -0.11 & -0.09 \\ -0.20 & -0.13 & -0.22 & -0.34 & 1.00 & 0.53 & -0.25 & 0.19 \\ -0.24 & -0.22 & -0.50 & -0.48 & 0.53 & 1.00 & 0.15 & 0.11 \\ 0.25 & -0.03 & 0.00 & -0.11 & -0.25 & 0.15 & 1.00 & 0.09 \\ -0.10 & 0.10 & 0.06 & -0.09 & 0.19 & 0.11 & 0.09 & 1.00 \end{pmatrix} \tag{4}$$

$$m = (18.36 \ 16.70 \ 3.43 \ 3.04 \ 0.95 \ 1.06 \ 0.63 \ 0.80) \tag{5}$$

$$\vec{\sigma} = (4.67 \ 3.59 \ 1.64 \ 1.67 \ 0.32 \ 0.25 \ 3.28 \ 0.14) \tag{6}$$

Table 1 shows Mahalanobis Distances for sample time series data. The ‘Left tilting road (neutral)’ case shown in the first row has nine distances from each unit space of road condition. The distance from ‘Left tilting road (neutral)’ indicated with ‘LTLT\_N’ is 1.2, the distance from ‘Left tilting road (discomfort)’ indicated with ‘LTLT\_D’ is 1.5. Similarly, RTLTL\_N is 13.1, RTLTL\_D is 4.4, NORM is 2.8, ROUH is 4.8, SLOP\_N is 20.3, SLOP\_D is 10.1, and STEP\_D is 2.3. According to

**Table 1** Mahalanobis distance from unit space for each condition

	LTLT_N	LTLT_D	RTLTL_N	RTLTL_D	NORM	ROUH	SLOP_N	SLOP_D	STEP_D
(1) Left tilting road (neutral)	1.2	1.5	13.1	4.4	2.8	4.8	20.3	10.1	2.3
(2) Left tilting road (discomfort)	3.6	1.2	13.7	4.7	2.8	4.5	22.5	13.4	2.3
(3) Right tilting road (neutral)	7.4	7.2	1.3	2.9	2.9	2.7	4.8	5.6	1.8
(4) Right tilting road (discomfort)	11.3	8.2	2.1	0.7	3.0	5.1	23.4	11.3	2.1
(5) Normal	9.0	6.7	5.0	3.8	1.6	2.0	19.0	8.4	1.6
(6) Rough surface	7.2	6.3	2.4	4.0	2.0	1.1	3.3	3.0	1.3
(7) Slope (neutral)	5.6	4.9	2.8	4.8	0.8	2.1	0.8	2.2	1.0
(8) Slope (discomfort)	10.2	7.8	7.8	4.1	2.1	3.1	4.9	1.0	1.1
(9) Step	10.1	7.5	9.3	5.2	1.7	5.9	5.3	6.0	1.0

the shortest distance of 1.2, '(1) Left tilting road' case in the first row is categorized into the 'Left tilting road (neutral)'. Similarly, '(2) Left tilting road (discomfort)' case in the second row is categorized into the 'Left tilting road (discomfort)' indicated with 'LTLT\_D' according to the shortest distance of 1.2. 223 of 247 sets were correctly categorized. As a result, overall correct answer ratio was 90.3 %. However, these sets are all used for calculation of Mahalanobis' unit spaces. Table 2 shows the result of 33 sample sets. In this case, all sets are not for the unit space calculation but for the confirmation of our proposed method. Cells surrounded by bold lines are correct answers for each row. Colored cells show the shortest distances. Among the 33 sets, 20 sets were correct. Therefore, the correct answer ratio was 60.6 %.

**Table 2** Mahalanobis distance from unit space for each condition

	LTLT_N	LTLT_D	RTLTL_N	RTLTL_D	NORM	ROUH	SLOP_N	SLOP_D	STEP_D
sample1 (step)	8.7	6.3	3.2	4.2	1.9	7.5	2.1	3.6	2.1
sample2 (step)	10.2	8.8	10.2	4.7	1.6	3.9	6.7	3.1	0.8
sample3 (step)	8.1	6.9	2.6	3.4	2.5	8.9	9.3	3.0	2.6
sample4 (step)	6.9	5.0	2.7	4.9	0.7	1.4	1.2	2.1	0.9
sample5 (step)	9.5	7.1	7.8	3.6	1.4	3.0	8.0	5.4	0.8
sample6 (step)	7.0	5.1	3.1	4.3	1.0	2.4	1.8	1.3	0.8
sample7 (left tilting road (neutral))	2.3	2.4	13.6	5.6	1.9	5.3	37.3	18.6	2.0
sample8 (left tilting road (neutral))	0.5	1.0	14.4	4.9	2.9	4.8	28.6	14.1	2.5
sample9 (left tilting road (discomfort))	3.4	1.5	14.6	5.3	3.3	5.4	34.0	15.4	2.8
sample10 (left tilting road (discomfort))	2.1	1.3	13.7	5.1	2.4	4.9	31.9	16.5	2.4
sample11 (right tilting road (neutral))	10.4	8.4	1.8	1.2	2.5	6.0	22.0	9.9	2.0
sample12 (right tilting road (neutral))	12.9	7.9	0.8	1.3	3.0	4.2	24.3	11.7	2.3
sample13 (right tilting road (discomfort))	10.7	7.8	1.3	1.0	2.7	5.9	16.9	7.7	2.0
sample14 (right tilting road (discomfort))	12.9	9.0	1.9	0.5	3.4	8.4	23.8	10.9	2.5
sample15 (step)	10.4	9.7	11.9	5.1	2.9	9.3	8.4	7.2	1.6
sample16 (step)	10.7	7.5	10.1	4.7	1.9	4.3	5.4	5.2	1.4
sample17 (normal)	4.6	6.2	6.6	5.9	0.7	3.2	3.8	3.2	1.4
sample18 (normal)	4.6	6.8	7.9	6.0	0.9	3.0	4.7	3.4	1.5
sample19 (normal)	5.4	6.9	3.8	5.4	1.4	3.2	1.9	3.3	1.6
sample20 (normal)	8.1	4.9	3.0	4.4	0.9	1.4	2.0	1.6	0.8
sample21 (rough surface)	7.1	6.2	3.6	4.8	1.1	1.4	4.2	2.7	1.1
sample22 (rough surface)	7.9	6.9	2.2	4.8	3.4	15.2	2.6	5.6	3.9
sample23 (slope (neutral))	8.8	6.6	3.5	4.8	3.0	11.7	1.6	4.7	3.2
sample24 (slope (neutral))	7.0	6.3	3.1	5.3	3.2	10.6	1.8	3.6	3.2
sample25 (slope (discomfort))	11.9	7.6	8.1	4.4	2.4	3.0	3.1	2.3	1.5
sample26 (slope (discomfort))	12.1	8.0	6.9	3.5	2.5	9.3	4.1	3.8	1.9
sample27 (normal)	4.8	6.2	5.6	6.0	1.1	2.7	3.4	4.2	1.8
sample28 (normal)	8.2	5.6	1.9	3.4	1.6	2.0	3.6	2.5	1.0
sample29 (step (discomfort))	10.1	7.6	8.4	4.1	1.0	3.7	5.4	3.9	0.5
sample30 (step (discomfort))	11.7	8.4	10.9	4.6	2.1	5.2	6.7	5.7	0.9
sample31 (normal)	4.4	7.7	7.0	6.3	1.6	4.3	4.3	5.0	2.0
sample32 (normal)	8.7	7.2	3.3	3.9	1.3	2.5	21.0	9.7	1.5
sample33 (normal)	4.4	3.8	4.1	4.3	0.7	1.6	8.8	4.3	0.9

## 7 Conclusion

This paper described a method to categorize road surface conditions for manual wheelchair based on Mahalanobis distance. In this paper, we first acquired time series handrim torque and 247 sets of waveform were extracted from the time series data and categorized into nine conditions. We then derived the unit spaces for the nine conditions from the acquired data. Finally, we confirmed that sample cases could be categorized with overall correct answer ratio of 60.6%. Our future work is to increase the number of sensor kinds for improvement of categorizing accuracy.

## References

- Ballast, D. K. (2013). *Interior Design Reference Manual* (6th ed.). Professional Publications, Inc.
- Brandstater, M., Mandac, R., Henderson, J., & Price, S. (1994). Efficacy of three measures to relieve pressure in seated persons with spinal cord injury. *Archives of Physical Medicine and Rehabilitation*, *75*, 535–539.
- Chugo, D., Fujita, K., Sakaida, Y., Yokota, S., & Takase, K. (2011). Depressurization assistance according to a posture of a seated patient. In *Proceedings of 2011 4th International Conference on Yokohama, Japan* (pp. 287–292).
- Hayashi, M., Goshi, K., Sumida, Y., & Matsunaga, K. (2012). Development of a route finding system for manual wheelchair users based on actual measurement data. In *Proceedings of Ubiquitous Intelligence & Computing and 9th International Conference on Autonomic & Trusted Computing (UIC/ATC)* (pp. 17–23).
- Redford, J. (1993). Seating and wheeled mobility in the disabled elderly population. *Archives of Physical Medicine and Rehabilitation*, *74*, 877–885.
- Sato, M., Kaneko, J., & Kojima, K. (2014). Development of pavement surface inspection system for wheelchair comfortability. In *Proceedings of 2014 IEEE 3rd Global Conference on Consumer Electronics (GCCE 2014)* (pp. 219–220).
- Taniguchi, G., Chowdury, S., & Wu, Y. (2000). *The Mahalanobis Taguchi System*. McGraw Hill.
- Taniue, H., Kaneko, J., & Kojima, K. (2015). Development of automatic barrier detection system for wheelchair. In *Proceedings of 2015 IEEE 4th Global Conference on Consumer Electronics (GCCE 2015)* (pp. 374–376).
- Tolerico, M., Ding, D., Cooper, R., Spaeth, D., Fitzgerald, S., Cooper, R., et al. (2007). Assessing mobility characteristics and activity levels of manual wheelchair users. *Journal of Rehabilitation Research and Development*, *44*, 561–572.

# Control of a Self-adjusting Lower Limb Exoskeleton for Knee Assistance

Viet Anh Dung Cai, Philippe Bidaud, Viet Thang Nguyen,  
Consuelo Granata and Minh Tam Nguyen

**Abstract** In this paper, the authors present the control architecture of a multi-contacts lower limb exoskeleton which is designed for knee rehabilitation purposes. The device's novel mechanical architecture, which comprises passive mechanical linkages connecting the user limbs to an external rigid mechanical structure, allows a more effective control of the system's transparency as only principal torque components are transmitted to the user's anatomical joints. Different types of sensors were used to capture the user's kinematics as well as to detect contacts between the user's soles and the ground. This data allow the estimation of the gait phases in realtime, using Principal Components Analysis (PCA) and Markov chain. Finally, a predictive controller was implemented on the device to assist the knee joints during specific gait phases.

## 1 Introduction

Recent works on the design of exoskeletons for human anatomical joints rehabilitation have figured out that a human anatomical joint is in most cases spatial and can not be reduced to simple elementary mechanical joints (Woltring et al. 1985). Thus, the

---

V.A.D. Cai (✉) · V.T. Nguyen · M.T. Nguyen  
Interactive Robotics Laboratory, University of Technology and Education,  
01 Vo Van Ngan Street, Thu Duc District, Ho Chi Minh City, Vietnam  
e-mail: dungcva@hcmute.edu.vn

V.T. Nguyen  
e-mail: thangnv@hcmute.edu.vn

M.T. Nguyen  
e-mail: tamnm@hcmute.edu.vn

P. Bidaud (✉) · C. Granata  
UPMC Univ Paris 06, Institut des Systèmes Intelligents et de Robotique,  
4 Place Jussieu, 75005 Paris, France  
e-mail: bidaud@isir.upmc.fr

C. Granata  
e-mail: consuelo.granata@gmail.com

© CISM International Centre for Mechanical Sciences 2016  
V. Parenti-Castelli and W. Schiehlen (eds.), *ROMANSY 21 - Robot Design, Dynamics and Control*, CISM International Centre for Mechanical Sciences 569,  
DOI 10.1007/978-3-319-33714-2\_43



design of exoskeletons for functional rehabilitation must take into account the complexity of anatomical joints. A misalignment between the instantaneous anatomical axis and the mechanism's actuated axis will create residual force/torque components that may limit the natural motion of the joint, or even cause permanent injuries in extreme cases. In 2006, (Schiele and Van der Helm 2006) presented a novel design for human arm exoskeleton which has 9 d.o.f. in total. In this design, a RPR mechanism is used at the elbow joint. Only the first rotational joint is actuated while the two other joints are passive, assuring that only the actuator torque is transmitted to the elbow. It was followed by different original designs in literature such as (Cai et al. 2011; Ergin and Patoglu 2012; Stienen et al. 2009). All these authors noticed the need of using passive linkages to eliminate undesired residual force/torque components.

Several authors (Popovic et al. 1989; Rabishong et al. 1975) have conducted research on modular exoskeletons since 1970s. These systems are designed to correct an individual joint during a specific task (such as walking). However, having no contact with the ground, a modular system must have low inertia in order to not disturb the user's movement. Meantime, full lower limb exoskeletons were also developed by several research teams (Banala et al. 2006; Vukobratovic et al. 1974). They were designed to assist paraplegic patients that have full upper-body capabilities during walking. The interaction with human limbs can be measured by force/torque sensors, and the assistance is provided when necessary during walking. As all the load of the system is transferred to the ground, in theory, the device won't affect natural motions if it is able to predict and follow the user motion. By this way, designers have less concerns about creating low mass and low inertia structure as in case of modular devices. To this end, several authors have been working on the kinematic measurement of human locomotion using passive exoskeletons (Kanjanapas and Tomizuka 2013) or using camera based motion capture systems with force plates (Popovic et al. 2005). This approach seems to be very promising, especially in functional rehabilitation applications, as the device can follow the subject's motion and assist one targeted joint during specific phases.

In this paper, the authors propose a novel mechanical design for lower limb exoskeleton and a hybrid predictive control solution developed for knee assistance during locomotion. The controller has the ability to provide torque assistance to the knee joint at precise moments during the gait cycle. This can be done using a robust gait phase detection method, based on the user's joints kinematic data measured by the exoskeleton itself.

## 2 Mechanical Design

The authors applied the design rule propose by (Cai et al. 2011) for the determination of the total general mobility of the mechanism and the number of passive joints that should be included into the mechanism to make the whole mechanical structure free of constraints when it is attached onto an anatomical joint. The idea is quite simple: one can consider two adjacent human corporal segments as two rigid solids which

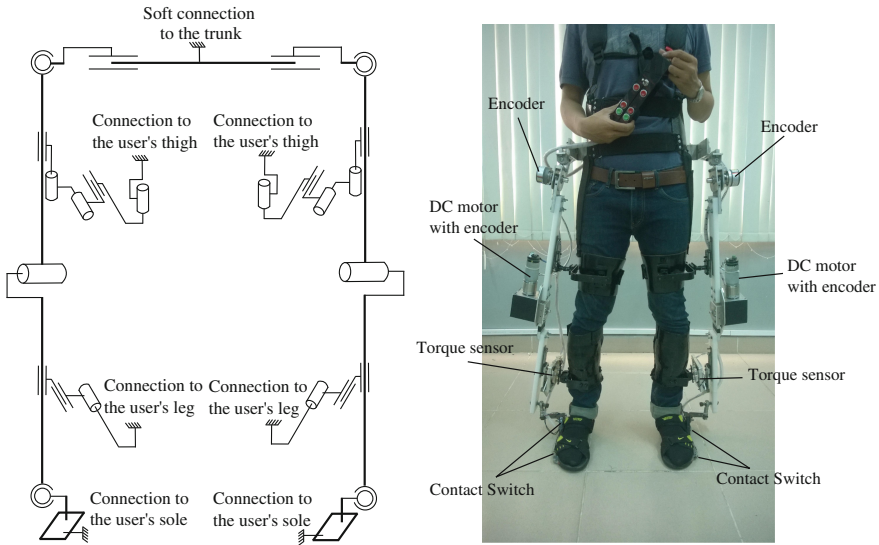


**Fig. 1** The complete kinematic scheme and the first prototype of the lower limb exoskeleton

are connected to each other by an anatomical joint. In space, the relative movement of a segment relative to the other one can be described by six parameters of movement (three translations and three rotations). As an anatomical joint is composed by bones, cartilages, menisci and other flexible elements such as ligaments, tendons and so on its kinematics is always variable depending on the load condition. Therefore, one must use in total 6 kinematic parameters to describe a complete human anatomical joint kinematics. As a result, an effective modular exoskeleton must have 6 degrees of freedom (including actuated and passive mechanical joints) in order to follow the natural motion of the subject without perturbing it. Obviously, to simplify the design, passive joints performing low angular variation amplitude during the user’s intended movement can be omitted. Other optimization factors such as force transmission capability or kinematic isotropy must also be considered by designers. This design rule is here generalized for full lower limb exoskeletons as shown in Fig. 1.

For the understanding of the design, one can divide the kinematic scheme into two parts: the anthropomorphic external structure which supports all the load of the system and the internal linkages, which connect the external structure to the user’s corporal segments. The external structure is composed by 2 spherical joints located at the ankles, 2 actuated rotational joints located at the knees, 2 other spherical joints at the hips and 2 prismatic joints which connect the whole structure to the user’s trunk. The internal linkages are composed by passive joints, which are used to connect the external structure to the human limbs (both the thighs and the legs). As it is demonstrated by several authors that the knee torque is essentially negative during walking (Kanjanapas and Tomizuka 2013; Popovic et al. 2005), the resistive motor torques can be provided at the knee during the stance phase to increase the stability

of the joint or at the Preswing phase (push-off) to assist the initiation of the swing movement. During other gait phases, the two motors are controlled in such a way that the mechanism can follow the intended movement of the user. This can be done using a zero torque controller. The interactive torques measurement can be assured via the torque sensors placed between the passive mechanical linkages connecting the external structure to the human legs.

Optical encoders are used to measure the movements of the mechanical structure's principal axes of rotation, that are located at the hip joints and knee joints levels. In addition, four switches are placed at the level of the soles as well to detect contacts between the external structure and the ground during walking. With these sensors data, one can detect the user's gait phases in realtime, therefore making possible the use of a predictive control for the knee assistance during locomotion.

### 3 Control of the System

The human gait cycle is a time-dependent process and is often divided into two specific locomotion phases denoted by percentages which are (Perry and Burnfield 2010):

- The stance phase, from 0 % to 62 % of the gait cycle. This phase is characterized by the contact between the foot's sole and the ground.
- The swing phase, from 62 % to 100 % of the gait cycle. This phase is characterized by the sole of the foot's lack of contact with the ground.

These 2 principal phases can be decomposed into 7 sub-phases that are: Loading Response (phase 1), Midstance (phase 2), Terminal Stance (phase 3), Preswing (phase 4), Initial Swing (phase 5), Midswing (phase 6) and Terminal Swing (phase 7). For a simpler classification, the gait phases can also be assembled into 4 sub-phases that are: Heel Strike (comprising the Terminal Swing and Loading Response), Stance Phase (comprising the Midstance and Terminal Stance), Push Off (Preswing) and Swing Phase (comprising Initial Swing and Midswing). This lengthens the phases' duration, and thus improves the robustness of the detection method. The details of the gait phases classification can be seen in Fig. 2.

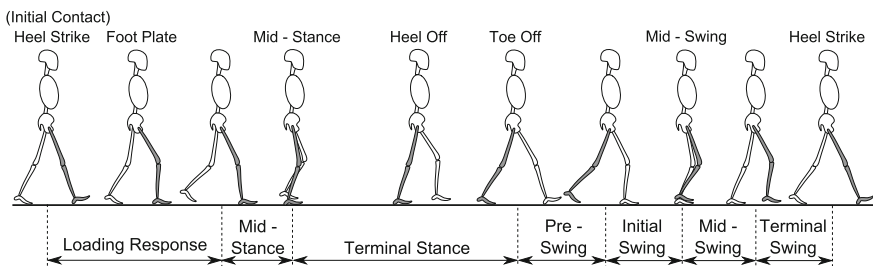
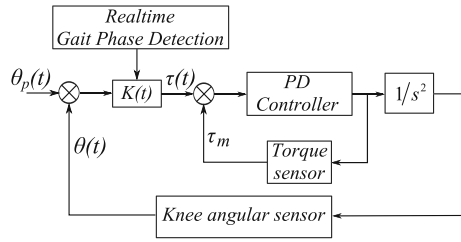


**Fig. 2** Human gait phases

**Fig. 3** The hybride predictive control scheme for knee assistance during locomotion



Here the switches data is coupled with the kinematic measurement of the external structure to estimate the gait phases during locomotion. Principal component analysis (PCA) is used to lower the data dimension in order to meet the requirements of estimation’s accuracy and high speed computation. To enhance the reliability of the gait phases recognition, a clustering algorithm using k-means method is implemented in order to identify the mean principal components vectors for each gait phase. It is followed by the use of a Markov chain which guarantees the robustness of the recognition by removing possible detection errors issued from the first classification step, exploiting the cyclical nature of the human gait.

In the very first experiments with the device, the authors aimed to evaluate its capacity to assist the knee joint during locomotion at a precise gait phase. Here the torque assistance is provided for the knee joint exactly at the initiation of the flexion movement (i.e. at the Preswing phase) in order to increase the knee range of motion during walking activities. To this end, a hybrid predictive control architecture is proposed for the control of the interactive torques measured between the user’s legs and the mechanical structure. The complete control scheme is shown if Fig. 3.

The interactive torque set-point  $\tau$  is in function of the predicted knee angle  $\theta_p(t)$  and the virtual stiffness  $K(t)$ . Its value is determined by the following equation:

$$\begin{cases} \theta_p(t) = \theta_p(t - 1) + \Delta\theta(t) \\ \tau = K(t)(\theta(t) - \theta_p(t)) \end{cases} \quad (1)$$

Here  $K(t)$  is an adjustable stiffness,  $\theta(t)$  is the measured knee angle at time  $t$ ,  $\theta_p(t)$  is the predicted knee angle at time  $t$ ,  $\Delta\theta(t)$  is the knee angular variation at time  $t$ , which is determined in advance experimentally. Besides,  $K(t)$  is in function of the gait phases. For the Preswing phase, its value can be a constant or a function of time, different from zero to create the assistance effect. Otherwise,  $K(t)$  is set to zero for the other phases so that the device could follow the knee intended motion. Low-level control of the interactive torque can be realized using a simple PD or LAG regulator. The stability of the control system is assured provided that the torque sensor axis remains nearly parallel to the user’s knee axis during its motion.

### 4 Experimental Result

Two experiments were realized. In each experiment, the user realized a 5 steps-walk with the device. The gait phase detection results as well as the measured knee angles and the interactive torques are shown in Fig. 4.

The sub-figure (1) presents the result of the first experiment. In this experiment, the motor torques were not controlled. As consequence, friction and inertia effects remained significant during the knee motion, therefore limiting its range of motion. As one can see in the sub-figure (1), the knee angular variation was only about 40° and the interactive torque amplitude was 4 N.m. The sub-figure (2) presents the second experiment in which the interactive torque was controlled by the predictive controller described in Sect. 3. Here one can state that the interactive torque's value increased significantly at the Preswing phases. As a result, the knee angle variation was much larger compared to that in the first experiment. Its amplitude was about 60° between full extension and full flexion. Additionally, the gait phase detection method remained robust during this experiment. These results highlight the fact that

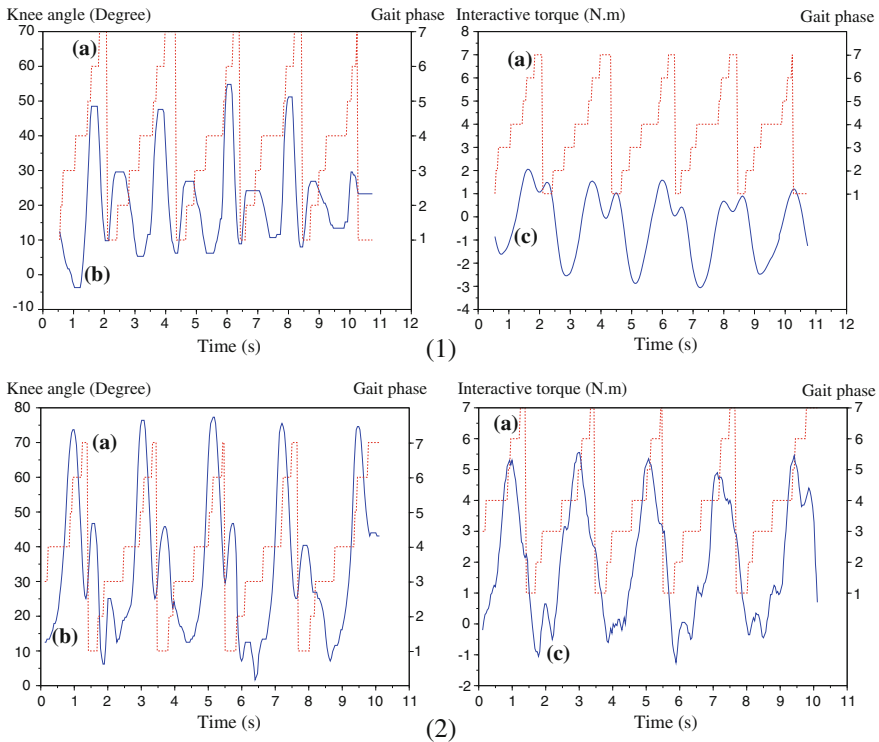


**Fig. 4** 1 First experiment: without motor torque control. 2 Second experiment: with predictive control. Curve (a): Gait phases. Curve (b): Knee angular variation. Curve (c): Interactive torque

this method can actually be used to assist the user's knee during a specific gait phase, while allowing the system to remain transparent during the other gait phases.

## 5 Conclusion

In this paper, the authors describe the control solution for a lower limb exoskeleton, which is designed to provide torque assistance for the knee joints during locomotion. The mechanical design of the prototype, comprising the kinematic solution for the external structure and passive linkages serving as connections between the latter and the user's body, was presented. Solutions for the control of the interaction between the user and the device, as well as for the gait phases detection were also discussed and experimented. The gait phases detection method was realized by using data collected by different displacement sensors placed at the hip joints and the knee joints levels, allowing an estimation in real time. The experiment results highlight the fact that a robust prediction model of the user's gait phases can help improving the control of the system's transparency, as well as the force/torque assistance capacity for a targeted anatomical joint during walking.

## References

- Banala, S. K., Agrawal, S. K., Fattah, A., Krishnamoorthy, V., Hsu, W., Scholz, J., et al. (2006). Gravity-balancing leg orthosis and its performance evaluation. *IEEE Transactions on Robotics*, 22(6), 1228–1239.
- Cai, V. A. D., Bidaud, P., Hayward, V., Gosselin, F., & Dessaily, E. (2011). Self-adjusting Isostatic Exoskeleton for the Human Knee Joint. In *Proceeding of Annual International Conference of the IEEE Engineering in Medicine and Biology Society* (pp. 612–618).
- Ergin, M. A., & Patoglu, V. (2012). ASSISTON-SE: A self-aligning shoulder-elbow exoskeleton. In *Proceeding of IEEE International Conference on Robotics and Automation (ICRA)* (pp. 2479–2485).
- Kanjanapas, K., & Tomizuka, M. (2013). *7 Degrees of Freedom Passive Exoskeleton for Human Gait Analysis: Human Joint Motion Sensing and Torque Estimation During Walking*, In *Proceedings of IFAC Symposium on Mechatronic Systems* (pp. 285–292).
- Perry, J., & Burnfield, J. (2010). *Gait Analysis Normal and Pathological Function*. Thorofare, New Jersey: Slack-Incorporated.
- Popovic, D. B., Tomovic, R., & Schwirtlich, L. (1989). *Hybrid assistive system-the motor neuro-prosthesis*. In *IEEE Transaction on Biomedical Engineering* (Vol. 36, no. 7).
- Popovic, M. B., Goswami, A., & Herr, H. (2005). Ground reference points in legged locomotion: Definitions, biological trajectories and control implications. *The International Journal of Robotic Research*, 24(12), 1013–1032.
- Rabishong, P., et al. (1975). *The AMOLL project (active modular orthosis for lower limbs)*. In *Proceedings of the International Symposium on External Control of Human Extremities* (pp. 33–42).
- Schiele, A., & Van der Helm, F. C. T. (2006). Kinematic design to improve ergonomics in human machine interaction. *IEEE Transactions on Neural Systems and Rehabilitation Engineering*, 14, 456–469.

- Stienen, A. H. A., Hekman, E. E. G., Van der Helm, F. C. T., & Van der Kooij, H. (2009). Self aligning exoskeleton axes through decoupling of joint rotations and translations. *IEEE Transaction on Robotics*, *25*, 628–633.
- Vukobratovic, M., Hristic, D., & Stojiljkovic, Z. (1974). Development of active anthropomorphic exoskeletons. *Medical & Biological Engineering*, *12*(1), 66–80.
- Woltring, H. J., Huiskes, R., & De Lange, A. (1985). Finite centroid and helical axis estimation from noisy landmark measurements in the study of human joint kinematics. *Journal of Biomechanics*, *18*(5), 379–389.

**Part IX**  
**Innovations and Applications**



# Pilot Experiments with the Human-Friendly Walking Assisting Robot Vehicle (hWALK)

Jorge Solis

**Abstract** Up to now, the embodiment of bodily-kinaesthetic, perceptual and cognitive capabilities for assistive robots has been scarcely studied. This research aims to incorporate and develop the concept of robotic human science and to enable its application in a human-friendly robot for assistive purposes. The author has introduced the development of a human-friendly walking assist robot vehicle designed to provide physical support to the elderly. The proposed system is composed by two-wheeled inverted pendulum mobile robot, a 3-DOFs desktop haptic interface, a mobile computer and a wireless module for communication purposes. Pilot experiments with healthy volunteers were carried out to verify the dynamic stability of the proposed system as well as the possibility to compensate the height error of the HI gripper under uneven terrain conditions.

**Keywords** Assistive robotics • Haptics • Force feedback

## 1 Introduction

In industrialized countries, regional disparities in healthcare and welfare services, increased medical expense caused by aging societies and shortages of medical staff have become serious problems. In Sweden, it is expected that about 25 % of Swedes population will be older than 65 years old by 2060 (Wilén and Ljungberg 2009). For this purpose, robot technology (RT) is expected to be an important key to find solutions to these problems. In particular, roboticists have been developing assistive robots for health care and welfare applications to improve the security, independence and quality of the elderly so they can stay in their homes longer (Bertmar 2012). As a consequence, this opens the opportunity to free up time so

---

J. Solis (✉)

Department of Engineering and Physics, Karlstad University, Karlstad, Sweden  
e-mail: jorge.solis@kau.se

that medical staff can provide care for the patients who really may need a human support (Ishii et al. 2009).

Nowadays most of the research has been mainly focused in developing assistive robots for the elderly in terms of telepresence robotic platforms designed for maintaining the elderly social contacts (Kristoffersson et al. 2007), wheeled walker platforms designed for turning away from obstacles and prevent elderly from accidents (Palopoli et al. 2015), pet-like robots designed for raising the quality of life among people with dementia in the later stage of their illness (Asplund and Gustafsson 2013). In particular, different walking-aid robots have been proposed during the last decades. In particular, the walking-aid robots can be classified in two main groups according to the mobility factor (Fukuda et al. 2015): active-type walkers driven by a servo motor (Dubowsky et al. 2000) and passive-type walkers driven by a servo brake (Hirata et al. 2004). Yu et al. (2003) proposed the PAMM system together with a smart cane robot with a relative small size but the maneuverability is compromised by the cost. Fukuda et al. (2015) introduced an intelligent cane robot consisting of a stick, a group of sensors for recognizing the user's intentions and an omnidirectional mobile platform. However, the physical support is provided by means of a fixed length and stiffness aluminum stick and cannot be customized depending on the needs of the specific user and environmental conditions. From those researches; a special focus has been done in terms to increase the level of multimodal interaction, sensing and control to facilitate the perception of the environment for a better guidance and provide a static physical support to avoid falling down. However, dynamic physical support, the adaptability to the user/task needs, and the multipurpose design concept has been scarcely studied.

For this purpose, at Karlstad University, Solis et al. (2015) has proposed to incorporate and develop the concept of robotic human science introduced by Takanishi (1995) and to enable its application in a multipurpose human-friendly robot for assisting elderly persons as well as assisting care givers. As first approach, Solis et al. (2015) presented the development of a human-friendly walking assistive robot vehicle (*hWALK*). The *hWALK* is composed by a two-wheeled inverted pendulum mobile robot, a 3-DOFs desktop haptic interface, a mobile computer and a wireless module for communication purposes. A PID controller has been implemented for the stability control and preliminary experiments were presented to verify the stability of the two-wheeled inverted pendulum. As a result, under static condition the *hWALK* was stabilized in about 16 s on a surface with carpet padding and 30 s on a surface with parquet (Solis et al. 2015).

In this paper, the author present pilot experiments to validate the dynamic stability of the proposed system as well as the possibility to compensate the height error due to the uneven terrain conditions. This paper is organized as follows: at first, a brief overview of the human-friendly walking assisting robot vehicle is described. Then, the details of the calculation of the force feedback to provide physical support to the user are provided. Finally, pilot experiments were proposed to provide physical support to healthy volunteers.

## 2 Human-Friendly Walking Assisting Robot Vehicle

The human-friendly *WALKing* assist robot vehicle (*hWALK*) has been designed to provide physical support to the elderly while walking. The *hWALK* is composed by (see Fig. 1): a mobile platform with on board controller and two actuated wheels (modified version from the one developed at Waseda University (Solis et al. 2011) and now commercially available as MiniWay<sup>®</sup>), a commercial available 3-DOFs desktop haptic interface (e.g. Novint Falcon), a mobile computer used for computing the force feedback processing and the wireless module TY24SK-E2025-01 (manufactured by NEC) for communication between the mobile computer and the mobile robot.

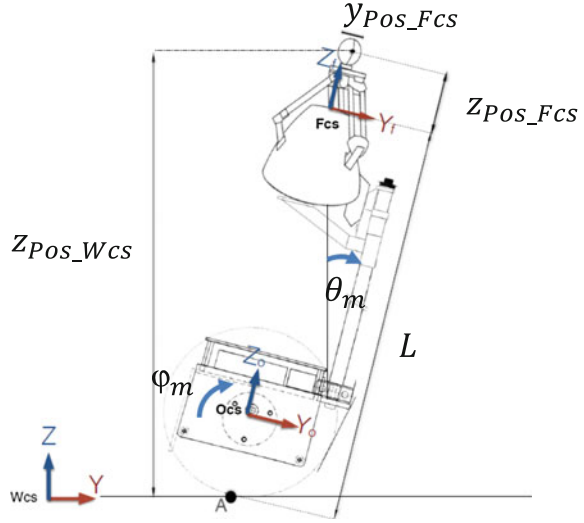
The principle for physical support is described as follows. If one considers  $d_z$  as the distance between the ground and the gripper of the HI; under even conditions of the ground, the distance will be kept constant so that no force feedback support should be exerted to the user during the walking motion ( $F_z = 0$ ). However; under uneven ground conditions, in order to keep the distance  $d_z$  constant, the HI should be programmed to exert force feedback support ( $F_z \neq 0$ ). As an example of the proposed robot system capabilities, elderly persons with walking difficulties may have vision difficulties to identify the ground conditions, so that the proposed system will not only be capable to sense and detect the ground conditions, but also it will be able to provide force feedback to the elder for better understanding the ground conditions and of course for providing walking support.

The model reference of the proposed system is shown in Fig. 2. In order to compute the force feedback for providing support to the user, the total force is computed by Eq. 1. In particular, the feedback force  $F_z$  was computed by means of a spring model as shown in Eq. 2, where  $z_{ref}$  is determined as Eq. 3 and  $k_{stiffness}$  and  $k_{damping}$  have been experimentally determined ( $k_{stiffness} = 5.91$  N/mm and  $k_{damping} = 0.079$  mN\*s/mm). The position of the gripper of the HI along the z-axis

**Fig. 1** Human-friendly walking assisting robot vehicle (*hWALK*) developed at Karlstad University



**Fig. 2** Model reference defined for the hWALK



respect to the world coordinate reference system ( $z_{Pos\_Wcs}$ ) is computed as Eq. 4. In order to define the desired position of the gripper of the HI ( $z_{Pos\_Fcs}$ ), the user must manually bring the gripper to the desired position and then press the lightning bolt button in the HI.

$$F_{Total\_z} = F_z + F_{z\_comp} \tag{1}$$

$$F_z = k_{stiffness} \cdot z_{ref} + k_{damping} \cdot \dot{z}_{ref} \tag{2}$$

$$z_{ref} = z_{Pos\_Wcs} - z_{Pos\_Fcs} \tag{3}$$

$$z_{Pos\_Wcs} = (L + z_{Pos\_Fcs}) \cdot \cos \theta_m - y_{Pos\_Fcs} \cdot \sin \theta_m \tag{4}$$

On the other hand; the control system for the two-wheeled inverted pendulum mobile robot is composed by 2 modules: the PID controller and the wireless module (acting as slave). In order to assure the stability of the two-wheeled inverted pendulum with an estimated load of 5 kg in the top of the pendulum, the integral part has been included in the proposed PD controller implemented in the commercial version as shown in Eqs. 5 and 6, where  $\theta_m$  is defined as the angular rotation of the chassis with respect to the ground,  $\psi$  is the angular rotation of the wheels with respect to the chassis and  $\varphi$  is the angular rotation of the wheels with respect to the ground. In addition,  $\alpha$  and  $\alpha_{REF}$  is the measured and desired heading direction respectively,  $i_{outR}$  and  $i_{outL}$  is the control signal for the right and left motor current motor respectively,  $i_R$  and  $i_L$  is the measured right and left motor current motor respectively,  $k_1$  is the chassis tilt angle control gain,  $k_2$  is the chassis tilt angular velocity control gain,  $k_3$  is the wheel angle control gain,  $k_4$  is the wheel angular velocity control gain,  $k_5$  is the chassis yaw angle control gain,  $k_6$  is the chassis yaw

angular velocity control gain,  $k_7$  is the left motor current control gain,  $k_8$  is the right motor current control gain,  $k_9$  is the angular rotation chassis integral control gain and  $k_{10}$  is the wheel angular rotation integral control gain. The gain parameters for the PID controller implemented for the *hWALK* were determined by using a heuristic method ( $k_1 = 186.3$ ;  $k_2 = 28.6$ ;  $k_3 = 5.8$ ;  $k_4 = 4.8$ ;  $k_5 = 0.024$ ;  $k_6 = 0.015$ ;  $k_7 = 1.942$ ;  $k_8 = 1.942$ ;  $k_9 = 0.01$  and  $k_{10} = 0.001$ ).

$$i_{outR} = k_1 \cdot \theta_m + k_2 \cdot \theta'_m + k_3 \cdot (\varphi - \varphi_{REF}) + k_4 \cdot (\varphi' - \varphi'_{REF}) + k_5 \cdot (\alpha - \alpha_{REF}) + k_6 \cdot (\alpha' - \alpha'_{REF}) + k_9 \int_0^T \theta_m dt + k_{10} \int_0^T \varphi dt \quad (5)$$

$$u_R = k_7 \cdot (i_{outR} - i_R)$$

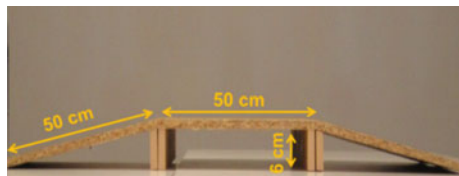
$$i_{outL} = k_1 \cdot \theta_m + k_2 \cdot \theta'_m + k_3 \cdot (\varphi - \varphi_{REF}) + k_4 \cdot (\varphi' - \varphi'_{REF}) - k_5 \cdot (\alpha - \alpha_{REF}) - k_6 \cdot (\alpha' - \alpha'_{REF}) + k_9 \int_0^T \theta_m dt + k_{10} \int_0^T \varphi dt \quad (6)$$

$$u_L = k_8 \cdot (i_{outL} - i_L)$$

### 3 Experiments and Results

In order to validate the dynamic stability as well as the possibility to compensate the height error of the HI's gripper under uneven terrain conditions, a pilot experiment setup was proposed by simulating a bump typically found in outdoor environments (Fig. 3). The bump was constructed with wood at our mechanical workshop (with an inclination angle of  $6.85^\circ$  with a length of 50 cm and a width of 50 cm). Seven healthy volunteers (between 24 to 48 years old) were requested randomly to carry the experiment. For this experiment six males and one women were shortly introduced about the aim of the experiment and each of them were allowed to try the *hWALK* a maximum of two trials before the actual experiment. For this purpose, after the calibration procedure of the two-wheeled inverted pendulum robot was completed, the subject was requested to hold the gripper of the HI and set the desired height by pressing the lightning bolt button. Then, the subject was requested to drive

**Fig. 3** Pilot experimental setup designed to simulate uneven terrain conditions



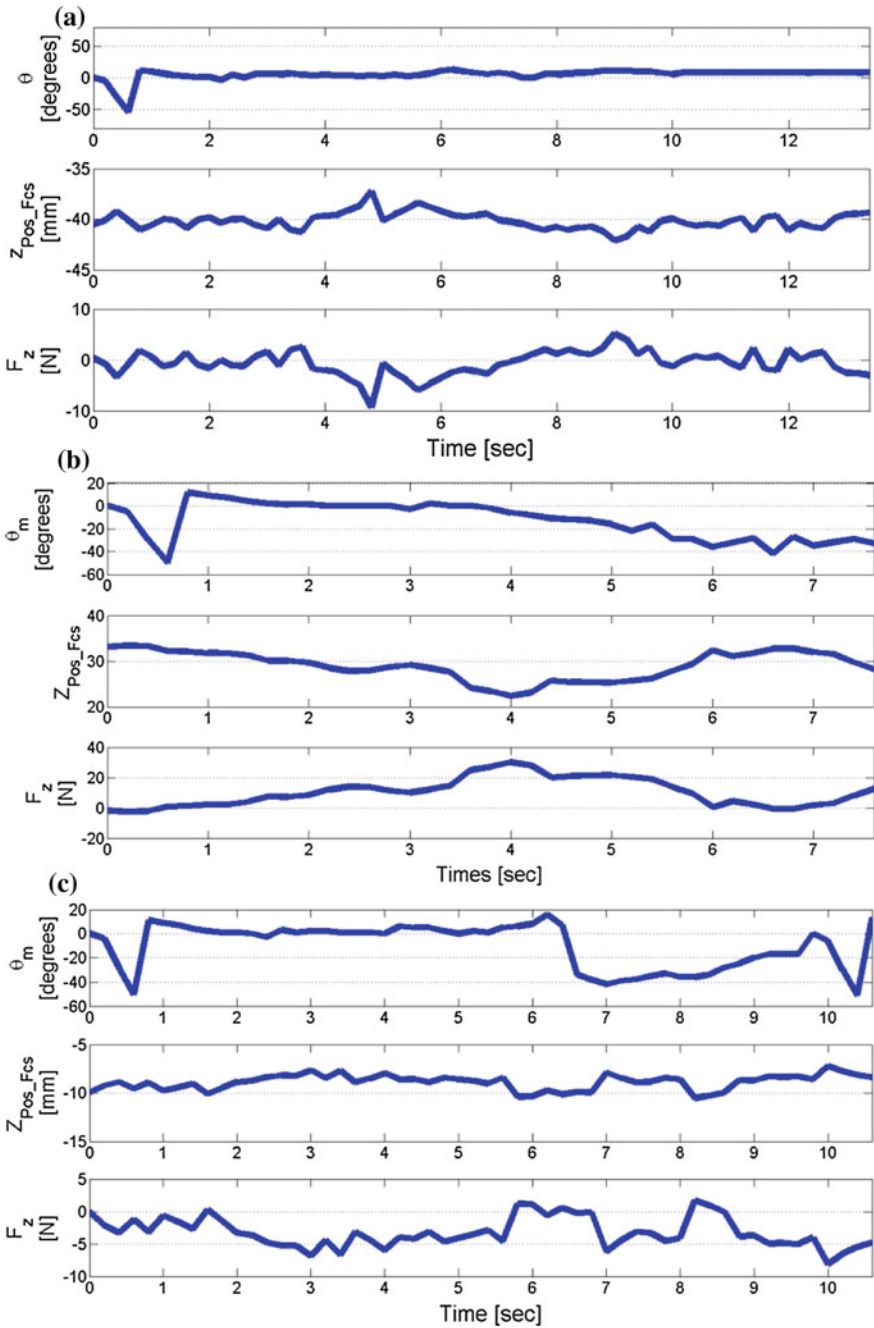


**Fig. 4** Experimental results from the subjects 1, 2 and 7 while exerting force feedback of 2.995 N/mm under dynamic conditions

up the *hWALK* over the bump in order to reach the final target position. At the time the subject has reached the final target position, he/she was requested to press the lightning bolt button again for indicating the conclusion of the task. At the end, they were asked about their impression of the performance system in terms of conform and sense of the physical support. After the testing phase, each volunteer were requested to perform the task and the HI was programmed to exert supporting force by setting the parameter  $k_{stiffness}$  as 2.955 N/mm. In order to validate the dynamic stability and possibility to compensate the height error under uneven terrain conditions, we have registered the following parameters (sampling time of 200 ms): the angular rotation of the chassis with respect to the ground ( $\theta_m$ ), the desired position of the gripper of the HI ( $z_{Pos\_Fcs}$ ) and the unsaturated feedback force ( $F_z$ ).

The experimental results are shown in Fig. 4. As we can observe, the subject 1 (Fig. 4a) didn't presented after 1 s any large variations of the angular rotation of the chassis with respect to the ground (similar results was observed for subjects 4, 5, and 6). As consequence, the level of exerted force was within the range of  $-10$  to  $5$  N during the motion and the maximum height deviation detected was about  $3.29$  mm from the initial desired height ( $z_{Pos\_Fcs}$ ). The subject 2 (Fig. 4b) presented a deviation within  $-40$  and  $10$  degrees on the angular rotation of the chassis with respect to the ground and the error was kept lower between  $2$  and  $4$  s which it corresponded to the ascending section of the simulated bump (similar result was noticed for subject 3). The level of exerted force from the HI was within the range of  $-2.5$  to  $30$  N and the maximum height deviation detected was about  $6.15$  mm from the initial desired one. As for the subject 7, we can observe that the angular rotation of the chassis was deviated about  $50$  degrees from the initial value around  $6$  s (corresponding to the descending section of the simulated bump) but the system was capable of recovering after  $4$  s. The level of exerted force from the HI was within the range of  $-2.0$  to  $8$  N and the maximum height deviation detected was about  $2.04$  mm from the initial desired one. From the above results, we can notice that even in presence of the disturbance introduced by the bump, the system was capable to recover larger deviations of the rotational angle of the chassis and reduce the desired height error. The level of exerted force for the subjects 1 and 7 during the motion was provided within the maximum feasible provided by the Novint Falcon ( $10$  N). As for the rest of the subjects, the level of force was saturated (particularly in the descending section of the simulated bump).

## 4 Conclusions

In this paper, the development of a human friendly walking assist robot vehicle for providing physical support to the elderly has been described. A pilot experiment was proposed in order to verify the dynamic stability of the proposed system while walking over uneven terrain conditions (e.g. a bump). From the experimental results, we could verify the dynamic stability and the possibility to compensate the height error of the HI gripper by exerting supporting force to health volunteers.

## References

- Asplund, L., & Gustafsson, C. (2013). Unique robot cat enhances quality of life among people with dementia. Retrieved from [http://www.mdh.se/unik-robotkatt-okar-livskvaliteten-hos-personer-med-demens-1.35302?l=en\\_UK](http://www.mdh.se/unik-robotkatt-okar-livskvaliteten-hos-personer-med-demens-1.35302?l=en_UK).
- Bertmar, H. (2012). Robotar som hjälper och vårdar, *Hjälpmedelsinstitutet*, 11318.
- Dubowsky, S., et al. (2000). PAMM-a robotic aid to the elderly for mobility assistance and monitoring: A helping-hand for the elderly. In *Proceedings of the International Conference on Robotics and Automation* (pp. 570–576).
- Fukuda, T., Huang, J., Pei, D., & Sekiyama, K. (2015). Motion control and fall detection of intelligent cane robot. In *Intelligent Assistive Robot. Springer Tracts in Advanced Robotics* (Vol. 106, pp. 317–337).
- Hirata, Y., Hara, A., & Kosuge, K. (2004). Passive-type intelligent walking support system RT Walker. In *Proceedings of the International Conference on Intelligent Robots and Systems* (pp. 3871–3876).
- Ishii, H., Solis, J., Takanishi, A., et al. (2009). Development and experimental evaluation of oral rehabilitation robot that provides maxillofacial massage to patients with oral disorders. *International Journal of Robotics Research*, 28(9), 1228–1239.
- Kristofferesson, A., et al. (2007). A review of mobile robotic telepresence. In *Advances in Human-Computer Interaction* (Vol. 2013).
- Palopoli, L., et al. (2015). Navigation assistance and guidance of older adults across complex public spaces: The DALi approach. In *Intelligent Service Robotics* (pp. 1–16).
- Solis, J., Takanishi, A., et al. (2011). Development of the waseda wheeled robot no. 2 refined II and pilot experiments with undergraduate students. In *13th World Congress in Mechanism and Machine Science* (pp. A20–345).
- Solis, J., et al. (2015). Towards the development of multipurpose assistive vehicle robot for the ambient assisted living. In *International Conference on Automation Science and Engineering* (pp. 1145–1150).
- Takanishi, A. (1995). Memoriam: Professor Ichiro Kato. *Autonomous Robots*, 2, 7–10.
- Yu, H., Spenko, M., & Dubowsky, S. (2003). An adaptive shared control system for an intelligent mobility aid for the elderly. *Autonomous Robots*, 15(1), 53–66.
- Wilén, A., & Ljungberg, A. (2009). The future population of Sweden 2009–2060, Statistics Sweden, Forecasting Institute, pp. 20.



# Conceptual Design of a Cable Driven Parallel Mechanism for Planar Earthquake Simulation

**Daisuke Matsuura, Shota Ishida, Muhamad Akramin, Emek Barış Küçüktabak, Yusuke Sugahara, Shinji Tanaka, Nobuo Fukuwa, Minoru Yoshida and Yukio Takeda**

**Abstract** Earthquake simulation is helpful in order for society to experience real seismic waves in safe environment. Cable-driven parallel mechanisms have advantages over conventional serial and parallel mechanisms. Prototype simulator which covers 1 m stroke in each direction has been built. In this paper, conceptual design of an earthquake simulator using cable driven parallel mechanism is presented. Spatial arrangement of cables is investigated in terms of the stability and safety of the simulator by dynamic analysis of the simulator. It was revealed that increasing the vertical angle of the cables with the ground while connecting them

---

D. Matsuura (✉) · S. Ishida · M. Akramin · E.B. Küçüktabak · Y. Sugahara · S. Tanaka · Y. Takeda

Department of Mechanical Sciences and Engineering, Tokyo Institute of Technology, Tokyo, Japan  
e-mail: matsuura@mech.titech.ac.jp

S. Ishida  
e-mail: ishida.s.ae@m.titech.ac.jp

M. Akramin  
e-mail: akramin059@gmail.com

E.B. Küçüktabak  
e-mail: baris.kucuktabak@gmail.com

Y. Sugahara  
e-mail: sugahara@mech.titech.ac.jp

S. Tanaka  
e-mail: tanakas@mech.titech.ac.jp

Y. Takeda  
e-mail: takeda@mech.titech.ac.jp

N. Fukuwa  
Disaster Mitigation Research Center, Nagoya University, Nagoya, Japan  
e-mail: fukuwa@sharaku.nuac.nagoya-u.ac.jp

M. Yoshida  
Hakusan Corporation, Tokyo, Japan  
e-mail: yoshida@hakusan.co.jp

closer to the center of mass of the output link with low coefficient of friction between the ground ensures the most stable motion.

**Keywords** Cable driven parallel mechanism • Earthquake simulator • Dynamic simulation

## 1 Introduction

Several massive earthquakes have occurred globally in the past decades, one of which is the Great East Japan Earthquake in 2011 with a magnitude of 9.0. The occurrence of earthquakes cannot be prevented, but their effect towards the public can be reduced by a variety of means. Earthquake simulation is helpful in order for society to experience real seismic waves in safe environment. This can be used to raise awareness towards disaster prevention. Cable-driven parallel mechanisms offer a remedy to some of the shortcomings of conventional serial and parallel mechanisms (Gosselin 2014). Using cables, they offer a large workspace, low inertia of moving parts, transportability and ease of assembly/disassembly. These advantages of cable-driven parallel mechanisms are especially beneficial for an earthquake simulator that is designed to be easily accessible for the public.

The Earthquake Simulator Vehicle, Kishinsha (Masaki 2013), is one of the simulators that is widely used in disaster prevention education throughout Japan. It is good in terms of transportability, but can only reproduce limited types of seismic waves. The E-Defence (Ohtani 2004), however, can reproduce various types of seismic waves with high precision. This simulator has a 20 m × 15 m moving platform which is driven by fourteen hydraulic actuators. Unfortunately, due to its massive size this simulator is lacking in transportability. On the other hand, Jishin-The-Vuton (Roh et al. 2013) is quite excellent in term of transportability. This is accomplished by basing the driving principle on the VUTON crawler developed by Hirose (Hirose 1993) for the purpose of reproducing seismic waves in a two-dimensional plane. By using the crawler, the simulator can achieve wide range of motion, but as a drawback the simulator is prone to tipping, due to the difference in height between the center of gravity of the moving parts and the driving mechanism (crawler).

In order to develop an earthquake simulator with high transportability that is capable of executing a wide range of planar seismic waves, a novel simulator composition was proposed (Shiwaku et al. 2012). The design consisted of a parallel mechanism driven by four cables arranged in a plane, and friction-reducing air bearings attached to the bottom of the output link. Since then, the authors have succeeded in the development of a practical-size simulator. There are numerous examples of research regarding cable driven parallel mechanisms (Khakpour et al. 2014; Liu et al. 2014; Babaghasabha et al. 2015), however, to the best knowledge of the authors research aiming at the development of an earthquake simulator

involving massive load and high acceleration have not yet been successfully accomplished.

Following its introduction the conceptual design of a planar earthquake simulator is presented, composed of a cable driven parallel mechanism with four cables, an elevated base, and low-friction air bearings to support the output link. The cable arrangement is then investigated by dynamic simulation with respect to stability, and finally a prototype design is presented.

## 2 Composition of the Planar Earthquake Simulator

Figure 1 shows the concept of our planar earthquake simulator. It is composed of a cable driven parallel mechanism (CDPM) with four cables, an elevated base, and four air bearings. Objects or human occupants are put on the output link of the CDPM in order to experience a simulated earthquake. As the first step, our target is to achieve large earthquake motions in the horizontal plane. To this end, the four air bearings are arranged between each corner of the output link of the CDPM and the elevated base. This composition contributes to the stable support of the output link by preventing tipping via small cable tension forces combined with smooth, fast, low-friction motion.

The arrangement of the cables is shown in Fig. 2. To achieve full motion control of the output link in the horizontal plane, four cables are used. As shown in the side view (Fig. 2c), the heights of the attachment points of the cables on the base,  $h_1$ , and the output link,  $h_2$ , are not the same, which is the main difference between the present mechanism configuration and the previous one. This means that the proposed CDPM has a spatial cable arrangement and constrained planar motion where

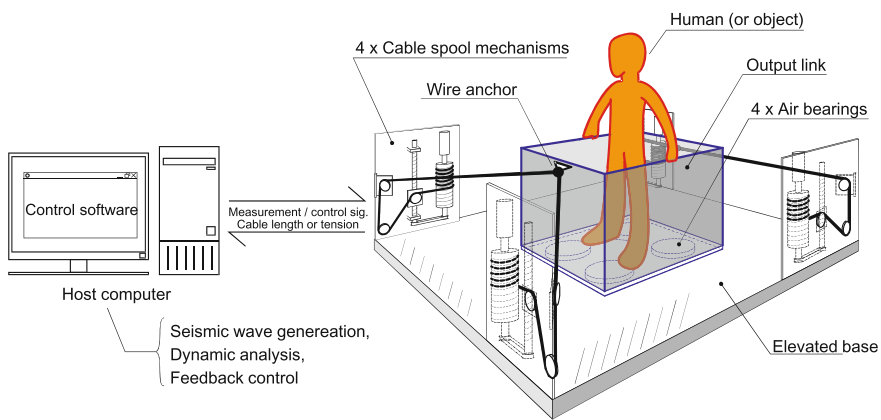


Fig. 1 Conceptual drawing of the planar earthquake simulator

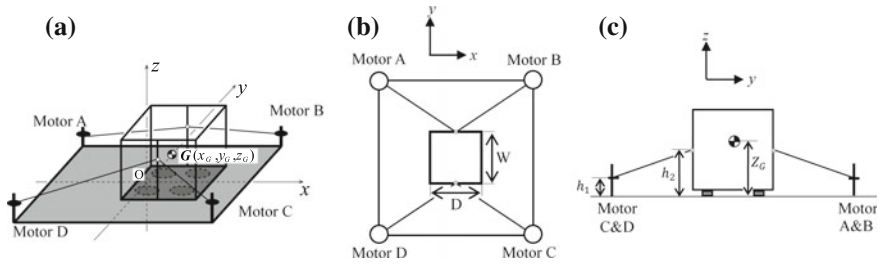


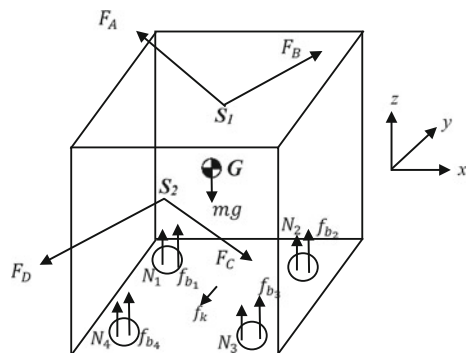
Fig. 2 Arrangement of the CDPM's cables. **a** isometric view **b** top view **c** side view

the planar pair consists of the air bearings and the elevated base. By this method, it is possible to achieve stable, smooth, and fast motions in a plane. The effect of this configuration is investigated through dynamic simulations in the following section.

### 3 Dynamic Simulation

The dynamic model of the CDPM is shown in Fig. 3.  $F_A, F_B, F_C$  and  $F_D$  are the cable tension forces applied on points  $S_1(F_A$  and  $F_B)$  and  $S_2(F_C$  and  $F_D)$ , and  $f_{b1}, f_{b2}, f_{b3}$  and  $f_{b4}$  are the bearing forces, applied on points  $B_1, B_2, B_3$  and  $B_4$ , respectively.  $N_1, N_2, N_3$  and  $N_4$  are the reaction forces between the ground and air bearings,  $f_k$  is the kinetic friction force, and  $\mu_k$  is the kinetic friction coefficient. To simplify the equations, instead of using four different reaction forces, their equivalent,  $N_{eq}$  is used.  $N_{eq}$  is applied on point N, and its  $x$  and  $y$  positions with respect to the center of mass of the output link G are denoted as  $x_N$  and  $y_N$ . A greater net moment from the other forces with respect to the  $x$  and  $y$  axes causes the position of N to increase, thus making it more prone to tipping.

Fig. 3 Dynamic model of the CDPM with air bearings



For planar motion, the dynamic equations become as follows:

$$m \begin{bmatrix} \ddot{x}_G \\ \ddot{y}_G \\ 0 \end{bmatrix} = \mathbf{F}_A + \mathbf{F}_B + \mathbf{F}_C + \mathbf{F}_D + \mathbf{f}_{b_1} + \mathbf{f}_{b_2} + \mathbf{f}_{b_3} + \mathbf{f}_{b_4} + \mathbf{N}_{eq} + \mathbf{f}_k + mg \begin{bmatrix} 0 \\ 0 \\ -1 \end{bmatrix} \quad (1)$$

$$\mathbf{I} \begin{bmatrix} 0 \\ 0 \\ \ddot{\psi} \end{bmatrix} = (\mathbf{GS}_1 \times \mathbf{F}_A) + (\mathbf{GS}_1 \times \mathbf{F}_B) + (\mathbf{GS}_2 \times \mathbf{F}_C) + (\mathbf{GS}_2 \times \mathbf{F}_D) + (\mathbf{GB}_1 \times \mathbf{f}_{b_1}) \\ + (\mathbf{GB}_2 \times \mathbf{f}_{b_2}) + (\mathbf{GB}_3 \times \mathbf{f}_{b_3}) + (\mathbf{GB}_4 \times \mathbf{f}_{b_4}) + (\mathbf{GN} \times \mathbf{N}_{eq}) + (\mathbf{GN} \times \mathbf{f}_k) \quad (2)$$

$$|\mathbf{f}_k| = -|\mathbf{N}_{eq}| \mu_k \quad (3)$$

As the system is redundantly actuated for planar motion in order to have a unique solution, one of the cable tensions,  $F_C = |\mathbf{F}_C|$  is preliminarily determined. The bearing forces, as well as the physical, kinematic, and dynamic parameters are known. The magnitudes of the three cable forces,  $|\mathbf{N}_{eq}|$ ,  $|\mathbf{f}_k|$ ,  $x_N$ , and  $y_N$  are unknown. These seven unknowns can be solved by using the seven scalar equations from Eqs. (1), (2) and (3).

Using the above equations, dynamic simulations were carried out. The standard values for the physical, kinematic, and dynamic parameters used are shown in Table 1. The simulation results are shown in Figs. 4 and 5, in which the trends of cable tension forces, friction force, magnitude, and position of the equivalent normal force with respect to  $h_1$  and with respect to kinetic friction coefficient, for two different  $z_G$  values are presented. In Fig. 4, the ideal case where the height of the center of gravity,  $z_G$ , and of the cable attachment point,  $h_2$ , are equal is considered. From this result, it is revealed that the position of  $\mathbf{N}_{eq}$  is independent from the height difference between the cable attachment points, and gets further from the center of gravity as  $\mu_k$  increases. In Fig. 5, the case where  $z_G \neq h_2$ , which should occur in practical usage, is considered where  $z_G = 0.65$  m and  $h_2 = 0.7$  m. In Fig. 5 (a), the hatched area shows the safe region without tipping. It can be seen that as the difference  $h_2 - h_1$  decreases, the output link becomes more prone to tipping.

**Table 1** Parameter values for simulation

Parameter	Value	Parameter	Value	Parameter	Value
$m$	40 kg	$F_C$	400 N	$\ddot{x}_G$	$9.8 \text{ m/s}^2$
$W$	1 m	$x_G$	-0.8 m	$\ddot{y}_G$	0
$D$	1 m	$y_G$	0	$\psi$	0
$h_2$	0.7 m	$\dot{x}_G$	0.1 m/s	$\dot{\psi}$	0
$f_b$	95 N	$\dot{y}_G$	0	$\ddot{\psi}$	0

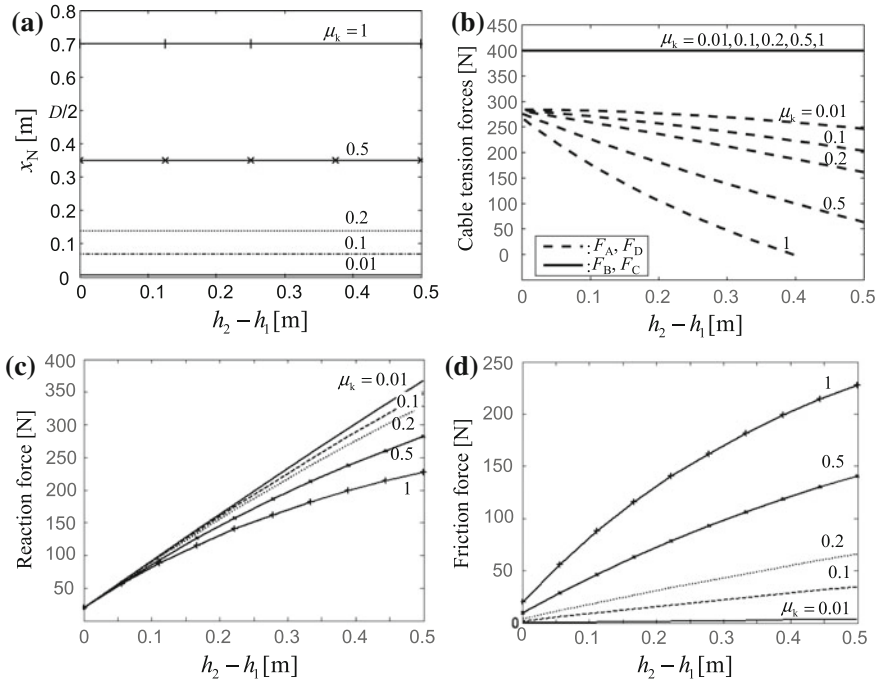


**Fig. 4** Simulation results (home position  $z_G = h_2 = 0.7$  m). **a**  $x_n$  versus  $h_2 - h_1$  **b** Cable forces versus  $h_2 - h_1$  **c**  $N_{eq}$  versus  $h_2 - h_1$  **d** Friction force versus  $h_2 - h_1$

By comparing the results in Figs. 4 and 5, it is revealed that the magnitudes are not dependent on the height of the center of mass ( $z_G$ ). In addition to this, it is also apparent that the height  $h_1$  has a maximum limit,  $h_{1,max}$ , to prevent tipping. The effect of the difference  $h_2 - z_G$  on  $h_{1,max}$ , is summarized in Fig. 6. Since there is no practical  $h_{1,max}$  value for cases with a high coefficient of friction, which can be confirmed in Fig. 4a and Fig. 5a, the values of  $\mu_k \leq 0.2$  are investigated. From this result, it is seen that if the friction coefficient is high, it is better to select  $h_2$  smaller than  $z_G$ , whereas if  $\mu_k$  is small, a higher  $h_2$  leads to greater safety. It is additionally worth noting that the effect of the coefficient of friction in terms of tipping decreases as the difference between  $h_2$  and  $z_G$  decreases.

In order to have the most stable system possible as indicated by the above trends, it is suggested to set the physical parameters as follows. To decrease the possibility of tipping,  $h_1$  should be set as low as the physical constraints allow. By using a lower coefficient of friction, cable tension forces can be kept in a desired region without loosening; however, it is important to make the connection point higher than the center of mass to obtain the most stable system in practice when the coefficient of friction is low.

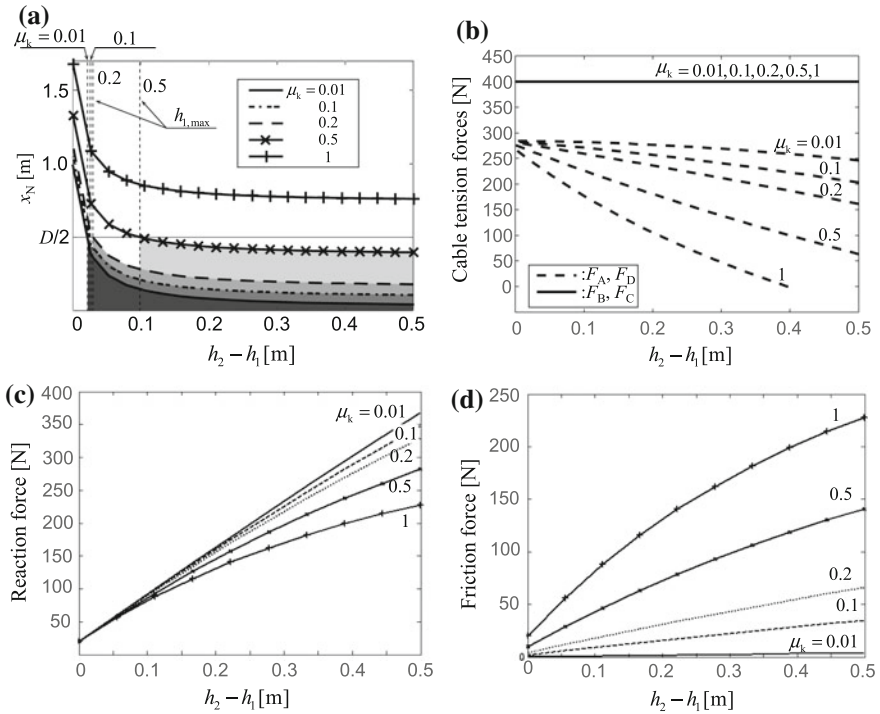


**Fig. 5** Simulation results (home position,  $z_G = 0.65$  m,  $h_2 = 0.7$  m). **a**  $x_N$  versus  $h_2 - h_1$  **b** Cable forces versus  $h_2 - h_1$  **c**  $N_{eq}$  versus  $h_2 - h_1$  **d** Friction force versus  $h_2 - h_1$

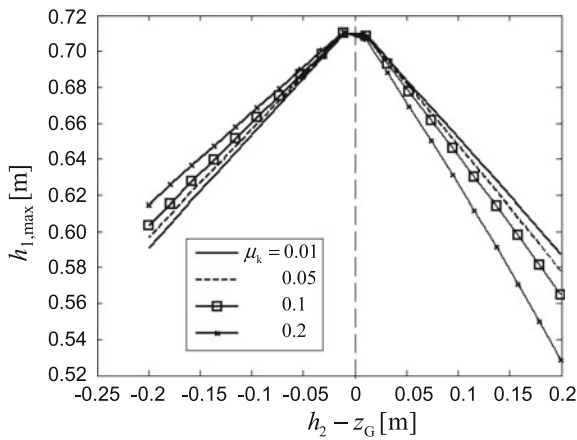
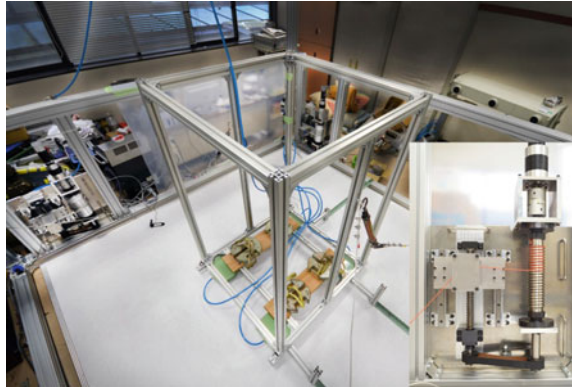


**Fig. 6** Relationship between  $h_2 - z_G$  and  $h_{1,max}$

**Fig. 7** Overview of the prototype earthquake simulator and a single cable spool mechanism



## 4 Simulator Prototype

Based on the results mentioned above, a prototype was constructed. As one of the key parts of the CDPM, the composition of a single cable spool mechanism, along with an overview of the prototype earthquake simulator is shown in Fig. 7. The width, depth, and height of the prototype are approximately 3.2 m, 3.2 m, and 1.5 m respectively. The cable spool mechanism is driven by a 400 W brushless DC servomotor with a planetary gear head of reduction ratio 1/14 (EC60/GP81, Maxon motor ag). The actuator units are driven by servo amplifiers (1BLDC, HiBot corp.) for the purpose of adjusting the lengths of the cables as calculated by pulse encoder signals of 500PPR with a PID feedback process. In addition, the tension of the one of four cables is measured using a tension sensor (pickup: LSP10-K25-B-S and amplifier: T300, Eiko Sokki corp.) in order to maintain a specific value. All of the above sensor signal processing, dynamic analysis, and feedback control are performed by a PC-based controller (Intel Core- 5 GHz, 16 GB RAM, operated by Windows-7 Enterprise Edition) at 1 kHz frequency triggered by a hardware timer interruption.

## 5 Conclusions

The conceptual design of an earthquake simulator using a cable driven parallel mechanism is presented. To achieve accurate seismic motion with high stability, a spatial arrangement of cables was investigated. A simulator prototype which covers a 1 m stroke in each direction has been constructed.



## References

- Babaghasabha, R., Khosravi, M. A. & Taghirad, H. D. (2015). Adaptive robust control of fully-constrained cable driven parallel robots. *Mechatronics*, 25, 27–36.
- Gosselin, C. M. (2014). Cable-driven parallel mechanisms: State of the art and perspectives. *Mechanical Engineering Review*, 1(1). doi:10.1299/mer.2014dsm0004.
- Hirose, S. & Amano, S. (1993). The VUTON: High payload, high efficiency holonomic omni-directional vehicle. In *Proceedings of the Sixth Symposium on Robotics Research* (pp. 253–260).
- Khakpour, H., Birglen, L., & Tahan, S. A. (2014). Synthesis of differentially driven planar cable parallel manipulators. *IEEE Transaction on Robotics*, 30(3), 619–630.
- Liu, H., Gosselin, C., & Laliberte, T. (2014). Conceptual design and static analysis of novel planar spring-loaded cable-loop-driven parallel mechanisms. *Journal of Mechanism and Robotics*, 4 (2). doi:10.1115/1.4005568.
- Masaki, Y. (2013). Duration of “feeling of being shaken” as assessed using an earthquake simulator vehicle. *Equilibrium Research*, 72, 459–466.
- Ohtani, K., Ogawa, N., Takayama, T. & Shibata H. (2004). Construction of E-defense (3-D full-scale earthquake testing facility). In *Thirteenth World Conference on Earthquake Engineering* (p. 189).
- Roh, S. G., Taguchi, Y., Nishida, Y., Yamaguchi, R., Fukuda, Y., Kuroda, S., et al. (2013). Development of the portable ground motion simulator of an earthquake. In *IEEE International Conference on Intelligent Robots and Systems* (pp. 5339–5344).
- Shiwaku, K., Roh, S. G., Nishida, Y., Yoshida, M. & Hirose, S. (2012). Proposition of cable driven earthquake simulator with pneumatic levitation. In *Proceedings of Robotic Society of Japan* (p.98) (in Japanese).

# Comparison of Dynamic Properties of Two KUKA Lightweight Robots

Lukasz Woliński and Marek Wojtyra

**Abstract** This paper concerns the comparison of dynamic properties of two LWR 4+ robots. As a preparation to the identification task, a series of joint torque measurements is performed to determine the variability of the dynamic parameters. The torque measurements from two robots are compared with each other and a simplified multibody model. The results are discussed.

**Keywords** Robot modeling · Multibody dynamics · Identification

## 1 Introduction

Modeling and control of robot manipulators require knowledge of the dynamic parameters which generally can be obtained only through the identification. It is usually a laborious and often an expensive process. This raises a question whether the dynamic parameters obtained from identification of one robot are sufficient to model all robots of that particular kind. Values and variability of dynamic parameters, such as friction, are not readily available from the manufacturer.

Having at the laboratory two KUKA Lightweight Robots (LWR 4+) (Bischoff et al. 1987) and planning to identify their dynamic parameters using adaptive control and neural networks approach, the authors are highly interested in gaining some insight into the parameters repeatability issue. Performing experiments on just two robots we cannot come to a definite conclusion regarding variations in parameters, however, we can find a clue what might be expected.

---

L. Woliński (✉) · M. Wojtyra  
Institute of Aeronautics and Applied Mechanics,  
Warsaw University of Technology, Warsaw, Poland  
e-mail: lwolinski@meil.pw.edu.pl

M. Wojtyra  
e-mail: mwojtyra@meil.pw.edu.pl

**Fig. 1** KUKA LWR 4+ robots



In this contribution two LWR 4+ robots (Fig. 1) are experimentally compared in terms of torques developed to execute required motion (the same desired trajectory in both cases). The results are contrasted against each other and against predictions of a rigid body model of an idealized robot. The differences between calculated (using the model) and measured quantities represent mainly the unmodelled dynamics; similarly, robot-to-robot differences are mostly due to variations in dynamic properties of the two manipulators. The observed differences are presented and discussed.

The article is organized as follows. Firstly, the multibody model of the LWR 4+ robot is presented. Then, organization of measurements is described. Next, the results are discussed, and finally, concluding remarks are formulated.

## 2 Model

A rigid body model of an idealized, frictionless manipulator was developed. The model is intended to guarantee fast calculations when providing an estimation of robot dynamics for control purposes. Since, as indicated by the similarities in results of independent studies performed by (Gaz et al. 2014) and (Jubien et al. 2014), geometry of masses is highly repeatable among LWR 4+ robots, the same model may be used for all units. For the robot control system, phenomena neglected in the model would be the subject for compensation.

Matrix-form equation of motion of a manipulator consisting of  $n$  rigid links can be written as (Featherstone and Orin 2008):

$$\mathbf{D}(\mathbf{q})\ddot{\mathbf{q}} + \mathbf{C}(\mathbf{q}, \dot{\mathbf{q}})\dot{\mathbf{q}} + \mathbf{G}(\mathbf{q}) + \boldsymbol{\tau}_{diss} = \boldsymbol{\tau} \quad (1)$$

where  $\mathbf{q} \in \mathbb{R}^{n \times 1}$  is a vector of joint coordinates,  $\mathbf{D}(\mathbf{q}) \in \mathbb{R}^{n \times n}$  is the inertia matrix of the manipulator,  $\mathbf{C}(\mathbf{q}, \dot{\mathbf{q}}) \in \mathbb{R}^{n \times n}$  is the Coriolis/centrifugal matrix,  $\mathbf{G}(\mathbf{q}) \in \mathbb{R}^{n \times 1}$  is the gravity vector,  $\boldsymbol{\tau}_{diss} \in \mathbb{R}^{n \times 1}$  is a vector of the dissipative torques (friction, etc.) and vector  $\boldsymbol{\tau} \in \mathbb{R}^{n \times 1}$  contains driving torques in joints.

Equation (1) was obtained using a recursive algorithm described in (Woliński and Malczyk 2015). There was, however, one slight change done—link coordinate frames were moved outside the centers of mass. The algorithm is briefly summarised in the following subsection.

### 2.1 Algorithm Formulation

Figure 2 presents fragment of a kinematic chain. Let  $\mathbf{h}_{ij}$  be a unit vector along the  $j$ th joint axis of rotation,  $\mathbf{r}_i$ —a vector locating the  $i$ th joint attachment point in the global reference frame,  $\mathbf{r}_{ij}$ —a vector originating at the  $i$ th joint attachment point and pointing to the  $j$ th joint attachment point. All quantities are represented in the global reference frame  $x_0y_0z_0$ .

Velocity of the  $j$ th link is (Bae and Haug 1987):

$$\mathbf{V}_j = \left[ \dot{\mathbf{r}}_j^T \ \boldsymbol{\omega}_j^T \right]^T = \mathbf{B}_{ij}\mathbf{V}_i + \mathbf{H}_j\dot{q}_j, \tag{2}$$

where  $\mathbf{B}_{ij}$  is a shift matrix and  $\mathbf{H}_j$  is a joint motion space matrix. Velocity equations for all  $n$  links can be written jointly in a form:

$$\mathbf{V} = \mathbf{B}\mathbf{V} + \mathbf{H}\dot{\mathbf{q}} = \boldsymbol{\Phi}\mathbf{H}\dot{\mathbf{q}}, \tag{3}$$

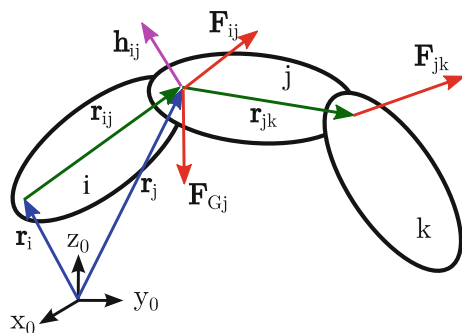
where  $\boldsymbol{\Phi} = (\mathbf{I} - \mathbf{B})^{-1}$ . Differentiation the above formula with respect to time allows to obtain equations for accelerations:

$$\dot{\mathbf{V}} = \boldsymbol{\Phi}((\dot{\mathbf{B}}\boldsymbol{\Phi}\mathbf{H} + \dot{\mathbf{H}})\dot{\mathbf{q}} + \mathbf{H}\ddot{\mathbf{q}}). \tag{4}$$

The  $i$ th link acts on the  $j$ th link with a force:

$$\mathbf{F}_{ij} = \mathbf{M}_j\dot{\mathbf{V}}_j + \mathbf{B}_{jk}^T\mathbf{F}_{jk} - \boldsymbol{\Omega}_j\mathbf{V}_j - \mathbf{F}_{Gj}, \tag{5}$$

**Fig. 2** Articulated bodies connected by revolute joints



where:  $\mathbf{M}_j$  is the  $j$ th link mass and inertia matrix,  $\mathbf{\Omega}_j = \begin{bmatrix} \mathbf{0} & -\tilde{\boldsymbol{\omega}}_j \tilde{\mathbf{S}}_j \\ \mathbf{0} & \tilde{\boldsymbol{\omega}}_j \mathbf{J}_j \end{bmatrix}$ ,  $\tilde{\boldsymbol{\omega}}_j$  is a skew-symmetric matrix associated with vector  $\boldsymbol{\omega}_j = \boldsymbol{\omega}_i + \mathbf{h}_{ij} \dot{q}_j$  which is the rotational velocity of the  $j$ th link, similarly  $\tilde{\mathbf{S}}_j$  is a skew-symmetric matrix associated with the first moment of mass of the  $j$ th link,  $\mathbf{F}_{G_j} = [m_j \mathbf{g}^T (\tilde{\mathbf{S}}_j \mathbf{g})^T]^T$  and  $\mathbf{F}_{jk}$  is the force exerted by the  $j$ th link on the  $k$ th link.

Force equations (5) for all  $n$  links can be written jointly in a form:

$$\mathbf{F} = \Phi^T (\mathbf{M}\dot{\mathbf{V}} - \mathbf{\Omega}\mathbf{V} - \mathbf{F}_G). \quad (6)$$

The following relation is obtained from the power-balance equation:

$$\mathbf{H}^T \mathbf{F} = \boldsymbol{\tau}. \quad (7)$$

Inserting Eq. (4) into Eq. (6) and the resulting equation into (7) gives finally relation (1), where:  $\mathbf{D}(\mathbf{q}) = \mathbf{H}^T \Phi^T \mathbf{M} \Phi \mathbf{H}$ ,  $\mathbf{G}(\mathbf{q}) = \mathbf{H}^T \Phi^T (-\mathbf{F}_G)$  and  $\mathbf{C}(\mathbf{q}, \dot{\mathbf{q}}) = \mathbf{H}^T \Phi^T (\mathbf{M} \Phi (\dot{\mathbf{B}} \Phi \mathbf{H} + \dot{\mathbf{H}}) - \mathbf{\Omega} \Phi \mathbf{H})$ .

## 2.2 Algorithmic Steps

To calculate matrices  $\mathbf{D}(\mathbf{q})$ ,  $\mathbf{C}(\mathbf{q}, \dot{\mathbf{q}})$  and  $\mathbf{G}(\mathbf{q})$ , the following algorithm is used:

1. Initialize matrices  $\mathbf{H} = \mathbf{0}_{6n \times 6}$ ,  $\dot{\mathbf{H}} = \mathbf{0}_{6n \times 6}$ ,  $\dot{\mathbf{B}} = \mathbf{0}_{6n \times 6n}$ ,  $\Phi = \mathbf{I}_{6n \times 6n}$ ,  $\mathbf{M} = \mathbf{0}_{6n \times 6n}$ ,  $\mathbf{\Omega} = \mathbf{0}_{6n \times 6n}$  and  $\mathbf{F}_G = \mathbf{0}_{6n \times 1}$ . Set  $j = 1$ .
2. Calculate  $\mathbf{H}_j$  and  $\dot{\mathbf{H}}_j$  and put them in rows  $6j - 5$  to  $6j$  and column  $j$  of  $\mathbf{H}$  and  $\dot{\mathbf{H}}$ . Put  $\mathbf{M}_j$  and  $\mathbf{\Omega}_j$  in rows  $6j - 5$  to  $6j$  and columns  $6j - 5$  to  $6j$  of  $\mathbf{M}$  and  $\mathbf{\Omega}$ . Put  $\mathbf{F}_{G_j}$  in rows  $6j - 5$  to  $6j$  of  $\mathbf{F}_G$ .
3. If  $j > 1$ , then set  $i = j - 1$  and calculate  $\mathbf{B}_{ij}$ ,  $\dot{\mathbf{B}}_{ij}$  and  $\Phi_j = \mathbf{B}_{ij} \Phi_i$  where  $\Phi_i$  is made of rows  $6i - 5$  to  $6i$  and columns 1 to  $6i$  of  $\Phi$ . Put  $\dot{\mathbf{B}}_{ij}$  into  $\dot{\mathbf{B}}$  in rows  $6j - 5$  to  $6j$  and columns  $6i - 5$  to  $6i$ . Put  $\Phi_j$  into  $\Phi$  in rows  $6j - 5$  to  $6j$  and columns 1 to  $6i$ .
4. Set  $j = j + 1$ . If  $j \leq n$ , then go to step 3, else go to 5.
5. Calculate  $\mathbf{D}(\mathbf{q})$ ,  $\mathbf{C}(\mathbf{q}, \dot{\mathbf{q}})$  and  $\mathbf{G}(\mathbf{q})$ .

After completion of the algorithm, a numerical form of Eq. (1) is obtained which can be used to solve the forward or inverse dynamics problem.

## 3 Measurements

Measurements were done on two KUKA LWR 4+ robots. They are 7 DOF redundant manipulators with anthropomorphic structure. Each robot is equipped with sensors measuring torques in joints on the link side, i.e. after the gear. Moreover, KUKA

provides the so-called *Fast Research Interface* (FRI) which allows communication between the robot controller and remote PC (Schreiber et al. 2010). FRI gives user the ability to specify motion commands and to acquire measurement data over the Ethernet with a time cycle ranging from 1 ms to 100 ms.

During the measurements robots were controlled in the joint space. Desired joint positions were calculated using cubic splines (Biagiotti and Melchiorri 2008, ch. 4.4.4) with the spline knots fulfilling the equations:

$$q_{dj}(t_k) = \frac{\pi}{2} \cos\left(\frac{\pi}{7}t_k\right) \quad j = 1, \dots, 7, \quad k = 1, \dots, 10 \quad (8)$$

and sent to the robot controllers using FRI. Desired motion lasted 14 seconds and was repeated 10 times on each robot. Measured joint torques were collected on the remote PC with the sample frequency 500 Hz. Sampled data was filtered using the 4th order Butterworth filter with a cutoff frequency of 1 Hz.

## 4 Results

Firstly, the repeatability of performance of both robots was checked. For each manipulator the average time course of joint torques was calculated (based on 10 measured cycles). The individual measurements were compared with respective averages in order to assess repeatability of results. To qualitatively compare the results, for each joint  $j$ , the mean square error was calculated:

$$\epsilon_j = \frac{1}{N} \sum_{i=1}^N (\tau_j^A(t_i) - \tau_j^B(t_i))^2 \quad j = 1, \dots, 7, \quad N = 7000, \quad (9)$$

where  $\tau_j^A$  and  $\tau_j^B$  are the torques being compared. Selected results, representative for all measurements, are presented in Table 1.

**Table 1** Mean square error ( $R_{avg}^1$ —1st robot average,  $R_{avg}^2$ —2nd robot average,  $R_i^1$ —1st robot  $i$ th measurement,  $R_i^2$ —2nd robot  $i$ th measurement)

Joint	$R_{avg}^1$ versus $R_1^1$	$R_{avg}^1$ versus $R_{10}^1$	$R_{avg}^2$ versus $R_1^2$	$R_{avg}^2$ versus $R_{10}^2$
1	0.0013	0.0102	0.0003	0.0003
2	0.00003	0.0001	0.0005	0.0005
3	0.0005	0.0005	0.00003	0.00003
4	0.0001	0.0001	0.0003	0.0001
5	0.0001	0.0002	0.0003	0.0003
6	0.0004	0.0003	0.00007	0.0001
7	0.00007	0.00006	0.0003	0.0002

Next, the recursive algorithm described in Sect. 2 was utilized to calculate the torques theoretically required to realize the desired trajectory. Geometry of masses for the dynamic model was taken from (Gaz et al. 2014) and (Jubien et al. 2014). Then, the modelled torques were compared with the average of measured torques from each robot separately. Results for the first two joints are presented in Figs. 3 and 4.

Note that absolute differences between torques being compared were moderate for all joints of the robots. Torque developed in joint 1 was small thus relative differences are clearly visible in Fig. 3. On the contrary, in the case of joint 2, the developed torque was large and the investigated differences are hardly visible in Fig. 4.

Equation (9) was used to calculate quantitative comparison of torques (first robot vs. second robot, model vs. first robot, model vs. second robot). The mean square error is presented in Table 2.

Fig. 3 First joint torques

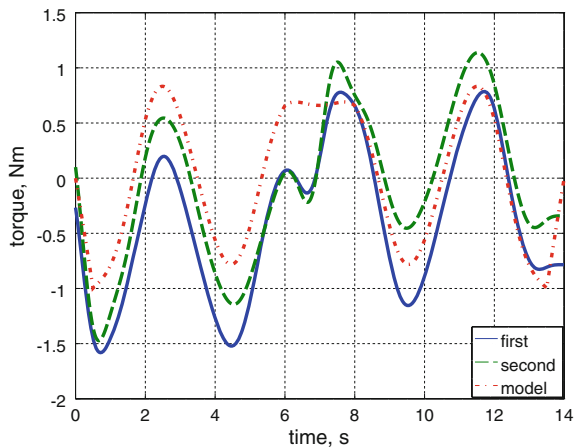
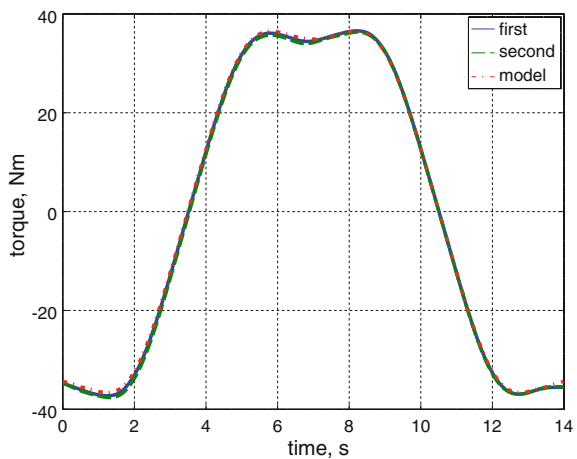


Fig. 4 Second joint torques



**Table 2** Mean square error (M—model,  $R_{avg}^1$ —1st robot average,  $R_{avg}^2$ —2nd robot average)

Joint	$R_{avg}^1$ versus $R_{avg}^2$	M versus $R_{avg}^1$	M versus $R_{avg}^2$
1	0.149	0.256	0.150
2	0.123	0.201	0.562
3	0.416	0.517	0.194
4	0.048	0.251	0.103
5	0.453	0.091	0.724
6	0.109	0.270	0.074
7	0.175	0.077	0.147

Differences between the modelled torques and torques measured on the robots are caused by the unmodelled effects. The idealized model is fast and efficient which predisposes it to control tasks. However, to achieve the desired tracking performance it has to be supplemented with the compensation of unmodelled dynamics, e.g. by means of neural network (Jiang et al. 2006).

## 5 Conclusions

The results of measurements show that dynamic properties of each individual robot are highly repeatable. Note that the numbers in Table 1 are two to three orders of magnitude smaller than numbers in Table 2.

In terms of dynamic properties, the differences between two robots are apparent. This indicates that in the case of applications for which the idealized model is insufficiently precise, the identification of unmodelled dynamics should be performed separately for each robot.

It is worth noting that robot-to-robot and robot-to-model differences are comparable in magnitudes (see Table 2). This suggests that there is no point in improving the general model for all robots, by including equations that describe previously neglected phenomena (predominantly joint friction) and trying to find additional parameters that match all robots. To improve the accuracy of modelling, the simple model of Sect. 2 should be accompanied by compensating terms tailored individually for each robot.

The presented conclusions must be treated cautiously, as only two robots were investigated.

**Acknowledgments** This research was supported by the National Science Centre (Poland) grant no. DEC-2012/07/B/ST8/03993.



## References

- Bae, D. S., & Haug, E. J. (1987). A recursive formulation for constrained mechanical system dynamics: Part I: Open loop systems. *Mechanics of Structures and Machines*, 15, 359–382.
- Biagiotti, L., & Melchiorri, C. (2008). *Trajectory Planning for Automatic Machines and Robots*. Berlin Heidelberg: Springer-Verlag.
- Bischoff, R., Kurth, J., Schreiber, G., Koeppe, R., Albu-Schäffer, A., Beyer, A., et al. (1987). The KUKA-DLR Lightweight Robot arm—a new reference platform for robotics research and manufacturing. In *Robotics (ISR), 2010 41st International Symposium on and 2010 6th German Conference on Robotics (ROBOTIK)* (pp. 741–748), June 2010.
- Featherstone, R., & Orin, D. E. (2008). Dynamics. In B. Siciliano & O. Khatib (Eds.), *Springer Handbook of Robotics* (pp. 35–65). Berlin Heidelberg: Springer-Verlag.
- Gaz, C., Flacco, F. & De Luca, A. (2014). Identifying the dynamic model used by the KUKA LWR: A reverse engineering approach. In *Proceedings of the IEEE International Conference on Robotics and Automation 2014* (pp 1386–1392), Hong Kong, China, 31 May–7 June 2014.
- Jiang, Z.-H., Ishida, T. & Sunawada, M. (2006). Neural network aided dynamic parameter identification of robot manipulators. In *Proceedings of the IEEE International Conference on Systems, Man and Cybernetics 2006* (pp. 3298–3303), Taipei, Taiwan, 8–11 October 2006.
- Jubien, A., Gautier, M. & Janot, A. (2014). Dynamic identification of the Kuka LightWeight Robot: comparison between actual and confidential Kuka's parameters. In *Proceedings of the IEEE/ASME International Conference on Advanced Intelligent Mechatronics 2014* (pp. 483–488), Besancon, France, 8–11 July 2014.
- Schreiber, G., Stemmer, A., & Bischof, R. (2010). The Fast research interface for the KUKA lightweight robot. In *IEEE ICRA 2010 Workshop on Innovative Robot Control Architectures* (pp. 15–21), May 2010.
- Woliński, Ł., & Malczyk, P. (2015). Dynamic modeling and analysis of a lightweight robotic manipulator in joint space. *Archive of Mechanical Engineering*, 62, 279–302.

# Comparison of Serial and Quasi-Serial Industrial Robots for Isotropic Tasks

Alexandr Klimchik, Evgeni Magid, Ilya Afanasyev  
and Anatol Pashkevich

**Abstract** The paper presents a new approach for comparison of serial and quasi-serial robots in industrial applications. In contrast to other works, it is based on evaluation of maximum compliance errors in the working area for isotropic tasks. It is proved that for large-scale isotropic tasks quasi-serial manipulators with kinematic parallelograms are preferable, while for small task dimensions' serial manipulators provide better accuracy.

**Keywords** Industrial robot · Serial manipulator · Quasi-serial manipulator

## 1 Introduction

In modern industrial applications, a number of technological tasks can be treated as isotropic ones, where required end-effector motion direction is almost uniform. Examples of such tasks can be found in milling of contemporary high performance metal and composite materials that generate essential force/torques causing non-negligible compliance errors of robotic manipulator. To minimize these errors, robot manufactures propose quasi-serial architectures with kinematic parallelograms that potentially provide better rigidity. For this reason, practicing engineers face the problem of well-grounded selection between serial and quasi-serial architectures for particular applications. This paper presents a novel technique that

---

A. Klimchik (✉) · E. Magid · I. Afanasyev  
Innopolis University, Universitetskaya 1, 420500 Innopolis, Russia  
e-mail: a.klimchik@innopolis.ru

E. Magid  
e-mail: e.magid@innopolis.ru

I. Afanasyev  
e-mail: i.afanasyev@innopolis.ru

A. Pashkevich  
Ecole des Mines de Nantes, 4 rue Alfred-Kastler, 44307 Nantes, France  
e-mail: anatol.pashkevich@mines-nantes.fr

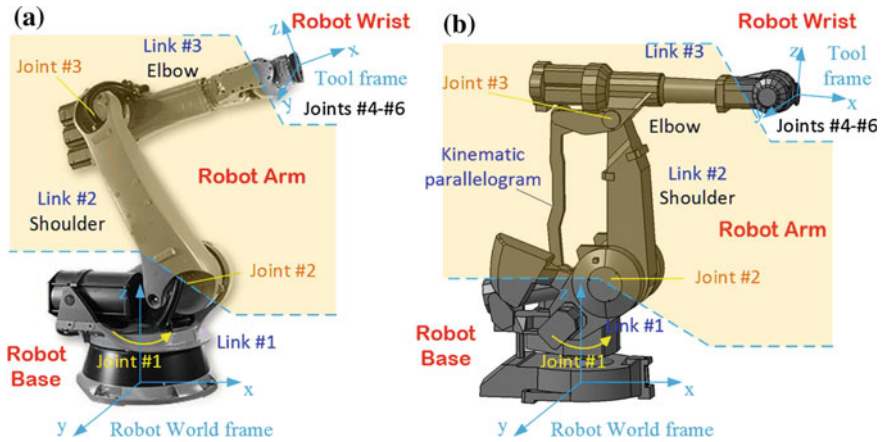


**Fig. 1** Architecture of a typical industrial robot. **a** typical serial manipulator **b** typical quasi-serial manipulator

allows user to evaluate manipulator performance numerically taking into account the manipulator stiffness properties and also particularity and size of a technological task.

In general, typical *serial manipulators* contain three main components: robot base, robot arm and robot wrist (Fig. 1a), where the robot base defines the arm orientation, the robot arm is responsible for the major movements of the robot end-effector, the orientation movements are provided by the robot wrist. *Quasi-serial robots* have roughly similar architecture (see Fig. 1b). In contrast to strictly serial counterparts, a quasi-serial manipulator arm contains a kinematic parallelogram, which can be treated as an internal closed-loop (and completely differ from hybrid serial-parallel manipulators). Usually the parallelogram does not affect essentially manipulator control and does not change manipulator direct/inverse kinematic equations. On the other hand, the stiffness model of a quasi-serial manipulator essentially differs from its serial counterpart since relocation of the manipulator compliant element influences stiffness behavior. For this reason, the results obtained for strictly serial manipulators cannot be used directly for quasi-serial manipulators.

The stiffness model of a robotic manipulator describes manipulator behavior under loading (Klimchik et al. 2014; Pashkevich et al. 2011; Yan et al. 2016). In addition to the conventional robot parameters (geometric ones), it includes a number of elastic parameters describing flexibility of manipulator links and joints. In number of industrial applications, manipulator elasticity cannot be ignored since high loading is applied to the robot, while required positioning accuracy is rather high. For example, in machining application, an end-effector deflection of industrial robots under the loading of 1kN may vary from 1 to 10 mm (Matsuoka et al. 1999), while demanded accuracy for machining process is about 0.1 mm. These compliance errors can be reduced down to admissible level using both on-line and off-line

error compensation techniques that are based on the appropriate stiffness model (Klimchik et al. 2013a), which may be either “*complete*” or “*reduced*”. The complete stiffness model of an industrial robot is rather complicated, as it takes into account all manipulator links and actuators compliances (Klimchik et al. 2015). However, in practice, a number of manipulator components may be treated as rigid ones, while the main compliance is concentrated in the actuator transmissions. This allows to apply so-called reduced models that take into account the joint elasticities only (Alici and Shirinzadeh 2005; Guo et al. 2015). Such models are quite common for stiffness modeling of heavy industrial robots (Klimchik et al. 2013b) where the links are massive and deflections under the force 1kN are lower than 0.1 mm. For this reason, the comparison study presented in this paper is based on the reduced stiffness model.

## 2 Motivation Example

To define the research problem and to demonstrate advantages/disadvantages of both serial and quasi-serial architectures, let us start with a motivation example showing that proper manipulator type selection essentially depends on the technological task dimension and external force orientation. This example deals with two manipulators (serial and quasi-serial ones) with the same basic geometric parameters  $l_2 = 1$  m,  $l_3 = 0.8$  m and similar joint compliances  $k = 10^{-6}$  rad/N m. These values are typical for industrial robots that are used in machining (Dumas et al., 2012). To compare stiffness behavior, let us compute the compliance errors caused by an external force 1.0 kN applied to the end-effector (details of related technique are presented in (Klimchik et al. 2014)). Relevant results have been obtained for two different external loadings and are presented in Fig. 2, which shows the compliance error distribution within the workspace.

As follows from Fig. 2, the elastostatic deflections vary from 0 to 3.83 mm for the serial manipulator and from 0 to 1.62 mm for the quasi-serial manipulator. These results show that for the considered case study the compliance errors range does not depend on the force direction, however the compliance error maps differ essentially. Summarizing these results, it is possible to define several research problems that are in the focus of this paper and are useful for optimal selection of robotic manipulator from the set of available ones. These problems can be formulated as follows:

- development of the manipulator selection methodology using the compliance maps and optimal task placement technique;
- defining boundary between the technological tasks which suit serial and quasi-serial architectures in the best way.

They will be studied in the following Sections.

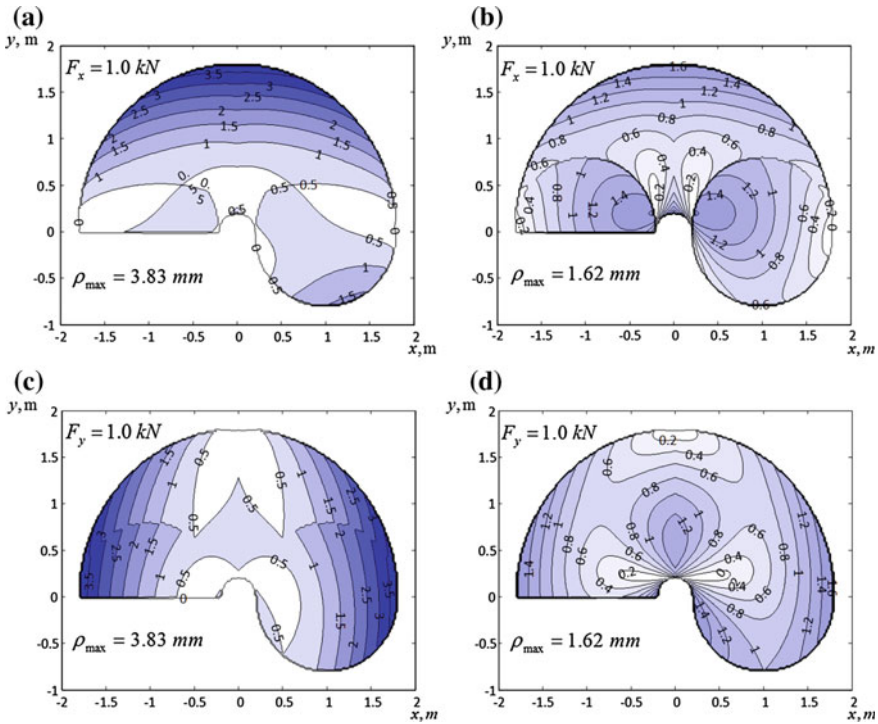


**Fig. 2** Compliance maps for serial and quasi-serial manipulators. **a** Compliance map for *serial manipulator* under the external loading in x-direction **b** Compliance map for *quasi-serial manipulator* under the external loading in x-direction **c** Compliance map for *serial manipulator* under the external loading in y-direction **d** Compliance map for *quasi-serial manipulator* under the external loading in x-direction

### 3 Performance Measure for Manipulator Accuracy Evaluation

The manipulator performance with respect to a number of technological tasks cannot be evaluated using elastic or geometrical properties only: an appropriate performance measure should take into account also the external force/torque directions and magnitudes. The problem becomes more complicated if external loadings are not given. In this case it is reasonable to consider all possible directions of external force and to estimate maximal compliance errors in the considered work-point:

$$\rho_p = \max_{\varphi_i} |\mathbf{k}_C \cdot \mathbf{F} \cdot \mathbf{R}(\varphi_i)|; \quad \varphi_i \in [-\pi, \pi] \tag{1}$$

where  $\mathbf{k}_C = \mathbf{J}(\mathbf{q}) \cdot \mathbf{k}_\theta \cdot \mathbf{J}(\mathbf{q})^T$  is the manipulator compliance for the configuration  $\mathbf{q}$ , the diagonal matrix  $\mathbf{k}_\theta$  collects the joint compliances,  $\mathbf{F}$  is the external loading applied to the manipulator end-effector,  $\mathbf{R}(\varphi_i)$  is the rotation matrix allowing us to estimate the compliance errors for any force direction  $\varphi_i$ .

In practice, the direction of maximal and minimal compliance errors can be obtained via the singular value decomposition of the compliance matrix  $\mathbf{k}_C$

$$\mathbf{k}_C = \mathbf{U} \cdot \Sigma \cdot \mathbf{V}^T \quad (2)$$

where the diagonal matrix  $\Sigma = \text{diag}(\sigma_{\max}, \dots, \sigma_{\min})$  contains the singular values,  $\mathbf{U}$  and  $\mathbf{V}$  are orthogonal matrices that in this particular case are equal. Here, the first line of the vector  $\mathbf{V}$  defines the force direction that causes the maximum compliance error of the end-effector. Similarly, the last line of vector  $\mathbf{V}$  defines the strongest direction. Corresponding values of  $\sigma_{\max}, \dots, \sigma_{\min}$  define the magnitude of compliance errors and the ratio between these values allows user to compare manipulator compliance in different directions. Hence, values  $\sigma_{\max}$  will be used further to estimate the manipulator stiffness properties in the configuration  $\mathbf{q}$ .

It is worth mentioning that manipulator architecture analysis cannot be performed in a single point. For this reason, we consider an *isotropic-shape tasks*, which can be circumscribed by a circle  $S$  of diameter  $d$ . Even though isotropic tasks may provide rather rough approximation for some complex technological problems, these it allows us to classify all technological tasks into typical groups and to analyze the manipulator performance for the group of tasks that meet certain requirements. Using the above notations, it is possible to evaluate the manipulator performance using maximum compliance error in accordance with expression

$$\rho_S = \max_{\mathbf{q}} \{ \sigma_{\max}(\mathbf{q}) \mid g(\mathbf{q}) \in S \} \quad (3)$$

where the function  $g(\mathbf{q})$  defines the manipulator geometry, and  $S$  is a workspace area corresponding to this task. By means of this performance measure it is possible to estimate potential compliance errors caused by the tool-workpiece interaction and to compare accuracy of different manipulators for the same type of technological tasks. In fact, here the product  $\rho_S \cdot |\mathbf{F}|$  corresponds to the guaranteed accuracy of robot-based machining if the cutting force does not exceed  $|\mathbf{F}|$  while the workpiece is placed inside of optimally located zone  $S$  within the robot workspace.

## 4 Comparison of Serial and Quasi-Serial Architectures

To compare serial and quasi-serial manipulators, let us compute and evaluate the error maps within the robot workspace using Eq. (3) and varying the size and location of task workspace  $S$ . For the error maps evaluation, let us apply the optimal task placement technique that provides the best task location  $\mathbf{p}_0^*$  for each given the size of  $d$

$$[\mathbf{p}_0^*, \rho_S^*] = \arg \left[ \min_{\mathbf{p}_0} \max_{\mathbf{q}} \{ \sigma_{\max}(\mathbf{q}) \mid g(\mathbf{q}) \in S(\mathbf{p}_0, d) \} \right] \quad (4)$$

It should be noted that for both serial and quasi-serial manipulators the compliance errors do not depend on the angle  $q_2$ . It means that for the *isotropic-shape tasks* the problem of the optimal task placement reduces to a one-dimensional one with respect to  $q_3$ . Relevant algorithm allowing us to define the optimal task placement and to evaluate manipulator accuracy is presented below. It provides the benchmark task accuracy  $\varepsilon_S$  and task optimal location corresponding to the task dimension  $d$ .

**Algorithm 1** – Optimal task placement for isotropic-shape tasks

**Input:** manipulator geometry  $l_1, l_2$ ; task diameter  $d$ ; stopping parameter  $\delta$

**Output:** optimal task location  $x_O$ ; obtained accuracy  $\varepsilon_S$

**Notations:**  $x_{\min} = |l_1 - l_2|$ ,  $x_{\max} = l_1 + l_2$

**Invoked function:** error function  $\varepsilon(x)$ ,  $x \in [x_{\min}, x_{\max}]$ ;  $\varepsilon(x) = \text{Inf}$  if  $x \notin [x_{\min}, x_{\max}]$

Verify  $d < x_{\max} - x_{\min}$ , return “No Solution” if false

Find minimum of error function  $[\varepsilon_{\min}, x^*] = \min(\varepsilon(x) \mid x \in [x_{\min}, x_{\max}])$

Set initial values of interval  $x_1 = x^*, x_2 = x^*$  and step size  $d_i = d / 2$

Repeat

    Compute  $\varepsilon_1 = \varepsilon(x_1 - d_i)$ ;  $\varepsilon_2 = \varepsilon(x_2 + d_i)$

    Enlarge interval  $[x_1, x_2]$ :

    if  $\varepsilon_1 \geq \varepsilon_2$

        than  $x_2 = x_2 + d_i$

        else  $x_1 = x_1 - d_i$

    Halve step size

    if  $x_2 - x_1 < d - \delta$

        than  $d_i = d_i / 2$

    while  $x_2 - x_1 < d$

Compute task accuracy  $\varepsilon_S = \max(\varepsilon(x_1), \varepsilon(x_2))$  and its location  $x_O = (x_1 + x_2) / 2$

Applying the above presented algorithm to the serial and quasi-serial manipulators, there were computed values of the benchmark accuracy  $\varepsilon_S$  for different task size  $d$  and different link lengths ratio  $\mu = l_3 / l_2$  (assuming that the total length is fixed, i.e.  $l_2 + l_3 = \text{const}$ , and all joint stiffness coefficients are equal). Relevant results are presented in Fig. 3, which allows us to compare potential accuracy for both architectures. As follows from them, for the *quasi-serial manipulator*, the best positioning accuracy is achieved for the link length ratio  $\mu = 1.0$ . It should be noted that this conclusion does not depend on the task size  $d$ . Moreover, the manipulator with such ratio may perform tasks of maximum size compared to the quasi serial manipulators with  $\mu > 1.0$  and  $\mu < 1.0$ . In contrast, for a *serial manipulator*, the optimal link length ratio essentially depends on the task size. In particular, for small tasks with  $d / (l_2 + l_3) < 0.25$  it is preferable to have the link length ratio  $\mu = 0.7$

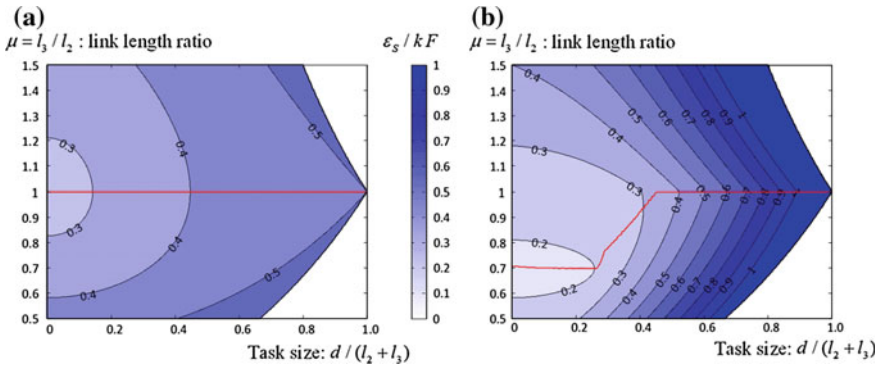


**Fig. 3** Normalized accuracy  $\varepsilon_S/kF$  for isotropic tasks. **a** Case of the quasi-serial manipulator **b** Case of the serial manipulator

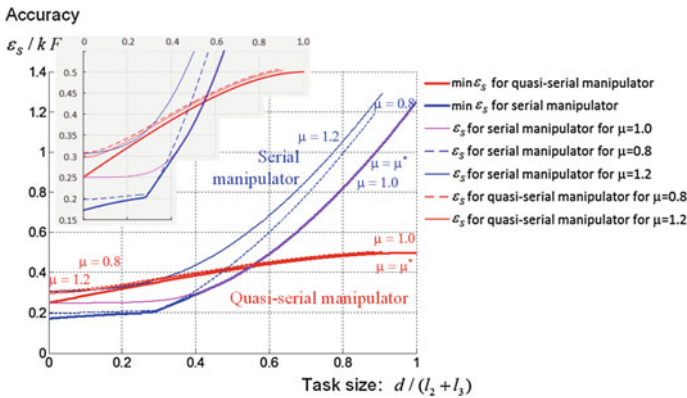


**Fig. 4** Accuracy of serial and quasi-serial manipulators for isotropic task

while for large tasks with  $d/(l_2+l_3) > 0.4$  the optimal ratio is  $\mu = 1.0$ . For convenience, optimal values of  $\mu$  are highlighted in Fig. 3 by red lines.

To make comparison of two architectures more evident, Fig. 4 presents potential accuracy (as well as zoom) for isotropic-shape tasks that is achieved for different link-length ratios  $\mu$ . The latter includes the optimal value of  $\mu = \mu^*$  as well as  $\mu = 0.8, 1.0, 1.2$  that are widely used in practice. The results show that for small isotropic-shape tasks the serial manipulators are preferable since they are able to ensure better accuracy. On the other side, the quasi-serial manipulators are better if the task size is rather big, i.e.  $d/(l_2+l_3) > 0.55$ . Besides, the quasi-serial manipulators provide similar performance for both small and large tasks while the properties of their serial counterparts essentially depend on the task size. It should be also emphasized that the link length ratio in the range  $\mu \in [0.8; 1.2]$  does not affect essentially the accuracy of a quasi-serial manipulator. In contrast, a serial



**Table 1** Accuracy of serial (SM) and quasi-serial (QSM) manipulators for isotropic tasks

Task dimension $d/(l_2 + l_3)$		Normalized accuracy, $\varepsilon_S/kF$							
		0.1		0.2		0.5		0.8	
Manipulator architecture		SM	QSM	SM	SM	SM	QSM	SM	QSM
Link-length ratio $\mu$	0.8	0.20	0.32	0.21	0.34	0.45	0.43	1.00	0.49
	1.0	0.25	0.28	0.25	0.32	0.37	0.42	0.82	0.48
	1.2	0.31	0.31	0.33	0.34	0.55	0.43	1.05	0.49
Minimum error		0.18	0.28	0.19	0.32	0.37	0.42	0.82	0.48

manipulator is very sensitive to its proper selection; for the range  $\mu \in [0.8; 1.2]$  the serial manipulator accuracy may be twice as worse compared to the minimum value. The results of this study are summarized in Table 1, which shows accuracy limits and preferred manipulators (for which the table cells are colored in green).

## 5 Conclusion

The paper presents the comparison analysis of serial and quasi-serial manipulators for isotropic-shape tasks. It proposes a new technique that evaluates robot positioning accuracy taking into account the manipulator stiffness behavior within the working area. It was demonstrated that serial manipulators are preferable for small tasks while quasi-serial manipulators better suit large tasks. Also it was shown that, from the manipulator compliance point of view, it is preferable to have serial manipulators with link-length ratio about 0.7 and quasi-serial with equal link lengths. In future, the developed approach will be applied to compare robot architectures from different manufactures.

## References

- Alici, G. & Shirinzadeh, B. (2005) Enhanced stiffness modeling, identification and characterization for robot manipulators. *Robotics, IEEE Tranaction. on* 21(4), 554–564.
- Dumas, C., Caro, S., Cherif, M., Garnier, S., & Furet, B. (2012). Joint stiffness identification of industrial serial robots. *Robotica*, 30, 649–659.
- Guo, Y., Dong, H., & Ke, Y. (2015). Stiffness-oriented posture optimization in robotic machining applications. *Robotics and Computer-Integrated Manufacturing*, 35, 69–76.
- Klimchik, A., Chablat, D., & Pashkevich, A. (2014). Stiffness modeling for perfect and non-perfect parallel manipulators under internal and external loadings. *Mechanism and Machine Theory*, 79, 1–28.
- Klimchik, A., Furet, B., Caro, S., & Pashkevich, A. (2015). Identification of the manipulator stiffness model parameters in industrial environment. *Mechanism and Machine Theory*, 90, 1–22.

- Klimchik, A., Pashkevich, A., Chablat, D., & Hovland, G. (2013a). Compliance error compensation technique for parallel robots composed of non-perfect serial chains. *Robotics and Computer-Integrated Manufacturing*, 29(2), 385–393.
- Klimchik, A., Wu, Y., Dumas, C., Caro, S., Furet, B. & Pashkevich, A. (2013b) Identification of geometrical and elastostatic parameters of heavy industrial robots. In *Robotics and Automation, 2013 IEEE International Conference on* (pp. 3707–3714).
- Matsuoka, S.-I., Shimizu, K., Yamazaki, N., & Oki, Y. (1999). High-speed end milling of an articulated robot and its characteristics. *Journal of Materials Processing Technology*, 95(1–3), 83–89.
- Pashkevich, A., Klimchik, A., & Chablat, D. (2011). Enhanced stiffness modeling of manipulators with passive joints. *Mechanism and Machine Theory*, 46(5), 662–679.
- Yan, S. J., Ong, S. K., & Nee, A. Y. C. (2016). Stiffness analysis of parallelogram-type parallel manipulators using a strain energy method. *Robotics and Computer-Integrated Manufacturing*, 37, 13–22.

# On the Dynamics and Emergency Stop Behavior of Cable-Driven Parallel Robots

Philipp Tempel, Alexander Verl and Andreas Pott

**Abstract** High dynamics of cable-driven parallel robots are beneficial to their use, however, the behavior of such robots during extreme maneuvers is yet to be investigated. In this paper, a simulation model is presented and validated in order to assess the emergency stop behavior of cable robots by simulation. Simulation results are evaluated using spectral analysis and validated against experimental data of a medium-sized redundantly restrained cable robot. The correctness and limitations of the model's accuracy in a range of the actual system's dynamics are furthermore shown.

## 1 Introduction

By replacing rigid links in the well-known Gough/Stewart platform with flexible bodies such as cables, certain properties inherent to Gough/Stewart platforms can be improved. Besides increasing the reachable workspace by use of cables, which can be coiled i.e., stored with minimum space requirements, dynamics of the system can greatly be improved due to decrease in total mass moved. These apparent changes were first studied in depth by the National Institute of Standards and Technology (NIST) for the NIST RoboCrane by Dagalakis (1989) and properties of the design were shown. Ever since the 1990s, research efforts on cable-driven parallel robots (in short *cable robots* or *CDPRs*, sketched in Fig. 1) have increased, inherent problems have been addressed and applications have emerged into the market.

Such cable robot applications can be found in many different fields. The well known Skycam by Cone (1985), providing a bird's-eye view of football or soccer

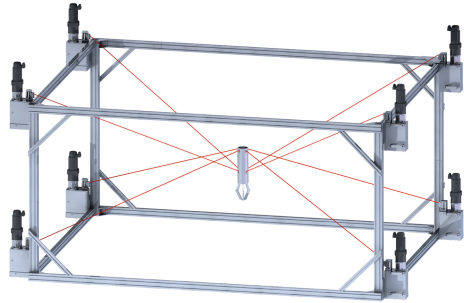
---

P. Tempel (✉) · A. Verl · A. Pott  
Institute for Control Engineering of Machine Tools and Manufacturing Units ISW,  
University of Stuttgart, Stuttgart, Germany  
e-mail: philipp.tempel@isw.uni-stuttgart.de

A. Verl  
e-mail: alexander.verl@isw.uni-stuttgart.de

A. Pott  
e-mail: andreas.pott@isw.uni-stuttgart.de

**Fig. 1** Technical rendering of the cable robot IPANema 1 by Fraunhofer IPA Pott et al. (2013)



matches, is a good example for cable robot technology in use. For use in logistics, Bruckmann et al. (2013) have developed a high rack storage and retrieval unit of large dimensions based on cable robot technology. Cable robots can also be used as locomotion devices as shown by Perreault and Gosselin (2008) or motion simulators providing large workspaces and high accelerations as presented in Zintz (2015). Lastly, in the German Pavilion at EXPO 2015 Universal Exposition hosted in Milan, Italy, two cable robots (see Fig. 2) mimicking the eyeballs of a bee showing its vision flying over Germany was implemented by Tempel et al. (2015b).

Challenges in the design and analysis of cable robots arise from both the flexibility and elasticity of cables as well as the unilateral constraint of cables only being able to transmit tensile forces and thus having to be kept under tension at all times. These challenges reflect not only in inverse kinematics, which generally is an easy task for rigid link parallel robots. They also reflect in forward kinematics and a field specific to cable robots: tension distribution and tension control. Most of the research on cable robots focuses on improving the kinematics, such as by introducing pulleys for guidance by Bruckmann et al. (2008) or considering cable mass Kozak et al. (2004). Other research focuses on the workspace analysis (e.g., Verhoeven 2004) or general application-driven design (e.g., Tempel et al. 2015b).

To the best of the authors' knowledge, all of current research focuses on exploiting advantages of cable robots while not riveting on understanding the dynamics during undesired motion such as induced through e.g., an emergency stop. Due to flexibility

**Fig. 2** Sketch of the show act in the German Pavilion with the two cable robots flying above visitor's heads displaying Germany from the perspective of a bee



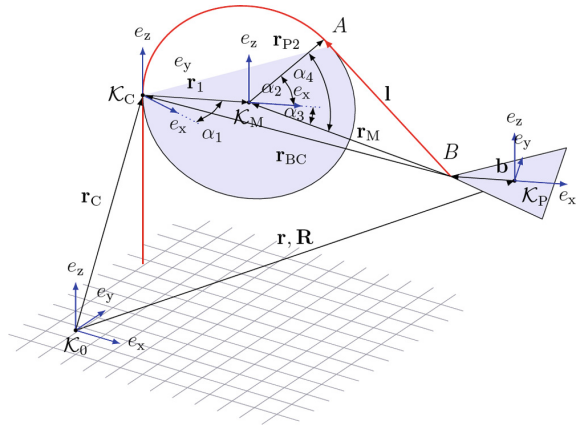
of employed cables, it is unclear and unpredictable how the system will behave when it is forced to come to a complete halt within a very short period of time. In order to ensure a system may be operated in a range suitable for the task but not harmful to the system or people surrounding it, the dynamics of the cable robot, especially at or very close to its maximum operative capabilities i.e., max speed and at the workspace border, are of interest. The main focus of this contribution will thus be providing experimental data insight on the emergency stop behavior of cable robots. This is mainly due to two reasons, one being the safety requirements imposed on the actual installation at EXPO 2015 (the robots are operated above visitors' heads). The other being the interest in cable robot behavior during emergency stops in order to quantify the impact of the platform's kinetic energy on cable tension and the drive's braking torques.

## 2 The Cable Robots at EXPO 2015

For the showroom in the German Pavilion, a technically unique setup was designed by Milla & Partner in cooperation with ISW. Two identical mobile platforms weighing 130 kg each with dimensions of approximately  $1.3 \times 2.2 \times 1.3$  m, are attached to eight steel cables routed from above yielding two redundantly restrained suspended cable robots. Each cable robot has an overall installation space of roughly  $6 \times 14 \times 7$  m of which, for safety reasons, it is not allowed to enter the lower 2.5 m during normal operation.

To meet the requirement of operating the mobile platforms above the audience, additional safety measurements were implemented both for off-line trajectory programming introduced in Tempel et al. (2015b) as well as on-site. On site, monitoring of cable tension and velocities was performed and checked against pre-computed limits stored inside a lookup table. However, additional safety measurements had to be provided determining the maximum allowed workspace which does not only consist of the wrench feasible workspace (see Verhoeven 2004), but which also accounts for the maximum distance of travel in case of an emergency stop. Determining this behavior and mapping it into quantitative values is difficult because of the system's highly non-linear properties depending on the system's current state i.e., Cartesian and articular position, velocity, and acceleration at the moment of initiating the emergency stop. Assuming the mobile platform moves perpendicular to the workspace hull at maximum velocity with maximum acceleration provides for the worst-case scenario for safety measurements.

**Fig. 3** Kinematic loop for pulley kinematics to determine cable length  $l = l(\mathbf{y})$  as a function of the mobile platform pose  $\mathbf{y} = \langle \mathbf{r}, \mathbf{R} \rangle$



### 3 System Model

For the sake of completeness, the kinematics, dynamics, and cable force model used in this work will be presented in the following considering a cable robot with  $n = 6$  degrees of freedom and  $m = 8$  cables/winchies.

#### 3.1 Kinematics

Inferring from Fig. 3, effective cable length set-points along a smooth trajectory can be determined using

$$l_i = \|l_i(\mathbf{y})\|_2 = \|\mathbf{a}_i - (\mathbf{r} + \mathbf{R}\mathbf{b}_i)\|_2, \tag{1}$$

where the tuple  $\mathbf{y} = \langle \mathbf{r}, \mathbf{R} \rangle$  is the arbitrarily parametrized pose and  $\mathbf{b}_i$  is the point of cable attachment on the platform. The cable outlet point  $\mathbf{a}_i$  is either fixed in space (considering standard kinematics) or changes as a function of the pose (considering pulley kinematics). Additional kinematics definitions considering cable mass exist (e.g., Gouttefarde et al. 2014; Kozak et al. 2004) but are not considered in this work due to known limitations in finding feasible solutions in real-time (c.f. Merlet 2015).

#### 3.2 Cable Tension Modeling

Modeling the cables as parallel combination of spring and damper, the restoring force of each cable  $i$ , ( $i = 1, \dots, m$ ), impinging on the mobile platform can be described by

$$f_i = \begin{cases} c_{i,\text{eff}}\Delta l_i + d_{i,\text{eff}}\Delta \dot{l}_i, & (\Delta l_i \wedge \Delta \dot{l}_i) \geq 0, \\ 0, & \text{else.} \end{cases} \quad (2)$$

where  $\Delta l$  and  $\Delta \dot{l}_i$  are the change of effective cable length and effective cable velocity, respectively. Cable stiffness coefficient  $c_{i,\text{eff}}$  and damping coefficient  $d_{i,\text{eff}}$  have to be determined either experimentally or from data sheets of the cables in use.

### 3.3 Dynamics

Based on the components of the dynamics model derived in Tempel et al. (2015a), the model used in this work consists of only the platform kinematics and dynamics and the cable model given as a linear spring-damper model which can be written in the form

$$\begin{bmatrix} m_p I & \mathbf{0} \\ \mathbf{0} & J_p P \end{bmatrix} \ddot{\mathbf{x}} = \begin{bmatrix} D_{\text{lin}} & \mathbf{0} \\ \mathbf{0} & D_{\text{rot}} P \end{bmatrix} \dot{\mathbf{x}} + A^T \mathbf{f} + \mathbf{w} - \mathbf{g}^C \quad (3)$$

where  $\mathbf{x} = [\mathbf{r}^T, \Theta^T]^T$  is the pose state parametrized with Cartesian position  $\mathbf{r} = [x, y, z]$  and quaternion rotation  $\Theta = [q_w, q_x, q_y, q_z]$ ,  $P$  projects quaternion velocities to angular velocities such that  $\boldsymbol{\omega} = P\dot{\Theta}$ ,  $D_{\text{lin}}$  and  $D_{\text{rot}}$  are linear and angular damping coefficients, respectively. Furthermore,  $\mathbf{f}$  is the vector of nominal cable forces,  $\mathbf{w}$  is the external wrench including gravity,  $\mathbf{g}^C$  is the vector of Coriolis force terms and  $A^T$  is the structure matrix (Verhoeven 2004) given by

$$A^T = \begin{bmatrix} \mathbf{u}_1, & \dots & \mathbf{u}_m \\ (Rb_1) \times \mathbf{u}_1, & \dots & (Rb_m) \times \mathbf{u}_m \end{bmatrix}. \quad (4)$$

## 4 Emergency Stop Behavior and Model Validation

To assess the dynamics of cable robots during emergency stops and to verify validity of the simulation model composed of Eqs. (2) and (3), experiments reflecting an abrupt stop of the platform were conducted. Due to necessity of abiding by safety regulations, an insight into the system had to be acquired before commissioning the actual installation. These experimental tests were conducted on a cable robot with similar proportions yet fully restrained i.e., cables are guided up- and downwards from the platform. In comparison to the EXPO cable robots, the experimental setup has a platform weight of 45 kg and is fitted with ultra-high-molecular-weight polyethylene fibers by Dyneema ( $\phi 6$  mm). Further the input/output behavior of commanded cable length to cable force is referred to for analysis which is carried out

using the System Identification Toolbox<sup>1</sup> of MATLAB.<sup>1</sup> Simulation data is acquired at 1 ms whereas experimental data is acquired at 10 ms. The frequency response of time-domain data is then estimated using the *spa* algorithm by aforementioned toolbox.

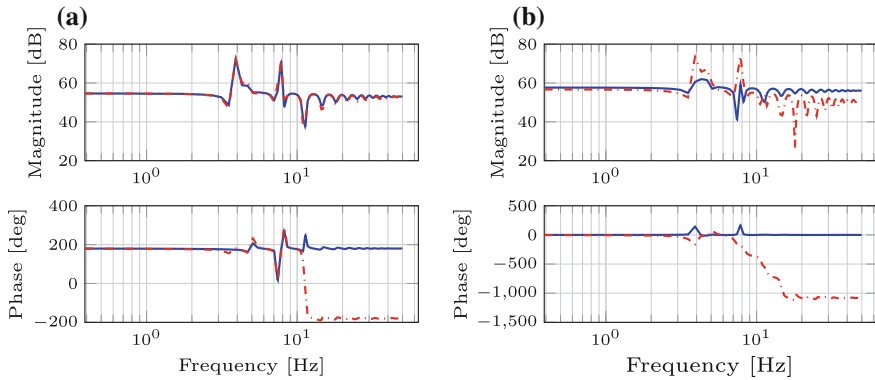


**Fig. 4** Exemplary magnitude and phase of simulative  $\text{—}$  and experimental  $\text{- - -}$  transfer function for cables 4 (a) and 8 (b)

Shown in Fig. 4 are the estimated transfer functions for simulation and experiment. It can be seen that simulation results are largely coherent with data acquired through experiments both in magnitude and phase for cable 2 shown in Fig. 4a. This holds true for cables 1–4 for excitation frequencies smaller than approximately 33 Hz. For cables 5 to 8 on the other hand, transfer functions match well for frequencies below 7 Hz, however, higher excitation frequencies lead to phase changes in the experimental data of more than 1000° which the simulative data does not reflect. This effect can be reduced to the cable robot configuration in use: Data was acquired on a fully restrained cable robot similar to the one shown in Fig. 1 with an additional payload of 40 kg. With such a high payload, the upper four cables are more tensed than usual and the lower four cables begin to slack changing the configuration from a fully restrained cable robot to a suspended one.<sup>2</sup> Slack cables act as low pass filter to any changes of their commanded length due to negligible tension. Furthermore, for cable 4, at a frequency of about  $f_{\text{crit}} \approx 66.5 \text{ rad/s} \approx 10 \text{ Hz}$ , the experimental data shows a phase shift of +360°. This phase shift also occurs for two of the lower four cables, cable 5 and 8 with a value of  $-1440^\circ$  and  $-1080^\circ$ , respectively (cable 8 is shown in Fig. 4b). Simulation data does not show this change in phase amongst any of the cables which leads to the assumption that there must be further, not yet considered effects in the cable, especially when it comes to slack cables being tensed again due to the motion of the mobile platform (in this case cables 5 through 8). On the

<sup>1</sup>System Identification Toolbox™ and MATLAB® are trademarks or registered trademarks of The MathWorks, Inc.®.

<sup>2</sup>Note: force control or payload compensation were not available in the actual installation.



one hand, this behavior also may be induced by transversal vibrations of the cable or by higher-order non-linear effects e.g., creep, fatigue, or the guiding over pulleys. Furthermore, the cable parameters are all assumed the same for all cables which is very unlikely to be applicable to real world scenarios. Material inconsistencies due to process tolerances during production of the cables leads to different cable characteristics thus to result variance amongst all cables which is already apparent when looking at the measured cable forces.

## 5 Conclusions

In this paper, the behavior of a cable robot undergoing an emergency stop was studied for a given cable robot configuration. With a simplified force transmission behavior of the cables represented by a spring-damper element, the frequency response can be approximated well over a good range of important frequencies. However, there are limitations of the model and discrepancies to the actual experimental data, especially for cables where the winch is located below the platform i.e., cables that are routed downwards from the platform. It can still be said that the model derived in this work is suitable for analyzing cable robots not only with regards to their designated task, but also with regard to their dynamics especially retardation dynamics.

**Acknowledgments** The University of Stuttgart as well as the Ministerium für Wissenschaft, Forschung und Kunst Baden-Württemberg (Ministry of Science, Research and Art Baden-Württemberg) supported the research for this project financially. These contributions are highly appreciated. We also want to thank Milla & Partner for their invitation to be part of the EXPO team. Especially, we want to acknowledge the many discussions with Ingo Kaske and Ulrich Kunkel which made the show in the German Pavilion technically possible.

## References

- Bruckmann, T., Mikelsons, L., Brandt, T., Hiller, M., & Schramm, D. (2008). Wire robots Part I: kinematics, analysis & design. In J.-H. Ryu (Ed.), *Parallel Manipulators*. New Developments: I-Tech Education and Publishing.
- Bruckmann, T., Lalo, W., Sturm, C., Schramm, D. & Hiller, M. (2013). Design and realization of a high rack storage and retrieval machine based on wire robot technology.
- Cone, L. (1985). Skycam, an aerial robotic camera system. *Byte Magazine*, 10, 122–132.
- Dagalakis, N. (1989). *Robot crane technology: Final report* (Vol. 1267). NIST technical note National Institute of Standards and Technology, Gaithersburg, CO: U.S. Dept. of Commerce.
- Gouttefarde, M., Nguyen, D. Q., & Baradat, C. (2014). Kinetostatic analysis of cable-driven parallel robots with consideration of sagging and pulleys. In J. Lenarčič & O. Khatib (Eds.), *Advances in Robot Kinematics* (pp. 213–221). Cham: Springer International Publishing.
- Kozak, K., Zhou, Q., & Jinsong, W. (2004) Static analysis of cable-driven manipulators with non-negligible cable mass. In *2004 IEEE Conference on Robotics, Automation and Mechatronics* (Vol. 2, pp. 886–891).

- Merlet, J.-P. (2015). The kinematics of cable-driven parallel robots with sagging cables: Preliminary results. In *2015 IEEE International Conference on Robotics and Automation (ICRA)*.
- Perreault, S., & Gosselin, C. (2008). Cable-driven parallel mechanisms: application to a locomotion interface. *Journal of Mechanical Design*, *130*(10), 102301.
- Pott, A., Mütterich, H., Kraus, W., Schmidt, V., Miermeister, P., & Verl, A. (2013). IPAnema: A family of cable-driven parallel robots for industrial applications. In T. Bruckmann & A. Pott (Eds.), *Cable-Driven Parallel Robots, Mechanisms and Machine Science* (Vol. 12, pp. 119–134). Berlin: Springer.
- Tempel, P., Miermeister, P., & Pott, A. (2015a). Kinematics and dynamics modeling for real-time simulation of the cable-driven parallel robot IPAnema 3. *Proceedings of the 14th IFToMM World Congress* (14th–2, pp. 117–123).
- Tempel, P., Schnelle, F., Pott, A. & Eberhard, P. (2015b). Design and programming for cable-driven parallel robots in the german pavilion at the EXPO 2015. *Machines*, *3*(3), 223–241. ISSN: 2075-1702.
- Verhoeven, R. (2004). *Analysis of the Workspace of Tendon-based Stewart Platforms*. Ph.D. thesis, Universität Duisburg-Essen, Duisburg-Essen. <http://purl.oclc.org/NET/duett-09112004-165148>.
- Zintz, K. (2015). Forschungsroboter mit Jahrmarktpotenzial. <http://j.mp/cdpr-4-human>.

# Automatic Robot Taping: Strategy and Enhancement

Qilong Yuan, Teguh Santoso Lembono and I-Ming Chen

**Abstract** Taping, covering the surfaces of objects with masking tapes, is a common process before conducting surface treatments like plasma spraying and painting. Manual taping is tedious and takes a lot of effort of the workers. The taping process is a special process which requires correct tape orientation and proper allocation of the masking tape for the coverage. We have introduced an automatic robot taping system consisting of a robot manipulator, a rotating platform, a 3D scanner and a specially designed novel taping end-effectors. With proper taping path planning methods, the taping of cylindrical and freeform surfaces have been achieved. With improvements on new sets of taping tools and path planning method, taping of general surfaces can be conducted using such system in future. This paper talks about the overall system design and discusses on the improvements needed to make the system available for parts with more general geometries. With further improvements, such taping solution with the taping tool and the taping methodology can be combined as a very useful and practical taping package to replace the work of human in such tedious and time consuming works.

**Keywords** Robot taping · Taping tool · Robot manipulation · Motion planning

---

Q. Yuan (✉) · T.S. Lembono · I.-M. Chen  
School of Mechanical and Aerospace Engineering, Nanyang Technological University,  
Singapore, Singapore  
e-mail: yu0017ng@e.ntu.edu.sg

T.S. Lembono  
e-mail: TLembono@ntu.edu.sg

I.-M. Chen  
e-mail: MIChen@ntu.edu.sg

# 1 Introduction

Taping, covering the surface of an object using masking tapes is a very important process for many industrial applications such as mechanical part repairing, surface protection and crack repairing. This taping process depends on manual workers to spend hours of work to finish for a single piece of repairing part.

Robot manipulations with 3D scanning models have been investigated in surface treatment applications like spray painting (Chen et al. 2002, 2008; Chen and Zhao 2013; Hegels et al. 2015) and laser coating removal (Baker et al. 2014). *These applications are scenarios that does not have contact requirement and there is no restriction other than the surface geometry* (Baker et al. 2014; Hegels et al. 2015). *Different from other Robot manipulations, taping request the special orientation of the masking tape so that it is not winkle and going towards the correct direction. Meanwhile, the pressing force is required to properly attach the masking tape to the correct location, as illustrated in Fig. 1. This brings difficulty to the taping process.* Taping regular shapes (tubes, bars, etc.) can be easily done through using some standard taping machines (Hottendorf 1972; Horiguchi et al. 1992). However, when the geometry of the taping part become complex, the taping problem becomes non-trivial. As a result, such taping works are mainly done manually by skilled workers.

In manual taping, the worker holds the roll of tape on one hand, and uses his fingers to attach the tape onto the surfaces, which is indeed a skillful work. To automate the taping process using robotic system, the following problems need to be solved: (1). To get the 3D model of the object. (2). To generate the taping path based on some planning strategy according to the parts' geometry. (3). Having a Proper taping end-effector. (4). Having a robot platform for the execution of the taping.

Previous works (Lembono et al. 2015; Yuan et al. 2015) have been done to tape regular shapes. This paper discusses on the current automatic taping system and its further improvements plans.

**Fig. 1** Manual Taping



## 2 Taping Path Planning Strategy

While the skilled workers do the manual taping, they firstly plan the strategy to use for certain geometry. This includes firstly the way to segment the surfaces of the part, and secondly the way to tape each segment—taping vertically, horizontally, or wrapping around). Also, the *width of the tape* also needs to be chosen for proper taping.

The taping strategy is largely dependent on the surface size and the curvature. For example, how to tape a spherical surface (with  $r$  being the radius) choosing a suitable tape with  $w_t$  being the tape width? To ensure that the tape is suitable for the surface, if the surfaces area is big, we firstly needs to segment entire surface into surface segments for taping.

The minimal curvature radius value on the surface  $r_m$  is required to be at least  $5w_t$  because if the radius is too small, the tape is not suitable for taping. The tape width also cannot be too small. Thus we apply the following constraints to choose the width of the tape.

$$20w_t > r_m > 5w_t \quad (1)$$

In general, the separation of the surface is a very challenging job that needs problem understanding. For example, how to tape a spherical surface? After problem understanding, we evenly divided the sphere surface into six square-like pieces as shown in Fig. 2.

The segmentation of the parts is a complex work that needs human understanding. The good thing is that, for the same model of parts, the surface separation strategy is the same. Therefore, it is reasonable to just create a database for the surface separation methods of all models based on human experience at the beginning, and use the strategies in database in path planning.

After the surface segmentation, the taping the entire part is divided into taping of multiple freeform surfaces.

Fig. 2 Surface Segmentation

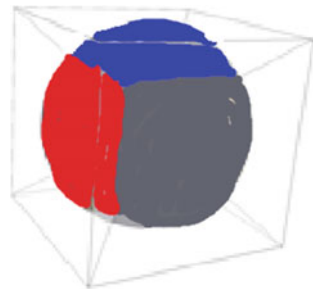
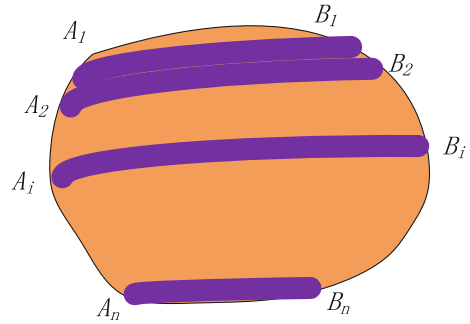


**Fig. 3** Area of interest for taping



## 2.1 Surface Area Taping Strategy

For a square-like shape, the general idea of the taping method is illustrated in Fig. 3.

Firstly, we can have a main taping direction based on the geometry of the area. The main direction is based on human input or database information. The group of point pairs,  $(A_i$  and  $B_i$  as shown in Fig. 3) are selected on the edges to make sure that surface curving with some preferable overlapping between adjacent tape segments.

After allocation of all the point pairs, each tape segment to cover the surface is actually a point to point taping across the surface. In this case, we need to figure out the following problems.

1. What orientation the tape should exactly start with in order to tape from a given point A to Point B on a square-like surface, with no or minimal wrinkle of the tape?
2. What is the taping path of the robot for the tape attachment?

The method is generally useful for planning with CAD models and point clouds. In this work, the 3D point cloud model is used. Therefore, the numerical calculations on quantities such as surface normal, projections etc. are needed, which is not detailed here.

## 2.2 Modeling of the Taping Process

As shown in Fig. 4, starting from point A, the mini tape element with very small length  $dl$  is attached on the surface. At a taping point  $p = (x, y, z)$ , the taping frame is defined follow the orientation of the mini taping element. The Z axis is defined by the surface normal at  $p$ . The Y axis is along the taping direction. The X axis is simple  $(Y \times Z)$ . The taping starting point  $p_i$  is the middle point of the starting edge of the mini tape element. The Z axis is defined to be along the normal vector direction,  $z_i = n_i$ . Then, the next taping point  $p_{i+1}$  is updated as follow:

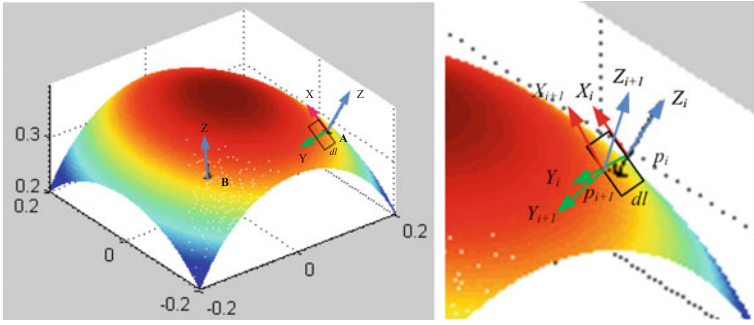


Fig. 4 3D surface model for taping

$$\hat{p}_{i+1} = p_i + y_i dl \tag{2}$$

Note that the taping point should lie on the surface. Therefore, a point  $\hat{p}_{i+1}$  is projected to the surface to get the next taping point  $p_{i+1}$ . Numerically, this is to search for the nearest point on the surface to be the next taping point.

In order to match the tape with the surface nicely, the tape elements need to be properly directed in order to satisfy the geometric constrain of the surface.

As shown in Fig. 5, while the tape attaches to the surface, it is understandable that the tape actually flip to the surface along a certain screw axis which depends on the surface geometry.

In the actual taping, as shown in Fig. 5, the small taping element flip to the surface along a line  $V_i$  is the intersection between the small taping element surface (flat)  $S_i$  and its next small taping element flat surface  $S_{i+1}$ . As a result, this twist axis  $V_i$  is perpendicular to both  $z_i$  and  $z_{i+1}$  (the surface normal of  $S_i$  and  $S_{i+1}$ ).

Therefore, we have,

$$V_i = \frac{z_i \times z_{i+1}}{|z_i \times z_{i+1}|} \tag{3}$$

The twist angle  $\varphi_i$  is,

Fig. 5 Flipping of the tape element while taping

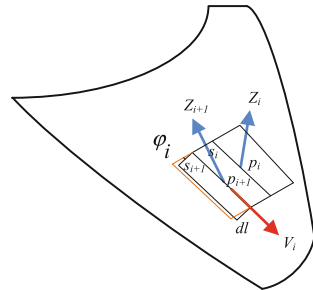
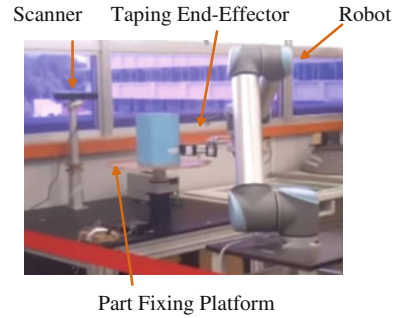


**Fig. 6** An automatic taping system



$$\varphi_i = a \cos(z_i \cdot z_{i+1}) \quad (4)$$

With such twist motion, it is understandable that the relationship between the orientation of the element frame of  $S_i$ ,  $R_i$ , and that of element frame of  $S_{i+1}$ , are connected by the twisting motion,  $R_{i+1} = e^{\varphi_i \hat{V}_i} R_i$ , where  $\hat{V}_i$  is the skew-symmetric matrix of vector  $V_i$ . Its corresponding rotation matrix is calculated by the  $SO(3)$  matrix  $e^{\varphi_i \hat{V}_i}$ , details can be found in (Murray et al. 1994; Yuan and Chen 2014).

Therefore the taping orientation will be  $y_{i+1} = e^{\varphi_i \hat{V}_i} y_i$ .

In this way, the taping process can be conducted following the geometry of the surface. Besides the surface following constraints while taping, it is important to figure out the initial taping orientation in order to correctly tape to the target point as expected.

In order to make sure that the tape correctly goes from starting point A to the target position B, the initial taping orientation needs to be determined. Numerical Method (Newton's Method) is used to search for the initial orientation.

With the taping locations, orientations, the surface normal and the posture of the part with respect to the robot, the robot end-effector pose can be determined (Fig. 6).

### 3 Automation of a Robot Taping System

The system includes a Kinect used as a 3D scanner, a taping robot with a taping end-effector. The part for taping is fixed on a rotation platform. A Central PC is used to synchronize the robot motion with the rotating platform.

The special design of the end-effector is required in order to meet the proper taping requirement. Meanwhile, the mechanism for cutting and holding the tape is also needed to accomplish the taping process.

The taping tool is used as the robot end-effector to handle the tapes and conduct the actual taping process. As shown in Fig. 7, the "tape holder" is used to handle



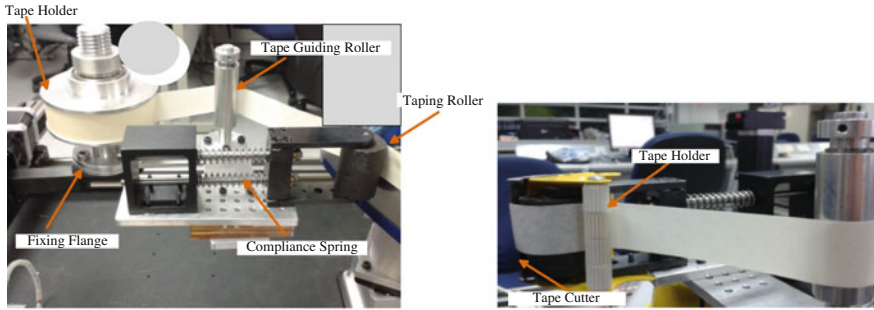


Fig. 7 Taping tool design

the masking tapes. The tape comes across the “tape guiding roller” so that it can be transmitted smoothly. The “tape roller” conducts the tape attachment task.

In addition, a “tape cutter” is needed to allow the separation of the tape segments. The requirements for this tape cutter are firstly to be able to cut the tape properly and secondly to maintain the tape in the location that is ready for the next taping step. As shown in Fig. 7, the tape cutter beside the taping roller is used for tape cutting. The taping holder is a thin roller that can have a line contact to stop the tape from going away from the tape roller.

#### 4 Execution of the Taping Process

Once the taping path planning is completed, the taping tool posture trajectories with respect to the part to be taped are known. In order to optimize the robot motion, the rotation platform rotates the parts while the robot conducts the taping. Therefore, the path of the robot end-effector is finalized according to the moving pattern of the rotation platform.

This module allows the robot system to execute the taping process based on the generated path. An example of taping a cylindrical surface is shown in Fig. 8a. Another example of taping freeform square-like surface is shown in Fig. 8b.

Because of modeling difficulties and the irregular shapes on the deformed surfaces, the taping testing is not completed while testing on a complex mechanical part Fig. 9. This will request us to update on the modeling accuracy and new taping head design to handle surface holes, damages, edges and corners etc.

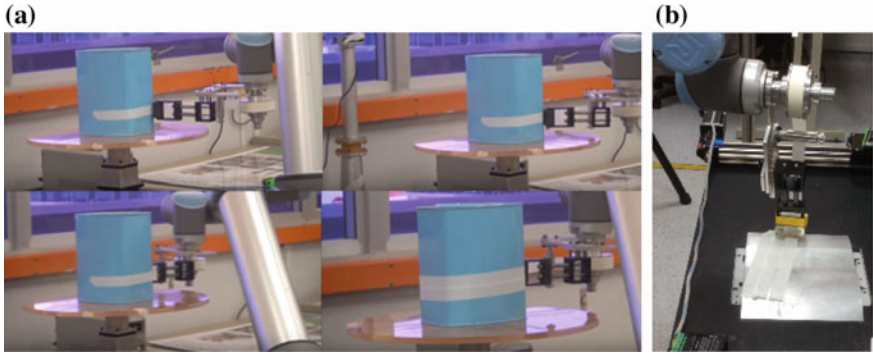


Fig. 8 Taping process of the automatic robot taping system

Fig. 9 Taping test on a complex irregular part



## 5 Conclusion and Discussion

This technical paper discloses the automatic robot taping system and corresponding methods for completing the robotic taping.

**Taping strategy:** A general computer algorithm to provide solutions on covering an arbitrary geometric part is not realistic since the planning strategy is based on problem understanding. For a specific application, the number of parts for taping is limited. Therefore, a more practical method is to apply human heuristic method to assist in building a taping strategy data. For each part, the experienced workers will advise on the key taping parameters—Area segmentation, taping direction, the type of tape, overlap of tape layers, initial points and tape cuttings etc. Such database can be applied on the path planning of a part after a part matching process.

**Accuracy:** Taping is a surface covering process where the surface covering method is the most critical. The accuracy is just moderate since the tasks can be completed within the tolerance of a few millimeters. However, to attach the tape on the surface, the taping tool needs to press the tape to the surface and apply some force for the attachment. This can be achieved based on compliant mechanisms on the end-effector. Precise force feedback can be helpful, but it also adds extra costs to the system.

**Taping speed:** In surface covering based on taping, the quality is priority instead of speed. Human taping is very slow, but human can handle very complex surface geometry with good quality (taping speed of human is normally several cm/s). For a robot the taping tools and the path need to be carefully considered in order to ensure good taping quality and a higher speed.

**Taping Tool and Sensors:** Currently, the taping tool is fine for taping of relatively large and flat area. For taping of different geometries such as corners or grooves, new taping head need to be designed. Meanwhile, it is expected to have distant sensors and force sensors added onto the system to provide distant and force feedback for better quality taping.

In very complex scenarios, a more suitable method is to let robot tape the major part, and let worker finish the minor but most challenging parts to ensure the efficiency.

**Acknowledgments** This work is supported in part by the Agency for Science, Technology and Research, Singapore, under SERC Grant 12251 00005.

## References

- Baker, C. L., Baker, C. R., Galati, D. G., Haines, J. C., Herman, H., Kelley, A. J., et al. (2014). A supervised autonomous robotic system for complex surface inspection and processing. Google Patents.
- Chen, H., Fuhlbrigge, T., & Li, X. (2008). Automated industrial robot path planning for spray painting process: a review. In *IEEE International Conference on Automation Science and Engineering, 2008. CASE 2008*. IEEE, 522–527.
- Chen, H., Sheng, W., Xi, N., Song, M., & Chen, Y. (2002). Automated robot trajectory planning for spray painting of free-form surfaces in automotive manufacturing. In *IEEE International Conference on Robotics and Automation, 2002. Proceedings. ICRA'02*. IEEE.
- Chen, W., and D. Zhao (2013). Path planning for spray painting robot of workpiece surfaces. *Mathematical Problems in Engineering* 2013.
- Hegels, D., Wiederkehr, T., & Müller, H. (2015). Simulation based iterative post-optimization of paths of robot guided thermal spraying. *Robotics and Computer-Integrated Manufacturing*, 35, 1–15.
- Horiguchi, N., Kaneko, Y., & Uda, S. (1992). Feeder of wrapping paper for coin wrapping machine, Google Patents.
- Hottendorf, W. J. (1972). Box Taping Machine, Google Patents.
- Lembono, T. S., Yuan, Q., Zou, Y., & Chen, I.-M. (2015). Automatic robot taping: System integration. In *IEEE International Conference on Advanced Intelligent Mechatronics (AIM), 2015*. IEEE.

- Murray, R., Li, Z., Sastry, S., & Sastry, S. (1994). *A mathematical introduction to robotic manipulation*. CRC.
- Yuan, Q., & Chen, I. (2014). Localization and velocity tracking of human via 3 IMU sensors. *Sensors and Actuators, A: Physical*, 212, 25–33.
- Yuan, Q., Lembono, T. S., Zou, Y., & Chen, I.-M. (2015). Automatic robot taping: auto-path planning and manipulation. In *2015 8th IEEE Conference on Robotics, Automation and Mechatronics (RAM)*. IEEE.